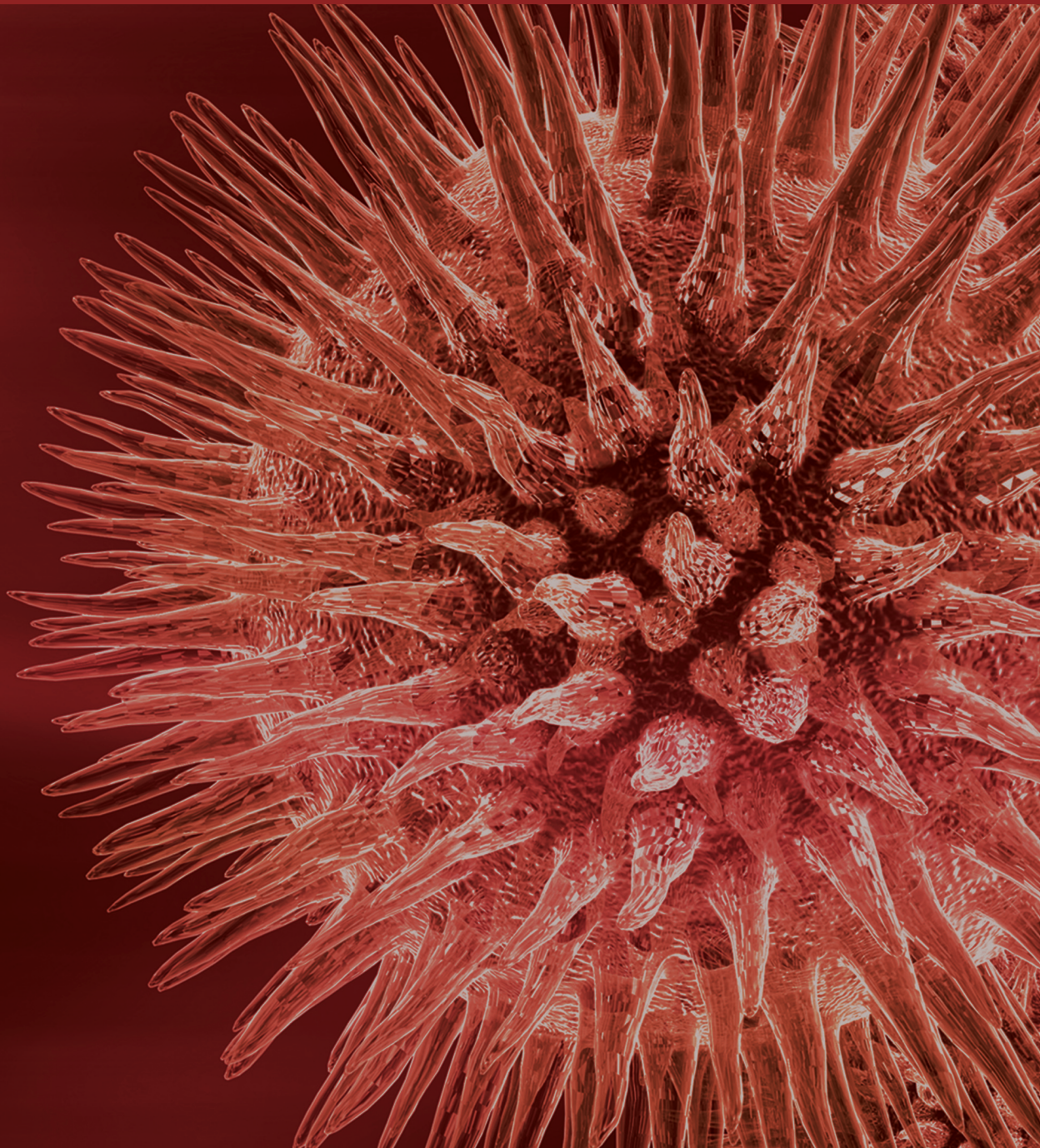


Journal of Biomedicine and Biotechnology

Advances in Muscle Physiology and Pathophysiology 2011

Guest Editors: Aikaterini Kontrogianni-Konstantopoulos, Guy Benian, and Henk Granzier





**Advances in Muscle Physiology and
Pathophysiology 2011**

Journal of Biomedicine and Biotechnology

**Advances in Muscle Physiology and
Pathophysiology 2011**

Guest Editors: Aikaterini Kontrogianni-Konstantopoulos,
Guy Benian, and Henk Granzier



Copyright © 2012 Hindawi Publishing Corporation. All rights reserved.

This is a special issue published in “Journal of Biomedicine and Biotechnology.” All articles are open access articles distributed under the Creative Commons Attribution License, which permits unrestricted use, distribution, and reproduction in any medium, provided the original work is properly cited.

Editorial Board

The editorial board of the journal is organized into sections that correspond to the subject areas covered by the journal.

Agricultural Biotechnology

Guihua H. Bai, USA	Hari B. Krishnan, USA	B. C. Saha, USA
Christopher P. Chanway, Canada	Carol A. Mallory-Smith, USA	Mariam B. Sticklen, USA
Ravindra N. Chibbar, Canada	Dennis P. Murr, Canada	Chiu-Chung Young, Taiwan
Ian Godwin, Australia	Rodomiro Ortiz, Sweden	

Animal Biotechnology

E. S. Chang, USA	Tosso Leeb, Switzerland	Lawrence B. Schook, USA
Bhanu P. Chowdhary, USA	James D. Murray, USA	Mari A. Smits, The Netherlands
Noelle E. Cockett, USA	Anita M. Oberbauer, USA	Leon Spicer, USA
Peter Dovc, Slovenia	Jorge A. Piedrahita, USA	J. Verstegen, USA
Scott C. Fahrenkrug, USA	Daniel Pomp, USA	Matthew B. Wheeler, USA
Dorian J. Garrick, USA	Kent M. Reed, USA	Kenneth L. White, USA
Thomas A. Hoagland, USA	Lawrence Reynolds, USA	

Biochemistry

Robert Blumenthal, USA	Paul W. Doetsch, USA	Wen-Hwa Lee, USA
David Ronald Brown, UK	Hicham Fenniri, Canada	Richard D. Ludescher, USA
Saulius Butenas, USA	Nick V. Grishin, USA	George Makhatadze, USA
Vittorio Calabrese, Italy	J. Guy Guillemette, Canada	Leonid Medved, USA
Miguel Castanho, Portugal	Paul W. Huber, USA	Susan A. Rotenberg, USA
Francis J. Castellino, USA	Chen-Hsiung Hung, Taiwan	Jason Shearer, USA
Roberta Chiaraluce, Italy	Michael Kalafatis, USA	Andrei Surguchov, USA
D. M. Clarke, Canada	B. E. Kemp, Australia	John B. Vincent, USA
Francesca Cutruzzolà, Italy	Phillip E. Klebba, USA	Y. George Zheng, USA

Bioinformatics

T. Akutsu, Japan	Stavros J. Hamodrakas, Greece	Florencio Pazos, Spain
Miguel A. Andrade, Germany	Paul Harrison, USA	Zhirong Sun, China
Mark Y. Borodovsky, USA	George Karypis, USA	Ying Xu, USA
Rita Casadio, Italy	Jack A. Leunissen, The Netherlands	Alexander Zelikovsky, USA
Artem Cherkasov, Canada	Guohui Lin, Canada	Albert Zomaya, Australia
David Corne, UK	Satoru Miyano, Japan	
Sorin Draghici, USA	Zoran Obradovic, USA	

Biophysics

Miguel Castanho, Portugal
P. Bryant Chase, USA
Kuo-Chen Chou, USA
Rizwan Khan, India

Ali A. Khraibi, Saudi Arabia
Rumiana Koynova, USA
Serdar Kuyucak, Australia
Jianjie Ma, USA

S. B. Petersen, Denmark
Peter Schuck, USA
Claudio M. Soares, Portugal

Cell Biology

Omar Benzakour, France
Sanford I. Bernstein, USA
Phillip I. Bird, Australia
Eric Bouhassira, USA
Mohamed Boutjdir, USA
Chung-Liang Chien, Taiwan
Richard Gomer, USA
Paul J. Higgins, USA
Pavel Hozak, Czech Republic

Xudong Huang, USA
Anton M. Jetten, USA
Seamus J. Martin, Ireland
Manuela Martins-Green, USA
Shoichiro Ono, USA
George Perry, USA
M. Piacentini, Italy
George E. Plopper, USA
Lawrence Rothblum, USA

Michael Sheetz, USA
James L. Sherley, USA
G. S. Stein, USA
Richard Tucker, USA
Thomas van Groen, USA
Andre Van Wijnen, USA
Steve Winder, UK
Chuan Yue Wu, USA
Bin-Xian Zhang, USA

Genetics

Adewale Adeyinka, USA
Claude Bagnis, France
J. Birchler, USA
Susan Blanton, USA
Barry J. Byrne, USA
R. Chakraborty, USA
Domenico Coviello, Italy
Sarah H. Elsea, USA
Celina Janion, Poland

J. Spencer Johnston, USA
M. Ilyas Kamboh, USA
Feige Kaplan, Canada
Manfred Kayser, The Netherlands
Brynn Levy, USA
Xiao Jiang Li, USA
Thomas Liehr, Germany
James M. Mason, USA
Mohammed Rachidi, France

Raj S. Ramesar, South Africa
Elliot D. Rosen, USA
Dharambir K. Sanghera, USA
Michael Schmid, Germany
Markus Schuelke, Germany
Wolfgang Arthur Schulz, Germany
Jorge Sequeiros, Portugal
Mouldy Sioud, Norway
Rongjia Zhou, China

Genomics

Vladimir Bajic, Saudi Arabia
Margit Burmeister, USA
Settara Chandrasekharappa, USA
Yataro Daigo, Japan
J. Spencer Johnston, USA

Vladimir Larionov, USA
Thomas Lufkin, Singapore
Joakim Lundeberg, Sweden
John L. McGregor, France
John V. Moran, USA

Yasushi Okazaki, Japan
Gopi K. Podila, USA
Momiao Xiong, USA

Immunology

Hassan Alizadeh, USA
Peter Bretscher, Canada
Robert E. Cone, USA
Terry L. Delovitch, Canada
Anthony L. DeVico, USA
Nick Di Girolamo, Australia
Don Mark Estes, USA
Soldano Ferrone, USA
Jeffrey A. Frelinger, USA
John Robert Gordon, Canada

James D. Gorham, USA
Silvia Gregori, Italy
Thomas Griffith, USA
Young S. Hahn, USA
Dorothy E. Lewis, USA
Bradley W. McIntyre, USA
R. Lee Mosley, USA
Marija Mostarica-Stojković, Serbia
Hans Konrad Muller, Australia
Ali Ouaiissi, France

Kanury V. S. Rao, India
Yair Reisner, Israel
Harry W. Schroeder, USA
Wilhelm Schwaeble, UK
Nilabh Shastri, USA
Yufang Shi, China
Piet Stinissen, Belgium
Hannes Stockinger, Austria
J. W. Tervaert, The Netherlands
Graham R. Wallace, UK

Microbial Biotechnology

Jozef Anné, Belgium
Yoav Bashan, Mexico
Marco Bazzicalupo, Italy
Nico Boon, Belgium

Luca Simone Cocolin, Italy
Peter Coloe, Australia
Daniele Daffonchio, Italy
Han de Winde, The Netherlands

Yanhe Ma, China
Bernd H. A. Rehm, New Zealand
Angela Sessitsch, Austria

Microbiology

D. Beighton, UK
Steven R. Blanke, USA
Stanley Brul, The Netherlands
Isaac K. O. Cann, USA
Stephen K. Farrand, USA
Alain Filloux, UK

Gad Frankel, UK
Roy Gross, Germany
Hans-Peter Klenk, Germany
Tanya Parish, UK
Gopi K. Podila, USA
Frederick D. Quinn, USA

Didier A. Raoult, France
Isabel Sá-Correia, Portugal
P. L. C. Small, USA
Michael Thomm, Germany
H. C. van der Mei, The Netherlands
Schwan William, USA

Molecular Biology

Rudi Beyaert, Belgium
Michael Bustin, USA
Douglas Cyr, USA
K. Iatrou, Greece
Lokesh Joshi, Ireland
David W. Litchfield, Canada

Wuyuan Lu, USA
Patrick Matthias, Switzerland
John L. McGregor, France
S. L. Mowbray, Sweden
Elena Orlova, UK
Yeon-Kyun Shin, USA

William S. Trimble, Canada
Lisa Wiesmuller, Germany
Masamitsu Yamaguchi, Japan

Oncology

Colin Cooper, UK
F. M. J. Debruyne, The Netherlands
Nathan Ames Ellis, USA
Dominic Fan, USA
Gary E. Gallick, USA
Daila S. Gridley, USA
Xin-yuan Guan, Hong Kong
Anne Hamburger, USA
Manoor Prakash Hande, Singapore
Beric Henderson, Australia

Steve B. Jiang, USA
Daehee Kang, Republic of Korea
Abdul R. Khokhar, USA
Rakesh Kumar, USA
Macus Tien Kuo, USA
Eric W. Lam, UK
Sue-Hwa Lin, USA
Kapil Mehta, USA
Orhan Nalcioğlu, USA
P. J. Oefner, Germany

Allal Ouhtit, Oman
Frank Pajonk, USA
Waldemar Priebe, USA
F. C. Schmitt, Portugal
Sonshin Takao, Japan
Ana Maria Tari, USA
Henk G. Van Der Poel, The Netherlands
Haodong Xu, USA
David J. Yang, USA

Pharmacology

Abdel A. Abdel-Rahman, USA
M. Badr, USA
Stelvio M. Bandiera, Canada
Ronald E. Baynes, USA
R. Keith Campbell, USA
Hak-Kim Chan, Australia
Michael D. Coleman, UK
J. Descotes, France

Dobromir Dobrev, Germany
Ayman El-Kadi, Canada
Jeffrey Hughes, USA
Kazim Husain, USA
Farhad Kamali, UK
Michael Kassiou, Australia
Joseph J. McArdle, USA
Mark J. McKeage, New Zealand

Daniel T. Monaghan, USA
T. Narahashi, USA
Kennerly S. Patrick, USA
Vickram Ramkumar, USA
Michael J. Spinella, USA
Quadiri Timour, France
Todd W. Vanderah, USA
Val J. Watts, USA

Plant Biotechnology

Prem L. Bhalla, Australia
J. R. Botella, Australia
Elvira Gonzalez De Mejia, USA
H. M. Häggman, Finland

Liwen Jiang, Hong Kong
Pulugurtha Bharadwaja Kirti, India
Yong Pyo Lim, Republic of Korea
Gopi K. Podila, USA

Ralf Reski, Germany
Sudhir Kumar Sopory, India

Toxicology

Michael Aschner, USA
Michael L. Cunningham, USA
Laurence D. Fechter, USA
Hartmut Jaeschke, USA

Youmin James Kang, USA
M. Firoze Khan, USA
Pascal Kintz, France
R. S. Tjeerdema, USA

Kenneth Turteltaub, USA
Brad Upham, USA

Virology

Nafees Ahmad, USA
Edouard Cantin, USA
Ellen Collisson, USA
Kevin M. Coombs, Canada
Norbert K. Herzog, USA
Tom Hobman, Canada
Shahid Jameel, India

Fred Kibenge, Canada
Fenyong Liu, USA
Éric Rassart, Canada
Gerald G. Schumann, Germany
Y.-C. Sung, Republic of Korea
Gregory Tannock, Australia

Ralf Wagner, Germany
Jianguo Wu, China
Decheng Yang, Canada
Jiing-Kuan Yee, USA
Xueping Zhou, China
Wen-Quan Zou, USA

Contents

Advances in Muscle Physiology and Pathophysiology 2011, Aikaterini Kontrogianni-Konstantopoulos, Guy Benian, and Henk Granzier
Volume 2012, Article ID 930836, 1 page

Distinct Effects of Contraction-Induced Injury *In Vivo* on Four Different Murine Models of Dysferlinopathy, Joseph A. Roche, Lisa W. Ru, and Robert J. Bloch
Volume 2012, Article ID 134031, 11 pages

Localization and Regulation of the N Terminal Splice Variant of PGC-1 α in Adult Skeletal Muscle Fibers, Tiansheng Shen, Yewei Liu, and Martin F. Schneider
Volume 2012, Article ID 989263, 8 pages

Force Characteristics of the Rat Sternomastoid Muscle Reinnervated with End-to-End Nerve Repair, Stanislaw Sobotka and Liancai Mu
Volume 2011, Article ID 173471, 9 pages

The Application of Three-Dimensional Collagen-Scaffolds Seeded with Myoblasts to Repair Skeletal Muscle Defects, Jianqun Ma, Kyle Holden, Jinhong Zhu, Haiying Pan, and Yong Li
Volume 2011, Article ID 812135, 9 pages

Localization of Magic-F1 Transgene, Involved in Muscular Hypertrophy, during Early Myogenesis, Flavio Ronzoni, Matilde Bongio, Silvio Conte, Luigi Vercesi, Marco Cassano, Carla Tribioli, Daniela Galli, Riccardo Bellazzi, Giovanni Magenes, Maria Gabriella Cusella De Angelis, and Maurilio Sampaolesi
Volume 2011, Article ID 492075, 9 pages

Facilitated Cross-Bridge Interactions with Thin Filaments by Familial Hypertrophic Cardiomyopathy Mutations in α -Tropomyosin, Fang Wang, Nicolas M. Brunet, Justin R. Grubich, Ewa A. Bienkiewicz, Thomas M. Asbury, Lisa A. Compton, Goran Mihajlović, Victor F. Miller, and P. Bryant Chase
Volume 2011, Article ID 435271, 12 pages

Electrophoretic Mobility of Cardiac Myosin Heavy Chain Isoforms Revisited: Application of MALDI TOF/TOF Analysis, Petra Arnostova, Petr L. Jedelsky, Tomáš Soukup, and Jitka Zurmanova
Volume 2011, Article ID 634253, 9 pages

Phasic and Tonic Smooth Muscle Function of the Partially Obstructed Guinea Pig Intestine, Jingbo Zhao, Donghua Liao, Jian Yang, and Hans Gregersen
Volume 2011, Article ID 489720, 9 pages

Distribution of Myosin Attachment Times Predicted from Viscoelastic Mechanics of Striated Muscle, Bradley M. Palmer, Yuan Wang, and Mark S. Miller
Volume 2011, Article ID 592343, 16 pages

Muscle Plasticity and β_2 -Adrenergic Receptors: Adaptive Responses of β_2 -Adrenergic Receptor Expression to Muscle Hypertrophy and Atrophy, Shogo Sato, Ken Shirato, Kaoru Tachiyashiki, and Kazuhiko Imaizumi
Volume 2011, Article ID 729598, 10 page

Titin-Actin Interaction: PEVK-Actin-Based Viscosity in a Large Animal, Charles S. Chung, Julius Bogomolovas, Alexander Gasch, Carlos G. Hidalgo, Siegfried Labeit, and Henk L. Granzier
Volume 2011, Article ID 310791, 8 pages

The IQ Motif is Crucial for Ca_v1.1 Function, Katarina Stroffekova
Volume 2011, Article ID 504649, 9 pages

Exact and Approximate Stochastic Simulation of Intracellular Calcium Dynamics, Nicolas Wieder, Rainer H. A. Fink, and Frederic von Wegner
Volume 2011, Article ID 572492, 5 pages

Thin Filament-Reconstituted Skinned Muscle Fibers for the Study of Muscle Physiology, Sayaka Higuchi, Yoshikazu Tsukasaki, Norio Fukuda, Satoshi Kurihara, and Hideaki Fujita
Volume 2011, Article ID 486021, 7 pages

Creep Behavior of Passive Bovine Extraocular Muscle, Lawrence Yoo, Hansang Kim, Andrew Shin, Vijay Gupta, and Joseph L. Demer
Volume 2011, Article ID 526705, 6 pages

Contractile Strength during Variable Heart Duration Is Species and Preload Dependent, Carlos A. A. Torres and Paul M. L. Janssen
Volume 2011, Article ID 294204, 6 pages

The Sarcomeric Z-Disc and Z-Discopathies, Ralph Knöll, Byambajav Buyandelger, and Max Lab
Volume 2011, Article ID 569628, 12 pages

Tropomodulin Capping of Actin Filaments in Striated Muscle Development and Physiology, David S. Gokhin and Velia M. Fowler
Volume 2011, Article ID 103069, 16 pages

The Evolution of the Mitochondria-to-Calcium Release Units Relationship in Vertebrate Skeletal Muscles, Clara Franzini-Armstrong and Simona Boncompagni
Volume 2011, Article ID 830573, 9 pages

Both Basic and Acidic Amino Acid Residues of IpTx_α Are Involved in Triggering Substate of RyR1, In Ra Seo, Dae Eun Kang, Dong Woo Song, and Do Han Kim
Volume 2011, Article ID 386384, 10 pages

The Recent Understanding of the Neurotrophin's Role in Skeletal Muscle Adaptation, Kunihiro Sakuma and Akihiko Yamaguchi
Volume 2011, Article ID 201696, 12 pages

Editorial

Advances in Muscle Physiology and Pathophysiology 2011

Aikaterini Kontrogianni-Konstantopoulos,¹ Guy Benian,² and Henk Granzier³

¹ Department of Biochemistry and Molecular Biology, University of Maryland, School of Medicine, Baltimore, MD 21201, USA

² Departments of Pathology and Cell Biology, Emory University, Atlanta, GA 30322, USA

³ Departments of Physiology and Molecular and Cellular Biology, The University of Arizona, Tucson, AZ 85721, USA

Correspondence should be addressed to Aikaterini Kontrogianni-Konstantopoulos, akons001@umaryland.edu

Received 18 December 2011; Accepted 18 December 2011

Copyright © 2012 Aikaterini Kontrogianni-Konstantopoulos et al. This is an open access article distributed under the Creative Commons Attribution License, which permits unrestricted use, distribution, and reproduction in any medium, provided the original work is properly cited.

The ordered assembly and synchronous contraction of striated muscle cells are highly complex processes that depend on the precise spatiotemporal formation of the sarcomeric and extrasarcomeric cytoskeleton alongside with specialized internal membranes that coordinately regulate Ca^{2+} cycling. The establishment of flexible molecular anchors that withstand stretch, between the contractile cytoskeleton and internal membranes, the superficial cytoskeleton and the sarcolemma, as well as the sarcolemma and the extracellular matrix, allows muscle cells to maintain their structural integrity and contractile activity. Recent advances using state-of-the-art, multidisciplinary, and integrated approaches have yielded a wealth of new information regarding these processes and have highlighted the next challenges for muscle physiologists, biochemists, and biophysicists.

In the second volume of our *Advances in Muscle Physiology and Pathophysiology* special emphasis issue, we continued to solicit original and review articles from leading and emerging scientists who study muscle structure and function and with diverse expertise and interests. A wide array of topics is covered, including, but not limited to, thin and thick filament assembly, regulation of cross-bridges formation, force generation, stress and stretch sensors, and Ca^{2+} dynamics as well as injury and disease models.

As the Editors of this special issue, we are grateful to all the authors who provided either original articles or comprehensive reviews of previous and current literature, making the second volume of this special issue attractive and interesting to a diverse audience of muscle researchers. Similar to our first volume, our aspiration was to include various aspects of muscle physiology and pathophysiology at the molecular, cellular, organ, and organismal levels. We

are pleased to see the outcome of our call in the form of this second, special emphasis volume, and as before we expect that it will provide a wealth of information that will further inspire outstanding muscle research.

Aikaterini Kontrogianni-Konstantopoulos
Guy Benian
Henk Granzier

Research Article

Distinct Effects of Contraction-Induced Injury *In Vivo* on Four Different Murine Models of Dysferlinopathy

Joseph A. Roche, Lisa W. Ru, and Robert J. Bloch

Department of Physiology, University of Maryland School of Medicine, 655 W. Baltimore Street, Baltimore, MD 21201, USA

Correspondence should be addressed to Robert J. Bloch, rbloch@umaryland.edu

Received 27 June 2011; Accepted 27 September 2011

Academic Editor: Aikaterini Kontrogianni-Konstantopoulos

Copyright © 2012 Joseph A. Roche et al. This is an open access article distributed under the Creative Commons Attribution License, which permits unrestricted use, distribution, and reproduction in any medium, provided the original work is properly cited.

Mutations in the *DYSF* gene, encoding dysferlin, cause muscular dystrophies in man. We compared 4 dysferlinopathic mouse strains: SJL/J and B10.SJL-*Dysf*^{flm}/AwaJ (B10.SJL), and A/J and B6.A-*Dysf*^{prmd}/GeneJ (B6.A/J). The former but not the latter two are overtly myopathic and weaker at 3 months of age. Following repetitive large-strain injury (LSI) caused by lengthening contractions, all except B6.A/J showed ~40% loss in contractile torque. Three days later, torque in SJL/J, B10.SJL and controls, but not A/J, recovered nearly completely. B6.A/J showed ~30% torque loss post-LSI and more variable recovery. Pre-injury, all dysferlinopathic strains had more centrally nucleated fibers (CNFs) and all but A/J showed more inflammation than controls. At D3, all dysferlinopathic strains showed increased necrosis and inflammation, but not more CNFs; controls were unchanged. Dystrophin-null *DMD*^{mdx} mice showed more necrosis and inflammation than all dysferlin-nulls. Torque loss and inflammation on D3 across all strains were linearly related to necrosis. Our results suggest that (1) dysferlin is not required for functional recovery 3 days after LSI; (2) B6.A/J mice recover from LSI erratically; (3) SJL/J and B10.SJL muscles recover rapidly, perhaps due to ongoing myopathy; (4) although they recover function to different levels, all 4 dysferlinopathic strains show increased inflammation and necrosis 3 days after LSI.

1. Introduction

The *DYSF* gene encodes dysferlin, a tail-anchored integral membrane protein of 230 kDa that is thought to mediate membrane stability or fusion through the action of calcium-binding C2 domains in its large cytoplasmic region [1–3]. Mutations in dysferlin have been linked to several muscular dystrophies in man, including limb girdle muscular dystrophy type 2B (LGMD2B) and Miyoshi myopathy (MM) [4, 5]. There are currently no treatments for these diseases, but several therapeutic approaches have been tested *in vitro* and in mice, including gene therapeutic studies. The success of these experiments and their ultimate translation to the clinic will rely on the availability of murine models of the human dysferlinopathies. Several such models exist, including two that, like the human dystrophies, arose spontaneously and two that were generated by targeted gene ablation [6, 7]. Although some of the properties of these strains of dysferlinopathic mice have been described, very few of their

characteristics have been directly compared to determine which, if any, most closely reproduce the characteristics of LGMD2B/MM. Here, we report the results of comparative studies on the two spontaneously occurring murine dysferlin mutants, SJL/J and A/J, and of the two strains derived from these mutants by breeding them into C57Bl mice, B10.SJL-*Dysf*^{flm}/AwaJ and B6.A-*Dysf*^{prmd}/GeneJ (referred to in this paper as B10.SJL and B6.A/J, resp.).

SJL/J mice show spontaneous myopathy [7–9], due to a mutation in the *Dysf* gene that results in the deletion of an exon encoding 57 amino acids in one of dysferlin's C2 domains [10, 11]. This mutation leads to a ~6-fold or greater reduction in dysferlin levels in SJL/J muscle [7, 12] and is associated with the development of fiber necrosis, central nucleation, inflammation, elevation of serum creatine kinase, and, in some muscles, fatty infiltration [13]. Some phenotypic changes occur in mice as early as 3 weeks of age and additional changes, including increases in centrally nucleated fibers (CNFs), are evident in 2-month-old mice

[9, 10, 12, 13]. The myopathy becomes more prominent with age, with a measurable loss of strength at 6 months of age and even greater compromise of histopathology and function in older animals [9, 13]. However, when compared to control strains, SJL/J mice also show behavioral differences, a high incidence of reticulum cell sarcomas [14], elevated levels of circulating T cells, and greater susceptibility to autoimmune diseases (<http://jaxmice.jax.org/strain/000686.html>). These traits are probably not linked to its dystrophic phenotype, which has been bred into the C57Bl/10J background [10, 12]. Extensive comparisons of SJL/J mice with their B10.SJL counterparts have not been reported, but preliminary studies of the time course of development of overt myopathy and the nature of the myopathy in these strains seem similar [9, 12]. They also share the property that proximal muscles, such as the quadriceps femoris, are more severely affected than distal muscles, such as the gastrocnemius and tibialis anterior [9, 12].

A/J, the other spontaneous dysferlinopathic mouse, has an ETn retrotransposon insertion in intron 4 of the murine *Dysf* gene that leads to the complete absence of dysferlin as assayed by immunoblots [7]. Paradoxically, the A/J mouse shows a milder phenotype at young ages and only becomes overtly myopathic at ages approaching 1 yr [7]. Nevertheless, serum creatine kinase is as elevated in 1-month-old A/J mice as it is in SJL/J mice [7]. As also seen in SJL/J and B10.SJL mice (see above), the effect of the A/J mutation is more pronounced in proximal than in distal muscles [7]. Ultrastructural images of A/J muscle, like those of SJL/J and dysferlin-null mice and human dysferlinopathies [6, 7, 15], show lesions in the sarcolemma and the accumulation of membrane-bound vesicles nearby as well as changes in the basal lamina [7]. Comparisons of A/J mice with mice carrying the same retrotransposon element in the C57Bl/6J background, B6.A/J, suggest that the hindlimb muscles of the latter develop myopathy more rapidly than A/J mice [16–18]. A/J mice carry a number of other mutations, however, that lead to hearing loss, a high incidence of lung carcinomas, lack of complement 5, and resistance to diabetes (<http://jaxmice.jax.org/strain/000646.html>). They also show much lower levels of spontaneous motor activity than many other strains of mice. These characteristics, or others, may modulate the extent and development of dysferlinopathy in A/J mice.

Our earlier studies, which focused on the A/J strain, showed that eccentric injuries caused by repetitive large-strain lengthening contractions had distinct effects on the ankle dorsiflexor muscles of A/J mice, compared to several control strains. In particular, both the A/J and control mice were equally susceptible to the large-strain injury, losing 40–50% of the contractile torque of their ankle dorsiflexors. Immediately after injury and for several days thereafter, the myofibers of A/J mice retained 10 kDa fluorescein-dextran, to the same extent as controls, suggesting that they had resealed their injured sarcolemmal membranes as well as controls. We interpreted these results to mean that, contrary to the conclusions reached by earlier studies performed on isolated myofibers *in vitro* [6], dysferlin is not needed for repairing sarcolemma damaged by a physiological injury *in vivo*. Differences between controls and A/J appeared

subsequent to injury, however, as controls recovered within 3 days of the injury, with little necrosis or inflammation and without requiring myogenesis, whereas the A/J mice required several weeks to recover, due to extensive fiber loss following necrosis and massive inflammation and subsequent regeneration via myogenesis.

Here we compare the responses of the four strains of mice, A/J, B6.A/J, SJL/J, and B10.SJL, to injury caused by large-strain lengthening contractions. In particular, we compare their baseline torque generated by the ankle dorsiflexor group, the susceptibility to injury of this muscle group to repetitive large-strain lengthening contractions, the recovery of torque 3 days after injury, and the histological status of the muscles before and after injury, including assessments of central nucleation, necrosis and inflammation. Our results suggest that the B6.A/J, SJL/J, and B10.SJL all recover from the injury within 3 days following injury, whereas A/J do not. Nevertheless, the response of the B6.A/J is distinct from that of SJL/J and B10.SJL. We also compare our findings on dysferlinopathic mice with dystrophin-deficient C57Bl/10ScSn-Dmd^{mdx}/J mice (DMD^{mdx}). We conclude that the dysferlinopathic strains of mice examined in this study are useful for studying different stages in the development of dysferlinopathy and the altered response to contraction-induced injury in the absence of dysferlin.

2. Materials and Methods

We studied baseline contractile torque, change in torque following large-strain lengthening contractions, and histological changes 3 days after injury in 4 different murine models of dysferlin deficiency and compared them to their respective control strains and a murine model of dystrophin deficiency.

All mice used in this study were obtained either directly from the Jackson Laboratory (Bar Harbor, ME) or were obtained from our animal colonies set up from breeding pairs initially obtained from the Jackson Laboratory (see Table 1). Mice used for this study were males between 12–16 wks of age. All experimental protocols involving animals were approved by the Institutional Animal Care and Use Committee of the University of Maryland School of Medicine, Baltimore.

2.1. Torque Measurement and Large-Strain Injury (LSI). Measurements of contractile torque and large-strain injury were performed *in vivo* as described [17–20] with the Small-animal Unit for Muscle Injury, Muscle Testing and Muscle Training (SUMITT, patent pending). Briefly, an anesthetized animal was placed on its back with its foot strapped onto a footplate in series with a torque transducer. The tibia was stabilized with a pin. The dorsiflexor muscles were stimulated via the peroneal nerve with a bipolar transcutaneous electrode. Twitches elicited by single 0.1 ms pulses were used to optimize electrode placement, current amplitude, and the optimal tibiotarsal angle for the dorsiflexors (typically 110° of plantarflexion). Post-LSI torque was measured at the same preinjury testing angle. In this study we did not test if LSI alters the torque-angle relationship of the dorsiflexors although our unpublished data suggest no change in

TABLE 1: Mouse strains. Mouse strains used in the study and number of animals studied per strain.

Strain	Source	JAX mice database stock #	DYSF mutation	N
A/WySnJ	School of Medicine University of Maryland. Breeding pairs from The Jackson Laboratory	000647	N/A. Control strain for A/J mice	8
A/J	School of Medicine University of Maryland. Breeding pairs from The Jackson Laboratory	000646	A retrotransposon insertion within intron 4, causing aberrant splicing of the gene	8
C57Bl/6J	The Jackson Laboratory	000664	N/A. Background strain for B6.A/J	8
B6.A/J	School of Medicine University of Maryland. Breeding pairs from The Jackson Laboratory	012767 B6.A-Dysf ^{prmd} /GeneJ	Progressive muscular dystrophy (prmd) allele from A/J introgressed into the C57BL/6J genetic background	8
SWR/J	The Jackson Laboratory	000689	N/A. Control strain for SJL/J mice	8
SJL/J	The Jackson Laboratory	000686	171 bp in-frame deletion in the encoded mRNA is predicted to remove 57 amino acids from dysferlin	8
C57BL/10J	The Jackson Laboratory	000665	Background strain for B10.SJL	8
B10.SJL	School of Medicine University of Maryland. Breeding pairs from The Jackson Laboratory, and Dr. A. J. Wagers, Harvard University, Cambridge, MA.	011128 B10.SJL-Dysf ^{im} /AwaJ	DYSF mutation (inflammatory myopathy, im) in the SJL strain introgressed into the C57BL/10ScSnHim strain and subsequently bred to C57BL/10J	8
DMD ^{mdx}	School of Medicine University of Maryland. Breeding pairs from The Jackson Laboratory	001801 C57BL/10ScSn-Dmd ^{mdx} /J	N/A. Dystrophin-deficient mice. C-to-T transition at position 3185, resulting in a termination codon in place of a glutamine codon	8

A/WySnJ and A/J after LSI. Increasing frequencies of pulses within a 300 ms pulse train were used to determine optimal tetanic frequency, which was 80 or 90 Hz for all control strains and A/J and 100–125 Hz for all other strains. After optimal baseline torque (maximal twitch and tetany) was recorded, 20 lengthening contractions were induced in the dorsiflexors by moving the foot into plantarflexion from 90–180° (starting with foot orthogonal to tibia) at 1200°/s, while the dorsiflexors were tetanically stimulated. While the 180° of plantarflexion is unlikely to occur in mice during normal motor activity, our injury model is physiological as it does not exceed the maximal range of plantarflexion of the ankle-foot complex recorded through gentle passive movement. A rest period of 1 min was allowed between successive lengthening contractions. Torques after LSI were recorded 4 min after the last lengthening contraction. Contractile data in Figures 1 and 2 are from 6 animals that were studied longitudinally on the day of injury (D0) and 3 days later (D3). We performed a terminal study on two animals of each strain at D0 to analyze histological changes immediately following injury (middle panels in Figure 3; contractile data from these animals are not shown).

2.2. Histological Studies. Histological studies were performed on the *Tibialis anterior* (TA) muscle, as it accounts for nearly

90% of the force produced by the dorsiflexors in mice [21]. Control and injured muscles were harvested from 2 animals per strain ~10 min after injury on D0 and from 6 animals per strain at D3 for histological studies. Collection of unfixed tissue, hematoxylin and eosin (H & E) staining, and labeling of macrophages with rat anti-mouse antibodies to CD68, which labels all murine macrophages [22], were performed as described [18, 23]. Quantitative data from H & E staining are from 8–10 unique visual fields (20x objective) from 3 different animals and expressed as a percentage of the total number of myofibers counted (~500 fibers counted for each strain of mice). Macrophage counts are from 3 animals per strain from 4 unique visual fields (40x objective) per muscle and expressed as the number of cells per square mm.

2.3. Statistical Methods. All statistical analyses were performed with SigmaStat (Ashburn, VA). Baseline torque data were analyzed with a one-way ANOVA, injury and recovery data were analyzed with a repeated measures two-way ANOVA. CNFs, necrotic fibers and macrophage counts (CD68+ cells) were analyzed by two-way ANOVAs. *Post hoc* analyses were performed according to the Student-Newman-Keuls method. Linear regression analyses of the effect of necrosis and macrophage counts torque as well the effect of macrophage counts on necrosis were performed with

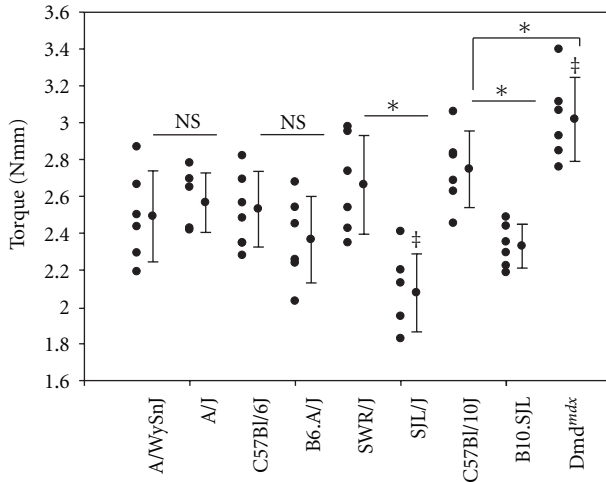


FIGURE 1: Baseline torque before large-strain injury. Maximum isometric tetanic torque of the dorsiflexor muscle group was measured prior to LSI. All control strains (A/WySnJ, C57Bl/6J, SWR/J, and C57Bl10/J) produced a similar level of contractile torque. Among the *Dysf* mutants, only SJL/J mice and B10.SJL mice were weaker than their corresponding controls. SJL/J mice were also weaker than A/J mice. Raw torque produced by DMD^{mdx} was the highest among the studied strains of mice. *Significant difference compared to control strain at same time point. NS:no significant difference. †Significant difference compared to A/J at same time point.

SigmaStat. Alpha was set at 0.05 *a priori*, and *P* values less than 0.05 were considered significant. Physiological data are reported as mean \pm S.D., and histological data are reported as mean \pm S.E.M.

3. Results

We used established physiological and morphological methods to compare 4 strains of dysferlin-deficient mice, A/J and SJL/J, which carry different mutations of dysferlin, and B6.A/J and B10.SJL, which carry their respective mutations in the C57Bl/6J and C57Bl/10J backgrounds. We used the latter as controls as well as SWR/J and A/WySnJ mice as controls in our studies of SJL/J and A/J mice, respectively (see Table 1). Our physiological experiments measured the contractile torque generated by the ankle dorsiflexor muscles, the loss of torque following a large-strain injury caused by repeated lengthening contractions, and the recovery of torque 3 days after injury. Our histological experiments measured the number of CNFs, necrotic myofibers, and inflammatory macrophages in TA muscles before and after injury. Our results indicate that these 4 strains of dysferlinopathic mice share some important features but differ significantly in others.

3.1. Physiological Assays. We first measured the torque generated by the ankle dorsiflexor muscles of the 4 types of dysferlinopathic mice, compared to the appropriate control strains (Figure 1). All control strains were statistically indistinguishable from each other. There was no statistical difference between A/J mice and its control, A/WySnJ mice,

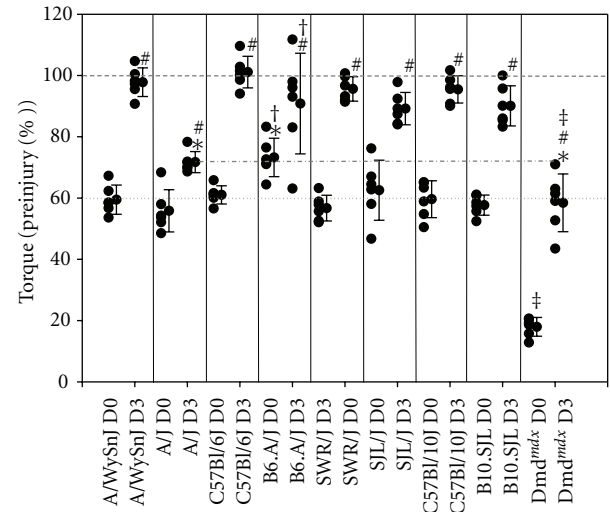


FIGURE 2: Torque after LSI. We measured maximum isometric torque \sim 4 min after the last lengthening contraction in the LSI protocol (D0) and again 3 days later (D3). All control strains lost a similar level of torque. All dysferlin mutant mice except B6.A/J showed a similar reduction in torque immediately after injury; B6.A/J mice showed less susceptibility to initial injury compared to control C57Bl/6J mice as well as other dysferlinopathic strains. DMD^{mdx} mice showed the highest level of torque loss immediately after injury. At D3, all control strains recovered to near baseline torque levels. All dysferlin mutants except A/J recovered to similar levels as their respective control strains. A/J mice and DMD^{mdx} mice showed a significant torque deficit at D3. *Significant difference compared to control strain at same time point. #Significant difference within same strain between D0 and D3. †Significant difference compared to same *Dysf* mutation at same time point. ‡Significant difference compared to A/J at same time point.

and between B6.A/J and its control, C57Bl/6J. SJL/J and B10.SJL mice generated similar levels of torque, but were weaker than their respective control strains, SWR/J and C57Bl/10J. All dysferlinopathic strains and their controls were significantly weaker than DMD^{mdx} mice, consistent with earlier reports that the latter are stronger than controls [24–26]. When normalized to muscle weight, however (see Table 2), TA muscles of DMD^{mdx} mice were \sim 38% weaker than muscles of C57Bl/10J mice.

We next subjected each murine strain to our large-strain injury protocol (LSI, see Methods). All strains except B6.A/J lost \sim 40% of their preinjury torque after LSI (Figure 2). B6.A/J mice only lost \sim 30% of their baseline torque, which was significantly less than its control C57Bl/6J and all other strains (Figure 2; supplementary data, Figures S1 and S2 available online at doi:10.1155/2011/134031). In contrast to all the control and dysferlinopathic strains we assayed, DMD^{mdx} mice showed a \sim 80% loss of contractile torque after LSI, significantly greater than any of the other strains, consistent with the greater susceptibility to injury by lengthening contractions characteristic of these mice [27–29].

We assayed the ability of mice of each strain to recover from the large-strain injury within the 3-day period that we previously found was sufficient for controls [17–19].

TABLE 2: Weights of TA muscles. Wet weights (in mg) of uninjured (right) and injured (left) TA muscles collected at D3 are given.

	A/Wy SnJ	A/J	C57Bl/6J	B6.A/J	SWR/J	SJL/J	C57Bl/10J	B10.SJL	DMD ^{mdx}
<i>N</i>	4	4	4	4	3	3	3	3	3
D3 control	43 ± 1	42 ± 1	51 ± 1	48 ± 1	45 ± 4	50 ± 2	43 ± 2	45 ± 1	79 ± 2
D3 injured	45 ± 3	40 ± 1	52 ± 1	47 ± 2	47 ± 5	48 ± 4	45 ± 2	46 ± 1	75 ± 4

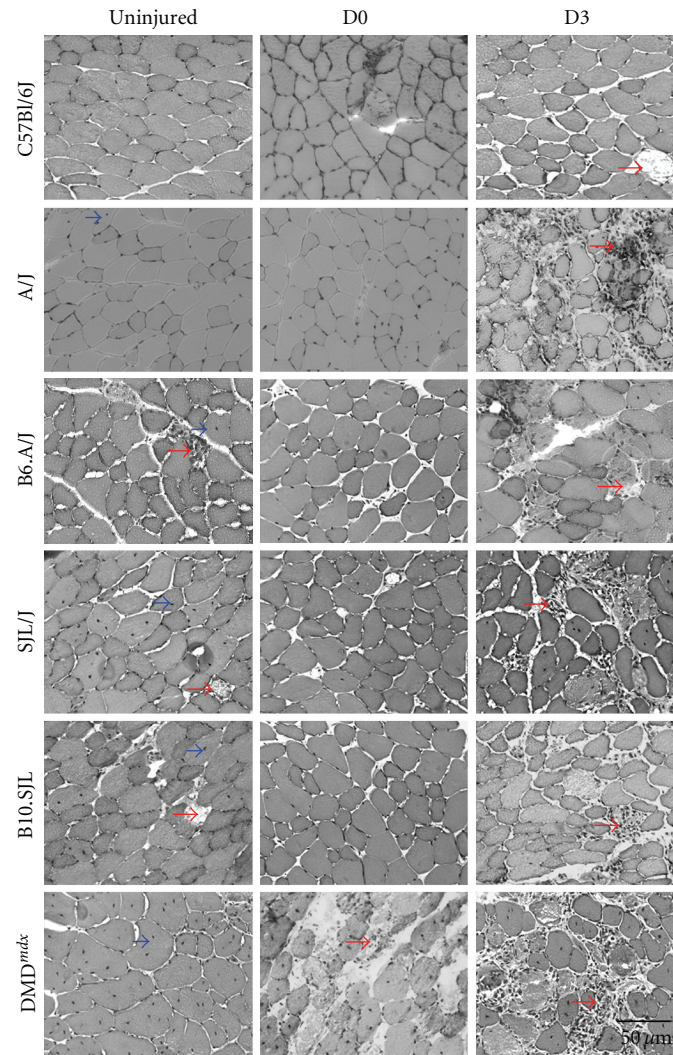


FIGURE 3: Histology before and after injury. We labeled TA muscles with H&E stains. In uninjured muscle, necrotic fibers identified by pale, disrupted cytoplasmic staining and infiltrated by mononuclear cells appeared in all dysferlinopathic strains except A/J (red arrows). All dysferlin mutants had many CNFs (blue arrow heads) before LSI. At D3 post-LSI, necrotic fibers increased in all mutants, with the most widespread area of necrosis in A/J muscle. Extensive myofiber damage soon after LSI was visible in DMD^{mdx} muscle, but not in control or dysferlinopathic muscle.

The mean torque for C57Bl/6J mice exceeded 100% baseline torque, suggesting complete recovery of function 3 days after LSI. All other control strains were statistically indistinguishable from C57Bl/6J at D3 post-LSI, indicating that they too had regained all of their lost contractile torque (Figure 2). As reported [17–19], A/J mice only recovered to only ~70% of their preinjury torque, equivalent to ~1/4 of the torque lost immediately after LSI. Surprisingly, B10.SJL and SJL/J recovered to ~90% of their original torque by D3 (Figure 2), which was also statistically indistinguishable from the level

of recovery shown by their respective control strains. This suggests that the absence or severe depletion of dysferlin is not sufficient to delay the recovery of torque 3 days after large-strain injury. The group mean for contractile torque for B6.A/J also recovered as well as their control C57Bl/6J mice. However, their recovery at D3 showed a wide range of values from a loss of 8% below initial injury in one animal to a gain of 10% above preinjury torque in another. Due to the high level of variability seen in the set of 6 B6.A/J animals, we performed physiological measurements on additional

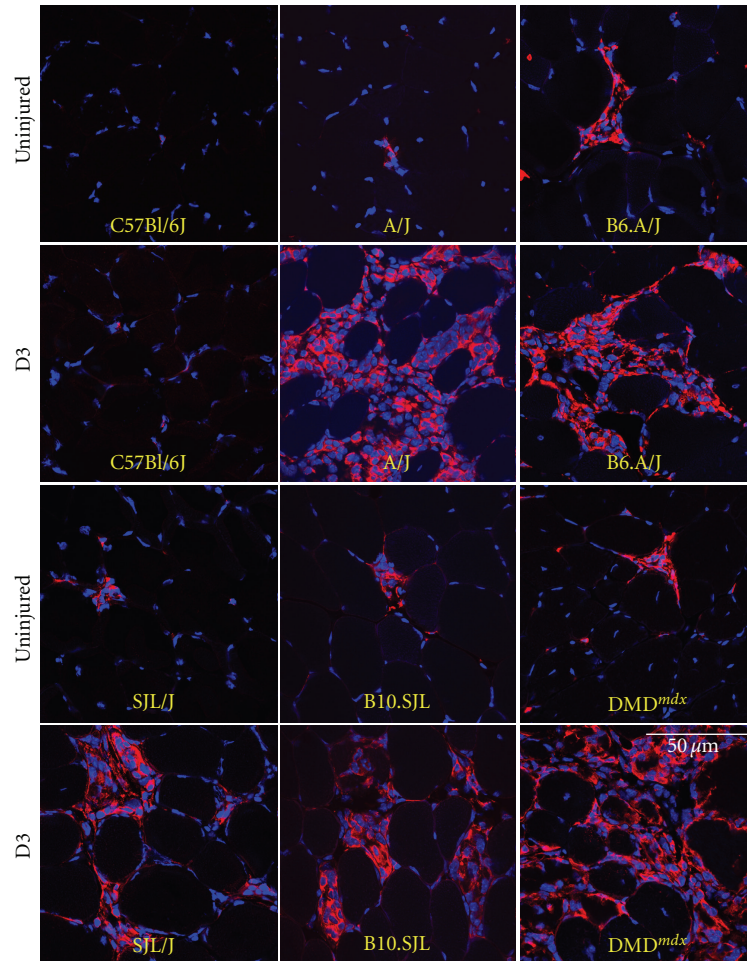


FIGURE 4: Macrophages (CD68+ cells) in muscle before and after injury. We labeled cross sections of uninjured and injured TA muscles with antibodies to CD68 to identify macrophages (red) and DAPI to mark nuclei (blue). Focal areas of macrophage infiltration were evident in uninjured muscle of all dysferlinopathic strains as well as DMD^{mdx} mice. At D3 following LSI, macrophage numbers increased significantly in these mutant strains.

sets of animals. With increased sample size, B6.A/J were statistically indistinguishable from C57Bl/6J and A/J at D0, but were different from both these strains at D3. They were also more variable (supplementary data, Figures S1 and S2). Just as they differed in their initial torque and susceptibility to injury, DMD^{mdx} mice also differed significantly from the control and dysferlinopathic strains in their extent of recovery from LSI, reaching only ~60% of their original torque by D3, equivalent to ~1/2 of the torque lost initially.

3.2. Histological Studies. We assessed 3 different morphological markers of myopathy, CNFs and necrotic fibers (both quantitated from H&E-stained sections) and macrophages (quantitated from sections immunolabeled with antibodies to CD68), in uninjured TA muscles and in muscles 3 days after injury (Figures 3 and 4). As all control strains were statistically indistinguishable at D0 and D3 in the number of CNFs, necrotic fibers, and CD68+ cells, we only show comparisons for these variables with C57Bl/6J data.

In uninjured muscles, CNFs were elevated in all dysferlinopathic mice as well as in DMD^{mdx} (Figure 5), compared

to controls. Uninjured SJL/J muscle had more CNFs than the other dysferlinopathic strains. We found no significant differences in central nucleation among B10.SJL, A/J, and B6.A/J. DMD^{mdx} mice showed much higher levels of CNFs, consistent with earlier reports [30, 31]. Except for DMD^{mdx} , we observed no significant increases in CNFs at D3 in any of the strains.

Although necrotic fibers were readily detected in the uninjured TA muscles of B6.A/J, B10.SJL, and SJL/J mice, the numbers were not significantly greater than control muscles (Figures 3 and 6). On D3 post-LSI, however, the number of necrotic fibers increased significantly in all of the dysferlinopathic mice (Figure 6). Necrotic fibers at D3 in A/J and SJL/J muscles were statistically indistinguishable, but B6.A/J and B10.SJL muscles had significantly fewer necrotic fibers than A/J and SJL/J, respectively. DMD^{mdx} had the highest levels of necrosis, which can be explained by severe myofiber damage seen immediately after injury, a feature not seen in dysferlinopathic muscle (Figure 6; also see middle panels in Figure 3). A regression analysis with % necrotic fibers as the independent variable and torque on D3

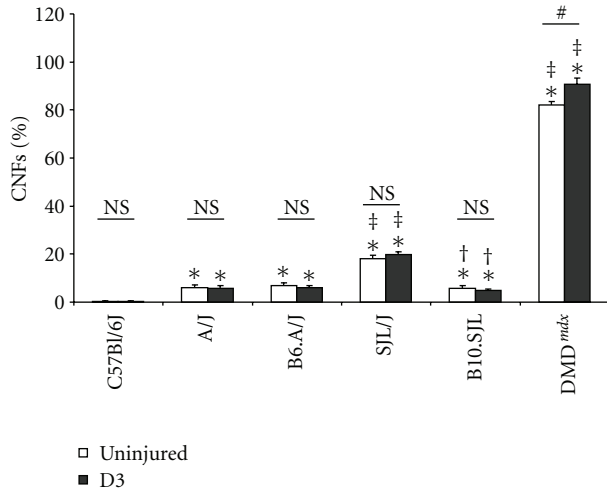


FIGURE 5: Quantitation of CNFs. We counted CNFs in H&E-stained cross sections of uninjured and injured TA muscles. In uninjured muscles, CNFs were elevated in all dysferlin mutants, with SJL/J muscle showing the greatest elevation. DMD^{mdx} muscle showed several-fold CNFs more than all the dysferlinopathic samples. Except for DMD^{mdx}, none of the strains showed changes in CNFs at D3. *Significant difference compared to control strain at same time point. #Significant difference within same strain between uninjured and D3. †Significant difference compared to same *Dysf* mutation at same time point. ‡Significant difference compared to A/J at same time point. NS:no significant difference.

as the dependent variable showed a linear relationship (Figure 7; adjusted $r_2 = 0.904$, $P = 0.002$). Thus, the deficit in torque 3 days after LSI was directly proportional to the number of necrotic myofibers at D3. SJL/J alone fell above the 95% confidence interval suggesting that their D3 contractile torque exceeds what would be expected based on the level of necrosis. Consistent with this, SJL/J mice have been shown to recover from other forms of injury very efficiently [32].

We also quantitated the number of macrophages (CD68+ cells) in TA muscles of each strain, both before and after injury. Focal areas of necrosis in uninjured muscles were invaded by macrophages in all dysferlinopathic strains (Figure 4). However, macrophage counts were not significantly different from uninjured C57Bl/6j (Figure 8). All dysferlinopathic strains showed significant increases in macrophages at D3 post-LSI (Figure 8), with the highest counts detected in A/J. DMD^{mdx} muscle at D3 had significantly greater macrophage infiltration than A/J. Regression analysis with D3 torque regressed on macrophage counts showed a linear relationship (Figure 9(a); adjusted $r_2 = 0.836$, $P = 0.007$), with all strains falling within the 95% confidence interval. Similarly, a regression analysis with macrophage counts regressed on necrosis at D3 also showed a linear relationship (Figure 9(b); adjusted $r_2 = 0.896$, $P = 0.003$), with all strains falling within the 95% confidence interval.

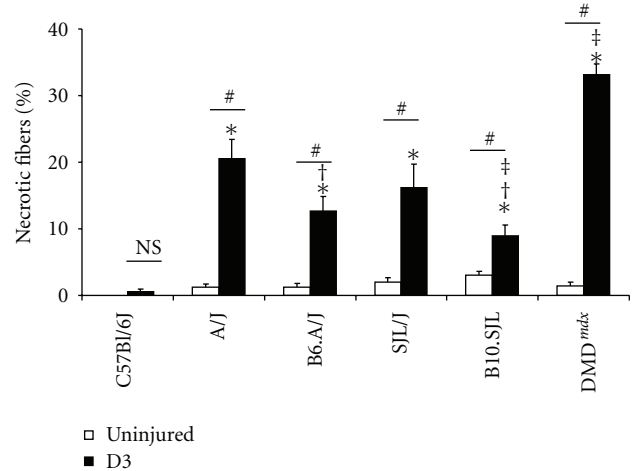


FIGURE 6: Quantitation of necrotic fibers. We counted necrotic fibers in H&E-stained cross sections of uninjured and injured TA muscles. Necrotic fibers increased significantly at D3 in all mutant strains. A/J muscle showed the largest increase among the dysferlin mutants, but the extent of necrosis in A/J muscles was significantly less than DMD^{mdx} at this time point. *Significant difference compared to control strain at same time point. #Significant difference within same strain between uninjured and D3. †Significant difference compared to same *Dysf* mutation at same time point. ‡Significant difference compared to A/J at same time point.

4. Discussion

Several strains of dysferlinopathic mice have been studied as possible models of human muscular dystrophies linked to mutations in the dysferlin gene. These include 2 different strains generated by gene ablation [6, 7], 2 strains with spontaneous mutations in the dysferlin gene, A/J and SJL/J, and the strains that were derived by breeding the A/J and SJL/J *Dysf* mutations into the well-established C57Bl/10J and C57Bl/6j genetic backgrounds, namely, B6.A/J and B10.SJL. Although several laboratories have compared some of these strains to each other, with results suggesting that they share similar properties [7, 12, 13], few direct comparisons have been made of mice carrying the SJL/J mutation to those carrying the ETn retrotransposon of A/J, and none have focused on their responses to injuries caused by lengthening contractions. Here we provide evidence to suggest that SJL/J and B10.SJL have a similar phenotype. We show further that they differ significantly from A/J and B6.A/J mice and, moreover, that the latter two strains differ significantly from each other.

Our LSI protocol, which differs from many other methods for injuring the hindlimb muscles of mice, has several advantages, including rapidity and reproducibility. Our LSI model also clearly distinguishes between some dysferlinopathic strains and controls, including A/J and A/WySnJ. Furthermore, the LSI model also distinguishes between some of the dysferlinopathic mice we have examined, discussed further below, as well as between dysferlin-deficient and dystrophin-deficient strains. LSI causes ~2-fold greater force deficit immediately after LSI in muscles lacking dystrophin

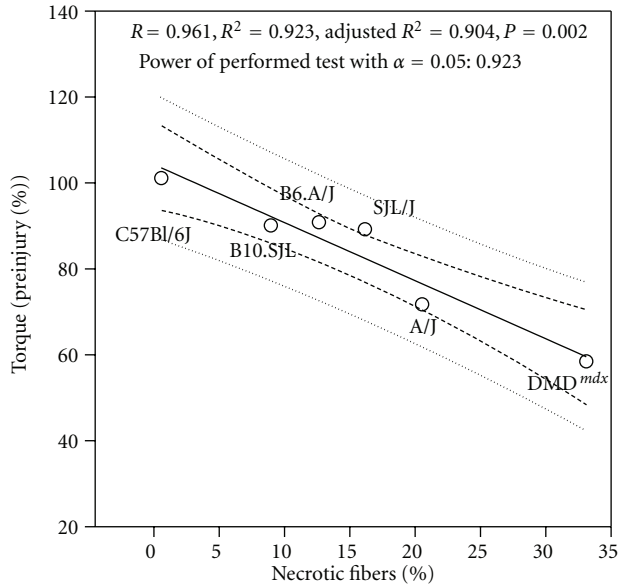


FIGURE 7: D3 contractile torque regressed on necrosis. A regression analysis of necrosis as the independent variable and D3 torque as the dependent variable showed a good linear fit, suggesting that the extent of necrosis is a reliable negative predictor of functional recovery at D3. The dashed and dotted lines represent the 95% confidence and prediction intervals, respectively.

than in muscles lacking dysferlin. Injury of DMD^{mdx} muscle is rapidly followed by significant myofiber degeneration (Figures 2 and 3). DMD^{mdx} mice are known to be much more susceptible than controls to injury induced by lengthening contractions [27–29], and the more pronounced effect of LSI on their muscles suggests that our injury model is indeed physiologically relevant to the study of sarcolemmal damage and repair.

Remarkably, however, although the physiological changes induced by LSI differ quantitatively from one strain to the other, they are qualitatively similar in all the strains we have studied, including control and dysferlinopathic strains. These are indistinguishable in their susceptibility to initial injury but differ 3 days later in necrosis and inflammation. By contrast, DMD^{mdx} mice are more susceptible to initial injury and also recover slowly. Consistent with this, regression analyses of loss of function on D3 following LSI, measured as torque loss, against the number of necrotic fibers on D3, show a strong linear correlation. Similarly, the number of macrophages in muscles on D3 post-LSI is a linear function of necrosis. In other studies, we have shown that the appearance of necrotic fibers precedes the appearance of macrophages in injured muscle by several hours (Roche JA and Bloch RJ, in preparation). These results therefore suggest that, despite the different mutations and genes affected in the dysferlinopathic and dystrophinopathic mice we have studied, and the different extents to which they recover contractile torque, the level of functional recovery and the extent of inflammatory cell infiltration are determined by the extent of myofiber necrosis. As macrophage infiltration in 3 dysferlinopathic strains (B6.A/J, SJL/J, and B10.SJL) is

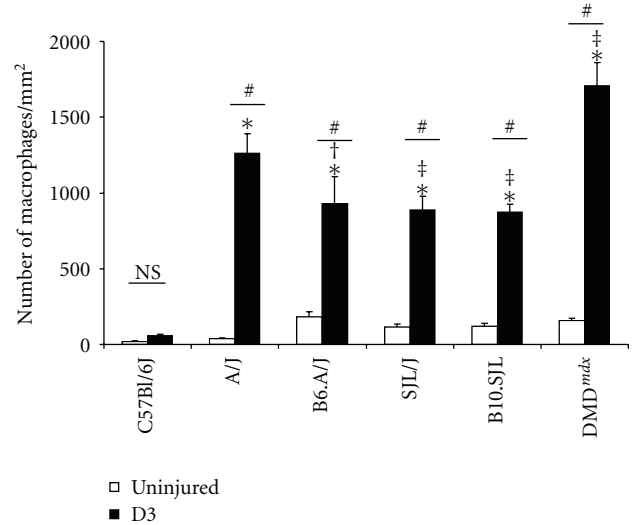


FIGURE 8: Quantitation of macrophages (CD68+ cells). We counted macrophages in cross sections of uninjured and injured TA labeled with antibodies to CD68 (see Figure 4). All dysferlin mutant strains showed elevated macrophage counts at D3 post-LSI, with A/J having significantly higher levels than the other strains. DMD^{mdx} muscle showed significantly higher macrophage infiltration than A/J. *Significant difference compared to control strain at same time point. #Significant difference within same strain between uninjured and D3. †Significant difference compared to same *Dysf* mutation at same time point. ‡Significant difference compared to A/J at same time point.

significantly elevated at D3 despite near complete functional recovery and moderate levels of myofiber necrosis, our results support a role for increased infiltration of monocytes and macrophages in dysferlinopathies, as reported by others [32–34].

Most of our attention in these studies was focused on the properties of 4 different dysferlinopathic strains of mice, two carrying a retrotransposon in the dysferlin gene (A/J and B6.A/J) and two carrying a mutation in the *Dysf* gene that results in the deletion of an exon encoding 57 amino acids in one of dysferlin's C2 domains. We find that the key characteristics of the TA muscles of 12–16 wk old SJL/J and B10.SJL mice are low but readily detectable levels of central nucleation, necrosis, and macrophage infiltration in uninjured muscles, consistent with the early stages of myopathy reported in these mice at this age [9, 12]. Consistent with their shared phenotypes, both strains lose similar fractions of their initial torque after LSI, and they both recover to near complete levels, similar to their respective control strains, within 3 days. However, SJL/J muscles show greater numbers of CNFs before injury and greater necrosis 3 days after LSI, suggesting that genes other than dysferlin that are differentially expressed play a role in the myopathy that has been reported in SJL/J mice.

Our previous studies on the effect of LSI on A/J and A/WySnJ mice suggest that the presence or absence of dysferlin does not have an immediate effect on the ability of the sarcolemma to reseal, trapping 10 kDa fluorescein dextran in

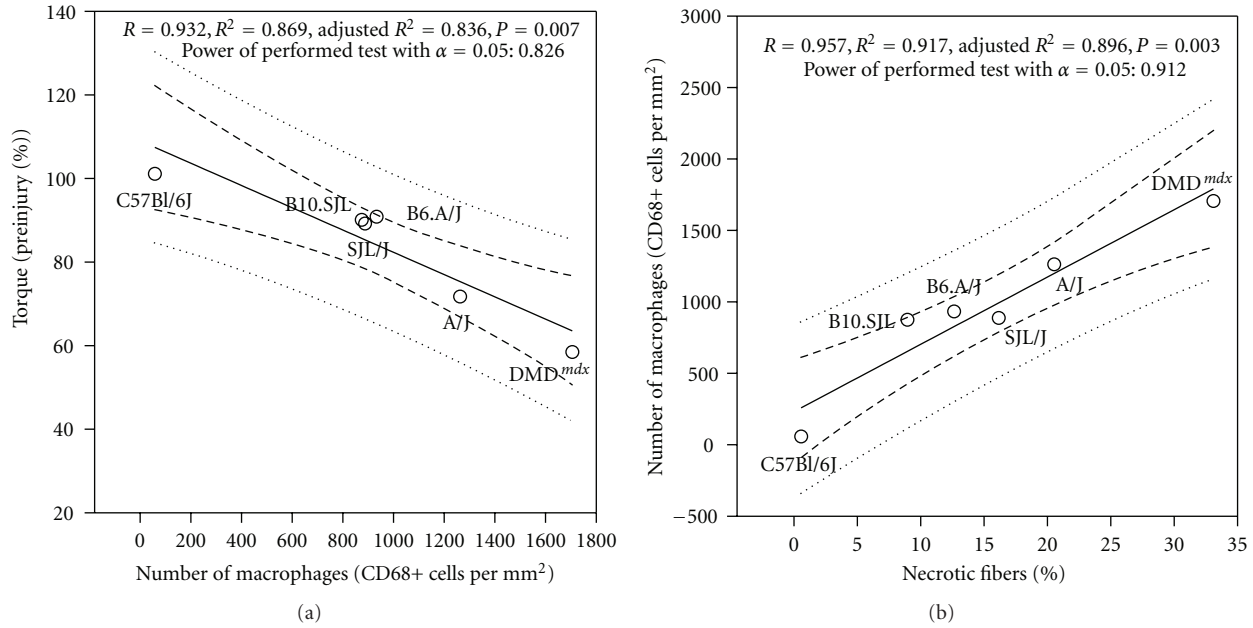


FIGURE 9: Regression analyses of contractile torque *versus* macrophage counts and macrophage counts *versus* necrosis. A regression analysis of the number of macrophages on D3 as the independent variable and torque at D3 as the dependent variable showed a good linear fit (a). Similarly, analysis of the number of necrotic fibers as the independent variable and the number of macrophages as the dependent variable also showed a good linear fit (b). The analyses suggest that that macrophage counts are a reliable negative predictor of functional recovery at D3 and that the number of necrotic fibers predicts the extent of macrophage invasion.

the myoplasm for several days after injury [18]. Rather, the damage to dysferlin-null muscle is a later event, subsequent to sarcolemmal resealing that manifests itself initially as a significant increase in necrosis followed later by increased inflammation. These changes are fully manifested by D3 after LSI, after which damaged myofibers are lost and replaced by myogenesis. Our results with the SJL/J and B10.SJL indicate that mutations in the dysferlin gene that reduce the levels of dysferlin protein in muscle to $\sim 15\%$ of control levels or less [7, 12] are not sufficient to lead to the persistent torque deficit seen in A/J muscle 3 days after injury. However, despite the near complete functional recovery of SJL/J and B10.SJL muscles 3 days after injury, they still showed significantly elevated counts of necrotic fibers and macrophages, albeit less than A/J. They are nevertheless consistent with the idea that wild-type dysferlin is not needed for sarcolemmal membranes to reseal immediately after injury and protect fibers against rapid degeneration, as we see in dystrophin-deficient DMD^{mdx} muscle. Indeed, the fact that these two strains of mice recover torque equally well after injury, and nearly as well as controls, suggests that the modified dysferlin they synthesize, albeit in very low amounts, may promote their accelerated recovery. Alternatively, the low levels of ongoing degeneration and regeneration, evident in uninjured muscles of these mice from their elevated numbers of CNFs, necrotic fibers, and macrophages, may accelerate their recovery from LSI, perhaps because they are already primed to regenerate.

Our current results with A/J and control, A/WySnJ, mice agree with our previous results, which indicate that A/J but not A/WySnJ muscle show more CNFs before injury, with a large increase in necrosis and inflammation 3 days after

injury [18]. CNFs only increase at later times, as A/J muscles regenerate [17, 18]. Consistent with this, torque is significantly depressed at D3 and recovers over 14 days after injury as myogenesis is activated to replace fibers lost as a result of the pathological changes that follow LSI.

Although they carry the same retrotransposon as A/J mice in their dysferlin gene and thus fail to express any dysferlin [7], B6.A/J mice respond differently to LSI. In particular, although they have similar levels of CNFs, necrotic fibers, and inflammation both before and after injury, the contractile torques we measure are highly variable. Moreover, their susceptibility to LSI appears lower than that of A/J mice (as well as SJL/J and B10.SJL), although the magnitude of this difference decreases as the sample size increases. We currently have no explanation for this variability. Until we can control it, however, we favor the A/J line for studying the role of dysferlin in muscles subjected to physiological injuries in living mice.

Our results suggest that A/J mice, and SJL/J and B10.SJL, are useful for studying different aspects of the muscular dystrophies linked to mutations in dysferlin. Because they show an earlier onset of myopathy, typical of the human disease, which is usually first observed in young adults, SJL/J and B10.SJL are potentially more useful for studying the progression of the disease *in vivo* and for testing the ability of drugs or other therapeutics to slow or block further myopathic changes. Given that C57Bl/10J mice are a better control for B10.SJL than SWR/J mice are for SJL/J, B10.SJL mice are a better choice for these types of experiments. Such studies will, however, require careful evaluation of the state of the muscles before any treatment, as they may already

be dystrophic. Because they show little pathology as young adults, but respond so differently to LSI than controls, A/J mice in our opinion remain very useful for studies designed to examine the specific role of dysferlin in muscles without the confounding effect of preexisting dystrophic changes. A/J mice also give insight into how apparently healthy muscles lacking dysferlin become dystrophic, thus modeling the subclinical phase of dysferlinopathies in humans. Given the differences between them, however, it seems advisable for laboratories to investigate both A/J and B10.SJL mice as they search for a cure for dysferlinopathies.

References

- [1] D. Bansal and K. P. Campbell, "Dysferlin and the plasma membrane repair in muscular dystrophy," *Trends in Cell Biology*, vol. 14, no. 4, pp. 206–213, 2004.
- [2] R. Han and K. P. Campbell, "Dysferlin and muscle membrane repair," *Current Opinion in Cell Biology*, vol. 19, no. 4, pp. 409–416, 2007.
- [3] L. Glover and R. H. Brown Jr., "Dysferlin in membrane trafficking and patch repair," *Traffic*, vol. 8, no. 7, pp. 785–794, 2007.
- [4] R. Bashir, S. Britton, T. Strachan et al., "A gene related to caenorhabditis elegans spermatogenesis factor fer-1 is mutated in limb-girdle muscular dystrophy type 2B," *Nature Genetics*, vol. 20, no. 1, pp. 37–42, 1998.
- [5] M. Vainzof, L. V. B. Anderson, E. M. McNally et al., "Dysferlin protein analysis in limb-girdle muscular dystrophies," *Journal of Molecular Neuroscience*, vol. 17, no. 1, pp. 71–80, 2001.
- [6] D. Bansal, K. Miyake, S. S. Vogel et al., "Defective membrane repair in dysferlin-deficient muscular dystrophy," *Nature*, vol. 423, no. 6936, pp. 168–172, 2003.
- [7] M. Ho, C. M. Post, L. R. Donahue et al., "Disruption of muscle membrane and phenotype divergence in two novel mouse models of dysferlin deficiency," *Human Molecular Genetics*, vol. 13, no. 18, pp. 1999–2010, 2004.
- [8] R. Hohlfeld, W. Müller, and K. V. Toyka, "Necrotizing myopathy in SJL mice," *Muscle and Nerve*, vol. 11, no. 2, pp. 184–185, 1988.
- [9] A. H. Weller, S. A. Magliato, K. P. Bell, and N. L. Rosenberg, "Spontaneous myopathy in the SJL/J mouse: pathology and strength loss," *Muscle and Nerve*, vol. 20, no. 1, pp. 72–82, 1997.
- [10] R. E. Bittner, L. V. B. Anderson, E. Burkhardt et al., "Dysferlin deletion in SJL mice (SJL-Dysf) defines a natural model for limb girdle muscular dystrophy 2B," *Nature Genetics*, vol. 23, no. 2, pp. 141–142, 1999.
- [11] E. Vafiadaki, A. Reis, S. Keers et al., "Cloning of the mouse dysferlin gene and genomic characterization of the SJL-Dysf mutation," *NeuroReport*, vol. 12, no. 3, pp. 625–629, 2001.
- [12] M. Von Der Hagen, S. H. Laval, L. M. Cree et al., "The differential gene expression profiles of proximal and distal muscle groups are altered in pre-pathological dysferlin-deficient mice," *Neuromuscular Disorders*, vol. 15, no. 12, pp. 863–877, 2005.
- [13] K. Kobayashi, T. Izawa, M. Kuwamura, and J. Yamate, "The distribution and characterization of skeletal muscle lesions in dysferlin-deficient SJL and A/J mice," *Experimental and Toxicologic Pathology*, vol. 62, no. 5, pp. 509–517, 2010.
- [14] W. M. Schmidt, M. H. Uddin, S. Dysek et al., "DNA damage, somatic aneuploidy, and malignant sarcoma susceptibility in muscular dystrophies," *PLoS Genetics*, vol. 7, no. 4, Article ID e1002042, 2011.
- [15] G. Cenacchi, M. Fanin, L. B. De Giorgi, and C. Angelini, "Ultrastructural changes in dysferlinopathy support defective membrane repair mechanism," *Journal of Clinical Pathology*, vol. 58, no. 2, pp. 190–195, 2005.
- [16] W. Lostal, M. Bartoli, N. Bourg et al., "Efficient recovery of dysferlin deficiency by dual adeno-associated vector-mediated gene transfer," *Human Molecular Genetics*, vol. 19, no. 10, pp. 1897–1907, 2010.
- [17] J. A. Roche, R. M. Lovering, and R. J. Bloch, "Impaired recovery of dysferlin-null skeletal muscle after contraction-induced injury in vivo," *NeuroReport*, vol. 19, no. 16, pp. 1579–1584, 2008.
- [18] J. A. Roche, R. M. Lovering, R. Roche, L. W. Ru, P. W. Reed, and R. J. Bloch, "Extensive mononuclear infiltration and myogenesis characterize recovery of dysferlin-null skeletal muscle from contraction-induced injuries," *American Journal of Physiology*, vol. 298, no. 2, pp. C298–C312, 2010.
- [19] D. P. Millay, M. Maillet, J. A. Roche et al., "Genetic manipulation of dysferlin expression in skeletal muscle: novel insights into muscular dystrophy," *American Journal of Pathology*, vol. 175, no. 5, pp. 1817–1823, 2009.
- [20] R. M. Lovering, J. A. Roche, M. H. Goodall, B. B. Clark, and A. Mcmillan, "An in vivo rodent model of contraction-induced injury and non-invasive monitoring of recovery," *Journal of Visualized Experiments*, no. 51, 2011.
- [21] C. P. Ingalls, G. L. Warren, J. Z. Zhang, S. L. Hamilton, and R. B. Armstrong, "Dihydropyridine and ryanodine receptor binding after eccentric contractions in mouse skeletal muscle," *Journal of Applied Physiology*, vol. 96, no. 5, pp. 1619–1625, 2004.
- [22] S. S. Rabinowitz and S. Gordon, "Macrosialin, a macrophage-restricted membrane sialoprotein differentially glycosylated in response to inflammatory stimuli," *Journal of Experimental Medicine*, vol. 174, no. 4, pp. 827–836, 1991.
- [23] J. A. Roche, D. L. Ford-Speelman, L. W. Ru et al., "Physiological and histological changes in skeletal muscle following in vivo gene transfer by electroporation," *American Journal of Physiology, Cell Physiology*, vol. 301, no. 5, pp. C1239–C1250, 2011.
- [24] G. R. Coulton, N. A. Curtin, J. E. Morgan, and T. A. Partridge, "The mdx mouse skeletal muscle myopathy: II. Contractile properties," *Neuropathology and Applied Neurobiology*, vol. 14, no. 4, pp. 299–314, 1988.
- [25] P. Sacco, D. A. Jones, J. R. T. Dick, and G. Vrbova, "Contractile properties and susceptibility to exercise-induced damage of normal and mdx mouse tibialis anterior muscle," *Clinical Science*, vol. 82, no. 2, pp. 227–236, 1992.
- [26] J. G. Quinlan, S. R. Johnson, M. K. McKee, and S. P. Lyden, "Twitch and tetanus in MDX mouse muscle," *Muscle and Nerve*, vol. 15, no. 7, pp. 837–842, 1992.
- [27] B. Weller, G. Karpati, and S. Carpenter, "Dystrophin-deficient mdx muscle fibers are preferentially vulnerable to necrosis induced by experimental lengthening contractions," *Journal of the Neurological Sciences*, vol. 100, no. 1-2, pp. 9–13, 1990.
- [28] C. Dellorusso, R. W. Crawford, J. S. Chamberlain, and S. V. Brooks, "Tibialis anterior muscles in mdx mice are highly susceptible to contraction-induced injury," *Journal of Muscle Research and Cell Motility*, vol. 22, no. 5, pp. 467–475, 2001.
- [29] S. I. Head, D. A. Williams, and D. G. Stephenson, "Abnormalities in structure and function of limb skeletal muscle fibres of dystrophic mdx mice," *Proceedings of the Royal Society B*, vol.

248, no. 1322, pp. 163–169, 1992.

- [30] J. Dangain and G. Vrbova, “Muscle development in mdx mutant mice,” *Muscle and Nerve*, vol. 7, no. 9, pp. 700–704, 1984.
- [31] L. F. B. Torres and L. W. Duchon, “The mutant mdx: inherited myopathy in the mouse. Morphological studies of nerves, muscles and end-plates,” *Brain*, vol. 110, no. 2, pp. 269–299, 1987.
- [32] C. A. Mitchell, J. K. McGeachie, and M. D. Grounds, “Cellular differences in the regeneration of murine skeletal muscle: a quantitative histological study in SJL/J and BALB/c mice,” *Cell and Tissue Research*, vol. 269, no. 1, pp. 159–166, 1992.
- [33] K. Nagaraju, R. Rawat, E. Veszelszky et al., “Dysferlin deficiency enhances monocyte phagocytosis: a model for the inflammatory onset of limb-girdle muscular dystrophy 2B,” *American Journal of Pathology*, vol. 172, no. 3, pp. 774–785, 2008.
- [34] C. A. Mitchell, M. D. Grounds, and J. M. Papadimitriou, “The genotype of bone marrow-derived inflammatory cells does not account for differences in skeletal muscle regeneration between SJL/J and BALB/c mice,” *Cell and Tissue Research*, vol. 280, no. 2, pp. 407–413, 1995.

Research Article

Localization and Regulation of the N Terminal Splice Variant of PGC-1 α in Adult Skeletal Muscle Fibers

Tiansheng Shen, Yewei Liu, and Martin F. Schneider

Department of Biochemistry and Molecular Biology, University of Maryland School of Medicine, Baltimore, MD 21201-1503, USA

Correspondence should be addressed to Martin F. Schneider, mschneid@umaryland.edu

Received 23 September 2011; Accepted 26 October 2011

Academic Editor: Aikaterini Kontrogianni-Konstantopoulos

Copyright © 2012 Tiansheng Shen et al. This is an open access article distributed under the Creative Commons Attribution License, which permits unrestricted use, distribution, and reproduction in any medium, provided the original work is properly cited.

The transcriptional coactivator peroxisome proliferator-activated receptor γ coactivator 1 α (PGC-1 α) regulates expression of genes for metabolism and muscle fiber type. Recently, a novel splice variant of PGC-1 α (NT-PGC-1 α , amino acids 1–270) was cloned and found to be expressed in muscle. Here we use Flag-tagged NT-PGC-1 α to examine the subcellular localization and regulation of NT-PGC-1 α in skeletal muscle fibers. Flag-NT-PGC-1 α is located predominantly in the myoplasm. Nuclear NT-PGC-1 α can be increased by activation of protein kinase A. Activation of p38 MAPK by muscle activity or of AMPK had no effect on the subcellular distribution of NT-PGC-1 α . Inhibition of CRM1-mediated export only caused relatively slow nuclear accumulation of NT-PGC-1 α , indicating that nuclear export of NT-PGC-1 α may be mediated by both CRM1-dependent and -independent pathways. Together these results suggest that the regulation of NT-PGC-1 α in muscle fibers may be very different from that of the full-length PGC-1 α , which is exclusively nuclear.

1. Introduction

The transcriptional coactivator peroxisome proliferator-activated receptor- γ co-activator 1 α (PGC-1 α) containing 797 amino acids (full-length) was first determined to be a cold inducible factor in a differentiated brown fat cell line [1]. Subsequent studies have shown that PGC-1 α plays important roles in mitochondrial biogenesis via coactivating several transcription factors such as nuclear respiratory factors and peroxisome proliferator-activated receptors [1–3]. PGC-1 α has also been found to mediate fast-to-slow skeletal muscle fiber-type transformation through coactivation of MEF2 [2, 4]. Exercise/muscle contraction has been found to increase PGC-1 α mRNA and protein levels [5, 6]. Both the activity and expression of PGC-1 α appear to be regulated by p38 MAPK, which phosphorylates PGC-1 α on Thr-262, Ser-265, and Thr-298 and increases its stability [7–9]. In addition, PGC-1 α expression is also modulated by AMPK-dependent phosphorylation at residues Thr-177 and Ser-570 [10, 11].

Recently, a novel biologically active 270-aa isoform of PGC-1 α (NT-PGC-1 α) was cloned by Zhang and his colleagues [12]. NT-PGC-1 α is produced by alternative splicing

of the full-length PGC-1 α through a premature stop codon between exons 6 and 7, generating a truncated N-terminal form of PGC-1 α containing the first 267 amino acids of full-length PGC-1 α and 3 additional amino acids from the insertion [12]. Two of the three p38 MAPK phosphorylation sites (Thr-262, Ser-265) and one of the two AMPK phosphorylation sites (Thr-177) of full-length PGC-1 α are present in NT-PGC-1 α . Although lacking the nuclear localization signals present in the full-length PGC-1 α , NT-PGC-1 α has a predicted size only about 30 kDa which should allow it to be freely diffusible between nucleus and cytosol via the nuclear pores [12]. However, recent studies found that NT-PGC-1 α is predominantly located in cytoplasm [12–14] and that the subcellular localization of NT-PGC-1 α is dynamically regulated by protein kinase A (PKA), which phosphorylates NT-PGC-1 α at residues Ser-194, Ser-241, and Thr-256 [13]. In adipocytes and in Chinese hamster ovary K1 (CHO-K1) cells, inhibition of CRM1 increased the nuclear content of NT-PGC-1 α [12, 13].

Although NT-PGC-1 α is found to be expressed in many tissues where PGC-1 α plays important roles, including the skeletal muscle [12], no reports of the subcellular

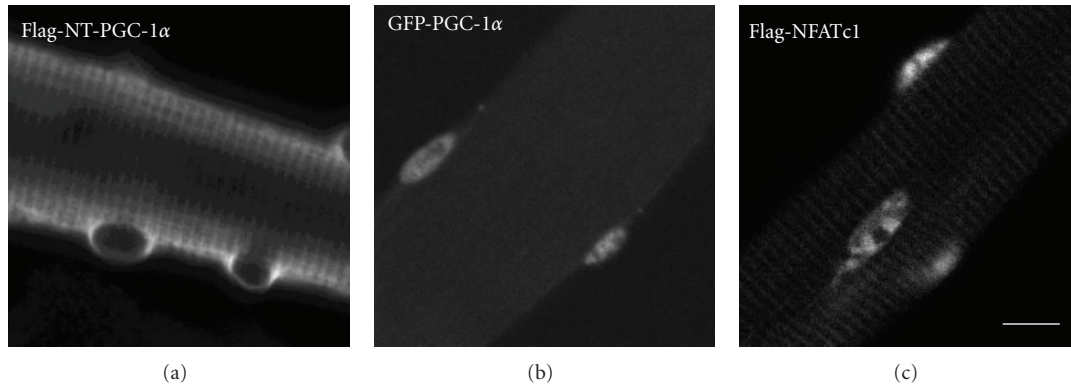


FIGURE 1: Localization of Flag-NT-PGC-1 α , GFP-PGC-1 α , and Flag-NFATc1 in muscle fibers. (a) A representative image of a muscle fiber expressing Flag-NT-PGC-1 α detected by anti-Flag antibody staining shows a predominantly cytoplasmic localization of Flag-NT-PGC-1 α in cultured adult skeletal muscle fibers. (b) A different fiber expressing the full-length PGC-1 α -GFP fusion protein shows that full length PGC-1 α is mainly located in the fiber nucleus. (c) A third muscle fiber expressing nuclear-targeted Flag-tagged NFATc1 detected by the same anti-Flag antibody procedure as in (a) has a strong nuclear staining, thus establishing nuclear penetration of the anti-Flag antibody. Scale bar, 10 μ m.

distribution and regulation of NT-PGC-1 α in skeletal muscle have been published. Therefore, in the present study, we use Flag-tagged NT-PGC-1 α to examine the subcellular distribution of NT-PGC-1 α in skeletal muscle fibers under control conditions and to demonstrate that the subcellular localization of NT-PGC-1 α in muscle fibers is dynamically regulated by PKA and by CRM1-dependent nuclear export, but not by p38 MAPK, or AMPK.

2. Materials and Methods

2.1. Materials. dbcAMP (N⁶, 2'-O-dibutyryladenosine 3':5'-cyclic monophosphate sodium) and monoclonal anti-Flag antibody were from Sigma (Saint Louis, MO). AICAR (5-aminoimidazole-4-carboxamide-1- β -D-ribose), anti-p38 MAPK, anti-phospho-p38 MAPK (Thr180/Tyr182), anti-AMPK, and anti-phospho-AMPK (Thr172) antibodies were purchased from Cell Signaling Technology (Boston, MA). Leptomycin B was obtained from LC Laboratories (Woburn, MA). The expression plasmid of GFP-PGC-1 α cDNA was obtained from Addgene (Cambridge, MA).

2.2. FDB Muscle Fiber Cultures. Experiments were carried out on skeletal muscle fibers obtained from 4–6-week-old CD-1 mice. Experimental protocols were approved by the University of Maryland Institutional Animal Care and Use Committee. Mice were euthanized and single muscle fibers were enzymatically dissociated from isolated flexor digitorum brevis (FDB) muscles. FDB muscle fibers were plated on laminin-coated glass coverslip floors glued over 1 cm holes in 35 mm plastic Petri dishes and cultured in MEM containing 10% fetal bovine serum and 25 μ g/mL gentamicin sulfate in 5% CO₂ at 37°C as previously described [15].

2.3. Adenovirus Infection. The recombinant adenovirus containing the Flag-tagged NT-PGC-1 α (Flag-NT-PGC-1 α) [13] was kindly provided by Dr. Thomas W. Gettys (Pennington

Biomedical Research Center, LA). The constructions of recombinant adenoviruses of NFATc1-GFP and nuclear targeted Flag-NFATc1 were described in detail previously [16]. All viral constructs were confirmed by sequencing the viral DNA. Infection of muscle fiber cultures by recombinant adenoviruses was carried out about 20 h after the fibers were plated as previously described [16]. After 48 hours of viral infection, muscle fibers expressing Flag-NT-PGC-1 α were either electrically stimulated or treated pharmacologically. Fiber electrical stimulation in culture was accomplished by mounting stainless steel electrodes in the floor of the culture dish. These electrodes were connected to a stimulator to give field stimulation. 28 V, 1 ms pulses produce visible fiber twitches and relaxation between stimuli without fiber detachment from the glass coverslip. After treatment, fibers were fixed immediately for immunostaining.

2.4. Fluorescence Immunocytochemistry. After electrical stimulation or pharmacological treatment, FDB muscle fibers were immediately fixed with 4% paraformaldehyde for 10 min and permeabilized with 0.5% Triton-X-100 in PBS for 20 min. Nonspecific binding sites were blocked by incubation with 5% normal serum. Immunostaining for Flag-tagged NT-PGC-1 α was performed using monoclonal anti-Flag antibody (1:1000) followed by incubation with the fluorescent protein-conjugated secondary antibody. The fluorescence of the stained fibers was visualized using a confocal laser scanning imaging system (Olympus FLUOVIEW 500) using constant settings of laser intensity and photomultiplier gain. In each fiber image the mean pixel background fluorescence (off the fiber) was determined and subtracted from each pixel throughout the image. The average pixel fluorescence within user specified areas of interest (AOI) over the whole nucleus or the cytoplasm in each image was quantified by software custom-written in the IDL programming language (Research Systems, Boulder, CO), similar as we used in our previous study [17], and the

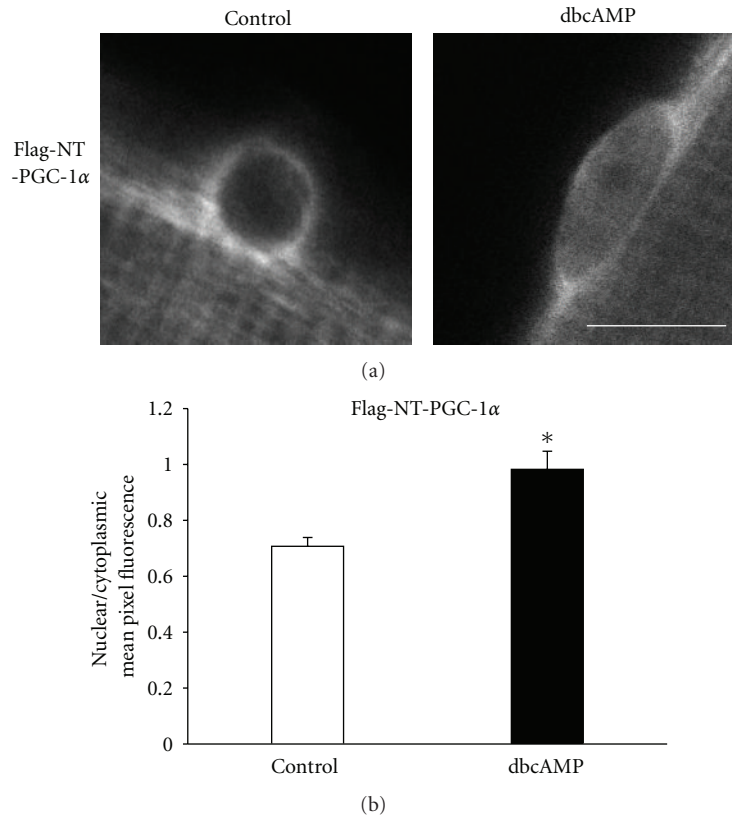


FIGURE 2: Activation of PKA increases nuclear Flag-NT-PGC-1 α . (a) Representative images of Flag-NT-PGC-1 α in a control fiber (control) and in another fiber after 1 h treatment with 1 mM dbcAMP in culture medium in the tissue culture incubator (dbcAMP). Scale bar, 10 μ m. (b) The n/c fluorescence ratio of Flag-NT-PGC-1 α in muscle fibers with (dbcAMP) or without (control) dbcAMP treatment. n/c values from 20 nuclei from 20 randomly selected fibers were averaged to give the mean value for each group. Asterisk indicates statistical significance between groups at $P < 0.05$.

ratio of nuclear to cytoplasmic mean pixel fluorescence was then calculated for each nucleus, which should correct for fiber to fiber differences in level of expression of Flag-NT-PGC-1 α or differences in overall staining level.

2.5. Western Blot Analysis. Cultured FDB muscle fibers were lysed with mammalian protein extraction reagent (Thermo Scientific, Rockford, IL) plus tablets of tissue protease inhibitor cocktail (Roche Diagnostics, Indianapolis, IN) and passed through a 21 gauge syringe 10 times. The lysates were subjected to centrifugation at 10,000 g for 10 min at 4°C. The supernatant was extracted and stored. Protein concentration was determined by the Bradford assay (Bio-Rad Laboratories, Inc., Hercules, CA). 30 μ g protein from each sample was fractionated by NuPAGE 3–8% Tris-Acetate Gel (Invitrogen, Carlsbad, CA) and transferred to PVDF membranes. Blots were probed with the appropriate primary and secondary antibodies and then visualized by Pierce ECL Western Blotting Substrate (Thermo Scientific, Rockford, IL) and exposed to X ray film (Amersham Hyperfilm, GE Healthcare, Piscataway, NJ). Film was scanned and band intensity was quantified by Image J software (National Institutes of Health, Bethesda, MD) after subtracting neighboring background intensity.

2.6. Statistics. Student's t -tests were used for comparisons of data obtained from two experimental conditions, and differences were considered significant if $P < 0.05$.

3. Results and Discussion

3.1. Subcellular Distribution of Flag-NT-PGC-1 α in Resting FDB Fibers. Using Flag-tagged NT-PGC-1 α expressed by adenoviral infection in cultured adult FDB skeletal muscle fibers, we found that Flag-NT-PGC-1 α is predominantly located in the myoplasm (Figure 1(a)), consistent with the recently described cytoplasmic localization of Flag-NT-PGC-1 α in adipocytes and CHO-K1 cells [12, 13]. Quantification of the mean pixel fluorescence in nuclear and cytoplasmic AOIs of 120 randomly selected resting fibers stained with anti-Flag antibody showed that the average value of nuclear/cytoplasmic mean pixel fluorescence ratio (n/c fluorescence ratio) was 0.63 ± 0.01 . This is in contrast to the distribution pattern of expressed full-length GFP-PGC-1 α fusion protein, which is predominantly located in the muscle fiber nuclei (Figure 1(b); n/c fluorescence ratio: 9.53 ± 2.86) as previously seen in COS cells [1]. As negative controls, fibers either not exposed to Flag-NT-PGC-1 α viral infection but stained with anti-Flag antibody or fibers with

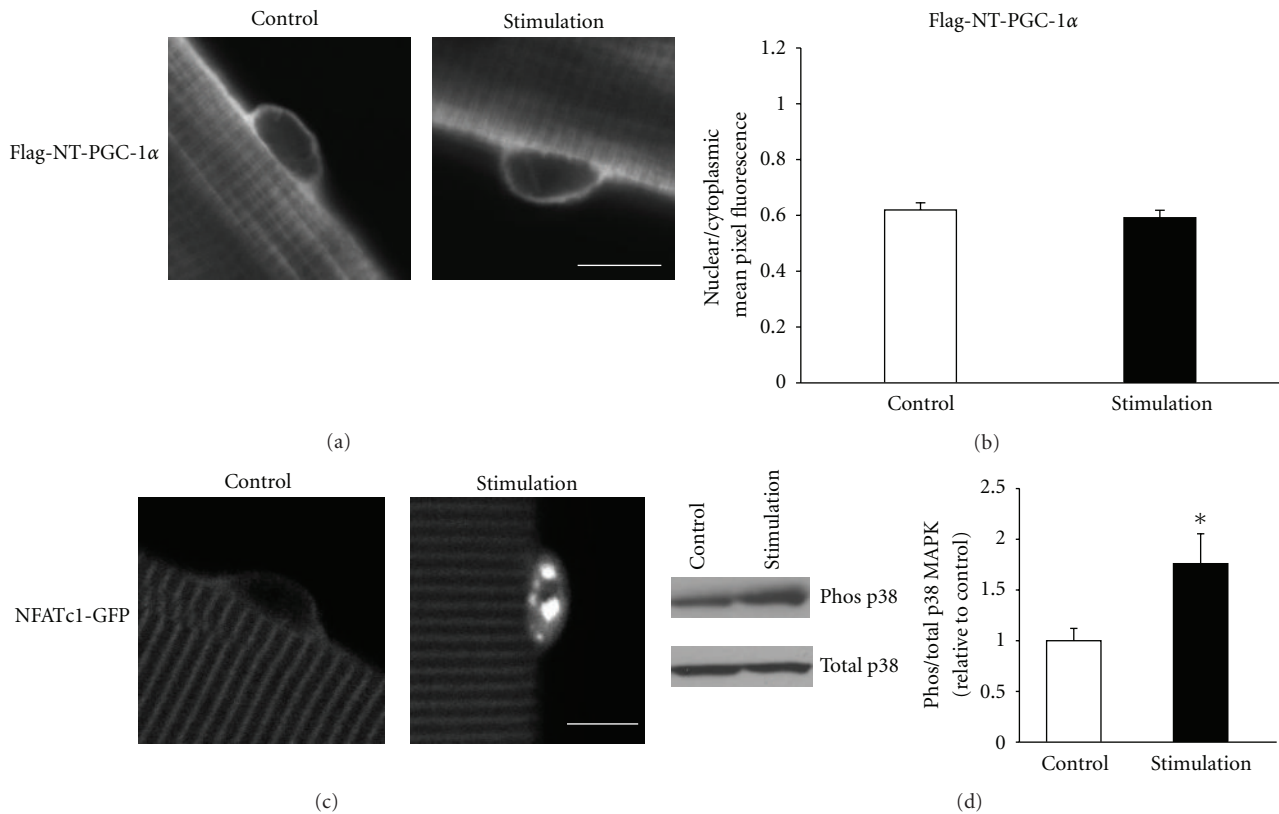


FIGURE 3: Muscle activity does not alter the subcellular distribution of Flag-NT-PGC-1 α . (a) Representative images of Flag-NT-PGC-1 α in a control fiber (control) and in another fiber stimulated continuously at 10 Hz for 4 h (stimulation). (b) The n/c fluorescence ratio of Flag-NT-PGC-1 α in muscle fibers with (stimulation) or without (control) electrical stimulation. n/c values from 20 nuclei from 20 randomly selected different fibers were averaged to give the mean value for each group. (c) Representative images of NFATc1-GFP in a control fiber (control) and in another fiber stimulated continuously at 10 Hz for 4 h (stimulation). Scale bars, 10 μ m for (a) and (c). (d) Representative Western blots showing the effect of muscle activity on p38 MAPK activation. Protein expression was quantified and averaged from 3 independent treatments. Phos p38, phospho-p38 MAPK; total p38, total p38 MAPK. Asterisk indicates statistical significance between groups at $P < 0.05$.

Flag-NT-PGC-1 α viral infection but without incubation with anti-Flag antibody show no evident fluorescence (data not shown), indicating the specificity of the anti-Flag antibody used. Finally, as a positive control for anti-Flag antibody accessibility to muscle fiber nuclei, we transfected muscle fibers with nuclear targeted Flag-tagged NFATc1 and found strong nuclear staining with anti-Flag antibody (Figure 1(c)), thus establishing nuclear penetration of the anti-Flag antibody.

3.2. Activation of PKA Increases Nuclear Flag-NT-PGC-1 α . Recent studies in adipocytes and CHO-K1 cells have shown that activation of PKA can significantly increase the nuclear content of NT-PGC-1 α [12, 13]. To test whether this regulation mechanism also exists in skeletal muscle fibers, we treated muscle fibers with 1 mM dbcAMP for 1 h in culture medium in the tissue culture incubator, as previously used to activate PKA in CHO-K1 cells [13]. Our results show that the Flag-NT-PGC-1 α fluorescent staining was stronger in nuclei of fibers exposed to dbcAMP (Figure 2(a), dbcAMP) than in control fibers (Figure 2(a), control). The Flag-NT-PGC-1 α n/c fluorescence ratio was significantly

increased from 0.71 ± 0.03 in control to 0.98 ± 0.07 in dbcAMP-treated fibers (Figure 2(b); $P < 0.05$), a 1.4-fold increase. The nuclear increase of Flag-NT-PGC-1 α after 1 h treatment of dbcAMP found here in skeletal muscle fibers is very close to what has been previously obtained in CHO-K1 cells (about 1.4 fold) and in differentiated adipocytes (about 1.5 fold) [13]. Together, these results support the notion that PKA regulates the subcellular distribution of NT-PGC-1 α and is thereby involved in modulation of the NT-PGC-1 α -dependent signaling pathway in muscle fibers. In brown adipocytes, it has been shown that PKA-dependent regulation of nuclear content of NT-PGC-1 α plays a role in the transcriptional activation of UCP1 and CIDEA [13], but the downstream signaling pathway of NT-PGC-1 α in skeletal muscle remains to be determined.

3.3. Muscle Activity Does Not Cause Nuclear Translocation of Flag-NT-PGC-1 α . In previous studies from our laboratory, we found that repetitive muscle fiber activity elicited by electric field stimulation of isolated FDB fibers is effective for activating nuclear-cytoplasmic redistribution of expressed GFP fusion proteins of the transcriptional regulators NFATc1

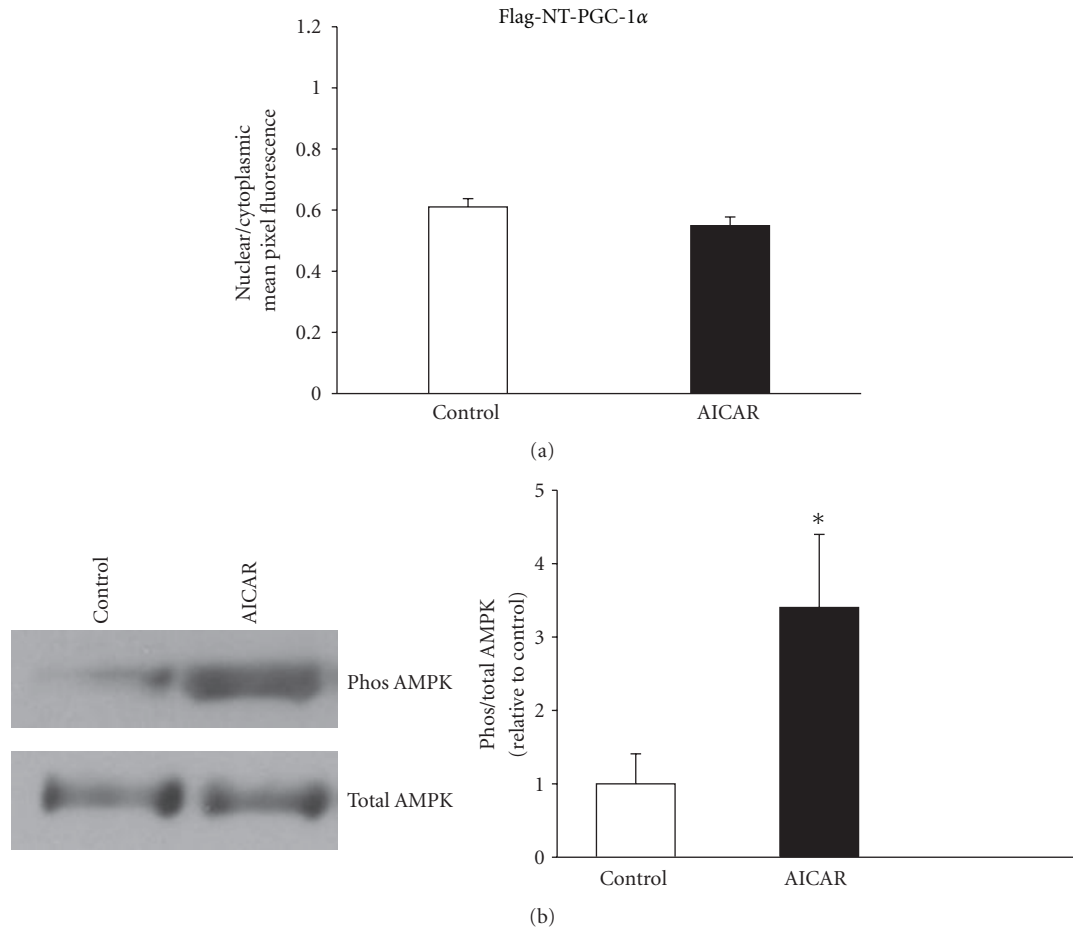


FIGURE 4: Activation of AMPK does not alter the subcellular distribution of Flag- NT-PGC-1 α in muscle fibers. (a) The n/c fluorescence ratio of Flag-NT-PGC-1 α in muscle fibers with (AICAR) or without (control) 2 mM AICAR treatment for 5 h in culture medium in the tissue culture incubator. n/c values from 20 nuclei from 20 randomly selected different fibers were averaged to give the mean value for each group. (b) Representative Western blots showing the effect of AICAR treatment on AMPK activation. Protein expression was quantified and averaged from 5 independent treatments. Phos AMPK, phospho-AMPK. Asterisk indicates statistical significance between groups at $P < 0.05$.

(NFATc1-GFP) and HDAC4 (HDAC4-GFP) and that both of these effects are mediated by elevated Ca^{2+} , NFATc1-GFP via Ca^{2+} dependent activation of calcineurin [16, 18], and HDAC4-GFP via Ca^{2+} dependent activation of CaM kinase [19]. Exercise/muscle contraction has also been found to increase the nuclear protein content of full-length PGC-1 α [5, 6]. Since nuclear NT-PGC-1 α has been shown to co-activate PPAR receptors as does the full-length PGC-1 α [12], it is of interest to determine whether stimulation of muscle fibers can also induce the nuclear accumulation of NT-PGC-1 α in FDB fibers. Our results show that the nuclear Flag-NT-PGC-1 α fluorescence of fibers stimulated continuously for 4 h at 10 Hz (Figure 3(a), stimulation) was essentially the same as in fibers from a parallel culture kept under control conditions without stimulation (Figure 3(a), control). The mean Flag-NT-PGC-1 α n/c fluorescence ratio was 0.62 ± 0.03 in control and 0.59 ± 0.03 in stimulated fibers (Figure 3(b); $P > 0.05$). Thus, Flag-NT-PGC-1 α does not translocate into the fiber nuclei in response to 4 h of continuous 10 Hz stimulation.

In order to verify the effectiveness of 10 Hz continuous stimulation on isolated FDB fibers, in separate experiments we infected fibers with adenovirus encoding NFATc1-GFP. Two days later, fibers were stimulated continuously for 4 h at 10 Hz, the same stimulation pattern used for the Flag-NT-PGC-1 α expressing fibers above. As previously reported [16, 18], NFATc1-GFP fusion protein is present predominantly at the sarcomeric Z line in the cytoplasm of nonstimulated cultured adult FDB fibers (Figure 3(c), control). 4 h of 10 Hz continuous stimulation markedly increased the nuclear NFATc1-GFP fluorescence (Figure 3(c), stimulation), so FDB fibers clearly respond to this stimulus pattern. Thus, 10 Hz muscle fiber activity can cause nuclear accumulation of the transcription factor NFATc1-GFP, but not of Flag-NT-PGC-1 α . However, it remains to be determined whether repetitive muscle activity results in modification of the expression level of endogenous NT-PGC-1 α .

It was previously reported that activation of p38 MAPK, which phosphorylates PGC-1 α on Thr-262, Ser-265, and Thr-298 [8], increases the activity and nuclear protein

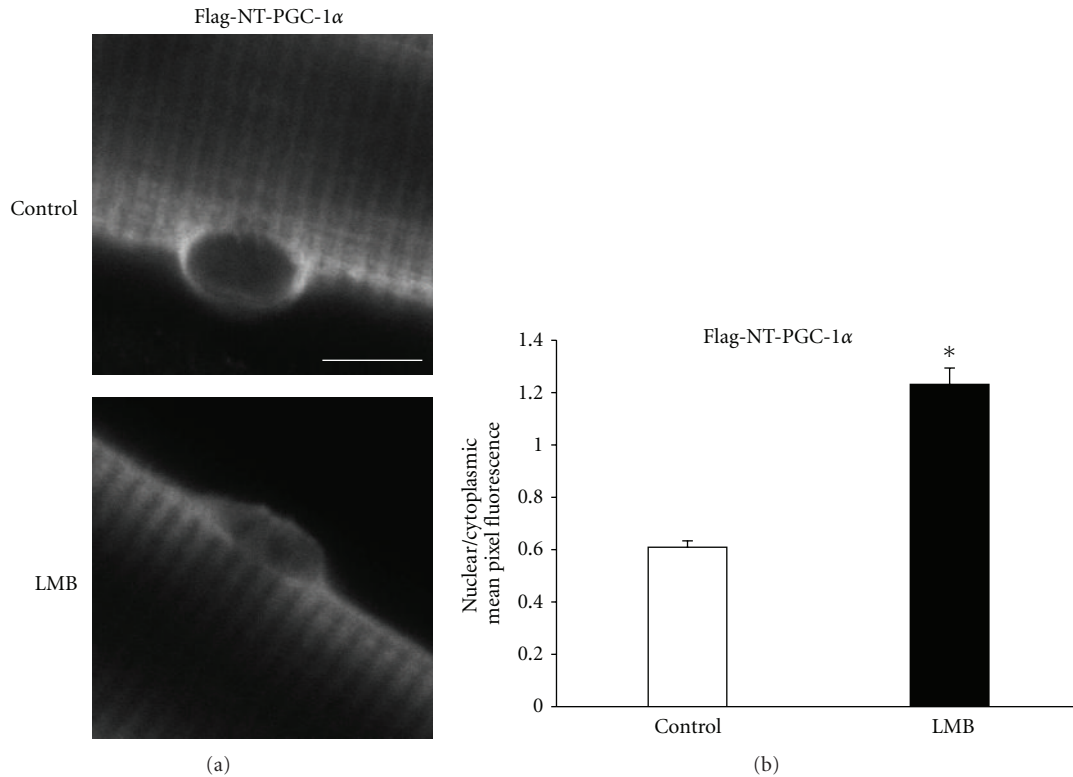


FIGURE 5: Inhibition of CRIM1 increases nuclear accumulation of Flag-NT-PGC-1 α . (a) Representative images of Flag-NT-PGC-1 α in a control fiber (control) and that of another fiber treated with 40 nM CRIM1 inhibitor leptomycin B (LMB) for 20 h in culture medium in the tissue culture incubator. Scale bar, 10 μ m. (b) The n/c fluorescence ratio of Flag-NT-PGC-1 α in muscle fibers with (LMB) or without (control) leptomycin B treatment. n/c values from 40 nuclei from 40 randomly selected different fibers were averaged to give the mean value for each group. Asterisk indicates statistically significant difference between groups at $P < 0.05$.

level of full length PGC-1 α in various tissues, including skeletal muscle [7–9]. Exercise/muscle contraction results in increased phosphorylation of p38 MAPK [9]. Using Western blot analysis, we found that 4 h of continuous stimulation can significantly increase the level of p38 MAPK phosphorylation in cultured FDB muscle fibers (Figure 3(d)). However, despite this increase in MAPK activation, there was no evident nuclear accumulation of Flag-NT-PGC-1 α as discussed above, even though NT-PGC-1 α contains two of the three p38 MAPK phosphorylation sites (Thr-262, Ser-265). These results suggest that p38 MAPK is not involved in the regulation of the subcellular distribution of NT-PGC-1 α in muscle fibers. Whether p38 MAPK plays a role or not in regulation of the protein stability and activity of endogenous NT-PGC-1 α as it does for the full-length PGC-1 α in muscle fibers will be an interesting question for future study.

3.4. Activation of AMPK Has No Effect on the Subcellular Distribution of Flag-NT-PGC-1 α . It was previously reported that AMPK can directly phosphorylate full-length PGC-1 α at residues Thr-177 and Ser-570 [11] and activate PGC-1 α -dependent signaling pathways in skeletal muscle [10, 11]. As NT-PGC-1 α contains one of the AMPK-phosphorylation sites, we next tested whether activation of AMPK can increase the nuclear accumulation of NT-PGC-1 α in skeletal muscle

fibers. Cultured FDB muscle fibers expressing Flag-NT-PGC-1 α were treated for 5 h with 2 mM of AICAR, a powerful cell permeable AMP mimic for activating AMPK [20]. After 5 h of incubation with or without AICAR, fibers were fixed and stained with anti-Flag antibody. Fibers treated with AICAR exhibited similar nuclear Flag-NT-PGC-1 α protein fluorescence as the control group. The mean Flag-NT-PGC-1 α n/c fluorescence ratio was 0.61 ± 0.03 in control and 0.55 ± 0.03 in AICAR-treated fibers (Figure 4(a); $P > 0.05$). Figure 4(b) shows that 5 h of AICAR treatment did significantly increase the phosphorylation of AMPK. These results demonstrate that activation of AMPK has no effect on the subcellular distribution of Flag-NT-PGC-1 α . One hour treatment with AICAR, or one hour of continuous electrical field stimulation at 10 Hz, caused no change in the nuclear/cytoplasmic distribution of Flag-NT-PGC-1 α (Supplementary Figure 1 available online at doi: 10.1155/2012/989263).

3.5. Inhibition of CRIM1 Induces Only Modest Nuclear Accumulation of Flag-NT-PGC-1 α . NT-PGC-1 α has a predicted size about 30 kDa which should allow it to be freely diffusible between nucleus and cytosol via the nuclear pores, a mechanism which is independent of CRIM1. However, previous studies showed that treatment with the CRIM1

nuclear export inhibitor leptomycin B (LMB) increased the nuclear content of NT-PGC-1 α in adipocytes and CHO-K1 cells [12, 13], suggesting that NT-PGC-1 α shuttles from the nucleus to the cytoplasm in these cells at least partially via a CRM1-dependent efflux pathway. Whether nucleocytoplasmic shuttling of NT-PGC-1 α proteins via a CRM1-dependent pathway also occurs in skeletal muscle is not known. To address this issue, we treated muscle fibers expressing Flag-NT-PGC-1 α with 40 nM leptomycin B. Our results show that the Flag-NT-PGC-1 α fluorescent staining was enhanced in nuclei of fibers exposed to leptomycin B (Figure 5(a), LMB) compared to control fibers (Figure 5(a), control). The Flag-NT-PGC-1 α n/c fluorescence ratio was significantly increased from 0.61 ± 0.02 in control to 1.23 ± 0.06 in fibers treated with leptomycin B for 20 h (Figure 5(b); $P < 0.05$). However, the extent of nuclear accumulation of Flag-NT-PGC-1 α in resting muscle fibers with blocked CRM1-dependent nuclear export is much lower than that previously observed for other transcriptional regulators such as NFATc1 and HDAC [18, 19], which are too large to pass passively through the nuclear pores.

The relatively low nuclear accumulation of Flag-NT-PGC-1 α in the presence of leptomycin B (Figure 5) compared to other transcriptional regulators such as NFATc1 [18] or HDAC4 [19] in adult muscle fibers indicates that either the unidirectional rate of nuclear influx of Flag-NT-PGC-1 α is extremely low so that there was little entry of Flag-NT-PGC-1 α into the muscle fiber nuclei during the 20 h exposure to leptomycin B or, more likely, that there is a CRM1-independent pathway [21] for nuclear efflux of Flag-NT-PGC-1 α . In this case, assuming that efflux is proportional to nuclear concentration and that the nuclear volume is negligible compared to the cytoplasm, the approximate doubling of n/c fluorescence ratio in exposure to leptomycin B indicates that nuclear efflux of Flag-NT-PGC-1 α via the leptomycin B insensitive pathway would have doubled in the presence of leptomycin B, so about half of the nuclear efflux in resting fibers in the absence of leptomycin B would be via the CRM1-independent pathway. If the CRM1-independent pathway is passive efflux via nuclear pores, which is likely since Flag-NT-PGC-1 α is below the cut off size for passive movement through the nuclear pores, Flag-NT-PGC-1 α would be distributed passively between nucleus and cytoplasm in the steady state in the case of full blockade of the CRM1-dependent pathway by leptomycin B. In that case the free concentration of Flag-NT-PGC-1 α would be the same in the nucleus and cytoplasm. The slightly higher nuclear than cytoplasmic concentration of total (i.e., free plus bound) Flag-NT-PGC-1 α (1.23 fold; see above) would indicate that fraction of bound Flag-NT-PGC-1 α would be slightly higher in the nucleus than in the cytoplasm. Whether the Flag tag on Flag-NT-PGC-1 α might influence its nuclear/cytoplasmic distribution in muscle fibers remains to be determined. The possibility of rapid intranuclear ubiquitination followed by proteasomal degradation [14] of Flag-NT-PGC-1 α within the nucleus as a mechanism for lowering nuclear Flag-NT-PGC-1 α is unlikely since ubiquitination occurs at the N-terminal residue [14], which is Flag tagged in our Flag-NT-PGC-1 α construct.

3.6. Other Considerations and Conclusion. Overexpression of full length PGC-1 α , which is predominantly nuclear, gives rise to an increase in mitochondrial number and oxidative capacity in skeletal muscle [2, 3]. It will be interesting to determine in future studies whether overexpression of NT-PGC-1 α , which is only partially nuclear, would also produce such effects on mitochondrial number and oxidative capacity.

In conclusion, our results suggest that in adult skeletal muscle fibers the nuclear-cytoplasmic distribution and regulation of NT-PGC-1 α is very different from that of the full-length PGC-1 α , which is exclusively nuclear.

Acknowledgments

The authors thank Dr. Thomas W. Gettys (Pennington Biomedical Research Center, LA) for providing the recombinant adenovirus of Flag-tagged NT-PGC-1 α and Minerva Contreras for technical assistance. This work was supported by NIH Grant R01-AR056477 from the National Institute of Arthritis and Musculoskeletal and Skin Diseases.

References

- [1] P. Puigserver, Z. Wu, C. W. Park, R. Graves, M. Wright, and B. M. Spiegelman, "A cold-inducible coactivator of nuclear receptors linked to adaptive thermogenesis," *Cell*, vol. 92, no. 6, pp. 829–839, 1998.
- [2] J. Lin, H. Wu, P. T. Tarr et al., "Transcriptional co-activator PGC-1 α drives the formation of slow-twitch muscle fibres," *Nature*, vol. 418, no. 6899, pp. 797–801, 2002.
- [3] Z. Wu, P. Puigserver, U. Andersson et al., "Mechanisms controlling mitochondrial biogenesis and respiration through the thermogenic coactivator PGC-1," *Cell*, vol. 98, no. 1, pp. 115–124, 1999.
- [4] O. H. Mortensen, L. Frandsen, P. Schjerling, E. Nishimura, and N. Grunnet, "PGC-1 α and PGC-1 β have both similar and distinct effects on myofiber switching toward an oxidative phenotype," *American Journal of Physiology, Endocrinology and Metabolism*, vol. 291, no. 4, pp. E807–E816, 2006.
- [5] A. S. Mathai, A. Bonen, C. R. Benton, D. L. Robinson, and T. E. Graham, "Rapid exercise-induced changes in PGC-1 α mRNA and protein in human skeletal muscle," *Journal of Applied Physiology*, vol. 105, no. 4, pp. 1098–1105, 2008.
- [6] S. Terada and I. Tabata, "Effects of acute bouts of running and swimming exercise on PGC-1 α protein expression in rat epitrochlearis and soleus muscle," *American Journal of Physiology, Endocrinology and Metabolism*, vol. 286, no. 2, pp. E208–E216, 2004.
- [7] D. Knutti, D. Kressler, and A. Kralli, "Regulation of the transcriptional coactivator PGC-1 via MAPK-sensitive interaction with a repressor," *Proceedings of the National Academy of Sciences of the United States of America*, vol. 98, no. 17, pp. 9713–9718, 2001.
- [8] P. Puigserver, J. Rhee, J. Lin et al., "Cytokine stimulation of energy expenditure through p38 MAP kinase activation of PPAR γ coactivator-1," *Molecular Cell*, vol. 8, no. 5, pp. 971–982, 2001.
- [9] Z. Yan, P. Li, and T. Akimoto, "Transcriptional control of the Pgc-1 α gene in skeletal muscle in vivo," *Exercise and Sport Sciences Reviews*, vol. 35, no. 3, pp. 97–101, 2007.

- [10] I. Irrcher, P. J. Adhietty, T. Sheehan, A. M. Joseph, and D. A. Hood, "PPAR γ coactivator-1 α expression during thyroid hormone- and contractile activity-induced mitochondrial adaptations," *American Journal of Physiology—Cell Physiology*, vol. 284, no. 6, pp. C1669–C1677, 2003.
- [11] S. Jäer, C. Handschin, J. St-Pierre, and B. M. Spiegelman, "AMP-activated protein kinase (AMPK) action in skeletal muscle via direct phosphorylation of PGC-1 α ," *Proceedings of the National Academy of Sciences of the United States of America*, vol. 104, no. 29, pp. 12017–12022, 2007.
- [12] Y. Zhang, P. Huypens, A. W. Adamson et al., "Alternative mRNA splicing produces a novel biologically active short isoform of PGC-1 α ," *Journal of Biological Chemistry*, vol. 284, no. 47, pp. 32813–32826, 2009.
- [13] J. S. Chang, P. Huypens, Y. Zhang, A. Kralli, and T. W. Gettys, "Regulation of NT-PGC-1 α subcellular localization and function by protein kinase A-dependent modulation of nuclear export by CRM1," *Journal of Biological Chemistry*, vol. 285, no. 23, pp. 18039–18050, 2010.
- [14] J. Trausch-Azar, T. C. Leone, D. P. Kelly, and A. L. Schwartz, "Ubiquitin proteasome-dependent degradation of the transcriptional coactivator PGC-1 α via the N-terminal pathway," *Journal of Biological Chemistry*, vol. 285, no. 51, pp. 40192–40200, 2010.
- [15] Y. Liu, S. L. Carroll, M. G. Klein, and M. F. Schneider, "Calcium transients and calcium homeostasis in adult mouse fast-twitch skeletal muscle fibers in culture," *American Journal of Physiology—Cell Physiology*, vol. 272, no. 6, pp. C1919–C1927, 1997.
- [16] Y. Liu, Z. Cseresnyés, W. R. Randall, and M. F. Schneider, "Activity-dependent nuclear translocation and intranuclear distribution of NFATc in adult skeletal muscle fibers," *Journal of Cell Biology*, vol. 155, no. 1, pp. 27–39, 2001.
- [17] T. Shen, Y. Liu, M. Contreras, E. O. Hernández-Ochoa, W. R. Randall, and M. F. Schneider, "DNA binding sites target nuclear NFATc1 to heterochromatin regions in adult skeletal muscle fibers," *Histochemistry and Cell Biology*, vol. 134, no. 4, pp. 387–402, 2010.
- [18] T. Shen, Y. Liu, Z. Cseresnyés, A. Hawkins, W. R. Randall, and M. F. Schneider, "Activity- and calcineurin-independent nuclear shuttling of NFATc1, but Not NFATc3, in adult skeletal muscle fibers," *Molecular Biology of the Cell*, vol. 17, no. 4, pp. 1570–1582, 2006.
- [19] Y. Liu, W. R. Randall, and M. F. Schneider, "Activity-dependent and -independent nuclear fluxes of HDAC4 mediated by different kinases in adult skeletal muscle," *Journal of Cell Biology*, vol. 168, no. 6, pp. 887–897, 2005.
- [20] R. C. Ho, N. Fujii, L. A. Witters, M. F. Hirshman, and L. J. Goodyear, "Dissociation of AMP-activated protein kinase and p38 mitogen-activated protein kinase signaling in skeletal muscle," *Biochemical and Biophysical Research Communications*, vol. 362, no. 2, pp. 354–359, 2007.
- [21] E. Saijou, T. Itoh, K. W. Kim, S. I. Iemura, T. Natsume, and A. Miyajima, "Nucleocytoplasmic shuttling of the zinc finger protein EZI is mediated by importin-7-dependent nuclear import and CRM1-independent export mechanisms," *Journal of Biological Chemistry*, vol. 282, no. 44, pp. 32327–32337, 2007.

Research Article

Force Characteristics of the Rat Sternomastoid Muscle Reinnervated with End-to-End Nerve Repair

Stanislaw Sobotka^{1,2} and Liancai Mu¹

¹Upper Airway Research Laboratory, Department of Research, Hackensack University Medical Center, 30 Prospect Avenue, Jurist Research Building, Hackensack, NJ 07601, USA

²Department of Neurosurgery, Mount Sinai School of Medicine, New York, NY 10029, USA

Correspondence should be addressed to Stanislaw Sobotka, ssobotka@humed.com

Received 1 June 2011; Revised 8 September 2011; Accepted 22 September 2011

Academic Editor: Henk Granzier

Copyright © 2011 S. Sobotka and L. Mu. This is an open access article distributed under the Creative Commons Attribution License, which permits unrestricted use, distribution, and reproduction in any medium, provided the original work is properly cited.

The goal of this study was to establish force data for the rat sternomastoid (SM) muscle after reinnervation with nerve end-to-end anastomosis (EEA), which could be used as a baseline for evaluating the efficacy of new reinnervation techniques. The SM muscle on one side was paralyzed by transecting its nerve and then EEA was performed at different time points: immediate EEA, 1-month and 3-month delay EEA. At the end of 3-month recovery period, the magnitude of functional recovery of the reinnervated SM muscle was evaluated by measuring muscle force and comparing with the force of the contralateral control muscle. Our results demonstrated that the immediately reinnervated SM produced approximately 60% of the maximal tetanic force of the control. The SM with delayed nerve repair yielded approximately 40% of the maximal force. Suboptimal recovery of muscle force after EEA demonstrates the importance of developing alternative surgical techniques to treat muscle paralysis.

1. Introduction

The sternocleidomastoid (SCM) is a long neck muscle with two bellies, a medially located sternomastoid (SM) and laterally positioned cleidomastoid (CM). Innervation of the SM originates from the accessory nerve (eleventh cranial pair) [1]. The SM is involved in the control of head movements and causes cranial displacement of the sternum and ribcage during conscious respiratory efforts [2–6]. It has been widely used as the muscle and myocutaneous flap for the reconstruction of oral cavity and facial defects [7, 8] and as a candidate for reinnervation studies [9].

The SM muscle is not active during resting ventilation but is recruited only during higher ventilatory demands [10]. Damage to the supplying nerve leads to significant atrophy in the muscle. The SM muscle is a good target for development of new reinnervation techniques due to its superficial location in the neck, easy surgical access, and a single nerve supply [9]. In addition, several neighboring cervical strap muscles (i.e., sternohyoid, sternothyroid, and omohyoid) and their innervating nerves could be potentially used as donors to reinnervate the paralyzed SM muscle [9].

End-to-end nerve repair has gained popularity in the use for restoring paralyzed muscles [11]. Many other techniques of reinnervation like end-to-side neurography, autologous nerve grafting, tubulization with a nerve guide tube, direct nerve implantation, and nerve-muscle pedicle transfer were also developed [9, 12]. However, despite advances in microsurgery and extensive studies on nerve repair, the presently used reinnervation methods result in poor functional recovery [13]. As reported, results of nerve repair to date have been no better than fair, with only about 50% of patients regaining useful function [14, 15]. Hall [16] reviewed the degree of functional recovery after traumatic injury to a peripheral nerve in humans and stated that such recovery is rarely satisfactory.

Poor motor recovery after nerve end-to-end anastomosis (EEA) could be attributed to the inability of denervated muscles to accept reinnervation and to recover from denervation atrophy. It could also result from a reduced ability of injured motoneurons to regenerate their axons after prolonged axotomy [16, 17].

A new reinnervation technique developed in this laboratory called nerve-muscle-endplate band grafting (NMEG)

has been described [9]. This method could be more effective as compared to the end-to-end nerve repair technique. In the NMEG experiments, the experimentally paralyzed SM muscle was reinnervated by transplanting an NMEG harvested from a sternohyoid (SH) muscle. The NMEG contained a muscle block, a nerve branch with nerve terminals, and a motor endplate (MEP) band with numerous neuromuscular junctions.

Muscle force measurement is an objective method used to evaluate the functional outcome of reinnervation. However, to evaluate the success of a new reinnervation technique, the reference data assessing muscle force in an intact SM and an SM repaired with the standard technique are needed. We recently described the results of muscle force studies in the intact SM muscle of the rat [18]. However, in literature there are no data available on force produced by SM muscle reinnervated with the EEA method.

In the present study, we described the force characteristics of the rat SM muscle reinnervated with the classical EEA method. Muscle force was studied 3 months after nerve anastomosis with different delays (from 0 to 3 months) between nerve transection and repair. The muscle force characteristics obtained in the present study using the classical EEA nerve repair can be used as a reference for evaluating the extent of functional recovery produced by new reinnervation techniques.

2. Materials and Methods

2.1. Subjects. The experiments were performed on 25 adult (3.5 months old) Sprague-Dawley female rats (Charles River Laboratories, Mass), weighing 350–450 grams. We used female rats because their body weights become stable in adulthood (starting at about 3 months) [19]. Studies by Cantillon and Bradford [20] showed that there is no difference between the male and female rat in the contractile properties of upper airway muscles, both in young and old animals. The rats were provided with *ad libitum* access to food and water and housed in standard cages in a 22°C environment with a 12:12-h light-dark cycle. All experimental procedures were reviewed and approved by the Institutional Animal Care and Use Committee prior to the onset of our experiments. The experiments were performed in accordance with the *Guide for Care and Use of Laboratory Animals* published by the US National Institutes of Health (NIH Publication no. 85-23, revised 1996). All efforts were made to minimize the number of animals and their suffering in the experiments.

2.2. Description of Nerve Transection and Repair with EEA. Particulars regarding the surgical procedures and postoperative assessment have been described in our previous papers [9, 18]. Briefly, during each of the two stages of the operation, rats underwent general anesthesia with a mixture of ketamine (80 mg/kg body wt) and xylazine (5 mg/kg body wt) administered intraperitoneally. Supplementary doses were administered to maintain a constant depth of anesthesia. Under an Olympus SZX12 Stereo zoom surgical microscope (Olympus America Inc., Center Valley, Pa), a

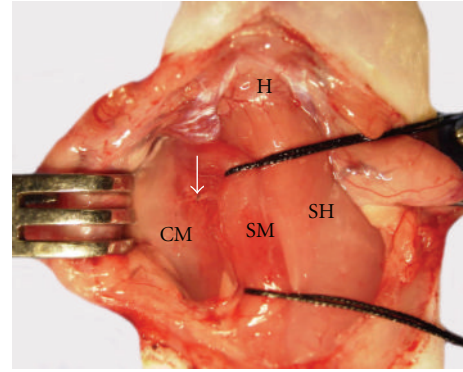


FIGURE 1: The SM nerve 3 months after transection and repair with EEA. Photograph from an open neck of a rat who underwent EEA procedure following transection of the SM nerve on the right side. After the SM was retracted medially by two sutures, its innervating nerve was visualized between the SM and cleidomastoid (CM) bellies. The SM nerve was transected and both nerve cut ends were united with two 10-0 nylon sutures (white arrow). H: hyoid bone; SH: sternohyoid muscle.

midline cervical incision was made extending from the hyoid bone to the sternum to expose the right SM muscle and its innervating nerve. During the first operation stage, the SM nerve was sharply transected approximately 3 mm proximal to the SM muscle. After surgery, the wound was closed in layers with interrupted simple sutures of 4-0 prolene. During the second operation stage, the transected right SM nerve was repaired in three different groups of rats (7 rats in each group) with two 10-0 interrupted epineurial sutures at different delay time points after nerve transection: immediately, 1-month delay, and 3-month delay. An additional group of 4 rats with SM nerve transection without nerve repair served as a denervation control for muscle weight evaluation. After the final operation, the rats were housed individually during a 3-month recovery period. Figure 1 illustrates the SM nerve 3 months after transection and repair with EEA.

2.3. Recording Setup. We built the acquisition system that provided user-controlled output signals (electrical stimulation to the nerve or muscle and the signal that controlled the length of the muscle) as well as recorded muscle force data. The system was assembled from a National Instruments multipurpose board (NI USB 6251, National Instruments, Austin, Tex) and an Aurora system (305-LR, Aurora Scientific, Aurora, Calif). It was controlled by a Dell laptop with the user written LabView (National Instruments) program. Data were analyzed offline with DIAdem software (National Instruments). The scheme of components and connections of the system is shown in Figure 2.

2.4. Muscle Attachment for Force Measurement. The details regarding the force measurement of the rat SM muscle have been provided in our recent publications [9, 18]. Briefly, the SM muscles on both sides were exposed under aseptic conditions. Each of the SM muscles was dissected free from the surrounding tissue. Care was taken so that the nerve branch

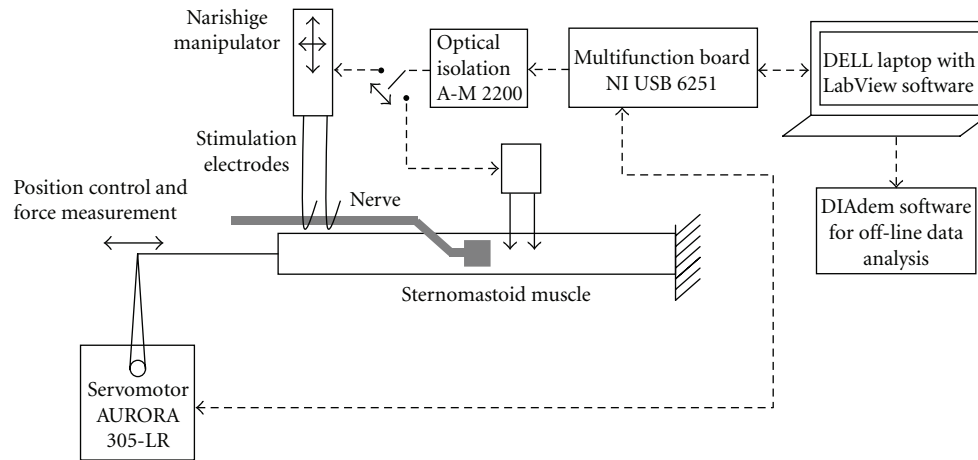


FIGURE 2: The schematic for the stimulation and recording system. The SM muscle is illustrated in the center. An Aurora Servomotor unit (305-LR) was used to stretch the SM muscle to optimal length and record muscle force. Electrical stimulation (200 ms trains of 200 Hz biphasic pulses) was generated by a National Instruments multifunction board (NI USB 6251). The stimulation trains were optically isolated from ground with an Optical Isolation Unit (A-M 2200) and directed to the SM nerve or directly to SM muscle. A Dell laptop with user-written LabView software was used to control the output signals (intensity of electrical stimulation and position of the servomotor lever) and to record the input signal (muscle force). Data were analyzed offline with National Instruments DIAdem software.

and blood vessels supplying the muscle remained intact. The rostral tendon of the SM was dissected free, cut close to the insertion, tied together with a 2-0 suture, and connected to a servomotor lever arm (Model 305B Dual-Mode Lever Arm System, Aurora Scientific Inc., Aurora, Ontario, Canada). The right SM nerve with EEA was identified, isolated from surrounding tissues, and placed on a bipolar stimulating electrode for nerve stimulation. On the control side, the muscle force of the left normal SM was measured by stimulating the intact SM nerve with the same bipolar electrode. In addition to nerve stimulation, direct muscle stimulation was also performed. The muscle was stimulated with a pair of needle electrodes inserted into the muscle at the level where the nerve enters the muscle. During the experiment, the rat was placed supine on a heating pad (homoeothermic blanket system, Stoelting, Wood Dale, Ill) and the core body temperature was monitored with a rectal thermistor and maintained at 36°C. The muscle and nerve examined were regularly bathed with warmed mineral oil throughout the testing to maintain muscle temperature between 35 and 36°C.

2.5. Stimulation Procedure. Functional reinnervation was evaluated using muscle force response to electrical stimulation at different intensities (0–1 mA). Optimal parameters of electrical stimulation of the SM nerve and muscle were established in our preliminary study on 10 control rats [18]. The stimulation signal used in this study consisted of a 200 ms train of biphasic pulses of constant current at a frequency of 200 pulses/s. Stimulation with a train duration of 200 ms was used to ensure that during stimulation, tetanic force reached a plateau in the fast-twitch SM muscle [21]. Each pulse was made of two opposite rectangular phases, with each phase lasting 0.2 ms. The stimulation was optically isolated from ground (optical isolation unit A-M 2200, A-M Systems, Sequim, Wash) and sent to two silver hook

electrodes separated by a 5 mm distance on which the stimulated nerve was placed. Alternately, the muscle was stimulated directly with two silver needle electrodes inserted in the muscle 10 mm rostral to the nerve entrance to the muscle. The separation distance between electrodes was 5 mm.

2.6. Statistical Analysis. Muscle force was analyzed with a two-factor repeated measure ANOVA followed by Tukey's test for post-hoc comparisons. Muscle weight was analyzed with a one-way ANOVA followed by Tukey's test. SAS/STAT 9.2 software (SAS Institute Inc., Cary, NC) was used in statistical comparisons.

3. Results

3.1. Stimulation of SM Muscle at Optimal Length. Muscle force characteristics were studied when the SM was stretched at an optimal length with a passive tension of 0.08 N. The selection of this tension level was based on the results of our previous study on 10 control rats [18]. That study showed that the SM muscle, when stretched with 0.08 N tension, is able to produce maximal muscle force (active muscle tension to electrical stimulation). The SM force declined to 60% at tensions of 0.02 N and 0.2 N. The same relationship between muscle force and muscle tension was confirmed in the present study in the reinnervated muscles. Figure 3 illustrates the group average of active muscle force produced by reinnervated SM muscles stretched at different passive tensions in rats which had EEA delayed for 3 months. Rats from this group were subjected to muscle denervation by a transection of the SM nerve. After a 3-month delay, the transected SM nerve was repaired with EEA. Three months after nerve repair, muscle force-tension characteristics were analyzed. The muscle force results from each subject were normalized by dividing muscle force data

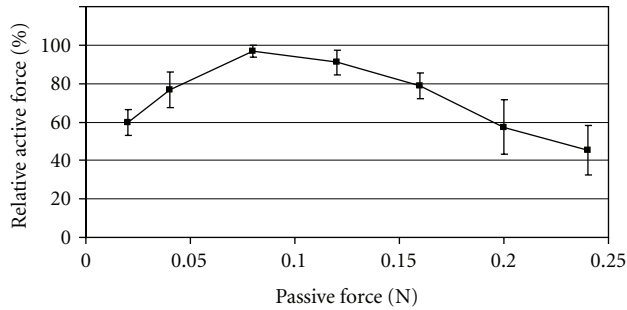


FIGURE 3: The active force generated by the SM muscle as a function of passive tension, with which the muscle was stretched just before stimulation. The active force was produced by the SM muscle in response to electrical stimulation of the SM nerve. A 200 ms train of 1 mA biphasic pulses at 200 pulses/s was used. Each phase of biphasic pulse lasted 0.2 ms. Data shown in this graph represent average active force, normalized by maximal force (observed at 0.08 N tension). Vertical bars represent standard error. The SM muscle was denervated for 3 months, repaired by end-to-end anastomosis, and left to recover for additional 3 months. The same muscle force-tension characteristic was observed in the noninjured control muscles [18].

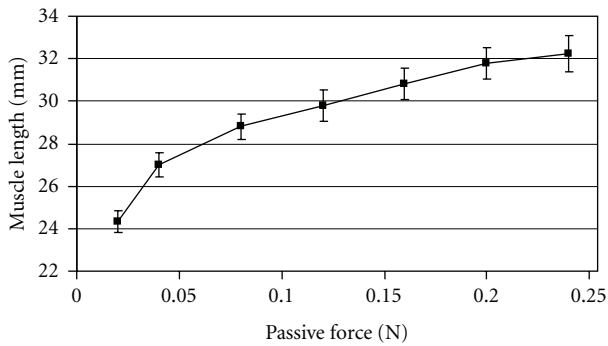


FIGURE 4: Length of the SM muscle as a function of the passive tension.

recorded at different tensions by the maximal muscle force observed at optimal tension (0.08 N). A 200 ms train of biphasic pulses (with a 0.2 ms pulse width) with a repetition frequency of 200 Hz was used to stimulate the SM nerve while the muscle was stretched with tensions ranging from 0.02 to 0.24 N. The stimulation current was set at 1 mA.

The length-tension relationship of the SM muscle is shown in Figure 4. The average length of the SM was 24.4 mm at a tension of 0.02 N, 28.8 mm at the optimal tension of 0.08 N and 31.8 mm at a tension of 0.2 N.

3.2. Force-Current Characteristics in Immediate EEA Group.

The averaged SM muscle force-current relationships observed in animals that underwent nerve transection and repair with EEA are shown in Figure 5 (immediate nerve repair group), Figure 6 (1-month delayed repair group), and Figure 7 (3-month delayed repair group). The contralateral intact SM muscle served as a control. Vertical bars illustrate standard error.

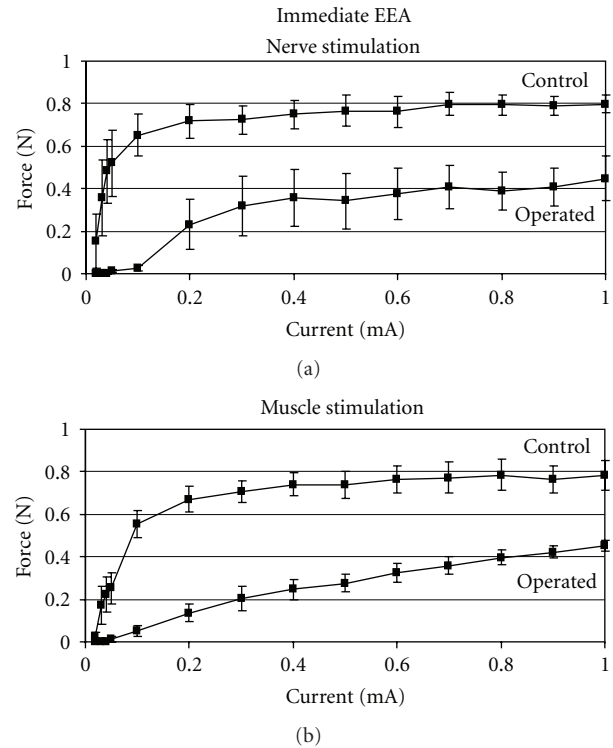


FIGURE 5: Force-current characteristics of the SM muscle in the immediate EEA group evoked by nerve stimulation or by direct muscle stimulation. (a) Illustrates superimposed force-current characteristics of the control and operated SM muscles evoked by stimulation provided to the SM nerve. In the control SM muscle the stimulation threshold, which produced noticeable muscle contraction, was 0.02 mA. Muscle force grew with increased stimulation current until it reached a plateau at 0.2 mA. The operated muscle had a larger stimulation threshold (with detectable muscle contraction at 0.1 mA) and produced a smaller force than the control muscle. (b) Shows superimposed force-current characteristics from the operated and control SM muscles evoked by direct SM muscle stimulation.

Averaged maximal muscle forces produced by the SM muscles using a 0–1 mA range of stimulation currents in different studied groups are shown in Figure 8. There is no significant difference in maximal muscle force between nerve and muscle stimulations on the control side (average data from control sides in all three EEA-operated groups are shown in Figure 8(b)). The maximal muscle force evoked by direct muscle stimulation was 97% of the maximal muscle force evoked by nerve stimulation in the group with immediate nerve repair, 91% in the group with 1 month delayed nerve repair, and 94% in the group with 3 month delayed nerve repair.

3.2.1. Control Muscle Force to Nerve Stimulation.

For the control SM muscle, the force-current function (Figure 5) had a threshold response at 0.02 mA. Muscle force grew with an increase of stimulation current until it reached a plateau at about 0.2 mA. Maximal muscle force produced by the SM muscle was about 0.8 N.

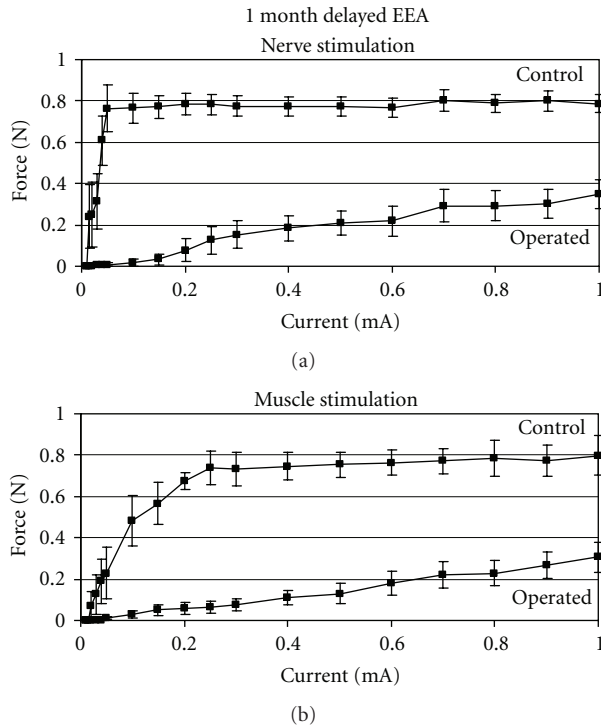


FIGURE 6: Force-current characteristics of the SM muscle in the 1-month delay EEA group. Muscle force in the operated and control SM muscles was produced by nerve stimulation (a) or by direct muscle stimulation (b). Note that the delayed reinnervation of the SM muscle produced a smaller muscle force as compared with immediate reinnervation (illustrated in Figure 5).

3.2.2. Operated Muscle Force to Nerve Stimulation. For the denervated and immediately repaired SM muscle, the nerve stimulation threshold to produce detectable muscle contraction was 0.1 mA (Figure 5). The maximal force of the operated muscle was 60.7% of the maximal force produced by the control, the nonoperated muscle on the contralateral side). A two-factor repeated ANOVA (group and intensity of stimulation as main factors) showed a statistically significant difference in muscle force between groups (operated and control muscles, $F = 17.94$, $P < 0.0005$) as well as the interaction of group with the intensity of stimulation ($F = 5.26$, $P < 0.005$ with a Greenhouse-Geisser correction).

3.2.3. Control Muscle Force to Muscle Stimulation. In addition to muscle force evoked by nerve stimulation, we also recorded muscle force produced in response to direct muscle stimulation. In the control muscles, similar maximal force-current relations were observed during nerve stimulation and direct muscle stimulation (Figure 5). Direct stimulation of the control muscle produced 97% of the maximal force observed during nerve stimulation. However, the stimulation threshold was smaller and the force-intensity curve reached a plateau earlier during nerve stimulation (as compared to direct muscle stimulation). A two-factor repeated ANOVA (group and intensity of stimulation as the main factors)

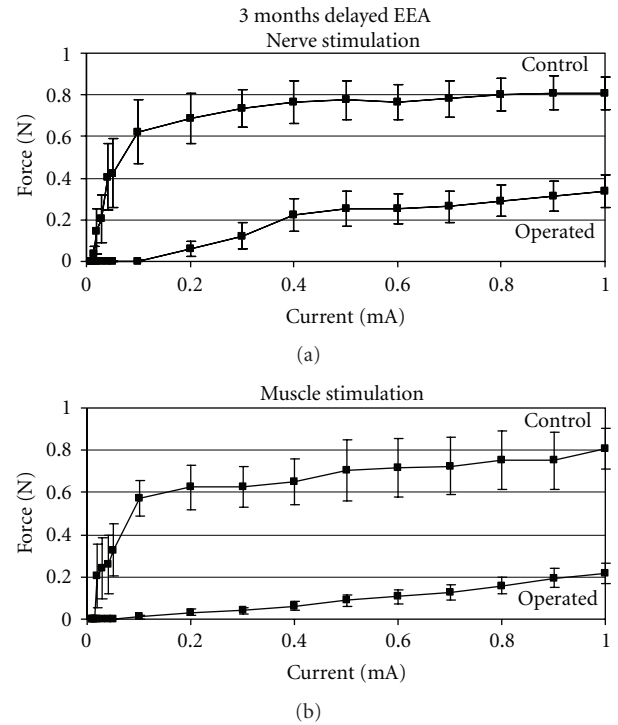


FIGURE 7: Force-current characteristics of the SM muscle in the 3-month delay EEA group. Muscle force in the operated and control SM muscles was produced by nerve stimulation (a) or by direct muscle stimulation (b).

showed no statistically significant difference between groups (force produced by muscle and nerve stimulation) but a statistically significant interaction of group with intensity of stimulation (14.08, $P < 0.0001$ with G-G correction).

3.2.4. Operated Muscle Force to Muscle Stimulation. Similar force-current relationships during nerve stimulation and during direct muscle stimulation were observed in the operated muscles (Figure 5). During muscle stimulation of the operated muscle, the threshold current of 0.1 mA produced visible muscle contractions. The maximal force of the operated muscle was 54.6% of the control (maximal force produced by the control, the nonoperated muscle on the contralateral side). Interestingly, variability of the muscle-force data to direct muscle stimulation was about 2-3 times smaller than that to nerve stimulation.

3.3. Force-Current Characteristics with Delayed Reinnervation. The SM muscles with a one-month as well as a three-month delay between nerve transection and repair showed a smaller muscle force as compared with the SM muscles, which were repaired immediately after denervation (Figures 5, 6, 7, and 8). The stimulation threshold was 0.1–0.2 mA. The maximal force of the operated muscle to nerve stimulation was reduced to about 39% of the maximal force produced by the control, the nonoperated muscle (39.8% in the 1-month delay EEA group and 38.0% in the 3-month

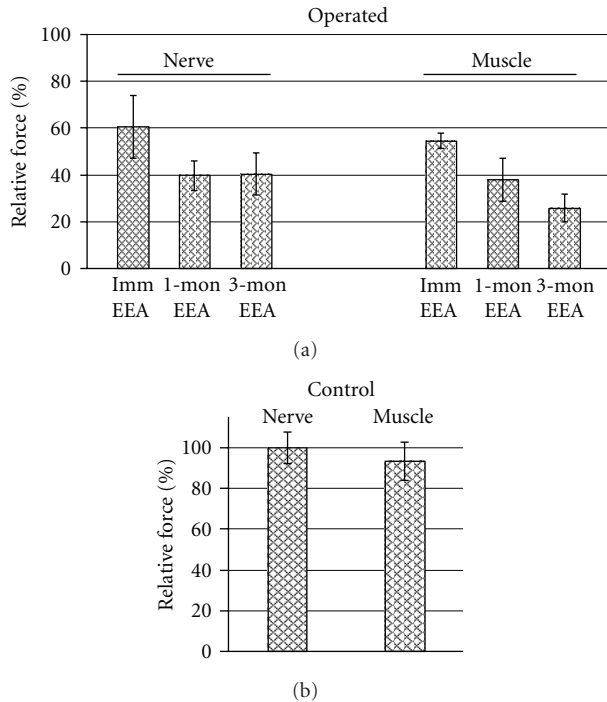


FIGURE 8: Average maximal muscle force of the SM muscle in different experimental conditions. (a) Shows maximal muscle force recorded from the operated SM muscles with immediate nerve repair after nerve transection (Imm EEA), with 1-month delay nerve repair (1-mon EEA) and with 3-month delay nerve repair (3-mon EEA). Data were normalized through dividing the maximal muscle force from the operated SM muscle by the maximal muscle force from the control SM muscle. Maximal muscle force produced by nerve stimulation is shown at the left side of the graph and by direct muscle stimulation at the right side of the graph. (b) Illustrates a comparison between the maximal muscle force evoked through nerve stimulation and through direct muscle stimulation of the control muscle (the intact muscle on the contralateral side). Muscle force (average from all three EEA groups) is presented as a percentage of maximal muscle force produced by nerve stimulation.

delay EEA group). A two-factor repeated ANOVA (group and intensity of stimulation as main factors) showed a statistically significant difference in muscle force between groups (control, immediately operated, and operated after 3-month delay, $F = 22.82$, $P < 0.0001$) as well as an interaction of group with intensity of stimulation ($F = 4.06$, $P < 0.002$ with a Greenhouse-Geisser correction). With direct muscle stimulation the maximal force of reinnervated muscle was reduced to 40.2% in 1-month delay EEA group and 25.8% in 3-month delay EEA group.

3.4. Muscle Weight. Figure 9 illustrates the effects of reinnervation on muscle mass. A normal SM muscle (on the control side) was compared to the operated SM muscle. The operated muscle was repaired with an immediate EEA (at the left), with a 3-month delayed EEA (in the middle) and was left denervated (at the right). The weight of the operated muscles

with immediate nerve repair was 78% of the weight of the muscles on control side (Figures 9 and 10).

Delayed EEA resulted in smaller muscle weight as compared with immediate EEA (Figures 9 and 10). Averaged muscle weight was 68% of the control for 1-month delay EEA and 64% of the control for 3-month delay EEA. The mean muscle weight of the EEA reinnervated muscles was greater than that of the denervated SM muscles (36% of the control). An ANOVA showed a significant difference between experimental groups ($F = 39.2$, $df = 3/21$, $P < 0.001$). Tukey's test showed that the immediate nerve repair group has a significantly larger weight than any other group. There was no significant difference in muscle weight between 1-month and 3-month delay EEA groups.

4. Discussion

4.1. Data Summary. Our present study provides the force characteristics of the rat SM muscle, which was denervated through an SM nerve transection and reinnervated at different time points with the classic EEA method.

The results showed only a partial recovery of muscle force at 3 months after reinnervation surgery. The recovery level of muscle force decreased when additional delay periods (1 or 3 months) were introduced between nerve transection and EEA nerve repair.

4.2. The Level of Force Recovery in the SM Muscle Reinnervated with EEA Immediately after Nerve Transection. The partial recovery of force generated by the reinnervated SM muscle was reflected in a higher stimulation threshold to produce any muscle contraction and smaller maximal muscle force. On the operated side, the threshold current needed to produce detectable SM muscle contraction was five times larger than that on the intact side. The maximal muscle force produced by a 0–1 mA nerve stimulation of the reinnervated SM muscle was reduced to about 60% of the force produced by the intact SM muscle.

Similar reduction of maximal muscle force after EEA repair was reported previously in other rat muscles. Meyer et al. [13] analyzed force produced by the soleus muscle following transection and traditional end-to-end epineurial repair of the sciatic nerve in the rat. By 32 weeks, the maximum isometric muscle force recovered to about 70% of the force of an intact muscle. Interestingly, recovery was much better (90% of normal) when the nerve went through a crush injury instead of transection. The authors concluded that poor recovery after nerve transection could be caused by the innervation of a muscle by inappropriate axons. Master et al. [22] studied the force produced by the gastrocnemius muscle in rats that had tibial nerve transected (4–5 mm proximal to the neuromuscular junction) followed by immediate neurorrhaphy. At 3 months postoperatively, the mean force of the operated gastrocnemius returned to 68% of the force produced by nonoperated one.

The mechanisms responsible for the reduced force produced by denervated and reinnervated muscles are not completely understood but may include muscle atrophy, reduced

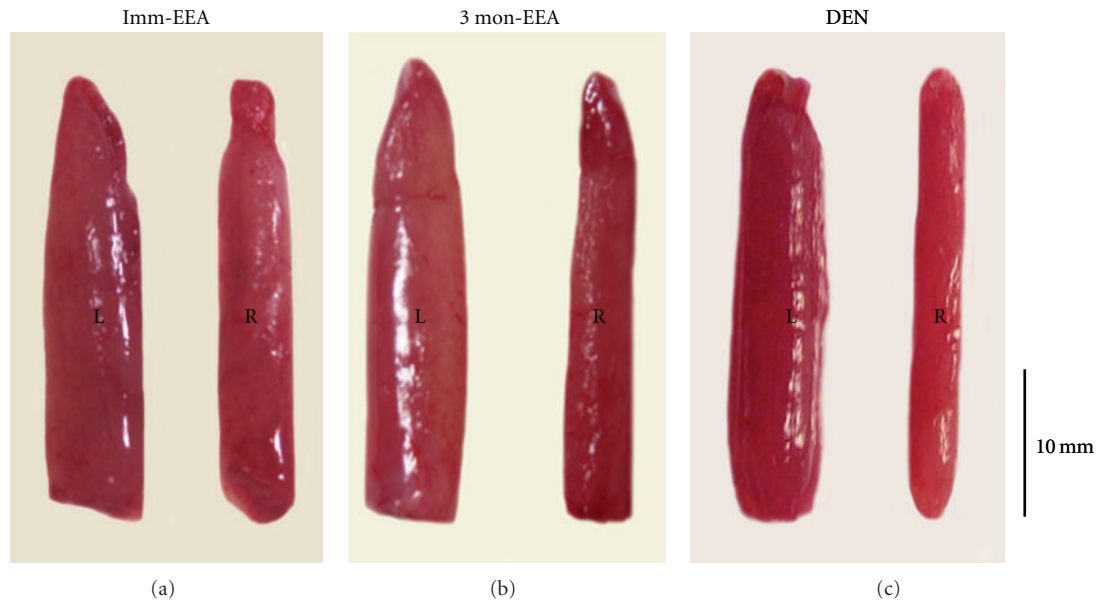


FIGURE 9: Photographs of the removed SM muscles showing the extent of muscle atrophy in three experimental groups. (a) A pair of SM muscles from a rat in the immediate EEA (Imm-EEA) group. (b) A pair of SM muscles from a rat in the 3-month delay EEA (3 mon-EEA) group. (c) A pair of SM muscles from a rat with denervation (DEN) of the right SM caused by nerve transection. In each rat, the left (L) SM was normal, whereas the right (R) SM was reinnervated or denervated.

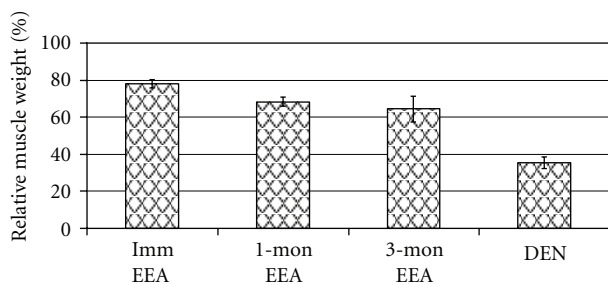


FIGURE 10: Average relative SM muscle weight in the denervation (DEN) and reinnervation experimental groups with immediate (Imm EEA), 1-month delay (1-mon EEA), and 3-month delay (3-mon EEA) nerve repair. SM muscle weight on the operated side was presented as a percentage of the SM muscle weight on the control side.

axonal numbers, altered axonal spatial organization, diminished muscle oxidative capacity, motor unit remodeling, and alternations in muscle fibers [23].

4.3. Decreased Level of Force Recovery in the SM Muscle with Delayed EEA Reinnervation. Delaying the process of reinnervation leads to an even larger decline in the ability of the SM muscle to generate force. As compared to immediate nerve repair, the 3-month delay between operation and reinnervation increased 2 times the threshold of current needed to produce muscle contraction. The maximal force produced by 0–1 mA nerve stimulation of SM muscle was reduced to about 40% of the force produced by the intact SM muscle.

Fu and Gordon [24] also reported poor functional recovery when nerve repair was delayed. They used a nerve cross-anastomosis paradigm in the rat. The tibial nerve was axotomized up to 12 months before it was cross-sutured to the distal stump of the freshly cut common peroneal nerve to innervate the freshly denervated tibialis anterior muscle. The authors concluded that prolonged axotomy significantly reduces the number of motor axons that regenerate and make functional connections with denervated muscle fibers.

Aydin et al. [25] denervated rat's gastrocnemius muscle via tibial nerve transection and delayed reconstruction of the nerve for periods ranging from 2 weeks to 1 year. They showed large deficits in muscle mass and maximum tetanic force caused by delayed reinnervation. The deficits were directly proportional to the denervation interval.

Swanson et al. [26] denervated the rat tibialis anterior by transecting the common peroneal nerve and after varying delays (ranging from 0 to 5 months) repaired the nerves with EEA. As in the present study, during muscle force testing, the muscle was stretched to the optimal tension needed to elicit a maximal force. Immediate reinnervation provided for very good maximal muscle force equal 94% of control (although this result was not very reliable because of large (30) standard error). After 3 months, muscle force fell to only 38%.

4.4. No Difference in Maximal Muscle Force Evoked by Muscle and Nerve Stimulations. One of physiological measures of muscle innervation is the ratio of tetanic muscle force to indirect and direct muscle stimulation. In normal muscles, this ratio is 100% and might be reduced in partially denervated muscles due to axonal damage, loss to neuromuscular junctions (NMJs), or severe defects in NMJ

synaptic transmission [27]. No difference in average maximal tetanic muscle force was observed in the present study when EEA reinnervated muscle contraction was evoked indirectly—through SM nerve stimulation, and with direct muscle stimulation. A similar observation that there is no difference between the maximal tetanic force evoked by nerve stimulation and by direct muscle stimulations, we reported previously in the SM muscle, which was repaired using the recently developed “nerve-muscle-endplate band grafting” (NMEG) technique [9]. Lack of power of the indirect/direct force ratio might be caused by “safety factor,” the excess of released transmitter during transmission of activity from nerve to muscle (the amount of transmitter released per nerve impulse is greater than that required to trigger an action potential in the muscle fiber). The safety factor allows neuromuscular transmission to remain effective under various difficult physiological conditions and stresses [28].

Interestingly, in the EEA reinnervated groups, the between-subject variability of maximal muscle force was larger during indirect (nerve) than during direct (muscle) stimulation. Gruner and Mason [29] showed considerable variation in recruitment of different muscle compartments during muscle force generation. The recruitment of different muscle compartments might be more variable in EEA group during indirect muscle stimulation (as compared to direct muscle stimulation), causing larger variability of the total tetanic muscle force.

4.5. Substantial Loss of Muscle Weight after Denervation. Large SM muscle atrophy (36% of the control muscle) caused by a 3-month denervation was illustrated in Figure 9. Similarly, strong denervation atrophy was observed in the rabbit tibialis anterior (TA) muscle by Ashley et al. [30]. After 2.5 months of denervation, muscle weight was reduced to 44% of weight observed in the innervated contralateral control TA. To prevent or at least limit the atrophy of the muscle during the denervation period (when final reinnervation had to be postponed) some authors used a two-stage operation process. In this process, an early temporary intermediate reinnervation (so called motor “baby sitting”) was followed by a final reinnervation [23]. However, the results of such double-stage operations produce worse outcomes than reinnervation made without intermediate reinnervation. Interestingly, muscle mass did not significantly differ between the normal and operated (denervated and repaired) groups which might suggest that denervation atrophy does not play a primary role in the reduction of tetanic force. Larger recovery of muscle mass (70% and 83%) than maximal tetanic force (43% and 70%) was observed in the rat soleus muscle, with its sciatic nerve transected, repaired with anastomosis, and studied 2 and 8 months after the repair [13]. However, a significant increase in muscle weight recovery was observed only in rats with long recovery time after reinnervation (between 4 and 8 months). There was no significant increase of muscle weight between 2 and 4 months after nerve repair. Swanson et al. [26] analyzed the weight of the rat tibialis anterior muscle and found that muscle weight after denervation and repair with EEA is reduced to 75% (of the

weight on the unoperated, contralateral side) for immediate EEA and to 59% after a 3-month delayed denervation. We observed similar levels of weight reduction in the present study in reinnervated SM muscles.

4.6. Need for the Search of Other Alternating Reinnervation Techniques. In general, nerve repair is accomplished by conventional end-to-end anastomosis when the two stumps can be approximated without tension [11, 31, 32]. A moderate functional recovery after nerve anastomosis points to the importance of developing new alternative surgical techniques, which may lead to the optimal reinnervation of paralyzed muscles. We hope that our new NMEG grafting method [9] has the potential to generate a better outcome than the commonly used EEA, especially with further refinement of the surgical procedure, the better placement of the donor NMEG graft at the recipient muscle, and by adding other factors facilitating the innervation process (e.g., electrical stimulation, neurotrophic factors, stem cells). Hall [16] in his review paper postulated that the next advances in nerve repair will depend upon manipulating the injury response around the injury site using cells and/or exogenous peptides rather than fine-tuning microsurgical techniques. Our recent studies [9] suggest that advances in muscle innervation techniques might be still critical component of a reinnervation strategy leading to optimal muscle reinnervation.

5. Conclusions

The present experiments describe characteristics of the force produced by the SM muscle of the rat with its supplying nerve severed and subsequently repaired with end-to-end anastomosis. Our study shows that a reinnervated SM muscle needs more than a 5-time larger nerve stimulation current to generate muscle contraction and is able to produce about 60% of tetanic force observed in the intact SM muscle.

The drop in the muscle force is more severe when there is an additional delay between nerve damage and repair. With a 3-month delayed reinnervation, the maximal tetanic muscle force drops to about 40% of the force observed in an intact SM muscle.

The results of this study provide reference levels for the tetanic force generated by the SM muscle in rats reinnervated with classic EEA. They can be used to assess the success of functional reinnervation produced by new reinnervation techniques.

Acknowledgments

This research was supported by NIH Grant no. 5R01DC008599 from the National Institute on Deafness and Other Communication Disorders (to L. Mu). The authors are grateful to Dr. Xiaolin Zhang for his excellent technical assistance during the surgical operations and data collection. They are also thankful to the anonymous reviewers for their constructive comments on the manuscript.

References

- [1] P. Caliot, P. Cabanie, V. Bousquet, and D. Midy, "A contribution to the study of the innervation of the sternocleidomastoid muscle," *Anatomia Clinica*, vol. 6, no. 1, pp. 21–28, 1984.
- [2] D. Costa, M. Vitti, D. De Oliveira Tosello, and R. Puglise Costa, "Participation of the sternocleidomastoid muscle on deep inspiration in man. An electromyographic study," *Electromyography and Clinical Neurophysiology*, vol. 34, no. 5, pp. 315–320, 1994.
- [3] A. De Troyer, P. A. Kirkwood, and T. A. Wilson, "Respiratory action of the intercostal muscles," *Physiological Reviews*, vol. 85, no. 2, pp. 717–756, 2005.
- [4] A. J. Raper, W. T. Thompson, W. Shapiro, and J. L. Patterson, "Scalene and sternomastoid muscle function," *Journal of Applied Physiology*, vol. 21, no. 2, pp. 497–502, 1966.
- [5] A. Legrand, E. Schneider, P. A. Gevenois, and A. De Troyer, "Respiratory effects of the scalene and sternomastoid muscles in humans," *Journal of Applied Physiology*, vol. 94, no. 4, pp. 1467–1472, 2003.
- [6] A. L. Hudson, S. C. Gandevia, and J. E. Butler, "The effect of lung volume on the co-ordinated recruitment of scalene and sternomastoid muscles in humans," *Journal of Physiology*, vol. 584, no. 1, pp. 261–270, 2007.
- [7] J. Hamilton, S. Avitia, and R. F. Osborne, "Designing a biped-icled sternocleidomastoid muscle flap for parotidectomy contour deformities," *Ear, Nose and Throat Journal*, vol. 85, no. 1, pp. 20–21, 2006.
- [8] V. Kumar, U. Gaud, M. Shukla, and M. Pandey, "Sternocleidomastoid island flap preserving the branch from superior thyroid artery for the reconstruction following resection of oral cancer," *European Journal of Surgical Oncology*, vol. 35, no. 9, pp. 1011–1015, 2009.
- [9] L. Mu, S. Sobotka, and H. Su, "Nerve-muscle-endplate band grafting: a new technique for muscle reinnervation," *Neurosurgery*, vol. 69, supplement 2, pp. 208–224, 2011.
- [10] G. A. Farkas and D. F. Rochester, "Contractile characteristics and operating lengths of canine neck inspiratory muscles," *Journal of Applied Physiology*, vol. 61, no. 1, pp. 220–226, 1986.
- [11] L. de Medinaceli, M. Prayon, and M. Merle, "Percentage of nerve injuries in which primary repair can be achieved by end-to-end approximation: review of 2,181 nerve lesions," *Microsurgery*, vol. 14, no. 4, pp. 244–246, 1993.
- [12] L. K. Kalliainen, P. S. Cederna, and W. M. Kuzon, "Mechanical function of muscle reinnervated by end-to-side neurotomy," *Plastic and Reconstructive Surgery*, vol. 103, no. 7, pp. 1919–1927, 1999.
- [13] R. S. Meyer, R. A. Abrams, M. J. Botte, J. P. Davey, and S. C. Bodine-Fowler, "Functional recovery following neurotomy of the rat sciatic nerve by epineurial repair compared with tubulization," *Journal of Orthopaedic Research*, vol. 15, no. 5, pp. 664–669, 1997.
- [14] B. J. F. Wong and R. L. Crumley, "Nerve wound healing: an overview," *Otolaryngologic Clinics of North America*, vol. 28, no. 5, pp. 881–895, 1995.
- [15] S. K. Lee and S. W. Wolfe, "Peripheral nerve injury and repair," *The Journal of the American Academy of Orthopaedic Surgeons*, vol. 8, no. 4, pp. 243–252, 2000.
- [16] S. Hall, "Nerve repair: a neurobiologist's view," *Journal of Hand Surgery*, vol. 26, no. 2, pp. 129–136, 2001.
- [17] X. Zhang, L. Mu, H. Su, and S. Sobotka, "Locations of the motor endplate band and motoneurons innervating the sternomastoid muscle in the rat," *Anatomical Record*, vol. 294, no. 2, pp. 295–304, 2011.
- [18] S. Sobotka and L. Mu, "Characteristics of tetanic force produced by the sternomastoid muscle of the rat," *Journal of Biomedicine and Biotechnology*, vol. 2010, Article ID 194984, 11 pages, 2010.
- [19] E. Uchino, T. Tsuzuki, and K. Inoue, "The effects of age and sex on seven elements in Sprague-Dawley rat organs," *Laboratory Animals*, vol. 24, no. 3, pp. 253–264, 1990.
- [20] D. Cantillon and A. Bradford, "Effects of age and gender on rat upper airway muscle contractile properties," *Journals of Gerontology*, vol. 55, no. 8, pp. B396–B400, 2000.
- [21] S. P. Cairns and A. F. Dulhunty, "The effects of β -adrenoceptor activation on contraction in isolated fast- and slow-twitch skeletal muscle fibres of the rat," *British Journal of Pharmacology*, vol. 110, no. 3, pp. 1133–1141, 1993.
- [22] D. Master, T. Cowan, S. Narayan, R. Kirsch, and H. Hoyen, "Involuntary, electrically excitable nerve transfer for denervation: results from an animal model," *Journal of Hand Surgery*, vol. 34, no. 3, pp. 479–e3, 2009.
- [23] K. Yoshimura, H. Asato, S. S. Jejurikar, P. S. Cederna, M. G. Urbanek, and W. M. Kuzon, "The effect of two episodes of denervation and reinnervation on skeletal muscle contractile function," *Plastic and Reconstructive Surgery*, vol. 109, no. 1, pp. 212–219, 2002.
- [24] S. Y. Fu and T. Gordon, "Contributing factors to poor functional recovery after delayed nerve repair: prolonged axotomy," *Journal of Neuroscience*, vol. 15, no. 5, pp. 3876–3885, 1995.
- [25] M. A. Aydin, S. E. Mackinnon, X. M. Gu, J. Kobayashi, and W. M. Kuzon, "Force deficits in skeletal muscle after delayed reinnervation," *Plastic and Reconstructive Surgery*, vol. 113, no. 6, pp. 1712–1718, 2004.
- [26] A. N. Swanson, S. W. Wolfe, M. Khazzam, J. Feinberg, J. Ehteshami, and S. Doty, "Comparison of neurotization versus nerve repair in animal model of chronically denervated muscle," *Journal of Hand Surgery*, vol. 33, no. 7, pp. 1093–1099, 2008.
- [27] A. Irintchev, A. Draguhn, and A. Wernig, "Reinnervation and recovery of mouse soleus muscle after long-term denervation," *Neuroscience*, vol. 39, no. 1, pp. 231–243, 1990.
- [28] S. J. Wood and C. R. Slater, "Safety factor at the neuromuscular junction," *Progress in Neurobiology*, vol. 64, no. 4, pp. 393–429, 2001.
- [29] J. A. Gruner and C. P. Mason, "Nonlinear muscle recruitment during intramuscular and nerve stimulation," *Journal of Rehabilitation Research and Development*, vol. 26, no. 2, pp. 1–16, 1989.
- [30] Z. Ashley, S. Salmons, S. Boncompagni et al., "Effects of chronic electrical stimulation on long-term denervated muscles of the rabbit hind limb," *Journal of Muscle Research and Cell Motility*, vol. 28, no. 4-5, pp. 203–217, 2007.
- [31] R. M. Braun, "Epineurial nerve suture," *Clinical Orthopaedics and Related Research*, vol. 163, pp. 50–56, 1982.
- [32] R. M. R. McAllister, S. E. A. Gilbert, J. S. Calder, and P. J. Smith, "The epidemiology and management of upper limb peripheral nerve injuries in modern practice," *Journal of Hand Surgery*, vol. 21, no. 1, pp. 4–13, 1996.

Research Article

The Application of Three-Dimensional Collagen-Scaffolds Seeded with Myoblasts to Repair Skeletal Muscle Defects

Jianqun Ma,^{1,2} Kyle Holden,^{1,3} Jinhong Zhu,³ Haiying Pan,^{1,3} and Yong Li⁴

¹The Laboratory of Molecular Pathology, Stem Cell Research Center, Children's Hospital of Pittsburgh, PA 15219, USA

²Department of Bioengineering, University of Pittsburgh, PA 15219, USA

³Department of Orthopedic Surgery, School of Medicine, University of Pittsburgh, PA 15213, USA

⁴Department of Pediatric Surgery, University of Texas, Medical School at Houston, TX 77030, USA

Correspondence should be addressed to Yong Li, yong.li.1@uth.tmc.edu

Received 30 June 2011; Accepted 11 September 2011

Academic Editor: Guy Benian

Copyright © 2011 Jianqun Ma et al. This is an open access article distributed under the Creative Commons Attribution License, which permits unrestricted use, distribution, and reproduction in any medium, provided the original work is properly cited.

Three-dimensional (3D) engineered tissue constructs are a novel and promising approach to tissue repair and regeneration. 3D tissue constructs have the ability to restore form and function to damaged soft tissue unlike previous methods, such as plastic surgery, which are able to restore only form, leaving the function of the soft tissue often compromised. In this study, we seeded murine myoblasts (C2C12) into a collagen composite scaffold and cultured the scaffold in a roller bottle cell culture system in order to create a 3D tissue graft *in vitro*. The 3D graft created *in vitro* was then utilized to investigate muscle tissue repair *in vivo*. The 3D muscle grafts were implanted into defect sites created in the skeletal muscles in mice. We detected that the scaffolds degraded slowly over time, and muscle healing was improved which was shown by an increased quantity of innervated and vascularized regenerated muscle fibers. Our results suggest that the collagen composite scaffold seeded with myoblasts can create a 3D muscle graft *in vitro* that can be employed for defect muscle tissue repair *in vivo*.

1. Introduction

Tissue loss usually results in significant dysfunction, physical deformities, and emotional pain long after treatment. Common causes of tissue loss include military injuries, such as high-velocity missiles, fragmenting exploding devices, and penetrating wounds associated with gunshots, and civilian injuries, such as blunt trauma attributed to automobile accidents [1]. Other causes of soft tissue removal include tumor removal, diabetic tissue damage, and irradiative injuries [2–5]. Current treatments of soft tissue injuries, such as skeletal muscle defects, resort to reconstructive plastic surgery, and skin grafting which are effective techniques to be employed in emergency repair and cosmetic applications, but often these techniques are unable to provide restoration of the function to the damaged tissue [6, 7].

Recent advances in biotechnology and bioengineering have offered novel approaches to repairing soft tissue defects by combining cell biology, gene transfer, biomaterials, and

bioreactors [8–12]. Among the new advances, three-dimensional biodegradable scaffolds provide the ability to restore form and also function to the injured area. In order to be successful, the 3D biodegradable scaffold needs to serve two purposes. First, the scaffold needs to have the physiologic and mechanical properties that mimic the *in vivo* native environment, and second, the scaffold needs to have the ability to allow for development and remodeling of the tissue in order to promote successful restoration of physiological function [13–15]. It is important for the scaffold to be biodegradable because nondegradable constructs implanted for prolonged time periods often induce an inflammatory response which can often compromise the tissue construct and the healing of the tissue [16–18].

Tissue and organ function are dependent on the presence of appropriate populations of differentiated cells, and therefore, it is important to incorporate proper cells in the 3D scaffold. This can be accomplished through rolling bottle cell culture systems which are advantageous, in comparison to

static cell seeding, in that a rolling bottle cell culture system improves cell seeding density and homogeneity within the scaffold [10, 19, 20]. This is accomplished through the slow revolutions of the culture bottles on the rolling device which produce a force significant enough to permit the cells to grow evenly in three dimensions [21]. Also the revolutions allow for nutrients to be provided to the cells while at the same time removing waste products through the constant movement of media bathing the cells [22].

In general, the artificial 3D scaffold provides an architecture on which seeded cells can organize and develop into the desired tissue for implantation. Once implanted in the soft tissue defect, the biodegradable scaffold provides an initial biomechanical structure for the replacement tissue until the cells produce an adequate extracellular matrix. During the deposition, organization, and formation of the newly generated extracellular matrix, the scaffold is either degraded or metabolized; eventually leaving a vital organ or tissue that restores, maintains, or improves tissue function. In this study, we built a 3D muscle graft by seeding C2C12 myoblasts into a biodegradable 3D collagen composite scaffold, and implanted it into a skeletal muscle defect mouse model *in vivo*. Immunostaining was employed to evaluate the effectiveness of the graft in improving vascularization, innervation, and regeneration of the damaged tissue.

2. Materials and Methods

2.1. C2C12 Myoblasts Transfected with Retroviral LacZ and LacZ Staining. C2C12 myoblasts were purchased from ATCC (American Type Culture Collection) and cultured in media (DMEM, Invitrogen) supplemented with 10% fetal bovine serum (FBS, Gibco, BR), 10% horse serum (HS), 1% penicillin/streptomycin (P/S), and 0.5% chick embryo extract (CEE). The culture media was removed and replaced with a 1:1 dilution of retroviral LacZ and culture media supplemented with 8 $\mu\text{g}/\text{mL}$ of polybrene. The cells were incubated in the solution for 6 hours at 5% CO_2 and 37°C. To ensure maximum transduction of the virus, the infection was done up to 3 times, and a LacZ staining was done after each infection to determine the efficiency of the infections. The LacZ staining consisted of fixing the cells in 1% glutaraldehyde solution (Sigma) for 2 minutes followed by washing with PBS. The cells were then incubated for 2 hours in a LacZ solution (225 mL PBS/25 mL KFE solution/250 μL of 2 M MgCl_2 /5 mL of X-gal) at 37°C. The cells were then visualized for analysis using bright field microscopy.

2.2. 3D Collagen Composite Scaffold and Cell Seeding. The 3D collagen composite scaffolds were purchased from BD Biosciences, (catalogue number 354613) and the scaffolds are of a cylindrical shape approximately 4.2–5.2 mm in diameter and 3.9–4.5 mm in height with a volume of 0.039 cm^3 . The average pore size of the scaffold is 100–200 μm and the hydration capacity is 25 μL . The weight and wet weight of the scaffolds are 3.5 mg and 45.0 mg, respectively, with an average wet tear strength of 0.48 ± 0.0131 lb/mm. The collagen composite scaffolds, derived from bovine hide, resemble the structure of collagen within the extracellular matrix, and are

able to support both short- and long-term differentiation of multiple cell types. The 3D scaffolds were individually placed into separate wells of a 48-well plate, and were immersed in a solution consisting of 200 μL of culture medium containing approximately 50,000 LacZ⁺ myoblasts. The scaffolds were then incubated in 37°C at 5% CO_2 for 1 hour.

2.3. Rolling Bottle Cell Culture System. The LacZ⁺ myoblast seeded scaffolds were transferred from the 48-well plates into Corning cell culture bottles containing 200 mL of culture media. The Corning cell culture bottles were placed on a Wheaton rolling device (Fischer Scientific) at a speed of 5 revolutions per minute (RPM). The Wheaton rolling device was then placed in an incubator at 37°C and 5% CO_2 for 3 weeks with periodic cell culture media changes.

2.4. Scaffold Sectioning and Immunostaining. *In vitro*, the scaffolds were harvested after 1, 2, and 3 weeks of culturing, and rinsed with PBS before being snap-frozen in 2-methyl butane precooled in liquid nitrogen and stored at -80°C . The scaffolds were then cryosectioned at 10 μm and prepared for immunostaining.

In vivo, scaffolds were harvested at various time points, and immunostaining was performed to detect CD31, vWF, dystrophin, neurofilament protein, and fast MyHC expression in injured GMs implanted with the myoblast seeded scaffolds. Tissue sections were fixed in 4% formalin for 5 minutes followed by washing with PBS. Nonspecific binding was blocked with 10% HS for 1 hour at room temperature (RT). Primary antibodies were diluted to 1:200 in 2% HS and incubated overnight at 4°C. The sections were then rinsed with PBS followed by secondary antibody incubation for 1 hour at RT in a 1:300 dilution. The sections were then rinsed with PBS before the nuclei were counterstained with DAPI.

2.5. Proliferation Assay. After 10 days of culturing the scaffolds in the Wheaton rolling device, a BrdU assay was performed in order to evaluate the proliferation capacity of the C2C12 myoblasts within the scaffold. BrdU was added to growth medium at dilution of 1:1000 for an incubation period of 24 hours. The scaffolds were then removed from the medium and rinsed with PBS before being snap-frozen in 2-methyl butane precooled in liquid nitrogen. The scaffolds were then sectioned and fixed with 4% formalin. The DNA was denatured for 10 min on ice with 1 N HCl followed by 2 N HCl at RT for 10 min, and finally 2 N HCl for 20 min at 37°C. Nonspecific binding was blocked with 10% HS for 1 hour. The primary antibody (biotin conjugated anti-BrdU) was added at a 1:250 dilution in 2% HS for 3 hours at RT. The secondary antibody (biotin streptavidin) was then added at a dilution of 1:400 for 1 hour at RT. The nuclei were then counterstained with DAPI.

2.6. Animal Experiments. The animal protocol was approved by the Animal Research and Care Committee at Children's Hospital of Pittsburgh. The mice included normal (C57BL/6J, 5–8 weeks of age, male), SCID (C57BL/6J-Prkdc^{scid}/SzJ, 4–8 weeks of age, female), and dystrophic/immunodeficient

mdx/SCID (C57BL/10ScSn-Dmd_{mdx} crossed with C57BL/6J-Prkdc_{scid}/SzJ, 4–8 weeks of age, female). All mice were purchased from Jackson Laboratory (Bar Harbor, Maine), and were housed individually with proper access to food and water and maintained on a 12-hour light/dark cycle. After the mice were anesthetized, an approximately $4 \times 4 \times 3$ mm³ defect was created in the belly of the gastrocnemius muscle (GM). The 3D muscle grafts and control nonseeded scaffolds were implanted in the defects followed by immediate wound closure. At designed time periods, mice were sacrificed, and the GMs were harvested and snap-frozen in 2-methylbutane precooled in liquid nitrogen, and they were cryosectioned for histological analysis.

3. Results

3.1. In Vitro. In the *in vitro* portion of the experiments, the C2C12 myoblast seeded scaffolds were cultured in a roller bottle cell culture system, and the scaffolds were harvested after 1, 2, and 3 weeks of culturing. After 1 week of culture, myoblasts were distributed throughout the interior of the scaffold which provides evidence that extensive migration was able to occur (Figures 1(a)–1(f)). Some of the cells migrated into the interior region of the scaffold, and this can be detected by either HE (Figures 1(a)–1(c)) or LacZ (Figures 1(d)–1(f)) staining. The sectioned scaffolds were also immunostained for CD31, an endothelial marker, and vWF, an endothelial cell-specific protein (Figures 2(a)–2(c)). After 1 week of culture, CD31-positive cells were seen within the scaffold (red, Figure 2(a)). Colocalization between CD31-positive (red) and vWF-positive (green) cells was visualized after 2 weeks of culture (yellow, Figure 2(b)). The detection of the colocalization of CD31 positive and vWF positive cells is indicative of vascular development within the scaffold. After 3 weeks of culturing, more extensive colocalized positive cells were seen (yellow, Figure 2(c)). A BrdU assay was performed in order to assess the viability and proliferative capacity of the myoblasts within the scaffold. We detected myoblasts with nuclei positive for BrdU (red, Figures 2(d), 2(e), and 2(f)), revealing that some of the myoblasts seeded within the scaffold were able to proliferate.

3.2. In Vivo. In the normal mouse model, implantation of a nonseeded control scaffold resulted in rejection from the host tissue, and this was seen 20 days after implantation (Figure 3(a)). In the SCID mouse model, the implanted nonseeded scaffolds were not rejected by the host tissue, but few host cells migrated into the area of the implantation (Figure 3(b)). In the same SCID mouse model, implantation of the 3D muscle graft with LacZ-positive myoblasts for a duration of 20 days, resulted in detection of large populations of LacZ-positive cells remaining in the transplantation site as well as extensive migration of the LacZ-positive cells into the surrounding host tissue, which demonstrates the success of the 3D graft implantation into the host tissue (Figure 3(c)). With immunostaining, we discovered CD31 and vWF positive cells present within the interior of the scaffold, and some of these cells expressed colocalization of the two markers

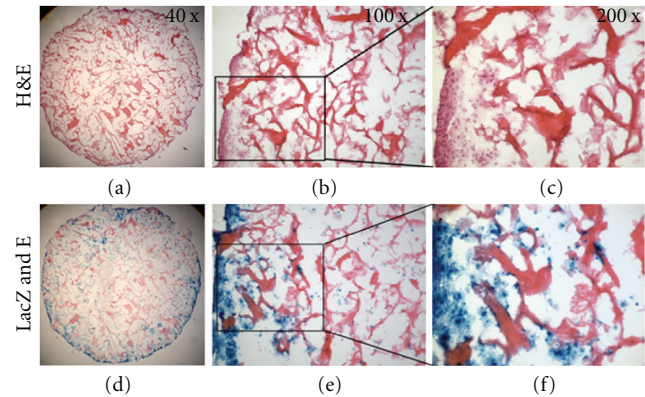


FIGURE 1: Cell growth examined after 1 week of culturing *in vitro*. Cells were visualized throughout the scaffold with a higher concentration of cells located on the periphery of the scaffolds; however, extensive migration is seen within the scaffolds. H&E staining of the scaffolds ((a)–(c)), and LacZ and eosin staining ((d)–(f)) are shown.

(Figure 3(d)), indicating that the vasculature process had begun to develop.

In the *mdx/SCID* mouse model, we followed the same procedure described above for the normal mouse model. We observed that the trauma sites were quickly healed in the 3D muscle graft implanted skeletal muscle after 10 (Figure 4(a)) and 20 days (Figure 4(c)) after surgery in comparison to the healing seen in the nonseeded scaffolds implanted into the muscle (Figures 4(b) and 4(d)). By histological analysis, the LacZ-positive cells were able to survive within the implanted scaffold as well as migrate throughout the scaffold. The scaffold began to breakdown as it was incorporated within the surrounding host tissue 10 days after implantation (Figures 4(e) and 4(f)). Twenty days after the graft implantation, we also detected that multiple cell types were spread homogeneously throughout the site of injury, and significantly, we detected CD31 and vWF positive cells present in the new tissue and some of these cells demonstrated colocalization between these two markers (Figures 4(g) and 4(h)). This result indicates that the vascularization process had started within the 3D muscle graft as early as 10 days after implantation.

We also investigated the histology of the long-term 3D muscle graft after implantation in the *mdx/SCID* mouse model. One month after implantation of the 3D muscle graft, LacZ and eosin staining provided evidence that the LacZ-positive myoblasts were able to survive within the implanted scaffold (Figure 5(a)). The site of injury was composed of LacZ-positive myoblasts and nondegraded residues of the scaffold (Figure 5(a) and 5(c) arrows). Some LacZ-positive myoblasts were detected at the periphery of the scaffold forming LacZ positive multinucleated myotubes (Figure 5(a), arrowheads). Many desmin positive cells (arrowheads), indicative of mature muscle cells, were detected within the area of implantation around nondegraded regions of the scaffold (Figure 5(b), arrows). With an H&E staining, we detected newly formed myofibers within the region of the degrading scaffold (Figure 5(d)).

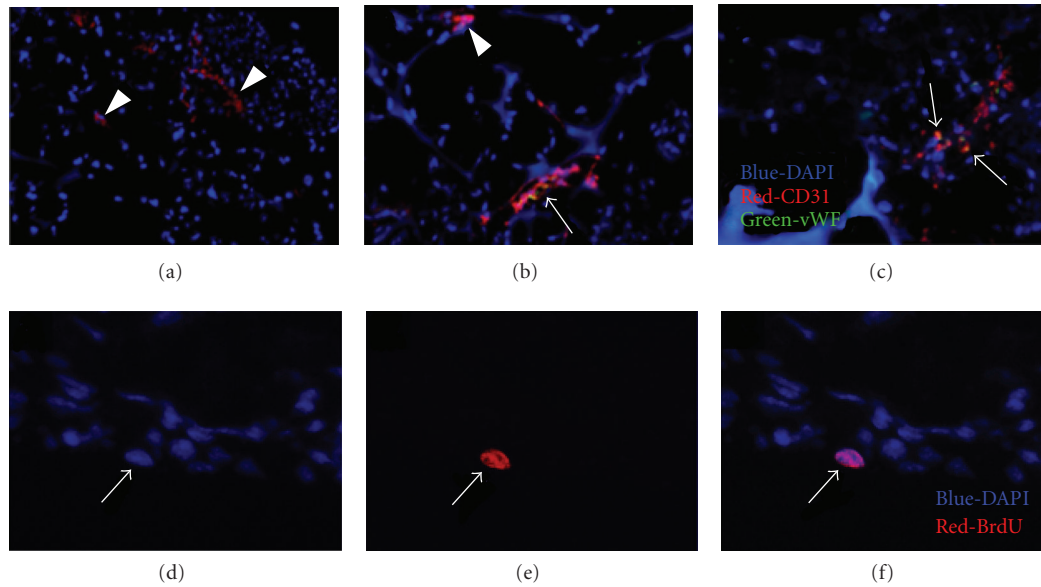


FIGURE 2: Immunofluorescent staining of the scaffolds after culturing for 1, 2, and 3 weeks *in vitro* for evidence of vasculature ((a)–(c)). After one week of culturing (a), CD31 positive cells (*red*) are detected within the scaffold. After two weeks of culturing (b), colocalization of CD31 (*red*) and vWF (*green*) positive cells are visualized. After three weeks of culturing (c), more extensive colocalization of CD31 and vWF is seen. A BrdU assay was performed *in vitro* after 10 days of culturing ((d)–(f)). BrdU positive nuclei (*red*) were seen revealing that proliferation was occurring throughout the scaffold (e).

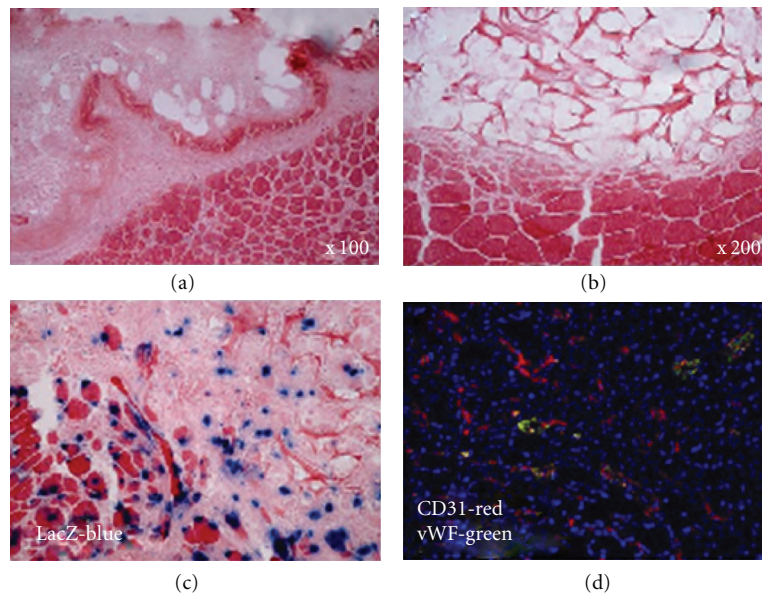


FIGURE 3: The immunocompatibility of the scaffolds was examined in normal mice and SCID mice *in vivo*. Twenty days after implantation in the normal mouse model, nonseeded scaffolds were rejected by the host tissue (a). Twenty days after implantation in the SCID mouse model, nonseeded scaffolds were not rejected by the host tissue, and few host cells migrated into the scaffold (b). Twenty days after implantation in the SCID mouse model, LacZ-labeled C2C12 myoblast seeded scaffolds were well received in the host tissue (c). Also, LacZ⁺ cells were able to migrate into the surrounding host tissue. An immunofluorescent staining of CD31 (*red*) and vWF (*green*) was performed on the implanted seeded scaffolds 20 days after implantation (d).

With immunostaining, dystrophin-positive myofibers were detected within the implantation region which suggests that regeneration was occurring within the site of injury (Figure 5(e), *arrowheads*). We also discovered that some CD31 positive cells were located within the site of injury,

revealing that the vascularization was an ongoing process (Figures 5(e) and 5(f), *arrows*).

Two months after implantation of the 3D muscle grafts, large dystrophin positive grafts were detected within the site of injury suggesting that muscle regeneration had taken

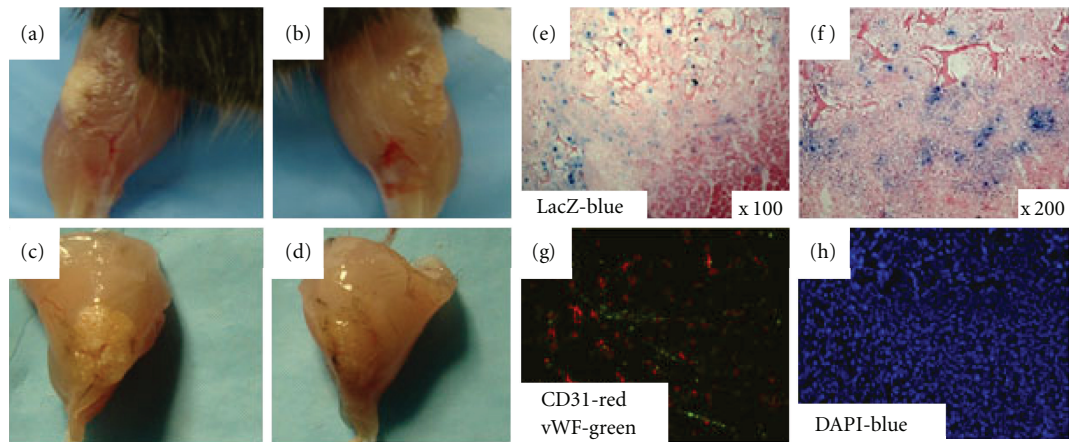


FIGURE 4: In the *mdx/SCID* mouse model, healthy healing was observed in the myoblast seeded scaffolds after 10 days (a) and 20 days (c). Nonseeded scaffolds implanted into *mdx/SCID* mice resulted in slower and less healthy healing at 10 days (b) and 20 days (d). LacZ staining of the implanted muscle graft region revealed extensive migration of the LacZ⁺ myoblasts into the surrounding host tissue (e) and (f). Immunofluorescent staining of CD31 (red) and vWF (green) showed vascularization developing in the implanted muscle graft region 20 days after implantation (g). A DAPI staining revealed that a variety of cell types were located homogeneously throughout the implanted muscle graft area (h).

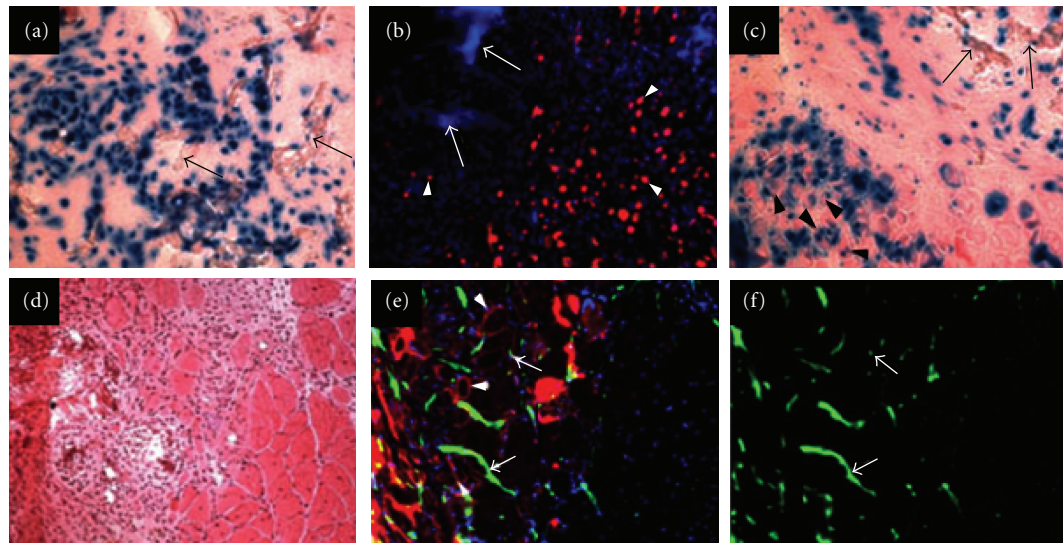


FIGURE 5: LacZ and eosin staining 1 month after implantation revealed that numerous LacZ⁺ myoblasts were able to survive within the implanted muscle graft region ((a) and (c)). Residues of nondegraded scaffold were also visualized within the implanted muscle graft area ((c), arrowheads). LacZ⁺ myoblasts were seen forming multinucleated myotubes within the implanted area ((a) arrows). Desmin positive myoblasts ((b) arrowheads) were detected within the vicinity of nondegraded portions of the scaffold ((b) arrows). An H&E staining revealed newly formed myofibers within the implantation site (d). Dystrophin-positive myofibers (red, arrowheads) were detected 1 month after implantation (e) as well as CD31-positive cells, ((e) and (f), green).

place in many regions of the injured area (Figures 6(a) B, E, and H). Also, the majority of the dystrophin-positive grafts stained positive for fast myosin-heavy chain protein (Figures 6(a) G–I). Similar to the previous time points, CD31 was visualized which provides evidence for extensive vascular development within the site of injury (Figures 6(a) A–C). Also neurofilament protein was detected within the dystrophin-positive grafts suggesting that innervations were being formed to the regenerating myofibers (Figure 6(a)

D–F). With histological analysis, we have detected a large area of scar tissue remaining in the implanted 3D graft sites three months after implantation through an H&E staining (Figure 6(b) A and B, stars). Also, we have detected regeneration of myofibers (Figure 6(b) B, arrows) and large amounts of dystrophin-positive myofibers within the new muscle graft (Figure 6(b) C and D, dystrophin-red, arrows) with revascularization (Figure 6(b) D, CD31-green, arrowheads). This existing scar tissue may be a major factor to

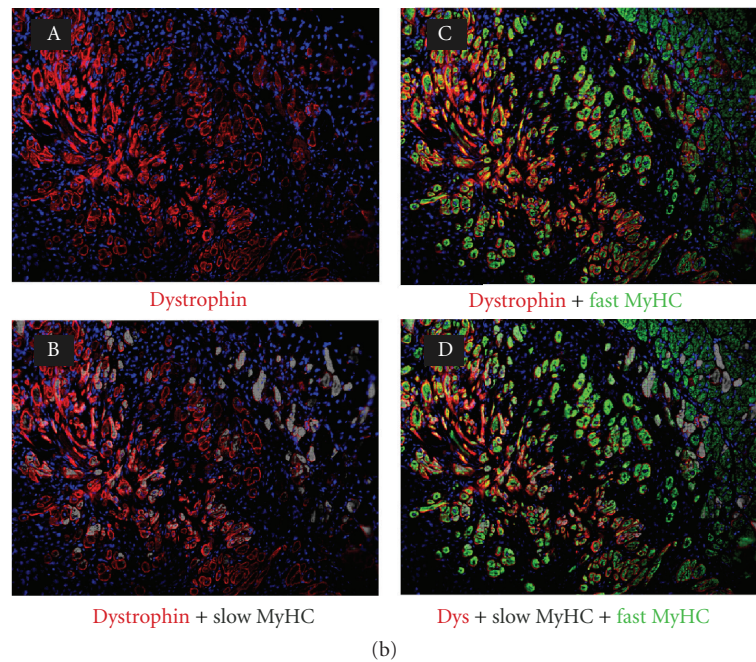
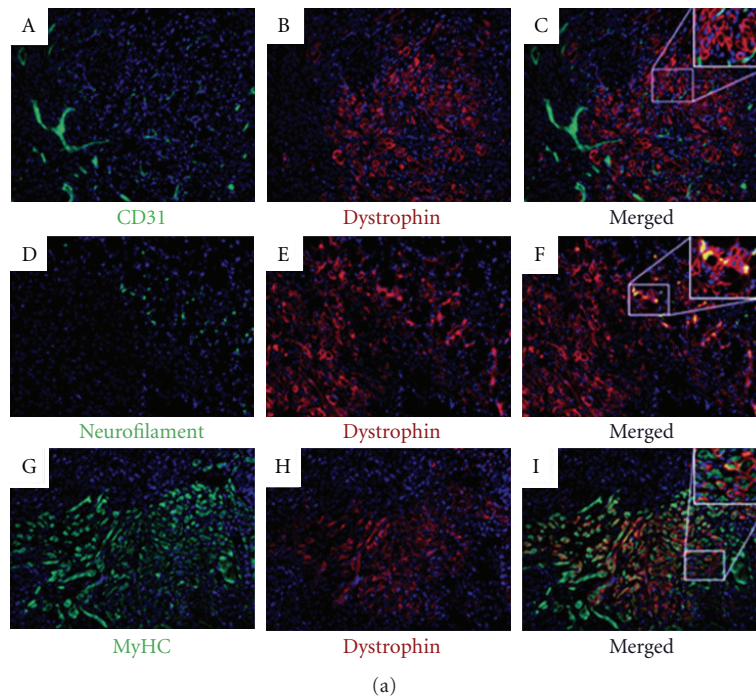


FIGURE 6: (a) Three months after implantation *in vivo*, large dystrophin-positive grafts were visualized ((a) B, E, H). CD31-positive cells were detected within the dystrophin-positive grafts indicative that vascularization and regeneration were occurring ((a) A–C). Neurofilament protein was visualized within the dystrophin-positive grafts revealing that innervations were forming along with the regenerating myofibers ((a) D–F). The majority of the dystrophin-positive grafts stained positively for fast myosin-heavy chain protein ((a) G–I). (b) Three months after implantation *in vivo*, all newly formed myofibers stained positive for dystrophin ((b) A *dystrophin-red*). A small quantity of the dystrophin-positive myofibers stained positive for slow myosin-heavy chain protein ((b) B *slow MyHC-gray*). A larger quantity of the dystrophin-positive myofibers stained positive for fast myosin-heavy chain protein ((b) C *fast MyHC-green*). (b) D displays a merged image revealing the distribution of the two types of myosin-heavy chain proteins.

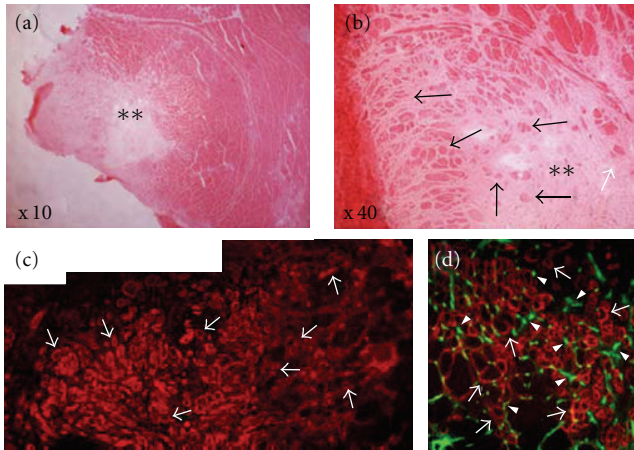


FIGURE 7: Three months after implantation, evaluation of the regenerative capacity of the seeded scaffolds. A hematoxylin and eosin staining revealed a large area of fibrosis in the muscle graft ((a) and (b), *sk*). However, within the muscle graft despite the area of fibrosis, we detected regenerating myofibers ((b), *arrows f*), and large quantities of dystrophin-positive myofibers ((c), *arrows f*). Within the areas of regeneration, revascularization was detected through the visualization of CD31-positive cells ((d) *green/arrows f*).

interfere with further muscle functional recovery, and can be a potential inducer of muscle reinjury with movement. Thus, prevention of fibrosis is necessary for the success of the bioengineered tissue in application.

4. Discussion

In the last few decades, advances in bioengineering have moved the field of tissue engineering significantly forward [15, 23, 24]. While 3D tissue constructs are still being developed, this field continues to grow from the intense efforts of military and civilian trauma researchers. Tissue engineering techniques combined with cell biology and material sciences hold great promise in developing appropriate strategies for the repair and regeneration of biological tissues. The necessary components for successful 3D engineered tissues have been identified to include the following: a biodegradable material that serves as a scaffold to facilitate new tissue growth, and pluripotent or stem cells to initiate new tissue growth as well as promoting vascularization and innervation once implanted within the patient. Our work focused primarily on creating functional 3D tissue constructs *in vitro*, through the use of a 3D biodegradable scaffold seeded with C2C12 primary myoblasts, which could then be implanted *in vivo* for the purpose of repairing and replacing damaged and lost tissue due to soft tissue defects.

Our results confirmed that C2C12 myoblasts are able to survive and migrate within the 3D collagen composite scaffold *in vitro*. This is a necessary step to occur prior to implantation in order to ensure that the implanted scaffolds are incorporating a rich source of myoblasts into the area of the skeletal muscle injury. Also, we discovered that *in vitro*, CD31-positive cells were present after 1 week of culturing.

CD31 is an endothelial marker that signifies progenitor blood vessel cells [25, 26] which means that the cell seeded scaffold had already started to develop some form of vasculature prior to implantation. This is furthered by evidence that after 2 weeks of culturing *in vitro*, colocalization between CD31- and vWF-positive cells was detected. These results indicate that the cell seeded scaffolds are capable of forming a type of prevascularization which is ideal for inducing vascular development within the defected muscle once implanted.

The ability to promote vascularization is an essential aspect of tissue engineering because often the vascularization to the area where the tissue loss took place is compromised by the trauma itself [4]. The vascularization that was seen *in vitro* was also present when the scaffolds were harvested at various time points after implantation *in vivo*. The detection of CD31-positive cells located throughout the scaffold provide evidence that vascularization was being incorporated within the scaffold from vessels located in the host tissue surrounding the defect. This incorporation of vasculature within the scaffold increased the cell survival of the myoblasts by providing nutrients and oxygen to the newly transplanted cells [27, 28]. In order for a tissue construct to be effective in becoming functional, vascularization needs to occur along with innervation. Techniques for repairing soft tissue defects, such as muscle and perforator flaps, result in providing vascularized coverage to the wound; however, due to the lack of innervations to the damaged area, sensitivity is often compromised [6]. Our results indicated that the seeded scaffold was successful in providing potential innervations to the damaged tissue based on the presence of neurofilament-positive cells. Neurofilament protein is a protein located in the intermediate filament of neurons [29]; therefore, its expression is indicative of neurogenesis and neural development.

Dystrophin-positive myofibers were found located within the area of the defect which signifies that new muscle fibers were being formed in the damaged area. The myoblasts that were seeded in the scaffold were able to successfully differentiate into myotubes which allowed for regeneration of the damaged tissue. This result is not surprising due to numerous previous studies that found that myoblast transplantation is an effective therapy for increasing dystrophin-positive myofibers in such muscle dystrophy diseases such as Duchenne muscular dystrophy [30–32]. A large quantity of the dystrophin-positive myofibers stained positively for fast-type myosin-heavy chain protein, and a lower quantity staining positively for slow-type myosin-heavy chain protein. This preferential difference may be contributed to the environment into which the myoblasts were implanted [33]. If more fast-type myosin-heavy chain myofibers were present in the surrounding area of host tissue around the defect, differentiation of the myoblasts into myotubes exhibiting fast-type myosin-heavy chain proteins may have been favored.

Although many challenges still remain in the successful restoration of soft tissue defects, our study provides a starting point for overcoming these challenges. The ability of the myoblast seeded collagen composite scaffolds to provide the initial architecture for rebuilding a functional tissue, as well as incorporating an appropriate population of cells that helps

to facilitate muscular regeneration through increasing innervation, vascularization, and the production of myofibers, makes the 3D collagen scaffold an ideal candidate for repairing soft tissue defects. However, immunocompatibility and fibrosis are two problems that still remain. As seen in our data, only immune-compromised mice were able to successfully integrate the 3D tissue graft into their host tissue which presents a limited scope of application for the scaffolds. Also, fibrosis is a pathological process that affects many tissues and organs after being afflicted by injuries or disease-like states [34]. The development of the fibrotic tissue can lead to chronic healing problems, which can result in tissue/organ dysfunction during the final healing stages, and can make the tissue more susceptible to reinjury after initial healing [35, 36]. Our study detected fibrosis formation in the skeletal muscles after long-term implantation, indicating that prevention or treatment of the fibrous scar tissue is essential for effective bioengineered tissues.

Author's Contributions

J. Ma and K. Holden contributed equally to this paper.

References

- [1] M. Dragas, L. Davidovic, D. Kostic et al., "Upper extremity arterial injuries: factors influencing treatment outcome," *Injury*, vol. 40, no. 8, pp. 815–819, 2009.
- [2] C. E. Attinger, I. Ducic, P. Cooper, and C. M. Zelen, "The role of intrinsic muscle flaps of the foot for bone coverage in foot and ankle defects in diabetic and nondiabetic patients," *Plastic and Reconstructive Surgery*, vol. 110, no. 4, pp. 1047–1054, 2002.
- [3] A. K. Singh, K. P. Gudehithlu, S. Patri et al., "Impaired integration of endothelial progenitor cells in capillaries of diabetic wounds is reversible with vascular endothelial growth factor infusion," *Translational Research*, vol. 149, no. 5, pp. 282–291, 2007.
- [4] M. M. Al-Qattan, "Severe, traumatic soft-tissue loss in the antecubital fossa and proximal forearm associated with radial and/or median nerve palsy: nerve recovery after coverage with a pedicled latissimus dorsi muscle flap," *Annals of Plastic Surgery*, vol. 46, no. 2, pp. 125–129, 2001.
- [5] A. Takeuchi, H. Tsuchiya, T. Shirai, K. Hayashi, H. Nishida, and K. Tomita, "Occlusive dressing for large soft tissue defects following soft tissue tumor excision," *Journal of Orthopaedic Science*, vol. 14, no. 4, pp. 385–390, 2009.
- [6] E. D. Rodriguez, R. Bluebond-Langner, C. Copeland, T. N. Grim, N. K. Singh, and T. Scalea, "Functional outcomes of post-traumatic lower limb salvage: a pilot study of anterolateral thigh perforator flaps versus muscle flaps," *The Journal of Trauma*, vol. 66, no. 5, pp. 1311–1314, 2009.
- [7] X. Shao, C. Chen, X. Zhang, Y. Yu, D. Ren, and L. Lu, "Coverage of fingertip defect using a dorsal island pedicle flap including both dorsal digital nerves," *Journal of Hand Surgery*, vol. 34, no. 8, pp. 1474–1481, 2009.
- [8] P. A. Janmey, J. P. Winer, and J. W. Weisel, "Fibrin gels and their clinical and bioengineering applications," *Journal of the Royal Society Interface*, vol. 6, no. 30, pp. 1–10, 2009.
- [9] S. G. Kumbar, S. P. Nukavarapu, R. James, L. S. Nair, and C. T. Laurencin, "Electrospun poly(lactic acid-co-glycolic acid) scaffolds for skin tissue engineering," *Biomaterials*, vol. 29, no. 30, pp. 4100–4107, 2008.
- [10] M. Pei, L. A. Solchaga, J. Seidel et al., "Bioreactors mediate the effectiveness of tissue engineering scaffolds," *The FASEB Journal*, vol. 16, no. 12, pp. 1691–1694, 2002.
- [11] S. A. Riboldi, M. Sampaolesi, P. Neuenschwander, G. Cossu, and S. Mantero, "Electrospun degradable polyesterurethane membranes: potential scaffolds for skeletal muscle tissue engineering," *Biomaterials*, vol. 26, no. 22, pp. 4606–4615, 2005.
- [12] L. G. Griffith, "Emerging design principles in biomaterials and scaffolds for tissue engineering," *Annals of the New York Academy of Sciences*, vol. 961, pp. 83–95, 2002.
- [13] L. E. Freed, F. Guilak, X. E. Guo et al., "Advanced tools for tissue engineering: scaffolds, bioreactors, and signaling," *Tissue Engineering*, vol. 12, no. 12, pp. 3285–3305, 2006.
- [14] D. W. Hutmacher, "Scaffold design and fabrication technologies for engineering tissues—state of the art and future perspectives," *Journal of Biomaterials Science, Polymer Edition*, vol. 12, no. 1, pp. 107–124, 2001.
- [15] L. Cen, W. Liu, L. Cui, W. Zhang, and Y. Cao, "Collagen tissue engineering: development of novel biomaterials and applications," *Pediatric Research*, vol. 63, no. 5, pp. 492–496, 2008.
- [16] J. M. Anderson and J. J. Langone, "Issues and perspectives on the biocompatibility and immunotoxicity evaluation of implanted controlled release systems," *Journal of Controlled Release*, vol. 57, no. 2, pp. 107–113, 1999.
- [17] J. E. Babensee, J. M. Anderson, L. V. McIntire, and A. G. Mikos, "Host response to tissue engineered devices," *Advanced Drug Delivery Reviews*, vol. 33, no. 1–2, pp. 111–139, 1998.
- [18] J. M. Anderson, "Inflammatory response to implants," *ASAIO Transactions*, vol. 34, no. 2, pp. 101–107, 1988.
- [19] G. Vunjak-Novakovic, B. Obradovic, I. Martin, P. M. Bursac, R. Langer, and L. E. Freed, "Dynamic cell seeding of polymer scaffolds for cartilage tissue engineering," *Biotechnology Progress*, vol. 14, no. 2, pp. 193–202, 1998.
- [20] M. Radisic, M. Euloth, L. Yang, R. Langer, L. E. Freed, and G. Vunjak-Novakovic, "High-density seeding of myocyte cells for cardiac tissue engineering," *Biotechnology and Bioengineering*, vol. 82, no. 4, pp. 403–414, 2003.
- [21] Y. Wang, H. L. Jiao, J. Z. Zhang, and R. Q. He, "Three-dimensional culture of hybridoma cells secreting anti-human chorionic gonadotropin by a new rolling culture system," *Journal of Biomedicine and Biotechnology*, vol. 2004, no. 1, pp. 35–40, 2004.
- [22] N. A. Bleckwenn and J. Shiloach, "Large-scale cell culture," *Current Protocols in Immunology*, Appendix 1, Appendix 1U, 2004.
- [23] D. H. Park, C. V. Borlongan, D. J. Eve, and P. R. Sanberg, "The emerging field of cell and tissue engineering," *Medical Science Monitor*, vol. 14, no. 11, pp. RA206–RA220, 2008.
- [24] D. W. Hutmacher, M. Sittinger, and M. V. Risbud, "Scaffold-based tissue engineering: rationale for computer-aided design and solid free-form fabrication systems," *Trends in Biotechnology*, vol. 22, no. 7, pp. 354–362, 2004.
- [25] C. -K. Perng, Y. -J. Wang, C. -H. Tsi, and H. Ma, "In vivo angiogenesis effect of porous collagen scaffold with hyaluronic acid oligosaccharides," *Journal of Surgical Research*, vol. 168, no. 1, pp. 9–15, 2011.
- [26] C. K. Chiang, M. F. Chowdhury, R. K. Iyer, W. L. Stanford, and M. Radisic, "Engineering surfaces for site-specific vascular differentiation of mouse embryonic stem cells," *Acta Biomaterialia*, vol. 6, no. 6, pp. 1904–1916, 2010.
- [27] M. K. Smith, M. C. Peters, T. P. Richardson, J. C. Garbern, and D. J. Mooney, "Locally enhanced angiogenesis promotes

- transplanted cell survival," *Tissue Engineering*, vol. 10, no. 1-2, pp. 63–71, 2004.
- [28] D. J. Tilkorn, A. Bedogni, E. Keramidaris et al., "Implanted myoblast survival is dependent on the degree of vascularization in a novel delayed implantation/prevascularization tissue engineering model," *Tissue Engineering—Part A*, vol. 16, no. 1, pp. 165–178, 2010.
- [29] R. Perrot, R. Berges, A. Bocquet, and J. Eyer, "Review of the multiple aspects of neurofilament functions, and their possible contribution to neurodegeneration," *Molecular Neurobiology*, vol. 38, no. 1, pp. 27–65, 2008.
- [30] T. A. Partridge, J. E. Morgan, G. R. Coulton, E. P. Hoffman, and L. M. Kunkel, "Conversion of mdx myofibres from dystrophin-negative to -positive by injection of normal myoblasts," *Nature*, vol. 337, no. 6203, pp. 176–179, 1989.
- [31] G. Q. Wallace, K. A. Lapidos, J. S. Kenik, and E. M. McNally, "Long-term survival of transplanted stem cells in immunocompetent mice with muscular dystrophy," *American Journal of Pathology*, vol. 173, no. 3, pp. 792–802, 2008.
- [32] Z. Liu, Y. Wu, and B. G. Chen, "Myoblast therapy: from bench to bedside," *Cell Transplantation*, vol. 15, no. 6, pp. 455–462, 2006.
- [33] Y. Matsuoaka and A. Inoue, "Controlled differentiation of myoblast cells into fast and slow muscle fibers," *Cell and Tissue Research*, vol. 332, no. 1, pp. 123–132, 2008.
- [34] Y. Li and J. Huard, "Differentiation of muscle-derived cells into myofibroblasts in injured skeletal muscle," *American Journal of Pathology*, vol. 161, no. 3, pp. 895–907, 2002.
- [35] Y. Li, W. Foster, B. M. Deasy et al., "Transforming growth factor- β 1 induces the differentiation of myogenic cells into fibrotic cells in injured skeletal muscle: a key event in muscle fibrogenesis," *American Journal of Pathology*, vol. 164, no. 3, pp. 1007–1019, 2004.
- [36] W. Wang, H. Pan, K. Murray, B. S. Jefferson, and Y. Li, "Matrix metalloproteinase-1 promotes muscle cell migration and differentiation," *American Journal of Pathology*, vol. 174, no. 2, pp. 541–549, 2009.

Research Article

Localization of Magic-F1 Transgene, Involved in Muscular Hypertrophy, during Early Myogenesis

Flavio Ronzoni,^{1,2} Matilde Bongio,¹ Silvio Conte,¹ Luigi Vercesi,¹ Marco Cassano,³ Carla Tribioli,⁴ Daniela Galli,^{1,2} Riccardo Bellazzi,² Giovanni Magenes,² Maria Gabriella Cusella De Angelis,^{1,2} and Maurilio Sampaolesi^{1,2,3,5}

¹ Human Anatomy Section, University of Pavia, Via Forlanini 8, 27100 Pavia, Italy

² Center for Tissue Engineering (CIT), University of Pavia, 27100 Pavia, Italy

³ Translational Cardiology (SCIL), Katholieke Universiteit Leuven, Herestraat 49, 3000 Leuven, Belgium

⁴ Institute of Molecular Genetics, CNR, 27100 Pavia, Italy

⁵ Stem Cell Research Institute, University Hospital Gasthuisberg, Herestraat 49, 3000 Leuven, Belgium

Correspondence should be addressed to Maurilio Sampaolesi, sampa@unipv.it

Received 31 May 2011; Revised 14 September 2011; Accepted 19 September 2011

Academic Editor: Aikaterini Kontrogianni-Konstantopoulos

Copyright © 2011 Flavio Ronzoni et al. This is an open access article distributed under the Creative Commons Attribution License, which permits unrestricted use, distribution, and reproduction in any medium, provided the original work is properly cited.

We recently showed that Magic-F1 (Met-activating genetically improved chimeric factor 1), a human recombinant protein derived from hepatocyte growth factor/scatter factor (HGF/SF) induces muscle cell hypertrophy but not progenitor cell proliferation, both *in vitro* and *in vivo*. Here, we examined the temporal and spatial expression pattern of Magic-F1 in comparison with Pax3 (paired box gene 3) transcription factor during embryogenesis. Ranging from 9.5 to 17.5 dpc (days post coitum) mouse embryos were analyzed by *in situ* hybridization using whole mounts during early stages of development (9.5–10.5–11.5 dpc) and cryostat sections for later stages (11.5–13.5–15.5–17.5 dpc). We found that Magic-F1 is expressed in developing organs and tissues of mesenchymal origin, where Pax3 signal appears to be downregulated respect to the wt embryos. These data suggest that Magic-F1 could be responsible of muscular hypertrophy, cooperating with Pax3 signal pathway in skeletal muscle precursor cells.

1. Introduction

Muscular hypertrophy is controlled by both muscle growth and muscle atrophy. These apparently contrasting biological processes share key molecules triggering active transcriptional programs to induce skeletal muscles atrophy or hypertrophy.

The IGF-1 (insulin-like growth factor-1) pathway affects both hypertrophy and atrophy, increasing protein synthesis and inhibiting the expression of transcription factor FOXO (forkhead box O), respectively. A key molecular player downstream of IGF-1 receptor is Akt (Abelson leukemia kinase) that when phosphorylated activates protein synthesis via mTOR (mammalian target of rapamycin). The two main actors to negatively control the muscle growth are myostatin and atrogen-1. Myostatin belongs to the TGF- β (transforming growth factor beta) family, and it is expressed and secreted predominantly in skeletal muscle, functioning

as negative regulator of muscle growth. Mice, sheep, cattle, and humans that present mutations in myostatin gene show a double-muscling phenotype, characterized by extensive muscular hypertrophy [1–4]. *In vitro* myostatin is able to positively affect the expression of ubiquitin ligases, involved in muscle atrophy [5]. Interestingly, myostatin treatment blocks the IGF1-AKT pathway, allowing the increased expression of atrogen-1, directly involved in muscle atrophy [6]. Among the muscle growth regulators, hepatocyte growth factor (HGF/SF) [7–9], initially unveiled as the major inducers of hepatogenesis, is involved in muscle stem-cell activation through its tyrosine kinase receptor Met [10–14], containing a Pax3-binding site. Pax3 is an early transcription factor involved in embryonic and adult myogenesis, and it is expressed in the lateral dermomyotome of all somites, where also is present Met [15]. Transgenic animals generated to interfere in HGF-Met signaling show abnormality in several muscles during embryogenesis [16–18]. Moreover, HGF-Met

pathway is important in muscle regeneration, since, sustains the proliferation of muscle stem cells after their activation [19–22]. However, HGF expression is downregulated during myogenesis in order to allow the satellite cells to exit the cell cycle, avoiding a delay in the regeneration process [23, 24].

The production of recombinant proteins allows the great advantage to select a specific biological effect of a given protein able to trigger different biological processes. We recently generated transgenic mice expressing an HGF-related recombinant protein, named Magic factor-1 (Met-activating genetically improved chimeric factor-1 or Magic-F1) and expressed exclusively in skeletal muscles [25]. This animal model develops muscular hypertrophy with no evident side effects or hyperplasia. However, the expression pattern of the transgene in early embryogenesis is unknown.

The effect of Magic-F1 recombinant protein in skeletal muscle tissue offers biological advantages over HGF. Magic-F1 is able to promote myocytes survival and enhance muscle regeneration and a lack of any mitogenic activity could allow a potential safe use of the recombinant protein as therapeutic cytokine for muscle degenerative disorders, promoting muscle regeneration without the potential risk of stimulating uncontrolled proliferation. Because of its selective stimulation of hypertrophy, Magic-F1 is a novel molecule with potential applicative perspective to counteract muscle wasting in muscle diseases such as cachexia or muscular dystrophy.

Here, we evaluate the localization of transgene Magic-F1 in comparison with Pax3, the earliest myogenic transcription factor, in early and late embryogenesis using *in situ* hybridization on whole-mount and cryosections of transgenic and wt mouse embryos.

2. Materials and Methods

2.1. Mouse Embryos and Staging. Embryos for *in situ* hybridization were dissected from CD1 wt (wild-type) female mice mated with homozygous Magic-F1 transgenic male mice (Stem Cell Research Institute, H. S. Raffaele, Milan, Italy). Embryos were generated using timed mating, with the morning vaginal plug designated as E0.5.

2.2. Genotyping of Magic-F1 Embryos. Magic-F1 is a recombinant protein containing two HGF NK2 domains joint by a linker. The exact amino acidic sequence of Magic-F1 corresponds to residues 1–285 of human HGF (Gene Bank no. M73239), a linker with the sequence (GGGGS)₃; residues 30–285 of human HGF, and a poly-histidine tag with the sequence DDDKHHHHHH. We generated transgenic mice expressing Magic-F1 construct into a plasmid containing the 1.500-bp (base pair) fragment of the MLC (myosin light chain) promoter, an 840-bp fragment of SV40 poly(A), and a 900-bp fragment from the 3' end of the MLC1f/3f gene, which acts as an enhancer as previously reported [25].

To determinate the genotypes of the embryos used in this study, the yolk sack was removed from each embryo and was used to prepare genomic DNA (deoxyribonucleic acid), according to a modified protocol using proteinase K digestion, isopropanol extraction, and ethanol

precipitation. Oligonucleotide primers *FW* (forward) (5'-GTGTCAAGGTTCTATTAGGCACTA-3') and *REV* (reverse) (5'-GTCCTTTACCAATGATGCAGTTTC-3'), were used to amplify a 331 bp fragment specific to *Magic-F1*. For each sample, 20 ng of genomic DNA was subjected to a cycle of predenaturation (94°C, 3 minutes and 30 seconds), then to 30 cycles of amplification consisting of denaturing (94°C, 15 seconds), annealing (56°C, 30 seconds) and extension (72°C, 45 seconds), followed by two additional extensions at 72°C, 7 minutes). The amplified products were analyzed by agarose gel electrophoresis in TBE (Tris Borate EDTA) 1X. To confirm that the absence of the band of some samples was due to the absence of *Magic-F1* gene and not to the absence of DNA, a PCR (polymerase chain reaction) has been performed for *GAPDH* (glyceraldehyde-3-phosphate dehydrogenase) gene, using oligonucleotide primers *FW* (5'-GGGTGGAGCCAAACGGGT-3') and *REV* (5'-GGAGTTGCTGTTGAAGTCGCA). For each sample, 20 ng of genomic DNA was subjected to a cycle of predenaturation (94°C, 5 minutes), then to 35 cycles of amplification consisting of denaturing (94°C, 60 seconds), annealing (60°C, 60 seconds) and extension (72°C, 60 seconds), followed by an additional extension at 72°C, 7 minutes.

2.3. Plasmid and Riboprobe Synthesis. As probes for hybridization experiments, human *Magic-F1* cDNA (complementary deoxyribonucleic acid) (1759 bp) was amplified using oligonucleotide primers *FW* (5'-ATGTGGGTGACCAACTCCTG-3') and *REV* (5'-CTAGTGGTGGTGGTGGTGGTGGT-3'). The amplified products were analyzed by agarose gel electrophoresis in TBE 1X. *Magic-F1* bands were excised from the gel, and the Magic-F1 DNA was extracted (QIAquick Gel Extraction Kit, QIAGEN). Magic-F1 fragments were subcloned into the *pGEM-T Easy Vector System* (Promega). Nonradioactive antisense and sense riboprobes were synthesized by *in vitro* transcription using digoxigenin-UTP following the manufactures instructions (Boehringer Mannheim). *Magic-F1* antisense and sense probes were synthesized using SP6/T7 RNA (ribonucleic acid) polymerase linearization at a suitable site: *pGEM-T* carrying *Magic-F1* was digested with BstXI and *Magic-F1* antisense probes were synthesized using T7 RNA polymerase; *Magic-F1* sense probes were synthesized using SP6 RNA polymerase after digestion with ApaI restriction enzyme. The *Pax3* antisense and sense probes were produced by T7 and SP6 RNA polymerase from *pCMV-sport6.1* (Invitrogen) carrying *Pax3* cDNA after proper linearization with EcoRI and BamHI, respectively.

2.4. In Situ Hybridization. Whole-mount *in situ* hybridization on mouse embryos was performed as described [26]. Briefly, embryos were dissected free of all membranes in phosphate-buffered saline (PBS) and fixed in 4% paraformaldehyde in PBS for 1–2 h at RT (Room Temperature) with slow rocking speed. After washing twice in PTW (PBS, 0.1% Tween-20), embryos were washed with 50% MeOH/PTW and 100% MeOH then stored in 100% MeOH at –20°C for less than a month. For hybridization,

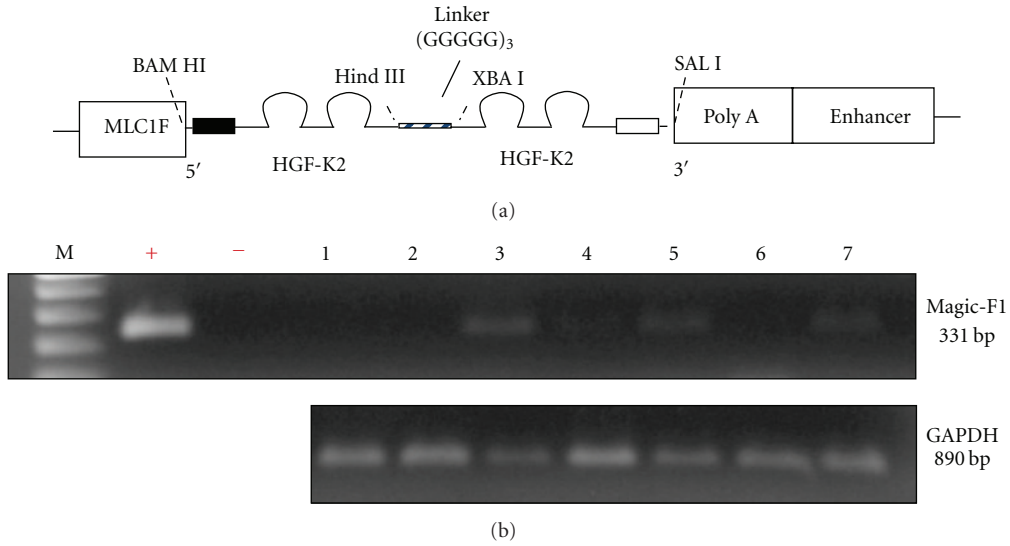


FIGURE 1: Magic-F1 transgenic mice. (a) Schematic representation of transgene. (b) Genotyping of 13.5 dpc mouse embryos derived by hemizygous-matched mice; +, - positive and negative control, respectively.

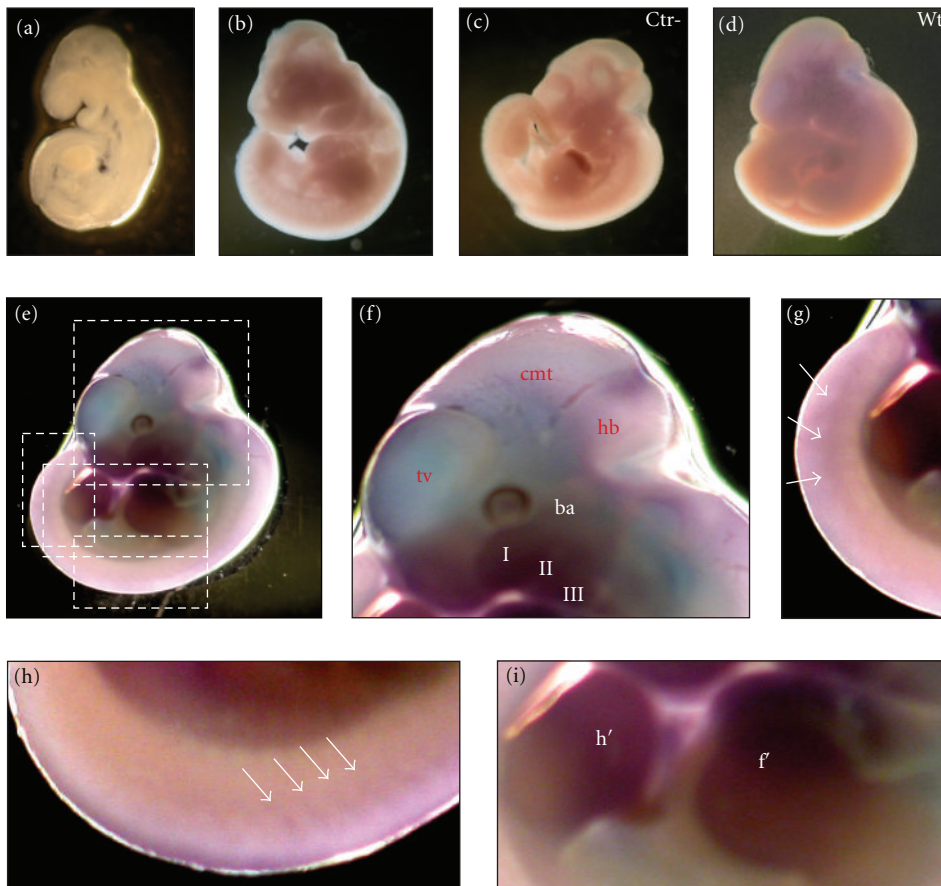


FIGURE 2: Expression of *Magic-F1* in whole mount embryos. Lateral view of whole-mount *in situ* hybridization with digoxigenin labeled antisense *Magic-F1* (a, b, d, e, f, g, h, and i) and sense *Magic-F1* (c) cRNA probes as negative control (ctr-). Specific hybrids are visualized as a purple precipitate in all panels except in (a), 9.5 dpc and (b) 10.5 dpc. (e) Specific *Magic-F1* transcripts are detected (f) in the mesodermal cells of the jaw and hyoid bone; in f, tv: telencephalic vesicles, cmt: mesenchymal cephalic tissue, hb: hindbrain, and ba: branchial arches where muscles are localized as well as around the eyes; a faint expression is also revealed in tail (g) and dorsal (h) somites, while a strong signal was selected in somites of fore (f') and hind (h') limb buds (i). In embryos hybridized with sense probe (c) background staining has not been detected as well as on 11.5 dpc wild type embryo (wt) hybridized with antisense probes (d).

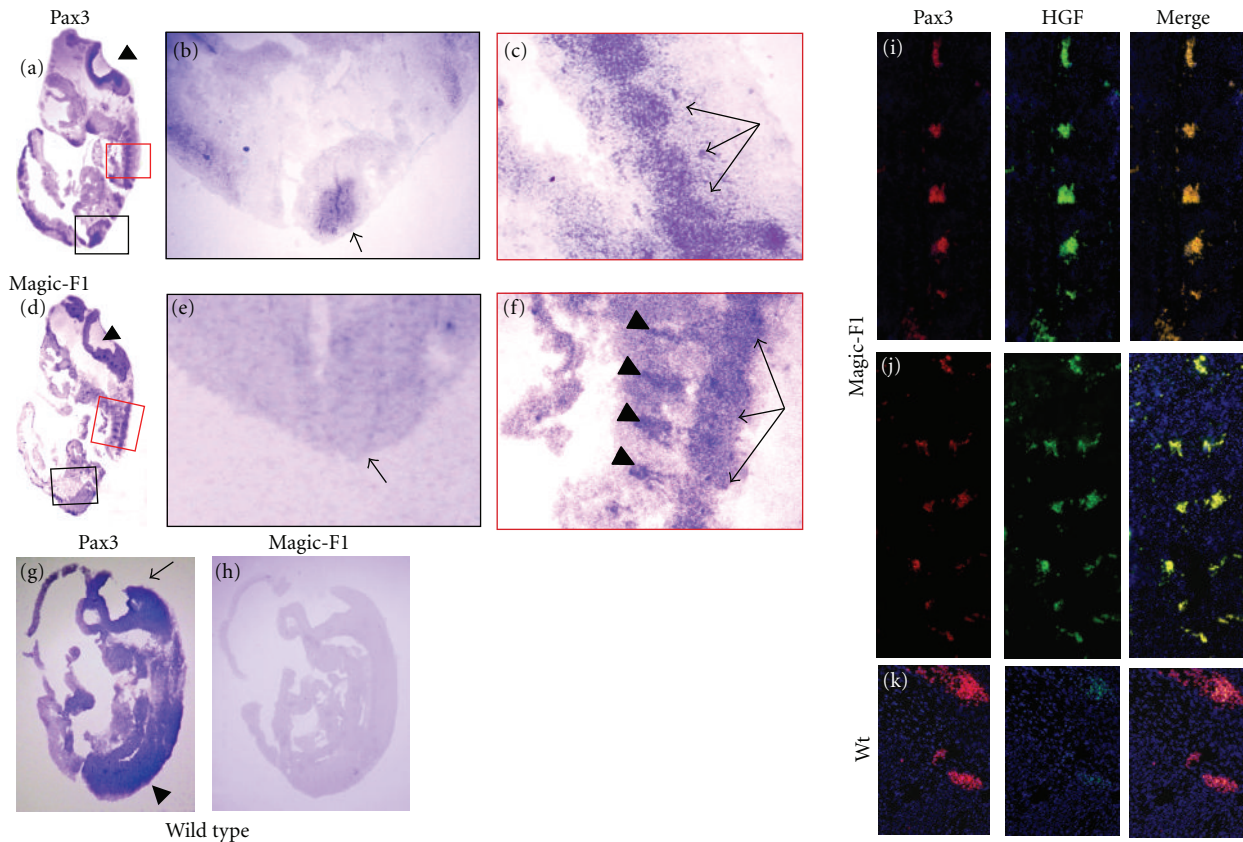


FIGURE 3: Transcription expression profile of *Pax3* (a–c) and *Magic-F1* (d–f) on 11.5 dpc mouse embryos of hemizygous *Magic-F1* (a–f) and wt (g, h) mice by *in situ* hybridization. In the sagittal section of transgenic embryo, *Pax3* riboprobes reveal a strong signal at the level of hindbrain (arrowhead in a), neuroepithelium of neural tube (arrow in b), and dorsal somites (c); sagittal section of 11.5 dpc embryo hybridized by *Magic-F1* riboprobes (d) shows a similar pattern of *Pax3* although no expression was detected at the level of neuroepithelium of neural tube (arrow in e); specific transcripts are observed in the cervical dorsal (posterior) root ganglion (arrows in c and f) and somites (arrowheads in f). In 11.5 dpc wt embryo hybridized with *Pax3* riboprobes (g), specific transcripts are detected mostly in the cerebellar primordium (cerebellar rudiment derived from dorsal part of the alar lamina of the Metencephalon) (arrow) and somites in lumbar region (arrowhead in g), whereas no signal for *Magic-F1* has been detected (h). Immunofluorescence analysis confirmed the presence of recombinant protein at the level of thoracic (i) and lumbar (j) somites in the transgenic embryos, whereas the signal was faint in the wt embryos (k), probably referred only to the HGF expression at this stage.

embryos were incubated horizontally at 65°C overnight in hybridization mix (50% deionized formamide, 1.3xSSC pH 5, 5 mM EDTA pH 8, 50 µg/mL Yeast RNA, 0.2% Tween-20, 0.5% CHAPS, 100 µg/mL Heparin, ddH₂O) with 1 µg/mL digoxigenin-labeled RNA probes. After *in situ* hybridization, the embryos were washed in MABT buffer (100 mM maleic acid (Sigma), 150 mM NaCl, 0.1% Tween-20, pH 7.5) and NTMT buffer (100 mM NaCl, 100 mM Tris-HCl pH 9.5, 50 mM MgCl₂, 0.1% Tween-20) and incubate with staining solution (4.5 µg/m NBT and 3.5 µg/mg BCIP). When the developed color reached the desired extent, embryos were washed twice with PTW and refixed in 4% HCHO/0.1% glutaraldehyde/PTW for 2 h at RT or 4°C overnight.

In situ hybridization on mouse cryostat sections was performed according to Sally Dunwoodie, NIMR. Briefly, the sections were fixed 4% paraformaldehyde in PBS, digested with proteinase K and postfixed. Sections were prehybridized in hybridization solution without probe (50% deionized

formamide, 10x salt, 250 µg/mL Yeast RNA, 5x Denhardt's, 50 µg/mL Heparin, 0.1% Tween, ddH₂O) in a humid environment at 67°C for 2 h. After incubation, the prehybridization buffer was removed and replaced with hybridization buffer containing everything in the prehybridization buffer plus 0.1–1 µg/mL labeled cRNA (complementary ribonucleic acid) riboprobe, denatured for 5 min at 80°C. A coverslip was placed over the hybridized area and the slides were then placed in a moist, closed plastic box and hybridized overnight at 67°C h. Following hybridization, the coverslips were washed off by dipping into 50% formamide, 1xSSC prewarmed to 67°C. The tissue was subjected to stringent washing at 67°C in 50% formamide, 1xSSC twice for 30 min, followed by two washes in MABT 1X at RT, for 30 min each. Slides were exposed to BMpurple (Roche) for 2 h. Slides were fixed in PFA 4% and washed in PBS, three times for 5 min. Hybridization signals were observed and photographed using a Nikon microscope. As a negative

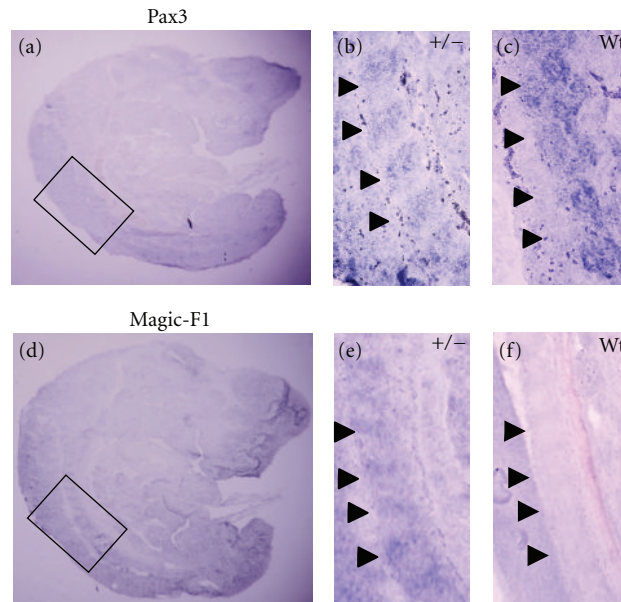


FIGURE 4: Expression of *Pax3* and *Magic-F1* in 13.5 dpc mouse embryos. (a) Sagittal section of 13.5 dpc mouse hybridized by *Pax3* riboprobes. A weak signal of *Pax3* transcripts have been detected in *Magic-F1* transgenic embryos (+/-) at the level of somites in thoracic (b) and lumbosacral region; in the wild-type age-matched embryo (wt) the signal appeared slightly stronger (c). A faint signal was detected at the same stage in transgenic embryos hybridized by *Magic-F1* antisense riboprobes (d); mainly, the transgenic expression was localized at the level of somites as shown at higher magnification in (e). No signal was detected in wild type embryos (wt) by *Magic-F1* antisense riboprobes (f). Arrowheads show somites.

control, specimens were incubated with hybridization buffer containing digoxigenin labeled riboprobes corresponding to the sense sequence of *Magic-F1*.

2.5. Immunocytochemistry. Cryosections placed in a humid, closed plastic box were fixed for 10 min in 4% paraformaldehyde in PBS, permeabilized in 0.2% Triton and incubated, first, with a blocking buffer (2% donkey serum) containing 1% blocking solution in PBS for 30 min at RT and, then, a second blocking buffer (0.5% mouse serum, 0.5% goat serum) containing 1% Blocking Solution (Candor-bioscience GmbH) in PBS for 30 min at RT, followed by incubation with primary antibodies (goat polyclonal antibody anti-HGF, 1 : 100 and Mouse monoclonal antibody anti-Pax3) diluted in 2% BSA (bovine serum albumine) in PBS overnight at 4°C. Sections were rinsed three times in PBS followed by a 2 h incubation with fluorescein-conjugated anti-mouse and anti-goat antibodies diluted 1/1500. Slides were stained with Hoechst dye and mounted in Fluor-Save. Stained cryosections were observed on an upright microscope Nikon Vico TE-2000 (Nikon, Japan).

3. Results and Discussion

3.1. PCR Analysis. PCR analysis of *Magic-F1* showed transgene expression in all the embryonic developmental stages analyzed and an example at stage 13.5 dpc is reported in Figure 1(b). As expected, no signal was detected in the wild-type embryos due to the high specificity of the primers able to discriminate between HGF and the recombinant protein *Magic-F1*.

3.2. Whole-Mount *In Situ* Hybridization. Whole-mount *in situ* hybridization was performed to detect *Magic-F1* and *Pax3* mRNA (messenger ribonucleic acid) in embryos at early stages of development (9.5, 10.5 and 11.5 dpc).

Magic-F1 expression was detected in bone cartilage primordia, dorsal somites, in tail and limb buds, where *Pax3* signal appears to be downregulated respect to the wt embryos. At 9.5 dpc (30 somite stage) and 10.5 dpc (40 somite stage) (Figures 2(a) and 2(b)), *in situ* hybridization analysis with digoxigenin- (DIG-) labeled antisense probes showed no expression of *Magic-F1* transcript. *Magic-F1* transcripts (Figure 2(e)) have been detected from stage of 11.5 dpc (58 somite stage) in developing organs and tissues of mesenchymal origin. Specifically, positive signal was observed in mesodermal cells of the jaw, hyoid bone and in pharyngeal (or brachial) arches from which branchiomeric muscles are formed. This expression profile confirmed the muscle specificity of the MLC1F (myosin light chain type 1F) promoter, regulating *Magic-F1* transcription. Furthermore, specific hybrids were also detected around the eyes at the level of the choroid coat and the sclera, both of mesenchymal origin, on the ventral and dorsal side of limb buds (Figure 2(d)), in the dorsal side of some rostral somites (Figure 2(h)), and in the tail bud (Figure 2(g)). No signal was observed in the embryos hybridized with the sense riboprobe (Figure 2(i)). The somites begin to form at the 7.75–8.0 dpc, and, after condensation, they begin to differentiate into three compartments: the sclerotome, the dermatome, and myotome. At 11.5 dpc (58 somite stage), *Magic-F1* transcripts have been detected in all three compartments (sclerotome, dermatome,

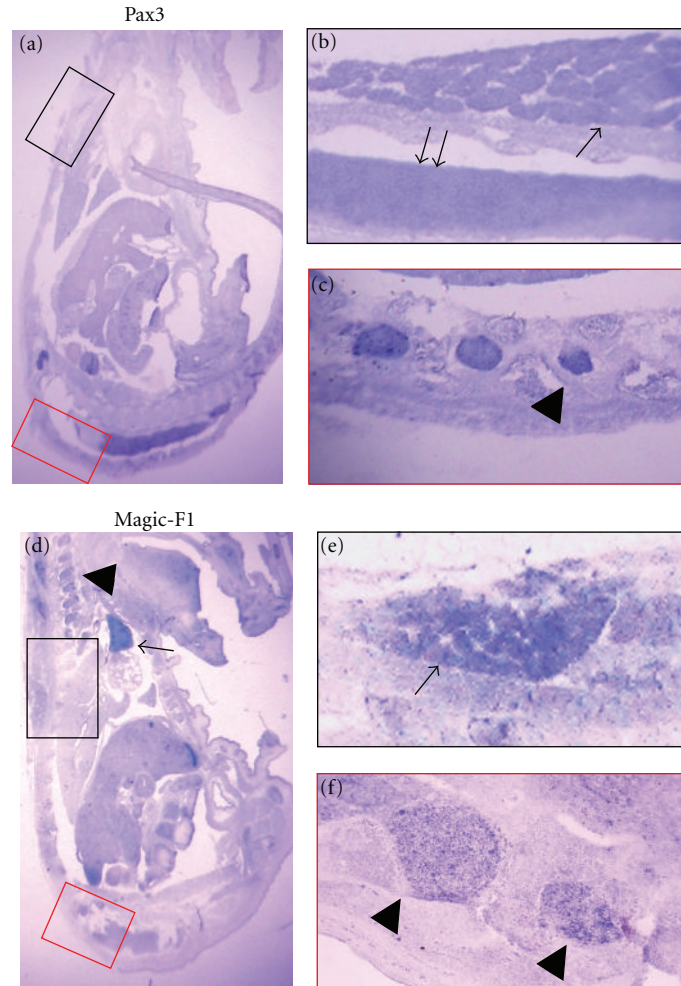


FIGURE 5: Expression of *Pax3* and *Magic-F1* at 15.5 dpc. Sagittal section of 15.5 dpc mouse hybridized with digoxigenin-labeled antisense *Pax3* riboprobes (a); specific *Pax3* transcripts are localized in cartilage primordium of tail vertebral body, cutaneous muscles (arrow) of thorax and trunk regions and in mid-cervical region of spinal cord (double arrow) as shown in (b); expression was also localized in cartilage primordium (arrowhead) of dorsal part of shaft region (c); (d) sagittal section of 15.5 dpc mouse hybridized with *Magic-F1* cRNA probes and signal is observed in cartilage primordium of anterior arch of cervical vertebra (arrowheads) and right lobe of thymus gland (arrow); specific *Magic-F1* transcripts are also localized in cutaneous muscles (arrow) of thorax and trunk regions (e); (f) higher magnification cartilage primordium of dorsal part of shaft region of ribs.

and myotome) originating from somites. No signal was detected in wt embryos at the same stage.

3.3. In Situ Hybridization on Cryostat Sections. *In situ* hybridization on 10 μm -cryostat sections was performed to localize *Magic-F1* and *Pax3* transcripts in embryos at later stages of development (11.5–13.5–15.5–17.5 dpc), since the large size of the samples did not allow a full penetration of the probes.

At 11.5 dpc, transgenic mouse embryos showed *Pax3* transcripts expression at the level of hindbrain (Figure 3(a)), neuroepithelium of neural tube (Figure 3(b)), and dorsal somites (Figure 3(c)). *Magic-F1* riboprobes showed a similar expression pattern (Figure 3(d)) reported for *Pax3* although the signal was not detected at the level of neuroepithelium of neural tube in embryos at the same stage (Figure 3(e)). Specific transcripts were also observed in the cervical dorsal

(posterior) root ganglion (Figures 3(c) and 3(f)) and somites (Figure 3(f)). In addition, at this stage, *Pax3* signal can be observed in wt embryos mainly in the cerebellar primordium and somites in lumbar region (Figure 3(f)), whereas no signal for *Magic-F1* has been detected (Figure 3(g)).

3.4. Localization of *Pax3* and *Magi-F1* Proteins and Transcripts. Immunofluorescence analysis was performed to localize the presence of recombinant protein. In transgenic embryos at 11.5 dpc, *MAGIC-F1* was mainly detected at the level of thoracic (Figure 3(i)) and lumbar (Figure 3(j)) somites, whereas a faint signal was detected in wt embryos (Figure 3(k)), probably due to the interference with HGF localization in the same area. At 13.5 dpc, transgenic embryos showed a weak signal of *Pax3* at the level of somites in thoracic (Figure 4(a)) and lumbosacral region (Figure 4(b)), whereas in the wild-type embryo, the signal appeared slightly

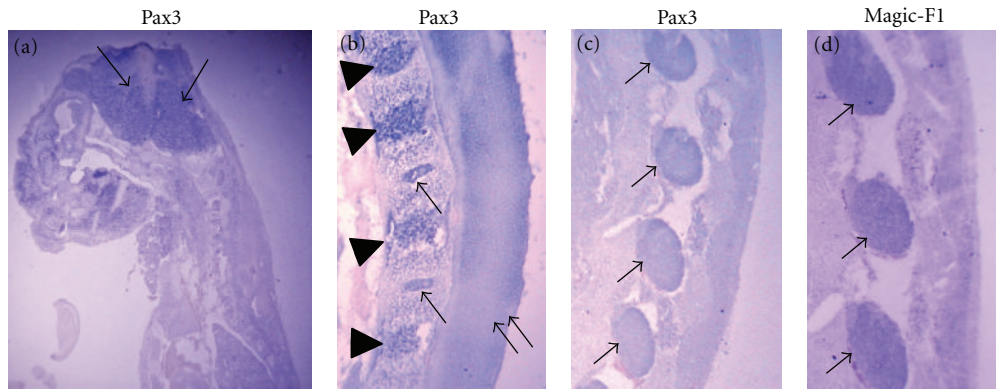


FIGURE 6: Expression of *Pax3* and *Magic-F1* at 17.5 dpc. Specific *Pax3* transcripts are localized on sagittal sections of 17.5 dpc at the level of the head (a), in the nucleus pulposus (b) of lumbar intervertebral disc (arrows) of the trunk, and in cartilage primordium (arrowheads) and wall of spinal cord in midlumbar region (double arrow) as shown in (b) and in cartilage primordium of dorsal part of ribs (c). (d) *Magic-F1* signal was observed at the level of cartilage primordium (arrows) of vertebrae.

stronger (Figure 4(c)). A weak signal have been detected in transgenic embryos hybridized by *Magic-F1* antisense riboprobes (Figure 4(d)), where *Magic-F1* was mainly expressed at the level of somites (Figure 4(e)), whereas no signal was detected in wild-type embryos (Figure 4(f)). Specific *Pax3* transcripts can be detected at later stage (15.5 dpc) (Figure 5(a)) in cartilage primordium of tail vertebral body, cutaneous muscles of thorax and trunk regions, and in mid-cervical region of spinal cord (Figure 5(b)). In addition, at this stage, *Pax3* expression demarcated also cartilage primordium of dorsal part of shaft region (Figure 5(c)). In sagittal section of 15.5 dpc embryo hybridized with *Magic-F1* cRNA probes a strong signal was detected in cartilage primordium of anterior arch of cervical vertebra and right lobe of thymus gland (Figure 5(d)). Consisted with this, *Magic-F1* resulted to be also expressed in cutaneous muscles of thorax and trunk regions (Figure 5(e)) and in primordium of dorsal part of shaft region of ribs (Figure 5(f)). From 17.5 dpc sagittal sections at the level of the head (Figure 6(a)), *Pax3* signal was detected in the trunk nucleus pulposus in central part of lumbar intervertebral disc (Figure 6(b)) and in cartilage primordium of dorsal part of ribs (Figure 6(c)). At this stage, *Magic-F1* expression was observed at the level of cartilage primordium of vertebrae (Figure 6(d)). These data suggest a role of this factor in muscle development possibly triggering the premature downregulation of *Pax3* signal pathway in skeletal muscle precursor cells.

4. Conclusion

Taken together, our data show that *Magic-F1* is localized in specific expression pattern in the developing muscular tissues. This could be relevant with the muscle phenotype previously observed in the transgenic animal model. The recombinant protein can be considered as a novel member of *Met* signaling, since it has been shown to interact with, and thus interfering with, cell migration and myogenesis. It is noteworthy that *Magic-F1* expression pattern is overlapping with *Pax3*, however, limited only in developing muscular

tissue, where exerts its myogenic potential. In fact, *Pax3* is able to activate *Myf5* (Myogenic factor 5) myogenic master gene [25], leading to the formation of skeletal muscle. In addition, *Pax3* orchestrates FGF (fibroblast growth factor) cascade [27], targeting directly *Fgfr4* (fibroblast growth factor receptor 4) and *Sprouty1* known to inhibit FGF pathway. *Magic-F1* may interfere with the balance between stem cell self-renewal and cell differentiation in developing muscles, mainly operated by *Pax3* and *Pax7* (paired box gene 7) [28]. It is unlikely that it is directly involved in stem-cell renewal; however, competing with HGF, the natural *Met* ligand could be move the balance towards muscle differentiation.

Further studies are necessary to elucidate *Magic-F1* specific role in cell specification and differentiation during embryogenesis.

Abbreviations

Akt:	Abelson leukemia kinase
ba:	Branchial arches
bp:	Base pair
BSA:	Bovine Serum Albumine
cmt:	Mesenchymal cephalic tissue
dpc:	Days post coitum
DNA:	Deoxyribonucleic acid
cDNA:	Complementary deoxyribonucleic acid
FGF:	Basic fibroblast growth factor
<i>Fgfr4</i> :	Fibroblast growth factor receptor 4
FOXO:	Forkhead box O protein
FW:	Forward
GAPDH:	Glyceraldehyde-3-phosphate dehydrogenase
hb:	Hindbrain
HGF:	Hepatocyte growth factor
MLC1F:	Myosin light chain type 1F
mTOR:	Mammalian target of rapamycin
<i>Myf5</i> :	Myogenic factor 5
<i>Pax3</i> :	Paired box gene 3
<i>Pax7</i> :	Paired box gene 7
PCR:	Polymerase chain reaction

REV: Reverse
 RNA: Ribonucleic acid
 cRNA: Complementary ribonucleic acid
 mRNA: Messenger ribonucleic acid
 RT: Room temperature
 TBE: Tris borate EDTA
 TGF- β : Transforming growth factor beta
 tv: Telencephalic vesicles
 wt: Wild type
 WB: Western blot.

Acknowledgments

This work is supported in part by FWO Odysseus no. G.0907.08, Wicka Funds no. zkb8720, Italian Ministry of University and Scientific Research (Grant no. 2005067555_003), CARIPO Rif. 2008.2005, and the Italian Research Programme no. PRIN2008RFNT8T_003. Flavio Ronzoni and Matilde Bongio contributed equally to this work.

References

- [1] A. Clop, F. Marcq, H. Takeda et al., "A mutation creating a potential illegitimate microRNA target site in the myostatin gene affects muscularity in sheep," *Nature Genetics*, vol. 38, no. 7, pp. 813–818, 2006.
- [2] S. J. Lee and A. C. McPherron, "Regulation of myostatin activity and muscle growth," *Proceedings of the National Academy of Sciences of the United States of America*, vol. 98, no. 16, pp. 9306–9311, 2001.
- [3] A. C. McPherron and S. J. Lee, "Double muscling in cattle due to mutations in the myostatin gene," *Proceedings of the National Academy of Sciences of the United States of America*, vol. 94, no. 23, pp. 12457–12461, 1997.
- [4] M. Schuelke, K. R. Wagner, L. E. Stolz et al., "Myostatin mutation associated with gross muscle hypertrophy in a child," *The New England Journal of Medicine*, vol. 350, no. 26, pp. 2682–2688, 2004.
- [5] C. McFarlane, E. Plummer, M. Thomas et al., "Myostatin induces cachexia by activating the ubiquitin proteolytic system through an NF- κ B-independent, FoxO1-dependent mechanism," *Journal of Cellular Physiology*, vol. 209, no. 2, pp. 501–514, 2006.
- [6] D. L. Allen and T. G. Unterman, "Regulation of myostatin expression and myoblast differentiation by FoxO and SMAD transcription factors," *American Journal of Physiology*, vol. 292, no. 1, pp. C188–C199, 2007.
- [7] L. Trusolino and P. M. Comoglio, "Scatter-factor and semaphorin receptors: cell signalling for invasive growth," *Nature Reviews Cancer*, vol. 2, no. 4, pp. 289–300, 2002.
- [8] L. Tamagnone and P. M. Comoglio, "Control of invasive growth by hepatocyte growth factor (HGF) and related scatter factors," *Cytokine and Growth Factor Reviews*, vol. 8, no. 2, pp. 129–142, 1997.
- [9] R. Zarnegar and G. K. Michalopoulos, "The many faces of hepatocyte growth factor: from hepatopoiesis to hematopoiesis," *The Journal of Cell Biology*, vol. 129, no. 5, pp. 1177–1180, 1995.
- [10] A. S. Woolf, M. Kolatsi-Joannou, P. Hardman et al., "Roles of hepatocyte growth factor/scatter factor and the met receptor in the early development of the metanephros," *The Journal of Cell Biology*, vol. 128, no. 1–2, pp. 171–184, 1995.
- [11] H. Takayama, W. J. La Rochelle, M. Anver, D. E. Bockman, and G. Merlino, "Scatter factor/hepatocyte growth factor as a regulator of skeletal muscle and neural crest development," *Proceedings of the National Academy of Sciences of the United States of America*, vol. 93, no. 12, pp. 5866–5871, 1996.
- [12] E. Andermarcher, M. A. Surani, and E. Gherardi, "Co-expression of the HGF/SF and c-met genes during early mouse embryogenesis precedes reciprocal expression in adjacent tissues during organogenesis," *Developmental Genetics*, vol. 18, no. 3, pp. 254–266, 1996.
- [13] F. Maina, M. C. Hilton, C. Ponzetto, A. M. Davies, and R. Klein, "Met receptor signaling is required for sensory nerve development and HGF promotes axonal growth and survival of sensory neurons," *Genes & Development*, vol. 11, no. 24, pp. 3341–3350, 1997.
- [14] L. Kos, A. Aronzon, H. Takayama et al., "Hepatocyte growth factor/scatter factor-MET signaling in neural crest-derived melanocyte development," *Pigment Cell Research*, vol. 12, no. 1, pp. 13–21, 1999.
- [15] S. Dietrich, F. Abou-Rebyeh, H. Brohmann et al., "The role of SF/HGF and c-Met in the development of skeletal muscle," *Development*, vol. 126, no. 8, pp. 1621–1629, 1999.
- [16] C. Schmidt, F. Bladt, S. Goedecke et al., "Scatter factor/hepatocyte growth factor is essential for liver development," *Nature*, vol. 373, no. 6516, pp. 699–702, 1995.
- [17] Y. Uehara, O. Minowa, C. Mori et al., "Placental defect and embryonic lethality in mice lacking hepatocyte growth factor/scatter factor," *Nature*, vol. 373, no. 6516, pp. 702–705, 1995.
- [18] F. Bladt, D. Riethmacher, S. Isenmann, A. Aguzzi, and C. Birchmeier, "Essential role for the c-met receptor in the migration of myogenic precursor cells into the limb bud," *Nature*, vol. 376, no. 6543, pp. 768–771, 1995.
- [19] S. M. Sheehan, R. Tatsumi, C. J. Temm-Grove, and R. E. Allen, "HGF is an autocrine growth factor for skeletal muscle satellite cells in vitro," *Muscle and Nerve*, vol. 23, no. 2, pp. 239–245, 2000.
- [20] K. J. Miller, D. Thaloor, S. Matteson, and G. K. Pavlath, "Hepatocyte growth factor affects satellite cell activation and differentiation in regenerating skeletal muscle," *American Journal of Physiology*, vol. 278, no. 1, pp. C174–C181, 2000.
- [21] R. Tatsumi, J. E. Anderson, C. J. Nevoret, O. Halevy, and R. E. Allen, "HGF/SF is present in normal adult skeletal muscle and is capable of activating satellite cells," *Developmental Biology*, vol. 194, no. 1, pp. 114–128, 1998.
- [22] Y. Leshem, D. B. Spicer, R. Gal-Levi, and O. Halevy, "Hepatocyte growth factor (HGF) inhibits skeletal muscle cell differentiation: a role for the bHLH protein Twist and the cdk inhibitor p27," *Journal of Cellular Physiology*, vol. 184, no. 1, pp. 101–109, 2000.
- [23] S. Anastasi, S. Giordano, O. Sthandier et al., "A natural hepatocyte growth factor/scatter factor autocrine loop in myoblast cells and the effect of the constitutive met kinase activation on myogenic differentiation," *The Journal of Cell Biology*, vol. 137, no. 5, pp. 1057–1068, 1997.
- [24] R. Gal-Levi, Y. Leshem, S. Aoki, T. Nakamura, and O. Halevy, "Hepatocyte growth factor plays a dual role in regulating skeletal muscle satellite cell proliferation and differentiation," *Biochimica et Biophysica Acta*, vol. 1402, no. 1, pp. 39–51, 1998.
- [25] M. Cassano, S. Biressi, A. Finan et al., "Magic-factor 1, a partial agonist of Met, induces muscle hypertrophy by protecting

- myogenic progenitors from apoptosis," *Plos One*, vol. 3, no. 9, Article ID e3223, 2008.
- [26] D. Henrique, J. Adam, A. Myat et al., "Expression of a Delta homologue in prospective neurons in the chick," *Nature*, vol. 375, no. 6534, pp. 787–790, 1995.
- [27] T. Sato, D. Rocancourt, L. Marques, S. Thorsteinsdóttir, and M. Buckingham, "A Pax3/Dmrt2/Myf5 regulatory cascade functions at the onset of myogenesis," *Plos Genetics*, vol. 6, no. 4, Article ID e1000897, 2010.
- [28] M. Lagha, J. D. Kormish, D. Rocancourt et al., "Pax3 regulation of FGF signaling affects the progression of embryonic progenitor cells into the myogenic program," *Genes & Development*, vol. 22, no. 13, pp. 1828–1837, 2008.

Research Article

Facilitated Cross-Bridge Interactions with Thin Filaments by Familial Hypertrophic Cardiomyopathy Mutations in α -Tropomyosin

Fang Wang,^{1,2} Nicolas M. Brunet,³ Justin R. Grubich,^{1,4}
Ewa A. Bienkiewicz,⁵ Thomas M. Asbury,^{6,7,8} Lisa A. Compton,^{1,9}
Goran Mihajlović,^{10,11} Victor F. Miller,^{1,12} and P. Bryant Chase¹

¹ Department of Biological Science, The Florida State University, Tallahassee, FL 32306-4295, USA

² Department of Neurobiology, College of Basic Medical Science, Southern Medical University, Guangzhou 510515, China

³ Donders Institute for Brain, Cognition and Behavior, Centre for Cognitive Neuroimaging, Radboud University Nijmegen, 6500 HB Nijmegen, The Netherlands

⁴ Department of Biology, American University in Cairo, Cairo 11835, Egypt

⁵ Department of Biomedical Sciences, The Florida State University College of Medicine, Tallahassee, FL 32306, USA

⁶ Institute of Molecular Biophysics, The Florida State University, Tallahassee, FL 32306, USA

⁷ Department of Mathematics, The Florida State University, Tallahassee, FL 32306, USA

⁸ Department of Biochemistry and Molecular Biology, Medical University of South Carolina, Charleston, SC 29425, USA

⁹ QIAGEN Inc., Valencia, CA 91355, USA

¹⁰ Department of Physics, The Florida State University, Tallahassee, FL 32306, USA

¹¹ Hitachi Global Storage Technologies, San Jose Research Center, San Jose, CA 95135, USA

¹² Agilent Technologies Inc., Santa Clara, CA 95051, USA

Correspondence should be addressed to P. Bryant Chase, chase@bio.fsu.edu

Received 1 June 2011; Accepted 24 August 2011

Academic Editor: Guy Benian

Copyright © 2011 Fang Wang et al. This is an open access article distributed under the Creative Commons Attribution License, which permits unrestricted use, distribution, and reproduction in any medium, provided the original work is properly cited.

Familial hypertrophic cardiomyopathy (FHC) is a disease of cardiac sarcomeres. To identify molecular mechanisms underlying FHC pathology, functional and structural differences in three FHC-related mutations in recombinant α -Tm (V95A, D175N, and E180G) were characterized using both conventional and modified *in vitro* motility assays and circular dichroism spectroscopy. Mutant Tm's exhibited reduced α -helical structure and increased unordered structure. When thin filaments were fully occupied by regulatory proteins, little or no motion was detected at pCa 9, and maximum speed (pCa 5) was similar for all tropomyosins. Ca^{2+} -responsiveness of filament sliding speed was increased either by increased $p\text{Ca}_{50}$ (V95A), reduced cooperativity n (D175N), or both (E180G). When temperature was increased, thin filaments with E180G exhibited dysregulation at temperatures $\sim 10^\circ\text{C}$ lower, and much closer to body temperature, than WT. When HMM density was reduced, thin filaments with D175N required fewer motors to initiate sliding or achieve maximum sliding speed.

1. Introduction

Familial hypertrophic cardiomyopathy (FHC) is a disease of cardiac sarcomeres, with causal mutations identified in a variety of myofilament proteins including thin filament Ca^{2+} -regulatory proteins [1–5]. Many mutations in cardiac troponin I (cTnI, the inhibitory subunit of the troponin complex, Tn) and cardiac troponin T (cTnT, Tn's tro-

pomyosin-binding subunit) enhance contractile function at subsaturating, and in some instances at saturating $[\text{Ca}^{2+}]$ [6–13]. Cardiac α -tropomyosin (α -Tm) is a third component of the thin filament associated with FHC [14, 15] that could have a central role in functional enhancement by FHC mutations, at least at subsaturating levels of $[\text{Ca}^{2+}]$, although wild-type Tm by itself (i.e., in the absence of Tn) does not enhance function [7, 16, 17].

The Tm molecule is an α -helical coiled-coil dimer that binds head to tail with adjacent Tm's to form a continuous strand, with two Tm strands associated with an F-actin [18]. Each Tm is associated with seven actin monomers and one ternary complex of Tn to form a structural regulatory unit that blocks strong myosin cross-bridge formation in the absence of Ca^{2+} (blocked state) [19]. Ca^{2+} binding to troponin C (TnC, Tn's Ca^{2+} -binding subunit) permits Tm movement on the thin filament to partially expose strong cross-bridge binding sites on actin (closed state), with further movement to the open state upon binding of myosin [19]. Some FHC mutations in α -Tm have been shown to reduce Tm's affinity for actin in vitro in the absence of Tn [20, 21] and may additionally destabilize Tn binding [22]; they further reduce the thermal stability of α -helix structure content in isolated Tm [21, 23, 24] or in actin-Tm [24]. It is not known, however, to what extent these structural changes and changes in thermal stability of Tm influence the function of regulated thin filaments.

Several FHC mutations in Tm may enhance some aspects of actomyosin function, but only at subsaturating and not saturating $[\text{Ca}^{2+}]$. V95A increased Ca^{2+} -sensitivity but also caused small decreases in the maximum solution ATPase activity, maximum speed of filament sliding in motility assays, and maximum Ca^{2+} -activatable tension in thin filament-reconstituted cardiac preparations [15, 22, 25]. E180G increased Ca^{2+} -sensitivity of tension in thin filament-reconstituted cardiac preparations [25], and both D175N and E180G increased Ca^{2+} -sensitivity of the fraction of motile filaments in motility assays [26]. Maximum filament sliding speed was unchanged by D175N or E180G when the ternary complex of cardiac Tn (cTn) was used [26] but increased with skeletal Tn (sTn) [20]. Vastus lateralis fibers from patients with the D175N mutation exhibited increased Ca^{2+} -sensitivity of isometric force compared with control fibers, with no change in maximum force or shortening velocity [27]. Maximum Ca^{2+} -activatable tension in thin filament-reconstituted cardiac preparations was decreased for D175N but not E180G, while total maximum tension was unchanged for D175N but increased for E180G; this was attributable to increases in Ca^{2+} -independent tension for both D175N and E180G, and V95A, too [25]. In a transgenic (Tg) mouse model, the E180G mutation leads to cardiac hypertrophy and increased mortality [28, 29]. These results from disparate assays indicate that FHC-related mutations require more thorough functional analysis at the level of single thin filaments to understand molecular mechanisms of the disease, and to allow for testing of potential therapeutic agents.

We therefore examined the influence of three FHC mutants in α -Tm on structure and Ca^{2+} activation of cardiac thin filaments under unloaded conditions. Thin filaments were reconstituted from recombinant, human α -GS-Tm WT, mutants E180G, D175N, or V95A, and cTn, and in vitro motility assays were used to examine function at the level of individual filaments. The three mutants increased Ca^{2+} -responsiveness of filament sliding speed at 30°C with no change in the maximum or minimum speeds at pCa 5 or pCa 9, respectively, when thin filaments were saturated with regulatory proteins. Increased Ca^{2+} -responsiveness by FHC

mutations was associated with greater structural disorder by circular dichroism spectroscopy (CD) at 25°C; E180G exhibited reduced functional stability at $\sim 10^\circ\text{C}$ lower than WT when temperature was varied in motility assays at pCa 5. Cross-bridge duty ratio was lower by $\sim 30\%$ with regulated thin filaments at pCa 5 and 30°C than with unregulated F-actin; duty ratio was similarly lower for thin filaments reconstituted with cTn and mutants D175N and E180G. In addition, enhancement of sliding speed for thin filaments reconstituted with D175N occurred at lower HMM densities than for WT or E180G. These results support the hypothesis that structural destabilization of α -Tm may play a role in functional enhancement by FHC-related mutations when there are few cross-bridges and could in some cases lead to loss of regulation (diastolic dysfunction) under normally minor perturbations of cellular conditions such as slight elevation of body core temperature during exercise.

2. Materials and Methods

2.1. Tropomyosin. Full-length human α -Tm (accession no. M19713) and, for comparison in structural assays, β -Tm (accession no. X06825) cDNAs were PCR amplified from a Marathon-Ready cDNA Library (CLONTECH Laboratories Inc., Palo Alto, Calif, USA) made from human cardiac tissue. Both PCR products were confirmed by sequencing. The α - and β -Tm constructs were engineered with a BamHI site just before the start codon and a Sall site just after the stop codon by PCR using Pfu Turbo DNA polymerase (Stratagene Inc., Cedar Creek, Tex, USA). Inserts were ligated to maltose-binding protein (MBP) fusion expression vector pMAL-c2 (New England BioLabs Inc., Beverly, Mass, USA) in which a thrombin cleavage site had been engineered. DH α cells were transformed with the ligation mixtures, and the positive clones were identified by PCR with the same primers used for cloning. The recombinant plasmids were extracted for expression and mutagenesis (α -Tm only).

Three α -Tm mutants, α -TmV95A, D175N, and E180G, were generated by PCR using QuikChange XL Site-Directed Mutagenesis system (Stratagene). Reactions were carried out per manufacturer's instructions with the template of α -Tm/pMAL-c2 plasmid and primer pairs:

pTmV95Af: 5'-CGCATCCAGCTGGCTGAGGAA-GAGTTGG-3'

pTmV95Ar: 5'-CCAACTCTTCCTCAGCCAGCTG-GATGCG-3'

pTmD175Nf: 5'-GGTCATCATTGAGAG-CAACCTGGAACGTGC-3'

pTmD175Nr: 5'-GCACGTTCCAGGTTGCTCTC-AATGATGACC-3'

pTmE180Gf: 5'-CGACCTGGAACGTGC-AGGAGAGCGGGCTGAGCTCTC-3'

pTmE180Gr: 5'-GAGAGCTCAGCCCGC-TCTCCTGCACGTTCCAGGTGC-3'

Plasmids extracted from three transformed mutants were sequenced with primers targeted at the flanks of MCS on

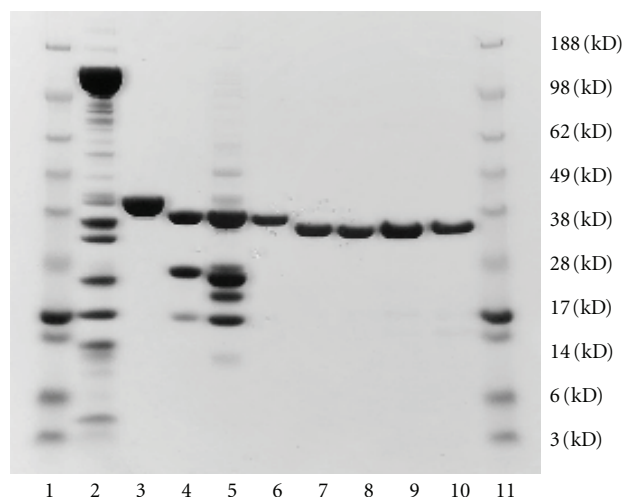


FIGURE 1: SDS-PAGE analysis of representative protein preparations. Gel was 4–12% polyacrylamide gradient (Invitrogen) and was stained with Coomassie brilliant blue. Lanes 1 and 11: MW markers (Invitrogen See Blue Plus 2; MWs given at right). Lane 2: rabbit skeletal muscle HMM. Lane 3: rabbit skeletal muscle actin. Lane 4: recombinant rat cardiac troponin (for reference only). Lane 5: human cTn (HcTn; Research Diagnostics). Lane 6: recombinant β -GS-Tm WT. Lane 7: recombinant α -GS-Tm WT. Lane 8: recombinant α -GS-Tm E180G. Lane 9: recombinant α -GS-Tm D175N. Lane 10: recombinant α -GS-Tm V95A.

pMAL-c2 vector to confirm sequence changes in the mutants.

For expression, competent *E. coli* BL21 (DE₃) cells (Novagen Inc., Madison, Wis, USA) were transformed with cDNA/pMAL-c2 plasmids for α -Tm, β -Tm, or the α -Tm mutants. Single colonies were grown at 37°C to an OD₆₀₀ of 0.5, followed by IPTG induction. The cells were harvested, resuspended in column buffer (20 mM Tris·Cl, pH 7.4, 10 mM β -mercaptoethanol, 200 mM NaCl, and 1 mM EDTA), lysed with mild sonication, centrifuged at 12,000 g, passed over an amylose affinity column (New England BioLabs Inc.), and eluted with column buffer containing 10 mM maltose. Fusion proteins were cleaved with thrombin (Sigma, St. Louis, Mo, USA) at 1 unit of thrombin per mg of protein in column buffer for 4 hrs at room temperature. The liberated recombinant Tm homodimers were purified on a Mono Q column (Pharmacia Biotech, Uppsala, Sweden) by high performance liquid chromatography (HPLC) with a gradient elution (buffer A: 20 mM Tris·Cl, pH 8.0, 25 mM NaCl; buffer B: buffer A containing 500 mM NaCl). The BamHI site on pMAL-c2 vector is integral to the thrombin cleavage region so all recombinant Tm's have two extra-amino acids (GS-) at the N-terminus; GS-represents a conservative alternative to the AS-dipeptide in bacterially expressed Tm that substitutes functionally for N-terminal acetylation [21, 30]. The purified recombinant proteins (Figure 1) were concentrated, aliquoted, and stored at -80°C in HPLC elution buffer until use [22, 25, 31].

2.2. Myosin, Heavy Meromyosin, Actin, and Troponin. Myosin and muscle acetone powder were made from rabbit back

and leg muscles as previously described [8, 31–34]. Animal handling was in accordance with the current US National Institutes of Health/National Research Council *Guide for the Care and Use of Laboratory Animals*. All procedures and protocols were approved by Florida State University's Institutional Animal Care and Use Committee. Adult male New Zealand white rabbits were anesthetized with 10 mg/kg Xylazine + 50 mg/kg of Ketamine + 3 mg Acepromazine in physiological saline (IM). Following verification of appropriate surgical depth of anesthesia, the animal was exsanguinated, skinned, eviscerated, and chilled on ice. Back and leg muscles were removed for the isolation of the desired proteins. F-actin was prepared from muscle acetone powder; aliquots of F-actin were labeled with rhodamine-phalloidin (RhPh) for fluorescence microscopy [8, 31, 32, 35]. Heavy meromyosin (HMM) was prepared by chymotryptic digestion of myosin [8, 31, 32, 35]. Native human cardiac troponin (HcTn) was obtained from Research Diagnostics (Flanders, NJ, USA). SDS-PAGE analysis of representative batches of proteins is shown in Figure 1.

2.3. SDS-PAGE and Western Blotting. Proteins were analyzed by SDS-PAGE and Western blotting. SDS-PAGE was conducted with 4–12% SDS-PAGE gels (Invitrogen Inc., Carlsbad, Calif, USA). Gels were either stained with Coomassie brilliant blue (Sigma) to visualize proteins (Figure 1) and analyzed with an EDAS-290 digital imaging system (Kodak, Rochester, NY, USA), or were used to transfer proteins to nitrocellulose (NC) membranes (BIO-RAD, Hercules, Calif, USA) at 30 mA, 4°C for overnight. NC membranes were rinsed for 2 min in TBS-T buffer (20 mM Tris·Cl, 150 mM NaCl, 0.05% Tween-20, pH 7.5), blocked for 1 hr at room temperature in TBS-T containing 2% BSA (Sigma), then incubated with rabbit anti-Tm antibody (Sigma, T3651) in TBS-T (1 : 3000) for 1 hr at room temperature. Bound antibody was detected using horseradish peroxidase-conjugated anti-rabbit IgG, followed by enhanced chemiluminescence reaction with ECL Plus Kit (Amersham Biosciences, Little Chalfont, Buckinghamshire, UK). Finally, the blots were exposed to Kodak X-ray film (Kodak, Rochester, NY, USA).

2.4. Circular Dichroism Spectroscopy. α -Tm, β -Tm, and three α -Tm mutants were dialyzed against CD buffer (20 mM sodium phosphate, 20 mM NaCl, pH 7.4) and concentrated using Centricon concentrators of 30,000 MW cut off (Millipore Corporation, Bedford, Mass, USA). Protein concentration was determined in CD buffer (in absence or presence [36] of 6 M urea) from A₂₈₀ using an extinction coefficient of 8700 M⁻¹ cm⁻¹ (<http://us.expasy.org/>). Data were collected at Tm concentrations of ~3–9 μ M on an AVIV model 202 spectrometer (Aviv Biomedical Inc, Lakewood, NJ, USA) using a 1 mm cuvette and wavelength range of 190–260 nm at 25°C. Each sample was equilibrated for 10 min prior to data collection and scanned three times with 0.4 or 0.5 nm wavelength steps and averaging time of 1 s. Molar ellipticity at 222 nm ($[\theta]_{222}$) was used to calculate α -helix content [37], and the elements of the secondary structure were analyzed with CDPro [38] using basis set 4. CD data represent the average of 2–3 independent experiments. The instrument

was calibrated with ammonium (+)-camphor-10-sulfonate (CSA) using the two-point method [39].

2.5. *In Vitro* Motility Assays. In vitro motility assays with regulated thin filaments were carried out essentially as described [8, 31, 32, 35, 40]. HMM was deposited in flow cells constructed with NC-coated coverslips. Motion of RhPh-labeled filaments was visualized by fluorescence microscopy and a SIT camera and recorded on VHS videocassettes. Motility assays were conducted at 30°C unless otherwise indicated. Control assays with unregulated F-actin were conducted in actin buffer (AB: 25 mM KCl, 25 mM imidazole, 4 mM MgCl₂, 1 mM EGTA, 1 mM DTT, and pH 7.4) [35] with 2 mM ATP and 0.3% methylcellulose (MC), or at pCa 5 without cTn or Tm. Solution composition for assays with regulated thin filaments was calculated as described [8, 31, 40]. Solutions contained 2 mM MgATP, 1 mM Mg²⁺, 10 mM EGTA, sufficient Ca(CH₃COO)₂ to achieve the desired pCa (pCa 9–4) (pCa = $-\log[\text{Ca}^{2+}]$, where $[\text{Ca}^{2+}]$ is in molar), 50 mM K⁺, 15 mM Na⁺, 20 mM MOPS, pH 7.00 at 30°C, 0.5% MC, and cTn and Tm (see below). $\Gamma/2$ was adjusted to 0.085 M with TrisOH and acetic acid. To minimize fluorophore photobleaching and photo-oxidative damage to the proteins, 3 mg/mL glucose, 100 $\mu\text{g}/\text{mL}$ glucose oxidase, 18 $\mu\text{g}/\text{mL}$ catalase, and 40 mM DTT were added to motility buffers.

Regulated thin filaments were reconstituted in the flow cell [8, 31, 40]. Regulatory protein concentrations were 125 nM in the reconstitution buffer and motility buffer. At 125 nM HcTn plus 125 nM Tm, filaments were “well regulated” as demonstrated by the absence of movement at pCa 9 and essentially all filaments moving rapidly at pCa 5.

2.6. Temperature Dependence of Filament Sliding Speed. Motility data were collected during continuously varying temperature transients as described [41, 42]. Flow cells were modified by photolithographic fabrication of a heater (thin Au film, 80–100 nm thick) and a gold resistive thermometer (10 mm wide and 80 nm thick stripes) onto opposite sides of the glass coverslip. The heater and thermometer were independently biased by two DC source meters (Keithley, MODEL 2400) that also measured the voltage drop over the thermometer stripe in a four-probe configuration. Experimental control and data acquisition were accomplished with a custom LabVIEW program. Thermometers were electrically insulated with GE varnish and calibrated over the temperature range 10–70°C. The thermoelectric heater covered most of the flow cell except for a small central window for observation of filament sliding, with the thermometer stripe located $\sim 500 \mu\text{m}$ from the window's edge. Flow cell heating was achieved using 0.8–0.9 A current which was turned off during cooling. The low starting temperature (14–18°C) and the cooling process were realized by chilled water flowing through a copper coil wrapped around the microscope objective.

2.7. Motion Analysis. Two approaches were used to quantify the speed of filament sliding. The first semiautomated approach was used to determine Ca²⁺-dependence of sliding

speed. Digital movies were recorded directly from the video signal or from videotape using a DC2 interface w/B&W adapter hardware (Miglia Tech., Ltd., Chesham, UK) connected to a Macintosh G4 with iMovie software. Movies were stored in QuickTime format. Custom software for filament tracking (motion analysis) was developed in the Linux environment and consists of image analysis software written in C++ with scripting and interface modules written in Python.

The image analysis software reads as input a series of images and outputs a list of filament paths. Initially, each frame of the digitized sequence was converted into a binary image using the Canny edge detection algorithm. For all detected edges, a centroid was computed and compared to the previous frame. Paths were constructed for objects whose current centroid was within a user-defined measure of tolerance of its predicted value. If a centroid was outside of these bounds, a new path was created and a current path may be ended. Each output path thus lists every member edge's centroid, length, head, and tail for all constituent frames. User-defined parameters control variables such as edge thresholding and minimum path length. Individual filament paths were retained when the centroid could be unambiguously tracked for ≥ 2 s. Speed statistics were calculated for each retained path. The ratio of SD/mean speed was calculated for each path as an indicator of uniformity of motion [32, 43], and filaments were accepted as moving uniformly when this ratio was < 0.3 . For each flow cell at a given condition, the fraction of uniformly moving filaments and their unweighted mean speed (\pm SD) was computed from all retained paths; the typical number of paths analyzed per flow cell was in the hundreds.

The second approach for motion analysis was used to determine the sliding speed of filaments during short time intervals (e.g., during continual variation of temperature) and to correlate sliding speed with the length of individual filaments (e.g., duty ratio experiments). This procedure utilized MetaMorph (Universal Imaging) and was carried out as described [41, 42]. Stacks of frames were created from digitized movies, and filament paths were visualized by superimposing all frames of one stack to form a projection and subtracting the image of the first frame. For each stack, 4–8 filaments were randomly selected, and the distance traveled (d) was determined by measuring the residual contour line for each filament path. Speed was determined as $d/(\Delta t(\#frames - 1))$, where Δt ($\Delta t = 0.0333$ s) is determined by the 30 frames-per-second video recording. Contour length of each filament was also recorded.

2.8. Cross-Bridge Duty Ratio during Unloaded Filament Sliding. Cross-bridge duty ratio (f) during unloaded filament sliding was estimated at pCa 5 using the method of Uyeda et al. [44]. Motility data were obtained as described above for regulated thin filaments and unregulated F-actin as a function of the density, ρ , of competent HMM on the flow cell surface, where ρ was varied by applying different concentrations of HMM in the initial sequence of solutions added to each flow cell. In separate experiments, ρ was determined from K-EDTA ATPase assays [16, 44]. Speeds of individual filaments and their contour lengths were measured as

described above. The filament length dependence of speed was fitted to an equation that describes the interaction between myosin and actin in a stochastic manner, based on the idea that f is equal to the probability that a myosin head is in the strong actin-binding state of its cross-bridge cycle, and that filaments will move at their maximum speed only if there is at least one cross-bridge at any given time [44]:

$$s = \eta(\rho) \times s_m \times \{1 - (1 - f)^N\}, \quad (1)$$

where s is the experimentally measured speed, s_m is the intrinsic maximum sliding speed, and $\eta(\rho)$ is a number between 0 and 1 that represents the efficiency by which force generated by a single myosin head is translated into sliding speed at a given ρ ; the regression parameters are f and $\eta(\rho) \times s_m$. The number of myosin motor domains (N) available for interaction with a filament of a given length l was calculated according to either the band model [44]:

$$N = 30\rho l, \quad (2)$$

where the constant 30 has units of nm and represents twice the reach of a myosin motor domain, or the nearest neighbor model [44, 45]:

$$N = l \left(\pi \times \frac{\rho}{\ln 2} \right)^{1/2}. \quad (3)$$

2.9. Statistical Analyses. Ca^{2+} -dependence of filament sliding speed was assessed by fitting data to a modified form of the Hill equation (4) by nonlinear least squares regression (SigmaPlot ver. 8.0; SPSS Inc., Richmond, Calif, USA):

$$s_u = \frac{s_{\max}}{1 + 10^{n(\text{pCa} - \text{pCa}_{50})}} + s_{\min}. \quad (4)$$

Equation (4) has four regression parameters: s_{\max} is the maximum Ca^{2+} -activated speed obtained at high $[\text{Ca}^{2+}]$ (low pCa); s_{\min} is the speed at low $[\text{Ca}^{2+}]$ (high pCa); pCa_{50} is an indicator of Ca^{2+} -sensitivity and is the pCa needed for the value $s_u - s_{\min}$ to reach 50% of s_{\max} ; n is an estimate of the slope around pCa_{50} and is an indicator of cooperativity. Regression parameter estimates are given \pm standard error of the regression. Statistical differences between regression parameter estimates (e.g., mutant versus WT) were evaluated for (4) by determining whether the difference deviated significantly from zero (SigmaPlot); parameters were considered to be significantly different when $P < 0.05$.

3. Results and Discussion

3.1. Maximum and Minimum Speeds of Filament Sliding. All motility assays with regulated thin filaments reconstituted with HcTn and α -GS-Tm WT, β -GS-Tm WT, or α -GS-Tm mutants were considered to be well regulated [31, 32, 40], that is, there was little or no motion at pCa 9, and fast uniform sliding at pCa 5 (Figure 2), indicating that both WT and mutants support complete Ca^{2+} -regulation when thin filaments are saturated with regulatory proteins. These unloaded motility data contrast with isometric force

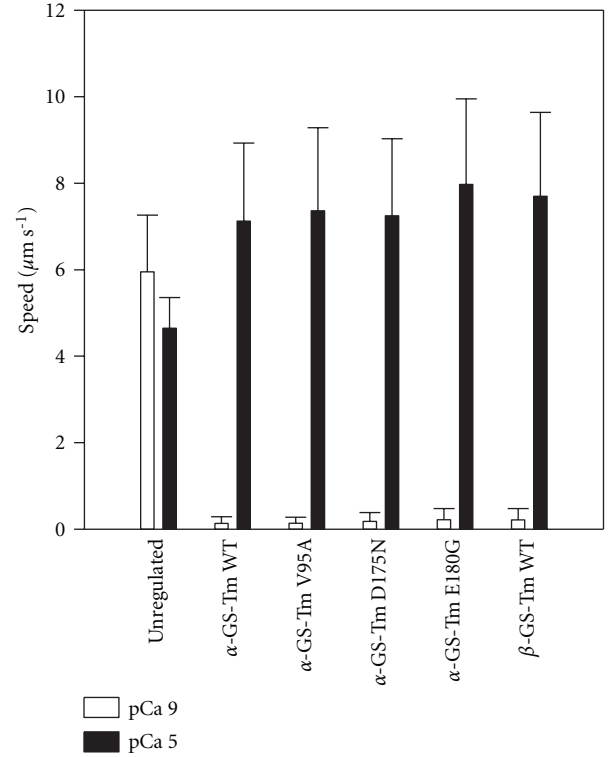


FIGURE 2: In vitro motility speeds at pCa 5 (solid bars) or pCa 9 (open bars) for regulated thin filaments (α -GS-Tm WT, α -GS-Tm V95A, α -GS-Tm D175N, α -GS-Tm E180G, or β -GS-Tm WT and HcTn), or at pCa 5 (solid bars) or in actin buffer (AB)-based motility buffer (pCa \sim 9; see Section 2.5) for unregulated F-actin. Values are the weighted mean \pm S.D. for 4–10 flow cells (weighted by the number of filament paths tracked in each flow cell).

measurements in thin filament-reconstituted cardiac preparations which exhibited active force generation in the absence of Ca^{2+} when V95A, D175N, or E180G replaced WT α -Tm [25] although this difference may at least partially reflect altered affinity of mutant Tm for F-actin and/or Tn [22] and experimental conditions where thin filaments may not have been fully saturated with regulatory proteins; it remains to be seen which condition more closely reflects diastole in FHC patients with these mutations. Unregulated F-actin exhibited similar speeds at both high and low $[\text{Ca}^{2+}]$ (Figure 2) as reported previously [32, 43]. At pCa 5, s_{\max} values for regulated thin filaments were 53–72% faster than for unregulated F-actin Figure 2; this result with HcTn and α -Tm agrees with our previous report [31] and compares with the enhancement of sliding speed by regulatory proteins from rabbit skeletal muscle [32, 46]. There was no significant difference between the speed at pCa 5 for thin filaments reconstituted with α -GS-Tm WT compared with any of the three mutants or β -GS-Tm WT (Figure 2). Tm alone (i.e., nonmutant Tm in the absence of troponin) does not enhance s_{\max} [7, 16, 17], and, thus, this effect may be more intimately linked to troponin than Tm [7, 47], as further implicated by FHC mutant data (Figure 2) [8]. In support of this idea, mutations D175N and E180G in human α -Tm were previously reported

TABLE 1: Motility speed-pCa regression parameter estimates for regulated thin filaments containing HcTn and WT or mutant tropomyosin.

	α -GS-Tm WT	α -GS-Tm V95A	α -GS-Tm D175N	α -GS-Tm E180G
pCa_{50}	6.52 ± 0.07	$6.63 \pm 0.03^*$	6.72 ± 0.12	$7.16 \pm 0.03^*$
n	2.3 ± 0.7	2.5 ± 0.4	$1.4 \pm 0.5^*$	$1.7 \pm 0.2^*$

Speed-pCa data from regulated motility assays (Figure 3) were fit to (4) by nonlinear least squares regression (Methods). Values are regression parameter estimates \pm SE. Parameter estimates of pCa_{50} and n that are significantly different from those for α -GS-Tm WT are indicated by * ($P < 0.05$).

to increase s_{\max} relative to WT, but only when coupled with rabbit sTn [20, 26] and not with human cTn (Figure 2) [26].

The data in Figure 2 are generally compatible with reports in which disparate experimental systems were used, with the exception of thin filament-reconstituted cardiac preparations at low Ca^{2+} , that these FHC-related mutations in α -Tm have generally small effects on function at very low or at saturating Ca^{2+} levels [15, 22, 25–27, 48, 49]. Decreased maximum ATPase activity and s_{\max} were found with V95A [15, 22] although these changes were small (<10%) and are not incompatible with our data (Figure 2). Increased maximum isometric force was previously reported in preparations from α -Tm E180G Tg mice [50] and thin filament-reconstituted cardiac preparations at saturating Ca^{2+} [25] although FHC-related changes in unloaded s_{\max} in motility assays or V_{\max} in fibers are not necessarily associated with corresponding changes in maximum isometric force [8, 11]. Thus, in conditions where thin filaments were saturated with Tn and Tm, the three mutations did not significantly affect the regulatory proteins' ability to inhibit actomyosin cycling at low [Ca^{2+}] and also had little or no effect on maximum unloaded filament sliding speed.

3.2. Ca^{2+} -Dependence of Filament Sliding. Sliding speed increased monotonically as [Ca^{2+}] increased (pCa decreased) for filaments reconstituted with HcTn and α -GS-Tm WT (Figure 3(a)). The data were well fit by the Hill relation, (4) ($R^2 = 0.928$; Figure 3(a)) and regression parameter estimates for pCa_{50} and n are given in Table 1. Ca^{2+} -dependence of sliding speed for regulated thin filaments containing mutant Tm was shifted leftward (increased Ca^{2+} -sensitivity) relative to α -GS-Tm WT (Figures 3(b)–3(d)). Regression estimates of pCa_{50} (4) increased by 0.11–0.64 pCa units relative to α -GS-Tm WT and were significant ($P < 0.05$) for the V95A and E180G mutations, although not for the D175N mutation (Table 1). The cooperativity parameter n (4) was significantly reduced for both the D175N and E180G mutations compared with WT (Table 1); this result translated into an increase in Ca^{2+} -responsiveness for the D175N mutant, too, even though pCa_{50} was not significantly affected (Figure 3; Table 1).

Our results with regulated thin filaments containing human α -Tm and cTn (Figure 3; Table 1) are in general agreement with previous studies when direct comparisons can be made (see Section 1), but there are also specific differences

in reported effects of these Tm mutations on contractile performance. Rat cardiac myocytes transfected with human α -Tm D175N exhibited no effect on the isometric force-pCa relation or maximum force [48] although Tg rats expressing human D175N exhibited a reduction in Ca^{2+} -sensitivity of force compared with WT [51]. Thin filament-reconstituted cardiac preparations exhibited increased Ca^{2+} -sensitivity of isometric force with V95A and E180G [25], as observed in motility assays (Figure 3; Table 1), and cooperativity was reduced for all three mutants [25]. Where differences were observed, they may depend on whether the assays test isometric or isotonic function which have different rate-limiting steps although another source of variability may derive from combining protein isoforms from different species. Differences could also stem from the use of homo-dimers of Tm (both with respect to isoforms and mutations) in most in vitro experiments, while varying proportions of homo- and heterodimers are expected in many experiments with Tg animal tissues or transfection of living cells. Where this has been examined however, the functional effects were linearly related to the amount of mutant present [49].

The E180G mutation increased pCa_{50} of motility by 0.64 pCa units (Figure 3(d); Table 1), which is a much greater extent than most other mutants, and similar to that observed for the same mutant's effect on Ca^{2+} -sensitivity of isometric force in thin filament-reconstituted cardiac preparations [25]. In some other reports, the E180G mutant also increased Ca^{2+} -sensitivity of various functional assays [26, 48, 50] but by lesser extents (~ 0.1 – 0.14 pCa units). An exception was ventricular strips from Tg rats expressing human α -Tm E180G mutation ($\sim 5\%$ of Tm mRNA) that exhibited no difference in Ca^{2+} -sensitivity of force relative to WT and also exhibited no cardiac hypertrophy [51]. Ca^{2+} -sensitivity of force increased more (~ 0.3 pCa units) in cardiac myocytes from Tg mouse hearts expressing $\sim 65\%$ α -Tm E180G, with a linear correlation between ΔpCa_{50} and fraction of α -Tm E180G that extrapolated to a large, ~ 0.4 pCa unit shift at 100% α -Tm E180G [49].

These differences in Ca^{2+} -sensitivity due to FHC-related mutations are in the same direction as observed with three C-terminal FHC-related mutations in cTnI although the cTnI mutants also exhibited substantial increases in s_{\max} [8]. α -Tm and cTnI mutants could affect s_{\max} differently because of differences in the molecular mechanisms by which cTnI and α -Tm mutants alter thin filament activation, or because of different sources for the regulatory proteins.

3.3. CD Spectroscopy. Ca^{2+} -sensitizing effects of the FHC mutations (Figure 3; Table 1) may be related to changes in Tm structure and are thus downstream in the signaling pathway from Ca^{2+} binding to TnC. Figure 4 shows CD spectra obtained from the five Tm samples. Each spectrum in Figure 4 is the average of 2–3 independent determinations from different batches of protein and each determination is the average of 3 scans. Spectra were quantified from $[\theta]_{222}$ and also by more extensive analysis (see Section 2) with CDPro software (Table 2). Both methods of analysis yielded similar, high estimates of α -helix content for both WT α - and β -Tm (78–85%) as expected for a protein that is largely

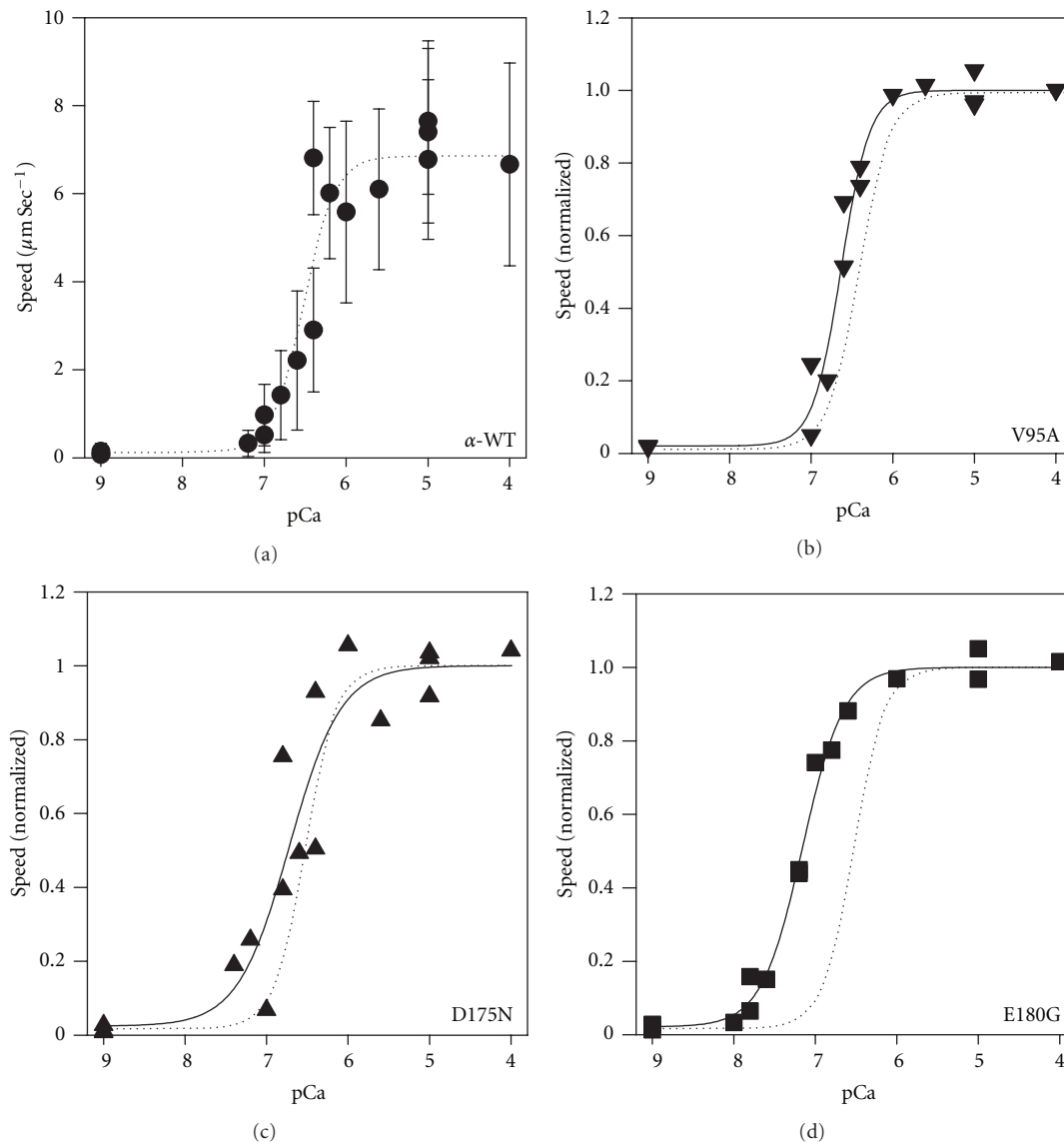


FIGURE 3: Ca^{2+} -dependence of in vitro motility speed for regulated thin filaments reconstituted with HcTn and either, (a) α -GS-Tm WT (\bullet), (b) α -GS-Tm V95A (\blacktriangledown), (c) α -GS-Tm D175N (\blacktriangle), or (d) α -GS-Tm E180G (\blacksquare). In (b–d), data and regressions for each Tm were normalized to $s_{\text{max}} + s_{\text{min}}$ from regression (4) for the same Tm. Each point represents the mean for one flow cell; error bars in (b–d) are comparable to those in (a). Solid lines are nonlinear least squares regression fits of the mutant Tm data to (4), and parameter estimates are given in Table 1. For comparison, the regression line for α -GS-Tm WT (a) was normalized as described above and plotted in panels (b–d) as a dotted line for reference.

α -helical coiled coil. CDPro and $[\theta]_{222}$ analyses indicated that α -helix content was lower in the three mutant proteins (61–73%; Table 2). Lower α -helix content of the mutant Tm's was correlated with higher fractions of unordered structure in CDPro analysis (Table 2). The V95A mutant had the lowest α -helix content, and reduced α -helix content of the E180G mutant is consistent with prediction from the COILS algorithm [52] of local destabilization around the mutation.

3.4. α -Tropomyosin E180G Mutation Alters Temperature Sensitivity of Filament Sliding at pCa 5. In addition to reduced α -helix content at 25°C (Figure 4), the E180G mutant exhibited decreased stability to thermal unfolding in the presence or

absence of actin [21, 24]. To test whether these structural changes are associated with functional effects in addition to the marked increase in Ca^{2+} -sensitivity (Figure 3(d)), we used a novel method for continuously varying temperature in motility assays [41, 42].

Speed of thin filaments reconstituted with α -Tm WT at pCa 5 increased with increasing temperature up to at least 50°C (Figure 5, open circles; note that these control data are a subset of the WT-regulated thin filament data replotted from Brunet et al. [42]). Above $\sim 54^\circ\text{C}$, thin filaments reconstituted with WT Tm/Tn exhibit an anomalous decline in sliding speed [42] that is likely due to dissociation of regulatory proteins from actin [24] and/or denaturation of

TABLE 2: Estimates of structural content of WT and mutant tropomyosins.

	α -helix (%)		β -sheet (%)	β -turn (%)	Unordered (%)
	$[\theta]_{222}$	CDPro	CDPro	CDPro	CDPro
α -GS-Tm WT	84.5 ± 4.6	79.1 ± 10.8	4.3 ± 3.4	7.0 ± 6.7	10.4 ± 5.8
α -GS-Tm V95A	60.6 ± 10.4	62.7 ± 6.4	8.2 ± 3.2	12.2 ± 3.5	17.0 ± 5.1
α -GS-Tm D175N	72.1 ± 0.7	72.9 ± 7.0	5.6 ± 3.7	11.3 ± 5.5	13.3 ± 6.0
α -GS-Tm E180G	69.7 ± 3.3	67.9 ± 5.6	5.9 ± 2.7	9.5 ± 4.7	17.3 ± 3.7
β -GS-Tm WT	83.6 ± 6.4	77.8 ± 13.1	5.2 ± 4.4	7.8 ± 6.5	10.1 ± 8.8

Estimates of structural content for each of the five recombinant Tm's were obtained from analyses of the individual CD spectra that were averaged for Figure 4. α -helical content was estimated from $[\theta]_{222}$ (Methods). Content of α -helix, β -sheet, and unordered structure was obtained using CDPro software (Methods). Values are mean \pm S.D. ($N = 2-3$ spectra); note that, for CDPro estimates, S.D. is the mean of S.D. values from CDPro.

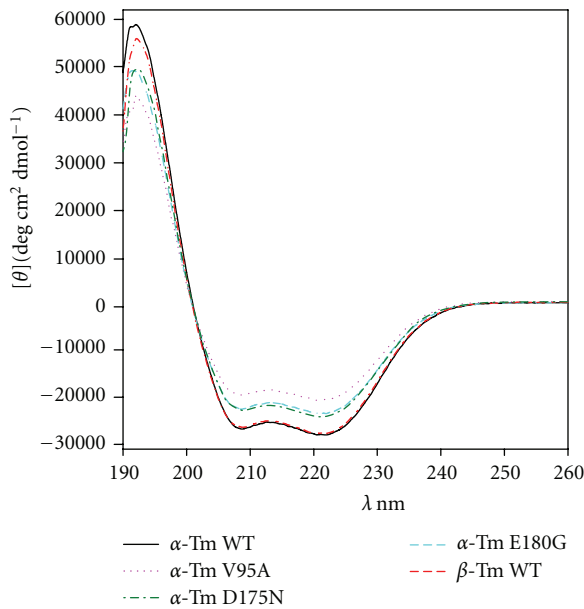


FIGURE 4: Circular dichroism spectra of WT and mutant recombinant tropomyosins in solution. Each spectrum is the average of 2-3 independent determinations. Estimates of structural content are given in Table 2. Note that curves for α -GS-Tm WT and β -GS-Tm WT overlap over most of the wavelength range.

Tm or Tn at elevated temperatures. Filament speed declines to that of unregulated F-actin [42] because actin and HMM denature at higher temperatures than Tm/Tn during these brief excursions to high temperatures.

When the assay was repeated with thin filaments reconstituted with α -Tm E180G (Figure 5, solid squares), the temperature dependence of speed deviated from WT at temperatures slightly above body temperature. At these higher temperatures, sliding speed was slower with mutant Tm than with WT. Above $\sim 44^\circ\text{C}$, there is a deflection in the speed-temperature relation for thin filaments reconstituted with α -Tm E180G (Figure 5). This deflection is likely indicative of structural destabilization, denaturation, and/or dissociation of mutant regulatory proteins at a substantially lower temperature ($\sim 10^\circ\text{C}$ lower) than for WT and is also indicative of a strong functional correlate of differential scanning calorimetry (DSC) measurements in solution [24].

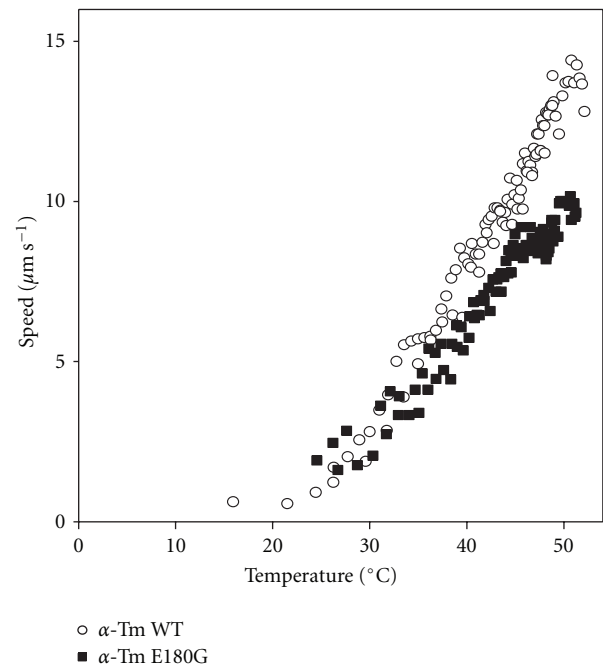


FIGURE 5: Temperature dependence of sliding speed at pCa 5 for regulated thin filaments reconstituted with HcTn and either α -GS-Tm E180G (■) or α -GS-Tm WT (○) [note that the control WT data are a subset of regulated thin filament data replotted from [42]]. Data were obtained during the heating phase of two cycles of heating and cooling in flow cells configured with a microfabricated thermo-electric heater for continuous variation of temperature (see Section 2). Points represent mean of the sliding speed for 3-8 filaments during one second. Note the deviation of mutant Tm data from WT as temperature increases.

The substantial increase in Ca^{2+} -sensitivity associated with the E180G mutation (Figure 3; Table 1) is thus correlated with reduced affinity for actin in vitro in the absence of Tn [20-22], destabilization of Tn binding to F-actin-Tm [22], reduced α -helix content (Figure 4; Table 2), and reduced thermal stability of structure [21, 24] and function (Figure 5). Structural destabilization of α -Tm by FHC mutations could reduce flexural rigidity, as suggested by Heller et al. [23] when considering other FHC-related mutations in α -Tm; modeling suggests that changes in protein compliance within sarcomeres could markedly affect

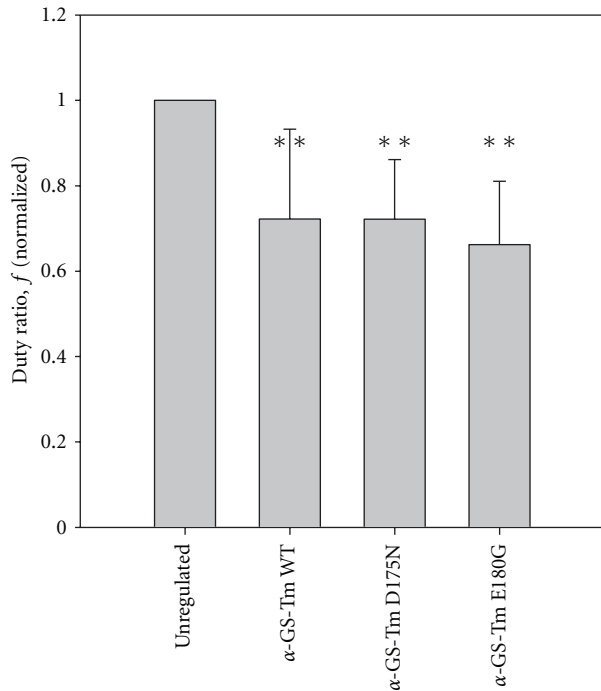


FIGURE 6: Cross-bridge duty ratio (f) during unloaded sliding of regulated thin filaments reconstituted with HcTn and either α -GS-Tm WT, α -GS-Tm D175N, or α -GS-Tm E180G is lower than for unregulated F-actin. Duty ratio was estimated using the method of Uyeda et al. [61] by varying HMM density (ρ) as described in Materials and Methods (see Section 2.8). Estimates of f were obtained by applying the band model and were normalized to the value obtained for WT at the same ρ . Bars indicate average normalized f for all ρ ($n = 5 - 8$); error bars indicate S.D. Duty ratios for all three types of regulated thin filaments were significantly lower than for unregulated F-actin (** $P < 0.01$) but were not statistically different from each other ($P > 0.05$).

muscle function [53–56]. The details of this mechanism are therefore distinct from the likely molecular basis for Ca^{2+} -sensitization by FHC-related mutations in the COOH-terminus of cTnI [8, 57]. Flexibility of Tm is clearly important for its structure and function [58] and changes related to FHC mutations could lead to a decrease in the already low-energy barrier for movement of Tm on actin [59]; detailed structural studies are needed to clarify the influence of FHC mutations on Tm structure and flexibility. In addition, coupling between adjacent regulatory units could be affected, as suggested by reduced cooperativity with the E180G mutation (Figure 3(d); Table 1) [25]. Significantly, the reduced thermal stability of thin filaments containing the E180G mutant α -Tm illustrated in Figure 5 suggests that patients with the FHC mutation could be more susceptible to diastolic dysfunction, and possibly sudden cardiac death, due to thin filament dysregulation during heavy exercise [24].

3.5. Dependence of Regulated Thin Filament Sliding at pCa 5 on Cross-Bridge Density and Number. Mutations in α -Tm could modulate the dependence of thin filament activation on cross-bridges and cross-bridge number [60]. To examine

this possibility for the D175N and E180G mutations—the two mutations associated with the largest effects on Ca^{2+} -responsiveness (Figure 3)—we measured sliding speed of regulated thin filaments at pCa 5 by varying the density of functional HMM (ρ) on the flow cell surface [44]. For each condition (Tm and ρ), speed (s) and the length (l) of individual filaments were used to determine $\eta(\rho) \times s_m$ and actomyosin duty ratio (f ; (1)) as described (see Section 2) [44]. Figure 6 shows that f was lower for WT-reconstituted thin filaments than for unregulated F-actin, and that f was similar for reconstituted thin filaments containing WT Tm or either of the two Tm mutants examined. Estimates of f in Figure 6 were obtained using the band model (2) and were averaged for all ρ . These results show that the structural and functional changes associated with mutants D175N and E180G of α -Tm do not lead to substantial changes in actomyosin duty ratio relative to WT-regulated thin filaments, consistent with regulated thin filament sliding speed being similar at saturating HMM density (Figure 2), and the distribution of cross-bridge states from sinusoidal analysis of isometric force in thin filament-reconstituted cardiac preparations [25].

For regulated thin filaments at pCa 5, s_m is a hyperbolic function of ρ (Figure 7). The ρ -dependence of $\eta(\rho) \times s_m$ was indistinguishable for α -Tm E180G compared with α -Tm WT (Figure 7). Thin filaments reconstituted with α -Tm D175N, on the other hand, exhibited motility and achieved maximum sliding speed at lower ρ 's than either E180G or WT (Figure 7). These results indicate that the D175N and E180G mutations increase Ca^{2+} -responsiveness of filament sliding (Figure 3; Table 1) by very different mechanisms even though the two mutations reside in close proximity and have similar effects on overall α -helical content as detected by CD spectroscopy (Figure 4). The data in Figures 3 and 7 suggest that effects of the D175N would be most evident at low levels of thin filament activation where the number of cross-bridges is small, and additional cross-bridges have the greatest impact.

3.6. Conclusions. Functional and structural differences in three FHC-related mutations in α -Tm (V95A, D175N, and E180G) were found using both conventional and modified in vitro motility assays and CD spectroscopy. Mutant Tm's exhibited lower α -helical content and more unordered structure than α -GS-Tm WT; these structural changes could result in alterations in flexural rigidity that, in turn, could be responsible for increased Ca^{2+} -responsiveness of regulated filament sliding that was observed with the mutants. α -GS-Tm E180G exhibited the greatest enhancement of Ca^{2+} -responsiveness of the mutants studied due to both a large increase in $p\text{Ca}_{50}$ and a reduction in n , and dysregulation at $\sim 10^\circ\text{C}$ lower temperature than WT. α -GS-Tm V95A exhibited a smaller but significant increase in $p\text{Ca}_{50}$. α -GS-Tm D175N exhibited lower n and a marked reduction in the minimum density of HMM necessary for initiating filament sliding and for achieving maximum sliding speed at saturating Ca^{2+} . These structural and functional changes provide insights into molecular mechanisms of pathological cardiac hypertrophy.

Increased Ca^{2+} -responsiveness of cardiac myofibrillar function appears to be a common feature of FHC-related

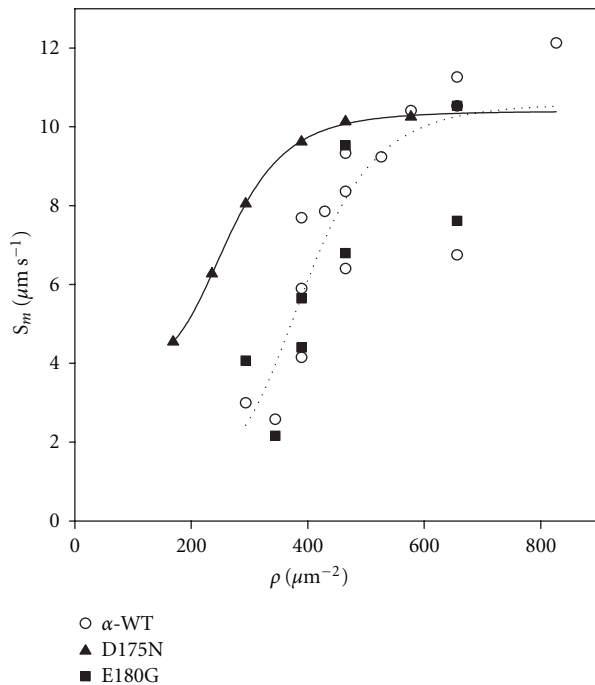


FIGURE 7: HMM density (ρ) dependence of maximum unloaded filament sliding speed (s_m) of regulated thin filaments reconstituted with HcTn and either α -GS-Tm WT (\circ), α -GS-Tm D175N (\blacktriangle), or α -GS-Tm E180G (\blacksquare). s_m was obtained at each ρ according to the method of Uyeda et al. [61] as described in Section 2.8; each point is from one flow cell. Note that $s_m(\rho)$ for thin filaments containing α -GS-Tm D175N is shifted leftward of that for thin filaments containing either α -GS-Tm WT or α -GS-Tm E180G.

mutations in α -Tm, cTnI, and cTnT (Figure 3) [8, 13, 15, 23, 25–27, 29, 48, 50, 62]. The extent of enhancement of Ca^{2+} -sensitivity is generally associated with clinical prognosis in FHC patients [57, 63] although it is not generally known the extent to which function in vivo with variable ratios of WT and mutant homo-dimers, and also presumptive heterodimers, might differ from that found using in vitro assays with pure homo-dimers such as those described here. Functional consequences of increased Ca^{2+} -sensitivity in the living heart, in the absence of adaptive responses, are expected to be slowed relaxation and increased duration of systole because the intracellular Ca^{2+} transient does not normally achieve sufficiently high Ca^{2+} concentrations to saturate TnC [56]. Observations on intact hearts from Tg mice with α -Tm mutation E180G are consistent with these expectations [28, 29, 49]. Thus, there are clear possibilities for direct links between thin filament mutations and hypertrophic signaling through altered mechanical and energetic load, and/or altered Ca^{2+} -cycling in myocytes [56].

Acknowledgments

The authors gratefully acknowledge Shanedah Williams Brown, Lori McFadden and Alyson Barnes for preparation of myosin and actin, Margaret Seavy for HPLC analyses, Kim Riddle and Tom Fellers from FSU's Biological Science Imag-

ing Resource for assistance with MetaMorph, Drs. Peng Xiong and Stephan von Molnár in Florida State University's Department of Physics and Ingetrative NanoScience Institute for expertise necessary to accomplish the experiments involving microfabrication and for critical comments, Campion Loong and Dr. Robin Maytum for helpful discussions; and Janina Bhuvorakul for assistance with preparation of figures and tables. They also thank the Physical Biochemistry Facility at the FSU Institute of Molecular Biophysics for use of the circular dichroism spectrometer. This work was supported by NIH/NHLBI Grant HL63974 (PBC), American Heart Association FL/PR Affiliate Predoctoral Fellowships 0315097B (NMB) and 0415104B (LAC), and NSF NIRT Grant ECS-0210332 (PX).

References

- [1] J. A. Towbin and N. E. Bowles, "The failing heart," *Nature*, vol. 415, no. 6868, pp. 227–233, 2002.
- [2] C. S. Redwood, J. C. Moolman-Smook, and H. Watkins, "Properties of mutant contractile proteins that cause hypertrophic cardiomyopathy," *Cardiovascular Research*, vol. 44, no. 1, pp. 20–36, 1999.
- [3] D. Fatkin and R. M. Graham, "Molecular mechanisms of inherited cardiomyopathies," *Physiological Reviews*, vol. 82, no. 4, pp. 945–980, 2002.
- [4] M. S. Parmacek and R. J. Solaro, "Biology of the troponin complex in cardiac myocytes," *Progress in Cardiovascular Diseases*, vol. 47, no. 3, pp. 159–176, 2004.
- [5] F. Ahmad, J. G. Seidman, and C. E. Seidman, "The genetic basis for cardiac remodeling," *Annual Review of Genomics and Human Genetics*, vol. 6, pp. 185–216, 2005.
- [6] K. Elliott, H. Watkins, and C. S. Redwood, "Altered regulatory properties of human cardiac troponin I mutants that cause hypertrophic cardiomyopathy," *Journal of Biological Chemistry*, vol. 275, no. 29, pp. 22069–22074, 2000.
- [7] E. Homsher, D. M. Lee, C. Morris, D. Pavlov, and L. S. Tobacman, "Regulation of force and unloaded sliding speed in single thin filaments: effects of regulatory proteins and calcium," *Journal of Physiology*, vol. 524, no. 1, pp. 233–243, 2000.
- [8] J. Köhler, Y. Chen, B. Brenner et al., "Familial hypertrophic cardiomyopathy mutations in troponin I (K183Δ, G203S, K206Q) enhance filament sliding," *Physiological Genomics*, vol. 14, pp. 117–128, 2003.
- [9] R. Lang, A. V. Gomes, J. Zhao, P. R. Housmans, T. Miller, and J. D. Potter, "Functional analysis of a troponin I (R145G) mutation associated with familial hypertrophic cardiomyopathy," *Journal of Biological Chemistry*, vol. 277, no. 14, pp. 11670–11678, 2002.
- [10] D. Lin, A. Bobkova, E. Homsher, and L. S. Tobacman, "Altered cardiac troponin T in vitro function in the presence of a mutation implicated in familial hypertrophic cardiomyopathy," *Journal of Clinical Investigation*, vol. 97, no. 12, pp. 2842–2848, 1996.
- [11] H. L. Sweeney, H. S. Feng, Z. Yang, and H. Watkins, "Functional analyses of troponin T mutations that cause hypertrophic cardiomyopathy: insights into disease pathogenesis and troponin function," *Proceedings of the National Academy of Sciences of the United States of America*, vol. 95, no. 24, pp. 14406–14410, 1998.
- [12] D. Szczesna, R. Zhang, J. Zhao, M. Jones, G. Guzman, and J. D. Potter, "Altered regulation of cardiac muscle contraction

- by troponin T mutations that cause familial hypertrophic cardiomyopathy," *Journal of Biological Chemistry*, vol. 275, no. 1, pp. 624–630, 2000.
- [13] F. Takahashi-Yanaga, S. Morimoto, K. Harada et al., "Functional consequences of the mutations in human cardiac troponin I gene found in familial hypertrophic cardiomyopathy," *Journal of Molecular and Cellular Cardiology*, vol. 33, no. 12, pp. 2095–2107, 2001.
- [14] L. Thierfelder, H. Watkins, C. MacRae et al., " α -Tropomyosin and cardiac troponin T mutations cause familial hypertrophic cardiomyopathy: a disease of the sarcomere," *Cell*, vol. 77, no. 5, pp. 701–712, 1994.
- [15] A. Karibe, L. S. Tobacman, J. Strand et al., "Hypertrophic cardiomyopathy caused by a novel α -tropomyosin mutation (V95A) is associated with mild cardiac phenotype, abnormal calcium binding to troponin, abnormal myosin cycling, and poor prognosis," *Circulation*, vol. 103, no. 1, pp. 65–71, 2001.
- [16] A. M. Gordon, Y. Chen, B. Liang, M. LaMadrid, Z. Luo, and P. B. Chase, "Skeletal muscle regulatory proteins enhance F-actin *in vitro* motility," *Advances in Experimental Medicine and Biology*, vol. 453, pp. 187–197, 1998.
- [17] P. VanBuren, K. A. Palmiter, and D. M. Warshaw, "Tropomyosin directly modulates actomyosin mechanical performance at the level of a single actin filament," *Proceedings of the National Academy of Sciences of the United States of America*, vol. 96, no. 22, pp. 12488–12493, 1999.
- [18] S. V. Perry, "Vertebrate tropomyosin: distribution, properties and function," *Journal of Muscle Research and Cell Motility*, vol. 22, no. 1, pp. 5–49, 2001.
- [19] A. M. Gordon, E. Homsher, and M. Regnier, "Regulation of contraction in striated muscle," *Physiological Reviews*, vol. 80, no. 2, pp. 853–924, 2000.
- [20] W. Bing, C. S. Redwood, I. F. Purcell, G. Esposito, H. Watkins, and S. B. Marston, "Effects of two hypertrophic cardiomyopathy mutations in α -tropomyosin, Asp175Asn and Glu180Gly, on Ca^{2+} regulation of thin filament motility," *Biochemical and Biophysical Research Communications*, vol. 236, no. 3, pp. 760–764, 1997.
- [21] N. Golitsina, Y. An, N. J. Greenfield et al., "Effects of two familial hypertrophic cardiomyopathy-causing mutations on α -tropomyosin structure and function," *Biochemistry*, vol. 38, no. 12, p. 3850, 1999.
- [22] M. C. Mathur, P. B. Chase, and J. M. Chalovich, "Several cardiomyopathy causing mutations on tropomyosin either destabilize the active state of actomyosin or alter the binding properties of tropomyosin," *Biochemical and Biophysical Research Communications*, vol. 406, no. 1, pp. 74–78, 2011.
- [23] M. J. Heller, M. Nili, E. Homsher, and L. S. Tobacman, "Cardiomyopathic tropomyosin mutations that increase thin filament Ca^{2+} sensitivity and tropomyosin N-domain flexibility," *Journal of Biological Chemistry*, vol. 278, no. 43, pp. 41742–41748, 2003.
- [24] E. Kremneva, S. Boussof, O. Nikolaeva, R. Maytum, M. A. Geeves, and D. I. Levitsky, "Effects of two familial hypertrophic cardiomyopathy mutations in α -tropomyosin, Asp175Asn and Glu180Gly, on the thermal unfolding of actin-bound tropomyosin," *Biophysical Journal*, vol. 87, no. 6, pp. 3922–3933, 2004.
- [25] F. Bai, A. Weis, A. K. Takeda, P. B. Chase, and M. Kawai, "Enhanced active cross-bridges during diastole: molecular pathogenesis of tropomyosin's HCM mutations," *Biophysical Journal*, vol. 100, no. 4, pp. 1014–1023, 2011.
- [26] W. Bing, A. Knott, C. Redwood et al., "Effect of hypertrophic cardiomyopathy mutations in human cardiac muscle α -tropomyosin (Asp175Asn and Glu180Gly) on the regulatory properties of human cardiac troponin determined by *in vitro* motility assay," *Journal of Molecular and Cellular Cardiology*, vol. 32, no. 8, pp. 1489–1498, 2000.
- [27] R. Bottinelli, D. A. Coviello, C. S. Redwood et al., "A mutant tropomyosin that causes hypertrophic cardiomyopathy is expressed *in vivo* and associated with an increased calcium sensitivity," *Circulation Research*, vol. 82, no. 1, pp. 106–115, 1998.
- [28] R. Prabhakar, N. Petrashevskaya, A. Schwartz et al., "A mouse model of familial hypertrophic cardiomyopathy caused by a α -tropomyosin mutation," *Molecular and Cellular Biochemistry*, vol. 251, no. 1–2, pp. 33–42, 2003.
- [29] R. Prabhakar, G. P. Boivin, I. L. Grupp et al., "A familial hypertrophic cardiomyopathy α -tropomyosin mutation causes severe cardiac hypertrophy and death in mice," *Journal of Molecular and Cellular Cardiology*, vol. 33, no. 10, pp. 1815–1828, 2001.
- [30] P. B. Monteiro, R. C. Lataro, J. A. Ferro, and F. D. C. Reinach, "Functional α -tropomyosin produced in *Escherichia coli*. A dipeptide extension can substitute the amino-terminal acetyl group," *Journal of Biological Chemistry*, vol. 269, no. 14, pp. 10461–10466, 1994.
- [31] B. Schoffstall, N. M. Brunet, S. Williams et al., " Ca^{2+} sensitivity of regulated cardiac thin filament sliding does not depend on myosin isoform," *Journal of Physiology*, vol. 577, no. 3, pp. 935–944, 2006.
- [32] A. M. Gordon, M. A. LaMadrid, Y. Chen, Z. Luo, and P. B. Chase, "Calcium regulation of skeletal muscle thin filament motility *in vitro*," *Biophysical Journal*, vol. 72, no. 3, pp. 1295–1307, 1997.
- [33] S. S. Margossian and S. Lowey, "Preparation of myosin and its subfragments from rabbit skeletal muscle," *Methods in Enzymology*, vol. 85, pp. 55–71, 1982.
- [34] J. D. Pardee and J. Aspudich, "Purification of muscle actin," *Methods in Enzymology*, vol. 85, pp. 164–181, 1982.
- [35] S. J. Kron, Y. Y. Toyoshima, T. Q. P. Uyeda, and J. A. Spudich, "Assays for actin sliding movement over myosin-coated surfaces," *Methods in Enzymology*, vol. 196, pp. 399–416, 1991.
- [36] H. Edelhoch, "Spectroscopic determination of tryptophan and tyrosine in proteins," *Biochemistry*, vol. 6, no. 7, pp. 1948–1954, 1967.
- [37] Y. H. Chen, J. T. Yang, and H. M. Martinez, "Determination of the secondary structures of proteins by circular dichroism and optical rotatory dispersion," *Biochemistry*, vol. 11, no. 22, pp. 4120–4131, 1972.
- [38] N. Sreerama and R. W. Woody, "Estimation of protein secondary structure from circular dichroism spectra: comparison of CONTIN, SELCON, and CDSSTR methods with an expanded reference set," *Analytical Biochemistry*, vol. 287, no. 2, pp. 252–260, 2000.
- [39] G. C. Chen and J. T. Yang, "Two-point calibration of circular dichrometer with d-10-camphorsulfonic acid," *Analytical Letters*, vol. 10, pp. 1195–1207, 1977.
- [40] B. Liang, Y. Chen, C. K. Wang et al., " Ca^{2+} regulation of rabbit skeletal muscle thin filament sliding: role of cross-bridge number," *Biophysical Journal*, vol. 85, no. 3, pp. 1775–1786, 2003.
- [41] G. Mihajlović, N. M. Brunet, J. Trbović, P. Xiong, S. Von Molnár, and P. B. Chase, "All-electrical switching and control mechanism for actomyosin-powered nanoactuators," *Applied Physics Letters*, vol. 85, no. 6, pp. 1060–1062, 2004.
- [42] N. M. Brunet, G. Mihajlović, K. Aledeat et al., "Micro-mechanical thermal assays of Ca^{2+} -regulated thin filament

- function and modulation by hypertrophic cardiomyopathy mutants of human cardiac troponin," *Journal of Biomedicine and Biotechnology*. In press.
- [43] E. Homsher, B. Kim, A. Bobkova, and L. S. Tobacman, "Calcium regulation of thin filament movement in an *in vitro* motility assay," *Biophysical Journal*, vol. 70, no. 4, pp. 1881–1892, 1996.
- [44] T. Q. P. Uyeda, S. J. Kron, and J. A. Spudich, "Myosin step size estimation from slow sliding movement of actin over low densities of heavy meromyosin," *Journal of Molecular Biology*, vol. 214, no. 3, pp. 699–710, 1990.
- [45] Y. Harada, K. Sakurada, T. Aoki, D. D. Thomas, and T. Yanagida, "Mechanochemical coupling in actomyosin energy transduction studied by *in vitro* movement assay," *Journal of Molecular Biology*, vol. 216, no. 1, pp. 49–68, 1990.
- [46] I. D. C. Fraser and S. B. Marston, "*In vitro* motility analysis of actin-tropomyosin regulation by troponin and calcium. The thin filament is switched as a single cooperative unit," *Journal of Biological Chemistry*, vol. 270, no. 14, pp. 7836–7841, 1995.
- [47] B. Schoffstall, V. A. LaBarbera, N. M. Brunet et al., "Interaction between troponin and myosin enhances contractile activity of myosin in cardiac muscle," *DNA and Cell Biology*. In press.
- [48] D. E. Michele, F. P. Albayya, and J. M. Metzger, "Direct, convergent hypersensitivity of calcium-activated force generation produced by hypertrophic cardiomyopathy mutant α -tropomyosins in adult cardiac myocytes," *Nature Medicine*, vol. 5, no. 12, pp. 1413–1417, 1999.
- [49] D. E. Michele, C. A. Gomez, K. E. Hong, M. V. Westfall, and J. M. Metzger, "Cardiac dysfunction in hypertrophic cardiomyopathy mutant tropomyosin mice is transgene-dependent, hypertrophy-independent, and improved by β -blockade," *Circulation Research*, vol. 91, no. 3, pp. 255–262, 2002.
- [50] E. M. Burkart, G. M. Arteaga, M. P. Sumandea, R. Prabhakar, D. F. Wiczorek, and R. J. Solaro, "Altered signaling surrounding the C-lobe of cardiac troponin C in myofilaments containing an α -tropomyosin mutation linked to familial hypertrophic cardiomyopathy," *Journal of Molecular and Cellular Cardiology*, vol. 35, no. 10, pp. 1285–1293, 2003.
- [51] D. Wernicke, C. Thiel, C. M. Duja-Isac et al., " α -tropomyosin mutations Asp175 Asn and Glu180 Gly affect cardiac function in transgenic rats in different ways," *American Journal of Physiology*, vol. 287, no. 3, pp. R685–R695, 2004.
- [52] A. Lupas, M. Van Dyke, and J. Stock, "Predicting coiled coils from protein sequences," *Science*, vol. 252, no. 5010, pp. 1162–1164, 1991.
- [53] T. L. Daniel, A. C. Trimble, and P. B. Chase, "Compliant realignment of binding sites in muscle: transient behavior and mechanical tuning," *Biophysical Journal*, vol. 74, no. 4, pp. 1611–1621, 1998.
- [54] D. A. Martyn, P. B. Chase, M. Regnier, and A. M. Gordon, "A simple model with myofilament compliance predicts activation-dependent crossbridge kinetics in skinned skeletal fibers," *Biophysical Journal*, vol. 83, no. 6, pp. 3425–3434, 2002.
- [55] P. B. Chase, J. M. Macpherson, and T. L. Daniel, "A spatially explicit nanomechanical model of the half-sarcomere: myofilament compliance affects Ca^{2+} -activation," *Annals of Biomedical Engineering*, vol. 32, no. 11, pp. 1559–1568, 2004.
- [56] A. Kataoka, C. Hemmer, and P. B. Chase, "Computational simulation of hypertrophic cardiomyopathy mutations in Troponin I: influence of increased myofilament calcium sensitivity on isometric force, ATPase and $[\text{Ca}^{2+}]_i$," *Journal of Biomechanics*, vol. 40, no. 9, pp. 2044–2052, 2007.
- [57] A. V. Gomes and J. D. Potter, "Molecular and cellular aspects of troponin cardiomyopathies," *Annals of the New York Academy of Sciences*, vol. 1015, pp. 214–224, 2004.
- [58] J. H. Brown, K. H. Kim, G. Jun et al., "Deciphering the design of the tropomyosin molecule," *Proceedings of the National Academy of Sciences of the United States of America*, vol. 98, no. 15, pp. 8496–8501, 2001.
- [59] W. Lehman, V. Hatch, V. Korman et al., "Tropomyosin and actin isoforms modulate the localization of tropomyosin strands on actin filaments," *Journal of Molecular Biology*, vol. 302, no. 3, pp. 593–606, 2000.
- [60] P. Vibert, R. Craig, and W. Lehman, "Steric-model for activation of muscle thin filaments," *Journal of Molecular Biology*, vol. 266, no. 1, pp. 8–14, 1997.
- [61] T. Q. P. Uyeda, H. M. Warrick, S. J. Kron, and J. A. Spudich, "Quantized velocities at low myosin densities in an *in vitro* motility assay," *Nature*, vol. 352, no. 6333, pp. 307–311, 1991.
- [62] B. Gafurov, S. Fredricksen, A. Cai, B. Brenner, P. B. Chase, and J. M. Chalovich, "The $\Delta 14$ mutation of human cardiac troponin T enhances ATPase activity and alters the cooperative binding of S1-ADP to regulated actin," *Biochemistry*, vol. 43, no. 48, pp. 15276–15285, 2004.
- [63] A. V. Gomes and J. D. Potter, "Cellular and molecular aspects of familial hypertrophic cardiomyopathy caused by mutations in the cardiac troponin I gene," *Molecular and Cellular Biochemistry*, vol. 263, no. 1, pp. 99–114, 2004.

Research Article

Electrophoretic Mobility of Cardiac Myosin Heavy Chain Isoforms Revisited: Application of MALDI TOF/TOF Analysis

Petra Arnostova,¹ Petr L. Jedelsky,^{2,3,4} Tomáš Soukup,⁵ and Jitka Zurmanova¹

¹Department of Physiology, Faculty of Science, Charles University in Prague, 12843 Prague, Czech Republic

²Department of Cell Biology, Faculty of Science, Charles University in Prague, 12843 Prague, Czech Republic

³Department of Parasitology, Faculty of Science, Charles University in Prague, 12843 Prague, Czech Republic

⁴Laboratory of Mass Spectrometry, Faculty of Science, Charles University in Prague, 12843 Prague, Czech Republic

⁵Institute of Physiology, Academy of Sciences of the Czech Republic, v.v.i., 14220 Prague, Czech Republic

Correspondence should be addressed to Jitka Zurmanova, jizurman@natur.cuni.cz

Received 24 June 2011; Accepted 9 September 2011

Academic Editor: Henk Granzier

Copyright © 2011 Petra Arnostova et al. This is an open access article distributed under the Creative Commons Attribution License, which permits unrestricted use, distribution, and reproduction in any medium, provided the original work is properly cited.

The expression of two cardiac myosin heavy chain (MyHC) isoforms in response to the thyroid status was studied in left ventricles (LVs) of Lewis rats. Major MyHC isoform in euthyroid and hyperthyroid LVs had a higher mobility on SDS-PAGE, whereas hypothyroid LVs predominantly contained a MyHC isoform with a lower mobility corresponding to that of the control soleus muscle. By comparing the MyHC profiles obtained under altered thyroid states together with the control soleus, we concluded that MyHC α was represented by the lower band with higher mobility and MyHC β by the upper band. The identity of these two bands in SDS-PAGE gels was confirmed by western blot and mass spectrometry. Thus, in contrast to the literature data, we found that the MyHC α possessed a higher mobility rate than the MyHC β isoform. Our data highlighted the importance of the careful identification of the MyHC α and MyHC β isoforms analyzed by the SDS-PAGE.

1. Introduction

Cardiac muscle contractility and its efficiency depend on myosin heavy chain (MyHC) isoforms being present. Mammalian heart muscle cells express two MyHC gene products, Myh6 and Myh7, which correspond to the α and β isoforms respectively [1]. The molecular masses of the rat α and β isoforms are both about 223 kDa (Rat Gene Database: <http://rgd.mcw.edu/>), and their amino acid sequences are 93% identical [2]. However, the isoforms differ in their ATPase activity and in their effect on heart contractility. MyHC α represents a “fast myosin” with higher ATPase activity and faster contraction, whereas MyHC β represents a “slow myosin” with lower ATPase activity and slower contraction [3–5]. In cardiac left ventricles (LVs), the α and β isoforms constitute three functional dimers marked V1, V2, and V3. V1 is the $\alpha\alpha$ homodimer, while V3 is the $\beta\beta$ homodimer, and V2 is the $\alpha\beta$ heterodimer. The ATPase activity of these three dimers corresponds to the α and β subunits involved [3, 6, 7]. The variations in the V-type ratio

(V1 : V2 : V3) correlate with the heart rate of different species [7, 8]. Fast-contracting ventricles of mice and rats (heart rate > 300/min) have a high proportion of V1, while slow-contracting ventricles of humans and cows (heart rate about 70/min) contain a V3 majority. Rabbit and guinea pig ventricles, with an intermediate speed, consist predominantly of V3 and still possess some V1 and V2 dimers [9]. *In vitro* experiments showed the difference in the hydrolytic and kinetic characteristics of the two α and β isoforms, which could explain the difference in the economy of force development and the basis for cardiac adaptation mechanism [10, 11]. In general, the experimental evidence suggests that hearts expressing primarily MyHC α isoform have a significantly higher rate of muscle shortening, whereas the hearts expressing mostly MyHC β possess the ability to generate force with higher efficiency [12].

The amount and changes in the ratio of V dimers have been determined using native gel electrophoresis under non-denaturing conditions, and it was found that the myosin

dimers mobility decreases in order $V1 > V2 > V3$ [6–8, 13–16]. On the other hand, the experiments studying the mobility of individual α and β monomers by the sodium dodecyl sulphate-polyacrylamide gel electrophoresis (SDS-PAGE) under denaturing conditions showed lower mobility of MyHC α compared to MyHC β [17–24].

The relative proportion of α and β isoforms in cardiac LVs can be influenced by several physiological and pathophysiological factors like hemodynamic overload, diabetes, or thyroid hormones, and it also corresponds with heart fitness [12]. Thyroid hormones were found to be the most potent regulators of cardiac MyHC gene expression [25]. Increased levels of thyroid hormones stimulate MyHC α (V1) and restrain MyHC β (V3) expression leading to the hyperthyroid phenotype, while lowered levels of thyroid hormones result in the inhibition of MyHC α (V1) and activation of MyHC β (V3) expression resulting in the hypothyroid phenotype [26–32]. Alterations to the thyroid hormone levels, in both experimental animals and humans, contribute to various pathological changes including some of the most life-threatening cardiac events, like atrial and ventricular fibrillations or malignant ventricular arrhythmias [33–35]. Changes in the expression of cardiac MyHC isoforms are supposed to be the important aspect of a failing heart [36, 37]. Since many cardiovascular diseases are accompanied by the shift between cardiac α and β MyHC isoforms, the unequivocal determination of both isoforms separated by SDS-PAGE is extremely important, even for human pathology.

In this study, we present data on the MyHC isoforms mobility obtained by SDS-PAGE technique and unambiguous identification of α and β isoforms by mass spectrometry (MALDI TOF/TOF) [38] and western blot (WB) analyses.

2. Material and Methods

2.1. Animals. Male and female 4-week-old inbred Lewis strain rats obtained from an authorized laboratory of the rat-breeding unit of the Institute of Physiology, Academy of Sciences of the Czech Republic, v. v. i., Prague, Czech Republic (accreditation no. 1020/491/A/00) were used for the experiments. Male euthyroid 250 g Wistar rats, obtained from Velaz s.r.o., Prague, Czech Republic, were used for comparison to the experimental Lewis strain rats. The maintenance and handling of the experimental animals were in accordance with the EU Council Directive (86/609/EEC) as well as with the local ethical committee guidelines of the Czech Ministry of Agriculture no. 1020/437/A/99. The investigation was approved by the Expert Committee of the Institute of Physiology, Academy of Sciences of the Czech Republic, v. v. i., Prague, Czech Republic.

2.2. Alteration of Thyroid Status. The hyperthyroid status (TH) was induced by intraperitoneal injections of 3,3',5-triiodo-L-thyronine (sodium salt, T_3 , 150 $\mu\text{g}/\text{kg}$ body weight) three times a week to the 4-week-old animals for 3 to 10 months. The hypothyroid (HY) status was induced with a 0.05% solution of methimazole (2-mercapto-1-methylimidazole) in drinking water given to the rats from the age

of 4 weeks for 4 to 11 months. The euthyroid (EU) rats were age-matched littermates of the experimental animals. All the rats analyzed in this study were part of a larger group in which thyroid states were previously checked by the measurement of biochemical and anatomical parameters that are known to be affected by thyroid hormone level alterations [39, 40].

2.3. Tissue Preparation. Cardiac tissue was obtained from adult EU, HY and TH inbred Lewis male and female rats. LVs from Wistar rats were used as a control of the MyHC band position in order to exclude strain differences. The animals were anesthetized with intraperitoneal injections of 1 mL (100 mg) of Narketan (Ketaminum ut hydrochloridum) per 1000 g of body weight, followed by 0.5 mL (10 mg) of the myorelaxant Xylapan (Xylazinum ut hydrochloridum) per 1000 g of body weight (Vetoquinol SA, France, and Vetoquinol Biowet, Poland, resp.). Whole hearts were quickly excised and placed in iced saline solution. LVs were readily isolated and immediately frozen in liquid nitrogen. Control soleus muscles (SOL) were excised immediately after the hearts and further treated with the same procedure described for LVs.

2.3.1. Homogenate Adjustment. The frozen LVs were pulverized in liquid nitrogen using porcelain mortar and homogenized 1:40 (w/v ratio) with homogenization buffer (5 M urea, 2 M thiourea, 0.4 M DL-dithiothreitol (DTT), 10 mM sodium pyrophosphate tetrabasic decahydrate) using a glass/glass homogenizer. The LV homogenates were aliquoted and stored at -80°C . Deep frozen tissue treatment and highly denaturing homogenization buffer protected proteins against eventual protease activity.

2.3.2. MyHC Extraction. The MyHC extraction was performed according to Agbulut et al. [41]. The LVs were pulverized in liquid nitrogen using a porcelain mortar. The powder was transferred into iced extraction buffer pH 6.5 containing 300 mM NaCl, 0.1 M NaH_2PO_4 monohydrate, 50 mM Na_2HPO_4 anhydrous, 10 mM sodium pyrophosphate, 1 mM MgCl_2 , 10 mM EDTA, and fresh 1.4 mM mercaptoethanol. MyHC were extracted for 1 hour on ice using four volumes of extraction buffer. The LV extracts were centrifuged at $12000 \times g$ for 10 minutes at 4°C and the supernatants were diluted 1:1 (v/v ratio) with conservation buffer pH 8.5 containing 40 mM sodium pyrophosphate and 50% glycerol, aliquoted and stored at -80°C .

2.4. MyHCs Separation. The SDS-PAGE method was performed on the Mini-PROTEAN Tetra Cell (BioRad) with gel thickness 0.75 mm according to a protocol used by Sant'Ana Pereira et al. [22] for gels running at constant current 13 mA (no pulse) for 7.5 hours. Separating and stacking gels were prepared on the same day as the electrophoresis was run. Separating gels (12% final concentration of acrylamide) contained 10% glycerol (v/v ratio), 12% acrylamide/bisacrylamide solution (the ratio of acrylamide/N,N'-methylenebisacrylamide was

200:1), 750 mM 2-amino-2-hydroxymethyl-propane-1,3-diol (TRIS) (pH 9.3), 0.1% sodium dodecyl sulphate (SDS) (w/v ratio), 0.03% ammonium persulphate (APS) (w/v ratio), and 0.14% tetramethylethylenediamine (TEMED). Stacking gels (3.7% final concentration of acrylamide) contained 10% glycerol, 3.7% acrylamide/N,N'-methylene-bisacrylamide (20:1 ratio), 125 mM TRIS (pH 6.8), 0.1% SDS, 0.03% APS, and 0.3% TEMED. Electrode buffer was composed of 0.05 M TRIS, 0.38 M glycine, and 0.346 mM SDS. Homogenates were diluted 1:1.5 (v/v ratio) with sample buffer (0.125 M TRIS pH 6.8, 0.5 mM EDTA pH 7, 5% SDS, 15 mM DTT, 20% glycerol, 0.1% Bromphenol Blue), LV extracts were diluted 1:1 (v/v ratio) with sample buffer, and SOL extracts were diluted 1:19 (v/v ratio) with sample buffer. Homogenates were loaded on the gels in the amount of 7 μ L per sample (5.5 μ g protein), LV extracts in the amount of 15 μ L (1 μ g protein) per sample, and SOL extracts of 4 μ L (2 μ g protein) per sample. As a control, we used SOL from hypothyroid animals (HY), containing basically 100% of the slow isoform identical with cardiac MyHC β . The gels were directly used for WB analyses or stained by a mixture of Coomassie Brilliant Blue and Bismarck Brown R (CBB&BBR) [42] for mass spectrometry and stained by silver nitrate for densitometry quantification (Quantity One Software, BioRad) [43].

2.5. MALDI TOF/TOF Sample Preparation. Each single CBB&BBR stained protein band was cut out from a single lane of the gel, placed to a microtube, and covered with 100 μ L 50 mM ammonium bicarbonate (ABC) buffer in 50% acetonitrile (ACN) with 50 mM DTT. All samples were subjected to sonication in an ultrasonic cleaning bath for 5 minutes. After 15 minutes the supernatant was discarded, and the gel was covered with 100 μ L of 50 mM ABC/50% ACN with 50 mM iodoacetamide and sonicated for 5 minutes. After 25 minutes, the supernatant was discarded and exchanged for 100 μ L 50 mM ABC/50% ACN with 50 mM DTT and sonicated for 5 minutes to remove any excess iodoacetamide. The supernatant was discarded, and the samples were sonicated for 5 minutes in 100 μ L of HPLC-grade water. The water was discarded, and samples were sonicated for another 5 minutes in 100 μ L of ACN. ACN was discarded, and the microtubes with the samples were left open for a couple of minutes to allow the rest of ACN to evaporate. Then, 5 ng of trypsin (Promega) in 10 μ L of 50 mM ABC were added to the gel. The samples were incubated at 37°C overnight. Trifluoroacetic acid (TFA) and ACN were added to the final concentration of 1% TFA, 30% ACN. The samples were sonicated for 10 minutes, and a 0.5 μ L drop was transferred onto MALDI targets and let to dry. The dried droplets were covered with a 0.5 μ L drop of α -cyano-4-hydroxycinnamic acid solution (2 mg/mL in 80% ACN) and let to dry.

2.6. MALDI TOF/TOF Analysis. Peptide mapping was performed in multiple independent experiments and independent samples. Spectra were acquired in the range of 800–3500 m/z using a 4800 Plus MALDI TOF/TOF Analyzer (Applied Biosystems/MDS Sciex) equipped with a Nd:YAG

laser (355 nm, firing rate 200 Hz). Peak lists from the MS spectra were generated by 4000 Series Explorer V 3.5.3 (Applied Biosystems/MDS Sciex) without smoothing, peaks with the local signal-to-noise ratio greater than 5 were picked automatically, deisotoped, and searched with local Mascot v. 2.1 (Matrix Science) against the nonredundant NCBI database of protein sequences as of 06/14/2010 (11186807 sequences; 3815639892 residues). The database search criteria were as follows—enzyme: trypsin, taxonomy: *Rattus norvegicus* (66703 sequences), fixed modification: carbamidomethylation, variable modification: methionine oxidation, peptide mass tolerance: 80 ppm, and one missed cleavage allowed. Only the hits that were scored by the Mascot software as significant ($P < 0.0001$) were accepted for further analyses.

2.6.1. Sequences Evaluation. Sequences for cardiac MyHC were obtained from GenBank databases: (MyHC α) P02563 and (MyHC β) P02564. Sequences were aligned with ClustalW 1.83: <http://www.ebi.ac.uk/clustalw/>.

2.7. Western Blot and Immunodetection. After SDS-PAGE, gels were quickly washed in ultrapure H₂O (mQ H₂O) (Millipore-Q system) and equilibrated for 15 min in transfer buffer containing 25 mM TRIS, 192 mM glycine, and 80 mM urea. Subsequently, the proteins were electrotransferred onto nitrocellulose membranes (0.2 μ m pore size, Protran BA 83, Whatman) at constant 100 V and 350 mA for 1 hour at 4°C using Mini Trans-Blot (BioRad). The membranes were quickly washed in mQ H₂O, dried, wrapped in polypropylene film, and stored overnight at –20°C.

On the following day, the membranes were washed for 15 minutes in 0.05% Tween in Tris-buffered saline (TTBS) solution and blocked for 1 hour at room temperature (RT) in 5% nonfat dry milk in TTBS. To detect α and β isoforms, membranes were incubated with NB300-284 (1:1000, Novus Biologicals) or anti-Slow (1:1000, provided by BioTrend and Novocastra) antibodies that recognized both cardiac MyHC isoforms on WB membranes; for specific detection of MyHC α , we used the BA.G5 antibody (1:5000, a kind gift by Professor S. Schiaffino). Incubations with primary antibodies were performed for 1 hour at RT in the TTBS solution. TTBS washing (3 \times 15 minutes) preceded and followed the membranes incubation with secondary anti-mouse IgG (Stabilized Goat Anti-Mouse IgG (H+L) – HRP Conjugated, no. 32430, Thermo Scientific Pierce) diluted 1:1000 under the same conditions as the primary antibodies. The membrane signals were detected by enhanced chemiluminescence (ECL) substrate (SuperSignal West Dura Extended Duration Substrate, no. 34076, Thermo Scientific Pierce) and visualized by the LAS-4000 system (Genetica, Fujifilm).

2.8. Statistical Analysis. Obtained data were analyzed by the GraphPad Prism 5 software. A one-way ANOVA and subsequent Student-Newman-Keuls test were used for comparison of differences in normally distributed variables between groups. Nonparametric Mann-Whitney's *U*-test and Kruskal-Wallis's test were used for a comparison of differences in nonnormally distributed variables between groups. All data

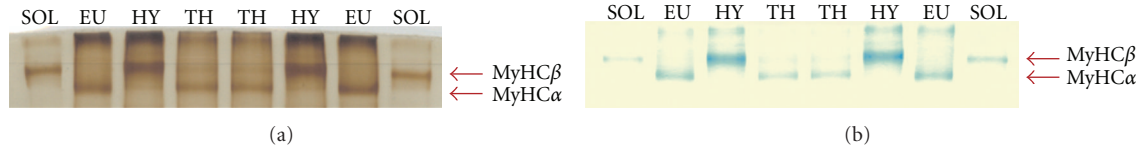


FIGURE 1: SDS-PAGE separation of cardiac MyHC isoforms from left ventricles of adult euthyroid (EU), hypothyroid (HY), and hyperthyroid (TH) Lewis rats. Control: soleus muscle (SOL) from the hypothyroid rat containing the MyHC1 isoform identical with cardiac MyHC β . The gel was silver stained (a) or stained by CBB+BBR (b) before MALDI TOF/TOF analysis.

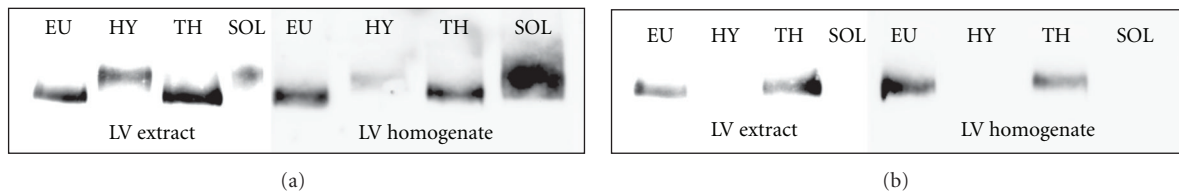


FIGURE 2: Western blot immunodetection of cardiac MyHC isoforms from left ventricle (LV) homogenates and extracts of adult euthyroid (EU), hypothyroid (HY), and hyperthyroid (TH) Lewis rats. The membranes were stained by NB300-284 antibody recognizing both MyHC α and MyHC β isoforms (a) or by BA.G5 antibody, which was solely specific for cardiac MyHC α isoform (b).

are expressed as mean \pm SD or as mean \pm SEM. The differences were considered as statistically significant when $P < 0.05$.

3. Results and Discussion

3.1. Separation of Cardiac MyHC Isoforms. The SDS-PAGE of cardiac MyHC isoforms revealed that a major MyHC isoform in EU and TH hearts was that with a greater mobility in polyacrylamide gels, whereas HY LVs contained the predominantly MyHC isoform with a lower mobility corresponding to the mobility of slow-type MyHC1 isoform in control HY SOL (Figures 1(a) and 1(b)). The same results were obtained by homogenate as well as MyHC extract separations. Based on the MyHC profiles observed in LVs at different thyroid states and in the control SOL, we assumed that MyHC α was represented by the lower band with a higher mobility and MyHC β by the upper band with a lower mobility. The densitometric quantification of the obtained bands supported our assumption, as the TH status was characterized by higher MyHC α expression, whereas the HY status significantly decreased MyHC α expression and increased MyHC β expression when compared with EU and TH states (Table 1). Since the observed mobilities of α and β isoforms in polyacrylamide gels were quite opposite to those reported in the literature, we decided to recheck our results by WB immunodetection and MALDI TOF/TOF analyses.

3.2. Identification of α and β MyHC Isoforms by WB Immunodetection and MALDI TOF/TOF Analyses. The WB analysis supported the conclusion based on results obtained by SDS-PAGE. The monoclonal BA.G5 antibody, shown to be specific for rat MyHC α [44], marked only the lower band with a higher mobility in EU and TH samples, while the HY samples and SOL control remained unstained with this antibody (Figure 2(b)). The NB300-284 antibody as well as anti-Slow

TABLE 1: Ratio of cardiac MyHC α /MyHC β isoforms from left ventricles of adult euthyroid (EU), hyperthyroid (TH), and hypothyroid (HY) Lewis rats. MyHC isoforms were separated by SDS-PAGE, silver-stained, and quantified by densitometric evaluation (Quantity One Software, BioRad). The data are expressed as a mean \pm SD, *significantly different from EU and TH, $P < 0.05$, number of animals = 5.

Thyroid status	The ratio
EU	3.84 ± 0.72
TH	4.39 ± 0.63
HY	$0.09 \pm 0.05^*$

antibody recognized both α and β isoforms. These antibodies marked the upper band with lower mobility in HY LVs and SOL samples and the lower band in the case of EU and TH rats (Figure 2(a)). The minor bands in all three thyroid states were under the detection limit of the WB method. These results confirm that cardiac LVs of EU and TH rats predominantly contain the MyHC α isoform showing higher mobility, whereas LVs of HY rats contain mainly the isoform MyHC β with the lower mobility.

The results of MALDI TOF/TOF analysis of EU, TH, HY, and SOL samples highly matched the sequences of MyHC α and MyHC β and unambiguously identified both isoforms. The overall sequence coverage for trypsin digested samples was 52% for MyHC α and 58% for MyHC β . Further experiments with Lys-C and Asp-N endoproteinases were used to increase the number of MyHC α isoform-specific (proteotypic) peptides and isoform-specific coverage which reached about 40% and 10% using Lys-C and Asp-N digestion, respectively. We highlighted the specific peptides resulting from different protease digestions in multiple sequence alignment (ClustalW 1.83) of MyHC α and MyHC β (Figure 3). Analysis of HY samples digested by trypsin identified 27 peptides specific for MyHC β (out of 61 in total). TH sample analysis

To estimate the effect of thyroid status on the heart function or fitness of the rats, we measured the heart index (heart mass in mg/body mass in g, expressed as a mean \pm SEM). In EU female and male rats, it was 3.23 ± 0.14 ($n = 11$) and 2.92 ± 0.06 ($n = 13$), respectively. The TH status led to cardiac hypertrophy, as the heart index significantly increased in female and male rats to 4.64 ± 0.23 ($n = 11$) and 3.78 ± 0.19 ($n = 8$), while the HY status resulted in cardiac atrophy, as the index significantly dropped to 2.9 ± 0.05 ($n = 16$) and 2.58 ± 0.11 ($n = 10$), respectively. Obviously, the application of thyroid hormones in our experiments corresponds to the physiological hypertrophy induced by chronic exercise and characterized by increased expression of MyHC α [45]. On the other hand, pathological hypertrophy, caused by pressure and volume overload in spontaneous hypertensive rats (SHR), leads to the shift from the MyHC α to the MyHC β [46]. Thyroid hormone applications as well as physical training by swimming were able to prevent or repair contractile protein abnormalities in pathological hypertrophy in rat hearts [46, 47].

3.4. Electrophoretic Mobility of Cardiac MyHC Isoforms. Our experiments showed unexpected results relating to the mobility of MyHC isoforms. Contrary to the literature data [17–24], we observed higher mobility of the α and lower mobility of the β isoform in polyacrylamide gels. However, these results can be considered reliable, the identity of the MyHC isoforms was successfully verified by WB immunodetection and mass spectrometry (MALDI TOF/TOF) methods. Both analyses showed that MyHC α (no. 62029: 223.508.76 Da; 1939 AA; pI = 5.4500; charge = -28.5 ; Rat Gene Database) represented by a lower band, moves with a higher mobility in 12% polyacrylamide separating gels than MyHC β (no. 62030: 222.899.28 Da; 1935 AA; pI = 5.4764; charge = -27 ; Rat Gene Database), represented by an upper band (Figures 1 and 2). Likewise, the control SOL sample analysis confirmed the position of MyHC β as the upper band. Nevertheless, the reason for the different band position observed in our experiments remains to be elucidated.

3.4.1. SDS-PAGE Modifications. Factors affecting the electrophoretic mobility of cardiac isoforms appear to have a crucial importance for the observed mobility changes. We tested various concentrations of acrylamide and glycerol and various ratios of acrylamide and bisacrylamide, but all these changes affected only the quality of separation, not the position of the bands.

It is known that the separation and mobility of cardiac myosins by a native electrophoresis depend on several factors, such as the molecular mass, acidic and basic residues [48], and helix content and amino acid composition [49], and on the pH of the separating gel. Unlike the native gel electrophoresis, the SDS-PAGE method under denaturing conditions is supposed to separate cardiac MyHC isoforms only by their molecular mass. The cardiac α and β isoforms have nearly identical molecular masses (~ 223 kDa), so that their separation is rather difficult. Several recent works have attempted to improve the electrophoretic resolution of the

cardiac MyHC isoforms. There were different concentrations of glycerol used: 5–45% [20], separating gels: 6% [24], 7% [21, 23], 8% [20], and 12% [22], and different acrylamide/bisacrylamide ratios: 37.5 : 1 [24], 50 : 1 [20, 21], and 200 : 1 [22]. All the mentioned papers, however, have reported an improvement of separation, but no change in the mobility of the isoforms.

For cardiac MyHC isoform separation, we used the method according to Sant'Ana Pereira et al. [22]: 12% separating gel, 200 : 1 acrylamide/bisacrylamide ratio, constant current 13 mA, temperature 10°C, and run time modified to 7.5 hours (7 hours originally). It is important to note that we used tissue processing according to Agbulut et al. [41] that differs significantly from the procedure used by Sant'Ana Pereira et al. [22] but in both cases the eventual activity of proteases was excluded. Furthermore, the same results were received with tissue homogenates and with MyHC extracts (cf. Figure 2).

The MyHC isoform mobility apparently depends on two forces acting against each other: the resistance and the electrical force. Thus, one of the possible explanations of the unexpected mobility observed might be the influence of the amount of bound SDS. MyHC α , which is slightly heavier, has 4 amino acids more than MyHC β . Therefore, MyHC α should be covered by more SDS molecules and pulled through the separating gel by a higher electrical force, which is in favor of its higher mobility. The resistance, of the separating gel at given concentration of acrylamide and bisacrylamide, increases with the molecular weight of separated proteins. This factor would then favor the higher mobility of MyHC β with a lower molecular weight. When these two factors were only taken into account, then the higher mobility of MyHC α could indicate that the electrical force have a greater impact on MyHC mobility than the resistance of the polyacrylamide gel.

3.4.2. Evaluation of Possible Mural Variability. A striking transmural variation of ATPase activity and MyHC isoform distribution was observed in rabbit [50] and rat [51] hearts. For our experiments, however, we have used longitudinal stripes containing epicardial, midwall, and endocardial portions in order to minimize any possible transmural variability.

3.4.3. Possible Strain Differences. To the best of our knowledge, this study was the first analysis of cardiac MyHCs performed on inbred Lewis strain rats. These animals have naturally higher levels of serum thyroxine compared with other routinely used rat strains [52]. Furthermore, in Lewis rats the fiber type compositions of skeletal muscles are very unique. When compared with other rat strains (Wistar, Sprague-Dawley, Fisher 344, WBN/Kob, Lister Hooded, and SHR rats), their soleus muscles were the slowest and their extensor digitorum longus muscles were the fastest [53]. However, we also analyzed cardiac MyHCs by the same methods in EU Wistar rats, and the positions of the MyHCs bands were quite similar to those obtained for the Lewis strain rats. In addition, no differences in cardiac MyHCs mobility among

several rat strains in SDS-PAGE gels (Sprague Dawley, Brown Norway, Copenhagen, SHR, and Wistar rats) were seen by Reiser et al. [54]. Strain differences can apparently affect the MyHC isoform ratio in the heart, but they obviously cannot explain the observed switch of the band position of both cardiac isoforms.

4. Conclusions

The data we obtained by SDS-PAGE in the three thyroid states showed that only the left ventricles of HY rats contained a significant amount of MyHC β , while the left ventricles of EU and TH rats were almost devoid of this isoform, expressing MyHC α as the major isoform. However, the higher mobility of MyHC α compared with that of MyHC β was contrary to the literature data. Therefore, the identity of both bands was confirmed by western blot immunodetection using specific antibodies (BA.G5 and NB300-284) and by MALDI TOF/TOF that showed the specific peptides resulting from different protease digestions in multiple sequence alignment (ClustalW 1.83) of MyHC α and MyHC β isoforms. The reasons for the observed unexpected mobility of the isoforms remain still unclear. The general conclusion from our results is that the order of migration of the two cardiac MyHC isoforms must always be verified and not just assumed.

Acknowledgments

The authors very grateful to Professor Stefano Schiaffino for BA.G5 antibody and Dr. Alberto C. Rossi for his help during experiments performed in Padua and for valuable comments during the preparation of the paper. They also thank to Professor Vaclav Pelouch for his kind advice during the experiments and to Bc. Eva Zikmundova for her excellent technical assistance. The study was supported by the Ministry of Education of the Czech Republic (Grant no. MSM0021620858), the Grant Agency of Academy of Sciences of the Czech Republic (Grant no. IAAX01110901), the Grant Agency of the Czech Republic (Grant no. 304/08/0256), and by the Research project AV0Z 50110509.

References

- [1] V. Mahdavi, M. Periasamy, and B. Nadal-Ginard, "Molecular characterization of two myosin heavy chain genes expressed in the adult heart," *Nature*, vol. 297, no. 5868, pp. 659–664, 1982.
- [2] E. M. McNally, R. Kraft, M. Bravo-Zehnder, D. A. Taylor, and L. A. Leinwand, "Full-length rat alpha and beta cardiac myosin heavy chain sequences. Comparisons suggest a molecular basis for functional differences," *Journal of Molecular Biology*, vol. 210, no. 3, pp. 665–671, 1989.
- [3] B. Pope, J. F. Hoh, and A. Weeds, "The ATPase activities of rat cardiac myosin isoenzymes," *FEBS Letters*, vol. 118, no. 2, pp. 205–208, 1980.
- [4] K. Schwartz, Y. Lecarpentier, and J. L. Martin, "Myosin isoenzymic distribution correlates with speed of myocardial contraction," *Journal of Molecular and Cellular Cardiology*, vol. 13, no. 12, pp. 1071–1075, 1981.
- [5] G. Ebrecht, H. Rupp, and R. Jacob, "Alterations of mechanical parameters in chemically skinned preparations of rat myocardium as a function of isoenzyme pattern of myosin," *Basic Research in Cardiology*, vol. 77, no. 2, pp. 220–234, 1982.
- [6] J. F. Y. Hoh, P. A. McGrath, and P. T. Hale, "Electrophoretic analysis of multiple forms of rat cardiac myosin: effects of hypophysectomy and thyroxine replacement," *Journal of Molecular and Cellular Cardiology*, vol. 10, no. 11, pp. 1053–1076, 1978.
- [7] A. M. Lompre, J. J. Mercadier, and C. Wisnewsky, "Species- and age-dependent changes in the relative amounts of cardiac myosin isoenzymes in mammals," *Developmental Biology*, vol. 84, no. 2, pp. 286–290, 1981.
- [8] W. A. Clark, R. A. Chizzonite, and A. W. Everett, "Species correlations between cardiac isomyosins. A comparison of electrophoretic and immunological properties," *The Journal of Biological Chemistry*, vol. 257, no. 10, pp. 5449–5454, 1982.
- [9] B. Swynghedauw, "Developmental and functional adaptation of contractile proteins in cardiac and skeletal muscles," *Physiological Reviews*, vol. 66, no. 3, pp. 710–771, 1986.
- [10] S. Sugiura, N. Kobayakawa, H. Fujita et al., "Comparison of unitary displacements and forces between 2 cardiac myosin isoforms by the optical trap technique: molecular basis for cardiac adaptation," *Circulation Research*, vol. 82, no. 10, pp. 1029–1034, 1998.
- [11] P. Vanburen, D. E. Harris, N. R. Alpert, and D. M. Warshaw, "Cardiac V1 and V3 myosins differ in their hydrolytic and mechanical activities in vitro," *Circulation Research*, vol. 77, no. 2, pp. 439–444, 1995.
- [12] M. P. Gupta, "Factors controlling cardiac myosin-isoform shift during hypertrophy and heart failure," *Journal of Molecular and Cellular Cardiology*, vol. 43, no. 4, pp. 388–403, 2007.
- [13] A. d'Albis, C. Pantaloni, and J. J. Bechet, "An electrophoretic study of native myosin isozymes and of their subunit content," *European Journal of Biochemistry*, vol. 99, no. 2, pp. 261–272, 1979.
- [14] A. M. Lompre, K. Schwartz, and A. d'Albis, "Myosin isoenzyme redistribution in chronic heart overload," *Nature*, vol. 282, no. 5734, pp. 105–107, 1979.
- [15] J. J. Mercadier, A. M. Lompre, and C. Wisnewsky, "Myosin isoenzymic changes in several models of rat cardiac hypertrophy," *Circulation Research*, vol. 49, no. 2, pp. 525–532, 1981.
- [16] H. Rupp and B. Maisch, "Separation of large mammalian ventricular myosin differing in ATPase activity," *Canadian Journal of Physiology and Pharmacology*, vol. 85, no. 3-4, pp. 326–331, 2007.
- [17] K. A. Esser, M. O. Boluyt, and T. P. White, "Separation of cardiac myosin heavy chains by gradient SDS-PAGE," *American Journal of Physiology*, vol. 255, no. 3, pp. H659–H663, 1988.
- [18] A. L. P. Caforio, M. Grazzini, J. M. Mann et al., "Identification of α - and β -cardiac myosin heavy chain isoforms as major autoantigens in dilated cardiomyopathy," *Circulation*, vol. 85, no. 5, pp. 1734–1742, 1992.
- [19] N. K. Sweitzer and R. L. Moss, "Determinants of loaded shortening velocity in single cardiac myocytes permeabilized with α -hemolysin," *Circulation Research*, vol. 73, no. 6, pp. 1150–1162, 1993.
- [20] P. J. Reiser and W. O. Kline, "Electrophoretic separation and quantitation of cardiac myosin heavy chain isoforms in eight mammalian species," *American Journal of Physiology*, vol. 274, no. 3, pp. H1048–H1053, 1998.
- [21] A. Mansén, F. Yu, D. Forrest, L. Larsson, and B. Vennström, "TRs have common and isoform-specific functions in regulation of the cardiac myosin heavy chain genes," *Molecular Endocrinology*, vol. 15, no. 12, pp. 2106–2114, 2001.
- [22] J. A. A. Sant'Ana Pereira, M. Greaser, and R. L. Moss, "Pulse electrophoresis of muscle myosin heavy chains in sodium

- dodecyl sulfate-polyacrylamide gels," *Analytical Biochemistry*, vol. 291, no. 2, pp. 229–236, 2001.
- [23] S. Piao, F. Yu, M. J. Mihm et al., "A simplified method for identification of human cardiac myosin heavy-chain isoforms," *Biotechnology and Applied Biochemistry*, vol. 37, no. 1, pp. 27–30, 2003.
- [24] C. M. Warren and M. L. Greaser, "Method for cardiac myosin heavy chain separation by sodium dodecyl sulfate gel electrophoresis," *Analytical Biochemistry*, vol. 320, no. 1, pp. 149–151, 2003.
- [25] S. Izumo, B. Nadal-Ginard, and V. Mahdavi, "All members of the MHC multigene family respond to thyroid hormone in a highly tissue-specific manner," *Science*, vol. 231, no. 4738, pp. 597–600, 1986.
- [26] A. M. Lompre, B. Nadal-Ginard, and V. Mahdavi, "Expression of the cardiac ventricular α - and β -myosin heavy chain genes is developmentally and hormonally regulated," *The Journal of Biological Chemistry*, vol. 259, no. 10, pp. 6437–6446, 1984.
- [27] E. Morkin, I. L. Flink, and S. Goldman, "Biochemical and physiologic effects of thyroid hormone on cardiac performance," *Progress in Cardiovascular Diseases*, vol. 25, no. 5, pp. 435–464, 1983.
- [28] E. Morkin, "Control of cardiac myosin heavy chain gene expression," *Microscopy Research and Technique*, vol. 50, no. 6, pp. 522–531, 2000.
- [29] K. Ojamaa and I. Klein, "In vivo regulation of recombinant cardiac myosin heavy chain gene expression by thyroid hormone," *Endocrinology*, vol. 132, no. 3, pp. 1002–1006, 1993.
- [30] A. K. Fletcher and A. P. Weetman, "Hypertension and hypothyroidism," *Journal of Human Hypertension*, vol. 12, no. 2, pp. 79–82, 1998.
- [31] L. W. Stevenson, "Beta-blockers for stable heart failure," *The New England Journal of Medicine*, vol. 346, no. 18, pp. 1346–1347, 2002.
- [32] S. Danzi, S. Klein, and I. Klein, "Differential regulation of the myosin heavy chain genes α and β in rat atria and ventricles: role of antisense RNA," *Thyroid*, vol. 18, no. 7, pp. 761–768, 2008.
- [33] S. Danzi and I. Klein, "Thyroid hormone and the cardiovascular system," *Minerva Endocrinologica*, vol. 29, no. 3, pp. 139–150, 2004.
- [34] G. J. Kahaly and W. H. Dillmann, "Thyroid hormone action in the heart," *Endocrine Reviews*, vol. 26, no. 5, pp. 704–728, 2005.
- [35] N. Tribulova, V. Knezl, A. Shainberg, S. Seki, and T. Soukup, "Thyroid hormones and cardiac arrhythmias," *Vascular Pharmacology*, vol. 52, no. 3–4, pp. 102–112, 2010.
- [36] S. Miyata, W. Minobe, M. R. Bristow, and L. A. Leinwand, "Myosin heavy chain isoform expression in the failing and nonfailing human heart," *Circulation Research*, vol. 86, no. 4, pp. 386–390, 2000.
- [37] P. J. Reiser, M. A. Portman, X. H. Ning, and C. S. Moravec, "Human cardiac myosin heavy chain isoforms in fetal and failing adult atria and ventricles," *American Journal of Physiology*, vol. 280, no. 4, pp. H1814–H1820, 2001.
- [38] S. M. Helmke, C. Y. Yen, K. J. Cios et al., "Simultaneous quantification of human cardiac alpha- and beta-myosin heavy chain proteins by MALDI-TOF mass spectrometry," *Analytical Chemistry*, vol. 76, no. 6, pp. 1683–1689, 2004.
- [39] T. Soukup, G. Zacharová, V. Smerdu, and I. Jirmanová, "Body, heart, thyroid gland and skeletal muscle weight changes in rats with altered thyroid status," *Physiological Research*, vol. 50, no. 6, pp. 619–626, 2001.
- [40] H. Rauchová, T. Mráček, P. Novák, M. Vokurková, and T. Soukup, "Glycerol-3-phosphate dehydrogenase expression and oxygen consumption in liver mitochondria of female and male rats with chronic alteration of thyroid status," *Hormone and Metabolic Research*, vol. 43, no. 1, pp. 43–47, 2011.
- [41] O. Agbulut, Z. Li, V. Mouly, and G. S. Butler-Browne, "Analysis of skeletal and cardiac muscle from desmin knock-out and normal mice by high resolution separation of myosin heavy-chain isoforms," *Biology of the Cell*, vol. 88, no. 3, pp. 131–135, 1996.
- [42] J. K. Choi, S. H. Yoon, H. Y. Hong, D. K. Choi, and G. S. Yoo, "A modified Coomassie blue staining of proteins in polyacrylamide gels with Bismark brown R," *Analytical Biochemistry*, vol. 236, no. 1, pp. 82–84, 1996.
- [43] H. Blum, H. Beier, and H. J. Gross, "Improved silver staining of plant proteins, RNA and DNA in polyacrylamide gels," *Electrophoresis*, vol. 8, pp. 33–99, 1987.
- [44] M. A. Rudnicki, G. Jackowski, L. Saggin, and M. W. McBurney, "Actin and myosin expression during development of cardiac muscle from cultured embryonal carcinoma cells," *Developmental Biology*, vol. 138, no. 2, pp. 348–358, 1990.
- [45] H. Rupp, "Differential effect of physical exercise routines on ventricular myosin and peripheral catecholamine stores in normotensive and spontaneously hypertensive rats," *Circulation Research*, vol. 65, no. 2, pp. 370–377, 1989.
- [46] J. Scheuer, A. Malhotra, and C. Hirsch, "Physiologic cardiac hypertrophy corrects contractile protein abnormalities associated with pathologic hypertrophy in rats," *The Journal of Clinical Investigation*, vol. 70, no. 6, pp. 1300–1305, 1982.
- [47] B. Wang, J. Ouyang, and Z. Xia, "Effects of triiodo-thyronine on angiotensin-induced cardiomyocyte hypertrophy: reversal of increased β -myosin heavy chain gene expression," *Canadian Journal of Physiology and Pharmacology*, vol. 84, no. 8–9, pp. 935–941, 2006.
- [48] Y. Yazaki and M. S. Raben, "Effect of the thyroid state on the enzymatic characteristics of cardiac myosin. A difference in behavior of rat and rabbit cardiac myosin," *Circulation Research*, vol. 36, no. 1, pp. 208–215, 1975.
- [49] P. T. Thyrum, E. M. Kritcher, and R. J. Luchi, "Effect of l-thyroxine on the primary structure of cardiac myosin," *Biochimica et Biophysica Acta*, vol. 197, no. 2, pp. 335–336, 1970.
- [50] B. R. Eisenberg, J. A. Edwards, and R. Zak, "Transmural distribution of isomyosin in rabbit ventricle during maturation examined by immunofluorescence and staining for calcium-activated adenosine triphosphatase," *Circulation Research*, vol. 56, no. 4, pp. 548–555, 1985.
- [51] L. B. Bugaisky, P. G. Anderson, R. S. Hall, and S. P. Bishop, "Differences in myosin isoform expression in the subepicardial and subendocardial myocardium during cardiac hypertrophy in the rat," *Circulation Research*, vol. 66, no. 4, pp. 1127–1132, 1990.
- [52] H. J. Esber, F. F. Menninger, and A. E. Bogden, "Variation in serum hormone concentrations in different rat strains," *Proceedings of the Society for Experimental Biology and Medicine*, vol. 146, no. 4, pp. 1050–1053, 1974.
- [53] P. Novák, G. Zacharová, and T. Soukup, "Individual, age and sex differences in fiber type composition of slow and fast muscles of adult lewis rats: comparison with other rat strains," *Physiological Research*, vol. 59, no. 5, pp. 783–801, 2010.
- [54] P. J. Reiser, M. Wick, and C. I. Pretzman, "Electrophoretic variants of cardiac myosin heavy chain- α in Sprague Dawley rats," *Electrophoresis*, vol. 25, no. 3, pp. 389–395, 2004.

Research Article

Phasic and Tonic Smooth Muscle Function of the Partially Obstructed Guinea Pig Intestine

Jingbo Zhao,^{1,2} Donghua Liao,^{1,2} Jian Yang,¹ and Hans Gregersen³

¹Mech-Sense, Aalborg Hospital, 9000 Aalborg, Denmark

²Institute of Clinical Medicine, Aarhus University Hospital, 8000 Aarhus, Denmark

³Sino-Danish Center for Education and Research, Aarhus University, 8000 Aarhus, Denmark

Correspondence should be addressed to Jingbo Zhao, jz@rn.dk

Received 28 June 2011; Accepted 29 August 2011

Academic Editor: Henk Granzier

Copyright © 2011 Jingbo Zhao et al. This is an open access article distributed under the Creative Commons Attribution License, which permits unrestricted use, distribution, and reproduction in any medium, provided the original work is properly cited.

This study was to generate phasic and tonic stress-strain curves for evaluation of smooth muscle function in the obstructed guinea pig jejunum. Partial and sham obstruction of the jejunum in guinea pigs was created surgically, with guinea pigs not being operated on served as normal controls. The animals survived 2, 4, 7, and 14 days, respectively. The jejunal segment was distended to 10 cm H₂O. The pressure and outer diameter changes were recorded. Passive conditions were obtained by using papaverine. Total phasic, tonic, and passive circumferential stress and strain were computed from the diameter and pressure data with reference to the zero-stress-state geometry. The active phasic and tonic stresses were defined as the total phasic and tonic stress minus the passive stress. The thickness of intestinal muscle layers increased in a time-dependent manner after obstruction. The amplitude of passive, total phasic, total tonic, active phasic, and active tonic circumferential stresses increased as function of strain 7 days after obstruction. However, when normalized to muscle layer thickness, the amplitude of active stresses did not differ among the groups. In conclusion, the long-term-obstructed intestine exhibits increased total smooth muscle contraction force. However, the contraction force per smooth muscle unit did not increase.

1. Introduction

Small bowel obstruction is a common clinical problem resulting from congenital [1–3] or acquired causes [4–7]. Small intestinal mechanical obstruction can be reproduced in laboratory animals using rings of different materials. Proximal to the partial obstruction site, the intestinal segment remodels morphologically and biomechanically [8–14]. Partial obstruction causes intestinal smooth muscle hyperplasia and hypertrophy [8, 9, 11, 12, 15–17]. Increased contraction force of remodeled smooth muscle layer has been reported, but the force was decreased when normalized to the tissue wet weight [15]. Furthermore, the obstructed intestinal wall became stiffer during longstanding partial obstruction [11, 12, 14]. Stiffening likely affects smooth muscle function. Therefore, it is important to study the function of remodeled intestinal smooth muscle due to partial obstruction.

It is possible to obtain isometric length-tension diagrams of phasic and tonic smooth muscle contraction *in vitro* [18].

Tools have now been developed for studying the active (phasic and tonic contractions) and passive length-tension behavior in the human gut *in vivo* using impedance planimetric distension [19–21]. From a biomechanical standpoint, muscle mechanical properties must be described in terms of stress and strain, that is, the force per area and tissue deformation. Computation of the stress depends on the wall thickness which cannot be directly measured *in vivo*. However, it is possible to measure the wall thickness *in vitro* and thus obtain the stress-strain relationship of the intestinal wall with reference to the zero-stress state [22]. Furthermore, the passive, tonic, and phasic stress-strain curves can be obtained when using papaverine to abolish smooth muscle activity [22].

In the present study we computed stress-strain data for assessment of the smooth muscle function of partially obstructed intestinal segments from guinea pigs. We hypothesized that the stress-strain properties of the remodeled small intestine change and that the remodeling is determined by the stress similar to the cardiovascular system [23].

2. Materials and Methods

2.1. Animals and Groups. The protocol was approved by the Danish Committee for Animal Experimentation. Male guinea pigs (600–800 g) were divided into four obstructed and four sham-obstructed groups living for 2, 4, 7, and 14 days, respectively. Ten age-matched guinea pigs not exposed to surgery were used as normal controls. We have long-term experience with the operative procedures [11, 12, 14], which is likely the reason for a mortality rate below 20%. The final number of animals was 6 in each obstructed group and 4 in each of the sham-obstructed group. The guinea pigs had access to water but were restricted from food intake from the night before the operations and experiments. The animals were weighted daily.

2.2. Creation of Partial Small Intestine Obstruction in Guinea Pig. The surgical procedure for partially obstructing the small intestine is well established [11, 14]. Atropine (Atropin DAK, Denmark) $0.3 \text{ mg} \cdot \text{kg}^{-1}$ s.c. was given 30 minutes prior to anesthesia with Hypnorm 0.5 mg and Dormicum 0.25 mg per 100 g body weight (Hypnorm:Dormicum:sterile water = 1:1:2; subcutaneous injection). A small midline laparotomy was done when surgical anesthesia was achieved. A loop of the midjejunum was selected, and the mesenterium was carefully incised close to the intestine to create a small window. Care was taken not to damage adjacent vessels or nerves.

A 3.5 mm wide polyurethane band was passed through the mesenteric window and closed antimesenterically with a 6–0 silk suture at a circumferential length about one mm longer than the outer circumference of the small intestine. Hence, a loose fit around the intestine was obtained without any apparent compression of the tissue. In the sham-obstructed group, the mesenteric incision was made and marked with a 6–0 silk suture but no band was placed. The abdominal wall was closed with 4–0 silk suture. Buprenorphine (Temgesic, Reckitt & Colman, UK) $0.05 \text{ mg} \cdot \text{kg}^{-1}$ was given subcutaneously to counter postoperative pain along with 10 mL saline to prevent dehydration. The animals were inspected and weighed daily after the operation. Animals in poor clinical condition were euthanized and excluded from the study.

2.3. In Vitro Intestinal Preparation. The guinea pigs were anesthetized with Hypnorm and Dormicum when the scheduled time had arrived. The abdominal cavity was opened and the intestine carefully dissected. A ten cm intestinal segment proximal to the band in the obstructed animals and segments from the corresponding location in sham-obstructed and normal animals were removed. A 0.5 cm long intestinal piece from the proximal end of the excised segment was cut and used for histological analysis. Further two short ring-shaped pieces perpendicular to the longitudinal axis were cut and used for zero-stress state analysis. The remaining segment was immediately put into the organ bath containing Krebs solution of the following composition ($\text{mmol} \cdot \text{L}^{-1}$): NaCl, 118; KCl, 4.7; NaHCO_3 , 25; NaH_2PO_4 , 1.0; MgCl, 1.2; $\text{CaCl}_2\text{-H}_2\text{O}$, 2.5; glucose, 11; ascorbic acid,

0.11. The 37°C Krebs solution was aerated with a gas mixture (95% O_2 and 5% CO_2 , pH 7.4). Thirty minutes equilibrating time was needed for recovery of the intestinal motility.

2.4. Ramp Distension Experimental Setup (Figure 1). The *in vitro* initial length of the intestinal segment was measured. The proximal end of the intestinal segment was tied on the cannula with silk threads. The cannula was via a tube connected to a syringe containing Krebs solution for applying luminal pressures ($0.8 \text{ mL} \cdot \text{min}^{-1}$). The lumen was pressurized by a pump (Genie Programmable Syringe Pump, World Precision Instrument, Stevenage, UK). The distal end of the intestinal segment was tied by a silk thread on the three-way tube connected to a micromanipulator that could stretch the intestinal segment in longitudinal direction. The ramp distension experiment with pressure up to 10.0 cm H_2O was done on the intestinal segment at the longitudinal stretch ratios 0%, 10%, and 20%. The pressure probe was inserted into the intestinal lumen through the cannula. The pressure was measured at three locations with 0.5 cm intervals. The location of the most proximal pressure hole was marked on the intestinal surface. The intestinal diameters at the locations where the pressure was recorded in the intestinal segments were videotaped by a CCD camera (Sony, Japan) on a stereomicroscope. The data sampling frequency for pressure and diameter data was 10/second.

2.5. The Zero-Stress State of the Intestinal Segment. The method for determination of the gastrointestinal zero-stress state has been described in detail previously [24, 25]. One-two mm wide rings were transferred to a calcium-free Krebs solution with EGTA and papaverine. This represented the no-load state that was photographed. Then, each ring-shaped segment was cut radially under the microscope resulting in an open sector geometry. Photographs representing the zero-stress state were taken ~ 60 min after the radial cutting to allow viscoelastic creep to occur.

2.6. Histological Analysis of the Small Intestine. The segment was fixed in 10% buffered formalin over 24 hours followed by dehydration in a series of graded ethanol (70%, 96%, and 99%) and embedding in paraffin. Five-micron sections were cut perpendicular to the mucosa surface, and the paraffin was cleared from the slides with coconut oil (over 15 min. 60°C). Redehydration occurred in 99%, 96%, and 70% ethanol followed by staining with hematoxylin and eosin. The layer thickness was measured by the same pathologist in a blinded review. Twelve determinations were made on each specimen and averaged.

2.7. Mechanical Data Analysis. Calculation was the assessment of the no-load state, zero-stress state dimensions and the outer diameters of the specimen at varying pressures. The Kirchhoff stress and Green's strain in the intestinal wall at a given pressure were computed assuming circular geometry as follows:

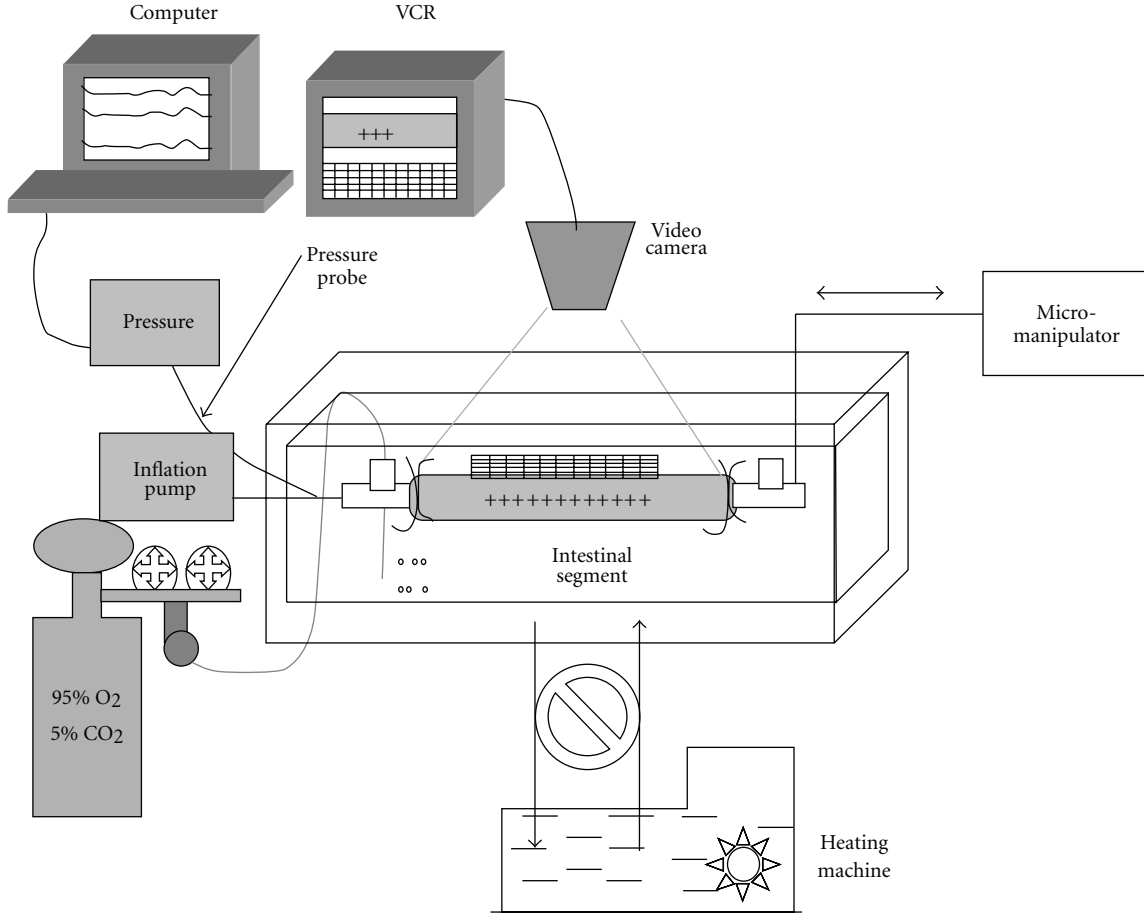


FIGURE 1: Experimental setup. The organ bath is composed of an inside chamber and an outside chamber. The Krebs solution contained in the small chamber was maintained constant at 37°C by circulating hot water in the big chamber using a heating machine. The intestinal segment was placed in the small organ bath in the Krebs solution. The intestinal distension was applied by a pump and the longitudinal length was set by a micromanipulator. The three-channel pressure probe was used to measure the pressures. The diameter changes of the intestinal segments were videotaped through a stereomicroscope.

Circumferential Kirchhoff's stress:

$$S_{\theta} = \frac{\Delta P r_{i-p}}{h_p \lambda_{\theta}^2}. \quad (1)$$

Circumferential midwall Green's strain:

$$E_{\theta} = \frac{\lambda_{\theta}^2 - 1}{2}, \quad (2)$$

where ΔP is the transmural pressure difference, r is the luminal radius h is the wall thickness and λ_{θ} is the circumferential stretch ratio.

Stress and strain data immediately before the contraction (stress and strain thresholds) and at maximal contraction (maximal amplitude of stress and strain) were used for further analysis.

The total phasic stress and the total tonic stresses (both composed of active and passive tissue properties) were extracted from the top points during contraction and the baseline between the contractions during the distension (Figure 2(a)). The passive stress was extracted from the

data obtained during distension after administration of papaverine. The strain points were not fixed; hence, it was not possible to directly compare between different samples and groups. Consequently curve fitting was applied.

The total tonic and passive stresses increased in an exponential-like way as function of strain. Consequently the stress-strain curves were fitted to the exponential function equation

$$S = (S^* + \beta)e^{\alpha(E-E^*)} - \beta, \quad (3)$$

where S^* and E^* are the stress and strain at a physiological reference level [25].

The total phasic circumferential stress-strain curves increased in a polynomial way as function of strain. As a consequence the stress-strain curves were fitted to the polynomial equation

$$S = S_0 + a_1 E^3 + a_2 E^2 + a_3 E^1, \quad (4)$$

where a_1 , a_2 , and a_3 are constants.

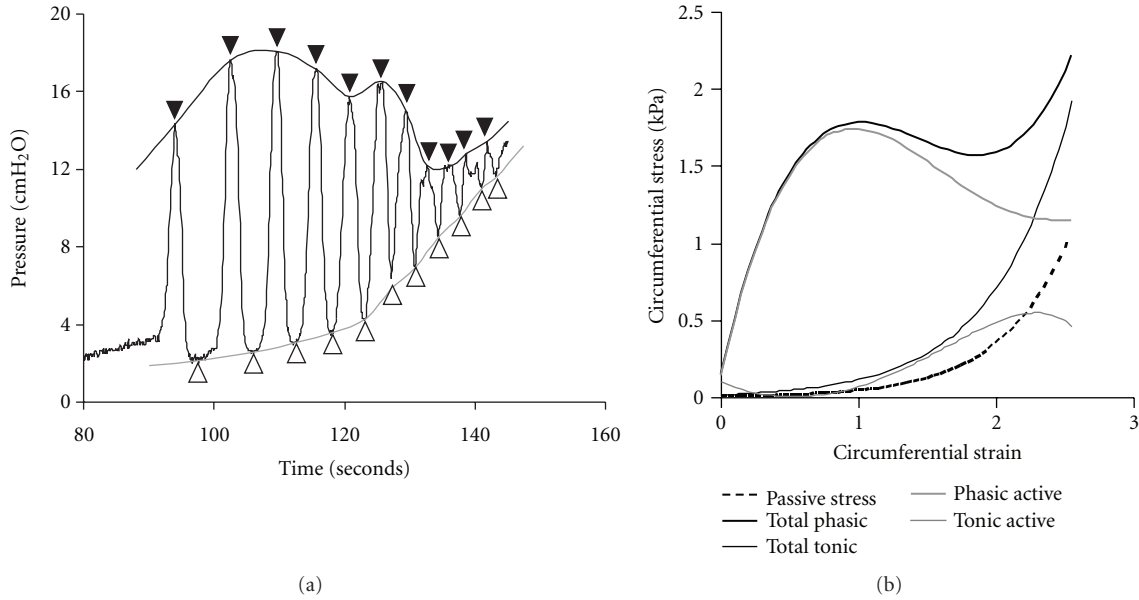


FIGURE 2: (a) illustrates maximum amplitudes during contraction and the baseline between the contractions during distension. The closed symbols above the curve mark the phasic part (black line). The open symbols under the curve mark the tonic part (gray line). The pressures from the phasic and tonic parts were used to compute the total phasic and tonic stress. (b) illustrates an example of passive, total phasic, total tonic, phasic active, and tonic active stresses as function of strains from a normal animal. The passive and the total tonic stress increased exponentially as function of strain, whereas the total phasic stress increased in a polynomial way. The phasic and tonic active stresses were obtained by the total phasic and tonic stresses minus the passive stress.

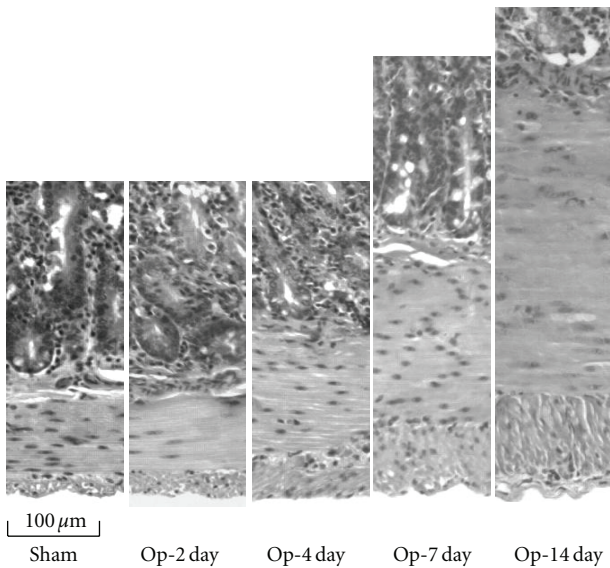


FIGURE 3: The typical pattern of the muscle layer proliferation. The hyperplasia of muscle layer was noted after two days of post-obstruction. Seven days after obstruction, the hypertrophy of both muscle layers was also observed. The circumferential muscle layer increased much more than the longitudinal muscle layer.

The active phasic and tonic stresses were defined as the total phasic and tonic stresses minus the passive stress (Figure 2(b))

$$\begin{aligned} \text{active phasic stress} &= \text{total phasic stress} - \text{passive stress}, \\ \text{active tonic stress} &= \text{total tonic stress} - \text{passive stress}. \end{aligned}$$

(5)

The active phasic and tonic stresses were normalized to muscle layer thickness as follows:

$$\begin{aligned} \text{normalized active phasic stress} &= \frac{\text{active phasic stress}}{\text{muscle thickness}}, \\ \text{normalized active tonic stress} &= \frac{\text{active tonic stress}}{\text{muscle thickness}}. \end{aligned} \quad (6)$$

The muscle layer thickness (μm) was obtained by histological measurement.

2.8. Statistical Analysis. The results were expressed as means \pm SEM unless indicated otherwise. The total phasic, total tonic, active phasic, and active tonic stresses were compared between different groups by ANOVA analysis. The normalized active phasic and tonic stresses as function of strain were also compared between groups. The results were regarded as significant when $P < 0.05$.

3. Results

3.1. General Data. The peritoneum had no signs of inflammation or adhesions that could potentially influence the mechanical properties and intestinal contraction.

The intestinal segments from the animals obstructed for 2 days and 4 days were clearly dilated. After seven days, intestinal hypertrophy was also visible. No changes were observed in the sham-obstructed and normal groups. Histological analysis showed that the thickness of both the submucosa layer and muscle layer increased during the development

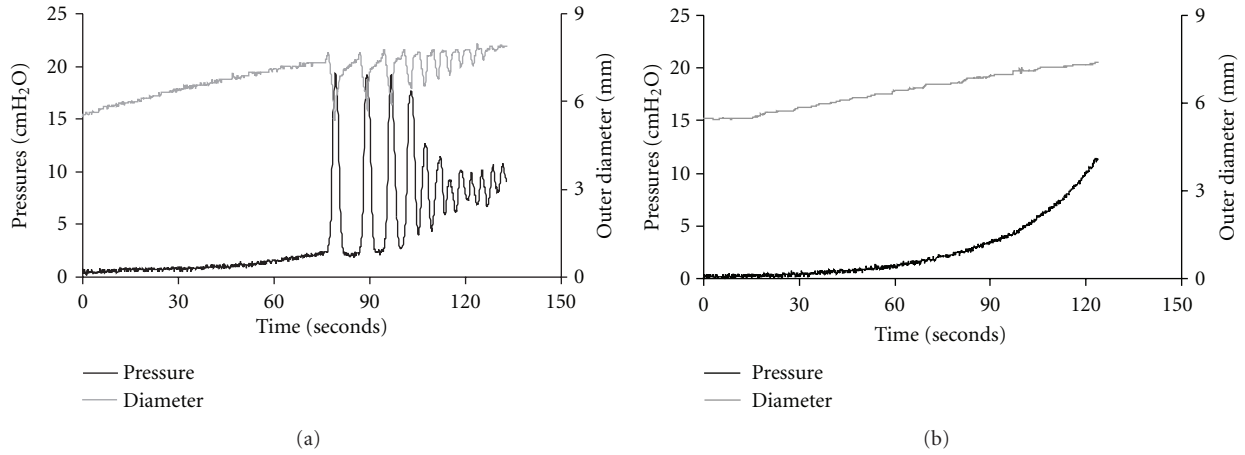


FIGURE 4: Illustration of ramp distension curves of the pressure and diameter of jejunal segment without longitudinal stretch obtained from a normal control animal. Waves of peristaltic contraction were clearly observed (a). The smooth muscle contraction was abolished by papaverine (b).

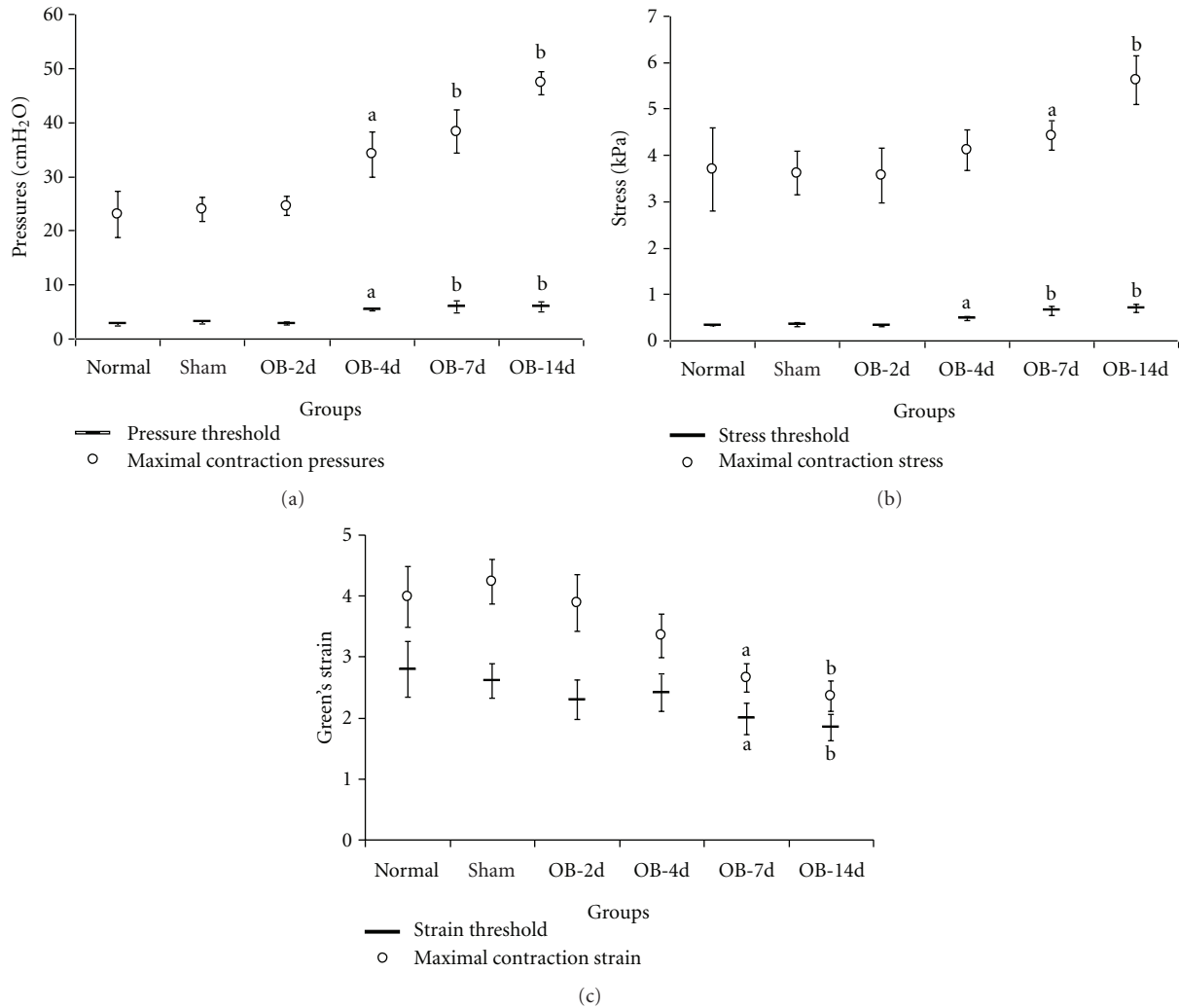


FIGURE 5: Illustration of the pressures (a), stresses (b), and strains (c) at the contraction threshold and at the maximum contraction in the groups. Threshold and maximal amplitude of pressures and stresses increased, and strain decreased as function of the obstruction period during ramp distension. Significant differences were found after 4 days of obstruction compared with normal and sham-obstructed controls (^a $P < 0.05$, ^b $P < 0.01$).

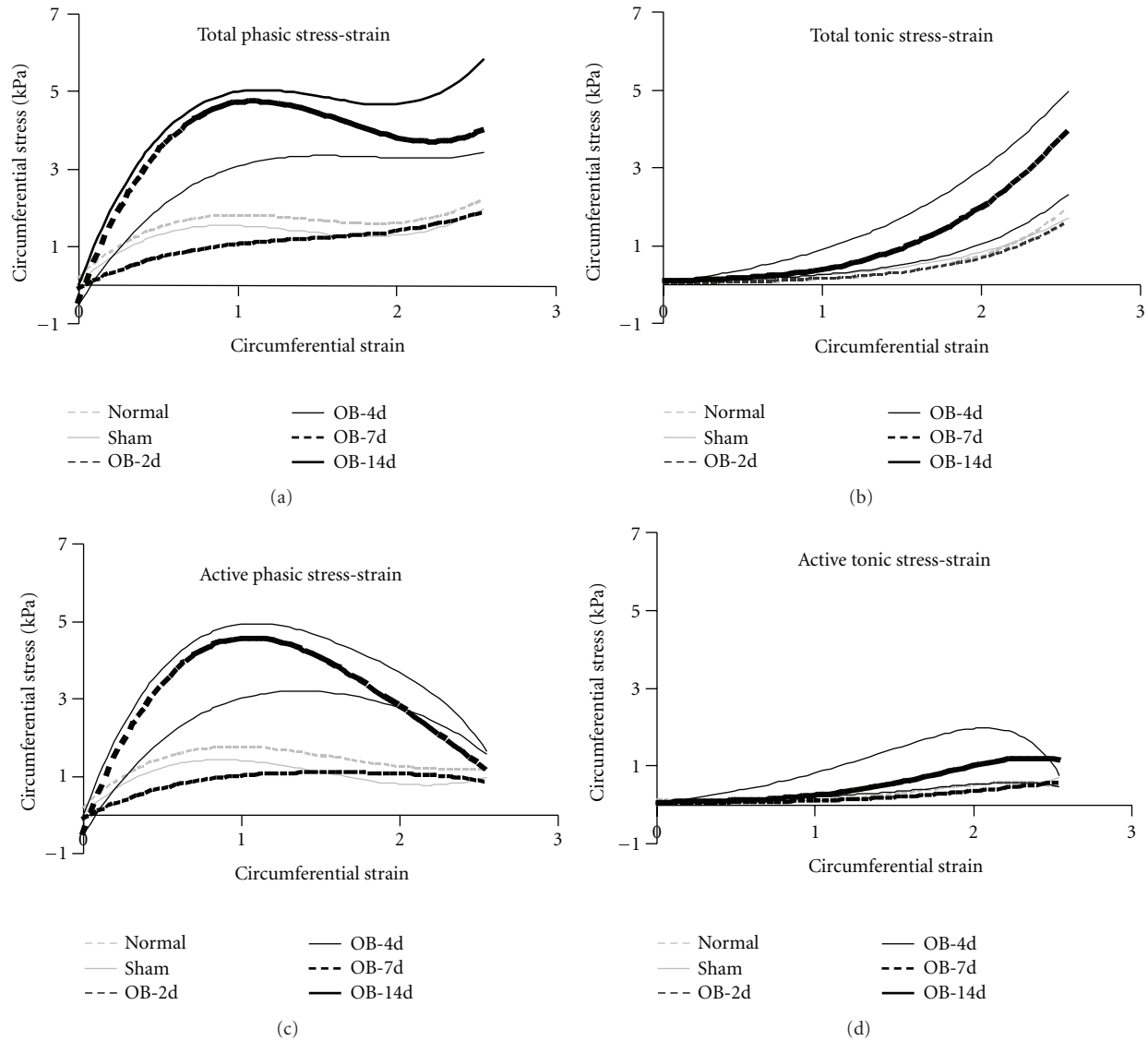


FIGURE 6: The total phasic and tonic stresses as function of strains are presented at the top panel and the computed active phasic and tonic stresses as function of strain at the bottom. The amplitude of total phasic, total tonic, active phasic, and active tonic circumferential stresses increased after 7 days obstruction compared with normal and sham controls ($P < 0.05$ and 0.01). Furthermore, the maximum for the active phasic and active tonic stresses differed.

of the obstruction (Table 1). Muscle layer thickening was observed after 4 days of obstruction whereas submucosal thickening was observed after 7 days of obstruction. The muscle hyperplasia was observed two days postobstruction. Seven days postobstruction the intestinal segments were also visibly hypertrophied. A typical pattern of the muscle layer proliferation is shown in Figure 3. The circumferential muscle layer increased much more than the longitudinal muscle layer. After 7 days of obstruction, hypertrophy is evident in both muscle layers.

3.2. Pressure-Diameter Curves. Figure 4 shows the pressure and diameter changes during the distension from a normal jejunal segment without longitudinal stretch applied. Waves of peristaltic contraction were clearly observed both from

pressure and diameter curves (Figure 4(a)). The pressure increased whereas the diameter decreased at each contraction wave. Peristaltic contractions were not observed when using papaverine (Figure 4(b)).

The pressures, stresses, and strains at the contraction threshold and maximal contraction points in different groups are shown in Figure 5. During ramp distension-induced contractions, the threshold and maximal pressure amplitude (Figure 5(a)) and stresses (Figure 5(b)) increased after obstruction. However, the strains at the contraction threshold and maximal contraction (Figure 5(c)) decreased during the development of the obstruction. Significant differences were found after 4 days of obstruction compared with normal and sham-obstructed controls ($P < 0.05$, $P < 0.01$). Thus the remodeled intestine due to obstruc-

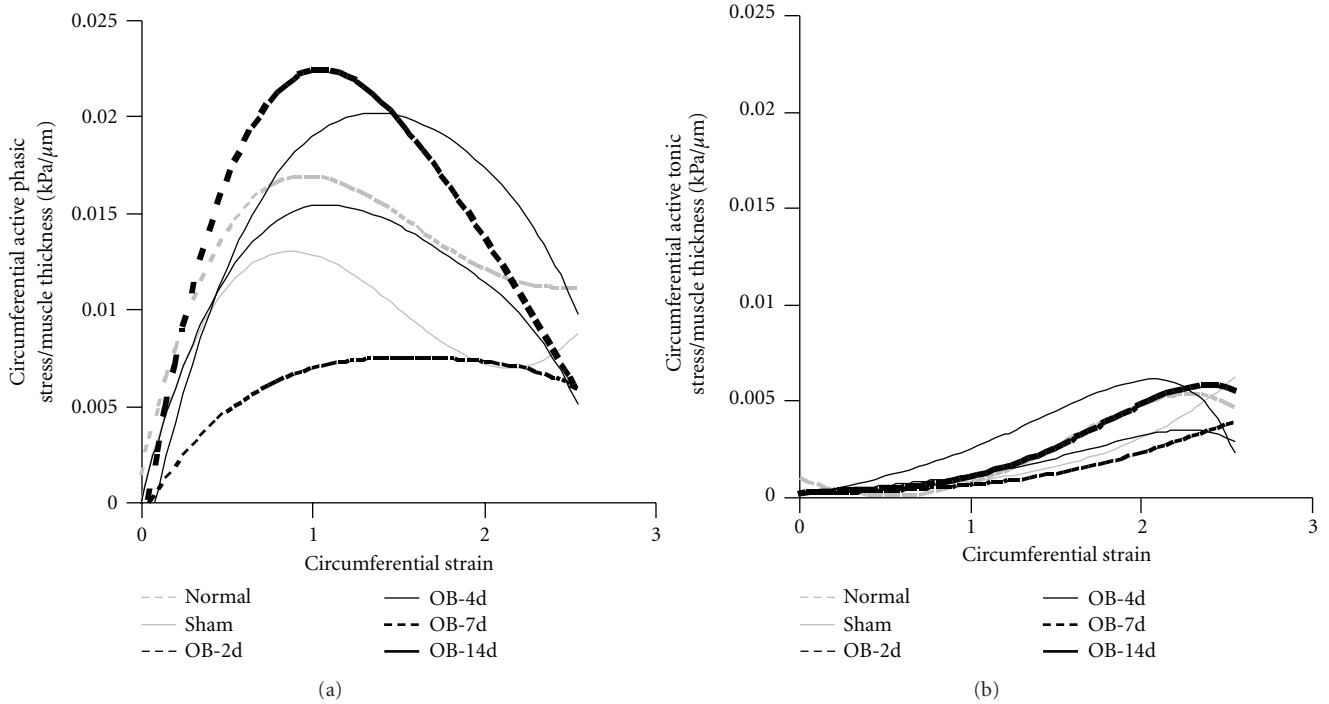


FIGURE 7: The normalized active phasic and tonic stresses illustrated as function of strains. When normalized to muscle layer thickness, the amplitude of active phasic and tonic stresses did not differ among the groups ($P > 0.05$).

TABLE 1: Layer thickness related to duration of obstruction (μm).

Groups	Mucosa	Submucosa	Circumferential muscle	Longitudinal muscle
Normal	861.1 \pm 134.3	42.9 \pm 11.2	79.3 \pm 24.1	36.2 \pm 7.5
Sham-obstructed	816.2 \pm 118.3	35.5 \pm 12.6	90.4 \pm 15.1	37.8 \pm 8.8
Obstructed for 2 days	905.3 \pm 109.9	45.3 \pm 11.8	107.3 \pm 31.4	37.4 \pm 9.5
Obstructed for 4 days	1001.1 \pm 135.9	34.5 \pm 8.5	116.5 \pm 42.3*	42.3 \pm 15.3*
Obstructed for 7 days	992.7 \pm 91.6	55.7 \pm 9.9*	145.5 \pm 57.9*	57.9 \pm 10.6*
Obstructed for 14 days	1028.1 \pm 167.2	71.8 \pm 18.7**	240.2 \pm 80.7**	80.7 \pm 28.9**

* $P < 0.05$; ** $P < 0.01$ (compared with normal and sham-obstructed groups).

tion required higher pressure and stress levels to induce contractions, and the induced contractions produced high pressures and stresses during ramp distension. However, the deformation of the intestinal wall became smaller indicating wall stiffening.

3.3. Analysis of Tonic and Phasic Stress-Strain Curves. In accordance with our previous study [22], the passive circumferential stress increased when the intestine was stretched longitudinally. Longitudinal stretching caused the active circumferential stress to decrease (data not shown). However, longitudinal stretch did not influence the differences of tonic and phasic stress-strain curves among the groups. The results below were obtained from the segments at longitudinal stretch of 10%.

Figure 6 illustrates the total phasic (a), total tonic (b), active phasic (c), and active tonic (d) stresses as function of strain in the different groups. The total phasic stress increased in a polynomial way as function of strain whereas

the total tonic stress increased in an exponential-like way. At corresponding circumferential strains, the amplitude of total phasic, total tonic, active phasic, and active tonic circumferential stresses increased after 7 days of obstruction compared with normal and sham-obstructed controls ($P < 0.05$ and 0.01). However, when normalized to the muscle layer thickness, the amplitude of active phasic and tonic stresses as function of strain did not differ among the groups (Figure 7, $P > 0.05$).

4. Discussion

The length-tension diagrams known from physiological and pharmacological studies of smooth muscle strips *in vitro* [19, 26] can be reproduced in intact segment of intestine *in vitro* as shown in the present and previous studies [22]. From a biomechanical standpoint, phasic and tonic stress-strain data are required for evaluation of smooth muscle mechanical function in intact intestinal segments. The main findings in the current study were that the amplitude of total phasic,

total tonic, active phasic, and active tonic circumferential stresses increased after 7 days of obstruction. However, when normalized to muscle layer thickness, the amplitude of active stresses did not differ among the groups.

The mechanical properties of the small intestine can be divided into properties arising from a “passive” or connective tissue element, an active (“tonic”) element, reflecting baseline muscle activity, and an active (“phasic”) element, reflecting the effects of distension-induced neuromuscular function. The passive and the active stress-strain curves depend on the wall structure, the wall mechanical properties, and the smooth muscle contractile properties. Longstanding nonoccluding intestinal obstruction results in structural changes with marked dilatation, increased collagen content, and hypertrophy of especially the muscle layer proximal to the obstruction site [9, 27]. Thus, stress-strain data are important for understanding the mechanical function of remodeled smooth muscle in the partially obstructed intestine. Length-tension diagrams have been derived from the human gastric antrum and duodenum [21, 28], though butylscopolamine may not have abolished all phasic activity. The present and previous [22] *in vitro* studies produced tonic and phasic stress-strain curves referenced to the passive stress-strain curve because papaverine completely abolished all smooth muscle activity. Computation of the stress depends on the wall thickness which cannot be directly measured *in vivo*. However it can be accounted for *in vitro*.

The partial obstruction narrows the intestine which will increase the resistance to flow during bolus passage. To compensate, the smooth muscle will proliferate to increase contraction force to overcome the resistance. Experimental evidence demonstrated that longstanding partial intestinal obstruction results in marked proliferation of the intestinal muscle layers [8, 9, 11, 12, 14–17]. In the present study the intestinal muscle layer, especially the circumferential muscle layer, thickness markedly increased during obstruction. The muscle layer increased circumferentially more than longitudinally probably due to increased circumferential stress. Previous studies on pressure contraction curves of obstructed intestinal segments have demonstrated that the total contractile ability of remodeled smooth muscle layer increased [12, 29]. In the present study the pressure curve (Figure 5(a)) confirmed that the maximal contraction pressure increased after obstruction. In agreement with the proliferation of the smooth muscle layer after 4 days of obstruction, the maximal contraction stress significantly increased indicating increased contraction force. Both muscle proliferation and stress increase in a time-dependent manner as function of obstruction time, indicating that muscle remodeling is determined by the stress. This phenomenon is known from the cardiovascular system [23]. However, the maximal contraction strain significantly decreased during the development of obstruction indicating the wall deformation became smaller due to stiffening [14]. Further stress-strain analysis demonstrated that the total phasic, total tonic, active phasic, and active tonic stresses as function of strain also significantly increased after 7 days of obstruction. Therefore, the increased total contraction force is mainly due to smooth muscle proliferation. As a result, increased total contraction

force can compensate to push the content through the partial obstruction site. Furthermore, it is worthwhile to notice that the maximum of active phasic and active tonic stress differ. This probably means that they are regulated in different ways.

Despite the fact that the total contraction force increased after obstruction, the contraction ability of single unit smooth muscle was decreased [15]. It is also interesting to notice at the present study that when normalized to muscle layer thickness, the active phasic and tonic stresses as function of strain did not differ between obstruction groups and sham-obstructed and normal groups. Therefore the remodeled smooth muscle cells may be somehow damaged due to long-term partial obstruction. Earlier studies demonstrated that the hypertrophied muscle cells exhibit ultrastructural changes of sarcoplasmic reticulum, gap connections, and cytoplasmic content and decreased ratio of myofilament to intermediate filament [30–32]. The relative decrease in myofilament content suggests a loss of contractile machinery in remodeled smooth muscle cells due to partial obstruction. Furthermore, it was reported that the stiffness of collagen fibrils could influence vascular smooth muscle cell phenotype and function [33]. The extracellular matrix including collagen was reported to increase due to the obstruction [11, 12]. We found that the submucosal thickness increased after intestinal obstruction. Therefore, the altered extracellular matrix may also affect the function of smooth muscle cells. This needs to be further studied. Furthermore, we noticed in the present study that the pressure and stress thresholds to induce contraction increased after obstruction. This can be caused by altered mechanosensory function such as resetting of the mechanoreceptors. This issue also requires further study.

The partially obstructed intestinal model has been validated previously [10, 11, 15] and demonstrated that it is a good model for studying histomorphological and biomechanical intestinal remodeling [14]. The size of the band relative to the circumference of the intestine is important for successful obstruction. If the band is too tight, the animal dies within 48 hours; if it is too loose, no changes will occur [11]. In the present study, the ring was one millimetre bigger than the outer diameter of the intestinal segment. The mortality rate was lower than 20%. Although the band does not compress the resting intestine, during bolus passage the band would increase the resistance during the propagation of contractions by compressing the intestinal wall.

5. Conclusions

The total active phasic and tonic stress increased in long-term-obstructed intestine which is likely related to increased total contraction force to push the content through the partial obstruction site. However, the contraction force per smooth muscle unit did not increase in obstructed intestine when compared to normal intestine.

Disclosure

The authors have no proprietary, financial, professional, or other personal interest related to the research.

Acknowledgments

The technicians O. Sørensen, T. Madsen, and J. Sørensen are thanked for handling the animals. This paper was supported by the Aalborg Hospital.

References

- [1] M. Hernanz-Schulman, "Infantile hypertrophic pyloric stenosis," *Radiology*, vol. 227, no. 2, pp. 319–331, 2003.
- [2] M. Miyamoto, K. Egami, S. Maeda et al., "Hirschsprung's disease in adults: report of a case and review of the literature," *Journal of Nippon Medical School*, vol. 72, no. 2, pp. 113–120, 2005.
- [3] W. Park and M. F. Vaezi, "Etiology and pathogenesis of achalasia: the current understanding," *American Journal of Gastroenterology*, vol. 100, no. 6, pp. 1404–1414, 2005.
- [4] J. Cheng, N. Vemula, and S. Gendler, "Small bowel obstruction caused by intramural hemorrhage secondary to anti-coagulant therapy," *Acta Gastro-Enterologica Belgica*, vol. 71, no. 3, pp. 342–344, 2008.
- [5] F. Froehlich, P. Juillerat, C. Mottet et al., "Obstructive fibrosclerotic Crohn's disease," *Digestion*, vol. 71, no. 1, pp. 29–30, 2005.
- [6] T. K. Hsieh, A. C. Chen, S. F. Wu, and W. Chen, "Postoperative intussusception in children with enterostomy," *Acta Paediatrica Taiwanica*, vol. 46, no. 3, pp. 166–169, 2005.
- [7] R. M. Zollinger Jr, W. C. Sternfeld, and H. Schreiber, "Primary neoplasms of the small intestine," *American Journal of Surgery*, vol. 151, no. 6, pp. 654–658, 1986.
- [8] S. Bertoni and G. Gabella, "Hypertrophy of mucosa and serosa in the obstructed intestine of rats," *Journal of Anatomy*, vol. 199, no. 6, pp. 725–734, 2001.
- [9] G. Gabella, "Hypertrophy of visceral smooth muscle," *Anatomy and Embryology*, vol. 182, no. 5, pp. 409–424, 1990.
- [10] K. Schulze-Delrieu, B. Brown, B. Herman et al., "Preservation of peristaltic reflex in hypertrophied ileum of guinea pig," *American Journal of Physiology*, vol. 269, no. 1, pp. G49–G59, 1995.
- [11] J. H. Storkholm, J. Zhao, G. E. Villadsen, H. Hager, S. L. Jensen, and H. Gregersen, "Biomechanical remodeling of the chronically obstructed guinea pig small intestine," *Digestive Diseases and Sciences*, vol. 52, no. 2, pp. 336–346, 2007.
- [12] J. H. Storkholm, J. Zhao, G. E. Villadsen, and H. Gregersen, "Spontaneous and bolus-induced motility in the chronically obstructed guinea-pig small intestine in vitro," *Digestive Diseases and Sciences*, vol. 53, no. 2, pp. 413–420, 2008.
- [13] B. V. Stromberg and L. Klein, "Collagen dynamics of partial small bowel obstruction," *American Journal of Surgery*, vol. 148, no. 2, pp. 257–261, 1984.
- [14] J. Zhao, D. Liao, J. Yang, and H. Gregersen, "Biomechanical remodelling of obstructed guinea pig jejunum," *Journal of Biomechanics*, vol. 43, no. 7, pp. 1322–1329, 2010.
- [15] S. Bertoni, G. Gabella, P. Ghizzardi et al., "Motor responses of rat hypertrophic intestine following chronic obstruction," *Neurogastroenterology and Motility*, vol. 16, no. 3, pp. 365–374, 2004.
- [16] J. Chen, H. Chen, K. M. Sanders, and B. A. Perrino, "Regulation of SRF/CARF-dependent gene transcription during chronic partial obstruction of murine small intestine," *Neurogastroenterology and Motility*, vol. 20, no. 7, pp. 829–842, 2008.
- [17] S. Geuna, S. Cardillo, and M. G. Giacobini-Robecchi, "Smooth muscle cell hypertrophy and hyperplasia in the partially obstructed gut of the rat: a quantitative evaluation," *Acta Anatomica*, vol. 163, no. 2, pp. 69–74, 1998.
- [18] P. A. Longhurst, J. S. Kang, A. J. Wein, and R. M. Levin, "Comparative length-tension relationships of urinary bladder strips from hamsters, rats, guinea-pigs, rabbits and cats," *Comparative Biochemistry and Physiology*, vol. 96, no. 1, pp. 221–225, 1990.
- [19] A. M. Drewes, K. P. Schipper, G. Dimcevski et al., "Multimodal induction and assessment of allodynia and hyperalgesia in the human oesophagus," *European Journal of Pain*, vol. 7, no. 6, pp. 539–549, 2003.
- [20] C. Gao, L. Arendt-Nielsen, W. Liu, P. Petersen, A. M. Drewes, and H. Gregersen, "Sensory and biomechanical responses to ramp-controlled distension of the human duodenum," *American Journal of Physiology—Gastrointestinal and Liver Physiology*, vol. 284, no. 3, pp. G461–G471, 2003.
- [21] H. Gregersen, O. H. Gilja, T. Hausken et al., "Mechanical properties in the human gastric antrum using B-mode ultrasonography and antral distension," *American Journal of Physiology—Gastrointestinal and Liver Physiology*, vol. 283, no. 2, pp. G368–G375, 2002.
- [22] J. Zhao, D. Liao, and H. Gregersen, "Phasic and tonic stress-strain data obtained in intact intestinal segment in vitro," *Digestive Diseases and Sciences*, vol. 53, no. 12, pp. 3145–3151, 2008.
- [23] Y. C. Fung, *Biomechanics: Motion, Flow, Stress, and Growth*, Springer-Verlag, New York, NY, USA, 1990.
- [24] H. Gregersen, G. S. Kassab, and Y. C. Fung, "The zero-stress state of the gastrointestinal tract: biomechanical and functional implications," *Digestive Diseases and Sciences*, vol. 45, no. 12, pp. 2271–2281, 2000.
- [25] H. Gregersen, *Biomechanics of the Gastrointestinal Tract. New Perspectives in Motility Research and Diagnostics*, Springer-Verlag, London, UK, 2002.
- [26] J. Pedersen, A. M. Drewes, and H. Gregersen, "New analysis for the study of the muscle function in the human oesophagus," *Neurogastroenterology and Motility*, vol. 17, no. 5, pp. 767–772, 2005.
- [27] G. Gabella, "Hypertrophy of intestinal smooth muscle," *Cell and Tissue Research*, vol. 163, no. 2, pp. 199–214, 1975.
- [28] J. Pedersen, C. Gao, H. Egekvist et al., "Pain and biomechanical responses to distention of the duodenum in patients with systemic sclerosis," *Gastroenterology*, vol. 124, no. 5, pp. 1230–1239, 2003.
- [29] S. Bertoni, V. Ballabeni, L. Flammini, T. Gobetti, M. Impicciatore, and E. Barocelli, "Intestinal chronic obstruction affects motor responsiveness of rat hypertrophic longitudinal and circular muscles," *Neurogastroenterology and Motility*, vol. 20, no. 11, pp. 1234–1242, 2008.
- [30] G. Gabella, "Hypertrophic smooth muscle. II. Sarcoplasmic reticulum, caveolae and mitochondria," *Cell and Tissue Research*, vol. 201, no. 1, pp. 79–92, 1979.
- [31] G. Gabella, "Hypertrophic smooth muscle. III. Increase in number and size of gap junctions," *Cell and Tissue Research*, vol. 201, no. 2, pp. 263–276, 1979.
- [32] G. Gabella, "Hypertrophic smooth muscle. IV. Myofilaments, intermediate filaments and some mechanical properties," *Cell and Tissue Research*, vol. 201, no. 2, pp. 277–288, 1979.
- [33] D. P. McDaniel, G. A. Shaw, J. T. Elliott et al., "The stiffness of collagen fibrils influences vascular smooth muscle cell phenotype," *Biophysical Journal*, vol. 92, no. 5, pp. 1759–1769, 2007.

Research Article

Distribution of Myosin Attachment Times Predicted from Viscoelastic Mechanics of Striated Muscle

Bradley M. Palmer, Yuan Wang, and Mark S. Miller

Department of Molecular Physiology and Biophysics, University of Vermont, 122 HSRF, Beaumont Avenue, Burlington, VT 05405, USA

Correspondence should be addressed to Bradley M. Palmer, bmpalmer@uvm.edu

Received 1 July 2011; Accepted 22 August 2011

Academic Editor: Henk Granzier

Copyright © 2011 Bradley M. Palmer et al. This is an open access article distributed under the Creative Commons Attribution License, which permits unrestricted use, distribution, and reproduction in any medium, provided the original work is properly cited.

We demonstrate that viscoelastic mechanics of striated muscle, measured as elastic and viscous moduli, emerge directly from the myosin crossbridge attachment time, t_{att} , also called time-on. The distribution of t_{att} was modeled using a gamma distribution with shape parameter, p , and scale parameter, β . At 5 mM MgATP, β was similar between mouse α -MyHC (16.0 ± 3.7 ms) and β -MyHC (17.9 ± 2.0 ms), and p was higher ($P < 0.05$) for β -MyHC (5.6 ± 0.4 no units) compared to α -MyHC (3.2 ± 0.9). At 1 mM MgATP, p approached a value of 10 in both isoforms, but β rose only in the β -MyHC (34.8 ± 5.8 ms). The estimated mean t_{att} (i.e., $p\beta$ product) was longer in the β -MyHC compared to α -MyHC, and became prolonged in both isoforms as MgATP was reduced as expected. The application of our viscoelastic model to these isoforms and varying MgATP conditions suggest that t_{att} is better modeled as a gamma distribution due to its representing multiple temporal events occurring within t_{att} compared to a single exponential distribution which assumes only one temporal event within t_{att} .

1. Introduction

Advances in optical techniques have allowed detailed analysis of the isolated single myosin crossbridge. Upon formation of a myosin crossbridge, isomerization of the myosin molecule provides a unitary force proportional to the length of the lever arm and the extent of the lever arm swing, also called the power stroke [1–4]. The time duration of crossbridge attachment, sometimes called time-on, is also measured by optical trapping. The distribution of attachment times has been found to depend upon the myosin isoform, nucleotide availability, point mutations, and several other factors [5–12]. This time duration of crossbridge attachment plays a significant role in determining muscle performance observed as force and velocity of contraction at the single fiber level.

There remains, however, a considerable challenge to understand and describe how the unitary force and the temporary attachment times of myosin molecules are manifested at the level of muscle tissue, which possesses a three-dimensional lattice structure and can be studied intact or submerged in physiological solutions after removal of

the plasma membrane. Viscoelastic mechanics of muscle tissue represents one such macroscopic consequence of these molecular phenomena. We describe in this paper a quantitative justification and methodology for estimating the distribution of myosin crossbridge attachment times based on viscoelastic mechanics measured in striated muscle fibers.

Length perturbation analysis of muscle provides a means to quantify viscoelastic mechanics and entails applying a small length change at one end of a muscle and recording the force response on the other end. The length perturbation and force response are then subjected to Fourier transformation, and the dynamic mechanical properties of the muscle are characterized by the complex ratio of the transformed force response normalized to cross-sectional area (or $\sigma(\omega)$ = Fourier transformed tensile stress) divided by the transformed length perturbation normalized to initial length (or $\varepsilon(\omega)$ = Fourier transformed strain). This complex ratio is also called the mechanical transfer function or complex modulus of the muscle, $Y(\omega) = \sigma(\omega)/\varepsilon(\omega)$. The real and imaginary parts are, respectively, termed the elastic modulus and viscous modulus of the muscle [13, 14].

The frequency characteristic dips (low values) and shoulders (high values) observed in the elastic and viscous moduli of activated muscle are sensitive to species of origin, myosin isoform, and varying concentrations of MgATP and therefore reflect the macroscopic consequence of myosin crossbridge kinetics [4, 11, 15–18]. The dips in the moduli, most notably the negatively valued viscous modulus, occur near the frequencies at which the muscle operates *in vivo* [14]. The shoulders of the moduli, however, are more prominent in magnitude. According to our previous modeling endeavor [19], the shoulders appearing at these higher frequencies of the moduli reflect the mechanical consequences of intermittent myosin crossbridge formation. In that work, we proposed that a two-state model of the acto-myosin crossbridge governed by first-order kinetics gives rise to a viscoelastic work-absorbing property, termed the C-process by Kawai and colleagues [13, 16, 20], which is characterized by an exponential rate constant equivalent to the myosin crossbridge off rate termed g by Huxley [21]. The mean myosin attachment time, based on a single exponential distribution of attachment times, could be estimated as the reciprocal of this exponential rate constant, $2\pi c$, after fitting (1) to a measured complex modulus [14, 19]:

$$Y(\omega) = A(i\omega)^k - B\left(\frac{i\omega}{2\pi b + i\omega}\right) + C\left(\frac{i\omega}{2\pi c + i\omega}\right). \quad (1)$$

While the single exponential representation of C-process and its interpretation have been valuable for examining a variety of muscle types under a number of conditions [7, 11, 13, 14, 19, 20, 22], the assumptions of first-order kinetics and a single exponential distribution of myosin attachment times are limiting. It is known, for example, that multiple time periods associated with multiple biochemical states make up the myosin crossbridge cycle. These multiple states constitute the entire myosin crossbridge attachment time. Such an addition of multiple smaller time periods would result in a multiple exponential distribution or a gamma distribution of the crossbridge attachment times rather than a single exponential distribution assumed by first-order kinetics.

In the present study, we examine the mechanical consequences of the distribution of myosin attachment times represented by a gamma distribution, which allows the description of more discrete and longer lived time-on and yet also allows for the possibility of a single exponential function. The consideration of the gamma distribution effectively poses the hypothesis that multiple temporal events which occur within the time of attachment can be discerned in the viscoelastic response of striated muscle at the macroscopic level. We provide an analytical solution to the mechanical consequences that emerge as the shoulders of the elastic and viscous moduli. We also demonstrate the validity of the analytical solution with computer simulations. Finally, we demonstrate the application of the gamma distribution representation of the C-process in a comparison of mouse cardiac myosin heavy chain isoforms, α -MyHC and β -MyHC, subjected to varying concentrations of MgATP.

2. Mathematical Modeling

Our goal in this section is to derive a mathematical expression that describes the viscoelastic component of a force response to a length perturbation that has been applied to an ensemble of myosin molecules intermittently attaching and detaching from actin within a half sarcomere of striated muscle. The force response and length perturbation will form the bases for a mechanical transfer function, which is equivalent to a viscoelastic complex modulus measured in frequency space. We use a two-state model of myosin attachment and detachment as our starting point in modeling the mechanical consequences of intermittently attached actomyosin crossbridges. It is important to point out that in the following development we do not assume first-order kinetics as governing myosin attachment and detachment; in doing so we will be able to provide a more generalized model of the viscoelastic mechanics due to the myosin crossbridges.

The time periods of attachment, t_{att} , and detachment, t_{det} , are considered here to be random variables whose values are governed by stochastic processes independent of force, stress, strain, length, velocity, and each other. The total time period for a myosin crossbridge cycle is also a random variable, $t_{\text{cycle}} = t_{\text{att}} + t_{\text{det}}$. All myosin heads are assumed independent of each other. During detachment, force due to an individual myosin head is zero. During attachment, force is given as the product of the unitary force due to the power stroke, the length displacement of an elastic element in series with the crossbridge, and the stiffness of that elastic element (Figure 1). We assume that length perturbations are sufficiently small to elicit a linear force response of the elastic element in series with the crossbridge.

The elastic element represents the most compliant structures between the M- and Z-lines of the sarcomere in series with the attached crossbridge. Previous work by others has identified the most compliant structures as the head and neck regions of the myosin S1 segment including the lever arm bound with the essential and regulatory light chains and that portion of myosin S2 segment not incorporated into the thick filament backbone [4, 23, 24]. We also assume that when the myosin is in a postpower stroke state the most compliant elements are taut, that is, not slack as might occur if the myosin bound to actin at a point too close to the M-line to stretch the S2 segment [4, 23, 24].

2.1. Viscoelastic Mechanical Response of Half Sarcomere. Here we provide a theoretical description of the force response of a half sarcomere to an externally applied length perturbation. We assume here that the total force that might be recorded from a half sarcomere, $F_{\text{total}}(t)$, is given as the sum of the forces produced by each attached myosin crossbridge due to its unitary force, F_{uni} , and its dynamic response due to the length perturbation, $f(t)$ (Figure 1). The total force produced by a summation of attached crossbridges will be denoted as

$$F_{\text{total}}(t) = \sum_{i=1}^M F_{\text{uni}(i)} + f(i)(t), \quad (2)$$

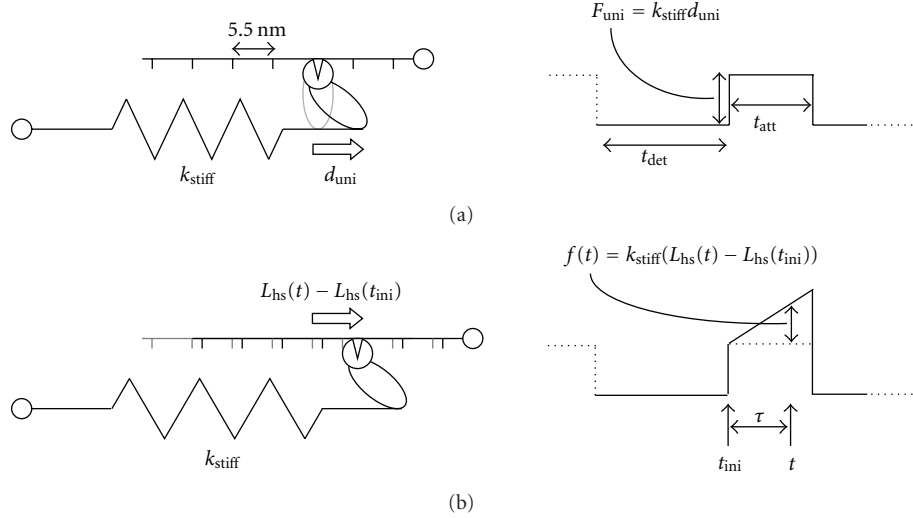


FIGURE 1: Force due to myosin crossbridges. (a) A unitary force, F_{uni} , is generated over a finite time of attachment, t_{att} (also called time-on), when the myosin power stroke swings the lever arm a net unitary displacement, d_{uni} . The time of detachment, t_{det} , refers to the time period between a crossbridge detaching from actin and before reattaching. (b) An additional crossbridge-dependent force is transmitted through the half sarcomere when an elastic element in series with the crossbridge and with stiffness k_{stiff} undergoes a length change due to an externally applied perturbation of the half sarcomere, L_{hs} . The force recorded at any time t , $f(t)$, due to the perturbation reflects the displacement of the elastic element since the initial time of crossbridge attachment, t_{ini} .

where M = the number of attached crossbridges in the half sarcomere at time t . When an external length perturbation is applied, the dynamic response of the i th attached crossbridge is given as the stiffness-displacement product, which is a linear approximation suitable for very small length perturbations:

$$f_{(i)}(t) = k_{\text{stiff}(i)}(L_{\text{hs}}(t) - L_{\text{hs}}(t_{\text{ini}(i)})), \quad (3)$$

where k_{stiff} = the stiffness coefficient of the crossbridge elastic element, $L_{\text{hs}}(t)$ = displacement imposed upon of the half sarcomere by an externally driven perturbation, and t_{ini} = the instant of initial crossbridge attachment. Under isometric conditions, the total force is simply equal to the total number of attached crossbridges, M , multiplied by the mean unitary force, \bar{F}_{uni} . The dynamic force recorded over the half sarcomere, $F_{\text{hs}}(t)$, can then be defined as the total force minus the isometric force and written as follows:

$$F_{\text{hs}}(t) = F_{\text{total}}(t) - M\bar{F}_{\text{uni}} = \sum_{i=1}^M k_{\text{stiff}(i)}(L_{\text{hs}}(t) - L_{\text{hs}}(t_{\text{ini}(i)})). \quad (4)$$

We now use the Inverse Fourier Transform definitions for $F_{\text{hs}}(t)$ and $L_{\text{hs}}(t)$, namely,

$$\begin{aligned} F_{\text{hs}}(t) &= \frac{1}{\sqrt{2\pi}} \int_{-\infty}^{\infty} \tilde{F}_{\text{hs}}(\omega) e^{i\omega t} d\omega, \\ L_{\text{hs}}(t) &= \frac{1}{\sqrt{2\pi}} \int_{-\infty}^{\infty} \tilde{L}_{\text{hs}}(\omega) e^{i\omega t} d\omega, \end{aligned} \quad (5)$$

where $\tilde{F}_{\text{hs}}(\omega)$ and $\tilde{L}_{\text{hs}}(\omega)$ are the Fourier Transform representations of $F_{\text{hs}}(t)$ and $L_{\text{hs}}(t)$, respectively; then (4) can be written as follows:

$$\begin{aligned} &\frac{1}{\sqrt{2\pi}} \int_{-\infty}^{\infty} \tilde{F}_{\text{hs}}(\omega) e^{i\omega t} d\omega \\ &= \frac{1}{\sqrt{2\pi}} \int_{-\infty}^{\infty} \sum_{i=1}^M k_{\text{stiff}(i)} \tilde{L}_{\text{hs}}(\omega) (e^{i\omega t} - e^{i\omega t_{\text{ini}(i)}}) d\omega. \end{aligned} \quad (6)$$

We now define the variable, $\tau = t - t_{\text{ini}}$, as the time period between time, t , and the instant of the most recent attachment of a crossbridge, t_{ini} . For the i th crossbridge, $t_{\text{ini}(i)} = t - \tau_{(i)}$. The term $(e^{i\omega t} - e^{i\omega t_{\text{ini}(i)}})$ in (6) then becomes $(1 - e^{-i\omega \tau_{(i)}}) e^{i\omega t}$ and we can remove the Inverse Fourier Integrals of (6):

$$\tilde{F}_{\text{hs}}(\omega) = \sum_{i=1}^M k_{\text{stiff}(i)} \tilde{L}_{\text{hs}}(\omega) (1 - e^{-i\omega \tau_{(i)}}). \quad (7)$$

The summation over a large number of attached crossbridges can be replaced as the product of M and the expected value of the summed terms. To do so would require our providing the probability density functions (PDFs) for those random variables represented as bearing the i -subscript in (7). We assume here that the random variables k_{stiff} and τ are independent of each other. Thus, the result for the expected value of k_{stiff} would be independent of its probability density function and equal to the mean value for k_{stiff} . Equation (7) can be written as

$$\tilde{F}_{\text{hs}}(\omega) = M\bar{k}_{\text{stiff}} \tilde{L}_{\text{hs}}(\omega) \int_0^{\infty} \text{PDF}_{\tau}(t) (1 - e^{-i\omega t}) dt, \quad (8)$$

where \bar{k}_{stiff} = mean stiffness of the elastic element and $\text{PDF}_{\tau}(t)$ = the probability density function for the random

variable τ as a function of time, t . Equation (8) represents the force response in frequency space due to an externally applied length perturbation on striated muscle with no strain dependence on myosin crossbridge kinetics.

The number of crossbridges attached at any time, M , can be replaced by the total number of myosin heads available to form crossbridges, N , multiplied by the probability that any one myosin head has formed a crossbridge, that is, the duty ratio $\bar{t}_{\text{att}}/\bar{t}_{\text{cycle}}$. The mechanical transfer function, which represents a measured viscoelastic complex modulus, can then be written as follows:

$$\frac{\tilde{F}_{\text{hs}}(\omega)}{\tilde{L}_{\text{hs}}(\omega)} = N \left(\frac{\bar{t}_{\text{att}}}{\bar{t}_{\text{cycle}}} \right) \bar{k}_{\text{stiff}} \int_0^{\infty} \text{PDF}_{\tau}(t) (1 - e^{-i\omega t}) dt, \quad (9)$$

where \bar{t}_{att} = mean time duration of crossbridge attachment and \bar{t}_{cycle} = mean time of a complete crossbridge cycle. Equation (9) represents a generalized mathematical description of the visco-elastic response of intermittently attaching myosin crossbridges. The form of (9) suggests that the force response is dictated by $\text{PDF}_{\tau}(t)$, so long as the other random variables are sufficiently represented by their respective means. A physical interpretation of $\text{PDF}_{\tau}(t)$ and its relation to the probability density function for t_{att} , $\text{PDF}_{t_{\text{att}}}(t)$, are presented below.

2.2. Survival Function. As defined above, the random variable τ represents the time period between any given time t and the instant any bound crossbridge was formed (Figure 1(b)). In other words, τ represents the time period any bound crossbridge has survived up to time t . The probability (Pr) that a crossbridge has survived for a time period τ , we will call it $S_{\tau}(t)$, is defined as the probability that τ is less than the time of crossbridge attachment, t_{att} [25]. The probability density function of crossbridge attachment time $\text{PDF}_{t_{\text{att}}}(t)$ and the survival function $S_{\tau}(t)$ are related as follows:

$$S_{\tau}(t) = \text{Pr}(t < t_{\text{att}}) = \int_t^{\infty} \text{PDF}_{t_{\text{att}}}(t) dt, \quad (10a)$$

$$-\frac{dS_{\tau}(t)}{dt} = \text{PDF}_{t_{\text{att}}}(t). \quad (10b)$$

The $\text{PDF}_{\tau}(t)$ needed in (8) is simply a normalization of $S_{\tau}(t)$ and is defined as the survival function of (10a) divided by its integral:

$$\text{PDF}_{\tau}(t) = \frac{S_{\tau}(t)}{\int_0^{\infty} S_{\tau}(t) dt}. \quad (11)$$

With (9) we have provided a mathematical representation of the energy-absorbing viscoelastic complex modulus that arises from intermittently attached myosin crossbridges, and we have not assumed a specific scheme for the biochemical steps that govern the distributions of the random variable t_{att} . Thus, any measure of the viscoelastic complex modulus, given by the left hand side of (9), can be used to calculate an estimate of $\text{PDF}_{\tau}(t)$ and by extension through (10b) also be used to calculate an estimate of $\text{PDF}_{t_{\text{att}}}(t)$.

2.3. Gamma Distribution Representation of $\text{PDF}_{t_{\text{att}}}(t)$. In our previous work we chose $\text{PDF}_{t_{\text{att}}}(t)$ to be represented by a single exponential distribution [19], which by extension of (10a), (10b), and (11) also defined $\text{PDF}_{\tau}(t)$ as the same single exponential distribution. That choice reflected an assumption of first-order kinetics governing the lifetime of the myosin crossbridge in the attached state. The result was a mathematical representation of the mechanical consequences of length perturbation that was equivalent to the historically represented C-process shown in (1).

Here we do not assume first-order kinetics. Instead, we consider $\text{PDF}_{t_{\text{att}}}(t)$ to be represented by a gamma distribution, which is used to describe random variables that represent a time period made up of the sum of several smaller time periods [26, 27]

$$\text{PDF}_{t_{\text{att}}}(t) = \frac{1}{\beta \Gamma(p)} \left(\frac{t}{\beta} \right)^{p-1} e^{-t/\beta}, \quad (12)$$

where p = a shape parameter reflecting the number of smaller time periods summed together to produce total time attached, t_{att} , β = a scale parameter reflecting the average duration of the smaller time periods. The mean t_{att} is calculated as $p\beta$, and $\Gamma(p)$ = the gamma function evaluated at p , a normalization factor.

The two parameters p and β are sufficient to provide a gamma distribution description of $\text{PDF}_{t_{\text{att}}}(t)$. The case of $p = 1$ is a special case that is equivalent to a single exponential function with mean β . Several examples of gamma distributions, including a case of $p = 1$, are illustrated in Figures 2(a) and 2(b), which demonstrate the effectiveness of the gamma distribution representation in accommodating a wide variety of probability density functions for t_{att} . Upon applying (10a), we attain the associated survival function $S_{\tau}(t)$:

$$S_{\tau}(t) = \frac{\Gamma(p, t/\beta)}{\Gamma(p)}, \quad (13a)$$

where $\Gamma(p, t/\beta)$ = the upper incomplete gamma function [26]. Example survival functions are illustrated in Figures 2(c) and 2(d) and correspond to the $\text{PDF}_{t_{\text{att}}}(t)$ examples in Figures 2(a) and 2(b). The integral of $S_{\tau}(t)$ over the abscissa, which is useful for normalization, is

$$\int_0^{\infty} S_{\tau}(t) dt = p\beta. \quad (13b)$$

Upon applying (13a) and (13b) to (11) we have

$$\text{PDF}_{\tau}(t) = \frac{\Gamma(p, t/\beta)}{p\beta\Gamma(p)}. \quad (14)$$

We can now state that the complex modulus that would arise from an ensemble of myosin crossbridges, whose distribution of t_{att} can be represented by a gamma distribution presented in (12), is given by the insertion of $\text{PDF}_{\tau}(t)$ of (14) into the expression for the mechanical transfer function of

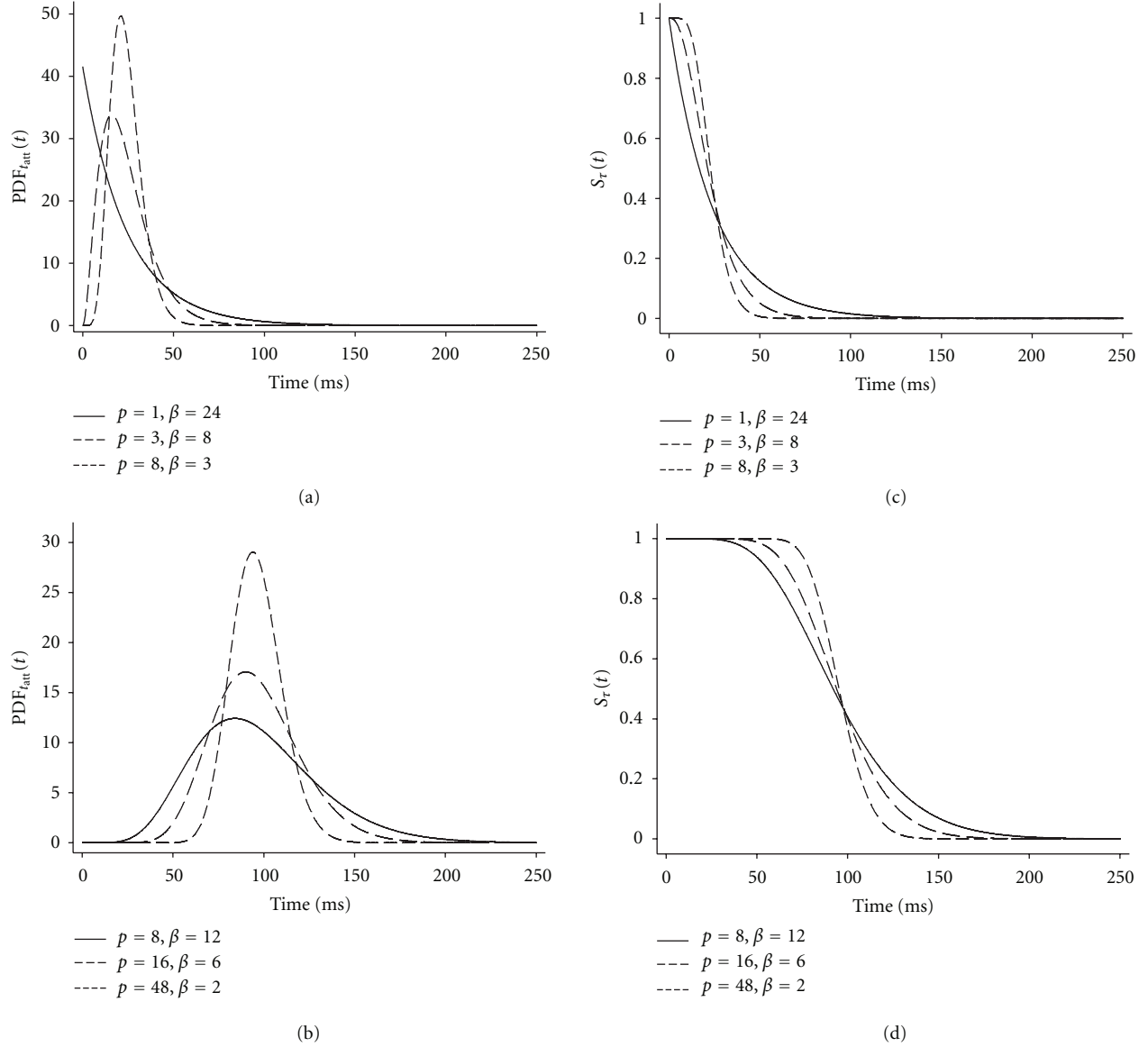


FIGURE 2: Examples of gamma distributions and associated survival functions. (a, b) The two parameters of the gamma distribution (p and β) permit description of a wide variety of distributions useful for representing the probability density function for myosin crossbridge attachment time, $\text{PDF}_{\text{att}}(t)$. Notably, a single exponential results when $p = 1$ (a), and a Gaussian distribution is approximated as p increases. (c, d) The survival function, $S_r(t)$, refers to the probability that an attached crossbridge will survive to time t . The analytical relationship between the $\text{PDF}_{\text{att}}(t)$ and $S_r(t)$ is provided by (10a) and (10b).

(9). Details of the evaluation of the integral in (9) after such a substitution are provided in the Appendix. The result is

$$\frac{\tilde{F}_{\text{hs}}(\omega)}{\tilde{L}_{\text{hs}}(\omega)} = \xi \left\{ 1 - \frac{1}{p i \omega \beta} \left(\frac{(i \omega \beta + 1)^p - 1}{(i \omega \beta + 1)^p} \right) \right\}, \quad (15)$$

where $\xi = N(\bar{t}_{\text{att}}/\bar{t}_{\text{cycle}})\bar{k}_{\text{stiff}}$.

Equation (15) describes the predicted complex modulus that would arise from length perturbation analysis of an ensemble of myosin crossbridges whose distribution of attachment times is represented by a gamma distribution. From a measured viscoelastic complex modulus represented

on the left-hand side of (15) we could use nonlinear least-squares methods to estimate the values of the three independent parameters ξ , p , and β , on the right-hand side of (15).

3. Methods

3.1. Computer Simulations. The force response of a virtual half sarcomere was simulated for a time period of two seconds for many (20,000) independent myosin heads alternately attaching and detaching to actin according to independent stochastic processes governing the random variables t_{att} and t_{det} . For any one computer simulation, random numbers representing t_{att} were generated to conform

with a gamma distribution with values for p ranging from 1 to 48 and for β ranging from 2 to 24 such that the mean time attached was either 24 ms or 96 ms. Random numbers representing t_{det} were generated with values for $p = 2$ and $\beta = 48$ ms such that the mean time detached was always 96 ms. Figure 3(a) illustrates the PDF $_{t_{\text{att}}}(t)$ when $p = 3$ and $\beta = 8$. Each random number generated from this PDF $_{t_{\text{att}}}(t)$ was used to dictate the time period over which a virtual crossbridge was attached for each occasion, as indicated in Figure 3(b). Figure 3(c) illustrates the PDF for t_{det} , PDF $_{t_{\text{det}}}(t)$, with $p = 2$ and $\beta = 48$. Each random number generated from this PDF $_{t_{\text{det}}}(t)$ was used to dictate the time over which a virtual crossbridge was detached for each occasion. Figure 3(b) illustrates an example of successive attachment and detachment time periods.

Sinusoidal length perturbations of the virtual half sarcomere were simulated as having amplitude 1 nm and frequencies over the range 1–250 Hz. Figure 3(d) illustrates an example perturbation at 1 Hz over a one-second time interval. Each crossbridge was assigned a stiffness constant of 1 pN/nm [28]. The change in length of the crossbridge relative to the time of initial attachment was multiplied by the stiffness constant to simulate the force resulting from the strain on the elastic element of the crossbridge. Figure 3(e) illustrates an example series of successive attachments and detachments over one second. Figure 3(f) illustrates the force deflection that would occur for a crossbridge during each time of attachment. The resulting force deflections of 20,000, independent crossbridges were summed to provide an equivalent two-second period for the ensemble in the virtual half sarcomere. An example of the resultant force from 20,000 crossbridges is given in Figure 3(g). This simulated force of the half sarcomere, $F_{\text{hs}}(t)$, was fit using a simplex method to a sine function, whose amplitude (Amp) and phase (ϕ) permitted the calculation of two components that were in phase and out of phase with respect to the length perturbation. The value of each moduli was then calculated from the amplitude and phase as elastic modulus = Amp cos(ϕ) and viscous modulus = Amp sin(ϕ). The smooth line in Figure 3(g) presents an example fit of a sine function to the resultant force, and Figure 3(h) presents the in-phase and out-of-phase components provided by the Simplex method. The resulting elastic and viscous moduli, given in units of pN/nm due to the lack of normalization factors used in the simulation, were fit simultaneously to (15) using a nonweighted Levenberg-Marquardt nonlinear least-squares routine. The diagonal of the resulting covariance matrix indicated the variances of parameter estimates. The square root of the variance thus provided the standard error for each parameter estimate, which was then multiplied 1.96 to provide the 95% confidence range. All computer simulations, random number generation, curve-fittings, and parameter estimation routines were performed using IDL Version 7.0 (ITT, Boulder, CO).

3.2. Solutions. All reagents were purchased from Sigma (St. Louis, Mo). Solutions were formulated by solving equations describing ionic equilibria [29]. Concentrations are expressed in mmol/L unless otherwise noted. Relaxing solu-

tion: pCa 8.0, 5.0 ethylene glycol-tetra-acetic acid (EGTA), 5.0 ATP, 1.0 Mg $^{2+}$, 20 hydroxyethyl-aminoethanesulfonic acid (BES), 35 phosphocreatine, 300 U/mL creatine kinase, ionic strength 200, pH 7.0. Activating solution: same as relaxing solution with pCa 4.0. Rigor solution: same as activating without added ATP, creatine kinase, or phosphocreatine. Storage solution: same as relaxing with 10 $\mu\text{g/mL}$ leupeptin and 50% wt/vol glycerol. Skinning solution: same as storage with 30 mM 2,3-butanedione monoxime (BDM) and 1% wt/vol Triton X-100.

3.3. Viscoelastic Mechanics. All procedures were reviewed and approved by the Institutional Animal Care and Use Committees of The University of Vermont. Male wild-type mice were fed either a normal mouse diet (WT) or an iodine deficient, 0.15% 6-N-propyl-2-thiouracil (PTU) diet for at least nine weeks prior to their being killed by rapid cervical dislocation. The PTU mice therefore became hypothyroid resulting in the expression of β -MyHC in the myocardium in contrast to the α -MyHC expressed in the WT mouse heart.

Mouse left ventricular skinned myocardial strips were prepared using methods similar to those described previously to yield thin strips ($\sim 140 \mu\text{m}$ diameter, $\sim 800 \mu\text{m}$ length) with longitudinally oriented parallel fibers [7]. These strips were chemically skinned for 2 hr at 22°C and stored at -20°C for no more than 5 days. At the time of study, aluminum T-clips were attached to the ends of a strip $\sim 150 \mu\text{m}$ apart. The strip was mounted between a piezoelectric motor (Physik Instrumente, Auburn, MA) and a strain gauge (SensoNor, Horten, Norway), lowered into a 30 μL droplet of relaxing solution maintained at 37°C and incrementally stretched to and maintained at 2.2 μm sarcomere length detected by videography and digital Fourier transform techniques (IonOptix, Milton, MA).

Strips were calcium activated at pCa 4.5 and subjected to decreasing concentrations of 5, 2, and 1 mM MgATP by exchanging equal volumes of rigor solution. Sinusoidal perturbations of amplitude 0.125% strip length were applied over the frequency range 0.125–250 Hz. The elastic and viscous moduli were calculated from the recorded tension transient as the relative magnitudes of the in-phase and out-of-phase components with respect to the imposed sinusoidal length perturbations [13, 20, 30]. The measured complex modulus was fit to (1), representing the single exponential distribution model of t_{att} , and to (16) below, representing the gamma distribution model of t_{att} , using a non weighted Levenburg-Marquardt non linear least-squares routine running within IDL Version 7.0 (ITT, Boulder, CO)

$$Y(\omega) = A(i\omega)^k - B\left(\frac{i\omega}{2\pi b + i\omega}\right) + \xi \left\{ 1 - \frac{1}{p i \omega \beta} \left(\frac{(i\omega\beta + 1)^p - 1}{(i\omega\beta + 1)^p} \right) \right\}. \quad (16)$$

Mean myosin time attached was calculated as $(2\pi c)^{-1}$ when the fit was performed with (1) and as $p\beta$ for fits using (16). The correlation coefficients between the recorded data and the fitted models were calculated as a Pearson

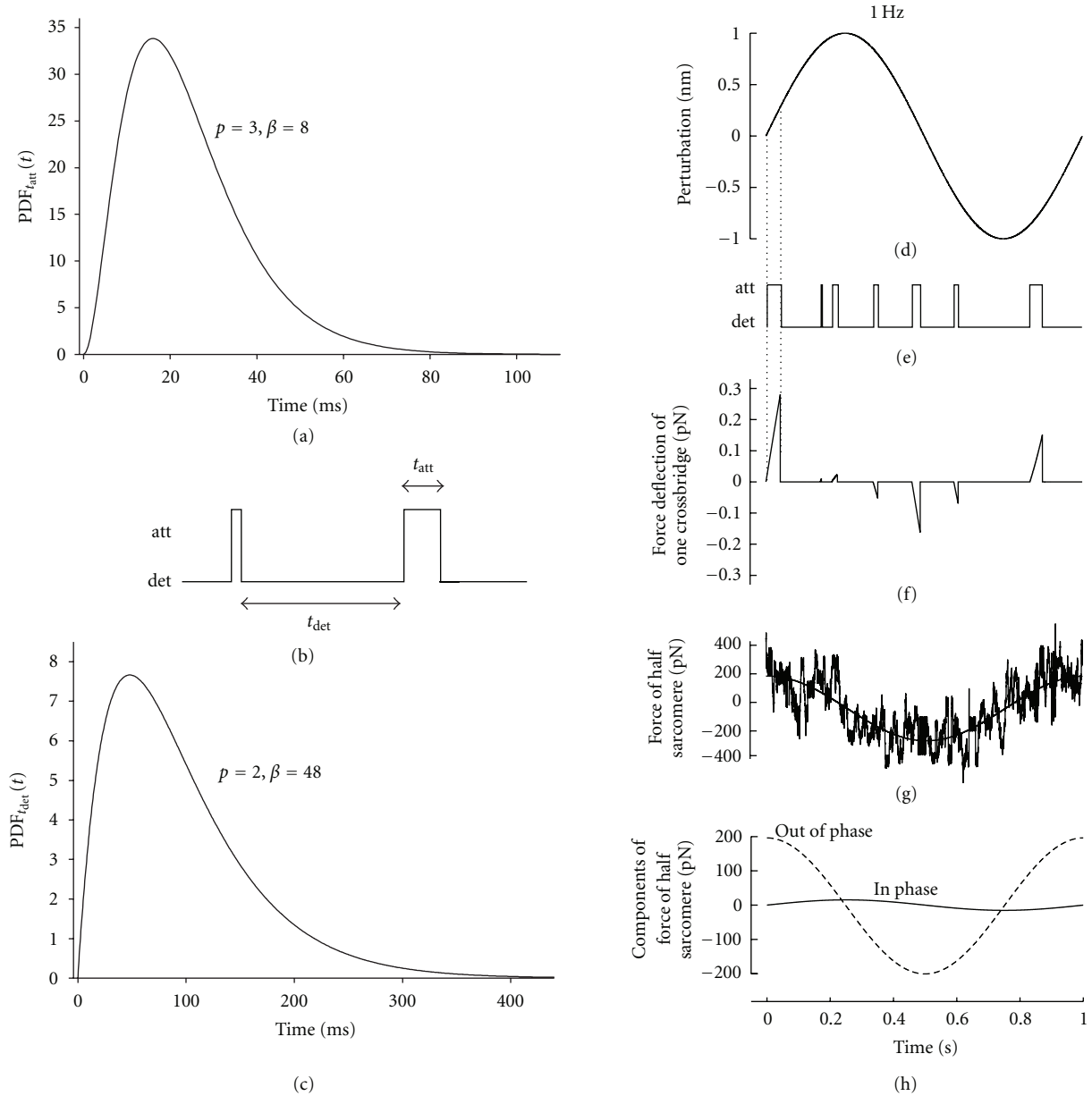


FIGURE 3: Schematic representation of computer-generated elastic and viscous moduli. (a)–(c) Random numbers generated from various $PDF_{att}(t)$ (one example shown in (a)) were used to dictate the attachment times, t_{att} , of a virtual crossbridge. (b) shows an example attachment and detachment sequence. (c) illustrates the $PDF_{t_{det}}(t)$, with $p = 2$ and $\beta = 48$, used to dictate the intermittent times of detachment. (d) A sinusoidal length perturbation with amplitude 1 nm was used to simulate an externally applied length perturbation. This example is at 1 Hz. (e) An example series of successive crossbridge attachments and detachments would be subject to the length perturbation. (f) The length change that occurs during the time of attachment results in a force deflection. (g) The sum of these force deflections from 20,000 crossbridges is then fit to a sinusoid (solid smooth line). (h) The magnitude of the component of the fitted sinusoid in phase with the length perturbation represents the elastic modulus at this frequency, the magnitude of the component out of phase represents the viscous modulus.

correlation coefficient. The two models used to calculate the mean myosin time attached were compared using linear correlation. Data points are presented as mean \pm sem.

4. Results

4.1. Computer Simulations. The computer simulations presented here served two purposes: first, to demonstrate the

accuracy of the analytical derivation resulting in (15) and second, to demonstrate that estimating the parameters of (15) by the nonlinear least-squares methods provided reasonable estimates of the parameters known *a priori* to underlie the computer generated elastic and viscous moduli.

Figures 4(a) and 4(b) illustrate example elastic and viscous moduli, which resulted from three separate computer simulations using the parameter pairs $p = 1$ and $\beta = 24$, $p = 8$

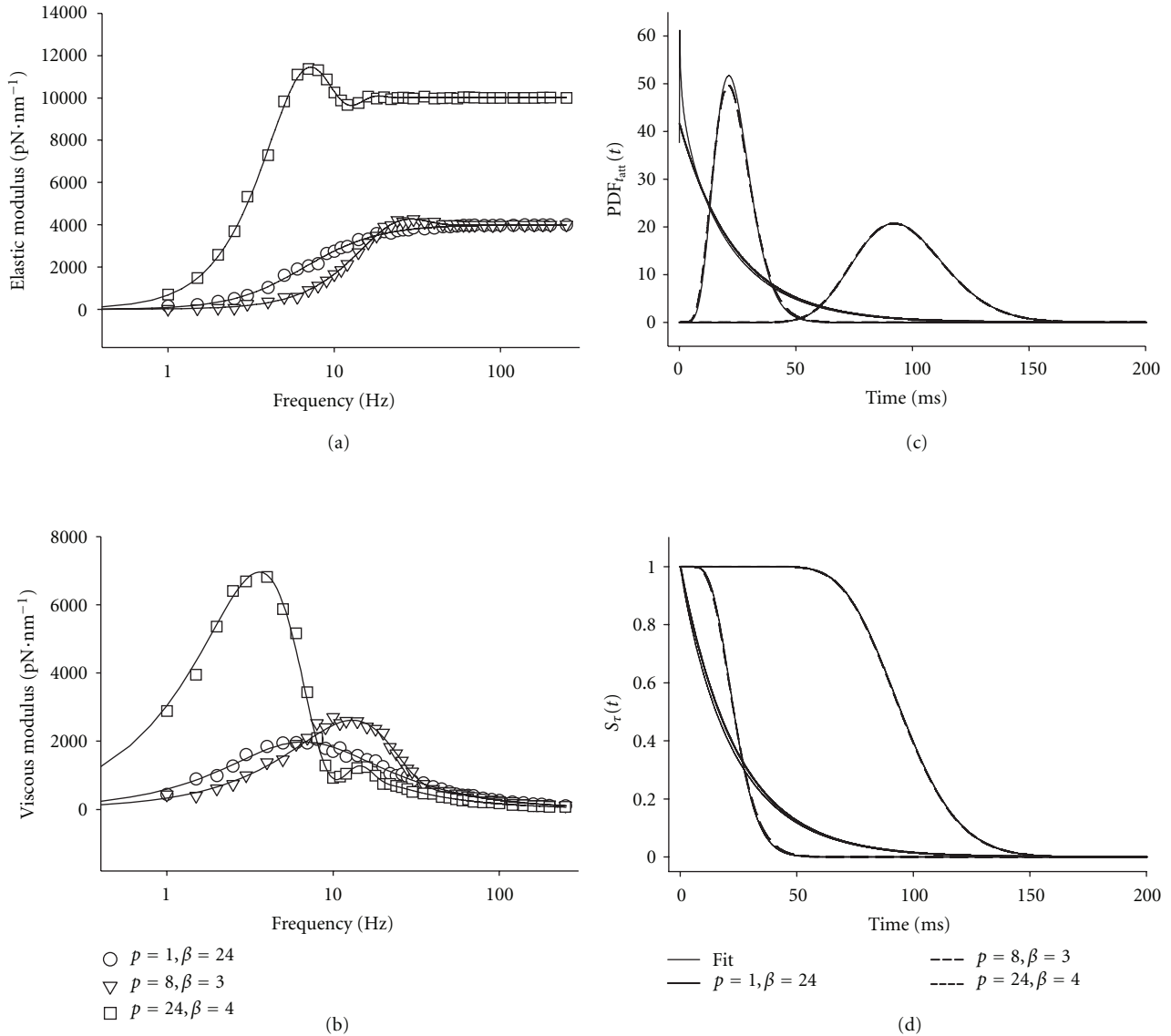


FIGURE 4: Examples of results from computer simulations. (a, b) The elastic and viscous moduli are plotted against frequency for three p and β pairs. Nonlinear least-squares fitting of (15) to the data produced a good fit shown as the line for each pair of p and β . (c) The parameters estimated from fitting (15) to the simulated data provided a comparison between the $PDF_{t_{att}}(t)$ used to generate the data and the gamma distribution predicted from the fits. In this case, the predicted gamma distributions are nearly indistinguishable from the original $PDF_{t_{att}}(t)$. (d) The survival function, $S_r(t)$, was also predicted from the parameter estimates and again very closely resembles the original $S_r(t)$.

and $\beta = 3$, and $p = 24$ and $\beta = 4$. The thin solid line represents the best fit of (15) to the simulated data. It is interesting to note that the first example, $p = 1$ and $\beta = 24$, represents the results from a single exponential model of $PDF_{t_{att}}(t)$. The elastic modulus monotonically rises to a maximum, and the viscous modulus monotonically rises to a max at 6.6 Hz and then monotonically falls. It is important to note that the shape of the viscous modulus when $p = 1$ is symmetrical about the peak when shown on the log-scaled axis. The other examples with $p > 1$ shown in Figures 4(a) and 4(b) do not demonstrate similarly smooth monotonic behavior. The elastic and viscous moduli instead show fluctuations, which result from the narrower distributions of t_{att} when $p > 1$

compared to the single exponential distribution. Also, the viscous modulus is no longer symmetrical about its peak.

Table 1 provides a comparison of parameter values used to generate the simulations and the parameter estimates calculated by the nonlinear least-squares routine fitting (15). For the three fitted parameters p , β , and ξ , the 95% confidence intervals for the parameter estimates were narrow compared to the magnitude of the values. These confidence intervals demonstrate the high precision and uniqueness of the parameter estimates. In addition, the correlation coefficients between values used and values estimated were consistently greater than 0.997. Based on the narrow confidence intervals for parameter estimates and the high correlation

TABLE 1: Parameter values used to generate random numbers in computer simulations of a force response due to myosin crossbridges subjected to sinusoidal length perturbations, and estimated parameter values from that force response fit to (15). For all simulations $\bar{t}_{\text{det}} = 96 \text{ ms}$, $N = 20,000$ and $k_{\text{stiff}} = 1 \text{ pN/nm}$. Est[] = estimated value of bracketed parameter, () indicates the $\pm 95\%$ confidence intervals for estimated value. The correlation between actual and estimated values resulted in a correlation coefficient greater than 0.997 for each parameter.

Sim number	p	β (ms)	\bar{t}_{att} (ms)	ξ (pN/nm)	Est[p]	Est[β] (ms)	Est[\bar{t}_{att}] (ms)	Est[ξ] (pN/nm)
(1)	1	24	24	4000	0.91 (0.01)	25.13 (0.06)	22.89	4005.0 (0.5)
(2)	2	12	24	4000	2.01 (0.01)	11.98 (0.03)	24.09	4019.8 (0.4)
(3)	3	8	24	4000	3.22 (0.01)	7.48 (0.02)	24.08	3981.2 (0.4)
(4)	6	4	24	4000	6.11 (0.02)	3.89 (0.01)	23.79	3986.4 (0.4)
(5)	8	3	24	4000	8.70 (0.03)	2.75 (0.01)	23.95	3997.4 (0.4)
(6)	4	24	96	10000	3.99 (0.01)	24.03 (0.03)	95.88	10007.0 (0.3)
(7)	8	12	96	10000	6.83 (0.01)	13.93 (0.02)	95.12	10003.8 (0.3)
(8)	12	8	96	10000	12.00 (0.02)	7.98 (0.01)	95.71	10012.8 (0.3)
(9)	16	6	96	10000	16.04 (0.03)	6.05 (0.01)	97.03	10022.6 (0.3)
(10)	24	4	96	10000	24.10 (0.06)	3.99 (0.01)	96.07	10017.2 (0.3)
(11)	48	2	96	10000	49.61 (0.15)	1.92 (0.01)	95.13	10004.0 (0.3)

Note: $\xi = N(\bar{t}_{\text{att}}/\bar{t}_{\text{cycle}})\bar{k}_{\text{stiff}}$.

between parameter estimates and actual parameter values, we are confident that the analytical expression provided by (15) accurately represents the mechanical consequences of temporarily attached myosin crossbridges, whose times of attachment are gamma distributed.

For the three examples given in Figures 4(a) and 4(b), the estimated parameter values were used to calculate the $\text{PDF}_{f_{\text{att}}}(t)$ and $S_{\tau}(t)$ using (12) and (13a), respectively. Figure 4(c) illustrates a comparison between the $\text{PDF}_{f_{\text{att}}}(t)$ used to generate the simulation and that calculated from the parameter estimates. Figure 4(d) provides a similar comparison for $S(\tau)$. For both $\text{PDF}_{f_{\text{att}}}(t)$ and $S_{\tau}(t)$, the estimated parameters reasonably reproduced the original functions used to generate the simulations. These comparisons illustrate the robustness with which parameters of the gamma distribution can be estimated using the nonlinear least-squares methods, which fit (15) to the elastic and viscous moduli.

4.2. Viscoelastic Mechanics. Muscle strips from both groups activated to a similar maximum developed tension of $20.7 \pm 1.8 \text{ mN}\cdot\text{mm}^{-2}$ for WT ($n = 6$) and $22.1 \pm 1.7 \text{ mN}\cdot\text{mm}^{-2}$ for PTU ($n = 6$). Figure 5 illustrates the elastic and viscous moduli recorded for maximally activated muscle strips isolated from WT and PTU mice, representing, respectively, the α -MyHC (Figures 5(a) and 5(b)) and β -MyHC (Figures 5(c) and 5(d)) isoforms. The myosin crossbridge kinetics in the α -MyHC are faster than those in β -MyHC and are reflected in the higher frequencies ranges for the dips and shoulders in the α -MyHC. For example, the most prominent dip and shoulder of the viscous modulus at 5 mM MgATP occur at ~ 9 and 90 Hz, respectively, in the α -MyHC and occur at lower frequencies 2 and 30 Hz in the β -MyHC. These observations are consistent with a longer-lived t_{att} in the β -MyHC compared to α -MyHC [5, 9].

As MgATP is reduced the dips and shoulders of the moduli shift to lower frequencies, as best seen in the

viscous modulus. The muscle also becomes stiffer, which is reflected in higher values of the elastic modulus, due to a greater fraction of crossbridges formed at any one time. These observations with lowering MgATP concentrations are consistent with a prolonged t_{att} due to a prolonged rigor state prior to MgATP binding to myosin and subsequent myosin detachment from actin.

4.3. Parameters of Gamma Distribution Model of t_{att} . Fits of (16) to the elastic and viscous moduli provided estimates of the gamma distribution parameters, p and β , and a calculation of mean t_{att} as the product $p\beta$. At 5 mM MgATP the shape parameter p was lower in the α -MyHC compared to β -MyHC (Figure 6(a)). At lower MgATP (1 and 2 mM), the shape parameter rises in both myosin isoforms and is not different between them. At all MgATP conditions and in both isoforms, the estimate for p was consistently near or greater than 2. This finding suggests that a single exponential distribution, which would have been represented by the gamma distribution with $p = 1$, did not fit the data as well as a gamma distribution with $p > 2$. Our finding $p > 2$ suggests two or more intermediate time periods within t_{att} . These results imply that the $\text{PDF}_{f_{\text{att}}}(t)$ reflected in the recorded elastic and viscous moduli is better represented by a distribution that describes multiple time intervals within t_{att} . In the strictest interpretation of the gamma distribution shape parameter, the rise in p with decreasing MgATP implies additional elemental time periods summed together to produce the total t_{att} . We would, however, caution that p approaching 10 as MgATP is lowered may be more reflective of an increasing t_{att} and not suggestive of additional biochemical states, as the lower MgATP would prolong only one biochemical state, the rigor state [4].

The parameter β effectively represents the duration of the intermediate time period that is summed p times to make up the total t_{att} . As illustrated in Figure 6(b), parameter β was found to be on the order of 1.5–2 ms for both α -MyHC and

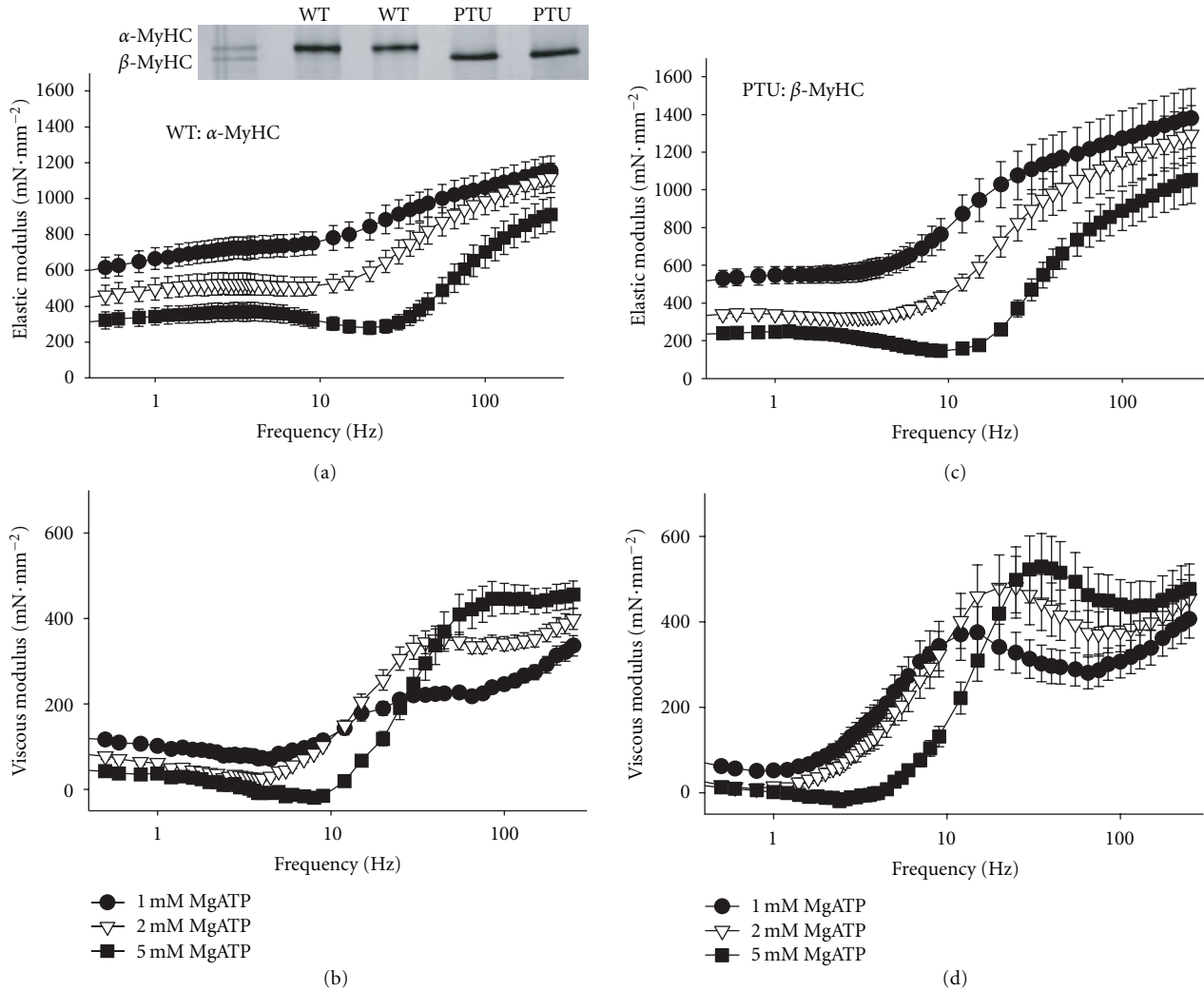


FIGURE 5: Example elastic and viscous moduli from mouse cardiac muscle strips. (a, b) The elastic and viscous moduli recorded at frequencies ranging 0.125–250 Hz for wild-type mouse cardiac muscle expressing α -MyHC at maximum calcium activation and 37°C. The frequency characteristics of the dips and shoulders are reflective of the underlying enzymatic activity and shift to lower frequencies as MgATP is reduced from 5 to 1 mM. (c, d) The elastic and viscous moduli recorded again for PTU-fed mouse cardiac muscle expressing β -MyHC. Frequency characteristics appear at lower frequencies compared to α -MyHC. Again, characteristics shift to lower frequencies as MgATP is reduced.

β -MyHC, except at 5 mM MgATP where β was 3.5 ms in the β -MyHC. We expected this parameter to have increased with decreasing MgATP, as lowering MgATP prolongs the rigor state. This parameter, however, was not as sensitive as p in describing the prolongation of t_{att} with decreasing MgATP.

Fluctuations and asymmetries in the elastic and viscous moduli, which are characteristic of the gamma distribution for $\text{PDF}_{t_{\text{att}}}(t)$, may not be easily seen in the averaged values for the moduli presented in Figure 5. To better demonstrate these fluctuations, an example pair of elastic and viscous moduli recorded from one β -MyHC muscle preparation at 1 mM MgATP is presented in Figures 6(c) and 6(d). The A- and B-processes have also been subtracted from the measured elastic and viscous moduli resulting in the C-process, which reflects the viscoelastic mechanics modeled here. The dotted lines shown in Figures 6(c) and 6(d)

represent the expected C-process when $p = 1$, the single exponential distribution. The recorded C-process, however, demonstrates fluctuations in the elastic modulus and an asymmetry in the viscous modulus different from the $p = 1$ case and consistent with the fluctuations and asymmetries for $p > 1$ illustrated in Figure 4.

The mean t_{att} was prolonged in the β -MyHC compared to α -MyHC at each MgATP examined and was also prolonged as MgATP was reduced (Figure 7(a)). These findings are consistent with known consequences of myosin isoform and MgATP availability [5, 9, 16]. The calculation of the mean t_{att} based on the gamma distributed t_{att} was generally higher than that calculated based on the exponential distributed t_{att} , showing that the shape of the $\text{PDF}_{t_{\text{att}}}(t)$ affects the calculated value of mean t_{att} . Notably, the correlation between t_{att} based on the gamma distribution and that based on the exponential

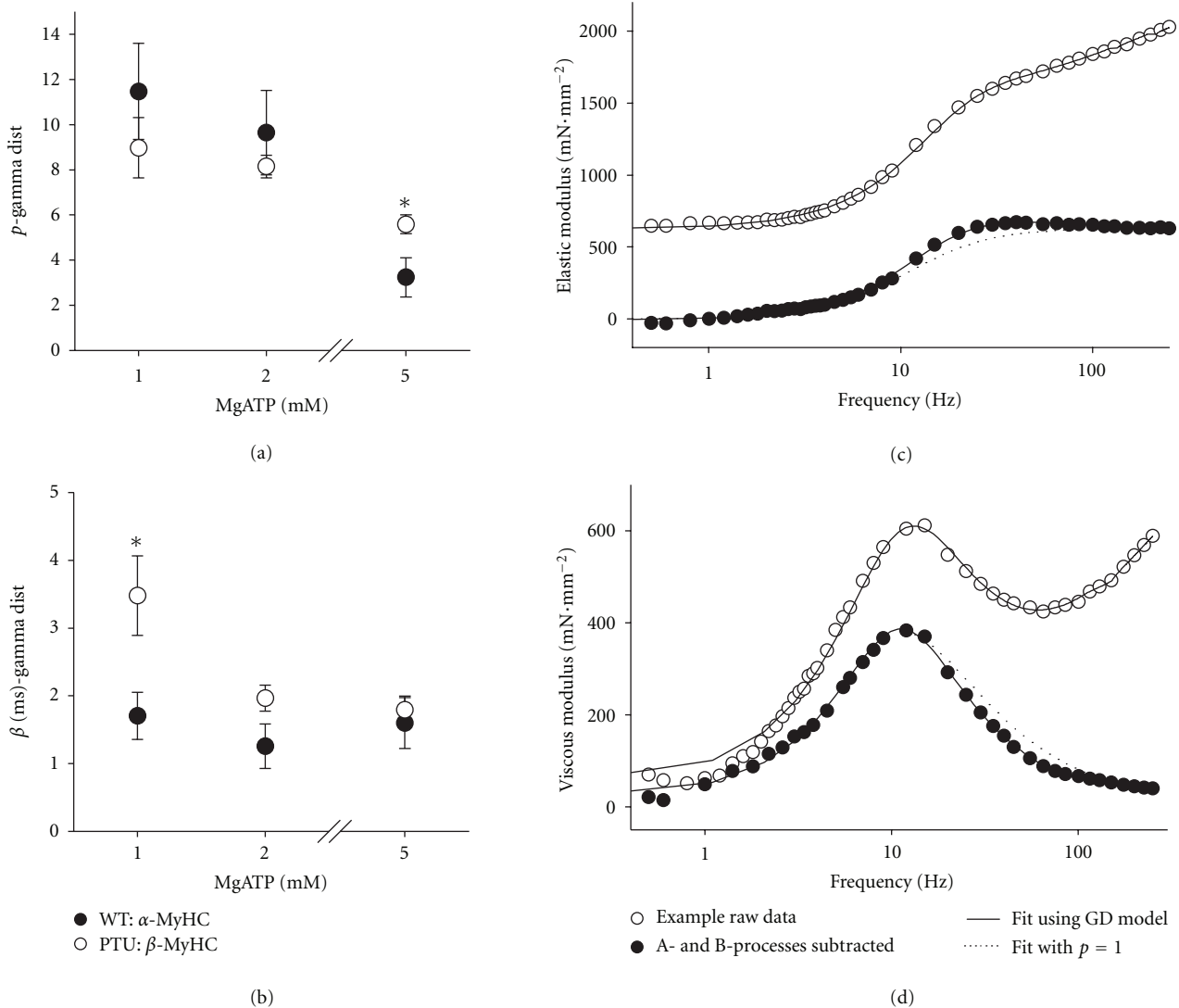


FIGURE 6: Results of fitting elastic and viscous modulus to gamma distributed and single exponential distributed models of $PDF_{t_{att}}(t)$. (a, b) The shape parameter, p , and the scale parameter, β , were estimated from fitting the gamma distribution model of (16) to the measured elastic and viscous moduli. * $P < 0.05$ by t -test between MyHC isoforms at same MgATP. (c) The elastic modulus recorded from one PTU β -MyHC muscle preparation at 1 mM MgATP is shown with its fit to (16), that is, the gamma distribution (GD) model. The goodness of fit is representative of the fits for all samples in this study. The A- and B-processes of (16) were then subtracted from the recorded elastic modulus to demonstrate fluctuations in the remaining C-process, which are more apparent when compared against the single exponential model ($p = 1$) of the t_{att} distribution (dotted line). These fluctuations are mechanical consequences of the gamma distributed t_{att} . (d) The corresponding viscous modulus was also subjected to fit and subtraction of A- and B-processes. The resulting C-process is compared against the single exponential model of the t_{att} distribution (dotted line). The asymmetry in the peak of the viscous modulus is subtle, but apparent at frequencies higher than 11 Hz.

distribution model was very strong, $r^2 = 0.932$ (Figure 7(b)), which indicates that both methods are capable of making comparisons of t_{att} among multiple groups or conditions. The Pearson correlation coefficient between the recorded data and the fitted models was very high, but was higher in the gamma distribution model ($r^2 = 0.986 \pm 0.002$) compared to single exponential model ($r^2 = 0.980 \pm 0.002$). We would expect the estimate of mean t_{att} based on the gamma distribution to be somewhat more accurate than those based on the single exponential distribution. Unfortunately, at this

time and without some other independent method to verify the actual mean t_{att} in the muscle strip, we cannot say with certainty what bias is introduced into our estimate of t_{att} using either model.

The parameter estimates resulting from the fits to (16) were used to predict the distributions of t_{att} , that is, $PDF_{t_{att}}(t)$, for each MyHC isoform and at each MgATP condition examined (Figure 8). The distributions for the α -MyHC (Figure 8(a)) appear at shorter time periods compared to those of β -MyHC (Figure 8(b)). The distributions in both

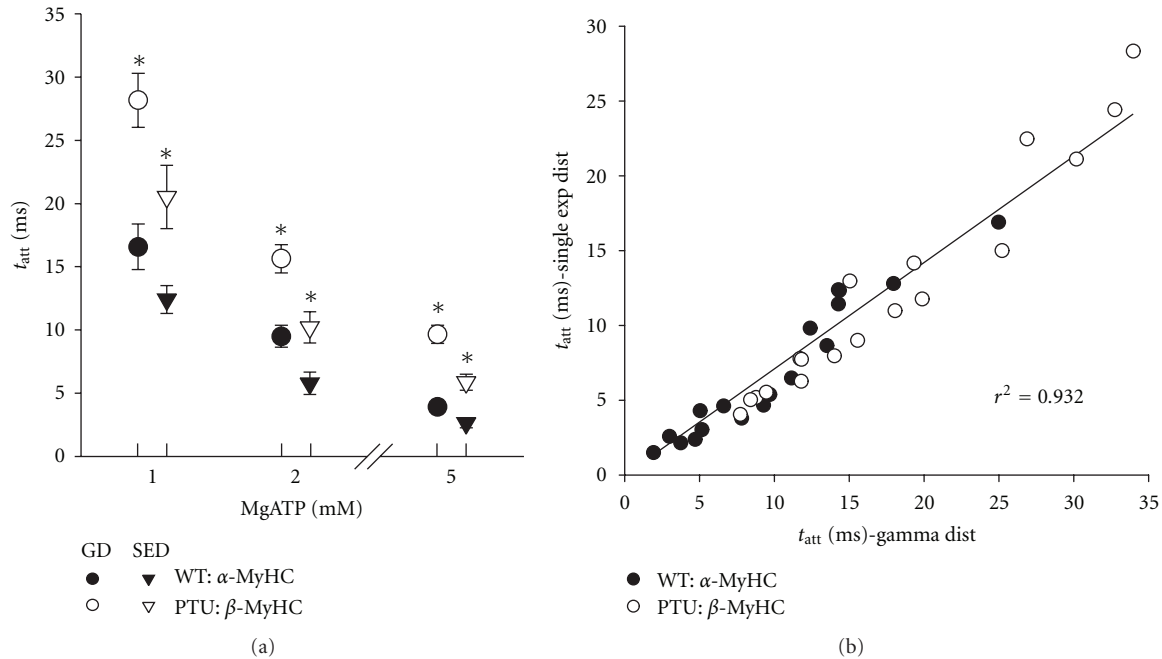


FIGURE 7: Mean time of crossbridge attachment. (a) The mean time of crossbridge attachment using both models of $PDF_{f_{att}}(t)$ demonstrated a longer t_{att} for β -MyHC and a prolongation in t_{att} as MgATP was reduced. The two models agreed qualitatively in these respects, but did not agree quantitatively as estimates using the gamma distribution (GD) model were $\sim 40\%$ higher than those using the single exponential distribution model (SED). (b) Values for t_{att} using the two models correlated strongly. Despite the relative differences in the estimates of t_{att} , either model produces similar results for comparing the effects of isoform and MgATP. * $P < 0.05$ by t -test between MyHC isoforms at same MgATP.

isoforms shift to longer time periods as MgATP is reduced. According to results from optical trapping [2, 4], in both isoforms inorganic phosphate P_i is released either prior to force production or very quickly after force production. Thus we depict P_i release in Figures 8(c)–8(f) to occur quickly. At saturating MgATP concentrations (i.e., 5 mM), the rigor state would be very short and the longest-lived state and the most significant contributor to the total t_{att} would be the ADP state (Figures 8(c) and 8(e)). Because lowering MgATP concentration would lengthen only the rigor state (Figures 8(d) and 8(f)), the mean t_{att} in both isoforms would have been prolonged due to longer rigor states. Particularly in the cases of lower MgATP, the value for t_{att} would be made up of the sum of multiple times periods, as indicated by the increased shape parameter, and the distribution of t_{att} is better represented by the gamma distribution.

5. Discussion

It is generally understood that force recorded in response to a length perturbation reflects (i) the number of myosin crossbridges bound to actin in a force-generating postpower stroke confirmation and (ii) a viscoelastic response that is the consequence of the length perturbation having been applied to temporarily formed crossbridges. The viscoelastic response, however, is often overlooked as a significant component of the dynamic force response. By frequency domain

analysis, however, it is clear that the viscoelastic response is substantial in magnitude, and the frequency characteristics of the viscoelastic response emerge as a consequence of cross-bridge kinetics [14, 16, 19]. The macroscopic measurements of viscoelastic mechanics in striated muscle combined with the modeling results presented in this paper can be used to estimate the microscopic temporal parameters reflecting myosin crossbridge kinetics, specifically the distribution of myosin attachment times (t_{att}) in a muscle fiber.

Our current modeling culminated in a specific mathematical representation of the mechanical transfer function that would arise from intermittently attached myosin crossbridges, (9). This representation was also provided previously [19], but without significant discussion regarding the normalized survival function, that is, the $PDF_{\tau}(t)$ term, in the integrand. We have provided here an explanation of the survival function, which underlies $PDF_{\tau}(t)$ and its relationship with the distribution of t_{att} , namely, $PDF_{f_{att}}(t)$ ((10a) and (10b)). Using the survival function and its relationship to the distribution of t_{att} was a very important step in demonstrating how the macroscopic viscoelastic mechanics emerge from molecular phenomena.

The gamma distribution model provided a more generalized representation of the many possible distributions of t_{att} and in so doing provided an opportunity to discern the more subtle consequences of the t_{att} distribution. The shape parameter in particular permits this more generalized description of the t_{att} distribution. The effect of the shape

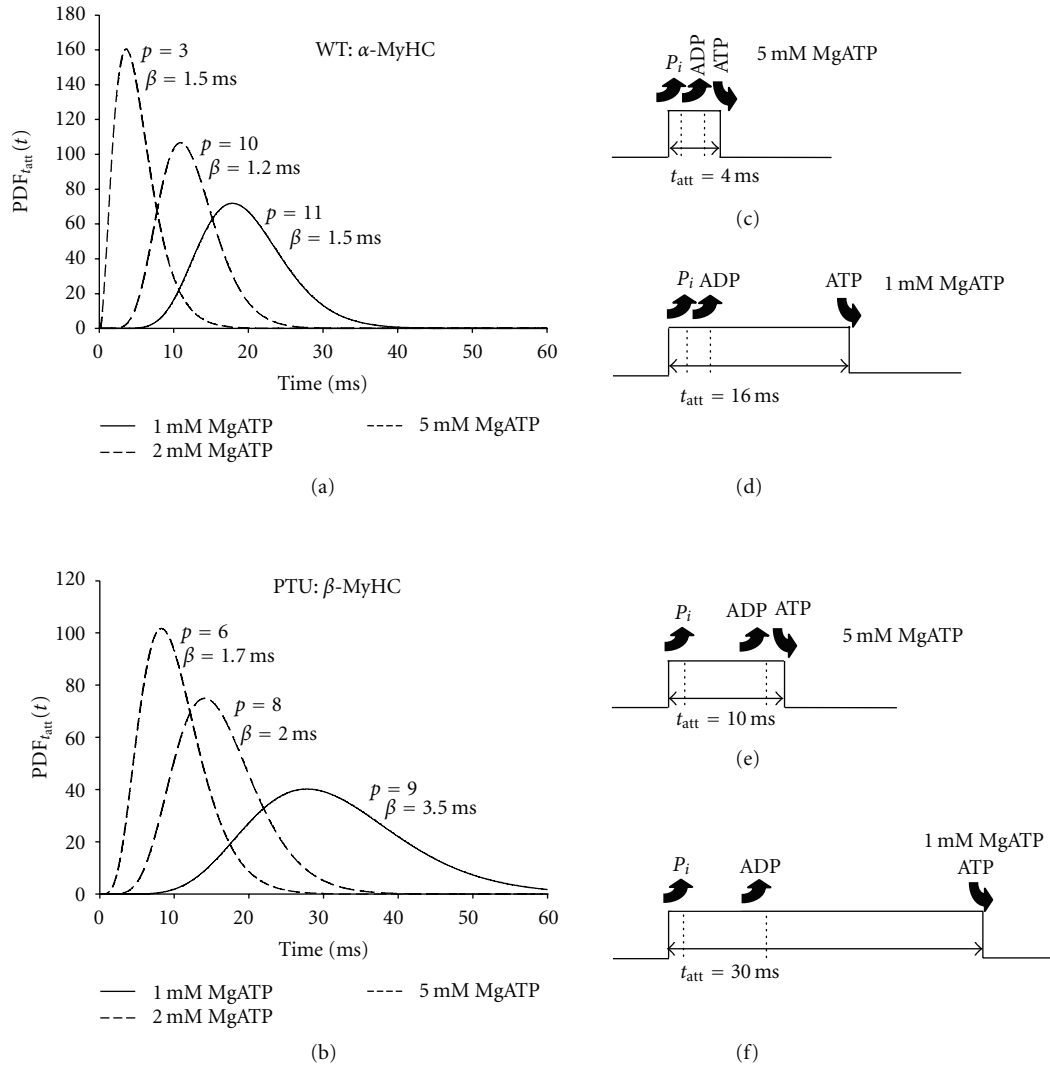


FIGURE 8: Predicted gamma distributed $PDF_{f_{att}}(t)$ for the two myosin isoforms under varying MgATP conditions at 37°C. (a) The parameter values estimated for the α -MyHC demonstrate an increasing shape parameter and prolonged t_{att} as MgATP was reduced. The resulting $PDF_{f_{att}}(t)$ looks more Gaussian in shape rather than exponential as MgATP was reduced. This would be consistent with a longer rigor state prior to MgATP binding and detachment of the myosin crossbridge. (b) The distributions for β -MyHC represent longer t_{att} compared to α -MyHC. Again, a longer rigor state would arise with lower MgATP. (c, d) In the α -MyHC at 5 mM MgATP, the release of P_i , release of ADP, and binding of ATP occur in relatively quick succession. The time periods that represent the P_i and ADP states, however, would not be affected by MgATP availability. With the reduction in MgATP concentration, the rigor state would be prolonged as detected in the viscoelastic mechanics. (e, f). In the β -MyHC, the ADP state is longer than that in the α -MyHC and the rigor state is more dramatically prolonged with decreasing MgATP compared to α -MyHC.

parameter, which was always estimated to be near or greater than 2, indicates that the distributions of t_{att} that underlie that recorded elastic and viscous moduli in both isoforms and under various MgATP conditions were distinct from the single exponential distribution and with lower MgATP begin to resemble Gaussian distributions. The increasing shape parameter with decreasing MgATP is consistent with the prolongation of the rigor state of the myosin crossbridge. We interpret these results for p and β to indicate that the crossbridge t_{att} is best represented by two or more intermediate time periods, but we caution that a p approaching a value of 10 may simply reflect a longer t_{att} and not additional biochemical states. The production of additional models

stipulating only 2- or 3-specific states may be warranted. Such a model may be useful in detecting which biochemical state of the crossbridge cycle is affected by an intervention such as that due to drug or posttranslational modification. We are aware, however, that increasing the number of fitted parameters may also lead to greater covariance among the parameters and less meaningful results.

We believe that our results demonstrate a benefit and utility of the gamma distribution model, which allows for near-zero occurrences of very short values for t_{att} , as would be expected for some cases such as low MgATP concentrations and lower temperatures. The single exponential model, on the other hand, presumes that the most

frequent values for t_{att} occur at the shortest times. Our results, particularly at lower MgATP, suggest that the single exponential model may not be sufficient to fully describe the distributions of t_{att} and the viscoelastic mechanical consequences as occurring in skinned muscle strips. It is notable, however, that while the gamma distribution model of t_{att} provides a generalized model of the mechanical consequences of the intermittent attachment of myosin to actin, we found that the single exponential model is sufficient for purposes of comparing estimated values of mean t_{att} based on the elastic and viscous moduli.

The gamma distribution model of myosin t_{att} leads to characteristics of elastic and viscous moduli that might not be obvious or intuitively predictable. Specifically, we did not expect the fluctuations and asymmetry in the elastic and viscous moduli that emerged from a gamma distributed t_{att} with $p > 1$. As the shape parameter increases and the t_{att} distribution becomes more Gaussian in shape, the fluctuations and asymmetries observed in the elastic and viscous moduli in the frequency domain became more pronounced. Only through completion of the analytical derivation and computer modeling were we able to demonstrate these particular mechanical consequences.

5.1. Limitations. Myosin kinetics are known to demonstrate dependencies on load or strain [10, 12], which were not considered in the present work. The modeling in the present work focuses on explaining only the viscoelastic mechanics at higher frequencies and specifically ignores any strain dependencies thus providing a limited model of the macroscopic mechanical consequences of myosin kinetics. A more complete model of viscoelastic mechanics would need to predict and explain the dips in the elastic and viscous moduli like those observed at the lower frequencies. The negative viscous modulus, which corresponds to mechanical energy production by the muscle preparation, may well be one particular outcome of a strain dependency on myosin kinetics. For example, the myosin time attached may be shortened during muscle lengthening at these lower frequencies, perhaps in a P_i -dependent manner [31–33], and the number of force-generating crossbridges attached during shortening versus lengthening would therefore contribute to an observation of mechanical work production.

5.2. Conclusion. The importance of experimental observations of the single myosin molecule using optical techniques cannot be overstated. Without these methods, we would not likely be able to discern the nature of muscle force production at the molecular level. Discerning the performance of myosin within the context of myofibrillar lattice structure like that found *in vivo* is also important. Mathematical and computer models of muscle performance, such as that presented in this work, are valuable in their providing the opportunity to detect a measure of myosin performance, that is, the distribution of t_{att} , within the context of *in vivo* sarcomeric structure that is not currently technologically possible by other means.

Appendix

In this appendix we provide a more detailed derivation of (15), which is the solution to (9) when $\text{PDF}_{t_{\text{att}}}(t)$ is represented by a gamma distribution. Therefore, $\text{PDF}_{\tau}(t)$ in the integrand of (9) is represented by a normalized upper incomplete gamma function shown in (14):

$$\frac{\tilde{F}_{\text{hs}}(\omega)}{\tilde{L}_{\text{hs}}(\omega)} = \left(\frac{\bar{t}_{\text{att}}}{\bar{t}_{\text{cycle}}} \right) N \bar{k}_{\text{stiff}} \left\{ \int_0^{\infty} \left(\frac{\Gamma(p, t/\beta)}{p\beta\Gamma(p)} \right) (1 - e^{-i\omega t}) dt \right\}. \quad (\text{A.1})$$

We choose to take the terms not containing t out of the integral:

$$\frac{\tilde{F}_{\text{hs}}(\omega)}{\tilde{L}_{\text{hs}}(\omega)} = N \left(\frac{\bar{t}_{\text{att}}}{\bar{t}_{\text{cycle}}} \right) \bar{k}_{\text{stiff}} \left\{ 1 - \frac{1}{p\beta\Gamma(p)} \int_0^{\infty} \Gamma\left(p, \frac{t}{\beta}\right) e^{-i\omega t} dt \right\}. \quad (\text{A.2})$$

For purposes of solving the definite integral above, we scale every occurrence of t within the integral by β as follows:

$$\begin{aligned} \frac{\tilde{F}_{\text{hs}}(\omega)}{\tilde{L}_{\text{hs}}(\omega)} &= N \left(\frac{\bar{t}_{\text{att}}}{\bar{t}_{\text{cycle}}} \right) \bar{k}_{\text{stiff}} \\ &\times \left\{ 1 - \frac{\beta}{p\beta\Gamma(p)} \int_0^{\infty} \Gamma\left(p, \frac{t}{\beta}\right) e^{-i\omega\beta(t/\beta)} d\left(\frac{t}{\beta}\right) \right\}. \end{aligned} \quad (\text{A.3})$$

The definite integral has been solved previously [34]:

$$\begin{aligned} \frac{\tilde{F}_{\text{hs}}(\omega)}{\tilde{L}_{\text{hs}}(\omega)} &= N \left(\frac{\bar{t}_{\text{att}}}{\bar{t}_{\text{cycle}}} \right) \bar{k}_{\text{stiff}} \\ &\times \left\{ 1 - \frac{\beta}{p\beta\Gamma(p)} \left[\frac{\Gamma(p)}{i\omega\beta} \left(1 - \frac{1}{(i\omega\beta + 1)^p} \right) \right] \right\}. \end{aligned} \quad (\text{A.4})$$

Upon canceling factors we get the following:

$$\frac{\tilde{F}_{\text{hs}}(\omega)}{\tilde{L}_{\text{hs}}(\omega)} = N \left(\frac{\bar{t}_{\text{att}}}{\bar{t}_{\text{cycle}}} \right) \bar{k}_{\text{stiff}} \left\{ 1 - \frac{1}{p i \omega \beta} \left(1 - \frac{1}{(i \omega \beta + 1)^p} \right) \right\}. \quad (\text{A.5})$$

We choose to write the bracketed term in the following form:

$$\frac{\tilde{F}_{\text{hs}}(\omega)}{\tilde{L}_{\text{hs}}(\omega)} = N \left(\frac{\bar{t}_{\text{att}}}{\bar{t}_{\text{cycle}}} \right) \bar{k}_{\text{stiff}} \left\{ 1 - \frac{1}{p i \omega \beta} \left(\frac{(i \omega \beta + 1)^p - 1}{(i \omega \beta + 1)^p} \right) \right\}. \quad (\text{A.6})$$

Equation (A.6) represents the predicted complex modulus that would arise from an ensemble of myosin crossbridges whose time attached is described by a gamma distribution with shape parameter p and scale parameter β .

When $p = 1$ we get the special case for the gamma distribution being equivalent to a single exponential distribution. The solution provided in (A.6) for $p = 1$ then reduces to the following.

$$\begin{aligned} \frac{\tilde{F}_{\text{hs}}(\omega)}{\tilde{L}_{\text{hs}}(\omega)} &= N \left(\frac{\bar{t}_{\text{att}}}{\bar{t}_{\text{cycle}}} \right) \bar{k}_{\text{stiff}} \left\{ \frac{i \omega \beta}{i \omega \beta + 1} \right\} \\ &= N \left(\frac{\bar{t}_{\text{att}}}{\bar{t}_{\text{cycle}}} \right) \bar{k}_{\text{stiff}} \left\{ \frac{i \omega}{i \omega + \beta^{-1}} \right\}. \end{aligned} \quad (\text{A.7})$$

The form of (A.7) is equivalent to that provided previously as a model for the C-process of sinusoidal analysis [19]. The mean time attached is represented here as β .

Acknowledgments

This paper is dedicated in honor of the authors' friend and mentor Dr. David W. Maughan. This work was supported by grants from NIH R01-HL086902 and P01-HL59408 (BMP, YW) and NIH K01-AG031303 (MSM).

References

- [1] J. T. Finer, R. M. Simmons, and J. A. Spudich, "Single myosin molecule mechanics: piconewton forces and nanometre steps," *Nature*, vol. 368, no. 6467, pp. 113–119, 1994.
- [2] J. A. Spudich, "How molecular motors work," *Nature*, vol. 372, no. 6506, pp. 515–518, 1994.
- [3] D. M. Warshaw, W. H. Guilford, Y. Freyzon et al., "The light chain binding domain of expressed smooth muscle heavy meromyosin acts as a mechanical lever," *Journal of Biological Chemistry*, vol. 275, no. 47, pp. 37167–37172, 2000.
- [4] M. J. Tyska and D. M. Warshaw, "The myosin power stroke," *Cell Motility and the Cytoskeleton*, vol. 51, no. 1, pp. 1–15, 2002.
- [5] S. Sugiura, N. Kobayakawa, H. Fujita et al., "Comparison of unitary displacements and forces between 2 cardiac myosin isoforms by the optical trap technique: molecular basis for cardiac adaptation," *Circulation Research*, vol. 82, no. 10, pp. 1029–1034, 1998.
- [6] S. Sugiura and H. Yamashita, "Functional characterization of cardiac myosin isoforms," *Japanese Journal of Physiology*, vol. 48, no. 3, pp. 173–179, 1998.
- [7] E. Blanchard, C. Seidman, J. G. Seidman, M. LeWinter, and D. Maughan, "Altered crossbridge kinetics in the α MHC^{403/+} mouse model of familial hypertrophic cardiomyopathy," *Circulation Research*, vol. 84, no. 4, pp. 475–483, 1999.
- [8] I. Morano, "Tuning the human heart molecular motors by myosin light chains," *Journal of Molecular Medicine*, vol. 77, no. 7, pp. 544–555, 1999.
- [9] N. R. Alpert, C. Brosseau, A. Federico, M. Krenz, J. Robbins, and D. M. Warshaw, "Molecular mechanics of mouse cardiac myosin isoforms," *American Journal of Physiology*, vol. 283, no. 4, pp. H1446–H1454, 2002.
- [10] C. Veigel, J. E. Molloy, S. Schmitz, and J. Kendrick-Jones, "Load-dependent kinetics of force production by smooth muscle myosin measured with optical tweezers," *Nature Cell Biology*, vol. 5, no. 11, pp. 980–986, 2003.
- [11] D. M. Swank, J. Braddock, W. Brown, H. Lesage, S. I. Bernstein, and D. W. Maughan, "An alternative domain near the ATP binding pocket of *Drosophila* myosin affects muscle fiber kinetics," *Biophysical Journal*, vol. 90, no. 7, pp. 2427–2435, 2006.
- [12] N. M. Kad, J. B. Patlak, P. M. Fagnant, K. M. Trybus, and D. M. Warshaw, "Mutation of a conserved glycine in the SH1-SH2 helix affects the load-dependent kinetics of myosin," *Biophysical Journal*, vol. 92, no. 5, pp. 1623–1631, 2007.
- [13] M. Kawai and P. W. Brandt, "Sinusoidal analysis: a high resolution method for correlating biochemical reactions with physiological processes in activated skeletal muscles of rabbit, frog and crayfish," *Journal of Muscle Research and Cell Motility*, vol. 1, no. 3, pp. 279–303, 1980.
- [14] D. Maughan, J. Moore, J. Vigoreaux, B. Barnes, and L. A. Mulieri, "Work production and work absorption in muscle strips from vertebrate cardiac and insect flight muscle fibers," *Advances in Experimental Medicine and Biology*, vol. 453, pp. 471–480, 1998.
- [15] M. Kawai and F. H. Schachat, "Differences in the transient response of fast and slow skeletal muscle fibers. Correlations between complex modulus and myosin light chains," *Biophysical Journal*, vol. 45, no. 6, pp. 1145–1151, 1984.
- [16] M. Kawai and H. R. Halvorson, "Role of MgATP and MgADP in the cross-bridge kinetics in chemically skinned rabbit psoas fibers. Study of a fast exponential process (C)," *Biophysical Journal*, vol. 55, no. 4, pp. 595–603, 1989.
- [17] B. L. Marcussen and M. Kawai, "Role of MgATP and inorganic phosphate ions in cross-bridge kinetics in insect (*Lethocerus colossicus*) flight muscle," *Progress in Clinical and Biological Research*, vol. 327, pp. 805–813, 1990.
- [18] G. Wang and M. Kawai, "Effects of MgATP and MgADP on the cross-bridge kinetics of rabbit soleus slow-twitch muscle fibers," *Biophysical Journal*, vol. 71, no. 3, pp. 1450–1461, 1996.
- [19] B. M. Palmer, T. Suzuki, Y. Wang, W. D. Barnes, M. S. Miller, and D. W. Maughan, "Two-state model of acto-myosin attachment-detachment predicts C-process of sinusoidal analysis," *Biophysical Journal*, vol. 93, no. 3, pp. 760–769, 2007.
- [20] M. Kawai, Y. Saeki, and Y. Zhao, "Crossbridge scheme and the kinetic constants of elementary steps deduced from chemically skinned papillary and trabecular muscles of the ferret," *Circulation Research*, vol. 73, no. 1, pp. 35–50, 1993.
- [21] A. F. Huxley, "Muscle structure and theories of contraction," *Progress in Biophysics and Biophysical Chemistry*, vol. 7, pp. 255–318, 1957.
- [22] M. Kawai and Y. Zhao, "Cross-bridge scheme and force per cross-bridge state in skinned rabbit psoas muscle fibers," *Biophysical Journal*, vol. 65, no. 2, pp. 638–651, 1993.
- [23] H. Higuchi, T. Yanagida, and Y. E. Goldman, "Compliance of thin filaments in skinned fibers of rabbit skeletal muscle," *Biophysical Journal*, vol. 69, no. 3, pp. 1000–1010, 1995.
- [24] M. F. Schmid and H. F. Epstein, "Muscle thick filaments are rigid coupled tubules, not flexible ropes," *Cell Motility and the Cytoskeleton*, vol. 41, no. 3, pp. 195–201, 1998.
- [25] M. Evans, N. Hastings, and B. Peacock, *Statistical Distributions*, Wiley, New York, NY, USA, 2000.
- [26] M. Abramowitz and I. A. Stegun, Eds., *Handbook of Mathematical Functions with Formulas, Graphs, and Mathematical Tables, 9th Printing*, Dover, New York, NY, USA, 1972.
- [27] D. L. Snyder, *Random Point Processes*, John Wiley and Sons, New York, NY, USA, 1975.
- [28] J. T. Finer, A. D. Mehta, J. A. Spudich et al., "Characterization of single actin-myosin interactions," *Biophysical Journal*, vol. 68, supplement 4, pp. 291S–297S, 1995.
- [29] R. E. Godt and B. D. Lindley, "Influence of temperature upon contractile activation and isometric force production in mechanically skinned muscle fibers of the frog," *Journal of General Physiology*, vol. 80, no. 2, pp. 279–297, 1982.
- [30] G. H. Rossmanith, "Tension responses of muscle to n-step pseudo-random length reversals: a frequency domain representation," *Journal of Muscle Research and Cell Motility*, vol. 7, no. 4, pp. 299–306, 1986.
- [31] M. E. Coupland, E. Puchert, and K. W. Ranatunga, "Temperature dependence of active tension in mammalian (rabbit psoas) muscle fibres: effect of inorganic phosphate," *Journal of Physiology*, vol. 536, no. 3, pp. 879–891, 2001.

- [32] B. M. Palmer, "A strain-dependency of Myosin off-rate must be sensitive to frequency to predict the B-process of sinusoidal analysis," *Advances in Experimental Medicine and Biology*, vol. 682, pp. 57–75, 2010.
- [33] K. W. Ranatunga and M. E. Coupland, "Crossbridge mechanism(s) examined by temperature perturbation studies on muscle," *Advances in Experimental Medicine and Biology*, vol. 682, pp. 247–266, 2010.
- [34] I. S. Gradshteyn and I. M. Ryzhik, Eds., *Tables of Integrals, Series, and Products*, Academic Press, 1980.

Review Article

Muscle Plasticity and β_2 -Adrenergic Receptors: Adaptive Responses of β_2 -Adrenergic Receptor Expression to Muscle Hypertrophy and Atrophy

Shogo Sato,^{1,2} Ken Shirato,¹ Kaoru Tachiyashiki,³ and Kazuhiko Imaizumi^{1,4}

¹ Laboratory of Physiological Sciences, Faculty of Human Sciences, Waseda University, 2-579-15 Mikajima, Tokorozawa, Saitama 359-1192, Japan

² Japan Society for the Promotion of Science, 8 Ichiban-cho, Chiyoda-ku, Tokyo 102-8472, Japan

³ Department of Natural and Living Sciences, Graduate School of Education, Joetsu University of Education, 1 Yamayashiki, Joetsu, Niigata 943-8512, Japan

⁴ Global COE Doctoral Program, Graduate School of Sport Sciences, Waseda University, 2-579-15 Mikajima, Tokorozawa, Saitama 359-1192, Japan

Correspondence should be addressed to Kazuhiko Imaizumi, imaizumi@waseda.jp

Received 1 June 2011; Accepted 23 August 2011

Academic Editor: Guy Benian

Copyright © 2011 Shogo Sato et al. This is an open access article distributed under the Creative Commons Attribution License, which permits unrestricted use, distribution, and reproduction in any medium, provided the original work is properly cited.

We discuss the functional roles of β_2 -adrenergic receptors in skeletal muscle hypertrophy and atrophy as well as the adaptive responses of β_2 -adrenergic receptor expression to anabolic and catabolic conditions. β_2 -Adrenergic receptor stimulation using anabolic drugs increases muscle mass by promoting muscle protein synthesis and/or attenuating protein degradation. These effects are prevented by the downregulation of the receptor. Endurance training improves oxidative performance partly by increasing β_2 -adrenergic receptor density in exercise-recruited slow-twitch muscles. However, excessive stimulation of β_2 -adrenergic receptors negates their beneficial effects. Although the preventive effects of β_2 -adrenergic receptor stimulation on atrophy induced by muscle disuse and catabolic hormones or drugs are observed, these catabolic conditions decrease β_2 -adrenergic receptor expression in slow-twitch muscles. These findings present evidence against the use of β_2 -adrenergic agonists in therapy for muscle wasting and weakness. Thus, β_2 -adrenergic receptors in the skeletal muscles play an important physiological role in the regulation of protein and energy balance.

1. Introduction

The skeletal muscle is the most abundant tissue in the human body comprising 40–50% of body mass. Skeletal muscle protein undergoes rapid turnover, which is regulated by the balance between the rates of protein synthesis and degradation. Physical activity (exercise training) and anabolic hormones and drugs (sports doping) increase muscle protein content. However, sarcopenia and muscle disuse (due to unloading, microgravity, or inactivity) and diseases decrease muscle protein content. The rate of protein synthesis is at least in part mediated by β_2 -adrenergic receptors (β_2 -ARs) in skeletal muscles in both anabolic and catabolic conditions.

ARs belong to the guanine nucleotide-binding G-protein-coupled receptor (GPCR) family. Skeletal muscle con-

tains a significant proportion of β -ARs. The β_2 subtype is the most abundant, while ~7–10% of ARs are the β_1 subtype [1, 2]. Furthermore, β_2 -AR is more dense in slow-twitch muscles than in fast-twitch muscles [3, 4]. However, the magnitude of anabolic responses to β_2 -adrenergic agonists is greater in fast-twitch muscles than in slow-twitch muscles [5–8].

The family of β -ARs was originally believed to signal predominantly via coupling with a stimulatory guanine nucleotide-binding protein, $G\alpha_s$; however, recent studies revealed that both β_2 - and β_3 -ARs in skeletal muscle are also capable of coupling to an inhibitory guanine nucleotide-binding protein, $G\alpha_i$ [9]. β_2 -AR activates the $G\alpha_s$ /adenylyl cyclase (AC)/cyclic adenosine monophosphate (cAMP)/cAMP-dependent protein kinase A (PKA) signaling

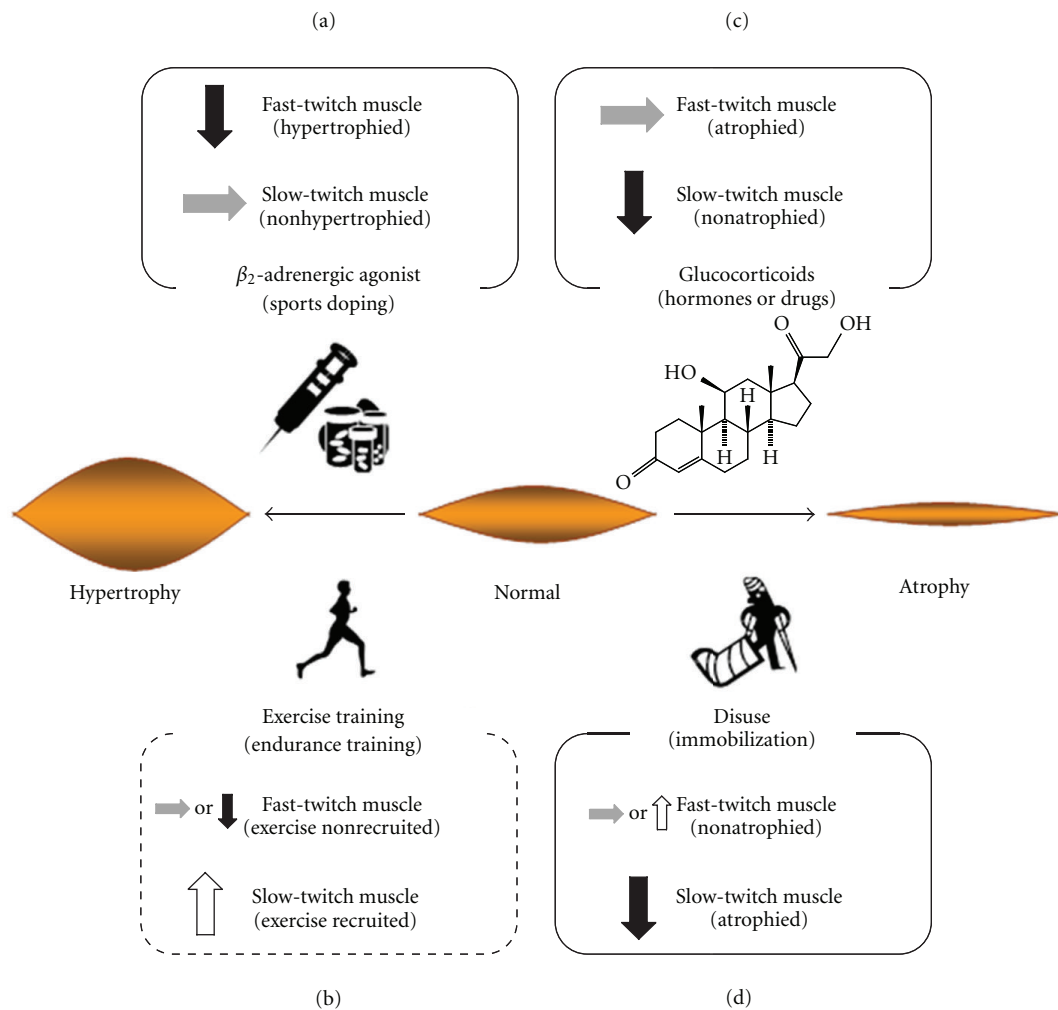


FIGURE 1: Changes in β_2 -AR expression in hypertrophied and atrophied skeletal muscles. (a) β_2 -AR stimulation using anabolic drugs downregulates β_2 -AR expression in hypertrophied fast-twitch muscles but not in slow-twitch muscles [4, 7, 8, 14–17]. (b) Exercise training such as endurance training upregulates β_2 -AR expression in exercise-recruited slow-twitch muscles, whereas no changes or downregulations are observed in fast-twitch muscles [18, 19], although muscle mass is not altered. However, although exercise training such as isometric strength training induces muscle hypertrophy, there is no insight regarding the effects of such exercise on β_2 -AR expression. The differential effects of types of exercise training on physiological responses such as β_2 -AR expression and muscle hypertrophy should be clarified in more detailed and are currently being investigated by our group. (c) Catabolic hormones or drugs such as glucocorticoids downregulate β_2 -AR expression in nonatrophied slow-twitch muscles but not fast-twitch muscles [16, 20, 21]. (d) Muscle disuse downregulates β_2 -AR expression in atrophied slow-twitch muscle, whereas no changes or upregulation of receptor expression are observed in fast-twitch muscles [14, 22]. Up arrow (open arrow): upregulation of β_2 -AR expression; down arrow (filled arrow): downregulation of β_2 -AR expression; lateral arrow (shade arrow): no change.

pathway. The signaling pathway is at least in part responsible for the anabolic response of skeletal muscle to β_2 -AR stimulation. Further, in addition to the well-documented inhibition of AC activity [10], β_2 -AR coupling to $G\alpha_i$ activates $G\alpha_s$ -independent pathways [11].

β_2 -AR has 7 transmembrane α helices forming 3 extracellular loops, including an NH_2 terminus and 3 intracellular loops that include a $COOH$ terminus [12]. β_2 -AR contains phosphorylation sites in the third intracellular loop and proximal cytoplasmic tail. Phosphorylation of these sites

triggers the agonist-promoted desensitization, internalization, and degradation of the receptor [13]. These regulatory mechanisms contribute to maintaining agonist-induced β_2 -AR responsiveness in various conditions.

The adaptive responses of β_2 -AR expression to anabolic and catabolic conditions in skeletal muscles are shown in Figure 1. Understanding the correlation between changes in muscle mass and β_2 -AR expression in several anabolic or catabolic conditions present scientific evidence to eradicate sports doping and identify novel approaches for attenuating

muscle atrophy concomitant with disuse and various diseases. This paper will discuss the effects of (1) pharmacological β_2 -AR stimulation (sports doping), (2) muscle hypertrophy (exercise training), and (3) muscle atrophy (catabolic conditions and hormones) on β_2 -AR expression in skeletal muscles.

2. Pharmacological Stimulation of β_2 -AR

2.1. Muscle Hypertrophy and β_2 -AR. A β_2 -adrenergic agonist, clenbuterol [1-(4-amino-3,5-dichlorobenzyl)-2-(tert-butylamino) ethanol], is used as a nonsteroidal anabolic drug for sports doping. According to the recent World Anti-Doping Agency (WADA) documents, clenbuterol was the seventh most commonly used anabolic agent in 2009 (67 cases; 2.0% of all anabolic agents used).

Numerous studies have shown that the administration of β_2 -adrenergic agonists induces muscle hypertrophy in many species [23–25]. Experiments using mice lacking β_1 -AR, β_2 -AR, or both demonstrate that β_2 -adrenergic agonist-induced functions such as muscle hypertrophy are mediated by β_2 -AR [26]. β_2 -Adrenergic agonists promote muscle growth by increasing the rate of protein synthesis and/or decreasing protein degradation [23–25]. Furthermore, β_2 -adrenergic agonists induce slow-to-fast [myosin heavy chain (MHC)]/ $\beta \rightarrow$ MHCIIa \rightarrow MHCIIId/x \rightarrow MHCIIb] transformation of muscle fibers.

The β_2 -AR signaling pathway involves the agonist-dependent activation of $G\alpha_s$, which in turn activates AC, resulting in increased cAMP production. Cyclic AMP-activated PKA initiates the transcription of many target genes via the phosphorylation of cAMP-response-element-(CRE-) binding protein (CREB) or adaptor proteins such as CREB-binding protein (CBP) and p300, subsequently promoting protein synthesis [23]. While β_2 -AR-mediated signaling was traditionally believed to involve selective coupling to $G\alpha_s$, recent studies revealed that β_2 -AR exhibits dual coupling to both $G\alpha_s$ and $G\alpha_i$ in skeletal muscles [9, 23]. In addition to $G\alpha_s$, $G\alpha_i$ -linked $G\beta\gamma$ subunits play an active role in various cell signaling processes such as the phosphoinositol 3 kinase (PI3 K)/protein kinase B (Akt)/mammalian target of rapamycin (mTOR)/p70S6 K and PI3 K/Akt/forkhead box-O (FOXO) pathways. These signaling pathways play important roles in β_2 -adrenergic agonist-induced hypertrophy in skeletal muscles [23].

In addition to promoting protein synthesis, the hypertrophic response of skeletal muscles following β_2 -adrenergic agonist administration is associated with decreased protein degradation. β_2 -Adrenergic agonists attenuate protein degradation predominantly via Ca^{2+} -dependent proteolysis and the ATP/ubiquitin-dependent pathway [27–31]. However, there is little knowledge regarding the preventive effects of β_2 -adrenergic agonists on the proteolysis system compared with the protein synthesis system.

The hypertrophic responses to β_2 -adrenergic agonists are observed much frequently in fast-twitch muscle than in slow-twitch muscle. Our group previously demonstrated that clenbuterol administration ($1.0 \text{ mg} \cdot \text{kg}^{-1} \cdot \text{day}^{-1}$) to rats for

10 days increases the mass of fast-twitch (extensor digitorum longus: EDL) muscle without altering in slow-twitch (soleus) muscle [7, 8]; other groups also observed the same tendency [5, 6, 32–35]. However, the mechanisms of the fiber-type-dependent effects of β_2 -adrenergic agonists on muscle hypertrophy remain unclear.

Pearen et al. [36, 37] and Kawasaki et al. [38] identified that β_2 -AR activation increases the expression of the orphan nuclear receptor, NOR-1 (NR4A3), a negative regulatory factor of myostatin (a member of the transforming growth factor- β superfamily and a potent negative regulator of muscle mass), in fast-twitch muscles without altering that in slow-twitch muscles. Furthermore, Shi et al. [32] demonstrate the possibility that β_2 -adrenergic agonist-induced fiber-type-dependent hypertrophy is in part due to the extracellular signal-regulated kinase (ERK)/mitogen activated protein kinase (MAPK) pathway. Moreover, the pharmacological inhibition of the PI3 K/Akt/mTOR signaling pathway revealed that the attenuation of the anabolic response to clenbuterol is greater in fast-twitch muscles than in slow-twitch muscles [30]. In addition to the protein synthesis system, Yimlamai et al. [35] found that clenbuterol inhibits ubiquitination more strongly in fast-twitch muscles than in slow-twitch muscles. Thus, β_2 -AR-mediated signaling pathways tend to promote muscle hypertrophy to a greater extent in fast-twitch muscle than in slow-twitch muscle.

2.2. Posttranslational Regulation of β_2 -AR. As shown in Table 1, some reports focus on the responses of β_2 -AR expression to β_2 -AR stimulation in skeletal muscles [4, 7, 8, 14–17]. This is because β_2 -AR functions such as muscle hypertrophy are maintained via receptor density, including synthesis and downregulation as well as receptor sensitivity, which includes receptor sensitization, desensitization, phosphorylation, and internalization [13, 39, 40].

The desensitization of β_2 -AR is associated with receptor phosphorylation. McCormick et al. [41] demonstrate that fast-twitch fibers mainly express nonphosphorylated β_2 -AR, whereas slow-twitch fibers predominantly express phosphorylated β_2 -AR. Furthermore, treating muscle fibers with β_2 -adrenergic agonists (e.g., clenbuterol, formoterol, and salbutamol) increases the phosphorylation of β_2 -AR in slow-twitch fibers but not in fast-twitch fibers [41]. On the other hand, the receptor phosphorylation occurs via the actions of protein kinases (such as PKA) and/or GPCR kinase (GRK). Rat skeletal muscles contain predominantly GRK2 and GRK5; GRK protein is expressed more in fast-twitch muscles than in slow-twitch muscles. These expression levels in each type of muscle fiber are not altered by β_2 -adrenergic agonist administration [42]. Thus, there is a negative correlation between the level of phosphorylated β_2 -AR and receptor kinase. Therefore, further investigation is needed to reveal the detailed mechanism of β_2 -AR phosphorylation.

Following β_2 -AR phosphorylation, the receptor is internalized into the cytosol. The internalized β_2 -AR is then degraded or dephosphorylated and subsequently recycled to the membrane [13, 43–45]. Prolonged administration of β_2 -adrenergic agonists leads to the downregulation of β_2 -AR density in skeletal muscles [15–17]. These posttranslational

TABLE 1: Responses of β_2 -AR expression in skeletal muscle to anabolic and catabolic conditions.

Conditions	Species	β_2 -AR		Other findings	References
		Protein	mRNA		
β_2 -AR stimulation					
Fenoterol (1.4 mg · kg ⁻¹ · day ⁻¹ , 4 weeks)	Rat	↓ (FT) → (ST)	n.d.		[4]
Clenbuterol (1.0 mg · kg ⁻¹ · day ⁻¹ , 10 days)	Rat	n.d.	↓ (FT) → (ST)	β_1 -AR mRNA ↓ (LV) β_2 -AR mRNA ↓ (LV)	[7] [8]
Clenbuterol (1.0 mg · kg ⁻¹ · day ⁻¹ , 10 days)	Rat	n.d.	↓ (FT) → (ST)	GR mRNA ↓ (FT) HuR mRNA ↓ (FT) AUF1 mRNA ↓ (FT)	
Fenoterol (1.4 mg · kg ⁻¹ · day ⁻¹ , 2–7 days)	Rat	→ (FT, ST)	↓ (FT, ST)	hnRNP A1 mRNA ↓ (FT) G α_s content → (FT, ST) AC activity → (FT, ST)	[14]
Clenbuterol (2.0 mg · kg ⁻¹ · day ⁻¹ , 18 days)	Rat	↓ (FT+ST)	n.d.		[15]
Clenbuterol (4.0 mg · kg ⁻¹ of feed, 10 days)	Rat	↓ (FT)	n.d.	β_2 -AR affinity → (FT)	[16]
Clenbuterol (0.2 mg · kg ⁻¹ · day ⁻¹ , 7 days)	Rat	↓ (FT+ST)	n.d.		[17]
Clenbuterol (50 μ M) Formoterol (100 μ M) Salbutamol (500 μ M)	Mouse (ex vivo)	Phosphorylated β_2 -AR ↑ (ST), → (FT)	n.d.	cAMP concentration ↑ (FT, ST)	[41]
Endurance training					
Treadmill (12 weeks)	Rat	↓ (FT)	n.d.	β_2 -AR affinity → AC activity ↓ G α_s content ↓	[18]
Treadmill (18 weeks)	Rat	→ (FT) ↑ (ST)	n.d.	AC activity ↑ (FT, ST) β_2 -AR density → (acute)	[19]
Catabolic conditions					
Dexamethasone (1.0 mg · kg ⁻¹ · day ⁻¹ , 10 days)	Rat	→ (FT, ST)	→ (FT) ↓ (ST)	GR mRNA ↓ (FT, ST) CREB mRNA ↓ (ST) AUF1 mRNA ↑ (FT)	[20]
Dexamethasone (1.0 mg · kg ⁻¹ · day ⁻¹ , 10 days)	Rat	n.d.	→ (FT) ↓ (ST)	GR mRNA ↓ (FT, ST) β_1 -AR mRNA ↑ (LV)	[21]
Dexamethasone (0.2 mg · kg ⁻¹ · day ⁻¹ , 10 days)	Rat	→ (FT)	n.d.	β_2 -AR affinity → (FT)	[16]
Casted-immobilization (10 days)	Rat	→ (FT, ST)	→ (FT) ↓ (ST)	GR mRNA ↓ (ST) GR protein ↓ (ST)	[22]
Aging	Rat	→ (FT, ST)	n.d.		[4]
Injury (bupivacaine injection)	Rat	↑ (FT) ↓ (ST)	↑ (FT) ↓ (ST)	G α_s content ↑ (FT), ↓ (ST) AC activity ↑ (FT, ST)	[14]

FT, fast-twitch muscle; ST, slow-twitch muscle; LV, left ventricle muscle. Up arrow, increase; down arrow, decrease; lateral arrow, no change. n.d., no data.

regulations are advantageous for maintaining the rate of muscle protein synthesis and/or degradation.

2.3. Short-Term and Chronic Transcriptional Regulation of β_2 -AR. β_2 -AR synthesis, including transcription and subsequent translation, is required to restore transmembrane receptor density. The process of β_2 -AR synthesis can be separated into 2 pathways: (1) the positive autoregulation of β_2 -AR gene transcription via receptor-mediated elevation of cAMP concentration followed by the phosphorylation and activation of CREB [46, 47] and (2) the transactivation of

the β_2 -AR gene via interaction between hormones and the nuclear receptor complex and response elements on the β_2 -AR promoter region [48]. In particular, the transcription of the β_2 -AR gene and the subsequent mRNA expression via cAMP-mediated CRE activation increased in response to short-term β_2 -adrenergic agonist exposure [46, 47]. Moreover, treatment with glucocorticoids or thyroid hormone transactivates the β_2 -AR gene both in vitro and in vivo [48–51].

Our previous reports demonstrate that clenbuterol administration (1.0 mg · kg⁻¹ · day⁻¹) for 10 days to rats

decreases β_2 -AR mRNA expression in the fast-twitch EDL muscle without altering that in the slow-twitch soleus muscle [7, 8]. Furthermore, the mRNA expression of glucocorticoid receptors (GRs) was also decreased with clenbuterol treatment in the EDL muscle but not in the soleus muscle [8]. Glucocorticoids and the GR complex activate the transcription of the β_2 -AR gene via interaction with glucocorticoid response elements (GREs), consensus *cis*-acting DNA sequences (i.e., AGA ACA nnn TGT TCT) on its promoter regions [48], thus upregulating β_2 -AR expression [16, 50, 51]. These findings corroborate our results that there is a positive correlation between the expression levels of β_2 -AR and GR in skeletal muscles. Beitzel et al. [14] also report that administrating the β -adrenergic agonist, fenoterol ($1.4 \text{ mg} \cdot \text{kg}^{-1} \cdot \text{day}^{-1}$, i.p.), for 5 days decreases β_2 -AR mRNA expression in the EDL and soleus muscles. Thus, in contrast to the transactivation of the β_2 -AR gene and increase in the mRNA level in response to short-term agonist exposure, chronic β_2 -adrenergic stimulation inhibits β_2 -AR synthesis in skeletal muscles.

2.4. Posttranscriptional Regulation of β_2 -AR. In addition to post-translational and transcriptional regulation, several groups focus on the posttranscriptional regulation of β_2 -AR mRNA. β_2 -AR mRNA contains an AU-rich element (ARE) within the 3'-untranslated region (3'-UTR) that can be recognized by several mRNA-binding proteins, including Hu antigen R (HuR), AU-rich element binding/degradation factor1 (AUF1), and heterogeneous nuclear ribonucleoprotein A1 (hnRNP A1) [52–55]. These factors play a role in the regulation of β_2 -AR mRNA stability [52–55]. Our study demonstrates that clenbuterol-induced stimulation of β_2 -AR decreases the mRNA expressions of these factors in the EDL but not in the soleus muscle [8], suggesting that the posttranscriptional process of β_2 -AR synthesis requires the stability of its mRNA to be regulated.

3. Exercise Training and β_2 -AR

Strength-resistance training increases muscle mass [56], fiber cross-sectional area [57], protein and RNA contents [58], and the capacity to generate force [59]. In contrast to strength training, endurance training is characterized by increased mitochondrial mass [60], increased oxidative enzymes [61], decreased glycolytic enzymes [62], increased slow contractile and regulatory proteins [62], and decreased fast fiber area [63]. These findings suggest that the functional roles of β_2 -AR in skeletal muscles differ with the type of exercise training.

3.1. Strength Exercise Training and β_2 -AR. Mounier et al. [64] investigated the changes in the weight of the EDL muscle induced by clenbuterol administration, strength training, and a combination of both. They found that the effects of strength training and clenbuterol on muscle hypertrophy were not additive in fast-twitch muscles. Their report also demonstrates that the strength-training-induced enhancement of lactate dehydrogenase-specific activity is completely inhibited by clenbuterol administration, while

the clenbuterol-induced decrease in monocarboxylate transporter1 mRNA expression is completely offset by strength training [64]. Thus, there are no synergetic effects of a combination of strength training and β_2 -AR stimulation on muscle mass. Furthermore, strength training counteracts molecular modifications such as glycolytic control induced by chronic clenbuterol administration in fast-twitch muscles to some extent. However, our evidence regarding the synergistic effects of strength training and β_2 -AR stimulation is insufficient because the experimental models of strength-trained animals are not fully established.

3.2. Endurance Exercise Training and β_2 -AR. In contrast to strength training, β_2 -AR stimulation affects endurance-training-induced modulations such as contractile activity [65], muscle fiber-type shift [65], metabolic enzyme activity [66], and insulin resistance [67, 68]. Lynch et al. [65] demonstrated that low-intensity endurance training prevents clenbuterol-induced slow-to-fast (type I fiber \rightarrow type II fiber) fiber-type transformation in the EDL and soleus muscles, and thereby offsets the clenbuterol-induced decrease in Ca^{2+} sensitivity in fast-twitch fibers. These results suggest that endurance-training-heightened muscle aerobic capacity is attenuated by β_2 -AR stimulation-induced muscle fiber-type transformations. Furthermore, pharmacological β -AR blockage diminishes the endurance-training-induced increase in citrate synthase activity in the fast-twitch plantaris muscle [66]. Moreover, clenbuterol administration prevents the endurance-training-induced improvement in insulin-stimulated glucose uptake and attenuates the increase in citrate synthase activity in the skeletal muscles of obese Zucker rats [67, 68]. These findings demonstrate that the endurance-training-induced increase in aerobic metabolism in skeletal muscles requires moderate but not excessive stimulation of β_2 -AR.

Recently, Miura et al. [69] demonstrated that an increase in peroxisome proliferator-activated receptor- γ coactivator-1 α (PGC-1 α) mRNA in response to exercise is mediated by β_2 -AR activation. Furthermore, the Ca^{2+} -signaling [70] and p38 MAPK pathways [71], which is downstream of β_2 -AR, are activated in skeletal muscles in response to exercise, which regulates PGC-1 α expression. Since PGC-1 α promotes mitochondrial biogenesis [72], the exercise-induced activation of β_2 -AR may in part enhance aerobic capacity by increasing PGC-1 α expression. Thus, β_2 -AR stimulation is essential for enhancing the effects of exercise training on muscle functions such as fiber-type shift as well as oxidative and anaerobic metabolism.

3.3. Response of β_2 -AR Expression to Exercise Training. As mentioned above, the functional roles of β_2 -AR during exercise training are physiologically important in skeletal muscles. Therefore, changes in the expression and sensitivity of β_2 -AR should be important for the metabolic, anabolic, and catabolic adaptations of skeletal muscles during exercise training. Nevertheless, there is little information on the response of β_2 -AR expression to exercise training in skeletal muscles. However, many studies demonstrate the effects of exercise training on β_2 -AR expression in several tissues

and cell types such as myocardia [73, 74], adipocytes [75], and macrophages [76]. Barbier et al. [73] demonstrated that exercise training induces changes in the distribution of β_1 -, β_2 -, and β_3 -AR densities in the rat left ventricle. In adipocytes, the exercise-induced trafficking of β_2 -AR into the cell membrane from the cytosol is coupled with adipocytes' function to increase intracellular cAMP production [75]. Kizaki et al. [76] also found a reduction in the expression of β_2 -AR mRNA in macrophages and highlight the significance of β_2 -AR in the exercise training-induced improvement of macrophages' innate immune function. Thus, changes in β_2 -AR expression play a role in physiological adaptations to exercise training in several tissues.

A few studies also report the effects of exercise training on β -AR in skeletal muscles [18, 19, 77, 78] (Table 1). Nieto et al. [18] demonstrate that β -AR density and $G\alpha_s$ content in the fast-twitch gastrocnemius muscle are significantly lower in endurance-exercised rats than in controls. They also reveal that exercise reduces receptor- and nonreceptor-mediated (i.e., pharmacological stimulation of AC by forskolin) AC activity in muscles [18]. However, Buckenmeyer et al. [19] report that endurance training increases β -AR density in slow-twitch muscles that are primarily recruited during endurance training, whereas β -AR density is not altered in fast-twitch muscles. Their report also demonstrates that receptor-mediated AC activity in slow-twitch muscles is increased by endurance training, and nonreceptor-mediated AC activity is increased by training in both fast- and slow-twitch muscles [19]. In contrast to chronic endurance training, the effects of acute exercise on β -AR density and AC activity in each type of muscle were not observed [19]. Therefore, endurance-exercise-training-induced changes in β_2 -AR expression and signaling in slow-twitch muscle contributes to the adaptation of metabolic and anabolic capacities during exercise.

4. Muscle Atrophy and β_2 -AR

4.1. Preventive Roles of β_2 -AR in Disuse-Induced Muscle Atrophy. Muscle wasting and weakness are common in physiological and pathological conditions, including aging, cancer cachexia, sepsis, other forms of catabolic stress, denervation, disuse (e.g., unloading, inactivity, and microgravity), burns, human immunodeficiency virus-(HIV)-acquired immunodeficiency syndrome (AIDS), chronic kidney or heart failure, chronic obstructive pulmonary disease (COPD), and muscular dystrophies. For many of these conditions, the anabolic properties of β_2 -adrenergic agonists provide therapeutic potential for attenuating or reversing muscle wasting, muscle fiber atrophy, and muscle weakness. These β_2 -adrenergic agonists also have important clinical significance for enhancing muscle repair and restoring muscle function after muscle atrophy.

In particular, muscle disuse, which is mainly reflected by increased myofibrillar protein breakdown, causes a progressive decrease in muscle strength associated with a decreased cross-sectional area of muscle fibers. Therefore, preventing disuse-induced muscle atrophy is a problem requiring urgent

attention and highlights β_2 -AR as a target of pharmacological stimulation. Since 2000, many groups have focused on the preventive effects of β_2 -adrenergic agonist on disuse-induced muscle atrophy [4, 34, 35, 79].

Yimlamai et al. [35] demonstrate that clenbuterol attenuates the hindlimb unweighting-induced atrophy and reduces ubiquitin conjugates only in fast-twitch plantaris and tibialis anterior muscles but not in the slow-twitch soleus muscle; this suggests that clenbuterol alleviates hindlimb unweighting-induced atrophy, particularly, in fast-twitch muscles at least in part through a muscle-specific inhibition of the ubiquitin-proteasome pathway. However, Stevens et al. [34] report that clenbuterol treatment accelerates hindlimb unweighting-induced slow-to-fast (MHCI/ β \rightarrow MHCIIa \rightarrow MHCIIId/x \rightarrow MHCIIb) transformation in the soleus muscle. β_2 -Adrenergic agonist also reverses muscle wasting and weakness in several conditions such as aging [4], muscular dystrophy [29], denervation [80], cancer cachexia [28], and myotoxic injury [81].

4.2. Preventive Roles of β_2 -AR in Catabolic Hormone-Induced Muscle Atrophy. Prolonged muscle disuse and/or unloading increases the secretion of glucocorticoids, which promotes the catabolism of muscle proteins via the ubiquitin-proteasome pathway [82, 83]. Sepsis also elevates plasma glucocorticoids and adrenocorticotrophic hormone (ACTH) levels [84]. Therefore, several studies focus on the counteractive effects of β_2 -AR stimulation on glucocorticoid-induced muscle atrophy [16, 85]. Huang et al. [16] report that clenbuterol almost prevents the decrease in the weight of gastrocnemius/plantaris muscle bundles induced by dexamethasone, a synthetic glucocorticoid. Pellegrino et al. [85] demonstrate that concurrent treatment of clenbuterol with dexamethasone minimizes MHC-transformation-induced by clenbuterol (slow-to-fast) or dexamethasone (fast-to-slow) alone. Thus, β_2 -AR stimulation plays an inhibitory role in muscle atrophy and weakness induced by catabolic diseases, mechanical unloading, catabolic hormones, and pharmacological agents.

4.3. Response of β_2 -AR Expression to Catabolic Hormones. Although the effectiveness of β_2 -AR stimulation on muscle atrophy is well documented, catabolic condition-induced changes in the expression of β_2 -AR in skeletal muscles are not fully understood. Understanding the responses of β_2 -AR expression to muscle atrophy is required to establish treatments for muscle atrophy.

Table 1 shows the catabolic-condition-induced changes in β_2 -AR expression in skeletal muscles. Our group investigated whether catabolic hormones or agents alter β_2 -AR expression in skeletal muscles [20, 21]. Dexamethasone administration ($1.0 \text{ mg} \cdot \text{kg}^{-1} \cdot \text{day}^{-1}$) to rats for 10 days decreases the expression of β_2 -AR mRNA in the soleus muscle without altering that in the EDL muscle, although the expression of β_2 -AR protein in the EDL and soleus muscles is not altered [20, 21]. Dexamethasone also does not alter β_2 -AR density in gastrocnemius/plantaris muscle bundles [16]. These phenomena are specifically observed in skeletal

muscles; meanwhile, glucocorticoids and the GR complex activate the transcription of β_2 -AR gene in the human hepatoma cell line (HepG2) [48], subsequently leading to the upregulation of β_2 -AR levels in DDT₁ MF-2 smooth muscle cells [50] and lung tissue [16, 51]. Furthermore, dexamethasone decreases the expression of GR mRNA in the soleus muscle [20, 21]. Dexamethasone also decreases and increases the expression of CREB mRNA, a transcription factor of the β_2 -AR gene [46, 47], in the soleus and EDL muscles, respectively [20]. These findings suggest that the dexamethasone-induced decrease in the expression of β_2 -AR mRNA in the slow-twitch soleus muscle is associated with transcriptional regulations.

4.4. Response of β_2 -AR Expression to Muscle Disuse. The effects of physiological and pathological catabolic-condition-induced muscle atrophy on β_2 -AR expression have also been studied (Table 1) [4, 14, 22]. Our recent investigation demonstrates that casted immobilization (knee and foot arthrodesis) for 10 days markedly induced atrophy in the soleus muscle, whereas it decreased the expression of β_2 -AR mRNA [22]. Decreased GR mRNA and protein expression was also detected in the soleus muscle [22]. These results suggest that casted immobilization decreases the expression of β_2 -AR mRNA in slow-twitch muscles via the downregulation of GR levels and subsequent glucocorticoid signals. On the other hand, Ryall et al. [4] demonstrate that aging-induced muscle wasting is observed in the EDL and soleus muscles, although there are no age-associated changes in β_2 -AR density in these muscles. Furthermore, in the regeneration process from muscle injury induced by bupivacaine injection, β_2 -AR density and mRNA expression as well as α_s content are decreased in the soleus but increased in the EDL muscle [14]. Thus, the effects of catabolic conditions such as disuse, aging, and injury on β_2 -AR expression are different from and/or dependent on the conditions, especially in fast-twitch muscles, whereas decreasing tendencies are observed in slow-twitch muscles.

Both pharmacological and mechanical studies indicate that the preventive effects of β_2 -AR stimulation on muscle atrophy and weakness are limited by decreased β_2 -AR synthesis and subsequently decreased density. In order to use β_2 -adrenergic agonists as a therapeutic agent for muscle wasting, further studies are necessary to obtain detailed evidence regarding the responses of β_2 -AR expression and function to muscle atrophy.

5. Conclusions

In this paper, we discussed adaptive responses of β_2 -AR expression in skeletal muscles to β_2 -adrenergic agonist treatment, exercise training, muscle disuse, and glucocorticoid treatment. This paper also outlined the functional roles of β_2 -AR in skeletal muscles. Skeletal muscle partly requires β_2 -AR activation for hypertrophy, regeneration, and atrophy prevention; however, its functions and responsiveness must be adaptively regulated by the receptor itself via downregulation, synthesis, and desensitization. New insight in the form

of scientific evidence is needed to eradicate sports doping and to identify new therapeutic targets for attenuating muscle atrophy induced by physiological and pathological conditions.

Acknowledgments

The authors would like to thank Professor Hideki Suzuki, Department of Health and Physical Education, Aichi University of Education, and Professor Hisaya Tsujimoto, Institute of Health and Sports Science, Kurume University, for their valuable advice and suggestions. This work was supported by Research Fellowships of the Japan Society for Promotion of Science for Young Scientists (2010–2011: S. Sato) and a Grant-in-Aid of the Global Center of Excellence (COE) program, Graduate School of Sport Sciences, Waseda University (2009–2013: K. Imaizumi) of the Ministry of Education, Culture, Sports, Science, and Technology, Japan.

References

- [1] Y. S. Kim, R. D. Sainz, P. Molenaar, and R. J. Summers, "Characterization of β_1 - and β_2 -adrenoceptors in rat skeletal muscles," *Biochemical Pharmacology*, vol. 42, no. 9, pp. 1783–1789, 1991.
- [2] R. S. Williams, M. G. Caron, and K. Daniel, "Skeletal muscle β -adrenergic receptors: variations due to fiber type and training," *American Journal of Physiology*, vol. 246, no. 2, part 1, pp. E160–E167, 1984.
- [3] J. G. Ryall, P. Gregorevic, D. R. Plant, M. N. Sillence, and G. S. Lynch, " β_2 -agonist fenoterol has greater effects on contractile function of rat skeletal muscles than clenbuterol," *American Journal of Physiology*, vol. 283, no. 6, pp. R1386–R1394, 2002.
- [4] J. G. Ryall, D. R. Plant, P. Gregorevic, M. N. Sillence, and G. S. Lynch, " β_2 -agonist administration reverses muscle wasting and improves muscle function in aged rats," *Journal of Physiology*, vol. 555, no. 1, pp. 175–188, 2004.
- [5] J. G. Burniston, W. A. Clark, L. B. Tan, and D. F. Goldspink, "Dose dependent separation of the hypertrophic and myotoxic effects of the β_2 agonist clenbuterol in rat striated muscles," *Muscle and Nerve*, vol. 33, no. 5, pp. 655–663, 2006.
- [6] J. G. Ryall, M. N. Sillence, and G. S. Lynch, "Systemic administration of β_2 -adrenoceptor agonists, formoterol and salmeterol, elicit skeletal muscle hypertrophy in rats at micro-molar doses," *British Journal of Pharmacology*, vol. 147, no. 6, pp. 587–595, 2006.
- [7] S. Sato, S. Nomura, F. Kawano, J. Tanihata, K. Tachiyashiki, and K. Imaizumi, "Effects of the β_2 -agonist clenbuterol on β_1 - and β_2 -adrenoceptor mRNA expressions of rat skeletal and left ventricle muscles," *Journal of Pharmacological Sciences*, vol. 107, no. 4, pp. 393–400, 2008.
- [8] S. Sato, S. Nomura, F. Kawano, J. Tanihata, K. Tachiyashiki, and K. Imaizumi, "Adaptive effects of the β_2 -agonist clenbuterol on expression of β_2 -adrenoceptor mRNA in rat fast-twitch fiber-rich muscles," *Journal of Physiological Sciences*, vol. 60, no. 2, pp. 119–127, 2010.
- [9] A. R. Gosmanov, J. A. Wong, and D. B. Thomason, "Duality of G protein-coupled mechanisms for β -adrenergic activation of NKCC activity in skeletal muscle," *American Journal of Physiology*, vol. 283, no. 4, pp. C1025–C1032, 2002.
- [10] S. N. Abramson, M. W. Martin, A. R. Hughes et al., "Interaction of β -adrenergic receptors with the inhibitory guanine

- nucleotide-binding protein of adenylate cyclase in membranes prepared from cyc-S49 lymphoma cells," *Biochemical Pharmacology*, vol. 37, no. 22, pp. 4289–4297, 1988.
- [11] C. Communal, W. S. Colucci, and K. Singh, "p38 mitogen-activated protein kinase pathway protects adult rat ventricular myocytes against β -adrenergic receptor-stimulated apoptosis. Evidence for G_i -dependent activation," *Journal of Biological Chemistry*, vol. 275, no. 25, pp. 19395–19400, 2000.
- [12] M. Johnson, "Molecular mechanisms of β_2 -adrenergic receptor function, response, and regulation," *Journal of Allergy and Clinical Immunology*, vol. 117, no. 1, pp. 18–24, 2006.
- [13] J. G. Krupnick and J. L. Benovic, "The role of receptor kinases and arrestins in G protein-coupled receptor regulation," *Annual Review of Pharmacology and Toxicology*, vol. 38, pp. 289–319, 1998.
- [14] F. Beitzel, M. N. Sillence, and G. S. Lynch, " β -Adrenoceptor signaling in regenerating skeletal muscle after β -agonist administration," *American Journal of Physiology*, vol. 293, no. 4, pp. E932–E940, 2007.
- [15] N. J. Rothwell, M. J. Stock, and D. K. Sudera, "Changes in tissue blood flow and β -receptor density of skeletal muscle in rats treated with the β_2 -adrenoceptor agonist clenbuterol," *British Journal of Pharmacology*, vol. 90, no. 3, pp. 601–607, 1987.
- [16] H. Huang, C. Gazzola, G. G. Pegg, and M. N. Sillence, "Differential effects of dexamethasone and clenbuterol on rat growth and on β_2 -adrenoceptors in lung and skeletal muscle," *Journal of Animal Science*, vol. 78, no. 3, pp. 604–608, 2000.
- [17] M. N. Sillence, M. L. Matthews, W. G. Spiers, G. G. Pegg, and D. B. Lindsay, "Effects of clenbuterol, ICI118551 and sotalol on the growth of cardiac and skeletal muscle and on β_2 -adrenoceptor density in female rats," *Naunyn-Schmiedeberg's Archives of Pharmacology*, vol. 344, no. 4, pp. 449–453, 1991.
- [18] J. L. Nieto, I. Diaz-Laviada, J. M. Malpartida, I. Galve-Roperh, and A. Haro, "Adaptations of the β -adrenoceptor-adenylyl cyclase system in rat skeletal muscle to endurance physical training," *Pflugers Archiv European Journal of Physiology*, vol. 434, no. 6, pp. 809–814, 1997.
- [19] P. J. Buckenmeyer, A. H. Goldfarb, J. S. Partilla, M. A. Pineyro, and E. M. Dax, "Endurance training, not acute exercise, differentially alters β -receptors and cyclase in skeletal fiber types," *American Journal of Physiology*, vol. 258, no. 1, pp. E71–E77, 1990.
- [20] S. Sato, K. Shirato, K. Tachiyashiki, and K. Imaizumi, "Synthesized glucocorticoid, dexamethasone regulates the expressions of β_2 -adrenoceptor and glucocorticoid receptor mRNAs but not proteins in slow-twitch soleus muscle of rats," *Journal of Toxicological Sciences*, vol. 36, no. 4, pp. 479–486, 2011.
- [21] F. Kawano, J. Tanihata, S. Sato et al., "Effects of dexamethasone on the expression of β_1 -, β_2 - and β_3 -adrenoceptor mRNAs in skeletal and left ventricle muscles in rats," *Journal of Physiological Sciences*, vol. 59, no. 5, pp. 383–390, 2009.
- [22] S. Sato, H. Suzuki, H. Tsujimoto, K. Shirato, K. Tachiyashiki, and K. Imaizumi, "Casted-immobilization downregulates glucocorticoid receptor expression in rat slow-twitch muscle," *Life Sciences*. in press.
- [23] G. S. Lynch and J. G. Ryall, "Role of β -adrenoceptor signaling in skeletal muscle: implications for muscle wasting and disease," *Physiological Reviews*, vol. 88, no. 2, pp. 729–767, 2008.
- [24] J. G. Ryall and G. S. Lynch, "The potential and the pitfalls of β -adrenoceptor agonists for the management of skeletal muscle wasting," *Pharmacology and Therapeutics*, vol. 120, no. 3, pp. 219–232, 2008.
- [25] Y. S. Kim and R. D. Sainz, " β -adrenergic agonists and hypertrophy of skeletal muscles," *Life Sciences*, vol. 50, no. 6, pp. 397–407, 1992.
- [26] R. T. Hinkle, K. M. B. Hodge, D. B. Cody, R. J. Sheldon, B. K. Kobilka, and R. J. Isfort, "Skeletal muscle hypertrophy and anti-atrophy effects of clenbuterol are mediated by the β_2 -adrenergic receptor," *Muscle and Nerve*, vol. 25, no. 5, pp. 729–734, 2002.
- [27] P. Costelli, C. Garcia-Martinez, M. Llovera et al., "Muscle protein waste in tumor-bearing rats is effectively antagonized by a β_2 -adrenergic agonist (clenbuterol). Role of the ATP-ubiquitin-dependent proteolytic pathway," *Journal of Clinical Investigation*, vol. 95, no. 5, pp. 2367–2372, 1995.
- [28] S. Busquets, M. T. Figueras, G. Fuster et al., "Anticachectic effects of formoterol: a drug for potential treatment of muscle wasting," *Cancer Research*, vol. 64, no. 18, pp. 6725–6731, 2004.
- [29] L. J. Harcourt, J. D. Schertzer, J. G. Ryall, and G. S. Lynch, "Low dose formoterol administration improves muscle function in dystrophic mdx mice without increasing fatigue," *Neuromuscular Disorders*, vol. 17, no. 1, pp. 47–55, 2007.
- [30] W. O. Kline, F. J. Panaro, H. Yang, and S. C. Bodine, "Rapamycin inhibits the growth and muscle-sparing effects of clenbuterol," *Journal of Applied Physiology*, vol. 102, no. 2, pp. 740–747, 2007.
- [31] L. C. C. Navegantes, N. M. Z. Resano, R. H. Migliorini, and C. Kettelhut, "Catecholamines inhibit Ca^{2+} -dependent proteolysis in rat skeletal muscle through β_2 -adrenoceptors and cAMP," *American Journal of Physiology*, vol. 281, no. 3, pp. E449–E454, 2001.
- [32] H. Shi, C. Zeng, A. Ricome, K. M. Hannon, A. L. Grant, and D. E. Gerrard, "Extracellular signal-regulated kinase pathway is differentially involved in β -agonist-induced hypertrophy in slow and fast muscles," *American Journal of Physiology*, vol. 292, no. 5, pp. C1681–C1689, 2007.
- [33] T. Kitaura, N. Tsunekawa, and H. Hatta, "Decreased monocarboxylate transporter 1 in rat soleus and EDL muscles exposed to clenbuterol," *Journal of Applied Physiology*, vol. 91, no. 1, pp. 85–90, 2001.
- [34] L. Stevens, C. Firinga, B. Gohlsch, B. Bastide, Y. Mounier, and D. Pette, "Effects of unweighting and clenbuterol on myosin light and heavy chains in fast and slow muscles of rat," *American Journal of Physiology*, vol. 279, no. 5, pp. C1558–C1563, 2000.
- [35] T. Yimlamai, S. L. Dodd, S. E. Borst, and S. Park, "Clenbuterol induces muscle-specific attenuation of atrophy through effects on the ubiquitin-proteasome pathway," *Journal of Applied Physiology*, vol. 99, no. 1, pp. 71–80, 2005.
- [36] M. A. Pearen, J. G. Ryall, M. A. Maxwell, N. Ohkura, G. S. Lynch, and G. E. O. Muscat, "The orphan nuclear receptor, NOR-1, is a target of β -adrenergic signaling in skeletal muscle," *Endocrinology*, vol. 147, no. 11, pp. 5217–5227, 2006.
- [37] M. A. Pearen, S. A. Myers, S. Raichur, J. G. Ryall, G. S. Lynch, and G. E. O. Muscat, "The orphan nuclear receptor, NOR-1, a target of β -adrenergic signaling, regulates gene expression that controls oxidative metabolism in skeletal muscle," *Endocrinology*, vol. 149, no. 6, pp. 2853–2865, 2008.
- [38] E. Kawasaki, F. Hokari, M. Sasaki, A. Sakai, K. Koshinaka, and K. Kawanaka, "The effects of β -adrenergic stimulation and exercise on NR4A3 protein expression in rat skeletal muscle," *Journal of Physiological Sciences*, vol. 61, no. 1, pp. 1–11, 2010.
- [39] K. L. Pierce, R. T. Premont, and R. J. Lefkowitz, "Seven-transmembrane receptors," *Nature Reviews Molecular Cell Biology*, vol. 3, no. 9, pp. 639–650, 2002.

- [40] A. Claing, S. A. Laporte, M. G. Caron, and R. J. Lefkowitz, "Endocytosis of G protein-coupled receptors: roles of G protein-coupled receptor kinases and β -arrestin proteins," *Progress in Neurobiology*, vol. 66, no. 2, pp. 61–79, 2002.
- [41] C. McCormick, L. Alexandre, J. Thompson, and G. Mutungi, "Clenbuterol and formoterol decrease force production in isolated intact mouse skeletal muscle fiber bundles through a β_2 -adrenoceptor-independent mechanism," *Journal of Applied Physiology*, vol. 109, no. 6, pp. 1716–1727, 2010.
- [42] S. W. Jones, D. J. Baker, and P. L. Greenhaff, "G protein-coupled receptor kinases 2 and 5 are differentially expressed in rat skeletal muscle and remain unchanged following β_2 -agonist administration," *Experimental Physiology*, vol. 88, no. 2, pp. 277–284, 2003.
- [43] S. M. DeWire, S. Ahn, R. J. Lefkowitz, and S. K. Shenoy, " β -arrestins and cell signaling," *Annual Review of Physiology*, vol. 69, pp. 483–510, 2007.
- [44] C. A. C. Moore, S. K. Milano, and J. L. Benovic, "Regulation of receptor trafficking by GRKs and arrestins," *Annual Review of Physiology*, vol. 69, pp. 451–482, 2007.
- [45] S. K. Shenoy and R. J. Lefkowitz, "Multifaceted roles of β -arrestins in the regulation of seven-membrane-spanning receptor trafficking and signalling," *Biochemical Journal*, vol. 375, no. 3, pp. 503–515, 2003.
- [46] S. Collins, M. Bouvier, M. A. Bolanowski, M. G. Caron, and R. J. Lefkowitz, "cAMP stimulates transcription of the β_2 -adrenergic receptor gene in response to short-term agonist exposure," *Proceedings of the National Academy of Sciences of the United States of America*, vol. 86, no. 13, pp. 4853–4857, 1989.
- [47] S. Collins, J. Altschmied, O. Herbsman, M. G. Caron, P. L. Mellon, and R. J. Lefkowitz, "A cAMP response element in the β_2 -adrenergic receptor gene confers transcriptional autoregulation by cAMP," *Journal of Biological Chemistry*, vol. 265, no. 31, pp. 19330–19335, 1990.
- [48] L. E. Cornett, F. C. Hiller, S. E. Jacobi, W. Cao, and D. W. McGraw, "Identification of a glucocorticoid response element in the rat β_2 -adrenergic receptor gene," *Molecular Pharmacology*, vol. 54, no. 6, pp. 1016–1023, 1998.
- [49] T. Bengtsson, B. Cannon, and J. Nedergaard, "Differential adrenergic regulation of the gene expression of the β -adrenoceptor subtypes β_1 , β_2 and β_3 in brown adipocytes," *Biochemical Journal*, vol. 347, no. 3, pp. 643–651, 2000.
- [50] J. R. Hadcock and C. C. Malbon, "Regulation of β -adrenergic receptors by "permissive" hormones: glucocorticoids increase steady-state levels of receptor mRNA," *Proceedings of the National Academy of Sciences of the United States of America*, vol. 85, no. 22, pp. 8415–8419, 1988.
- [51] J. C. W. Mak, M. Nishikawa, H. Shirasaki, K. Miyayasu, and P. J. Barnes, "Protective effects of a glucocorticoid on downregulation of pulmonary β_2 -adrenergic receptors in vivo," *Journal of Clinical Investigation*, vol. 96, no. 1, pp. 99–106, 1995.
- [52] J. D. Port, L. Y. Huang, and C. C. Malbon, " β -Adrenergic agonists that down-regulate receptor mRNA up-regulate a M(r) 35,000 protein(s) that selectively binds to β -adrenergic receptor mRNAs," *Journal of Biological Chemistry*, vol. 267, no. 33, pp. 24103–24108, 1992.
- [53] B. G. Tholanikunnel, J. G. Granneman, and C. C. Malbon, "The M(r) 35,000 β -adrenergic receptor mRNA-binding protein binds transcripts of G-protein-linked receptors which undergo agonist-induced destabilization," *Journal of Biological Chemistry*, vol. 270, no. 21, pp. 12787–12793, 1995.
- [54] A. Pende, K. D. Tremmel, C. T. DeMaria et al., "Regulation of the mRNA-binding protein AUF1 by activation of the β -adrenergic receptor signal transduction pathway," *Journal of Biological Chemistry*, vol. 271, no. 14, pp. 8493–8501, 1996.
- [55] B. C. Blaxall, A. C. Pellett, S. C. Wu, A. Pende, and J. D. Port, "Purification and characterization of β -adrenergic receptor mRNA-binding proteins," *Journal of Biological Chemistry*, vol. 275, no. 6, pp. 4290–4297, 2000.
- [56] K. Baar and K. Esser, "Phosphorylation of p70(S6k) correlates with increased skeletal muscle mass following resistance exercise," *American Journal of Physiology*, vol. 276, no. 1, pp. C120–C127, 1999.
- [57] P. A. Tesch and J. Karlsson, "Muscle fiber types and size in trained and untrained muscles of elite athletes," *Journal of Applied Physiology*, vol. 59, no. 6, pp. 1716–1720, 1985.
- [58] T. S. Wong and F. W. Booth, "Skeletal muscle enlargement with weight-lifting exercise by rats," *Journal of Applied Physiology*, vol. 65, no. 2, pp. 950–954, 1988.
- [59] E. B. Colliander and P. A. Tesch, "Effects of eccentric and concentric muscle actions in resistance training," *Acta Physiologica Scandinavica*, vol. 140, no. 1, pp. 31–39, 1990.
- [60] J. O. Holloszy, "Biochemical adaptations in muscle. Effects of exercise on mitochondrial oxygen uptake and respiratory enzyme activity in skeletal muscle," *Journal of Biological Chemistry*, vol. 242, no. 9, pp. 2278–2282, 1967.
- [61] J. O. Holloszy, L. B. Oscai, I. J. Don, and P. A. Molé, "Mitochondrial citric acid cycle and related enzymes: adaptive response to exercise," *Biochemical and Biophysical Research Communications*, vol. 40, no. 6, pp. 1368–1373, 1970.
- [62] D. Pette and C. Heilmann, "Transformation of morphological, functional and metabolic properties of fast twitch muscle as induced by long term electrical stimulation," *Basic Research in Cardiology*, vol. 72, no. 2-3, pp. 247–253, 1977.
- [63] R. S. Staron, R. S. Hikida, and F. C. Hagerman, "Human skeletal muscle fiber type adaptability to various workloads," *Journal of Histochemistry and Cytochemistry*, vol. 32, no. 2, pp. 146–152, 1984.
- [64] R. Mounier, H. Cavalié, G. Lac, and E. Clottes, "Molecular impact of clenbuterol and isometric strength training on rat EDL muscles," *Pflugers Archiv European Journal of Physiology*, vol. 453, no. 4, pp. 497–507, 2007.
- [65] G. S. Lynch, A. Hayes, S. P. Campbell, and D. A. Williams, "Effects of β_2 -agonist administration and exercise on contractile activation of skeletal muscle fibers," *Journal of Applied Physiology*, vol. 81, no. 4, pp. 1610–1618, 1996.
- [66] S. K. Powers, M. Wade, D. Criswell et al., "Role of beta-adrenergic mechanisms in exercise training-induced metabolic changes in respiratory and locomotor muscle," *International Journal of Sports Medicine*, vol. 16, no. 1, pp. 13–18, 1995.
- [67] C. E. Torgan, G. J. Etgen, J. T. Brozinick Jr., R. E. Wilcox, and J. L. Ivy, "Interaction of aerobic exercise training and clenbuterol: effects on insulin-resistant muscle," *Journal of Applied Physiology*, vol. 75, no. 4, pp. 1471–1476, 1993.
- [68] C. E. Torgan, J. T. Brozinick Jr., E. A. Banks, M. Y. Cortez, R. E. Wilcox, and J. L. Ivy, "Exercise training and clenbuterol reduce insulin resistance of obese Zucker rats," *American Journal of Physiology*, vol. 264, no. 3, pp. E373–E379, 1993.
- [69] S. Miura, K. Kawanaka, Y. Kai et al., "An increase in murine skeletal muscle peroxisome proliferator-activated receptor- γ coactivator-1 α (PGC-1 α) mRNA in response to exercise is mediated by β -adrenergic receptor activation," *Endocrinology*, vol. 148, no. 7, pp. 3441–3448, 2007.

- [70] C. Handschin, J. Rhee, J. Lin, P. T. Tarr, and B. M. Spiegelman, "An autoregulatory loop controls peroxisome proliferator-activated receptor γ coactivator 1 α expression in muscle," *Proceedings of the National Academy of Sciences of the United States of America*, vol. 100, no. 12, pp. 7111–7116, 2003.
- [71] T. Akimoto, S. C. Pohnert, P. Li et al., "Exercise stimulates Pgc-1 α transcription in skeletal muscle through activation of the p38 MAPK pathway," *Journal of Biological Chemistry*, vol. 280, no. 20, pp. 19587–19593, 2005.
- [72] Z. Wu, P. Puigserver, U. Andersson et al., "Mechanisms controlling mitochondrial biogenesis and respiration through the thermogenic coactivator PGC-1," *Cell*, vol. 98, no. 1, pp. 115–124, 1999.
- [73] J. Barbier, F. Rannou-Bekono, J. Marchais, P. M. Berthon, P. Delamarche, and F. Carré, "Effect of training on $\beta_1\beta_2\beta_3$ adrenergic and M₂ muscarinic receptors in rat heart," *Medicine and Science in Sports and Exercise*, vol. 36, no. 6, pp. 949–954, 2004.
- [74] R. Stones, A. Natali, R. Billeter, S. Harrison, and E. White, "Voluntary exercise-induced changes in β_2 -adrenoceptor signalling in rat ventricular myocytes," *Experimental Physiology*, vol. 93, no. 9, pp. 1065–1075, 2008.
- [75] J. Ogasawara, M. Sanpei, N. Rahman et al., " β -Adrenergic receptor trafficking by exercise in rat adipocytes: roles of G-protein-coupled receptor kinase-2, β -arrestin-2, and the ubiquitin-proteasome pathway," *FASEB Journal*, vol. 20, no. 2, pp. 350–352, 2006.
- [76] T. Kizaki, T. Takemasa, T. Sakurai et al., "Adaptation of macrophages to exercise training improves innate immunity," *Biochemical and Biophysical Research Communications*, vol. 372, no. 1, pp. 152–156, 2008.
- [77] W. H. Martin, A. R. Coggan, R. J. Spina, and J. E. Saffitz, "Effects of fiber type and training on β -adrenoceptor density in human skeletal muscle," *American Journal of Physiology*, vol. 257, no. 5, pp. E736–E742, 1989.
- [78] R. P. Farrar, K. A. Monnin, D. E. Fordyce, and T. J. Walters, "Uncoupling of changes in skeletal muscle β -adrenergic receptor density and aerobic capacity during the aging process," *Aging*, vol. 9, no. 1-2, pp. 153–158, 1997.
- [79] N. M. Herrera Jr., A. N. Zimmerman, D. D. Dykstra, and L. V. Thompson, "Clenbuterol in the prevention of muscle atrophy: a study of hindlimb-unweighted rats," *Archives of Physical Medicine and Rehabilitation*, vol. 82, no. 7, pp. 930–934, 2001.
- [80] R. J. Zeman, R. Ludemann, and J. D. Etlinger, "Clenbuterol, a β_2 -agonist, retards atrophy in denervated muscles," *American Journal of Physiology*, vol. 252, no. 1, pp. E152–E155, 1987.
- [81] F. Beitzel, P. Gregorevic, J. G. Ryall, D. R. Plant, M. N. Sillence, and G. S. Lynch, " β_2 -adrenoceptor agonist fenoterol enhances functional repair of regenerating rat skeletal muscle after injury," *Journal of Applied Physiology*, vol. 96, no. 4, pp. 1385–1392, 2004.
- [82] I. J. Smith, N. Alamdari, P. O'Neal, P. Gonnella, Z. Aversa, and P. O. Hasselgren, "Sepsis increases the expression and activity of the transcription factor Forkhead Box O 1 (FOXO1) in skeletal muscle by a glucocorticoid-dependent mechanism," *International Journal of Biochemistry and Cell Biology*, vol. 42, no. 5, pp. 701–711, 2010.
- [83] W. Zhao, W. Qin, J. Pan, Y. Wu, W. A. Bauman, and C. Cardozo, "Dependence of dexamethasone-induced Akt/FOXO1 signaling, upregulation of MAFbx, and protein catabolism upon the glucocorticoid receptor," *Biochemical and Biophysical Research Communications*, vol. 378, no. 3, pp. 668–672, 2009.
- [84] X. Sun, D. R. Fischer, T. A. Pritts, C. J. Wray, and P. O. Hasselgren, "Expression and binding activity of the glucocorticoid receptor are upregulated in septic muscle," *American Journal of Physiology*, vol. 282, no. 2, pp. R509–R518, 2002.
- [85] M. A. Pellegrino, G. D'Antona, S. Bortolotto et al., "Clenbuterol antagonizes glucocorticoid-induced atrophy and fibre type transformation in mice," *Experimental Physiology*, vol. 89, no. 1, pp. 89–100, 2004.

Research Article

Titin-Actin Interaction: PEVK-Actin-Based Viscosity in a Large Animal

Charles S. Chung,¹ Julius Bogomolovas,² Alexander Gasch,² Carlos G. Hidalgo,¹ Siegfried Labeit,² and Henk L. Granzier¹

¹Molecular Cardiovascular Research Program, Sarver Heart Center, Department of Physiology, University of Arizona, Tucson, AZ 85724, USA

²Department of Integrative Pathophysiology, Universitätsmedizin Mannheim, University of Heidelberg, Theodor-Kutzer-Ufer 1-3, 68167 Mannheim, Germany

Correspondence should be addressed to Henk L. Granzier, granzier@email.arizona.edu

Received 23 July 2011; Accepted 1 September 2011

Academic Editor: Guy Benian

Copyright © 2011 Charles S. Chung et al. This is an open access article distributed under the Creative Commons Attribution License, which permits unrestricted use, distribution, and reproduction in any medium, provided the original work is properly cited.

Titin exhibits an interaction between its PEVK segment and the actin filament resulting in viscosity, a speed dependent resistive force, which significantly influences diastolic filling in mice. While diastolic disease is clinically pervasive, humans express a more compliant titin (N2BA:N2B ratio ~0.5–1.0) than mice (N2BA:N2B ratio ~0.2). To examine PEVK-actin based viscosity in compliant titin-tissues, we used pig cardiac tissue that expresses titin isoforms similar to that in humans. Stretch-hold experiments were performed at speeds from 0.1 to 10 lengths/s from slack sarcomere lengths (SL) to SL of 2.15 μm . Viscosity was calculated from the slope of stress-relaxation vs stretch speed. Recombinant PEVK was added to compete off native interactions and this found to reduce the slope by 35%, suggesting that PEVK-actin interactions are a strong contributor of viscosity. Frequency sweeps were performed at frequencies of 0.1–400 Hz and recombinant protein reduced viscous moduli by 40% at 2.15 μm and by 50% at 2.25 μm , suggesting a SL-dependent nature of viscosity that might prevent SL “overshoot” at long diastolic SLs. This study is the first to show that viscosity is present at physiologic speeds in the pig and supports the physiologic relevance of PEVK-actin interactions in humans in both health and disease.

1. Introduction

Diastolic (dys)function is of major clinical importance and is characterized by both elastic [1–4] and viscous properties [5–7]. The giant elastic protein titin (also known as connectin [8, 9]) is well known to be related to the elasticity of cardiac muscle impacting the end diastolic pressure volume relationship (for current reviews see [10–12]). These elastic properties arise from the three extensible segments localized in the I-band of the sarcomere: the tandem Ig segments, the proline-glutamic acid-lysine-valine rich PEVK element, and the N2B unique sequence. Viscosity is a speed-dependent resistive property of all biological tissues [13]. Viscosity in cardiac tissues impacts diastolic filling by slowing ventricular pressure relaxation and causing a delayed relaxation phenotype during early filling [2, 5, 6].

The Ig domains that make up the tandem Ig segments of titin’s spring region are a possible intrinsic source of viscosity. Individual Ig domains were originally thought to unfold during stretch and refold during release causing a viscosity [14, 15], but single molecule and simulation studies suggest that the domain unfolding is unlikely to be a prominent process under physiologic conditions [16–20]. Interactions between elements of the extensible I-band of titin and other structures in the sarcomere are another possible source of viscosity. The interaction between titin and actin was hypothesized due to evidence of a viscoelastic interaction in the sarcomere [21], close proximity of the two filament types, and in vitro evidence of titin binding to actin [22–25]. Yamasaki et al. first demonstrated by cosedimentation assays that the PEVK region, but not the N2B element or Ig domains, interacted with actin [13];

Kulke et al.'s F-actin cosedimentation assays supported this finding [26]. Both studies showed that F-actin sliding in the in vitro motility assays was slowed by the addition of recombinant PEVK protein to the assay buffer suggestive that the PEVK adds a viscous force that slows filament sliding. Mechanically, Yamasaki found a reduction in the stress-response of rat cardiac myofibers using exogenously added recombinant PEVK proteins [13]. Kulke utilized gelsolin extraction of thin filaments to abolish native actin-PEVK interaction in myofibrils and found that this reduced viscous stress relaxation [26] (although such extraction potentially releases near-Z-disk titin that is normally firmly bound to actin [27]). Both studies confirmed in the fiber/fibril that a viscous response was due to PEVK-actin interactions. The development of a PEVK KO mouse model [28] provided a new tool to study PEVK-actin interactions and its effect on viscosity. Utilizing skinned cells and fibers from this KO mouse, a 50% reduction was found in the viscosity in stress-relaxation and viscous moduli in sinusoidal experiments using protocols identical to the ones used in this study [29]. Recently, using a PEVK KO mouse, we quantified the contribution of PEVK-actin interactions to viscosity in an ex vivo and in vivo whole heart preparation, and we showed a key physiologic consequence that PEVK-actin interactions control 30% of viscosity during early rapid filling [29].

Cardiac muscle of large mammals, including human, coexpresses both the stiffer N2B isoform and more compliant N2BA isoform unlike that of small rodents that is dominated by expression of the N2B cardiac isoform [10, 12]. The PEVK element of the N2B isoform contains 7 exons with 5 PPAK (proline-rich) motifs that are negatively charged and involved in actin binding [28, 30]. The PEVK region of the cardiac N2BA isoform contains all of the elements expressed in the N2B isoform and additional PEVK exons, including additional PPAK repeats as well as two PolyE (glutamic acid rich) motifs [30]. The PolyE motifs appear to have a stronger binding affinity to actin than the PPAK motifs [31]. Because of these changes in PEVK expression and the expression of additional Ig domains in N2BA dominant tissues [12], direct extrapolations from the findings in small animals to humans are difficult. Thus, while characterization of the PEVK-actin interaction shows physiologic relevance in small animals, actual application in large mammals including humans remains unclear. To study viscosity in tissues containing a high N2BA:N2B ratio, we utilized tissues from the pig. Viscous properties were probed using both stretch hold and frequency sweep perturbations to quantify viscosity and we utilized a competition assay with recombinant PEVK proteins to disrupt the native PEVK-actin interactions.

2. Methods

2.1. Porcine-Skinned Fiber Preparation and Mechanics. Porcine LV tissue was obtained as previously described [32]. Animal experiments were approved by the University of Arizona Institutional Animal Care and Use Committee and followed NIH guidelines for "Using Animals in Intramural Research." Briefly, the heart was rapidly obtained from the pig <5 minutes after sacrifice, washed with a calcium-free

HEPES-buffered solution ([in mM] 10 HEPES; 133.5 NaCl, 5 KCl, 1.2 NaH₂PO₄; 1.2 MgSO₄, 11 glucose, 4 Na-Pyruvate with 2.5 U/L insulin, pH 7.44), dissected into small strips, and placed in a skinning solution composed of relaxing solution ([in mM]: 10 BES, 10 EGTA, 6.56 MgCl₂, 5.88 Na-ATP, 1 DTT, 46.35 potassium-propionate, 15 creatine phosphate) with 1% Triton X-100 (Thermo Scientific, Waltham, Mass) and a high concentration of protease inhibitors ([in mM] 0.1 E64, 0.4 Leupeptin and 0.5 PMSF) for 24–48 hrs at 4°C. After skinning, tissues were washed with Triton-free relaxing solution with protease inhibitors then infiltrated with a 50% (vol/vol) solution of relaxing solution and glycerol at 4°C then stored at –20°C. Small fibers were dissected, glued to aluminum clips, and attached at either end to a force transducer (AE801, SensorOne, Sausalito, Calif) and length motor (308B, Aurora Scientific, Aurora ON, Canada) and washed with relaxing solution with inhibitors. Cross-sectional area (CSA) was measured ($0.023 \pm 0.002 \text{ mm}^2$). All fibers activated at 2.0 μm sarcomere lengths (SL) using a pCa 4.0 solution to confirm fiber quality, achieving tensions of $39.5 \pm 2.5 \text{ mN/mm}^2$. Length perturbations and force measurements were performed using a custom LabVIEW interface (National Instruments, Austin, Tex)

Cardiac muscle fibers were stretched with two length perturbations to evaluate viscosity [29]. The fibers were stretched using a stretch-hold-release protocol from their slack sarcomere length to a SL of 2.15 μm at 3 speeds: 0.1, 1.0, and 10.0 lengths/s. After stretch, the fibers were held at their stretched length for 90 seconds, followed by a symmetric release. A sinusoidal frequency sweep was applied at the end of hold of the 0.1 length/s stretch with frequencies from 0.1 to 400 Hz at an amplitude of $\pm 2\%$ of the fiber length. 10 minutes of recovery time in between stretches was used. In order to probe the dependence on sarcomeric strain, frequency sweeps were also imparted at a SL of 2.25 μm (fibers were stretched from slack to a SL of 2.25 μm at 0.1 lengths/sec).

To test the magnitude of PEVK-actin interactions, recombinant PEVK fragments were expressed in *E. coli* and purified as previously described [32]. Briefly, cDNA fragments were amplified from human cDNA with primer pairs corresponding to the human cardiac I27-PEVK-I84 fragment with the flanking Ig domains included to enhance the stability of the protein. Amplified cDNA fragments were inserted into a pETM11 vector, expressed in *E. coli*, and the obtained fragments were sequence verified. Fragments were purified then dialyzed into PBS ([in mM] 2.7 KCl, 1.5 KH₂PO₄, 137 NaCl, 8 Na₂PO₄) and 10% glycerol, aliquoted, flash frozen, and stored at –80°C. For use, proteins were thawed and dialyzed in relaxing solution with protein inhibitors. PEVK fragments were added to the pig fibers to a final concentration of 22 μM in relaxing solution with protease inhibitors, allowed to incubate for >1 hr, and probed with the mechanical protocol described above.

2.2. Analysis of Skinned Muscle Mechanics. Data was analyzed offline in a custom LabVIEW VI. Stress was calculated by dividing measured force by cross-sectional area. For stretch-hold experiments, stress was measured at the end of the

stretch to calculate the peak stress and again at the end of the hold (90 sec after peak) to calculate a steady state stress. Analysis methodology was adapted from previous work [33, 34]. The viscous stress is calculated as the peak minus steady-state stress during the hold. The viscosity was calculated as the slope between the viscous stress and the \log_{10} of the stretch speed (in lengths/s).

Frequency sweep data was analyzed to obtain viscous moduli [35]. The stress was used to first calculate the complex stiffness as the stress divided by the amplitude of the imposed length change (normalized to fiber length). Phase delay was calculated as the phase difference between the stress and strain signals. The viscous modulus was then calculated as complex stiffness times the sine of the phase delay [35] (see inset of Figure 3(a)) at all frequencies.

2.3. Statistics. Data analysis was performed in MS Excel. Student *t*-test was used to compare the viscosity (slope and viscous modulus at a given frequency) between groups. A *P* value < 0.05 was considered significant.

3. Results

Using titin protein gels, we first established the titin isoform expression ratio of porcine cardiac LV tissues and found that the N2BA:N2B isoform ratio is ~ 1.0 (Figures 1(a) and 1(b)). This expression ratio is much higher than that of the mouse LV (~ 0.2) and is slightly higher than that of normal human LV and similar to that of human LV of DCM patients (Figure 1(b)). To quantify viscosity, we stretched skinned pig LV muscle from their slack SL ($\sim 1.9 \mu\text{m}$) to $2.15 \mu\text{m}$ and then held length constant for 90 sec to observe stress relaxation, followed by a release back to the slack length. Figure 1(c) shows two examples of such stretch-hold-release experiments, one carried out in relaxing solution (Ctrl) and the other in relaxing solution to which exogenous PEVK had been added (we confirmed the purity of the expressed PEVK using gels, see inset of Figure 1(c)). We measured viscous stress (σ_v) from the stress relaxation during the hold phase of the protocol (explained at top of Figure 2(a)). Viscous stress was measured at three stretch speeds encompassing subphysiologic (0.1 lengths/s) to supraphysiologic speeds (10 lengths/s) and the magnitude of the stress relaxation, defined by the peak minus steady-state stress (Figure 2(a), inset), was determined at each speed. Viscosity was quantified as the slope of stress relaxation versus (log) speed. At SL of $2.15 \mu\text{m}$, the viscosity (slope) was reduced by 35% ($P = 0.03$) when fibers were incubated with recombinant PEVK (Figure 2(b)). These results indicate that PEVK-actin interactions are present and relevant in tissues expressing high levels of the compliant titin N2BA isoform.

We also measured the viscous moduli during a sinusoidal oscillation protocol at frequencies from 0.1 to 400 Hz and using an amplitude of 2% of the fiber length and repeated the protocol in the absence and presence of recombinant PEVK. Frequency analysis provides a robust method to quantify the viscous response of a tissue at a wide array of speeds

[29, 35]. To quantify the modulus, the ratio of the stress response and length perturbation was first used to calculate a complex stiffness and the phase delay between stress and length is used to calculate the viscous modulus (Figure 3(a)). The viscous modulus was reduced by 40% by the treatment with recombinant PEVK at SL of $2.15 \mu\text{m}$ (Figure 3(b)). We also performed experiments at a SL of $2.25 \mu\text{m}$ and found that the viscous moduli were reduced by 50% at all frequencies (Figure 3(c)). Importantly, the viscous modulus maintained a constant reduction at physiologic frequencies (~ 0.5 – 2 Hz corresponding to the heart rate in the pig) for both SL ranges. These data indicate that the introduction of recombinant PEVK does reduce the viscosity of the system at all frequencies, including frequencies corresponding to physiologic heart rates, and reveals that it does this in a SL-dependent manner.

4. Discussion

In resisting the rapid expansion of the left ventricle, viscosity is an important modulator of diastolic function [2, 5–7]. While previous work has shown a contribution of PEVK-actin interactions to viscosity both in vitro [13, 26, 36, 37] and in vivo [29], such findings were largely obtained in small rodents that express titin that is stiffer than in larger mammals and often at speeds below [13, 36] or above [26] physiologic rates. Yet the relevance to human cardiac function and dysfunction is not direct, owing to the increased expression of the compliant N2BA isoform that contains additional Ig domains and a longer PEVK domain. To determine the viscous properties of titin in a large animal model with a human-like titin isoform expression ratio, we investigated pig myocardial tissues. Additionally, we utilized recombinant PEVK proteins to interrupt native PEVK-actin interactions.

PEVK-actin interactions in the pig were significantly reduced by competitive binding of recombinant PEVK to the actin filament. This reduced the viscous response to stretch by 35% and the viscous moduli by more than 40% at a SL of $2.15 \mu\text{m}$ (Figures 2 and 3). At longer sarcomere lengths ($2.25 \mu\text{m}$) that are likely to be reached during diastole in pigs [38], the viscous moduli obtained with the sinusoidal analysis increased to $\sim 50\%$. Thus, PEVK-actin interaction is a major source of viscosity in large mammals like the pig. These novel findings are the first to quantify viscosity across physiologic speeds in tissues expressing high levels of compliant N2BA isoforms.

Our findings indicate that PEVK-actin interaction is likely to be physiologically important in humans where viscosity influences relaxation [2, 5, 6]. The characterization of delayed relaxation [39] has long been a clinical indicator of diastolic dysfunction in echocardiography. Recent advances in modeling further support that the delayed relaxation phenotype is caused by a viscous force [2]. Recently, we used transmitral Doppler echocardiography in a KO mouse deficient in PEVK and found a significant reduction in viscosity during early rapid filling [29]. The ability to translate the echocardiographic findings in mice to humans could not be fully appreciated until the present results on

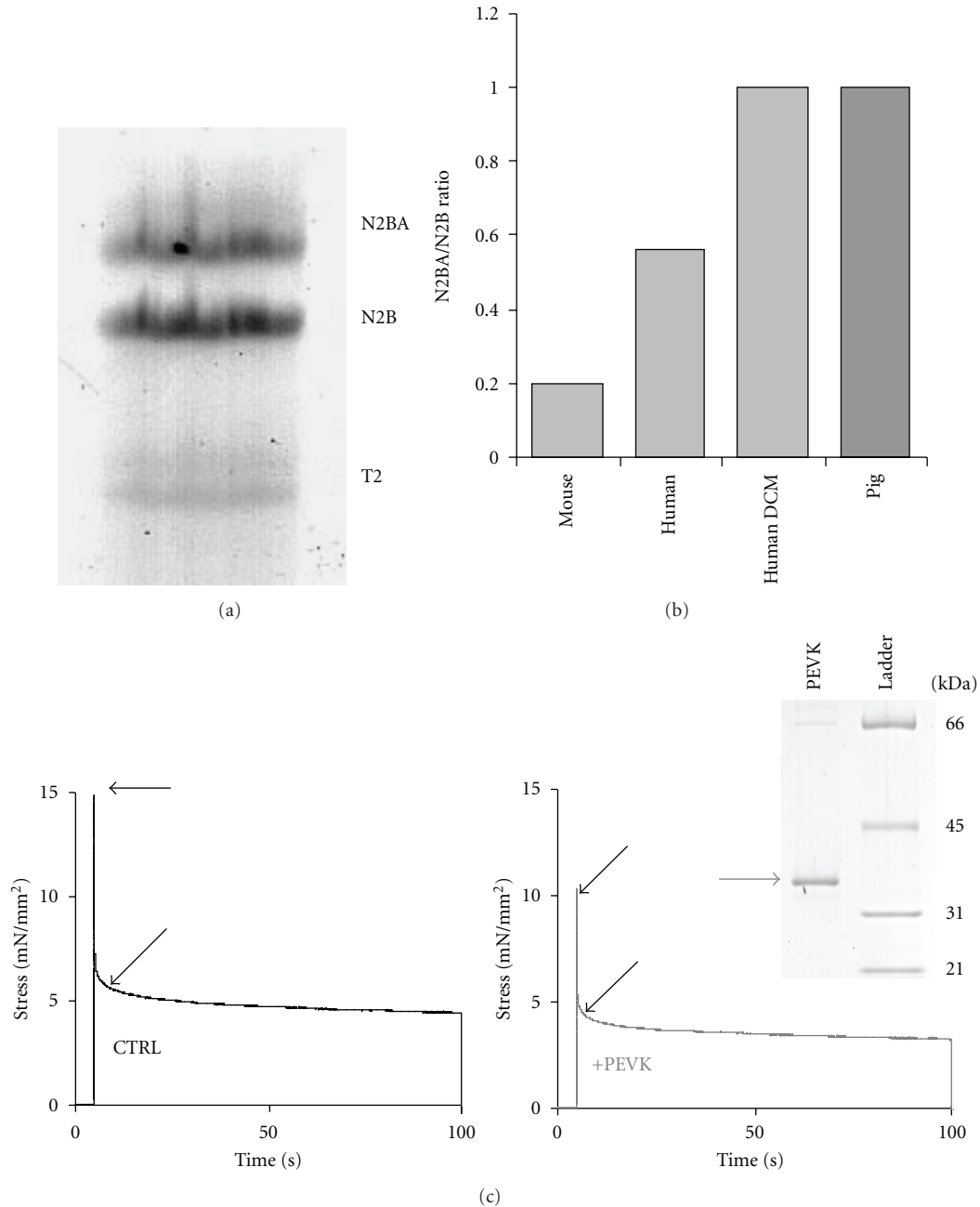


FIGURE 1: Porcine myocardial characteristics. (a) Pig LV tissues electrophoresed on a large pore 1% agarose gel indicate a nearly 1:1 N2BA:N2B ratio. (b) N2BA/N2B ratios range from 0.2 in small animals to 1.0 in human dilated cardiomyopathy (DCM). (c) Example mechanical perturbation of pig tissue from slack SL to $2.15 \mu\text{m}$ at 10.0 lengths/s in control conditions and incubated with recombinant PEVK protein to inhibit native PEVK-actin interactions showing reduced stress relaxation (arrows). Inset: SDS-PAGE indicating the high purity of the recombinant PEVK protein fraction that was used. See text for details.

pig myocardium that showed a clear presence of viscosity in tissues with a high N2BA:N2B ratio. Our work establishes that despite the longer PEVK element and distinct sequence composition of the N2BA PEVK, PEVK-actin interactions are present in myocardial tissues with human-like titin isoform expression. Thus, this interaction is conserved across species, supporting the importance of these interactions to diastolic function.

The SL-dependence of the viscous modulus (Figure 3) was unexpected and may indicate that at longer SL where the PEVK is stretched to a higher degree additional binding site for actin are available than at short SL or, alternatively, that the lattice compression that occurs at long SL enhances the interaction [29]. The increased viscosity at longer SL might reduce any potential SL “overshoot” during filling [36, 40] and may allow for more precise end-diastolic SL control.

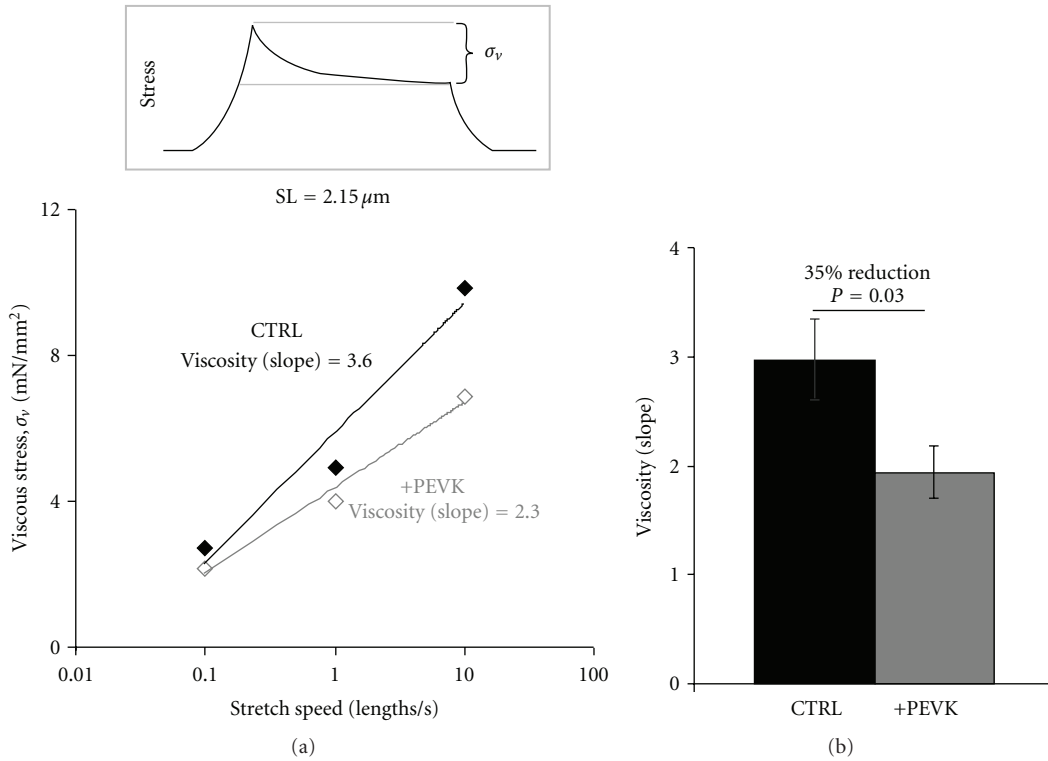


FIGURE 2: Measurement of viscosity from stress relaxation data in pig tissue. (a) Example viscosity data derived from stress relaxation in a fiber untreated (CTRL, black) and in presence of recombinant PEVK protein (+PEVK, gray). Inset: schematic of explaining how viscous stress (σ_v) was determined. (b) Exogenously added PEVK reduces the viscosity (slope) by 35%. See text for details.

The competition assays with recombinant PEVK reduced viscosity by only 40–50%. This incomplete inhibition is possibly due to the inability of the added PEVK to compete off all native PEVK-actin interactions. Alternatively, it indicates that there is an additional source of viscosity, a possibility that is consistent with results of the PEVK KO mouse model that also show that in absence of the PEVK element myocardial tissue continues to display ~50% of the viscosity found in wildtype myocardium [29]. Stretch-hold and frequency sweep protocols in myofilament extracted mouse fibers have negligible viscosity suggesting that the extracellular matrix contributes little to viscosity of the myocardium [29]. Thus, the non-PEVK source of viscosity is likely to arise from interactions that involve the myofilaments. In our studies, in PEVK KO mice, we evaluated microtubules, a known source of viscosity under pathological conditions [34, 41, 42]. However, colchicine treatment produced no effect on viscosity of the intact heart neither in WT nor in PEVK KO mice [29], suggesting that, in normal hearts, there is little contribution of microtubules to viscosity. Thin-thick filament interaction is unlikely because this predicts that viscosity would be increased when the myofilament lattice is compressed in PEVK KO tissue and this is not what we observed in our previous studies [29]. Possibilities that require future testing are intermolecular interactions between adjacent titin molecules and interactions between intermediate filaments and any

of the myofilament types. In summary, although additional sources of viscosity are likely to exist, the PEVK-actin interaction is the only well-established molecular source of viscosity in cardiac tissues and contributes up to half of the total viscosity of skinned myocardium in relaxing solution.

It has previously been shown that PEVK-actin interaction can be regulated by S100A1, a calcium binding protein present in cardiac tissues (for recent review see [43]). S100A1 is a member of the S100 calcium binding proteins that is preferentially found in cardiac tissues. S100A1 normally targets to calcium handling proteins (the sarcoplasmic reticulum, RyR2), but also localizes in the I-band of the sarcomere [13]. When present in the sarcomere and activated by the presence of physiological calcium levels, S100A1 inhibits PEVK-actin interactions [13, 36]. Thus, PEVK-actin interaction-based viscosity can be turned off during systole when high calcium levels are present in the cytosol and turned on again during diastole when calcium levels fall. A second mechanism shown to influence PEVK-actin interactions is protein kinase C- α (PKC α) phosphorylation of titin. PKC α phosphorylation occurs at two sites in the PEVK element that are conserved across a large number of mammalian species including the mouse, pig, and human [32]. In both pig and mouse skinned cardiac fibers [32, 44], PKC α treatment increased viscosity by 20–30% at physiological speeds; the effect was amplified by pretreating

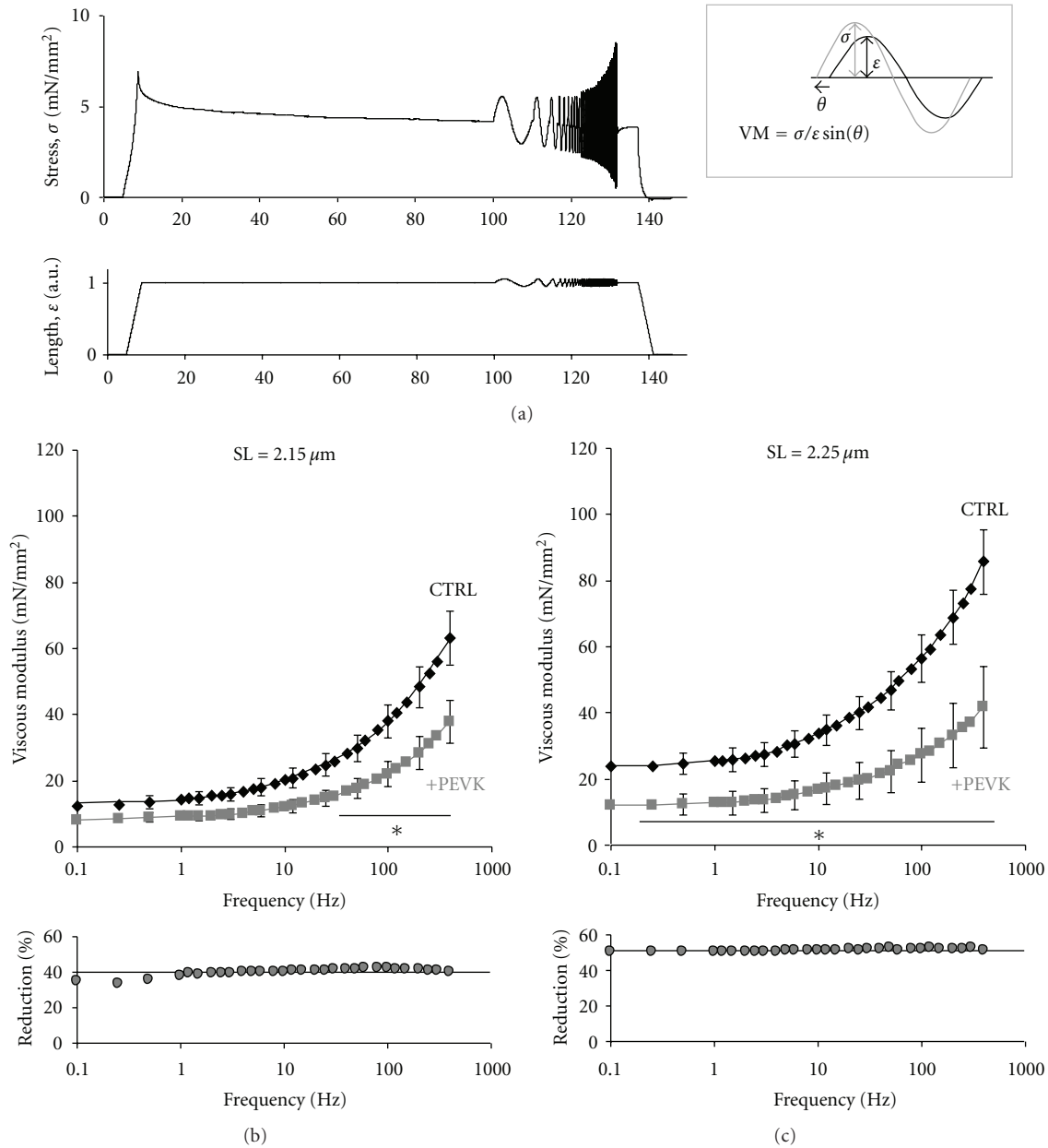


FIGURE 3: Measurement of viscous moduli via sinusoidal analysis in pig tissue. (a) The frequency sweep perturbation is imparted after a 90-second hold at SL of 2.15 or 2.25 μm . The viscous modulus is calculated utilizing the magnitude of the stress response, magnitude of the length perturbation and phase delay (schematic, right). (b) The viscous modulus measured in control tissues at SL of 2.15 μm (CTRL, black) is reduced in the presence of recombinant PEVK proteins (+PEVK, gray) by 40%. (c) At a SL of 2.25 μm , adding PEVK protein (+PEVK, gray) reduces the viscous modulus at all frequencies. * indicates $P < 0.05$ across the frequencies noted by the horizontal bar. See text for details.

the fibers by protein phosphatase 1 (PP1) to dephosphorylate titin [32]. These changes in viscosity indicate a potentially large dynamic range by which viscosity can be modulated. The understanding of the functional effects of PKC α phosphorylation and its regulation may aid in our understanding of the underlying dysfunction, for example, in heart failure where PKC α is upregulated [45, 46]. These factors provide a potential path for clinical management of cardiac diastolic dysfunction.

5. Conclusion

This study establishes the presence of PEVK-actin interactions in a large mammal, the pig, and is the first to conclusively determine with physiological stretch protocols the magnitude of PEVK-actin interactions in hearts with a human-like titin isoform expression ratio. Competition assays with exogenous recombinant protein show that the magnitude of this contribution is up to 50% of the total

viscosity seen in these tissues. Furthermore, we found that PEVK-based viscosity is larger at longer SL, a property that might aid in preventing SL overshoot at the end of filling, and because of the influence of PEVK-actin interactions on early rapid filling, modulation of these interactions are of potential clinical importance.

Acknowledgments

The authors gratefully acknowledge the assistance of Luann Wyly for expert animal care and other lab members for advice and assistance. This work was supported by grants from the American Heart Association (0825748G) and the NIH (T32 HL07249-31) to C. S. Chung; by the Deutsche Forschungsgemeinschaft to S. Labeit; the NIH (R01 HL062881) and a generous gift from Alan and Alfie Norville to H. L. Granzier.

References

- [1] M. Ohno, C. P. Cheng, and W. C. Little, "Mechanism of altered patterns of left ventricular filling during the development of congestive heart failure," *Circulation*, vol. 89, no. 5, pp. 2241–2250, 1994.
- [2] L. Shmuylovich and S. J. Kovács, "E-wave deceleration time may not provide an accurate determination of LV chamber stiffness if LV relaxation/viscoelasticity is unknown," *American Journal of Physiology—Heart and Circulatory Physiology*, vol. 292, no. 6, pp. H2712–H2720, 2007.
- [3] M. R. Zile and D. L. Brutsaert, "New concepts in diastolic dysfunction and diastolic heart failure: part I: diagnosis, prognosis, and measurements of diastolic function," *Circulation*, vol. 105, no. 11, pp. 1387–1393, 2002.
- [4] C. S. Chung and H. L. Granzier, "Contribution of titin and extracellular matrix to passive pressure and measurement of sarcomere length in the mouse left ventricle," *Journal of Molecular and Cellular Cardiology*, vol. 50, no. 4, pp. 731–739, 2011.
- [5] C. S. Chung and S. J. Kovács, "Physical determinants of left ventricular isovolumic pressure decline: model prediction with in vivo validation," *American Journal of Physiology—Heart and Circulatory Physiology*, vol. 294, no. 4, pp. H1589–H1596, 2008.
- [6] D. A. Kass, J. G. F. Bronzwaer, and W. J. Paulus, "What mechanisms underlie diastolic dysfunction in heart failure?" *Circulation Research*, vol. 94, no. 12, pp. 1533–1542, 2004.
- [7] S. J. Kovács, B. Barzilai, and J. E. Pérez, "Evaluation of diastolic function with Doppler echocardiography: the PDF formalism," *American Journal of Physiology—Heart and Circulatory Physiology*, vol. 252, no. 1, part 2, pp. H178–H187, 1987.
- [8] K. Wang, J. McClure, and A. Tu, "Titin: major myofibrillar components of striated muscle," *Proceedings of the National Academy of Sciences of the United States of America*, vol. 76, no. 8, pp. 3698–3702, 1979.
- [9] K. Maruyama, "Connectin, an elastic protein from myofibrils," *Journal of Biochemistry*, vol. 80, no. 2, pp. 405–407, 1976.
- [10] M. M. Lewinter and H. Granzier, "Cardiac titin: a multifunctional giant," *Circulation*, vol. 121, no. 19, pp. 2137–2145, 2010.
- [11] W. A. Linke and M. Krüger, "The giant protein titin as an integrator of myocyte signaling pathways," *Physiology*, vol. 25, no. 3, pp. 186–198, 2010.
- [12] H. L. Granzier and S. Labeit, "The giant protein titin: a major player in myocardial mechanics, signaling, and disease," *Circulation Research*, vol. 94, no. 3, pp. 284–295, 2004.
- [13] R. Yamasaki, M. Berri, Y. Wu et al., "Titin-actin interaction in mouse myocardium: passive tension modulation and its regulation by calcium/S100A1," *Biophysical Journal*, vol. 81, no. 4, pp. 2297–2313, 2001.
- [14] H. P. Erickson, "Reversible unfolding of fibronectin type III and immunoglobulin domains provides the structural basis for stretch and elasticity of titin and fibronectin," *Proceedings of the National Academy of Sciences of the United States of America*, vol. 91, no. 21, pp. 10114–20118, 1994.
- [15] L. Tskhovrebova, J. Trinick, J. A. Sleep, and R. M. Simmons, "Elasticity and unfolding of single molecules of the giant muscle protein titin," *Nature*, vol. 387, no. 6630, pp. 308–312, 1997.
- [16] M. Rief, M. Gautel, A. Schemmel, and H. E. Gaub, "The mechanical stability of immunoglobulin and fibronectin III domains in the muscle protein titin measured by atomic force microscopy," *Biophysical Journal*, vol. 75, no. 6, pp. 3008–3014, 1998.
- [17] M. Gautel, E. Lehtonen, and F. Pietruschka, "Assembly of the cardiac I-band region of titin/connectin: expression of the cardiac-specific regions and their structural relation to the elastic segments," *Journal of Muscle Research and Cell Motility*, vol. 17, no. 4, pp. 449–461, 1996.
- [18] K. Trombitás, M. Greaser, S. Labeit et al., "Titin extensibility in situ: entropic elasticity of permanently folded and permanently unfolded molecular segments," *Journal of Cell Biology*, vol. 140, no. 4, pp. 853–859, 1998.
- [19] K. Trombitás, Y. Wu, M. McNabb et al., "Molecular basis of passive stress relaxation in human soleus fibers: assessment of the role of immunoglobulin-like domain unfolding," *Biophysical Journal*, vol. 85, no. 5, pp. 3142–3153, 2003.
- [20] M. Helmes, K. Trombitás, T. Centner et al., "Mechanically driven contour-length adjustment in rat cardiac titin's unique N2B sequence: titin is an adjustable spring," *Circulation Research*, vol. 84, no. 11, pp. 1339–1352, 1999.
- [21] H. Granzier, M. Kellermayer, M. Helmes, and K. Trombitás, "Titin elasticity and mechanism of passive force development in rat cardiac myocytes probed by thin-filament extraction," *Biophysical Journal*, vol. 73, no. 4, pp. 2043–2053, 1997.
- [22] T. Funatsu, E. Kono, H. Higuchi et al., "Elastic filaments in situ in cardiac muscle: deep-etch replica analysis in combination with selective removal of actin and myosin filaments," *Journal of Cell Biology*, vol. 120, no. 3, pp. 711–724, 1993.
- [23] M. S. Kellermayer and H. L. Granzier, "Calcium-dependent inhibition of in vitro thin-filament motility by native titin," *FEBS Letters*, vol. 380, no. 3, pp. 281–286, 1996.
- [24] S. Kimura, K. Maruyama, and Y. P. Huang, "Interactions of muscle β -connectin with myosin, actin, and actomyosin at low ionic strengths," *Journal of Biochemistry*, vol. 96, no. 2, pp. 499–506, 1984.
- [25] A. Soteriou, M. Gamage, and J. Trinick, "A survey of interactions made by the giant protein titin," *Journal of Cell Science*, vol. 104, no. 1, part 1, pp. 119–123, 1993.
- [26] M. Kulke, S. Fujita-Becker, E. Rostkova et al., "Interaction between PEVK-titin and actin filaments origin of a viscous force component in cardiac myofibrils," *Circulation Research*, vol. 89, no. 10, pp. 874–881, 2001.
- [27] W. A. Linke, M. Ivemeyer, S. Labeit, H. Hinssen, J. C. Ruegg, and M. Gautel, "Actin-titin interaction in cardiac myofibrils: probing a physiological role," *Biophysical Journal*, vol. 73, no. 2, pp. 905–919, 1997.

- [28] H. L. Granzier, M. H. Radke, J. Peng et al., "Truncation of titin's elastic PEVK region leads to cardiomyopathy with diastolic dysfunction," *Circulation Research*, vol. 105, no. 6, pp. 557–564, 2009.
- [29] C. S. Chung, M. Methawasin, O. L. Nelson et al., "Titin based viscosity in ventricular physiology: an integrative investigation of PEVK-actin interactions," *Journal of Molecular and Cellular Cardiology*, vol. 51, no. 3, pp. 428–434, 2011.
- [30] M. Greaser, "Identification of new repeating motifs in titin," *Proteins*, vol. 43, no. 2, pp. 145–149, 2001.
- [31] A. Nagy, P. Cacciafesta, L. Grama, A. Kengyel, A. Málnási-Csizmadia, and M. S. Kellermayer, "Differential actin binding along the PEVK domain of skeletal muscle titin," *Journal of Cell Science*, vol. 117, part 24, pp. 5781–5789, 2004.
- [32] C. Hidalgo, B. Hudson, J. Bogomolovas et al., "PKC phosphorylation of titin's PEVK element: a novel and conserved pathway for modulating myocardial stiffness," *Circulation Research*, vol. 105, no. 7, pp. 631–638, 2009.
- [33] P. P. de Tombe and H. E. ter Keurs, "An internal viscous element limits unloaded velocity of sarcomere shortening in rat myocardium," *Journal of Physiology*, vol. 454, pp. 619–642, 1992.
- [34] T. S. Harris, C. F. Baicu, C. H. Conrad et al., "Constitutive properties of hypertrophied myocardium: cellular contribution to changes in myocardial stiffness," *American Journal of Physiology—Heart and Circulatory Physiology*, vol. 282, no. 6, pp. H2173–H2182, 2002.
- [35] H. L. Granzier and K. Wang, "Interplay between passive tension and strong and weak binding cross-bridges in insect indirect flight muscle: a functional dissection by gelsolin-mediated thin filament removal," *Journal of General Physiology*, vol. 101, no. 2, pp. 235–270, 1993.
- [36] H. Fukushima, C. S. Chung, and H. Granzier, "Titin-isoform dependence of titin-actin interaction and its regulation by S100A1/ Ca²⁺ in skinned myocardium," *Journal of Biomedicine and Biotechnology*, vol. 2010, Article ID 727239, 9 pages, 2010.
- [37] W. A. Linke, M. Kulke, H. Li et al., "PEVK domain of titin: an entropic spring with actin-binding properties," *Journal of Structural Biology*, vol. 137, no. 1-2, pp. 194–205, 2002.
- [38] M. M. Lewinter, J. Popper, M. McNabb, L. Nyland, S. B. Bell, and H. Granzier, "Extensible behavior of titin in the miniswine left ventricle," *Circulation*, vol. 121, no. 6, pp. 768–774, 2010.
- [39] S. F. Nagueh, C. P. Appleton, T. C. Gillebert et al., "Recommendations for the evaluation of left ventricular diastolic function by echocardiography," *Journal of the American Society of Echocardiography*, vol. 22, no. 2, pp. 107–133, 2009.
- [40] L. Shmuylovich, C. S. Chung, and S. J. Kovács, "Point: left ventricular volume during diastasis is the physiological in vivo equilibrium volume and is related to diastolic suction," *Journal of Applied Physiology*, vol. 109, no. 2, pp. 606–608, 2010.
- [41] J. D. Stroud, C. F. Baicu, M. A. Barnes, F. G. Spinale, and M. R. Zile, "Viscoelastic properties of pressure overload hypertrophied myocardium: effect of serine protease treatment," *American Journal of Physiology—Heart and Circulatory Physiology*, vol. 282, no. 6, pp. H2324–H2335, 2002.
- [42] S. Nishimura, S. Nagai, M. Katoh et al., "Microtubules modulate the stiffness of cardiomyocytes against shear stress," *Circulation Research*, vol. 98, no. 1, pp. 81–87, 2006.
- [43] M. Vlkers, D. Rohde, C. Goodman, and P. Most, "S100A1: a regulator of striated muscle sarcoplasmic reticulum Ca²⁺ handling, sarcomeric, and mitochondrial function," *Journal of Biomedicine and Biotechnology*, vol. 2010, Article ID 178614, 10 pages, 2010.
- [44] B. D. Hudson, C. G. Hidalgo, M. Gotthardt, and H. L. Granzier, "Excision of titin's cardiac PEVK spring element abolishes PKC α -induced increases in myocardial stiffness," *Journal of Molecular and Cellular Cardiology*, vol. 48, no. 5, pp. 972–978, 2010.
- [45] E. Churchill, G. Budas, A. Vallentin, T. Koyanagi, and D. Mochly-Rosen, "PKC isozymes in chronic cardiac disease: possible therapeutic targets?" *Annual Review of Pharmacology and Toxicology*, vol. 48, pp. 569–599, 2008.
- [46] S. S. Palaniyandi, L. Sun, J. C. Ferreira, and D. Mochly-Rosen, "Protein kinase C in heart failure: a therapeutic target?" *Cardiovascular Research*, vol. 82, no. 2, pp. 229–239, 2009.

Research Article

The IQ Motif is Crucial for Ca_v1.1 Function

Katarina Stroffekova^{1,2}

¹ Department of Biophysics, P. J. Šafárik University, Košice 04001, Slovakia

² Department of Biology, Utah State University, Logan, UT 84322, USA

Correspondence should be addressed to Katarina Stroffekova, katarina.stroffekova@upjs.sk

Received 14 July 2011; Revised 19 August 2011; Accepted 22 August 2011

Academic Editor: Guy Benian

Copyright © 2011 Katarina Stroffekova. This is an open access article distributed under the Creative Commons Attribution License, which permits unrestricted use, distribution, and reproduction in any medium, provided the original work is properly cited.

Ca²⁺-dependent modulation via calmodulin, with consensus CaM-binding IQ motif playing a key role, has been documented for most high-voltage-activated Ca²⁺ channels. The skeletal muscle Ca_v1.1 also exhibits Ca²⁺-/CaM-dependent modulation. Here, whole-cell Ca²⁺ current, Ca²⁺ transient, and maximal, immobilization-resistant charge movement (Q_{\max}) recordings were obtained from cultured mouse myotubes, to test a role of IQ motif in function of Ca_v1.1. The effect of introducing mutation (IQ to AA) of IQ motif into Ca_v1.1 was examined. In dysgenic myotubes expressing YFP-Ca_v1.1_{AA}, neither Ca²⁺ currents nor evoked Ca²⁺ transients were detectable. The loss of Ca²⁺ current and excitation-contraction coupling did not appear to be a consequence of defective trafficking to the sarcolemma. The Q_{\max} in dysgenic myotubes expressing YFP-Ca_v1.1_{AA} was similar to that of normal myotubes. These findings suggest that the IQ motif of the Ca_v1.1 may be an unrecognized site of structural and functional coupling between DHPR and RyR.

1. Introduction

Calcium entering the cell through voltage-gated Ca²⁺ channels plays an important role in mediating a wide variety of cellular events and includes feedback processes that regulate activity of the channel itself. The Ca²⁺-dependent modulation of channel activity mediated by the Ca²⁺-binding protein calmodulin (CaM) is found in many ion channels including the Ca_v1 family [1]. Ca²⁺-dependent inactivation (CDI) of Ca_v1.2 is mediated by CaM, and its structural determinants have been assigned to the proximal region of the C-terminus of Ca_v1.2 [1, 2]. Three domains have been identified within this region: a Ca²⁺ binding EF-hand motif, a CaM-tethering site, and a CaM-binding IQ motif. The EF-hand motif, located ~16 residues beyond the end of the last transmembrane segment (IVS6), is absolutely necessary for CDI. The CaM-tethering site, which consists of both preIQ₃ and IQ motifs, resides 50 amino acids downstream from the EF-hand motif and binds Ca²⁺-free CaM (apo-CaM) at resting [Ca²⁺]_i. The IQ motif resides downstream from the EF-hand motif and the pre-IQ₃ domain, and it binds Ca²⁺-CaM. When the interaction of CaM with either of these domains is compromised, CDI is reduced or eliminated [1, 2].

Recently, it has been demonstrated that the skeletal muscle L-type Ca²⁺ channel (Ca_v1.1) also displays CDI mediated by CaM and that CaM associates with Ca_v1.1 *in vivo* [3]. The initial 200 amino acids of the C-terminus of the Ca_v1.1 are highly conserved and contain the above-described domains including the IQ motif. CaM binding to the IQ motif of Ca_v1.2 channel has been shown to be necessary for CDI, and the mutation of the isoleucine (I1624) and glutamine (Q1625) to alanines (AA) in the IQ motif of Ca_v1.2 resulted in ablation of CDI and significant reduction of apoCaM binding to Ca_v1.2 [1, 2, 4]. Whether the IQ motif in Ca_v1.1 plays a similar role remains to be determined.

In the present work, myotubes cultured from normal and dysgenic (lacking endogenous Ca_v1.1) mice were used to investigate the role of the IQ motif in the function of Ca_v1.1. The results presented demonstrate that the IQ motif in the C-terminus of Ca_v1.1 is critical for function of Ca_v1.1 as a voltage sensor as well as Ca²⁺ channel. Furthermore, the results indicate that the IQ motif may be a previously unrecognized site of protein-protein interaction between Ca_v1.1 and the skeletal muscle ryanodine receptor (RyR1) and may play a role in skeletal muscle excitation-contraction (EC) coupling.

2. Experimental Procedures

2.1. Molecular Biology. The coding sequence of yellow fluorescent protein- (YFP-) tagged $\text{Ca}_v1.1$ channel (YFP- $\text{Ca}_v1.1$) was a gift from Dr. K. Beam and is described in detail elsewhere [5]. The residues isoleucine (I) and glutamine (Q) at codons 1529-1530 of rabbit $\text{Ca}_v1.1$ [6] were substituted with alanine (A) using the QuikChange II mutagenesis kit (Stratagene, La Jolla, CA), using the YFP- $\text{Ca}_v1.1$ as a template. The construct YFP- $\text{Ca}_v1.1_{AA}$ was verified by restriction digest analysis and sequencing.

2.2. Cell Cultures. Primary myotubes were cultured from normal or dysgenic newborn mouse skeletal muscle as previously described [3]. For confocal microscopy purposes, primary cultures of myotubes were plated onto 35 mm culture dishes with integral no. 0 glass coverslip bottoms (MatTek) instead of Primaria dishes. Approximately one week after plating, dysgenic myotubes were injected with expression plasmids (cDNAs) encoding either YFP- $\text{Ca}_v1.1$ or YFP- $\text{Ca}_v1.1_{AA}$ at concentrations of $0.2 \mu\text{g}/\mu\text{L}$, respectively. In experiments assessing the effects of CaM on Ca^{2+} transients, normal myotubes (~one week in culture) were injected with expression plasmids encoding CaM_{wt} or CaM₁₂₃₄ (gift of Dr. Yue) and green fluorescent protein (pEGFP-C1, BD Biosciences Clontech, CA) at concentrations of 0.1 and $0.02 \mu\text{g}/\mu\text{L}$, respectively. Successfully transfected myotubes were identified 36–48 hours after injection by their *yellow* or *green* fluorescence under UV illumination.

2.3. Electrophysiology. Patch pipettes were constructed of borosilicate glass and had resistances of 1.8–2.5 M Ω when filled with the standard internal solution, which contained (in mM) 145 Cs-aspartate, 10 Cs₂-EGTA, 5 MgCl₂, and 10 HEPES (pH 7.4 with CsOH). The external solution contained (in mM) 145 tetraethylammonium chloride (TEA-Cl), 10 CaCl₂, 0.003 tetrodotoxin, and 10 HEPES (pH 7.4 with TEA-OH). The holding potential was -80 mV , and test pulses were preceded by a 1-s prepulse to -30 mV to inactivate endogenous T-type Ca^{2+} currents. Recorded membrane currents were corrected off line for linear components of leakage and capacitance by digitally scaling and subtracting the average of 10 preceding control currents, elicited by hyperpolarizing voltage steps (30 mV amplitude) from -50 mV . Ca^{2+} currents were normalized by linear cell capacitance (expressed in pA/pF). Values for G_{max} , the maximal Ca^{2+} conductance, were obtained by fitting the measured currents according to the following equation:

$$I_{\text{peak}} = \frac{G_{\text{max}} (V - V_R)}{\{1 + \exp [-(V - V_{1/2})/k]\}}, \quad (1)$$

where I_{peak} is the peak current activated at the test potential V , V_R is the extrapolated reversal potential, $V_{1/2}$ is the potential for half-maximal activation of the Ca^{2+} conductance, and k is a slope factor.

The fraction of current remaining at the end of an 800 ms test pulse (r_{800}) was determined by dividing the current

remaining at the end of test pulse by the peak current, and this ratio was used to quantify the level of inactivation

$$r_{800} = \frac{I_{\text{end}}}{I_{\text{peak}}}. \quad (2)$$

For measurements of charge movement, 0.5 mM Cd^{2+} and 0.1 mM La^{3+} were added to the external solution to block Ca^{2+} currents. Charge movements were elicited in response to a prepulse protocol that consisted of a 1-s prepulse to -30 mV and a subsequent 40 ms repolarization to a pedestal potential (-50 mV), followed by a 25 ms depolarization to $+40 \text{ mV}$. The maximum amount of charge that can be moved (Q_{max}) was obtained by integrating the charge movement current at test potential of $+40 \text{ mV}$. Linear leak and capacity currents were subtracted on line using $-P/4$ delivered from the holding potential (-80 mV) before each pulse. Charge movements were normalized to total cell capacitance (nC/ μF).

To measure relative changes in voltage-gated Ca^{2+} release from the SR, the Ca^{2+} indicator K₅-Fluo-3 (0.5 mM) (Molecular Probes) was included in the pipette solution. After rupture of the cell membrane and entry into the whole cell configuration, cells were allowed to dialyze for about 5 min before recording in order to achieve adequate loading with indicator dye. Fluorescent emission was measured by a photomultiplier system (Biomedical Instrumentation Group, University of Pennsylvania). The set of filters used to record the fluorescent signal from Fluo-3 was as follows: excitation band-pass filter of 470/20 nm; dichroic long-pass mirror (510 nm); emission long-pass filter of 520 nm. After rupture and dye loading into the cell, the baseline fluorescence (F_{base}) was monitored. The increase in fluorescent signal during depolarization was expressed as $\Delta F/F$, where ΔF represents the increase in fluorescence above baseline fluorescence ($\Delta F = F_{\text{transient}} - F_{\text{base}}$), and F is F_{base} . Peak fluorescence during each test pulse was plotted as a function of test potential V and fitted according to the following equation:

$$\frac{\Delta F}{F} = \frac{(\Delta F/F)_{\text{max}}}{\{1 + \exp[(V_{F1/2} - V)/k_F]\}}, \quad (3)$$

where $(\Delta F/F)_{\text{max}}$ is the maximal fluorescent change, $V_{F1/2}$ is the potential for half-maximal activation of the Ca^{2+} transient, and k_F is a slope factor.

All recordings were performed at room temperature ($\sim 20^\circ\text{C}$), and data are reported as mean \pm SEM; n indicates the number of myotubes tested. Data sets were statistically compared by an unpaired, two-sample Student's t -test, with a confidence interval of at least 95%.

2.4. Confocal Microscopy. Cells were bathed in rodent ringer (in mM: 146 NaCl, 5 KCl, 2 CaCl₂, 1 MgCl₂, 11 glucose, 10 HEPES; pH 7.4 adjusted with NaOH) and examined with an LSM 510 META laser scanning microscope (Zeiss, Thornwood, New York) with 40X oil immersion objective. The laser line (514 nm) of the argon laser (30 mW maximum output, operated at 50% or 6.3 A) was used to excite YFP

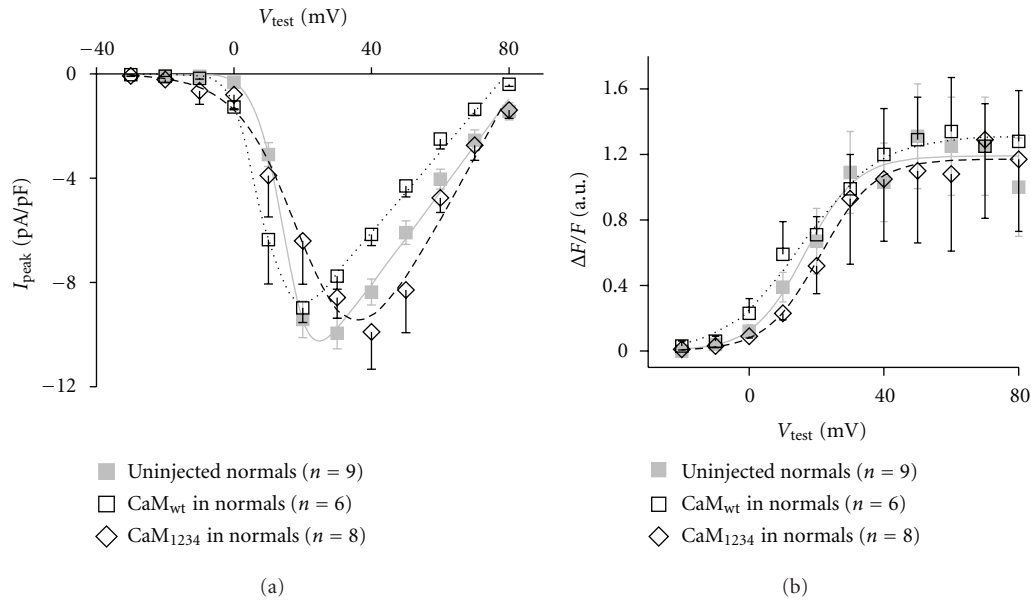


FIGURE 1: Ca^{2+} -binding ability of CaM does not affect skeletal muscle EC coupling. (a) The average peak current density (I_{peak}) is plotted as a function of membrane potential (V_{test}). Data were obtained from the indicated number of myotubes for each group. The smooth lines through the data were generated by using equation (1) (see Methods) and the average values. (b) The average peak fluorescence ($\Delta F/F$) is plotted as a function of membrane potential (V_{test}). Data were obtained from the indicated number of myotubes for each group. The smooth lines through data represent Boltzmann fits to the average data using equation (3) (see Methods).

fluorophore. Emissions of YFP were recorded in single-track configuration with a long-pass filter of 530 nm (Chroma, Rockingham, Vermont). Fluorescence signals were analyzed by the 510 LSM Image Examiner software (Zeiss, Thornwood, New York).

2.5. Immunocytochemistry. Primary cell cultures were plated onto 35 mm culture dishes with integral no. 0 glass coverslip bottoms (MatTek). Myotubes expressing constructs of $Ca_v1.1$ were identified by fluorescence. The cultures will be fixed with 100% methanol at $-20^{\circ}C$ for a minimum of 20 min. Cells were then incubated for 1 hour in PBS (phosphate-buffered saline) containing 1% BSA (bovine serum albumin) and 10% goat serum to block unspecific labeling. After 3 washes with PBS/BSA (.2%), cell cultures were incubated with specific primary antibody against the RyR1 (34C, Developmental Studies Hybridoma Bank (DSHB), UI) (dilution 1:4000) overnight at $4^{\circ}C$. Cells were washed out 3 times with PBS/BSA (.2%), followed by 1 hour of incubation with secondary antibody conjugated with Alexa 568 (at final dilution 1:5,000, goat anti-rabbit IgG, Invitrogen). Cells were then washed 3 times with PBS/BSA (.2%) to remove unbind secondary antibody and assessed with a confocal microscope.

3. Results

Ca^{2+} -binding ability of CaM does not affect skeletal muscle EC coupling. First, I addressed the question whether the Ca^{2+} -binding ability of CaM plays any role in skeletal muscle

EC coupling. Overexpressed mutant CaM which does not bind Ca^{2+} (CaM_{1234}) can displace approximately 70% of endogenous CaM, as reflected by abolishment of CDI of $Ca_v1.1$ [3]. However, overexpression of either CaM_{wt} or CaM_{1234} in normal myotubes did not significantly affect either current-voltage (I/V) relationship (Figure 1(a)) or voltage-gated Ca^{2+} release from SR as indicated by similar peak fluorescence-voltage relationship ($\Delta F/F-V$) in comparison with uninjected normal myotubes (Figure 1(b)). This result suggests that either the Ca^{2+} -binding ability of CaM or CaM itself does not play a role in skeletal muscle EC coupling. However, CaM associates with $Ca_v1.1$ *in vivo* [3] and that indicates the possibility that CaM may still serve as a structural subunit of $Ca_v1.1$, that is, that interaction between CaM and $Ca_v1.1$ can stabilize the DHPR complex. By doing so, it may also ensure proper structural and functional coupling between DHPR and RyR1.

Therefore, I examined whether CaM association with $Ca_v1.1$ is necessary for its function as a voltage sensor for EC coupling. The IQ motif of $Ca_v1.1$ has been shown to bind CaM similar to IQ motifs of $Ca_v1.3$ and Ca_v2 channels [7]. Introduction of the mutation IQ/AA in the IQ motif of the cardiac L-type Ca^{2+} channel ($Ca_v1.2$) resulted in abolishment of CDI and significant reduction of apoCaM binding to $Ca_v1.2$ [2, 4]. Thus, corresponding IQ motif mutation in the C-terminus of $Ca_v1.1$ was obvious place to start.

The mutation (IQ/AA) in the CaM-binding site of $Ca_v1.1$ disables function of $Ca_v1.1$ as a Ca^{2+} channel and voltage sensor for EC coupling. I introduced the IQ/AA mutation in the C-terminus of $Ca_v1.1$ and investigated how this

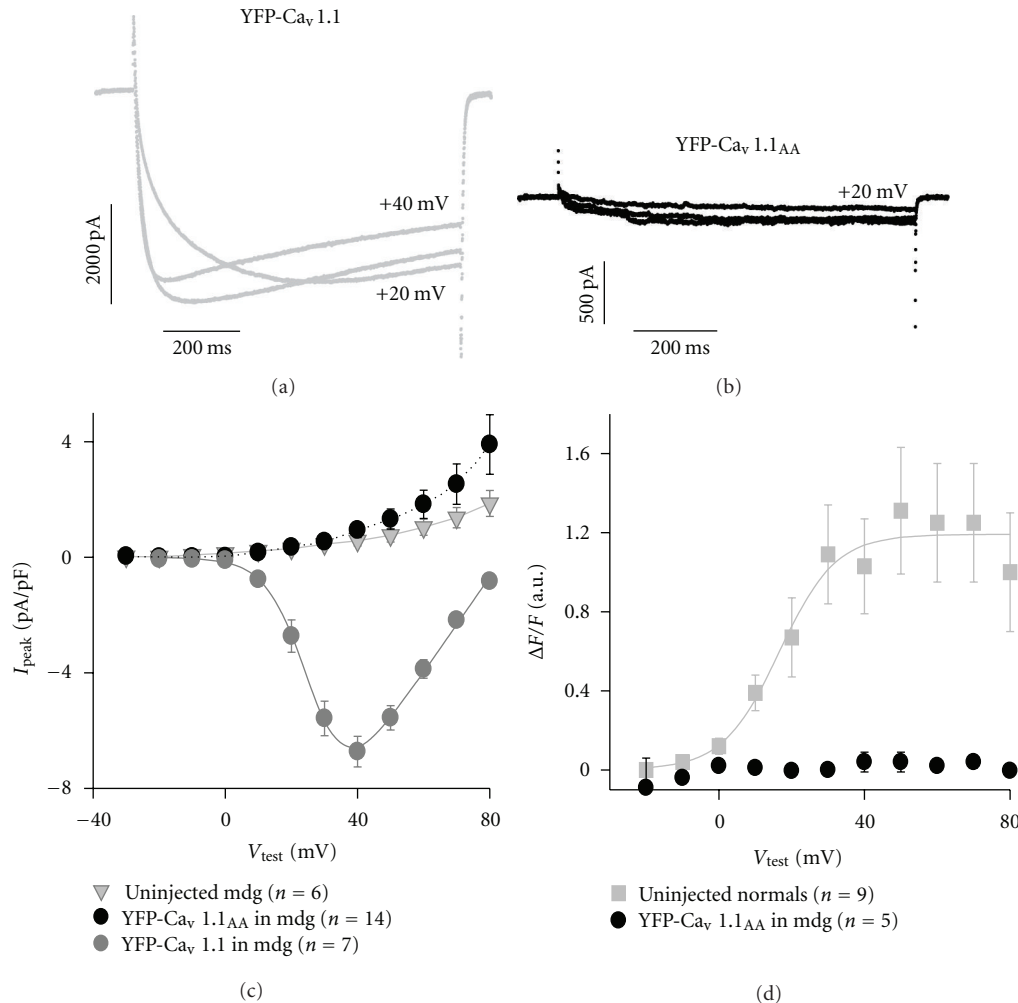


FIGURE 2: The IQ/AA mutation disables function of Ca_v1.1 as a Ca²⁺ channel and voltage sensor for EC coupling. Representative whole-cell L-type Ca²⁺ currents recorded from dysgenic myotubes expressing either (a) YFP-Ca_v1.1 (cell 1 (05-10-02); linear capacitance $C = 587$ pF) or (b) YFP-Ca_v1.1_{AA} (cell 1 (01-13-03); linear capacitance $C = 201$ pF). Note that the current scales are different in (a) and (b). (c) The average peak current density (I_{peak}) is plotted as a function of membrane potential (V_{test}). Data were obtained from the indicated number of myotubes for each group. The smooth lines through the data were generated by using equation (1) (see Methods) and the average values. (d) The average peak fluorescence ($\Delta F/F$) is plotted as a function of membrane potential (V_{test}). Data were obtained from the indicated number of myotubes for each group. The smooth lines through data represent Boltzmann fits to the average data using equation (3) (see Methods).

mutation will alter Ca_v1.1 function as Ca²⁺ channel and voltage sensor for EC coupling. Introduction of the mutation IQ/AA in the IQ motif of Ca_v1.2 resulted in abolishment of CDI and significant reduction of apoCaM binding to Ca_v1.2 [2, 4]. Whether IQ motif in the Ca_v1.1 plays a similar role is unknown. Dysgenic myotubes expressing either YFP-Ca_v1.1 or YFP-Ca_v1.1_{AA} were used to examine the role of IQ motif in Ca²⁺-dependent inactivation (CDI) of Ca_v1.1. Injections of plasmids encoding various constructs of Ca_v1.1 into dysgenic myotubes at concentrations of 0.2–0.5 μg/μL have been previously demonstrated to produce a similar extent of maximal, immobilization-resistant charge movement and similar Ca²⁺ current densities as normal myotubes, which corresponds to similar protein expression levels [3, 6, 8–10].

Figure 2(a) shows Ca²⁺ currents mediated by YFP-Ca_v1.1 expressed in dysgenic myotube. The fraction of current remaining at the end of the pulse (r_{800}) displayed a U-shaped voltage dependence (data not shown), consistent with a current-dependent inactivation process. In such a process, the extent of inactivation varies in proportion with the amplitude of the inward calcium current, which in turn depends on the number of conducting channels and the electrochemical driving force on calcium. Inactivation was minimal at a test potential of +10 mV, as reflected by an r_{800} value of 0.9 ± 0.08 ($n = 7$), and maximal at a test potential of +40 mV, as reflected by a minimum r_{800} value of 0.74 ± 0.03 ($n = 7$). Correspondingly, the Ca²⁺ current attained its maximum conductance at +40 mV (Figure 1(c)). Thus, Ca²⁺ currents mediated by YFP-Ca_v1.1

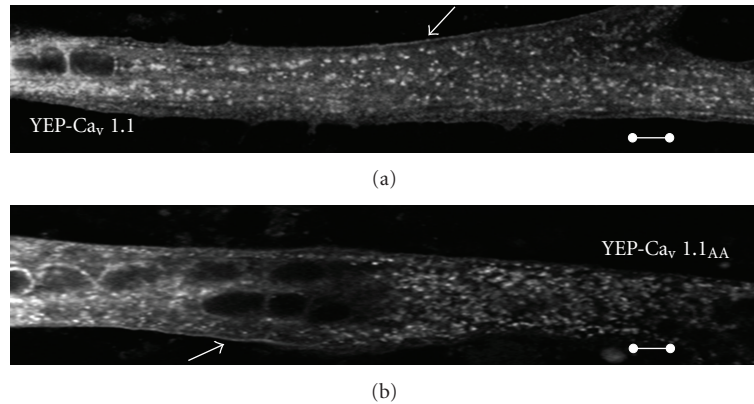


FIGURE 3: YFP- $\text{Ca}_v1.1_{AA}$ displays similar expression pattern as YFP- $\text{Ca}_v1.1$ in dysgenic myotubes. Confocal images of either YFP- $\text{Ca}_v1.1$ (a) or YFP- $\text{Ca}_v1.1_{AA}$ (b) yellow fluorescence in dysgenic myotubes. Bar 50 μm .

displayed a current-dependent inactivation process, current-voltage (I - V) relationship (Figure 2(c)), and maximal Ca^{2+} ion conductance ($G_{\text{max}} = 166 \pm 18 \text{ nS/nF}$; $n = 7$) similar to the endogenous $\text{Ca}_v1.1$ of normal myotubes [3]. These results suggest that YFP fused to the N-terminus of $\text{Ca}_v1.1$ does not interfere with channel function.

In contrast, dysgenic myotubes expressing YFP- $\text{Ca}_v1.1_{AA}$ (Figures 2(b) and 2(c)) displayed either very small ($<1 \text{ pA/pF}$) or no measurable Ca^{2+} currents. This is a very dramatic and surprising result considering that the corresponding mutation (IQ/AA) in the IQ motif of $\text{Ca}_v1.2$ resulted only in ablation of CDI but did not affect the I - V relationship of Ca^{2+} currents mediated by $\text{Ca}_v1.2$ [2]. Further voltage-gated Ca^{2+} currents and SR Ca^{2+} release were measured simultaneously from dysgenic myotubes expressing YFP- $\text{Ca}_v1.1_{AA}$ and compared with recordings from uninjected normal myotubes and normal myotubes overexpressing CaM_{wt} or CaM_{1234} . The voltage-gated Ca^{2+} release from SR was completely abolished in dysgenic myotubes expressing YFP- $\text{Ca}_v1.1_{AA}$ (Figure 2(d)).

The loss of $\text{Ca}_v1.1_{AA}$ function could be a result of several scenarios such as that mutation caused misfolding of protein and insufficient membrane targeting or that protein-protein interaction between RyR1 and $\text{Ca}_v1.1$ was significantly disturbed. If the latter possibility is the case, this result suggests that either the IQ motif itself or association of CaM with $\text{Ca}_v1.1$ is necessary for *orthograde* signaling from $\text{Ca}_v1.1$ to RyR1, which underlies skeletal muscle EC coupling.

The IQ/AA mutation does not prevent proper targeting of $\text{Ca}_v1.1$ into sarcolemma. The severe loss of function, abolished Ca^{2+} current and orthograde signaling mediated by the $\text{Ca}_v1.1_{AA}$, could be explained by compromised targeting of $\text{Ca}_v1.1$ to the T-SR junction as a result of incomplete protein folding.

Figure 3 shows confocal images of yellow fluorescence from a dysgenic myotube expressing either YFP- $\text{Ca}_v1.1$ or YFP- $\text{Ca}_v1.1_{AA}$. Expression of YFP- $\text{Ca}_v1.1$ (a) or YFP- $\text{Ca}_v1.1_{AA}$ (b) resulted in the appearance of small yellow fluorescence puncta located near the cell surface. The small

puncta correspond to groups of $\text{Ca}_v1.1$ localized to T-SR junctions; these puncta are similar in size and distribution to those of $\text{Ca}_v1.1$ foci revealed by immunohistochemistry [11]. There is a similar staining of the membrane and distribution of puncta in both myotubes, suggesting that both constructs are likely targeted to T-SR junctions.

To confirm targeting of YFP- $\text{Ca}_v1.1_{AA}$ to the sarcolemma, the Q_{max} was measured at +40 mV (Figure 4). The Q_{max} in dysgenic myotubes expressing $\text{Ca}_v1.1_{AA}$ ($5.9 \pm 0.5 \text{ nC}/\mu\text{F}$; $n = 27$) was similar to that of normal myotubes ($5.5 \pm 0.4 \text{ nC}/\mu\text{F}$; $n = 16$), but significantly larger ($P < 0.001$) than in dysgenic myotubes alone ($2.5 \pm 0.2 \text{ nC}/\mu\text{F}$; $n = 18$). This finding suggests that IQ/AA mutation in $\text{Ca}_v1.1$ did not prevent the protein from being properly targeted or undergoing voltage-dependent conformational changes, which strongly suggest proper folding as intramembrane segment S4 of $\text{Ca}_v1.1$ is responsible for voltage-dependent movement.

To further confirm $\text{Ca}_v1.1_{AA}$ proper targeting into T-SR junctions and site of EC coupling, I investigated colocalization of $\text{Ca}_v1.1$ and RyR1. Dysgenic myotubes expressing either YFP- $\text{Ca}_v1.1$ or YFP- $\text{Ca}_v1.1_{AA}$ (yellow fluorescence: YFP was artificially assigned as green) were incubated with specific primary antibody against the RyR1 followed by incubation with secondary antibody conjugated with Alexa 568 (red fluorescence). Colocalization of green and red fluorescence results in yellow pattern suggests colocalization of YFP- $\text{Ca}_v1.1$ and RyR1 in T-SR junctions *in vivo* (see Figures 5(g) and 5(h)). Colocalization patterns of YFP- $\text{Ca}_v1.1_{AA}$ with RyR1 were compared to YFP- $\text{Ca}_v1.1$ and RyR1 patterns in 5 different experiments. Colocalization patterns of either YFP- $\text{Ca}_v1.1$ or YFP- $\text{Ca}_v1.1_{AA}$ with RyR1 were similar and have been analyzed by MetaMorph 7 software (Molecular Devices). Colocalization in near surface slices of z-stacks of YFP- $\text{Ca}_v1.1$ and RyR1 was $83 \pm 4\%$ ($n = 7$), and colocalization of YFP- $\text{Ca}_v1.1_{AA}$ and RyR1 was $85 \pm 2\%$ ($n = 7$). These results strongly suggest that YFP- $\text{Ca}_v1.1_{AA}$ is targeted into T-SR junctions.

Together these results suggest that the IQ/AA mutation is not likely to affect protein folding within membrane. Furthermore, much more drastic alternation or deletions

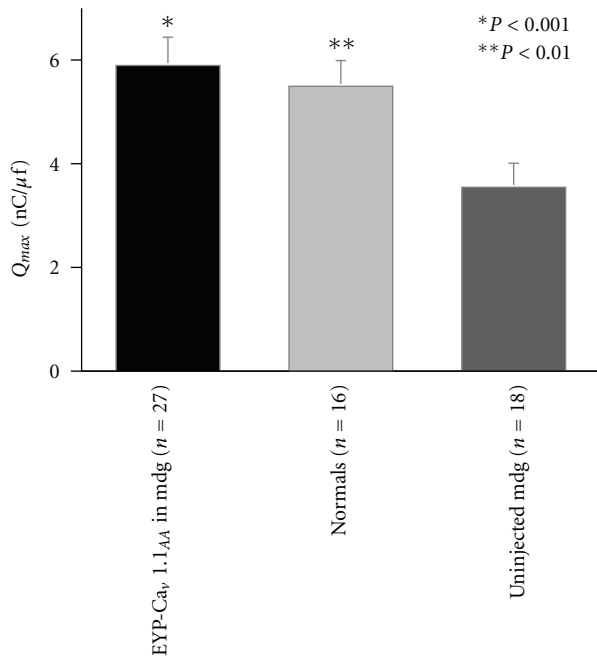


FIGURE 4: Ca_v1.1_{AA} generates normal densities of intramembrane charge movement. The average maximal, immobilization-resistant charge movement at +40 mV (Q_{max}) obtained from the indicated number of myotubes for each group. The charge movements were elicited by 25 ms depolarizations from a pedestal potential (-50 mV) to +40 mV. Symbols and error bars represent mean \pm SEM.

in Ca_v1.1 sequence did not have such dramatic effects [12, 13].

Taking altogether, the loss of both ionic Ca²⁺ current and skeletal muscle EC coupling in Ca_v1.1_{AA} along with charge movement similar to normal myotubes suggests that the IQ motif of the Ca_v1.1 may be unrecognized site of protein-protein interaction between Ca_v1.1 and RyR1 and play a role in both *orthograde* and *retrograde* signaling.

4. Discussion

The present study provides new information about the skeletal muscle L-type Ca²⁺ channel (Ca_v1.1). Specifically, the data demonstrate *in vivo* that the IQ motif in the C-terminus of Ca_v1.1 is critical for function of Ca_v1.1 as a voltage sensor as well as a Ca²⁺ channel. Furthermore, the results indicate that the IQ motif, in addition to II-III loop, may be a previously unrecognized site of protein-protein interaction between Ca_v1.1 and RyR1 and, thus, may play a role in skeletal muscle EC coupling.

Ca_v1.1 is localized in regions of the T-tubular membrane that are closely apposed to the sarcoplasmic reticulum (i.e., the T-SR junction), and the primary role of Ca_v1.1 is to serve as the voltage sensor for skeletal muscle EC coupling. The second protein that plays a major role in this process is the skeletal muscle ryanodine receptor (RyR1). RyR1 is localized in junctional SR membrane and functions as calcium release channel. The mechanism of signal transmission between

Ca_v1.1 and RyR1 is still incompletely understood, but the most accepted view is that they are mechanically coupled and interact with each other through protein-protein interaction (*orthograde* and *retrograde* signaling). *Orthograde* signaling is the signal from Ca_v1.1 to RyR1, in which movement of the voltage sensors in Ca_v1.1 trigger opening of RyR1 and release of Ca²⁺ from the SR (EC coupling). *Retrograde* signaling is communication from RyR1 to Ca_v1.1, in which RyR1 somehow increases the amount of L-type Ca²⁺ current mediated by Ca_v1.1 [8, 9].

The Ca²⁺ conductance of Ca_v1.1 channel is not necessary for functional excitation-contraction coupling between RyR1 and Ca_v1.1; however, a direct protein-protein interaction between these two proteins in multiple sites is. It has been shown that cytoplasmic loops of Ca_v1.1 and several regions of RyR1 play important role for normal physiological EC coupling in skeletal muscle [10, 14–17]. It has been also shown that protein-protein interaction between RyR1 and Ca_v1.1 is necessary for Ca_v1.1 display of Ca²⁺ conductance (retrograde signaling) [8]. It is clear that there are multiple contact sites between RyR1 and Ca_v1.1 and not all of them are recognized and understood, yet. The most investigated region of contact between RyR1 and Ca_v1.1 in Ca_v1.1 is II-III cytoplasmic loop, but other regions play a role [14, 15].

In the present experiments, normal myotubes and dysgenic myotubes expressing either YFP-Ca_v1.1 or YFP-Ca_v1.1_{AA} were used to examine the role of the IQ motif in both functions of Ca_v1.1, as a voltage sensor in EC coupling and Ca²⁺ channel. The primary cultures of skeletal muscle myotubes provide a natural cellular environment for Ca_v1.1. First, I examined whether a fusion of YFP to Ca_v1.1 would interfere with its function. The Ca²⁺ currents mediated by YFP-Ca_v1.1 displayed an *I-V* relationship similar to the endogenous Ca_v1.1 [3], suggesting that YFP fused on the N-terminus of Ca_v1.1 does not interfere with its channel function, as was also shown by others [5]. Endogenous Ca_v1.1 also exhibits CaM-mediated Ca²⁺-dependent inactivation (CDI) [3]. The Ca²⁺ currents mediated by YFP-Ca_v1.1 also displayed current-dependent inactivation similar to the CDI of endogenous Ca_v1.1, further supporting observation that fusion of YFP with Ca_v1.1 does not interfere with channel function.

Second, I examined how IQ/AA mutation in Ca_v1.1 will affect its function. Surprisingly, the intriguing finding of the present study was that dysgenic myotubes expressing YFP-Ca_v1.1_{AA} displayed either very small or no measurable Ca²⁺ currents. Significant decrease or abolishment of Ca²⁺ current through Ca_v1.1 could have resulted from improper targeting or folding of the protein. If Ca_v1.1_{AA} was retained inside of myotubes due to incorrect folding and targeting, neither Ca²⁺ currents nor Q_{max} would be obtained. The absence of Ca²⁺ currents in some of the dysgenic myotubes expressing YFP-Ca_v1.1_{AA} would suggest both. However, even though the Ca²⁺ current was absent, Q_{max} comparable with normal myotubes was observed. The Q_{max} measured in dysgenic myotubes expressing Ca_v1.1_{AA} was significantly larger ($P < 0.001$) than in dysgenic myotubes alone, but similar to that of normal myotubes measured here and

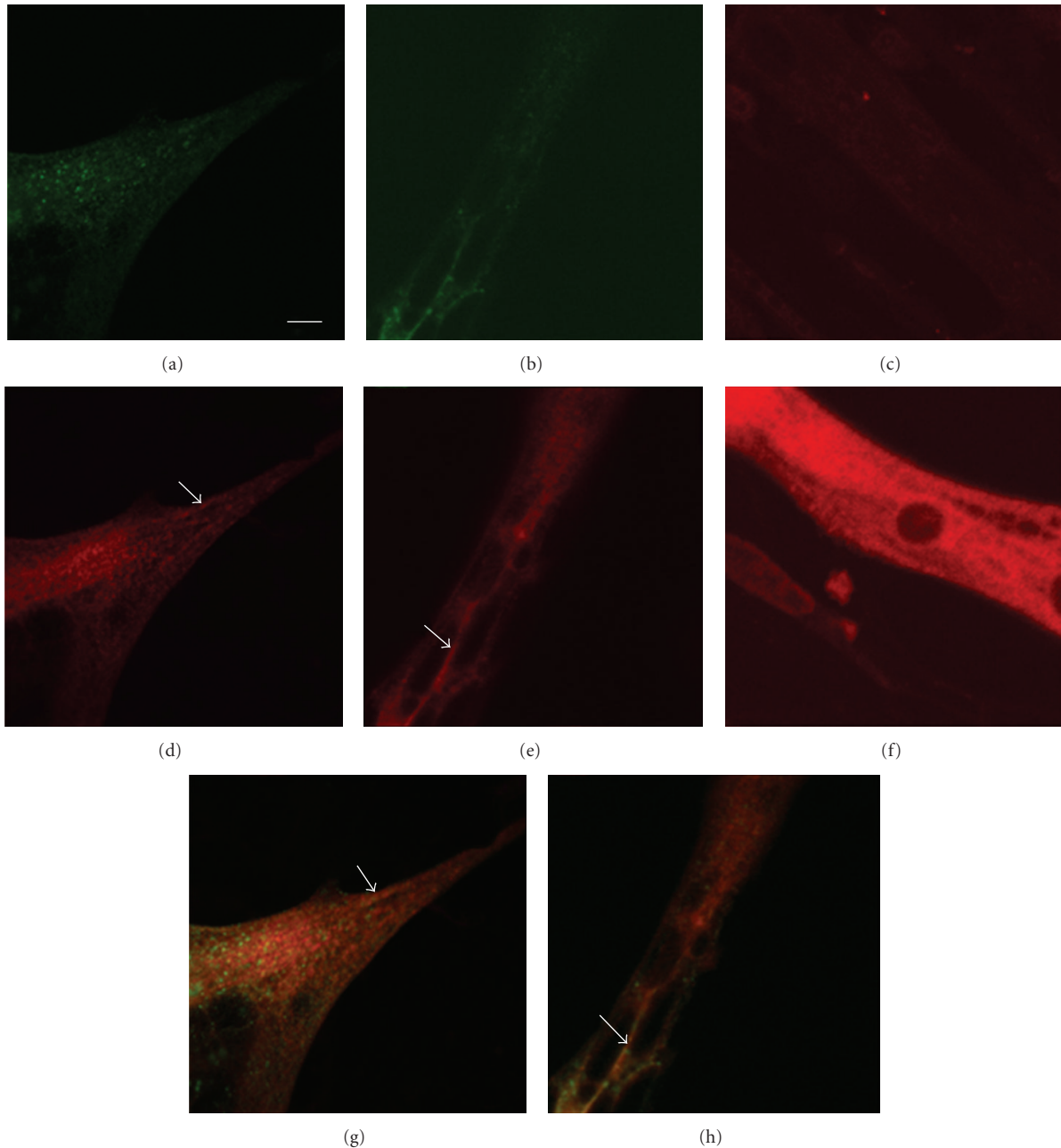


FIGURE 5: $\text{Ca}_v1.1_{AA}$ is targeted to T-SR junctions. Confocal images of colocalization of either YFP- $\text{Ca}_v1.1$ (a) or YFP- $\text{Ca}_v1.1_{<term?>AA_{<term?>}$ (b) green fluorescence and immunolabeled RyR1 ((d) and (e) red fluorescence in dysgenic myotubes. (g) and (h) represent overlay of (a) and (d), and (b) and (e), respectively. The control dysgenic myotube (no $\text{Ca}_v1.1$) immunolabeled without (c) and with (f) primary Ab(34C). Bar, 20 μm .

to the Q_{max} measured in dysgenic myotubes expressing various constructs of wt $\text{Ca}_v1.1$ at the similar experimental conditions elsewhere [6, 7].

The amount of Q_{max} in dysgenic myotubes expressing YFP- $\text{Ca}_v1.1_{AA}$ suggests that IQ/AA mutation in $\text{Ca}_v1.1$ did not prevent the protein from being properly targeted and that protein can undergo voltage-dependent conformational changes. The size of small measurable Ca^{2+} currents measured in some (6 out of 14) of the dysgenic myotubes

expressing $\text{Ca}_v1.1_{AA}$ (<1pA/pF) was similar to L-type Ca^{2+} currents measured in dyspedic (lacking a functional gene of RyR1) myotubes [7], suggesting a loss of retrograde signaling from RyR1. Endogenous $\text{Ca}_v1.1$ channels are present in sarcolemma of the dyspedic myotubes in similar density as in normal myotubes, as was demonstrated by comparable Q_{max} (dyspedic: $4.0 \pm 1.4 \text{ nC}/\mu\text{F}$; normal: $6.4 \pm 2.8 \text{ nC}/\mu\text{F}$) [7]. Thus, the amount of Q_{max} measured in dysgenic myotubes expressing $\text{Ca}_v1.1_{AA}$ ($5.9 \pm 0.5 \text{ nC}/\mu\text{F}$) is in

good agreement with the previously published values, and indicates that the IQ/AA mutation may have also disrupted *retrograde* signaling between $\text{Ca}_v1.1$ and RyR1. The similar expression patterns and comparable colocalization of YFP- $\text{Ca}_v1.1$ and YFP- $\text{Ca}_v1.1_{AA}$ with RyR1 in dysgenic myotubes obtained by confocal microscopy and immunocytochemistry further support the argument that YFP- $\text{Ca}_v1.1_{AA}$ seems to be folded and targeted properly to the T-SR junctions. In addition, much more drastic alternation or deletions in $\text{Ca}_v1.1$ sequence did not have such dramatic effects [12, 13].

Third, the IQ/AA mutation in C-terminus of $\text{Ca}_v1.1$ had a dramatic effect on its function as a voltage sensor for EC coupling. Even though amount of Q_{max} in dysgenic myotubes expressing YFP- $\text{Ca}_v1.1_{AA}$ is sufficient to support EC coupling (see above), the voltage-gated Ca^{2+} release from SR was completely abolished in these cells. This finding suggests that either tethering of CaM to $\text{Ca}_v1.1$ as a structural subunit or the IQ motif itself is necessary for orthograde signaling between $\text{Ca}_v1.1$ and RyR1 (EC coupling). Overexpression of CaM_{wt} and CaM_{1234} in normal myotubes did not significantly affect the peak fluorescence-voltage relationship ($\Delta F/F-V$) in comparison with uninjected normal myotubes, suggesting that the Ca^{2+} -binding ability of CaM does not play a role in skeletal muscle EC coupling in single twitch contractions.

For the first time, the present study shows that the IQ motif plays a role in both *orthograde* (skeletal muscle EC coupling) and *retrograde* (Ca^{2+} current) signaling between $\text{Ca}_v1.1$ and RyR1 *in vivo*. Several regions of RyR1 were shown to participate in protein-protein interactions between $\text{Ca}_v1.1$ and RyR1. However, until recently only the II-III loop of the $\text{Ca}_v1.1$ has been thought to be necessary to convey *orthograde* and *retrograde* signaling between $\text{Ca}_v1.1$ and RyR1. The present findings suggest that the C-terminus in addition to the II-III loop participates in and is necessary for the correct transmission of signals between $\text{Ca}_v1.1$ and RyR1. These results support previously published *in vivo* findings that in addition to the II-III loop of $\text{Ca}_v1.1$ additional intracellular loops of $\text{Ca}_v1.1$ are necessary to restore the full extent of *orthograde* and *retrograde* signaling between $\text{Ca}_v1.1$ and RyR1 [15]. The present findings also support *in vitro* results from pull-down assays, where it was demonstrated that CaM-binding region of RyR1 (3614–3543) interacts with the proximal C-terminus of $\text{Ca}_v1.1$ (1393–1527) in the absence of CaM [18, 19]. It was also shown that CaM binding to the RyR1 is not essential for skeletal EC coupling [20]. This would indicate together with binding studies [18] that CaM association to either $\text{Ca}_v1.1$ or RyR1 is not crucial for skeletal muscle EC coupling, but CaM-binding domains of both $\text{Ca}_v1.1$ and RyR1 are. For example, it has been shown that CaM-binding region of RyR1 binds to IQ peptide of $\text{Ca}_v1.2$ and in pull-down assay binds to $\text{Ca}_v1.1$ [18]. It still remains to be determined whether CaM itself needs to be tethered to $\text{Ca}_v1.1$ to ensure signaling and more experiments are in progress.

In conclusion, the results from confocal microscopy, immunocytochemistry, charge movement, and Ca^{2+} transients obtained from dysgenic myotubes expressing YFP- $\text{Ca}_v1.1_{AA}$ indicate that the IQ motif in the C-terminus of

$\text{Ca}_v1.1$ plays a crucial role in both *orthograde* (EC coupling) and *retrograde* (Ca^{2+} current) signaling between $\text{Ca}_v1.1$ and RyR1.

Acknowledgments

The authors thanks Dr. David Yue for kindly providing CaM_{wt} and CaM_{1234} constructs Dr. Kurt Beam for discussions, providing YFP- $\text{Ca}_v1.1$ construct, and for his support of preliminary studies and Dr. Brett Adams for his helpful insights and constructive criticism of the paper. This work was supported by MDA Research Grant and PIRG06-GA-2009-256580, Marie Curie Actions FP7-PEOPLE-2009-RG, EU.

References

- [1] H. Liang, C. D. DeMaria, M. G. Erickson, M. X. Mori, B. A. Alseikhan, and D. T. Yue, "Unified mechanisms of Ca^{2+} regulation across the Ca^{2+} channel family," *Neuron*, vol. 39, no. 6, pp. 951–960, 2003.
- [2] R. D. Zühlke, G. S. Pitt, R. W. Tsien, and H. Reuter, " Ca^{2+} - sensitive inactivation and facilitation of L-type Ca^{2+} channels both depend on specific amino acid residues in a consensus calmodulin-binding motif in the α_{1C} subunit," *Journal of Biological Chemistry*, vol. 275, no. 28, pp. 21121–21129, 2000.
- [3] K. Stroffekova, " Ca^{2+} /CaM-dependent inactivation of the skeletal muscle L-type Ca^{2+} channel ($\text{Ca}_v1.1$)," *Pflugers Archiv European Journal of Physiology*, vol. 455, no. 5, pp. 873–884, 2008.
- [4] W. Tang, D. B. Halling, D. J. Black et al., "Apocalmodulin and Ca^{2+} calmodulin-binding sites on the $\text{Ca}_v1.2$ channel," *Biophysical Journal*, vol. 85, no. 3, pp. 1538–1547, 2003.
- [5] S. Papadopoulos, V. Leuranguer, R. A. Bannister, and K. G. Beam, "Mapping sites of potential proximity between the dihydropyridine receptor and RyR1 in muscle using a cyan fluorescent protein-yellow fluorescent protein tandem as a fluorescence resonance energy transfer probe," *Journal of Biological Chemistry*, vol. 279, no. 42, pp. 44046–44056, 2004.
- [6] B. A. Adams, T. Tanabe, A. Mikami, S. Numa, and K. G. Beam, "Intramembrane charge movement restored in dysgenic skeletal muscle by injection of dihydropyridine receptor cDNAs," *Nature*, vol. 346, no. 6284, pp. 569–572, 1990.
- [7] P. Pate, J. Mochca-Morales, Y. Wu et al., "Determinants for calmodulin binding on voltage-dependent Ca^{2+} channels," *Journal of Biological Chemistry*, vol. 275, no. 50, pp. 39786–39792, 2000.
- [8] M. Grabner, R. T. Dirksen, N. Suda, and K. G. Beam, "The II-III loop of the skeletal muscle dihydropyridine receptor is responsible for the Bi-directional coupling with the ryanodine receptor," *Journal of Biological Chemistry*, vol. 274, no. 31, pp. 21913–21919, 1999.
- [9] B. A. Adams, T. Tanabe, and K. G. Beam, " Ca^{2+} current activation rate correlates with α_{1S} subunit density," *Biophysical Journal*, vol. 71, no. 1, pp. 156–162, 1996.
- [10] C. M. Wilkens, N. Kasielke, B. E. Flucher, K. G. Beam, and M. Grabner, "Excitation-contraction coupling is unaffected by drastic alteration of the sequence surrounding residues L720–L764 of the α_{1S} II-III loop," *Proceedings of the National Academy of Sciences of the United States of America*, vol. 98, no. 10, pp. 5892–5897, 2001.

- [11] B. E. Flucher, N. Kasielke, and M. Grabner, "The triad targeting signal of the skeletal muscle calcium channel is localized in the COOH terminus of the α_{1S} subunit," *Journal of Cell Biology*, vol. 151, no. 2, pp. 467–477, 2000.
- [12] C. Proenza, C. M. Wilkens, and K. G. Beam, "Excitation-contraction coupling is not affected by scrambled sequence in residues 681-690 of the dihydropyridine receptor II-III loop," *Journal of Biological Chemistry*, vol. 275, no. 39, pp. 29935–29937, 2000.
- [13] K. Stroffekova, C. Proenza, and K. G. Beam, "The protein-labeling reagent FLASH-EDT2 binds not only to CCXXCC motifs but also non-specifically to endogenous cysteine-rich proteins," *Pflügers Archiv—European Journal of Physiology*, vol. 442, no. 6, pp. 859–866, 2001.
- [14] C. A. Ahern, D. Bhattacharya, L. Mortenson, and R. Coronado, "A component of excitation-contraction coupling triggered in the absence of the T671-L690 and L720-Q765 regions of the II-III loop of the dihydropyridine receptor α_{1S} pore subunit," *Biophysical Journal*, vol. 81, no. 6, pp. 3294–3307, 2001.
- [15] L. Carbonneau, D. Bhattacharya, D. C. Sheridan, and R. Coronado, "Multiple loops of the dihydropyridine receptor pore subunit are required for full-scale excitation-contraction coupling in skeletal muscle," *Biophysical Journal*, vol. 89, no. 1, pp. 243–255, 2005.
- [16] J. Nakai, N. Sekiguchi, T. A. Rando, P. D. Allen, and K. G. Beam, "Two regions of the ryanodine receptor involved in coupling with L-type Ca^{2+} channels," *Journal of Biological Chemistry*, vol. 273, no. 22, pp. 13403–13406, 1998.
- [17] F. Protasi, C. Paolini, J. Nakai, K. G. Beam, C. Franzini-Armstrong, and P. D. Allen, "Multiple regions of RyR1 mediate functional and structural interactions with α_{1S} -dihydropyridine receptors in skeletal muscle," *Biophysical Journal*, vol. 83, no. 6, pp. 3230–3244, 2002.
- [18] S. Sencer, R. V. L. Papineni, D. B. Halling et al., "Coupling of RYR1 and L-type calcium channels via calmodulin binding domains," *Journal of Biological Chemistry*, vol. 276, no. 41, pp. 38237–38241, 2001.
- [19] L. Xiong, J. Z. Zhang, R. He, and S. L. Hamilton, "A Ca^{2+} -binding domain in RyR1 that interacts with the calmodulin binding site and modulates channel activity," *Biophysical Journal*, vol. 90, no. 1, pp. 173–182, 2006.
- [20] K. M. S. O'Connell, N. Yamaguchi, G. Meissner, and R. T. Dirksen, "Calmodulin binding to the 3614–3643 region of RyR1 is not essential for excitation-contraction coupling in skeletal myotubes," *Journal of General Physiology*, vol. 120, no. 3, pp. 337–347, 2002.

Review Article

Exact and Approximate Stochastic Simulation of Intracellular Calcium Dynamics

Nicolas Wieder, Rainer H. A. Fink, and Frederic von Wegner

Medical Biophysics Group, Institute of Physiology and Pathophysiology, University of Heidelberg, 69120 Heidelberg, Germany

Correspondence should be addressed to Nicolas Wieder, nwieder@ix.urz.uni-heidelberg.de and Frederic von Wegner, frederic.wegner@urz.uni-heidelberg.de

Received 1 July 2011; Accepted 25 August 2011

Academic Editor: Aikaterini Kontrogianni-Konstantopoulos

Copyright © 2011 Nicolas Wieder et al. This is an open access article distributed under the Creative Commons Attribution License, which permits unrestricted use, distribution, and reproduction in any medium, provided the original work is properly cited.

In simulations of chemical systems, the main task is to find an exact or approximate solution of the *chemical master equation* (CME) that satisfies certain constraints with respect to computation time and accuracy. While *Brownian motion* simulations of single molecules are often too time consuming to represent the mesoscopic level, the classical *Gillespie algorithm* is a stochastically exact algorithm that provides satisfying results in the representation of calcium microdomains. *Gillespie's algorithm* can be approximated via the *tau-leap* method and the *chemical Langevin equation* (CLE). Both methods lead to a substantial acceleration in computation time and a relatively small decrease in accuracy. Elimination of the noise terms leads to the classical, deterministic reaction rate equations (RRE). For complex multiscale systems, hybrid simulations are increasingly proposed to combine the advantages of stochastic and deterministic algorithms. An often used exemplary cell type in this context are striated muscle cells (e.g., cardiac and skeletal muscle cells). The properties of these cells are well described and they express many common calcium-dependent signaling pathways. The purpose of the present paper is to provide an overview of the aforementioned simulation approaches and their mutual relationships in the spectrum ranging from stochastic to deterministic algorithms.

1. Introduction

Ca^{2+} is a vital second messenger in many cell types. The ubiquitous appearance as well as its often crucial role in functional important signaling pathways are the reasons for the great scientific interest in Ca^{2+} dynamics. Oscillations in the typically low-intracellular Ca^{2+} concentration carry information which is processed (filtered) via signal cascades (e.g., calmodulin-dependent pathways) to induce a variety of cellular responses on different spatiotemporal scales (e.g., muscle contraction [1], fertilization [2], and regulation of gene expression [3]).

Oscillations are induced by sequences of random calcium “puffs” or “sparks”, that are highly localized Ca^{2+} release events from intracellular Ca^{2+} stores (sarcoplasmic and endoplasmic reticulum) [4]. However, the link between the dynamics of individual molecules involved in microdomain Ca^{2+} dynamics (e.g., Ca^{2+} channels) and the resulting cellular responses are not completely understood yet. This is where computational simulation algorithms come into play. The great number of biological functions as well as the simple

structure of Ca^{2+} ions are the reason for its well-described chemical and physical properties. Those circumstances make the *in silico* examination of Ca^{2+} dynamics very promising. Microdomains controlled by Ca^{2+} channels play an important role in the context of Ca^{2+} oscillations and waves [5]. For an accurate model of these domains, we have to consider stochastic processes at the mesoscopic level. Many regulatory and signaling processes are only inadequately described by deterministic simulation approaches [6].

An often used exemplary cell type in this context is given by striated muscle cells (e.g., cardiac and skeletal muscle cells) where a large amount of electrophysiological, biochemical, and ultrastructural data exists. Furthermore, these cells express many of the ubiquitous calcium-dependent signaling pathways which make it easy to transfer the methods and results to other cell types.

2. Background

Every chemical system is defined by a set of properties. First of all, there are N chemical species, $S = \{S_1, \dots, S_N\}$, in

the system volume Ω . The state vector $\mathbf{x}(t) = (x_1(t), \dots, x_N(t))$ denotes the number of molecules $x_k(t)$, $k = 1, \dots, N$ of each species S_k at time t in Ω . Events define transitions between different system states, where an event is any biophysical process which is characterized by a rate constant. It is possible to derive an event propensity a_j by its stochastic rate constant c_j and the stoichiometric coefficients of the underlying process. A chemical system contains M events $R = \{R_1, \dots, R_M\}$ which are represented through a state change vector $\mathbf{v}_j = (d_{j,1}, \dots, d_{j,N})$, $j = 1, \dots, M$, where component $d_{j,i}$ denotes the change in the number of molecules S_i due to the event R_j . Even more complex processes, which do not affect $\mathbf{x}(t)$, but other system properties, can easily be considered, for instance, voltage-gated ion channels have been introduced into stochastic simulation algorithms. To introduce the continuously varying membrane potential regulating the channel, its effect on the subunit transition rates was modeled as a time-varying stochastic event rate [10]. In the following, we exemplify the calculation of some relevant event propensities.

2.1. Reaction Events. $a_j(\mathbf{x}, t) = c_j h_j(\mathbf{x}, t)$, where $h_j(\mathbf{x}, t)$ denotes the number of possible molecular combinations available for reaction R_j at time t .

For first- and second-order reactions, the stochastic rate constants c_j are calculated from the macroscopic reaction rate constants k_j as $c_j = k_j$ for monomolecular reactions and as $c_j = k_j/\Omega$ for bimolecular reactions given the system volume Ω .

2.2. Diffusion Events. $a_k(\mathbf{x}, t) = c_k x_k(t)$, where $x_k(t)$ denotes the number of molecules of the diffusing species k at time t .

$c_k = D_k/A$, where D_k denotes the specific diffusion coefficient and A the diffusion area.

2.3. Channel Gating. Channel gating, that is, subunit transitions, are naturally described by a discrete stochastic process. Their biological properties force us to differentiate between ligand-gated and voltage-gated ion channels.

The interaction of ligands and channel subunits can be modeled as ordinary reaction events. Keeping track of the subunit states and depending on the gating scheme, we can decide whether the channel is in an open state or not.

The introduction of voltage-gated ion channels is more complex and requires a characteristic function, representing the membrane potential. The transition rates between the open/close states of the channels are based on the actual function value.

2.4. Channel Conductance. Ion permeation through a channel protein is modeled by translating the electrical conductance to a rate constant which can then be transformed into a permeation probability.

$c_j = I_{ch}/(e \cdot z_{ion})$, where e is the elementary charge and z_{ion} is the charge of the permeating ion. I_{ch} denotes the mean current of the channel in C/s.

All further considerations assume a well-stirred chemical system, and the velocities and positions of individual molecules in Ω are ignored. This assumption is based on

the fact that nonreactive molecular collisions that lead to a mixing of the system are far more likely than the occurrence of reactive events. This leads to uniformly randomized positions and thermally randomized velocities throughout the system volume (Maxwell-Boltzmann distribution) [7].

All simulation strategies can finally be derived from the chemical master equation (CME). The CME is a differential (or difference) equation that describes the time evolution of the probability density $P(\mathbf{x}, t)$ that is the multivariate distribution of the state vector $\mathbf{x}(t)$. Using the notation introduced above, the CME reads

$$\partial_t P(\mathbf{x}, t) = \sum_{j=1}^M [a_j(\mathbf{x} - \mathbf{v}_j, t) P(\mathbf{x} - \mathbf{v}_j, t) - a_j(\mathbf{x}, t) P(\mathbf{x}, t)]. \quad (1)$$

In words, (1) states that the change in $P(\mathbf{x}, t)$ is calculated as the net probability flow conveyed by the flows from state $\mathbf{x} - \mathbf{v}_j$ to \mathbf{x} (via event R_j) and the reverse flows out of state \mathbf{x} .

3. The Gillespie Algorithm

While the simulation of the Brownian motion of all individual molecules would provide an accurate model of Ca^{2+} dynamics, the computational effort is very high to examine signaling pathways on an adequate spatiotemporal scale. Increasing system volume and increasing numbers of molecules lead to extreme increases in computation time. Gillespie's algorithm is an alternative to accurately simulate small system volumes under the assumption of a well stirred system. Sample paths generated using this approach are samples of a multivariate Markov process. This means that given a system state $\mathbf{x}(t)$, the state $\mathbf{x}(t + \tau)$ at any future time $t + \tau$ only depends on $\mathbf{x}(t)$ and not on the previous history of the system. Transitions between system states are performed by generating independent, exponentially distributed waiting times τ_j for each possible event R_j (according to the event propensities) and choosing the event with the minimum waiting time. The computational procedure is the same for all event types R_j . It uses the current event propensity $a_j(\mathbf{x}, t)$ and a uniformly distributed random variable $r \sim U[0, 1]$:

$$\tau_j = \frac{-\log r}{a_j(\mathbf{x}, t)}. \quad (2)$$

Equation (2) leads to exponentially distributed waiting times τ which are characteristic for Markov processes. After selection of the event R_j with the smallest τ -value τ_j , the current simulation time t is advanced to $t \leftarrow t + \tau_j$, and the system state is changed to $\mathbf{x}(t) \leftarrow \mathbf{x}(t) + \mathbf{v}_j$. To improve the computational performance, the Gibson-Bruck algorithm introduced a dependency graph which leads to an efficient update rule where only those reaction propensities are updated that are influenced by the last reaction realized. A reaction R_b depends on a reaction R_a if one of the educts of R_b is changed by reaction R_a [8]. A complete overview of improvements of the classical Gillespie algorithm can be found in the literature [9].

The algorithm reads as follows.

- (0) *Initialization*: to initialize the system, set the initial number of each species S_i to $\mathbf{x}(t) = \mathbf{x}(t_0)$, $t = t_0$, and calculate the waiting times τ_j , $j = 1, \dots, M$ for each event R_j .
- (1) *Event selection*: select the event R_j that minimizes the associated τ -value (2).
- (2) *Update time and state*: increment the system time $t \leftarrow t + \tau_j$ and change the state vector according to R_j : $\mathbf{x}(t + \tau_j) = \mathbf{x}(t) + \mathbf{v}_j$.
- (3) *Exit condition*: if $(t + \tau_j > T_{\max})$ then *Exit*, where T_{\max} is the maximum simulation time.
- (4) *Update*: recalculate τ -values of related events as stored in the dependency graph.
- (5) *Go to step 1*.

The Gillespie algorithm quickly meets its limits when systems with increasing system volumes Ω and large numbers of implemented events are simulated. In particular, the presence of different time scales can decrease the efficiency crucially (e.g., diffusion events outnumber Ca^{2+} buffer association/dissociation events by far [10]). The τ -leaping method, which is introduced in the next paragraph, partially solves these problems.

4. The τ -Leaping Method

Frequently, it is not necessary to track all individual events explicitly because event propensities do not change significantly in a certain time interval of length τ . Using the classical Gillespie algorithm, this fact leads to a high computational effort which is not always necessary in terms of accuracy. The τ -leaping method takes advantage of this observation by evaluating how many times each event R_j will occur in the discrete time interval $[t, t + \tau)$. To apply the τ -leaping method to model systems, it is necessary to find an appropriate τ value for every simulation step. The so-called leaping condition requires the time interval to be small enough to assure that no propensity function a_j undergoes an appreciable change. This is traditionally accomplished by bounding $\Delta_\tau a_j(\mathbf{x}, t)$ to the product of a defined error control parameter ϵ and the sum of all propensity functions a_0 [9]:

$$\Delta_\tau a_j(\mathbf{x}, t) \leq \epsilon \cdot a_0(\mathbf{x}, t). \quad (3)$$

Considering chemical reaction systems exhibiting a wide range of temporal scales, this approach might lead to inaccuracies due to the high variability of the involved event propensities. To satisfy the leap condition in such cases, Cao et al. [11] suggested a new τ -selection procedure which bounds the relative changes in a_j by a fixed factor ϵ . A detailed discussion of different τ -selection procedures can be found in the literature [11].

In this context, $a_j(\mathbf{x})\tau$ denotes the average occurrence of R_j in $[t, t + \tau)$, which is adequately approximated by

a Poisson-distributed random variable $\xi_j(a_j(\mathbf{x}), \tau)$. This approach leads to the τ -leaping approximation which reads

$$\mathbf{x}(t + \tau) = \mathbf{x}(t) + \sum_{j=1}^M \mathbf{v}_j \xi_j(a_j(\mathbf{x})\tau). \quad (4)$$

Poisson random variables are unbounded and some reaction networks can produce the impossible scenario of negative copy numbers for certain chemical species. Especially, small reactant populations with copy numbers close to zero are affected by this. Different solutions have been proposed to solve this problem. Tian and Burrage [12] developed an alternative by replacing the Poisson-distributed random variable by a binomial random variable which can be bounded by the actual number of reactants of each species.

Cao et al. [11] introduced the modified (nonnegative) Poisson τ -leaping approach. It is based on the idea of subdividing the set of all events into critical and noncritical events depending on their risk to induce negative reaction species populations in $[t, t + \tau)$. Simulating critical events with the classical Gillespie algorithm and non-critical events using τ -leaping, the probability of negative molecule counts becomes nearly zero.

5. The Chemical Langevin Equation

The approximation of the event count occurring in a carefully chosen time interval $[t, t + \tau)$ can be taken a step further. If a chemical reaction system not just fulfills (a) the leaping condition but also satisfies (b) $a_j\tau \gg 1$, for all $j \in [1, M]$, the Poisson-distributed random variable ξ_j can be approximated by a normally (Gaussian-) distributed random variable with mean and variance equal to $a_j(\mathbf{x})\tau$:

$$\xi_j(a_j(\mathbf{x})\tau) \approx N(a_j(\mathbf{x})\tau, a_j(\mathbf{x})\tau). \quad (5)$$

With the linear combination theorem of random variables and (4), we can deriviate the “white noise form” of the Langevin equation:

$$\mathbf{x}(t + dt) = \mathbf{x}(t) + \sum_{j=1}^M \mathbf{v}_j a_j(\mathbf{x}(t))dt + \sum_{j=1}^M \mathbf{v}_j \sqrt{a_j(\mathbf{x}(t))}dB(t), \quad (6)$$

where $dB(t)$ denotes a temporally uncorrelated Gaussian white noise process (the increments of a Brownian motion $B(t)$).

The CLE approach implies some notable consequences. First, the integration time interval dt is fixed. Second, due to the transformation of the Poisson to a Gaussian random variable, the resulting molecule counts become real values rather than integers. The change of the state vector $\mathbf{x}(t)$ is dependent on a deterministic part (first sum of (6)), and a stochastic part (second sum of (6)). When the number of reactants tends to infinity, the stochastic term can be neglected compared to the deterministic part, and (6) reduces to the deterministic *reaction rate equation* approach. This extrapolation provides the link between conventional

deterministic chemical kinetics and the stochastic approach. A complete derivation of the CLE can be found in the literature [13].

Furthermore, the theory of stochastic processes allows a transformation of the Langevin equation to an associated *Fokker-Planck equation* (FPE) that describes the temporal evolution of the probability density $P(\mathbf{x}, t)$ [14]. The FPE method has been applied to calcium dynamics in the dyadic cleft of cardiomyocytes [15]. Given that researchers are often more interested in explicit sample paths of a model than in probability distributions, the CLE approach is more common.

6. Hybrid Simulations

The simulation of complex chemical systems, including a set of events with a high variability of propensity functions, often cannot be conveniently approximated by the CLE. The resulting loss in accuracy ignores important events on slow temporal scales that affect the evolution of the whole system (e.g., ion channels). A promising way to avoid the high computational effort of the classical Gillespie algorithm while achieving a satisfying degree of accuracy is *Hybrid simulation algorithms* that combine deterministic and stochastic approaches.

Rüdiger et al. [16] successfully proposed a hybrid stochastic and deterministic approach for the simulation of Ca^{2+} blips, describing the state transitions between the subunits of an IP_3R calcium channel with the classical Gillespie algorithm and the surrounding Ca^{2+} -dynamics (buffering, diffusion) as a deterministic process. Similar approaches have been introduced by Stern et al. [17] and Greenstein and Winslow [18] using cardiac and skeletal muscle cells as model systems. Kalantzis [19] and Choi et al. [20] proposed hybrid algorithms that switch adaptively between the classical Gillespie algorithm, the τ -leaping method, and the chemical Langevin equation. Skupin et al. introduced a spatially resolved multiscale model which combines detailed stochastic channel gating on the scale of a channel cluster with a linearized spatial bidomain model to integrate them on a microscopic scale [21].

7. Conclusion

High-resolution confocal laser microscopy and mathematical models of calcium signaling showed that stochastic effects can be essential for intracellular information processing. At the same time, we observe a continuous improvement in data quality through advanced measurement techniques and increasing accuracy and availability of physical and chemical properties of signaling molecules. Thus, stochastic simulation approaches are increasingly used to simulate subcellular signaling pathways. New tendencies in developing integrated simulation algorithms that case-dependently switch between different approaches are very promising and may provide efficient solutions for the simulation of large systems with complex event interactions. Most importantly, future work has to prove the validity of those approaches on different spatiotemporal scales.

The degree of stochasticity necessary to model Ca^{2+} microdomains is still discussed. Tanskanen et al. [22] as well as Hake and Lines [23] both proposed two different models of the cardiac dyadic cleft, using different algorithms. The dyadic cleft is a functionally important microdomain in cardiac myocytes where the process of excitation-contraction coupling takes place. This microdomain is located between the sarcolemma and the endoplasmic reticulum membrane and is characterized by steep Ca^{2+} -concentration gradients and attoliter volumes. The interaction between L type calcium channels (LCC) and clusters of Ryanodine receptor calcium channels is the key event of this process. Tanskanen et al. [22] introduced a model using a spatially resolved Markov process, taking into account the positions of individual Ca^{2+} -ions, dyadic proteins, the membrane surface charges, and channel gating [22]. They conclude that the full stochasticity of their approach is necessary for an exact description of the dyad. On the other hand, Hake and Lines [23] also used the dyadic cleft as the structural basis of their work. Comparing a hybrid model, combining a deterministic continuous model with stochastic receptor gating and a fully stochastic *Random Walk* (RW) approach, they conclude that under certain limitations of the simulation parameters, the deterministic approach reproduces the RW results sufficiently well. Thurley and Falcke [24] recently used a hybrid simulation approach to study the relation of robustness and sensitivity of calcium-dependent subcellular pathways based on the statistical properties of interspike intervals. Even though there is a high diversity of deterministic, stochastic, and hybrid simulation strategies, the specifying system parameters are equal. The open source community has consistently developed the *System Biology Markup Language* (SBML) [25] which defines a universal XML file format to ensure the interchangeability of model definitions between different software packages. Therefore, one of the major goals of future efforts should be a support of the SBML or an equivalent file format to help with the advance of a flexible, barrier-free system biology community.

References

- [1] A. Tsugorka, E. Rios, and L. A. Blatter, "Imaging elementary events of calcium release in skeletal muscle cells," *Science*, vol. 269, no. 5231, pp. 1723–1726, 1995.
- [2] S. A. Stricker, "Repetitive calcium waves induced by fertilization in the nemertean worm *Cerebratulus lacteus*," *Developmental Biology*, vol. 176, no. 2, pp. 243–263, 1996.
- [3] R. E. Dolmetsch, K. Xu, and R. S. Lewis, "Calcium oscillations increase the efficiency and specificity of gene expression," *Nature*, vol. 392, no. 6679, pp. 933–936, 1998.
- [4] G. Dupont, A. Abou-Lovergne, and L. Combettes, "Stochastic aspects of oscillatory Ca^{2+} dynamics in hepatocytes," *Biophysical Journal*, vol. 95, no. 5, pp. 2193–2202, 2008.
- [5] G. Dupont and L. Combettes, "Modelling the effect of specific inositol 1,4,5-trisphosphate receptor isoforms on cellular Ca^{2+} signals," *Biology of the Cell*, vol. 98, no. 3, pp. 171–182, 2006.
- [6] D. T. Gillespie, "Stochastic simulation of chemical kinetics," *Annual Review of Physical Chemistry*, vol. 58, pp. 35–55, 2007.

- [7] D. T. Gillespie, "Exact stochastic simulation of coupled chemical reactions," *Journal of Physical Chemistry*, vol. 81, no. 25, pp. 2340–2361, 1977.
- [8] M. A. Gibson and J. Bruck, "Efficient exact stochastic simulation of chemical systems with many species and many channels," *Journal of Physical Chemistry A*, vol. 104, no. 9, pp. 1876–1889, 2000.
- [9] D. T. Gillespie, "Approximate accelerated stochastic simulation of chemically reacting systems," *Journal of Chemical Physics*, vol. 115, no. 4, pp. 1716–1733, 2001.
- [10] F. Von Wegner and R. H. A. Fink, "Stochastic simulation of calcium microdomains in the vicinity of an L-type calcium channel," *European Biophysics Journal*, vol. 39, no. 7, pp. 1079–1088, 2010.
- [11] Y. Cao, D. T. Gillespie, and L. R. Petzold, "Efficient step size selection for the tau-leaping simulation method," *The Journal of chemical physics*, vol. 124, no. 4, Article ID 044109, 2006.
- [12] T. Tian and K. Burrage, "Binomial leap methods for simulating stochastic chemical kinetics," *Journal of Chemical Physics*, vol. 121, no. 21, pp. 10356–10364, 2004.
- [13] D. T. Gillespie, "Chemical Langevin equation," *Journal of Chemical Physics*, vol. 113, no. 1, pp. 297–306, 2000.
- [14] C. Gardiner, *Handbook of Stochastic Methods: For Physics, Chemistry and the Natural Sciences*, Springer, 3rd edition, 2004.
- [15] R. L. Winslow, A. Tanskanen, M. Chen, and J. L. Greenstein, "Multiscale modeling of calcium signaling in the cardiac dyad," *Annals of the New York Academy of Sciences*, vol. 1080, pp. 362–375, 2006.
- [16] S. Rüdiger, J. W. Shuai, W. Huisinga et al., "Hybrid stochastic and deterministic simulations of calcium blips," *Biophysical Journal*, vol. 93, no. 6, pp. 1847–1857, 2007.
- [17] M. D. Stern, G. Pizarro, and E. Ríos, "Local control model of excitation-contraction coupling in skeletal muscle," *Journal of General Physiology*, vol. 110, no. 4, pp. 415–440, 1997.
- [18] J. L. Greenstein and R. L. Winslow, "An integrative model of the cardiac ventricular myocyte incorporating local control of Ca²⁺ release," *Biophysical Journal*, vol. 83, no. 6, pp. 2918–2945, 2002.
- [19] G. Kalantzis, "Hybrid stochastic simulations of intracellular reaction-diffusion systems," *Computational Biology and Chemistry*, vol. 33, no. 3, pp. 205–215, 2009.
- [20] T. Choi, M. R. Maurya, D. M. Tartakovsky, and S. Subramaniam, "Stochastic hybrid modeling of intracellular calcium dynamics," *Journal of Chemical Physics*, vol. 133, no. 16, Article ID 165101, 2010.
- [21] A. Skupin, H. Kettenmann, and M. Falcke, "Calcium signals driven by single channel noise," *PLoS Computational Biology*, vol. 6, no. 8, Article ID e1000870, 2010.
- [22] A. J. Tanskanen, J. L. Greenstein, A. Chen, S. X. Sun, and R. L. Winslow, "Protein geometry and placement in the cardiac dyad influence macroscopic properties of calcium-induced calcium release," *Biophysical Journal*, vol. 92, no. 10, pp. 3379–3396, 2007.
- [23] J. Hake and G. T. Lines, "Stochastic binding of Ca²⁺ ions in the dyadic cleft; Continuous versus random walk description of diffusion," *Biophysical Journal*, vol. 94, no. 11, pp. 4184–4201, 2008.
- [24] K. Thurley and M. Falcke, "Derivation of Ca²⁺ signals from puff properties reveals that pathway function is robust against cell variability but sensitive for control," *Proceedings of the National Academy of Sciences of the United States of America*, vol. 108, no. 1, pp. 427–432, 2011.
- [25] M. Hucka, A. Finney, B. J. Bornstein et al., "Evolving a lingua franca and associated software infrastructure for computational systems biology: the Systems Biology Markup Language (SBML) project," *Systems biology*, vol. 1, no. 1, pp. 41–53, 2004.

Review Article

Thin Filament-Reconstituted Skinned Muscle Fibers for the Study of Muscle Physiology

Sayaka Higuchi,¹ Yoshikazu Tsukasaki,¹ Norio Fukuda,²
Satoshi Kurihara,² and Hideaki Fujita¹

¹Laboratory for Comprehensive Bioimaging, Riken Quantitative Biology Center, OLABB, 6-2-3 Furuedai, Suita, Osaka 565-0874, Japan

²Department of Cell Physiology, The Jikei University School of Medicine, Tokyo 105-8461, Japan

Correspondence should be addressed to Hideaki Fujita, hideaki.fujita@riken.jp

Received 21 July 2011; Accepted 12 August 2011

Academic Editor: Henk Granzier

Copyright © 2011 Sayaka Higuchi et al. This is an open access article distributed under the Creative Commons Attribution License, which permits unrestricted use, distribution, and reproduction in any medium, provided the original work is properly cited.

We review the use of thin filament-reconstituted muscle fibers in the study of muscle physiology. Thin filament extraction and reconstitution protocol is a powerful technique to study the role of each component of the thin filament. It is also useful for studying the properties of genetically modified molecules such as actin and tropomyosin. We also review the combination of this protocol with sinusoidal analysis, which will provide a solid technique for determining the effect of regulatory proteins on actomyosin interaction and concomitant cross-bridge kinetics. We suggest that thin filament-reconstituted muscle fibers are an ideal system for studying muscle physiology especially when gene modifications of actin or tropomyosin are involved.

1. Introduction

Striated muscle has a highly ordered structure where muscle proteins are arranged in an array of filaments [1, 2]. It is critically important that these structures are maintained so that muscle proteins retain their physiological functions. Thus, physiological functions of muscle proteins must be studied using a model that preserves their native higher-order structure. Thin filaments involving actin, tropomyosin and troponin can be reconstituted in vitro which preserves Ca²⁺ sensitivity, and, in this model, the measurement of active tension or sliding speed is possible (in vitro motility assay system) [3, 4]. In the in vitro motility assay system, the higher-order structure of thin filaments is reconstituted but myosin or the motor domain of myosin is randomly placed on glass-coverslip, which differs from the physiological condition. The higher-order structure of thick filaments can be reconstituted relatively easily in vitro by lowering the ionic strength of the solution [5] although force or sliding velocity could not be measured until single-molecule manipulation techniques were developed [6, 7]. These in vitro experiments with reconstituted filaments revealed that

muscle proteins show altered kinetics when the higher-order structure is conserved, indicating the importance of the higher-order structure in the study of muscle proteins. Although filament structures can be reconstituted in vitro using purified proteins, it is still difficult to reconstruct the 3D structure of muscle where thick and thin filaments are arranged in a hexagonal lattice. Recently, a new in vitro assay system was developed which used an isolated A-band and reconstituted actin filament to measure the active force developed in the thick filament lattice structure [8]. This approach enables the study of the physiology of muscle proteins preserving higher-order structure of muscle but, because the preparation of A-band is labor consuming and the setup is relatively complicated, this technique did not become widely used. Another approach is to exchange the small molecules such as troponin and myosin light chain in skinned muscle [9–12]. Although this approach enables the study of the properties of some muscle proteins, most other proteins such as myosin, actin, and tropomyosin are difficult to exchange; thus another approach is needed.

Removal and reconstitution of the filament in skinned muscle is another way to exchange muscle proteins with

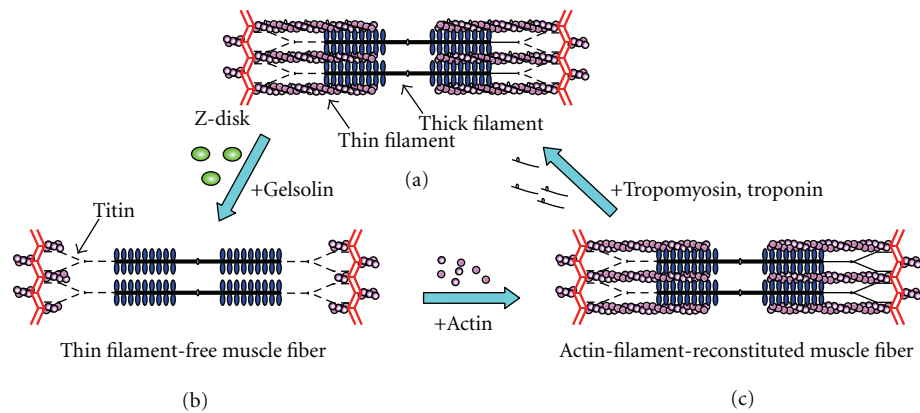


FIGURE 1: Schematic diagram illustrating the thin filament removal and reconstitution protocol. By applying gelsolin to skinned muscle fibers (a), thin filament free muscle fibers (b) can be obtained. By adding actin monomer to these thin filament free muscle fibers, actin-filament-reconstituted muscle fibers without regulatory proteins (c) can be obtained. Thin filament can be reconstituted by adding regulatory proteins to these actin-filament-reconstituted muscle fibers.

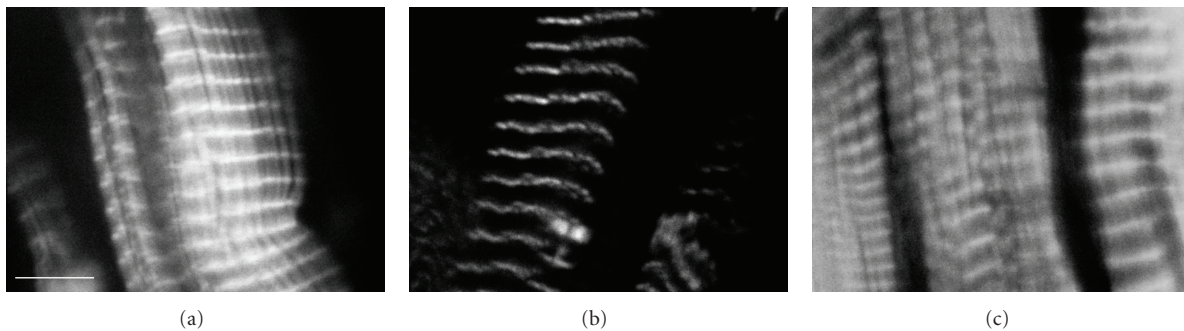


FIGURE 2: Confocal fluorescent micrograph of muscle fibers at each step of thin filament removal and reconstitution. (a) Control cardiac muscle fibers. (b) Gelsolin-treated muscle fibers. (c) Actin-filament-reconstituted muscle fibers. Actin filament was stained with rhodamine-phalloidin. Scale bar: 5 μm .

purified proteins. Because thick filaments can be removed relatively easily by increasing the ionic strength [13], several attempts were made to reconstitute thick filaments using purified myosin. Although myosin filaments can be reconstituted relatively easily *in vitro*, reconstitution of thick filaments inside skinned muscle fibers is not possible due to the spontaneous polymerization of myosin filament. On the other hand, thin filaments cannot be removed by simply changing the ionic strength of the surrounding environment. Selective removal of thin filaments was achieved by using the actin filament severing protein, gelsolin, as a molecular tool, which enabled elimination of actin, troponin, and tropomyosin from skinned muscle fibers [14–16]. Because gelsolin requires Ca^{2+} for actin filament severing, actomyosin ATPase inhibitor was initially used during gelsolin treatment, which was followed by the use of actin filament severing domain of gelsolin [17]. Using these thin filament-removed (thin filament-free) skinned muscle fibers, reconstitution of thin filaments was performed [18]. Figure 1 illustrates the procedure for the removal and reconstitution of thin filaments. When purified actin monomer was added to thin filament-free skinned muscle fibers under the polymerizing condition, the actin filament polymerizes nucleated by a

short fragment of the thin filament remaining at the Z-disk, reconstituting the actin filament. These investigators [18] used potassium iodide rather than potassium chloride and low temperature in order to slow the spontaneous nucleation of actin polymerization. These actin-filament-reconstituted muscle fibers can be used to study the properties of the actin filament without regulatory proteins. By the addition of the tropomyosin-troponin complex to actin-filament-reconstituted skinned muscle fibers, Ca^{2+} sensitivity was recovered [19]. Figure 2 shows confocal micrographs of muscle fibers stained for actin filament before and after the thin filament removal and after the reconstitution of actin filament. The confocal image clearly shows that thin filaments were removed by gelsolin treatment and restored after reconstitution of actin filament. When skinned skeletal muscle fibers were used for thin filament removal and reconstitution, only ~20% of active tension was recovered regardless of the duration of actin filament reconstitution [18]. This was attributed to the damage of the Z-disk due to the overremoval of actin fragments which constitute the Z-disk and/or by proteases contaminated in the gelsolin solution. When skinned cardiac muscle was used, active tension was recovered by more than 100%, average being

~140% [19]. The successful recovery of active tension when cardiac muscle fibers were used was probably due to the stronger Z-disk structure of cardiac muscle. Active tension augmentation (by ~40%) was attributed to the length distribution of thin filaments in cardiac muscle, where length distribution is broad and the average length is shorter compared to skeletal muscle [20]. The longer length of thin filaments after reconstitution is likely to increase active force of the muscle fibers. When the skeletal tropomyosin-troponin complex was used in place of cardiac muscle, reconstituted muscle fibers showed a pCa-tension relationship that resembles that of the skeletal muscle fibers, showing successful exchange of the regulatory proteins.

The primary function of striated muscle is to generate active force; thus, when studying the physiological function of muscle proteins, it is important that active tension is measured. Unlike the *in vitro* motility assay system where expensive equipment, such as optical tweezers, is needed to measure force generation, it is comparatively easy to measure active force generated by thin filament-reconstituted skinned muscle fibers. Thus, thin filament-reconstituted muscle fibers are an ideal model for studying the physiology of thin filament proteins [21].

2. Study of the Effect of Regulatory Proteins in Muscle Physiology Using Thin Filament-Reconstituted Skinned Muscle Fibers

Unlike small proteins such as troponin or myosin light chains, tropomyosin is bound to seven actin monomers and it is extremely difficult to remove without damaging other muscle proteins. Using actin-filament-reconstituted muscle fibers before reconstitution of regulatory proteins, it is possible to measure the properties of bare actin filament without regulatory proteins in force generation. This is also possible by using *in vitro* motility experiments, but actin filaments are usually stained with fluorescent phalloidin, which may affect the active tension generating capability of actomyosin complex. Generally speaking, the *in vitro* motility system requires expensive experimental setups, such as optical tweezers, for force measurement, and the experiment is labor intensive, requiring numerous experiments to compensate for the large variation of the results. In addition, the *in vitro* motility assay system can only be performed at very low ionic strength, such as ~50 mM, which is different from physiological conditions where ionic strength is ~200 mM [22]. In the actin-filament-reconstituted muscle model, active force generated by naked actin filament can be measured without phalloidin staining and at a physiological ionic strength. Moreover, the lattice structure of thick filament is conserved, offering a more natural physiological condition. Here, we show examples of the use of a thin filament removal and reconstitution protocol for studying the role of regulatory proteins in muscle physiology.

During muscle fatigue or the onset on ischemia, intracellular pH of muscle decreases, resulting in a decrease in active tension, Ca^{2+} sensitivity, and shortening velocity [23, 24].

It is known that even in skinned muscle fibers where only thick and thin filament is involved, active tension generation capability is affected by pH, but whether regulatory protein affects the pH dependence of active tension is unknown. Using a thin filament removal and reconstitution protocol, the effect of regulatory proteins on the pH effect was studied [25]. In skinned cardiac muscle fibers, active tension increased linearly with an increase in pH, consistent with previous reports [26, 27]. This was also the case in actin-filament-reconstituted fibers, but the slope was much steeper than that with regulatory proteins. When regulatory proteins were reconstituted, the muscle fibers regained the original pH-force relationship [25]. The pH-force relationship was also recovered by the reconstitution of tropomyosin only, showing the importance of tropomyosin in the modulation of the pH-force relationship of muscle. When regulatory proteins from skeletal muscle were used, the pH-force relationship resembled that of skeletal muscle, which is larger than cardiac muscle. This result indicates that regulatory proteins protect muscle fibers from active tension decrease due to acidosis, especially in cardiac muscle where active tension loss by acidosis may be critical.

Sliding velocity and the active tension generation capability of striated muscle is also influenced by temperature where both the sliding velocity and active tension are larger at higher temperatures below 40°C [28, 29]. An increase in the sliding velocity indicates an increase in actomyosin ATPase activity, whereas an increase in active force suggests an increase in the number of force-generating cross-bridges. This shows that ATPase activity in the cross-bridge cycle is not equally affected by temperature [29], hypothesizing that the force generated by each cross-bridge does not change. Although the effect of temperature in muscle physiology has been well studied, the influence of regulatory proteins in the effect of temperature remains unknown. Using the thin filament removal and reconstitution protocol, the effect of regulatory proteins in temperature sensitivity of active force was studied [30]. In actin-filament-reconstituted muscle fibers without regulatory proteins, the effect of temperature on active tension was much less than the native fibers. When regulatory proteins were reconstituted, muscle fibers regained the temperature-force relationship of native fibers. Stiffness of muscle during contraction, an indicator of the amount of strong binding cross-bridges, decreased when temperature was increased in muscle fibers without regulatory proteins. Detailed study has revealed that cross-bridge detachment is enhanced by increasing temperature when regulatory proteins are absent [30]. This study showed that regulatory proteins may influence the actomyosin ATPase by modifying the surface of thin filaments.

One of the interesting features of striated muscle is its autooscillatory mechanism. Skinned striated muscle self-oscillates at few Hertz without Ca^{2+} oscillation in the presence of both MgADP and inorganic phosphate (Pi) at relaxing conditions (SPOC) [30, 31]. Under these conditions, both active tension and sarcomere length oscillate periodically. To investigate whether tropomyosin is involved in the SPOC, actin-filament-reconstituted muscle fibers have been used [32]. When active tension was decreased

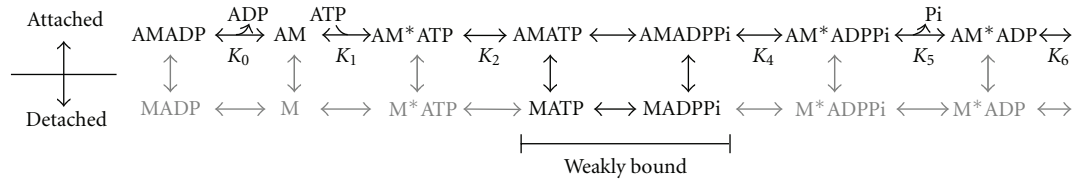


FIGURE 3: Kinetic model of actomyosin (AM) ATPase. The main pathway is shown in black and the minor pathway in grey. Upper row is in attached state and lower row is in detached state. A: actin; M: myosin. The asterisks show the difference in the conformation of the molecule.

by 2,3-butanedione 2-monoxime (BDM), the inhibitor of actomyosin ATPase, SPOC was observed in the presence of MgADP and Pi even when regulatory proteins were absent. This result clearly showed that tropomyosin is not required in SPOC and that oscillatory mechanisms are inherent in the actomyosin motor system. Recently, the mechanism of SPOC was clarified where the change in lattice spacing by mutual sliding of thick and thin filaments is the key point in the generation of oscillation [33]; this also indicated that the regulatory system is not a requirement for SPOC. Thus, the prediction made by the actin-filament-reconstituted model was shown to reflect the properties of muscle.

3. Combination with Sinusoidal Analysis

The thin filament removal and reconstitution protocol enables the exchange of actin and tropomyosin in skinned muscle fibers which is not possible in other methods, thus it is expected to be useful in studying the physiology of genetically engineered actin, troponin, and tropomyosin. Although the change in the active force by altering the surrounding environment such as pH or temperature is possible in the thin filament removal and reconstitution protocol, it is not possible to compare the active force before and after reconstitution of the actin filament because active tension recovery varies largely between experiments. This is problematic when the study of genetically engineered muscle protein is considered, because the first parameter that is to be compared is tension generation capability. To avoid this problem, it is ideal to measure the force per cross-bridge. This can be achieved by measuring the stiffness of the muscle fibers during activation to determine the number of strongly bound cross-bridges and by measuring the kinetic parameters of the actomyosin ATPase scheme to calculate the number of cross-bridges among various states. To study the kinetics of actomyosin ATPase cycle, perturbation which can alter the ATPase kinetics at a speed faster than the reaction to be studied is needed. For example, temperature jump study (T-jump) can deduce several apparent rate constants relating to the actomyosin ATPase and by changing the concentration of MgATP, MgADP, or Pi, and, accordingly, the details of actomyosin ATPase can be presumed [28, 29]. The T-jump study revealed that muscle force generation is endothermic, and several cross-bridge states exist in actomyosin complex [28, 29]. Other such “jump” experiments such as pressure [34], Pi [35, 36], or ATP [37, 38] can also deduce the elementary steps of the actomyosin ATPase. Perturbation to actomyosin ATPase can also be achieved by step length

change; the kinetics were studied using both release and stretch protocols [39–41]. Other than applying step length change, sinusoidal length change was also used, which gives a higher signal-to-noise ratio than the step length change experiments [42, 43]. Sinusoidal analysis revealed three exponential processes in response to length changes, which were attributed to six steps of the elementary steps of the cross-bridge cycle, and three equilibrium constants and four rate constants associated with this scheme were deduced [44]. Because sinusoidal analysis can characterize all of the equilibrium constants between the elementary steps of the cross-bridge cycle, calculation of the distribution of the cross-bridge species is possible. Measurement of the stiffness enables estimation of the amount of strong binding cross-bridges during activation, and consequently force per cross-bridge can also be estimated. Since sinusoidal analysis can reveal the details of the actomyosin ATPase cycle, the combination with the thin filament removal and reconstitution protocol is expected to yield many interesting results.

Investigations using the thin filament removal and reconstitution protocol and sinusoidal analysis revealed the influence of regulatory protein on the elementary steps of the cross-bridge cycle [42, 43]. These studies showed that the regulatory proteins promote cross-bridge detachment by increasing K_2 and decreasing K_4 , which was primarily caused by tropomyosin (Figure 3). This finding implies that the regulatory system inhibits actomyosin interaction even in the presence of Ca^{2+} . At the same time, active force generated by each cross-bridge was larger in the presence of regulatory proteins, which may be induced by the conformational change of actin filaments due to the presence of regulatory proteins. The combination of the thin filament removal and reconstitution protocol and sinusoidal analysis is particularly useful in studying genetically modified actin and tropomyosin. Several actin mutants were studied in which the N-terminal negative charges were changed using sinusoidal analysis [45]. Electrostatic force between the N-terminal charge of actin and the cationic loop 2 of myosin is believed to be important in the initial association with myosin. The result showed that the stronger negative charge at the N-terminal enhances active force during contraction. The effect of genetically engineered tropomyosin on cross-bridge kinetics was also studied using the thin filament reconstitution protocol and sinusoidal analysis. Tropomyosin is a coiled-coil dimeric protein that binds to seven actin monomers and its sequence shows a 7-fold repeat relating to the sites which bind to actin [46]. The seven

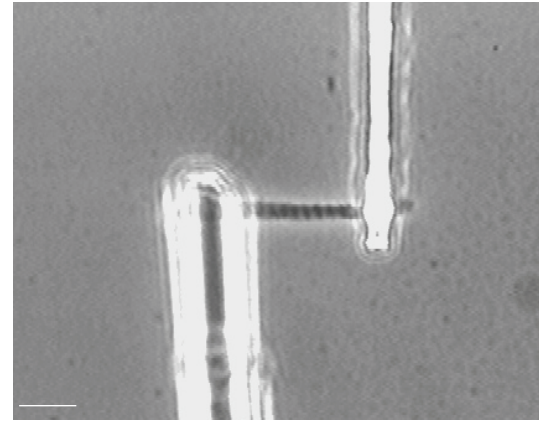
repeats are quasi-equivalent but solution studies show the differences in their functions, where the first and last periods are important in the head-to-tail association of tropomyosin molecule and period 4 involved in troponin binding. Using the thin filament reconstitution protocol, Kawai et al. showed that period 3 of tropomyosin is essential in the enhancement of isometric tension [47]. The physiological properties of tropomyosin mutations (V95A, D175N, and E180G) regarding hypertrophic cardiomyopathy (HCM) were also studied using the same method and showed that contractility was decreased and relaxation was impaired in HCM tropomyosin [48]. Likewise, the effects of phosphorylation and/or dephosphorylation of tropomyosin were investigated by using this technique [49]. These studies showed that the combination of the thin filament reconstitution protocol and sinusoidal analysis is very useful in the study of genetically modified actin and tropomyosin.

4. Studying Titin Using Thin Filament-Free Muscle Fibers

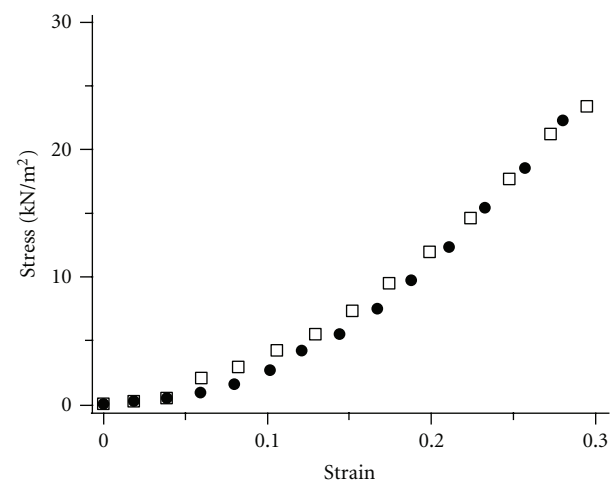
Titin (also known as connectin) is a muscle-specific giant protein with a molecular weight of 3~4MDa [50]. Titin spans from Z-disk to M-line in half sarcomere constituting a third filament in muscle, and it functions as a molecular spring during stretch which determines the passive force. The property of titin is particularly important in cardiac muscle physiology because titin's property as a spring is a major determinant of diastolic force. Mechanical properties of titin can be studied by stretching muscle fibers during relaxation, but there is an effect from slow cycling weakly bound cross-bridges [51]. The effect of weakly bound cross-bridges can be eliminated by using the thin filament-free muscle fibers, which is the state before the reconstitution of actin filament in the thin filament removal and reconstitution protocol. Figure 4 shows the stress-strain relationship of cardiac myofibril treated with gelsolin. When skinned skeletal muscle fibers were stretched after removal of thin filament, the stress-strain relationship differed from those in the presence of thin filament showing the presence of weakly-bound cross-bridges [17]. The effect of Ca^{2+} on passive force was investigated using thin filament-free muscle fibers [52]; in the presence of Ca^{2+} , it is important to eliminate the effect of cross-bridges to measure passive force, as the coexistence of Ca^{2+} and ATP will activate the cross-bridges. Studies have shown that Ca^{2+} increases the stiffness of titin, which may play a role during systole and diastole [52, 53].

5. Conclusions

The thin filament removal and reconstitution protocol is useful in the study of the physiology of actin and tropomyosin in muscle contraction. It is particularly valuable when combined with sinusoidal analysis. Actin-filament-reconstituted muscle fibers are useful in studying the properties of genetically modified actin. Thin filament-reconstituted model is helpful in studying the properties of tropomyosin. Muscle fibers without thin filament can be used to study the mechanical property of giant protein titin.



(a)



(b)

FIGURE 4: (a) Phase-contrast image of cardiac myofibril treated with gelsolin. Myofibril was held with two glass needles. Thick needle was moved to the left to stretch the myofibril and force was measured by the bending of the thin needle. Scale bar: $10\ \mu\text{m}$. (b) Stress-strain relationship of myofibril treated with gelsolin. Two examples are shown. Strain is expressed relative to the slack length.

Acknowledgment

The work of the authors was supported in part by Grants-in-Aid for Scientific Research (N.F. and S.K.), Scientific Research on Innovative Areas (N.F. and S.K.) and for Challenging Exploratory Research (N.F.) from the Ministry of Education, Culture, Sports, Science and Technology of Japan and by grants from the Japan Science and Technology Agency (CREST) (N.F.), the Vehicle Racing Commemorative Foundation (S.K.), the Institute of Seizon and Life Sciences (S.K.) and the CASIO Science Promotion Foundation (N.F.).

References

- [1] A. F. Huxley and R. Niedergerke, "Structural changes in muscle during contraction: interference microscopy of living muscle fibres," *Nature*, vol. 173, no. 4412, pp. 971–973, 1954.
- [2] H. Huxley and J. Hanson, "Changes in the cross-striations

- of muscle during contraction and stretch and their structural interpretation," *Nature*, vol. 173, no. 4412, pp. 973–976, 1954.
- [3] A. M. Gordon, M. A. LaMadrid, Y. Chen, Z. Luo, and P. B. Chase, "Calcium regulation of skeletal muscle thin filament motility in vitro," *Biophysical Journal*, vol. 72, no. 3, pp. 1295–1307, 1997.
 - [4] E. Homsher, D. M. Lee, C. Morris, D. Pavlov, and L. S. Tobacman, "Regulation of force and unloaded sliding speed in single thin filaments: effects of regulatory proteins and calcium," *Journal of Physiology*, vol. 524, no. 1, pp. 233–243, 2000.
 - [5] R. Niederman and T. D. Pollard, "Human platelet myosin. II. In vitro assembly and structure of myosin filaments," *Journal of Cell Biology*, vol. 67, no. 1, pp. 72–92, 1975.
 - [6] A. Ishijima, Y. Harada, H. Kojima, T. Funatsu, H. Higuchi, and T. Yanagida, "Single-molecule analysis of the actomyosin motor using nano-manipulation," *Biochemical and Biophysical Research Communications*, vol. 199, no. 2, pp. 1057–1063, 1994.
 - [7] M. Kaya and H. Higuchi, "Nonlinear elasticity and an 8-nm working stroke of single myosin molecules in myofilaments," *Science*, vol. 329, no. 5992, pp. 686–689, 2010.
 - [8] M. Suzuki, H. Fujita, and S. Ishiwata, "A new muscle contractile system composed of a thick filament lattice and a single actin filament," *Biophysical Journal*, vol. 89, no. 1, pp. 321–328, 2005.
 - [9] M. Hatakenaka and I. Ohtsuki, "Effect of removal and reconstitution of troponins C and I on the 2^+ -activated tension development of single glycerinated rabbit skeletal muscle fibers," *European Journal of Biochemistry*, vol. 205, no. 3, pp. 985–993, 1992.
 - [10] F. Shiraishi, M. Kambara, and I. Ohtsuki, "Replacement of troponin components in myofibrils," *Journal of Biochemistry*, vol. 111, no. 1, pp. 61–65, 1992.
 - [11] J. M. Metzger and R. L. Moss, "Myosin light chain 2 modulates calcium-sensitive cross-bridge transitions in vertebrate skeletal muscle," *Biophysical Journal*, vol. 63, no. 2, pp. 460–468, 1992.
 - [12] S. Lowey, G. S. Waller, and K. M. Trybus, "Skeletal muscle myosin light chains are essential for physiological speeds of shortening," *Nature*, vol. 365, no. 6445, pp. 454–456, 1993.
 - [13] H. Higuchi and S. Ishiwata, "Disassembly kinetics of thick filaments in rabbit skeletal muscle fibers. Effects of ionic strength, 2^+ concentration, pH, temperature, and cross-bridges on the stability of thick filament structure," *Biophysical Journal*, vol. 47, no. 3, pp. 267–275, 1985.
 - [14] T. Funatsu, H. Higuchi, and S. Ishiwata, "Elastic filaments in skeletal muscle revealed by selective removal of thin filaments with plasma gelsolin," *Journal of Cell Biology*, vol. 110, no. 1, pp. 53–62, 1990.
 - [15] H. L. M. Granzier and K. Wang, "Interplay between passive tension and strong and weak binding cross-bridges in insect indirect flight muscle: a functional dissection by gelsolin-mediated thin filament removal," *Journal of General Physiology*, vol. 101, no. 2, pp. 235–270, 1993.
 - [16] T. Funatsu, E. Kono, H. Higuchi et al., "Elastic filaments in situ in cardiac muscle: deep-etch replica analysis in combination with selective removal of actin and myosin filaments," *Journal of Cell Biology*, vol. 120, no. 3, pp. 711–724, 1993.
 - [17] H. L. M. Granzier and K. Wang, "Passive tension and stiffness of vertebrate skeletal and insect flight muscles: the contribution of weak cross-bridges and elastic filaments," *Biophysical Journal*, vol. 65, no. 5, pp. 2141–2159, 1993.
 - [18] T. Funatsu, T. Anazawa, and S. Ishiwata, "Structural and functional reconstruction of thin filaments in skeletal muscle," *Journal of Muscle Research and Cell Motility*, vol. 15, no. 2, pp. 158–171, 1994.
 - [19] H. Fujita, K. Yasuda, S. Niitsu, T. Funatsu, and S. Ishiwata, "Structural and functional reconstitution of thin filaments in the contractile apparatus of cardiac muscle," *Biophysical Journal*, vol. 71, no. 5, pp. 2307–2318, 1996.
 - [20] T. F. Robinson and S. Winegrad, "Variation of thin filament length in heart muscle," *Nature*, vol. 267, no. 5606, pp. 74–75, 1977.
 - [21] M. Kawai and S. Ishiwata, "Use of thin filament reconstituted muscle fibres to probe the mechanism of force generation," *Journal of Muscle Research and Cell Motility*, vol. 27, no. 5–7, pp. 455–468, 2006.
 - [22] D. W. Maughan and R. E. Godt, "A quantitative analysis of elastic, entropic, electrostatic, and osmotic forces within relaxed skinned muscle fibers," *Biophysics of Structure and Mechanism*, vol. 7, no. 1, pp. 17–40, 1980.
 - [23] M. J. Dawson, D. G. Gadian, and D. R. Wilkie, "Muscular fatigue investigated by phosphorus nuclear magnetic resonance," *Nature*, vol. 274, no. 5674, pp. 861–866, 1978.
 - [24] K. A. P. Edman and A. R. Mattiazzi, "Effects of fatigue and altered pH on isometric force and velocity of shortening at zero load in frog muscle fibres," *Journal of Muscle Research and Cell Motility*, vol. 2, no. 3, pp. 321–334, 1981.
 - [25] H. Fujita and S. Ishiwata, "Tropomyosin modulates pH dependence of isometric tension," *Biophysical Journal*, vol. 77, no. 3, pp. 1540–1546, 1999.
 - [26] S. P. Robertson and W. G. Kerrick, "The effects of pH on 2^+ -activated force in frog skeletal muscle fibers," *Pflugers Archiv European Journal of Physiology*, vol. 380, no. 1, pp. 41–45, 1979.
 - [27] P. B. Chase and M. J. Kushmerick, "Effects of pH on contraction of rabbit fast and slow skeletal muscle fibers," *Biophysical Journal*, vol. 53, no. 6, pp. 935–946, 1988.
 - [28] K. W. Ranatunga, "Endothermic force generation in skinned cardiac muscle from rat," *Journal of Muscle Research and Cell Motility*, vol. 20, no. 5–6, pp. 489–496, 1999.
 - [29] Y. E. Goldman, J. A. McCray, and K. W. Ranatunga, "Transient tension changes initiated by laser temperature jumps in rabbit psoas muscle fibres," *Journal of Physiology*, vol. 392, pp. 71–95, 1987.
 - [30] H. Fujita and M. Kawai, "Temperature effect on isometric tension is mediated by regulatory proteins tropomyosin and troponin in bovine myocardium," *Journal of Physiology*, vol. 539, part 1, pp. 267–276, 2002.
 - [31] N. Fukuda, H. Fujita, T. Fujita, and S. Ishiwata, "Spontaneous tension oscillation in skinned bovine cardiac muscle," *Pflugers Archiv European Journal of Physiology*, vol. 433, no. 1–2, pp. 1–8, 1996.
 - [32] H. Fujita and S. Ishiwata, "Spontaneous oscillatory contraction without regulatory proteins in actin filament-reconstituted fibers," *Biophysical Journal*, vol. 75, no. 3, pp. 1439–1445, 1998.
 - [33] K. Sato, M. Ohtaki, Y. Shimamoto, and S. Ishiwata, "A theory on auto-oscillation and contraction in striated muscle," *Progress in Biophysics and Molecular Biology*, vol. 105, no. 3, pp. 199–207, 2011.
 - [34] N. S. Fortune, M. A. Geeves, and K. W. Ranatunga, "Contractile activation and force generation in skinned rabbit muscle fibres: effects of hydrostatic pressure," *Journal of Physiology*, vol. 474, no. 2, pp. 283–290, 1994.

- [35] J. A. Dantzig, Y. E. Goldman, N. C. Millar, J. Lacktis, and E. Homsher, "Reversal of the cross-bridge force-generating transition by photogeneration of phosphate in rabbit psoas muscle fibres," *Journal of Physiology*, vol. 451, pp. 247–278, 1992.
- [36] E. Homsher and N. C. Millar, "Caged compounds and striated muscle contraction," *Annual Review of Physiology*, vol. 52, pp. 875–896, 1990.
- [37] K. Horiuti, K. Kagawa, and K. Yamada, "Transient contraction of muscle fibers on photorelease of ATP at intermediate concentrations of 2^+ ," *Biophysical Journal*, vol. 67, no. 5, pp. 1925–1932, 1994.
- [38] J. A. Dantzig, M. G. Hibberd, D. R. Trentham, and Y. E. Goldman, "Cross-bridge kinetics in the presence of MgADP investigated by photolysis of caged ATP in rabbit psoas muscle fibres," *Journal of Physiology*, vol. 432, pp. 639–680, 1991.
- [39] G. Piazzesi, F. Francini, M. Linari, and V. Lombardi, "Tension transients during steady lengthening of tetanized muscle fibres of the frog," *Journal of Physiology*, vol. 445, pp. 659–711, 1992.
- [40] G. Piazzesi, M. Linari, M. Reconditi, F. Vanzi, and V. Lombardi, "Cross-bridge detachment and attachment following a step stretch imposed on active single frog muscle fibres," *Journal of Physiology*, vol. 498, no. 2, part 1, pp. 3–15, 1997.
- [41] M. Linari, V. Lombardi, and G. Piazzesi, "Cross-bridge kinetics studied with staircase shortening in single fibres from frog skeletal muscle," *Journal of Muscle Research and Cell Motility*, vol. 18, no. 1, pp. 91–101, 1997.
- [42] H. Fujita, D. Sasaki, S. Ishiwata, and M. Kawai, "Elementary steps of the cross-bridge cycle in bovine myocardium with and without regulatory proteins," *Biophysical Journal*, vol. 82, no. 2, pp. 915–928, 2002.
- [43] H. Fujita, X. Lu, M. Suzuki, S. Ishiwata, and M. Kawai, "The effect of tropomyosin on force and elementary steps of the cross-bridge cycle in reconstituted bovine myocardium," *Journal of Physiology*, vol. 556, part 2, pp. 637–649, 2004.
- [44] M. Kawai and H. R. Halvorson, "Two step mechanism of phosphate release and the mechanism of force generation in chemically skinned fibers of rabbit psoas muscle," *Biophysical Journal*, vol. 59, no. 2 I, pp. 329–342, 1991.
- [45] X. Lu, M. K. Bryant, K. E. Bryan, P. A. Rubenstein, and M. Kawai, "Role of the N-terminal negative charges of actin in force generation and cross-bridge kinetics in reconstituted bovine cardiac muscle fibres," *Journal of Physiology*, vol. 564, part 1, pp. 65–82, 2005.
- [46] A. D. McLachlan and M. Stewart, "The 14 fold periodicity in α tropomyosin and the interaction with actin," *Journal of Molecular Biology*, vol. 103, no. 2, pp. 271–293, 1976.
- [47] M. Kawai, X. Lu, S. E. Hitchcock-Degregori et al., "Tropomyosin period 3 is essential for enhancement of isometric tension in thin filament-reconstituted bovine myocardium," *Journal of Biophysics*, vol. 2009, Article ID 380967, 17 pages, 2009.
- [48] F. Bai, A. Weis, A. K. Takeda et al., "Enhanced active cross-bridges during diastole: molecular pathogenesis of tropomyosin's HCM mutations," *Biophysical Journal*, vol. 10, no. 4, pp. 1013–1023, 2011.
- [49] X. Lu, D. H. Heeley, L. B. Smillie, and M. Kawai, "The role of tropomyosin isoforms and phosphorylation in force generation in thin-filament reconstituted bovine cardiac muscle fibres," *Journal of Muscle Research and Cell Motility*, vol. 31, no. 2, pp. 93–109, 2010.
- [50] S. Labeit and B. Kolmerer, "Titins: giant proteins in charge of muscle ultrastructure and elasticity," *Science*, vol. 270, no. 5234, pp. 293–296, 1995.
- [51] R. Horowitz, E. S. Kempner, M. E. Bisher, and R. J. Podolsky, "A physiological role for titin and nebulin in skeletal muscle," *Nature*, vol. 323, no. 6084, pp. 160–164, 1986.
- [52] H. Fujita, D. Labeit, B. Gerull, S. Labeit, and H. L. Granzier, "Titin isoform-dependent effect of calcium on passive myocardial tension," *American Journal of Physiology*, vol. 287, no. 6, pp. H2528–H2534, 2004.
- [53] D. Labeit, K. Watanabe, C. Witt et al., "Calcium-dependent molecular spring elements in the giant protein titin," *Proceedings of the National Academy of Sciences of the United States of America*, vol. 100, no. 23, pp. 13716–13721, 2003.

Research Article

Creep Behavior of Passive Bovine Extraocular Muscle

Lawrence Yoo,^{1,2} Hansang Kim,² Andrew Shin,^{1,2} Vijay Gupta,^{2,3} and Joseph L. Demer^{1,3,4,5}

¹ Department of Ophthalmology, Jules Stein Eye Institute, University of California Los Angeles, 100 Stein Plaza, UCLA, Los Angeles, CA 90095-7002, USA

² Department of Mechanical Engineering, University of California, Los Angeles, CA, USA

³ Biomedical Engineering Interdepartmental Program, University of California, Los Angeles, CA, USA

⁴ Neuroscience Interdepartmental Program, University of California, Los Angeles, CA, USA

⁵ Department of Neurology, University of California, Los Angeles, CA, USA

Correspondence should be addressed to Joseph L. Demer, jld@ucla.edu

Received 6 June 2011; Accepted 16 August 2011

Academic Editor: Henk Granzier

Copyright © 2011 Lawrence Yoo et al. This is an open access article distributed under the Creative Commons Attribution License, which permits unrestricted use, distribution, and reproduction in any medium, provided the original work is properly cited.

This paper characterized bovine extraocular muscles (EOMs) using creep, which represents long-term stretching induced by a constant force. After preliminary optimization of testing conditions, 20 fresh EOM samples were subjected to four different loading rates of 1.67, 3.33, 8.33, and 16.67%/s, after which creep was observed for 1,500 s. A published quasilinear viscoelastic (QLV) relaxation function was transformed to a creep function that was compared with data. Repeatable creep was observed for each loading rate and was similar among all six anatomical EOMs. The mean creep coefficient after 1,500 seconds for a wide range of initial loading rates was at 1.37 ± 0.03 (standard deviation, SD). The creep function derived from the relaxation-based QLV model agreed with observed creep to within 2.7% following 16.67%/s ramp loading. Measured creep agrees closely with a derived QLV model of EOM relaxation, validating a previous QLV model for characterization of EOM biomechanics.

1. Introduction

Since strabismus surgery manipulates extraocular muscles (EOMs) mechanically to correct binocular misalignment, accurate determination of quasistatic biomechanical properties of EOMs may be important. Classical studies investigated the uniaxial force and length relationship for EOMs [1–4]. More recently, comprehensive biomechanical methods have been employed to characterize constitutive models [5] for EOMs, representing their viscoelastic, or history-dependent relationship between stress and strain [6, 7]. Several important mechanical behaviors reflect viscoelasticity: hysteresis, relaxation, attenuation of acoustic waves, and creep.

Hysteresis is history dependent variation in mechanical behavior, resulting in differences in stress between loading and unloading phases. Hysteresis implies work, energy dissipation due to loading and unloading [5, 8, 9]. Relaxation describes how a material deformed by external perturbation returns to equilibrium. In stress relaxation testing, a material is rapidly subjected to displacement and then maintained over an extended time interval at the same displacement by

external feedback while a decline in required external force is observed [6, 10–13].

Creep is the tendency of a material to deform permanently under constant force. To characterize creep, tensile loading is rapidly imposed and maintained at a constant level while specimen elongation is observed over an extended time [13, 14]. Creep is likely to be particularly significant in binocular alignment and strabismus, where agonist and antagonist EOMs remain under loading for extended time periods, and where such loading is purposely altered by, for example, strabismus surgery that alters EOM tension.

While viscoelastic properties have often been neglected in interpretation of conventional EOM length-tension data, realistic constitutive modeling is essential for accurate finite element models (FEMs) that graphically simulate interactions of EOMs with orbital connective tissues. Supporting this contention, Quaia et al. [7] and our previous investigation [6] highlighted the need for valid constitutive models of EOMs in application of quasilinear viscoelastic (QLV) theory to constitutive modeling.

Linear elasticity theory is well established for strains of $\leq 3\%$ in generic materials. Soft tissues generally, however, undergo larger physiological strains in the range of tens of percent where behavior becomes nonlinear. Modeling of EOMs should consider the hyperelastic nature of soft tissue, which means that it is highly nonlinearly elastic [12, 15–20] Fung’s QLV theory [5, 21–23] is appropriate because it incorporates both linear viscoelastic and nonlinear elastic characteristics. We previously reported that a QLV model based upon *in vitro* relaxation data was effective in describing mechanical behavior of passive bovine EOMs [6].

Quaia et al. found limitations in QLV describing constitutive properties of *in vivo* simian EOMs at short-time scale and proposed a modification that they termed adaptive quasilinear viscoelasticity (AQLV) [7]. Although AQLV was superior to QLV in describing EOM properties relevant to the most rapid eye movements (saccades), the approach is computationally intensive and requires extensive data collection that would limit its practicality for FEM. We supposed that the simpler QLV formulation might be adequate to quasistatic, passive behavior of EOMs relevant in binocular alignment and strabismus.

Since the EOMs are not contracting when under tensile loading, we emulated a previous study with the assumption that absence of perfusion and innervation would not strongly influence constitutive properties [6]. By investigating EOM creep, we aimed to extend understanding of their time-dependent stress-strain behavior and to validate the previously reported relaxation-based QLV model applicable to FEM [6].

2. Methods

The approach was similar to that previously published [6]. The EOM specimens prepared from heads of cattle freshly slaughtered for food. The total time from slaughter to mechanical testing ranged from 3 to 4 hours. During the preparation of specimens, the tissues were constantly irrigated with lactated Ringer solution, which was kept at 37°C , to prevent any dehydration. The EOM specimens were cut into 2–3 cm long rectangular prisms (length of actual bovine EOMs) having $2\text{ mm} \times 2\text{ mm}$ cross-section. Actual test length of each specimen was 10 mm, with $\leq 5\text{ mm}$ on both ends that was clamped on the load cell, excluding the terminal tendon. As in the previous study, a tabletop microtensile load cell, Instron model 4411 (Instron, Norwood, Mass, Series IX software) was enclosed in a plastic chamber where warm water vapor and radiant heat maintained physiologic 97% humidity and 37°C temperature as indicated by a sensor (Fisher Scientific, Chino, Calif). Preconditioning was omitted because a previous investigation of passive EOM relaxation properties demonstrated that preconditioning did not influence results [6]. For both creep testing and preliminary experiments to optimize the testing parameters, total of 60 EOM specimens from 8 different bovine orbits were used.

2.1. Creep Testing. We determined the reduced creep ($\epsilon(t)/\epsilon(0)$). In ideal creep testing, an initial tensile force should be

imposed on the specimen instantaneously and then maintained at a constant level for an extended time [5, 13]. Since instantaneous imposition of tensile force is physically impossible, tensile force is rapidly increased at a constant ramp rate to a level that is subsequently maintained. Based upon tensile-loading results [6], we selected 0.2 N, which produces 30% strain that is well within the linear range, as an appropriate ramp force. Although the maximum loading rate of the load cell was 550 mm/min, it was necessary to limit the rate to 100 mm/min to maintain stable force feedback. Therefore, all the creep tests were performed at the following four rates: 10, 20, 50, and 100 mm/min, equivalent to 1.67, 3.33, 8.33, and 16.67%/s, respectively. After the initial loading of 0.2 N was imposed, this force was then maintained by the load cell’s feedback servo for 1,500 s during recording of specimen length.

2.2. Fung’s Quasilinear Viscoelasticity Theory. It represents stress as a function of strain and time. In stress relaxation testing, strain is held constant and the stress declines as a function of time alone:

$$\sigma(\mathbf{t}) = \sigma_0 \mathbf{G}(\mathbf{t}), \quad (1)$$

where $\mathbf{G}(\mathbf{t})$ is the time dependent reduced relaxation function with $\mathbf{G}(\mathbf{0}) = \mathbf{1}$, and σ_0 is initial stress. Similarly, for static creep in which stress is held constant, strain varies as a function of time alone:

$$\epsilon(\mathbf{t}) = \epsilon_0 \mathbf{J}(\mathbf{t}), \quad (2)$$

where $\mathbf{J}(\mathbf{t})$ is the time dependent reduced creep function with $\mathbf{J}(\mathbf{0}) = \mathbf{1}$ and ϵ_0 is the initial strain. For linear viscoelasticity [5], which is a special case of the more general QLV theory [24], time-varying stress relaxation function $\mathbf{G}(\mathbf{t})$ and creep function $\mathbf{J}(\mathbf{t})$ should be related as follows:

$$\mathbf{G}(\mathbf{0}) = \frac{\mathbf{1}}{\mathbf{J}(\mathbf{0})}, \quad (3)$$

$$\mathbf{G}(\infty) = \frac{\mathbf{1}}{\mathbf{J}(\infty)},$$

or

$$\mathbf{G}(\mathbf{s})\mathbf{J}(\mathbf{s}) = \frac{\mathbf{1}}{\mathbf{s}^2}, \quad (4)$$

where $\mathbf{G}(\mathbf{s})$ and $\mathbf{J}(\mathbf{s})$ are Laplace transforms of the functions $\mathbf{G}(\mathbf{t})$ and $\mathbf{J}(\mathbf{t})$, respectively. A nonlinear least square method was used in previous study fit the stress relaxation data, determining constants \mathbf{a} , \mathbf{b} , \mathbf{c} , \mathbf{d} , \mathbf{g} , and \mathbf{h} [6]:

$$\mathbf{G}(\mathbf{t}) = \mathbf{a}e^{(-\mathbf{b}\mathbf{t})} + \mathbf{c}e^{(-\mathbf{d}\mathbf{t})} + \mathbf{g}e^{(-\mathbf{h}\mathbf{t})}. \quad (5)$$

Using the Laplace transform of the stress relaxation function and (4), a predicted creep function for EOM was determined using MatLab (The Mathworks Inc, Natick, Mass, USA).

3. Results and Discussion

As is typical for creep testing generally [5, 24, 25], a logarithmically increasing displacement was observed after

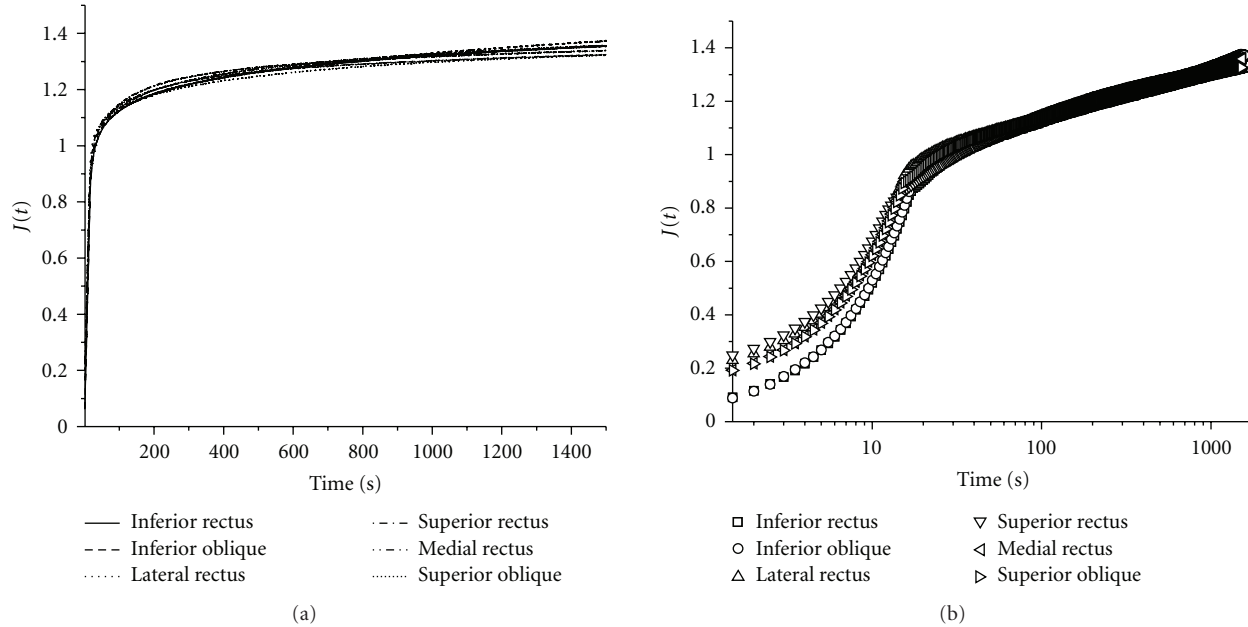


FIGURE 1: Mean normalized displacement $J(t)$ plotted for two specimens each of the six bovine EOMs in both linear and semi-log scales. All EOMs exhibited similar creep to 1.34 ± 0.02 (SD) maximum.

initial ramp loading of each specimen, without asymptote. Data were plotted as normalized displacement $J(t)$, the ratio of instantaneous specimen length to initial length.

3.1. Creep for Each Anatomical EOM. Although relaxation and tensile properties were similar among the four rectus and both oblique bovine EOMs in the previous study [6], preliminary experiments were conducted on two specimens of each of the six EOMs to determine if they exhibit similar creep at 3.33%/s strain rate. As can be seen from Figure 1, creep was essentially identical for all six EOMs.

3.2. Dependence of Creep on Ramp-Loading Rate. In order to determine if EOM properties depend on initial loading, experiments were conducted for five specimens each at four ramp-loading rates: 1.67, 3.33, 8.33, and 16.67%/s. As an example, Figures 2(a) and 2(b) show the force displacement and creep plots for 0.2 N force. Since all EOMs exhibited similar creep, differentiation of each anatomical EOM was unnecessary.

Creep at other ramp-loading rates was similar to Figure 2, with maximum standard deviations (SDs) for five specimens each of 0.029, 0.056, and 0.036 for 3.33, 8.33, and 16.67%/s loading, respectively.

As seen in Figure 3, for all four initial loading rates, creep coefficients at the end of 1,500 seconds were similar at 1.37 ± 0.033 . Despite the ultimate similarity of creep behavior, the linear part of each curve under initial loading steepened as loading rate increased, and the shape of each curve varied with loading rate (Figure 3). As loading rate decreased, the curve showed slower elongation. Since EOM is a soft tissue,

TABLE 1: QLV relaxation model parameters.

a	2.81
b (1/sec)	1.57
c	0.86
d (1/sec)	1.4×10^{-4}
g	0.34
h (1/sec)	1.7×10^{-2}

reaching a true asymptotic value during creep testing is neither practical nor theoretically necessary [5, 25]. Although the creeping behavior exhibited by EOM after ramp loading is used in its viscoelastic characterization, the rate-dependent ramp behavior can also be used to understand the contribution of EOM elasticity in its overall creep behavior. With behavior of the EOM during the ramp phase being less affected by viscosity as the loading rate is decreased, one can optimize the loading rate for tensile testing to extract the tensile elasticity of the EOM.

3.3. Conversion of Relaxation Function to Creep Function. All constants in the reduced relaxation function were derived from the published relaxation function [6] and are shown in Table 1.

Using parameters extracted from the QLV relaxation model, (4) in the time domain was converted to a reduced creep function using the inverse Laplace transform function and symbolic toolbox in Matlab, 6 constant values from the Laplace S domain (6), and 7 constants from the time

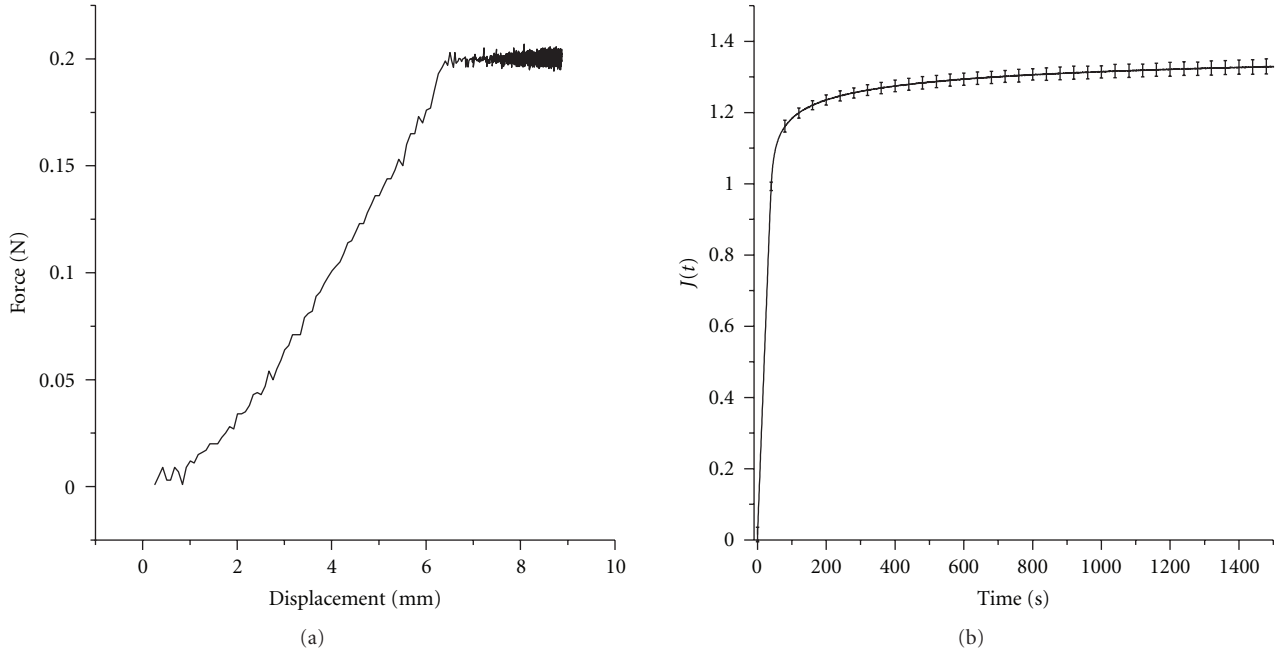


FIGURE 2: Mean creep for 1.67%/s loading rate for 5 EOM specimens. (a) Force versus displacement. After initial ramp loading achieved at around 6 mm deformation, the force was held constant at 0.2 N. (b) Reduced creep coefficients over 1,500 seconds. Maximum creep coefficient SD was 0.023.

TABLE 2: Constants in Time and Laplace S Domain for Creep (6) and (7).

a_1	2.81	C_1	1.6137×10^{-4}
a_2	1.57	C_2	4.0473×10^{21}
a_3	0.86	C_3	0.2312
a_4	1.4×10^{-4}	C_4	1.5097×10^{22}
a_5	0.34	C_5	1.6788×10^{22}
a_6	1.7×10^{-2}	C_6	0.2434
		C_7	1.1487

domain (7) of the resulting reduced creep function are listed in Table 2

$$J(s) = \frac{1}{S^2(a_1/(s+a_2) + a_3/(s+a_4) + a_5/(s+a_6))}, \quad (6)$$

$$J(t) = C_1 t + \frac{C_2 \sinh(C_3 t) - C_4 \cosh(C_3 t)}{C_5 \exp(C_6 t)} + C_7. \quad (7)$$

Since ideal initial loading is assumed instantaneous, data obtained at higher rates of initial ramp loading should more closely reflect ideal creep. Hence, the reduced creep function derived from the reduced relaxation function was compared with experimental data for the highest ramp-loading rate, showing close agreement (Figure 4). Experimental creep coefficient values fell within $\pm 2.7\%$ of theoretical values for all time points tested.

When an EOM is innervated and perfused with oxygenated blood, it is constantly under tension. It is important to understand EOM creep properties for simulation of the

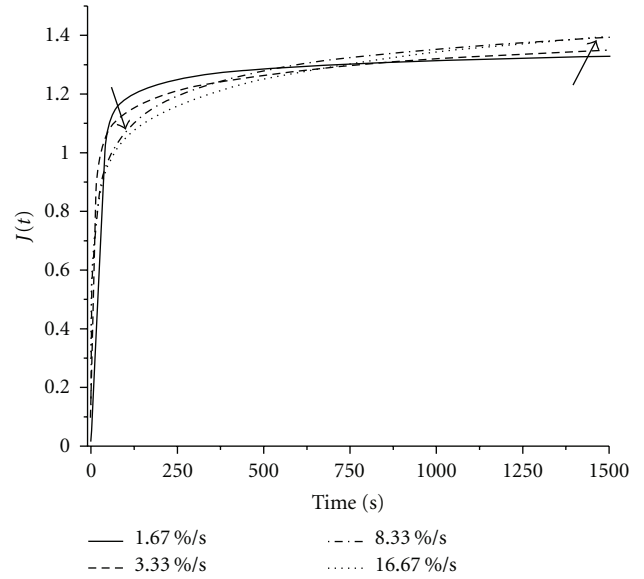


FIGURE 3: Comparison of creep at 4 different initial loading rates. The left arrow indicates that a lower reduced creep coefficient is reached at the end of initial ramp loading as the ramp-loading rate increases. The right arrow indicates that a higher creep coefficient is reached after 1500 seconds as ramp-loading rate increases.

common situation where a physiologically relaxing EOM is still experiencing tensile force exerted by its antagonist. In the current study, passive bovine EOM creep was investigated within the framework of linear viscoelasticity by comparing converted creep function from QLV model based upon stress

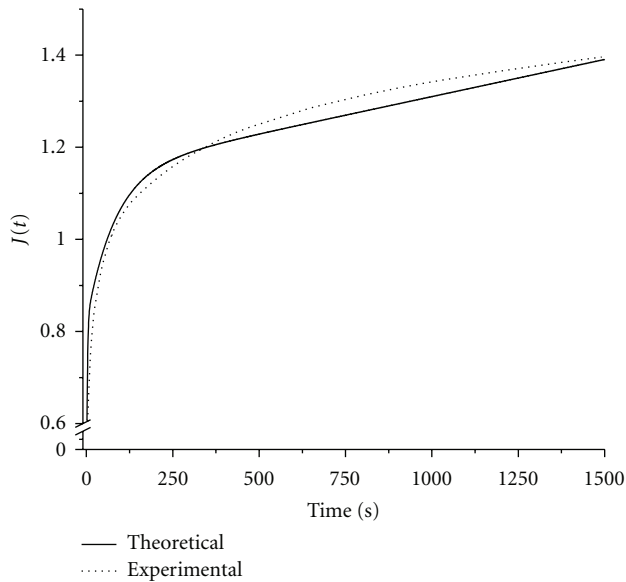


FIGURE 4: Observed reduced EOM creep function, and theoretical function derived from the reduced relaxation function.

relaxation data [6]. The current experiment varied initial elongation rate and demonstrated excellent agreement with the theoretical prediction based upon QLV relaxation model. It has been suggested that initial ramp loading for creep testing of articular cartilage should occur within 250 ms [20]; however, even over a longer time of 800 ms, the data for bovine EOMs agreed closely with values derived from relaxation function.

Regardless of which anatomical rectus or oblique EOM was tested, creep for initial ramp-loading rates from 1.67 to 16.7%/s showed similar asymptotic creep coefficients of 1.37 ± 0.03 over 1,500 s. However, dynamic creep varied with initial strain rate. Creep coefficient $J(t)$ reached a higher initial value when the loading rate was lower, but subsequently increased more slowly (Figure 3). It seems reasonable to assume that each EOM specimen has the same elasticity. It is a well-accepted notion that when solid specimen is stretched slowly, dynamic contributions are reduced because at low initial loading speed, elasticity predominates over viscous effects [26–28]. With predominantly elastic effects, less energy is dissipated than when initial loading is rapid. Since the present models were based upon data from low strain rates, we suggest that the QLV models derived from these investigations are most applicable to slow eye movements such as fixations and pursuit. Since loading for both relaxation and creep tests closely approximates ideal step loading, the relaxation and creep functions are likely to accurately reflect EOM viscosity.

4. Conclusion

This paper validated a previously reported QLV model for EOM relaxation. Since a reduced creep function is the inverse Laplace transform of a reduced relaxation function, agreement between experimental creep and the previously

published reduced relaxation function constitutes a strong test of the relaxation-based QLV model for passive EOMs, with experimental agreement to within $\pm 2.7\%$ of theoretical values. Hence, we can infer that a QLV model based upon relaxation effectively describes the constitutive properties of passive EOMs. The present validation of the quantitative viscoelastic constitutive relationship for passive bovine EOM provides better understanding of EOM biomechanics, in a theoretical framework practical for graphical simulation of quasistatic ocular motility using FEM.

Acknowledgments

This paper is supported by US Public Health Service, National Eye Institute: Grants EY08313 and EY00331; Research to Prevent Blindness. J. Demer is Leonard Apt Professor of Ophthalmology.

References

- [1] D. A. Robinson, D. M. O'Meara, A. B. Scott, and C. C. Collins, "Mechanical components of human eye movements," *Journal of Applied Physiology*, vol. 26, no. 5, pp. 548–553, 1969.
- [2] C. C. Collins, M. R. Carlson, A. B. Scott, and A. Jampolsky, "Extraocular muscle forces in normal human subjects," *Investigative Ophthalmology and Visual Science*, vol. 20, no. 5, pp. 652–664, 1981.
- [3] H. J. Simonsz, "Force-length recording of eye muscles during local anesthesia surgery in 32 strabismus patients," *Strabismus*, vol. 2, no. 4, pp. 197–218, 1994.
- [4] C. Quaia, H. S. Ying, A. M. Nichols, and L. M. Optican, "The viscoelastic properties of passive eye muscle in primates. I: static and step responses," *PLoS ONE*, vol. 4, no. 4, Article ID e4850, 2009.
- [5] Y. C. Fung, *Biomechanics: Mechanical Properties of Living Tissues*, Springer, New York, NY, USA, 1993.
- [6] L. H. Yoo, H. Kim, V. Gupta, and J. L. Demer, "Quasi-linear viscoelastic behavior of bovine extra-ocular muscle tissue," *Investigative Ophthalmology and Visual Science*, vol. 50, no. 8, pp. 3721–3728, 2009.
- [7] C. Quaia, H. S. Ying, and L. M. Optican, "The viscoelastic properties of passive eye muscle in primates. II: testing the quasi-linear theory," *PLoS ONE*, vol. 4, no. 8, Article ID e6480, 2009.
- [8] M. S. Shall, D. M. Dimitrova, and S. J. Goldberg, "Extraocular motor unit and whole-muscle contractile properties in the squirrel monkey: summation of forces and fiber morphology," *Experimental Brain Research*, vol. 151, no. 3, pp. 338–345, 2003.
- [9] S. Sklavos, D. M. Dimitrova, S. J. Goldberg, J. Porrill, and P. Dean, "Long time-constant behavior of the oculomotor plant in barbiturate-anesthetized primate," *Journal of Neurophysiology*, vol. 95, no. 2, pp. 774–782, 2006.
- [10] J. C. Downs, J. K. F. Suh, K. A. Thomas, A. J. Bellezza, R. T. Hart, and C. F. Burgoyne, "Viscoelastic material properties of the peripapillary sclera in normal and early-glaucoma monkey eyes," *Investigative Ophthalmology and Visual Science*, vol. 46, no. 2, pp. 540–546, 2005.
- [11] H. C. Lin, M. K. W. Kwan, and S. L. Y. Woo, "On the stress relaxation properties of the anterior cruciate ligament(ACL)," in *Proceedings of the Annual Meeting of the American Society of Mechanical Engineers*, pp. 5–6, Advances in Bioengineering, 1987.

- [12] C. E. Miller and C. L. Wong, "Trabeculated embryonic myocardium shows rapid stress relaxation and non-quasi-linear viscoelastic behavior," *Journal of Biomechanics*, vol. 33, no. 5, pp. 615–622, 2000.
- [13] V. C. Mow, S. C. Kuei, W. M. Lai, and C. G. Armstrong, "Biphasic creep and stress relaxation of articular cartilage in compression: theory and experiments," *Journal of Biomechanical Engineering*, vol. 102, no. 1, pp. 73–84, 1980.
- [14] I. S. Nash, P. R. Greene, and C. S. Foster, "Comparison of mechanical properties of keratoconus and normal corneas," *Experimental Eye Research*, vol. 35, no. 5, pp. 413–424, 1982.
- [15] J. G. Pinto and Y. C. Fung, "Mechanical properties of the heart muscle in the passive state," *Journal of Biomechanics*, vol. 6, no. 6, pp. 597–616, 1973.
- [16] J. M. Huyghe, D. H. van Campen, T. Arts, and R. M. Heethaar, "The constitutive behaviour of passive heart muscle tissue: a quasi-linear viscoelastic formulation," *Journal of Biomechanics*, vol. 24, no. 9, pp. 841–849, 1991.
- [17] B. S. Myers, J. H. McElhaney, and B. J. Doherty, "The viscoelastic responses of the human cervical spine in torsion: experimental limitations of quasi-linear theory, and a method for reducing these effects," *Journal of Biomechanics*, vol. 24, no. 9, pp. 811–817, 1991.
- [18] S. R. Toms, G. J. Dakin, J. E. Lemons, and A. W. Eberhardt, "Quasi-linear viscoelastic behavior of the human periodontal ligament," *Journal of Biomechanics*, vol. 35, no. 10, pp. 1411–1415, 2002.
- [19] C. E. Miller, M. A. Vanni, and B. B. Keller, "Characterization of passive embryonic myocardium by quasi-linear viscoelasticity theory," *Journal of Biomechanics*, vol. 30, no. 9, pp. 985–988, 1997.
- [20] S. L.-Y. Woo, B. R. Simon, S. C. Kuei, and W. H. Akeson, "Quasi-linear viscoelastic properties of normal articular cartilage," *Journal of Biomechanical Engineering*, vol. 102, no. 2, pp. 85–90, 1980.
- [21] Y. C. Fung, "Elasticity of soft tissues in simple elongation," *The American Journal of Physiology*, vol. 213, no. 6, pp. 1532–1544, 1967.
- [22] Y. C. Fung, *Stress-Strain-History Relations of Soft Tissues in Simple Elongation*, *Biomechanics: Its Foundations and Objectives*, Prentice-Hall, Englewood Cliffs, NJ, USA, 1972.
- [23] N. Simin, L. E. Bilston, and N. Phan-Thien, "Viscoelastic properties of pig kidney in shear, experimental results and modelling," *Rheologica Acta*, vol. 41, no. 1, pp. 180–192, 2002.
- [24] G. M. Thornton, C. B. Frank, and N. G. Shrive, "Ligament creep behavior can be predicted from stress relaxation by incorporating fiber recruitment," *Journal of Rheology*, vol. 45, no. 2, pp. 493–507, 2001.
- [25] B. R. Simon, R. S. Coats, and S. L. Y. Woo, "Relaxation and creep quasilinear viscoelastic models for normal articular cartilage," *Journal of Biomechanical Engineering*, vol. 106, no. 2, pp. 159–164, 1984.
- [26] X. Hu and G. S. Daehn, "Effect of velocity on flow localization in tension," *Acta Materialia*, vol. 44, no. 3, pp. 1021–1033, 1996.
- [27] W. Ze-Ping, "Void-containing nonlinear materials subject to high-rate loading," *Journal of Applied Physics*, vol. 81, no. 11, pp. 7213–7227, 1997.
- [28] T. Nicholas, "Tensile testing of materials at high rates of strain," *Experimental Mechanics*, vol. 21, no. 5, pp. 177–185, 1981.

Research Article

Contractile Strength during Variable Heart Duration Is Species and Preload Dependent

Carlos A. A. Torres^{1,2} and Paul M. L. Janssen¹

¹Department of Physiology and Cell Biology, The Ohio State University, Columbus, OH 43210, USA

²Department of Emergency Medicine, The Ohio State University, Columbus, OH 43210, USA

Correspondence should be addressed to Paul M. L. Janssen, janssen.10@osu.edu

Received 1 July 2011; Accepted 15 August 2011

Academic Editor: Henk Granzier

Copyright © 2011 C. A. A. Torres and P. M. L. Janssen. This is an open access article distributed under the Creative Commons Attribution License, which permits unrestricted use, distribution, and reproduction in any medium, provided the original work is properly cited.

We investigate the effect of beat-to-beat variability on cardiac contractility. Cardiac trabeculae were isolated from the right ventricle of rabbits and beagle dogs and stimulated to isometrically contract, alternating between fixed steady state versus variable interbeat intervals. Trabeculae were stimulated at physiologically relevant frequencies for each species (dog 1 and 4 Hz; rabbit 2 and 4 Hz) intercalating fixed periods with 40% variability. A subset of the trabeculae (at 90% of optimal length) was stretched prior to stimulation between 5 and 13% and stimulated at the same frequencies with a fixed versus 40% variation. Fixed rate response at the same base frequency was measured before and after each variable period and the average force reported. In canine preparations no change in force was observed as a result of the imposed variability in beat-to-beat duration. In the rabbit, we observed a non-significant decrease in force between fixed and variable pacing at both 2 and 4 Hz ($n = 8$) when 40% variability was introduced. When a 5% and 13% stretch was applied, the correlation coefficient sharply increased, indicating a more prominent impact of the prebeat duration on the following cycle with higher preload.

1. Introduction

Bowditch [1] described the influence of the interval between beats on force development over 100 years ago. His landmark experiments in frog hearts ascribed prime importance to the effect of the interval between beats on the strength of contraction. Widely recognized as one of the most important relationships in cardiac physiology, the force frequency relationship has ever since been subject of intense investigation in the field of cardiac mechanics. The force-frequency relationship (FFR) describes that an increase in force development is observed as the interval between beats decreases (higher frequency) and has been shown *in vivo* and *in vitro*, occurs in all healthy mammals [2], and this FFR is impaired in patients with heart failure [3]. Typically, these changes in contractile force develop over several beats and are generally derived from steady-state observations at different frequencies [4].

Other intrinsic and seemingly opposite phenomena in mammalian myocardium act on a more immediate non-steady-state beat-to-beat basis. Postrest potentiation des-

cribes the stronger force development seen when stimulation is resumed after a longer than usual interval, that is, a period or rest, between beats [5]. Mechanical restitution describes the dependency of the recovery of contractile force on the interval between contractions, namely, that a shorter interval leads to a weaker beat and a longer interval leads to a stronger beat [6, 7]. Postextrasystolic potentiation is yet another mechanism whereby a shorter interval that precedes a longer interval determines a stronger contraction in the subsequent beat [8].

In our previous work in rat, we were able to show small gains in average contractile force over the fixed rate period given an equivalent number of beats in each period [9]. Here, to translate these findings to species that more closely resemble human cardiac function, we investigated R-R interval modulation (such as what may occur during atrial fibrillation) may have on the inotropic status of the myocardium in rabbits and dogs and seek to verify the impact of this strategy on different species with different calcium handling and EC coupling properties.

2. Methods

Male NZW rabbits (2-3 months) were anesthetized with pentobarbital (at 60 mg/kg intraperitoneal). In dogs (weighing 19.0 ± 0.4 kg, range, 13.6–24.1 kg, 2-3 years old), an intravenous catheter was placed in the cephalic vein and a surgical plane of anesthesia was induced by the bolus injection (over 1-2 min) of sodium pentobarbital (50 mg/kg, Nembutal, Abbott, North Chicago, ILL). Under deep anesthesia, the hearts were rapidly removed and perfused retrogradely through the aorta with Krebs Henseleit solution (120 mM NaCl, 5 mM KCl, 2 mM MgSO_4 , 1 mM NaH_2PO_4 , 20 mM NaHCO_3 , 0.25 mM Ca^{2+} , and 10 mM glucose) in equilibrium with 95% O_2 /5% CO_2 . 2,3-Butanedione monoxime (BDM) was added to the dissection solution to stop the heart from beating and to prevent damage during dissection [10]. This investigation conforms with the *Guide for the Care and Use of Laboratory Animals published by the US national Institutes of Health (NIH Publication Ns 83-23, revised 1996)*. Suitable thin, uniform, nonbranched trabeculae along the free wall of the right ventricle were dissected carefully and without touching the muscle mounted in the bath as previously described for rabbit [11] and dog [12]. Average width was ~ 120 – $140 \mu\text{m}$ in order to prevent hypoxic cores of the muscles [13]. The dissected specimen contained small cubes of ventricular tissue attached to each end to facilitate mounting the muscle onto the experimental setup. The cube of ventricular tissue at one end of the trabecula was connected to a hook, and the cube at the other end rested in a basket-shaped extension of the force transducer. The muscle was bathed in a continuous flow of oxygenated K-H solution (without BDM), and with 1.75 mM Ca^{2+} , at 37°C . The dimensions (length, width, and thickness) of the muscle were measured under 30x magnification. Initially, the muscle was stimulated at 1 Hz at a temperature of 37°C and stretched until small increases in length resulted in about equal increases in resting tension and active developed tension. This fixed optimal preload is equivalent to that near the end diastolic volume in the *in vivo* situation (sarcomere length of $\sim 2.2 \mu\text{m}$) [14]. Trabeculae were stimulated at physiologic frequencies for each species (1 and 4 Hz in dog, $n = 9$, and 2 and 4 Hz in rabbit, $n = 8$) with or without a 40% variation imposed on interbeat duration. In order to define the load dependence of contractility during heart rate variability (HRV), a subset of rabbit trabeculae was subsequently subjected to a variable preload protocol by utilizing a high-speed high-accuracy servomotor as a displacement device ($n = 5$). One end of the trabeculae was attached to a length displacement device (i.e., a high-speed, high-accuracy servomotor). Once peak tension is reached and forces start declining (150 ms after initiation of the twitch), the servomotor reduces the muscle length by 10% (to 90% of optimal) within 2 ms, after which it is immediately stretched at the velocity of one muscle length per second until the next beat is triggered. At that point, the muscle length is kept constant. This range of lengths was chosen to be close to the *in vivo* sarcomere length range the heart undergoes during a contraction [14]. The protocol is then repeated (Figure 1). By actively stretching the muscle at a rate of 1 muscle length

per second, a certain percent stretch of muscle length will result, which is identical to the percentage of muscle that is released. Thus, average preload is identical both during the fixed preload and variable preload protocol.

In all protocols, total number of beats in each fixed versus variable period was the same. A fixed-rate steady-state response at the same base frequency was measured before and after each variable period, and average force was reported.

Data Analysis. Data were obtained and analyzed through custom written software (LABVIEW). Correlation coefficients and slopes were obtained for prebeat duration and force development. Kaleidagraph statistical package was utilized to perform Students *t*-test and repeated measures ANOVA where appropriate. All data are reported as means \pm SEM.

3. Results

First, we compared the average active force development between protocols with base frequency with a random 40% variation in the interval between beats compared. In dog myocardium (Figure 2), there was no significant change on average force development at both 1 Hz (cycle time of 1000 ms) and 4 Hz (cycle time of 250 ms).

Next, we compared these protocols in the rabbit. Since during *in vivo* beats, a prolonged beat-interval increases filling time, we mimicked this increase an increase in preload by stretching the muscle during the interbeat period until stimulated. In Figure 3, we depict the observed nonsignificant decrease in strength when imposing a 40% variable protocol until a stretch (increased pre load) is applied. Albeit not significant, there is a reversal of the negative tendency at 5% stretch for both baseline frequencies 2 and 4 Hz. Only at the more extreme 13% stretch at 4 Hz (the high end of the frequency range for rabbit) do we again observe a nonsignificant trend towards a negative effect.

In Figure 4, we show the correlation between prebeat duration and average force development in the dog at both 1 and 4 Hz during a 40% variable pacing protocol. Note the static relationship at the different frequencies. There is no difference with the increase in frequency.

In Figure 5, we show that as the preload stretch increases, while the baseline frequency increases too, a much higher correlation between beatduration and developed force. At 4 Hz, the increase in correlation becomes statistically significant. The longer the prebeat duration, the higher the contractile force observed, and the shorter the interval, the weaker the following beat.

4. Discussion

In our previous work, we had suggested and shown that an algorithm that imposed a beat-to-beat variability can lead to an average slight increase in force in rat myocardium [9]. In subsequent studies, we showed that in the rabbit, up to three preceding beats contribute to the amplitude of a given beat but that the average amplitude is not significantly

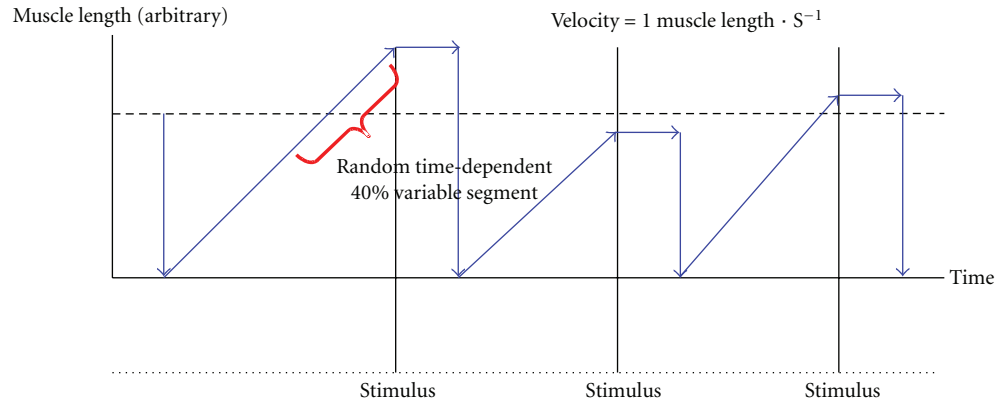


FIGURE 1: Following a stimulus, muscle length (y -axis) is kept constant till well after peak active force development has been reached. At 150 ms after the stimulation, muscle length is quickly reduced to 90% of optimal length and thereafter restretched at 1 muscle length per second. The duration of this stretch varied resulting in successive beats with different preloads, where the preload is increased linearly with the interbeat duration.

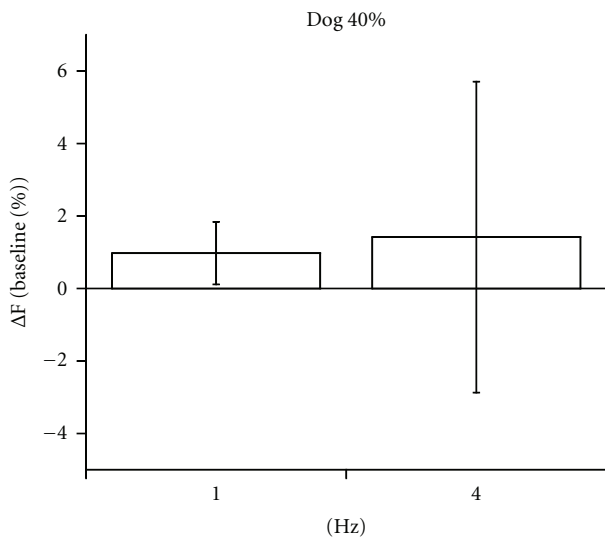


FIGURE 2: In dog trabeculae, at 40% variability, the average active developed force was not increased at 4 or 1 Hz. Results are expressed compared to baseline.

affected by a pseudovisible heart rate compared to the average of that rate applied as steady state [15, 16]. Here, we tested the efficacy of this initial randomized beat duration strategy in the rabbit and dog. The current data suggest that neither canine or rabbit myocardium seem to benefit (i.e., increase inotropy) from a variable rate with no negative or positive effect of variability on force development or kinetics noticed. The explanation for this species differences is more than likely found in the distinct manner in which EC coupling and calcium regulation are handled in each animal. Of particular interest is the increased contribution of the L-type calcium channels to the overall intracellular calcium pool during each contraction: $\sim 70\%$ in rabbit and dog compared to less only 2–5% in rat [17, 18]. In addition, it is known that also myofilament isoform composition differs between small and larger mammals, most notably in the

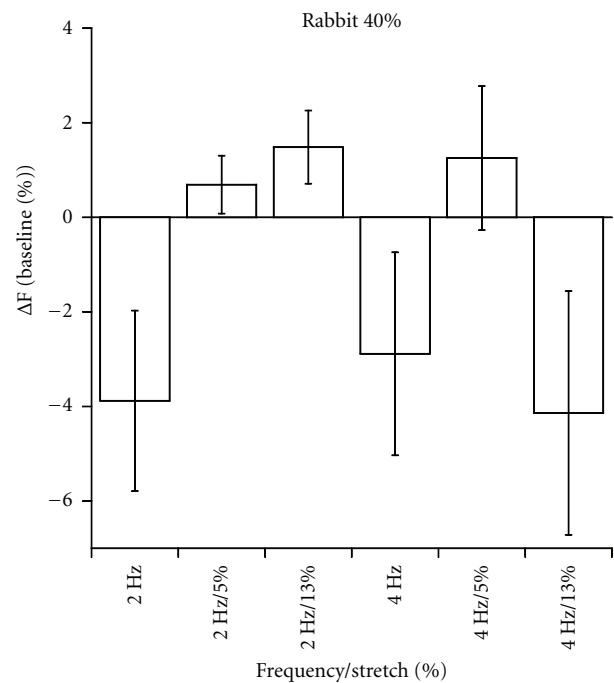


FIGURE 3: At a variability of 40% in the rabbit at both 2 and 4 Hz, there was no statistically significant difference between variable and base protocols. The addition of a 5% and/or 13% stretch just prior to contraction did not seem to improve or impair the average force development.

myosin heavy chain (MHC) isoform [19]. However, since the force of contraction highly depends on time passed since the last contraction, dynamic calcium handling and distribution of calcium fluxes that are very much time-dependent are thus more likely contributors, versus fixed differences in isoforms of MHC, or other differences in myofilament protein expression, although these cannot be excluded to contribute to the species differences at this point.

When next we investigated the effect of a variable length (load) under a variable pacing protocol on the rabbit heart,

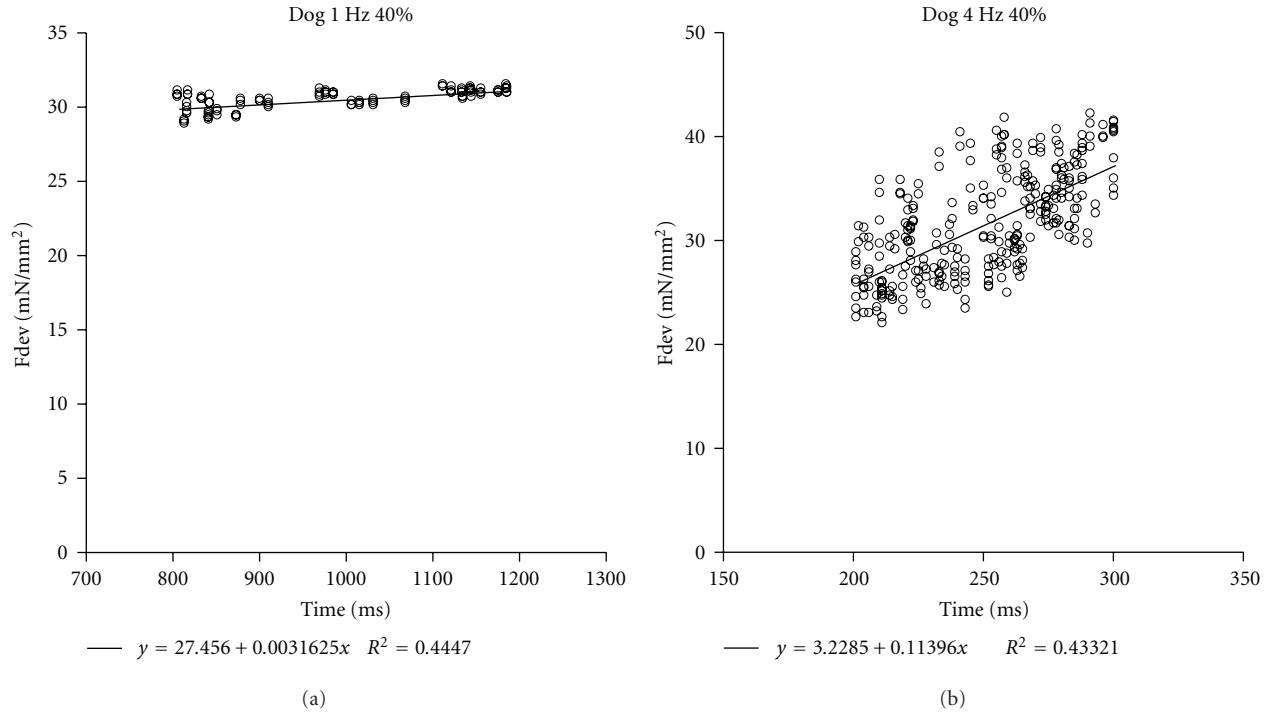


FIGURE 4: The correlation between prebeat duration and average force development in the dog is demonstrated for both 1 and 4 Hz. There is no difference with the increase in frequency.

we noticed a discrete increase on average force of the variable over the fixed rate base frequency that was constant at both 2 and 4 Hz for the 5% stretch group. At 13% stretch, a similar effect was noticed at the 2 Hz frequency group, whereas, at 4 Hz, there was a nonsignificant weakening effect. This latter finding may have resulted as these higher frequencies from the additional stretch may have caused some damage to the myofilament structure by a too rapid stretch.

Of greater importance was the significantly tighter correlation R^2 observed between the prebeat duration and the developed force once a small variable stretch was applied. This correlation was much tighter as the frequency and stretch increased ($P < 0.001$ at 4 Hz). This suggests that while the interval between beats is important, there is considerable effect that is load dependent affecting the subsequent beat. While several studies have shown an independent and strong effect of the interbeat duration alone and with contribution of the Frank Starling mechanism put into question [7, 20], there are others with findings similar to ours during *in vivo* investigations [21, 22]. At the heart of the problem lie two seemingly opposite phenomena: on one hand a sustained decrease in interbeat duration (thus an increase in frequency) leads to increased contractility, whereas instantaneous decreases in interbeat duration lead to a weaker immediate first beat [23]. We here now show that this interplay appears to be nonlinear in the time domain and that, by manipulating the frequency and variability a host of factors interact dynamically in a non-steady-state of equilibrium that changes every instant. The mechanism of the stretch-dependent “tightening” of the correlation is likely to be found in the interaction between load and calcium handling

and could include stretch-dependent calcium channels and ion homeostasis [24] on one hand, an interaction of the higher calcium sensitivity at greater sarcomere length [25], or a greater contribution of predominantly passive elements such as collagen or titin [26]. Potentially, at larger sarcomere length, the increase in the absolute myofilament calcium buffer capacity is nonlinear with stretch and promotes retention of calcium between two subsequent beats. However, more detailed experiments would be required to test such hypothesis.

On a beat-to-beat basis with instantaneous switching intervals away from steady state, the phenomena of mechanical restitution and postrest potentiation and postextrasystolic potentiation likely play an important role in determining the immediate contractile state of the heart [27]. We speculate that the direction and the magnitude of force modulation possibly relate to the different relative contributions of the sodium calcium exchanger (NCX) versus the sarcoplasmic reticulum calcium ATPase (SERCA) to the contractile process in each species. This paper uniquely highlights the influence of heart rate variability on a beat-to-beat basis and the different effects in diverse species while attempting to account for real life *in vivo* events such as preload stretching of the fibers.

We conclude that, in larger mammals, no changes in contractile force can be obtained by introducing variation in the beat-to-beat duration, and we confirm the evidence that prebeat duration has an important effect on developed strength [15]. The addition of a prebeat stretch effectively tightens this association that also becomes more significant as the frequency increases. Short-term manipulation of the beat-to-beat

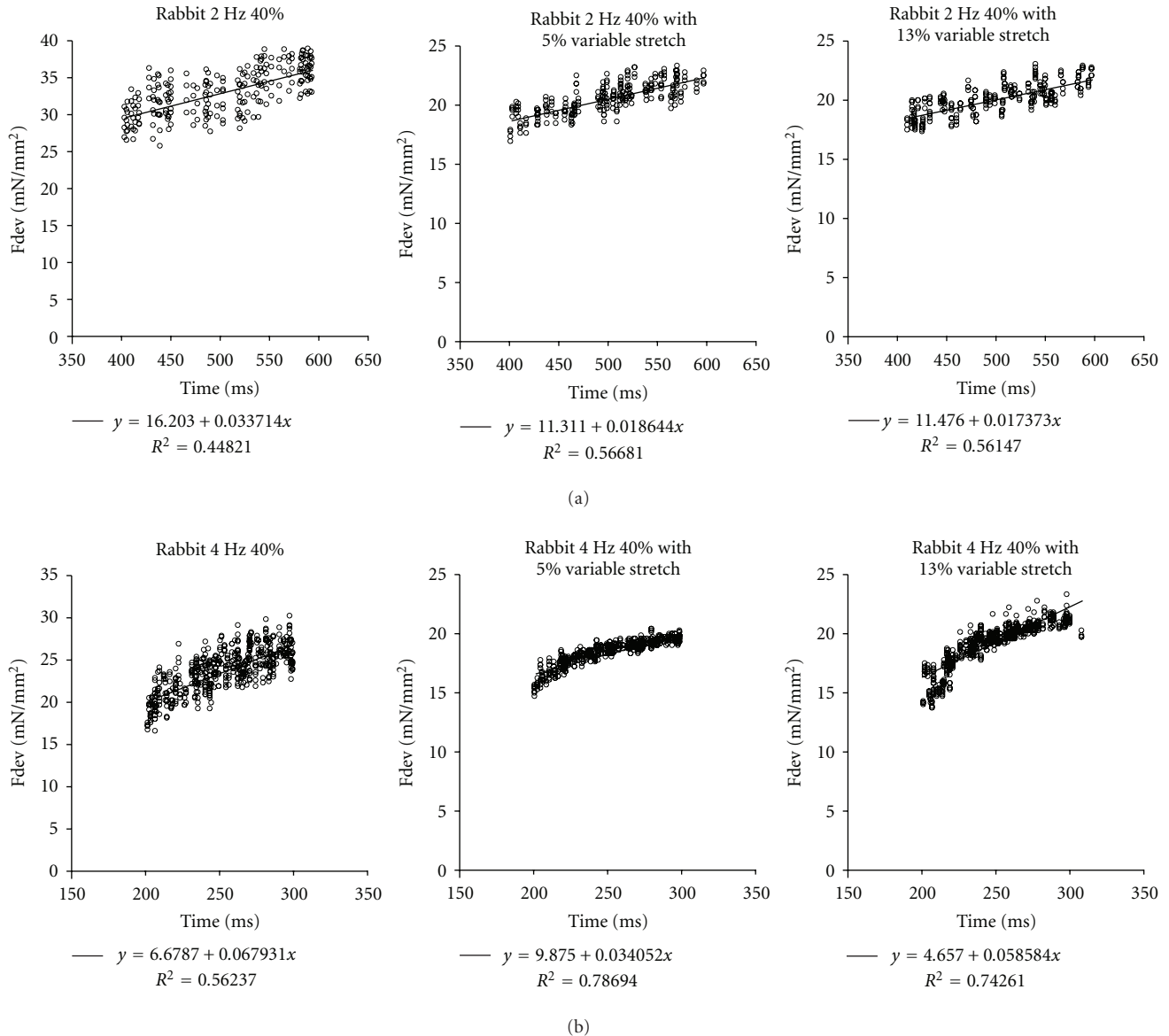


FIGURE 5: Top half displays the interaction between prebeat duration and force development at 2 Hz. The correlation coefficients are increasingly tighter as the preload stretch is increasingly applied. On the bottom half, we depict the same phenomena at the higher frequency (4 Hz). The correlation here is more evident and significantly different statistically ($P < 0.01$) from the initial nonstretch correlation value of 0.56.

interval thus can have variable effects that are species dependent. Its underlying mechanisms require further *in vivo* experiments as well as potential investigation of the long-term effects on protein expression and posttranslational modifications that are known to occur as a result of length [28] of frequency changes [11, 29].

Acknowledgments

This study was supported by an American Heart Association Established Investigator Award 0740040N (to P. M. L. Janssen) and by NIH K02HL083957 (to P. M. L. Janssen).

References

- [1] H. P. Bowditch, "Ueber die Eigenthuemlichkeiten der Reizbarkeit, welche die Muskelfasern des Herzens zeigen," *Berichte über die Verhandlungen der Königlich-Sächsischen Gesellschaft der Wissenschaften zu Leipzig*, vol. 23, pp. 652–689, 1871.
- [2] P. M. L. Janssen and M. Periasamy, "Determinants of frequency-dependent contraction and relaxation of mammalian myocardium," *Journal of Molecular and Cellular Cardiology*, vol. 43, no. 5, pp. 523–531, 2007.
- [3] L. A. Mulieri, G. Hasenfuss, B. Leavitt, P. D. Allen, and N. R. Alpert, "Altered myocardial force-frequency relation in human heart failure," *Circulation*, vol. 85, no. 5, pp. 1743–1750, 1992.

- [4] P. M. L. Janssen, "Myocardial contraction-relaxation coupling," *American Journal of Physiology*, vol. 299, no. 6, pp. H1741–H1749, 2010.
- [5] B. Pieske, M. Sütterlin, S. Schmidt-Schweda et al., "Diminished post-rest potentiation of contractile force in human dilated cardiomyopathy: functional evidence for alterations in intracellular Ca²⁺ handling," *Journal of Clinical Investigation*, vol. 98, no. 3, pp. 764–776, 1996.
- [6] D. Burkhoff, D. T. Yue, M. R. Franz, W. C. Hunter, and K. Sagawa, "Mechanical restitution of isolated perfused canine left ventricles," *American Journal of Physiology*, vol. 246, no. 1, pp. H8–16, 1984.
- [7] S. M. C. Hardman, M. I. M. Noble, T. Biggs, and W. A. Seed, "Evidence for an influence of mechanical restitution on beat-to-beat variations in haemodynamics during chronic atrial fibrillation in patients," *Cardiovascular Research*, vol. 38, no. 1, pp. 82–90, 1998.
- [8] F. L. Meijler, J. Strackee, J. L. Van Capelle, and J. C. Du Peron, "Computer analysis of the RR interval-contractility relationship during random stimulation of the isolated heart," *Circulation Research*, vol. 22, no. 5, pp. 695–702, 1968.
- [9] C. A. A. Torres, K. D. Varian, and P. M. L. Janssen, "Variability in interbeat duration influences myocardial contractility in rat cardiac trabeculae," *The Open Cardiovascular Medicine Journal*, vol. 2, pp. 96–100, 2008.
- [10] L. A. Mulieri, G. Hasenfuss, F. Ittleman, E. M. Blanchard, and N. R. Alpert, "Protection of human left ventricular myocardium from cutting injury with 2,3-butanedione monoxime," *Circulation Research*, vol. 65, no. 5, pp. 1441–1444, 1989.
- [11] K. D. Varian and P. M. L. Janssen, "Frequency-dependent acceleration of relaxation involves decreased myofilament calcium sensitivity," *American Journal of Physiology*, vol. 292, no. 5, pp. H2212–H2219, 2007.
- [12] G. E. Billman, Y. Nishijima, A. E. Belevych et al., "Effects of dietary omega-3 fatty acids on ventricular function in dogs with healed myocardial infarctions: in vivo and in vitro studies," *American Journal of Physiology*, vol. 298, no. 4, pp. H1219–H1228, 2010.
- [13] S. Raman, M. A. Kelley, and P. M. L. Janssen, "Effect of muscle dimensions on trabecular contractile performance under physiological conditions," *Pflugers Archiv*, vol. 451, no. 5, pp. 625–630, 2006.
- [14] E. K. Rodriguez, W. C. Hunter, M. J. Royce, M. K. Leppo, A. S. Douglas, and H. F. Weisman, "A method to reconstruct myocardial sarcomere lengths and orientations at transmural sites in beating canine hearts," *American Journal of Physiology*, vol. 263, no. 1, pp. H293–H306, 1992.
- [15] K. D. Varian, Y. Xu, C. A. A. Torres, M. M. Monasky, and P. M. L. Janssen, "A random cycle length approach for assessment of myocardial contraction in isolated rabbit myocardium," *American Journal of Physiology*, vol. 297, no. 5, pp. H1940–H1948, 2009.
- [16] Y. Xu, M. M. Monasky, N. Hiranandani, K. M. Haizlip, G. E. Billman, and P. M. L. Janssen, "Effect of Twitch Interval Duration on the Contractile Function of Subsequent Twiches in Isolated Rat, Rabbit, and Dog Myocardium under Physiological Conditions," *Journal of Applied Physiology*. In press.
- [17] D. M. Bers, "Cardiac excitation-contraction coupling," *Nature*, vol. 415, no. 6868, pp. 198–205, 2002.
- [18] M. M. Monasky and P. M. L. Janssen, "The positive force-frequency relationship is maintained in absence of sarcoplasmic reticulum function in rabbit, but not in rat myocardium," *Journal of Comparative Physiology B*, vol. 179, no. 4, pp. 469–479, 2009.
- [19] A. M. Lompre, J. J. Mercadier, C. Wisnewsky et al., "Species- and age-dependent changes in the relative amounts of cardiac myosin isoenzymes in mammals," *Developmental Biology*, vol. 84, no. 2, pp. 286–290, 1981.
- [20] A. T. M. Gosselink, P. K. Blanksma, H. J. G. M. Crijns et al., "Left ventricular beat-to-beat performance in atrial fibrillation: contribution of Frank-Starling mechanism after short rather than long RR intervals," *Journal of the American College of Cardiology*, vol. 26, no. 6, pp. 1516–1521, 1995.
- [21] H. J. Muntinga, A. T. M. Gosselink, P. K. Blanksma, P. J. De Kam, E. E. Van Der Wall, and H. J. G. M. Crijns, "Left ventricular beat to beat performance in atrial fibrillation: dependence on contractility, preload, and afterload," *Heart*, vol. 82, no. 5, pp. 575–580, 1999.
- [22] M. Petretta, M. L. E. Vicario, L. Spinelli et al., "Combined effect of the force-frequency and length-tension mechanisms on left ventricular function in patients with dilated cardiomyopathy," *European Journal of Heart Failure*, vol. 4, no. 6, pp. 727–735, 2002.
- [23] C. Dumitrescu, P. Narayan, Y. Cheng, I. R. Efimov, and R. A. Altschuld, "Phase I and phase II of short-term mechanical restitution in perfused rat left ventricles," *American Journal of Physiology*, vol. 282, no. 4, pp. H1311–H1319, 2002.
- [24] C. Luers, F. Fialka, A. Elgner et al., "Stretch-dependent modulation of [Na⁺]_i, [Ca²⁺]_i, and pHi in rabbit myocardium—a mechanism for the slow force response," *Cardiovascular Research*, vol. 68, no. 3, pp. 454–463, 2005.
- [25] P. P. de Tombe, R. D. Mateja, K. Tachampa, Y. A. Mou, G. P. Farman, and T. C. Irving, "Myofilament length dependent activation," *Journal of Molecular and Cellular Cardiology*, vol. 48, no. 5, pp. 851–858, 2010.
- [26] H. L. Granzier, Y. Wu, L. Siegfried, and M. LeWinter, "Titin: physiological function and role in cardiomyopathy and failure," *Heart Failure Reviews*, vol. 10, no. 3, pp. 211–223, 2005.
- [27] M. W. Cooper, "Postextrasystolic potentiation: do we really know what it means and how to use it?" *Circulation*, vol. 88, no. 6, pp. 2962–2971, 1993.
- [28] M. M. Monasky, B. J. Biesiadecki, and P. M. L. Janssen, "Increased phosphorylation of tropomyosin, troponin I, and myosin light chain-2 after stretch in rabbit ventricular myocardium under physiological conditions," *Journal of Molecular and Cellular Cardiology*, vol. 48, no. 5, pp. 1023–1028, 2010.
- [29] R. R. Lamberts, N. Hamdani, T. W. Soekhoe et al., "Frequency-dependent myofilament Ca²⁺ desensitization in failing rat myocardium," *Journal of Physiology*, vol. 582, no. 2, pp. 695–709, 2007.

Review Article

The Sarcomeric Z-Disc and Z-Discopathies

Ralph Knöll, Byambajav Buyandelger, and Max Lab

Centre for Research Excellence, British Heart Foundation, National Heart & Lung Institute, Imperial College, South Kensington Campus, Flowers Building, 4th Floor, London SW7 2AZ, UK

Correspondence should be addressed to Ralph Knöll, r.knoell@imperial.ac.uk

Received 5 July 2011; Accepted 12 August 2011

Academic Editor: Henk Granzier

Copyright © 2011 Ralph Knöll et al. This is an open access article distributed under the Creative Commons Attribution License, which permits unrestricted use, distribution, and reproduction in any medium, provided the original work is properly cited.

The sarcomeric Z-disc defines the lateral borders of the sarcomere and has primarily been seen as a structure important for mechanical stability. This view has changed dramatically within the last one or two decades. A multitude of novel Z-disc proteins and their interacting partners have been identified, which has led to the identification of additional functions and which have now been assigned to this structure. This includes its importance for intracellular signalling, for mechanosensation and mechanotransduction in particular, an emerging importance for protein turnover and autophagy, as well as its molecular links to the t-tubular system and the sarcoplasmic reticulum. Moreover, the discovery of mutations in a wide variety of Z-disc proteins, which lead to perturbations of several of the above-mentioned systems, gives rise to a diverse group of diseases which can be termed Z-discopathies. This paper provides a brief overview of these novel aspects as well as points to future research directions.

1. Introduction

Z-discs (Z-disk, Z-line, Z-band) delineate the lateral borders of sarcomeres and are the smallest functional units in striated muscle. The core of a Z-disc consists of actin filaments coming from adjacent sarcomeres which are crosslinked by α actinin molecules [1]. Mature Z-discs are probably composed of hundreds of different proteins, and one regards them as one of the most complex macromolecular structures in biology [2]. Z-discs, which are difficult to detect in conventional light microscopy, appear in the longitudinal view of electron microscopy as electron dense bands with varying sizes, ranging between 30 and 50 nm in fast muscle and between 100 and 140 nm in slow muscle and cardiac myocytes. In the transverse view, they appear as a “basketweave” or as “small square lattices” [3]. F-actin filaments, titin, and the nebulin/nebulette system directly attach to the Z-disc, and, because of their importance for sarcomere mechanics, the Z-disc has initially been regarded as important for mechanical stability only.

However, within the last decade, our knowledge with regard to this structure increased steadily, and it is now clear that the sarcomeric Z-disc serves as a nodal point for

signalling in general and mechanosensation and mechanotransduction in particular. The Z-disc also links to the t-tubular system, the sarcoplasmic reticulum, and several E3 ubiquitin ligases localized to the Z-disc and link this structure to protein turnover and probably autophagy.

While excellent reviews with regard to the structural aspects of the Z-disc [4, 5] and with emphasis on its role in signalling [6–9] have been published recently, we will focus more on the role of the Z-disc in disease and will highlight recent developments in the exciting field of Z-disc biology.

Although we use the term “Z-disc protein” in this paper, such a protein is difficult to define. This is because (i) a protein at the Z-disc may not always be confined to the disc—depending on developmental stage and physiological circumstances; (ii) it may be found at other locations within the sarcomere, such as the I- and M-bands (i.e., FHL1 and 2); (iii) these proteins can also be in multiple localizations, including the nucleus (such as muscle LIM protein, (MLP)), costamere (such as integrin linked kinase, (ILK)), cytoplasm, intercalated disc, sarcoplasmic reticulum, and t-tubules. Another example is desmin, which is present at the sarcomeric Z-disc but as an intermediate filament (IF); it connects not only this structure with the desmosomes but has other

links to other compartments, linking these to the nucleus as well. Other examples of Z-disc proteins include the giant protein titin, where only the amino-terminus is located to the Z-disc, and nebulin/nebulette, where only the carboxy-terminus is localized to the Z-disc and/or F-actin. In this context, an NCBI online search (<http://www.ncbi.nlm.nih.gov/guide/>) revealed that currently about 227 gene products or proteins are associated with the Z disc, and at least about 50 human and about 60 mouse gene products have been assigned to it. Due to space restrictions, this paper cannot discuss all of these proteins, but will focus on some significant recent developments and point out some important and particularly disease-associated proteins and their genes.

2. Structural Aspects

Z-discs can be defined as plate-like structures in sarcomeres to which the plus ends of actin filaments are localized, or they can be defined as the centre of the I-band. As pointed out above, they are probably composed of hundreds of different proteins and are regarded as one of the most complex macromolecular structures in biology [2]. Major Z-disc proteins include cardiac actin which is crosslinked by α actinin and “capped” by CapZ, titin, which spans a complete half sarcomere, and nebulin/nebulette which runs along actin filaments.

Z-discs, which are difficult to detect in conventional light microscopy, appear in the longitudinal view of electron microscopy as dense zigzag bands with varying but myofibre-specific sizes, ranging between 30 to 50 nm in fast muscle and between 100 to 140 nm in slow muscle and cardiac myocytes. Z-disc widths are determined by the layers of α actinin, which can range from two to six or even more molecules [10, 11]. It is interesting to find the thinnest Z-discs in the fastest muscle fibres, which, functionally, produce the highest sarcomere-shortening velocities, and the widest Z-discs in slow muscle. It is difficult to give an explanation for this phenomenon, but, if the Z disc contributes to series elasticity, perhaps via its connection to titin, thinner discs may provide less elasticity (=stiffer cell). As the contractile apparatus is activated, it has to stretch the discs in series before force transmits—so cellular force transmission throughout the muscle would have a shorter delay and be faster. Also, may be via z-disc/titin/actomyosin interaction crossbridge that cycling may be faster. In the transverse view, Z-discs appear as “basketweaves” or “small square lattices” [3], and it has been proposed by Goldstein and coworkers [12–14] as well as by Yamaguchi et al. [15], that the Z-disc changes its structure, from small square lattice in resting muscle to a wider basketweave form in activated muscle [13]. A study of α actinin binding to actin within the Z-disc revealed that the angles between both proteins varied preferentially between 60 and 120 degrees [16]. Both the conformational change of the Z-disc during contraction as well as the changes of the angles between α actinin and actin could well be part of a stress-sensing mechanism.

3. Z-Disc-Related Proteins

3.1. α Actinin. α actinin belongs to the spectrin gene super-family which includes a wide variety of different cytoskeletal components including dystrophin, utrophin, fimbrin, and alpha and beta spectrins. The skeletal and cardiac muscle isoforms are localized to the sarcomeric Z-discs and are important for actin localization. Various splice variants have been reported, the largest of which contains 892 amino acids. The mature protein is about 35 nm in length and occurs as an antiparallel homodimer. The single protein consists of four spectrin repeats at its centre as well as of an actin-binding domain (ABD) at its amino-terminus and two EF hands (calmodulin homology domains) at the carboxy-terminus, which enable α actinin to crosslink actin filaments within the Z-disc. A single mutation in α actinin (Q9R) has been found in an individual affected by DCM [17], and via linkage analysis the gene for α actinin (ACTN2) has been linked recently to HCM [18, 19] (please see also Table 1 and Figure 1). The α actinin Q9R mutation in particular disrupts the interaction with MLP and seems to affect cellular differentiation.

3.2. Muscle LIM Protein (MLP). Muscle LIM protein (for Lin11, Isl 1, and Mec 3 (LIM)) is a 194 amino acid LIM-only protein localized not only to the sarcomeric Z-disc, where it interacts most probably with α actinin [20], calcineurin [21], and telethonin [22, 23], but is also present in the nucleus where this protein is able to interact with myoD, myogenin, and MRF4 [24], as well as at the intercalated discs where it interacts with NRAP [25], and at the costameres where it interacts with zyxin [20], integrin linked kinase (ILK) [26], and β 1 spectrin [27]. MLP-deficient animals develop a severe form of heart failure, and patients with mutations in this gene develop forms of cardiomyopathy—either dilated cardiomyopathy DCM (dilated, enlarged ventricular chambers and inadequate systolic function) or hypertrophic cardiomyopathy HCM (increase in myocardial wall thicknesses which may or may not be associated with fatal arrhythmias) [28, 29]. MLP interacts with a variety of additional proteins such as cofilin 2 [30] and actin [31] and is involved in actin polymerization. Moreover, the protein has been implicated in various signal transduction cascades, including mechanosensation and mechanotransduction, calcium metabolism, and myofibrillogenesis. Of note, MLP has also been reported to be deacetylated by histone deacetylase 4 (HDAC4) and acetylated by the histone acetylase (HAT) PCAM and that its acetylation is linked to an increase myofibrillar calcium sensitivity [32]. Although little is known about the role of HDACs and HATs with regard to their effects on calcium sensitivity, a possible link between these molecules, the Z-disc, and contractility is of great interest because a direct link between the Z-disc and calcium sensitivity has never been shown before. However, future research will have to elucidate this link in much more detail (for a recent review on MLP, see [33]).

3.3. Telethonin (TCAP). Telethonin (titin cap, t-cap, TCAP) is a small 167 amino acid protein (molecular weight ~19 kDa)

TABLE 1: Z-disc proteins involved in human disease.

Name of gene	Type of disease
α actinin (central Z-disc)	Cardiomyopathy
Muscle LIM protein (MLP)	Cardiomyopathy
Telethonin (TCAP)	Cardiomyopathy, LGMD2G
Actin	Cardiomyopathy
Integrin-linked kinase (ILK)	DCM
Calsarcin1 (Myozenin, ZASP)	Cardiomyopathy, myofibrillar myopathy (MFM) zaspopathies
FHL1 (four and a half LIM domain protein)	X-linked myopathy with postural muscle atrophy (XMPMA), scapuloperoneal (SP), reducing body myopathy (RBM)
Cypher (Zasp, Oracle)	Cardiomyopathy, MFM
Desmin (Z-disc related)	Multiple
Nebulin/Nebulette	Nemaline myopathy
Myotilin	LGMD, MFM, myotilinopathy
BAG3	Cardiomyopathy, MFM
Titin (Z-disc)*	Cardiomyopathy (titinopathies)

Z-disc protein mutations cause a wide spectrum of diseases, which may be called “Z-discopathies”. Titin mutation itself cause a broad spectrum of diseases (here we refer only to mutations affecting the Z-disc). The term cardiomyopathy includes at least HCM and DCM, other types of heart failure such as arrhythmogenic right ventricular myopathy.

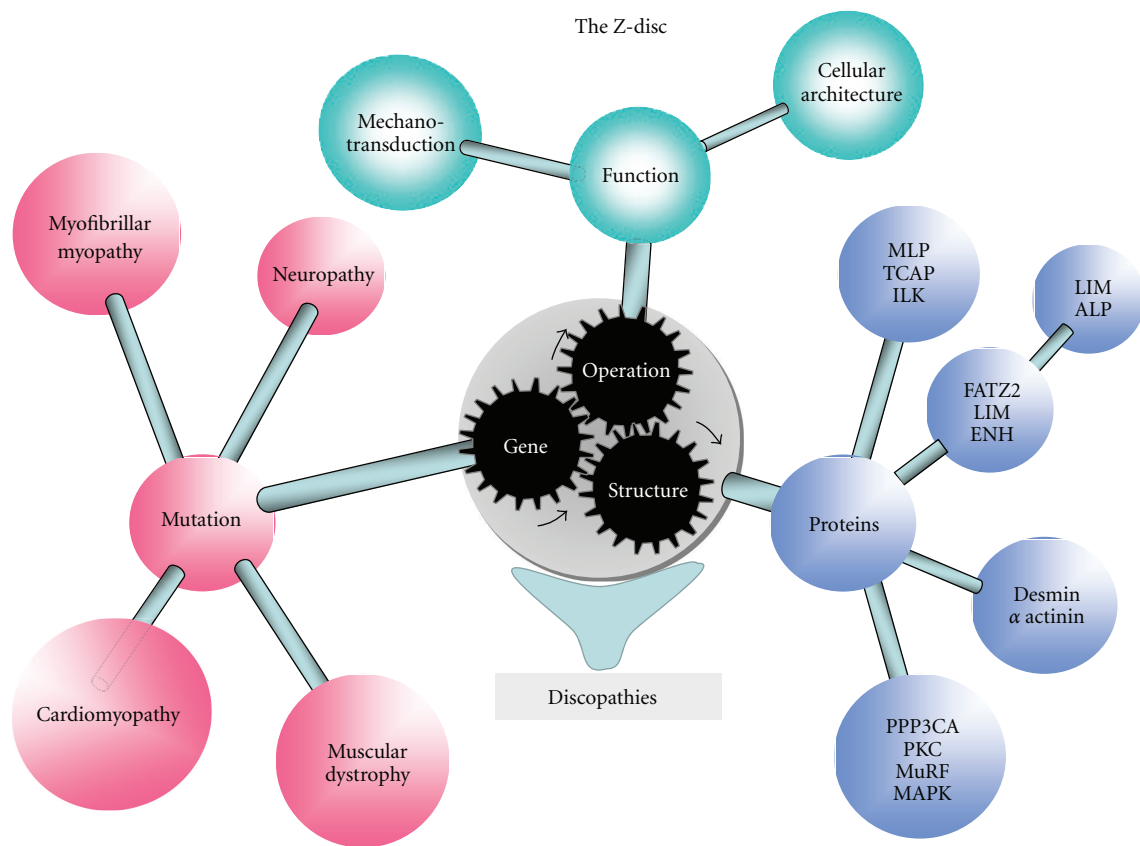


FIGURE 1: The sarcomeric Z-disc—multiple functions and links to maladaptation. The figure links various functions and structural aspects to maladaptation and disease, such as mutations in Z-disc proteins which are linked to different diseases. Defects in mechanosensation and mechanotransduction are linked to Z-disc mediated autophagy and UPS which in turn are linked to skeletal and cardiac muscle disease.

striated-muscle-specific protein with a unique β -sheet structure. This protein, with unknown homologue genes, binds in an antiparallel (2:1) sandwich complex at the periphery of the sarcomeric Z-disc to the titin Z1-Z2 domains and essentially “glues” together the N-termini of two adjacent titin molecules [2]. This interaction represents also the strongest protein-protein interaction observed to date [34]. In this regard, it will be interesting to analyze telethonin’s function during biomechanical stress. Telethonin is an *in vitro* substrate of titin kinase, an interaction thought to be critical during myofibril growth [35], and the protein also can be phosphorylated by protein kinase D (PKD) which might link telethonin to the regulation of G-protein-coupled receptor (GPCR) signalling [36].

Telethonin interacts also with a wide variety of additional and very different proteins, such as ankyrin repeat protein 2, small ankyrin 1 (a transmembrane protein of the sarcoplasmic reticulum) [37], minK, a potassium channel β -subunit, as well as with sodium channels such as $\text{Na}_v1.5$ [38, 39]. Interestingly, the interaction with mink indicates a link between telethonin and the t-tubular system, a connection also observed in a telethonin-deficient zebrafish model [40]. However, the precise interplay between telethonin and the t-tubular system needs to be elucidated.

In addition, telethonin interacts with MDM2 and muscle ring fingers 1/2 (MuRF1/2) [41, 42]—E3 ubiquitin ligases strongly impacting cardiac protein turnover. It remains to be elucidated which telethonin domains are involved in the interaction with MuRF 1/2 and whether mutations affect the degradation process of telethonin. It might well be that some telethonin mutations may lead to forms of proteinopathies, which are characterized by aggresome formation, autophagy, and apoptosis (see next chapter).

Moreover, telethonin may participate in the regulation of myocardial hypertrophy by interacting with calsarcin-1 (also known as FATZ-2 or myozenin-2) [43], which is a mediator of calcineurin activity. Telethonin interacts with, as well as regulates, the secretion of myostatin, an important negative regulator of muscle growth [44], and interacts with BMP10, a positive regulator of hypertrophy [45]. Therefore, telethonin is well suited to influence the delicate balance between atrophy and hypertrophy or myocardial remodelling [28]. However, this link needs to be analyzed in more detail. Telethonin may also affect cell survival by interacting with the proapoptotic protein Siva [46] and is involved in cardiac mechanosensation [22].

Nonsense mutations in the telethonin gene are associated with limb-girdle muscular dystrophy type 2G (LGMD 2G) [47–49], heterozygous missense mutations, with dilated and hypertrophic forms of cardiomyopathy [18, 22, 50], as well as with intestinal pseudoobstruction [39]. However, a recently discovered telethonin mutation (R76C), found in an individual affected by intestinal pseudoobstruction, affected the $\text{Na}_v1.5$ (SCN5A) channel when coexpressed in HEK 293 cells altering steady-state activation kinetics [39]. Whether this effect can also be observed in the heart or whether other telethonin mutations also affect ion channels requires elucidation.

To date it is not all clear why and how telethonin mutations cause these broad-spectrum diseases. Ion channels, E3 ubiquitin ligases, autophagy, and apoptosis could well play a role. In this regard, telethonin deficiency in a genetically altered mouse model is not associated with a spontaneous cardiac phenotype but leads to severe maladaptation and heart failure following biomechanical stress. Telethonin interacts with the proapoptotic protein p53 and facilitates its degradation via MDM2. Loss of telethonin in the presence of biomechanical stress increases p53 as well as apoptotic cell death [51]. This novel link might help to explain some of the pathologies observed in patients affected by mutations in this gene.

3.4. Integrin-Linked kinase (ILK). ILK has been identified as an integrin-binding protein and has also been localized to the sarcomeric Z-disc, but the functionality of its kinase domain *in vivo* has recently been questioned [52]. The ternary complex of ILK, Pinch and Parvin (IPP) interacts with the cytoplasmic tail of β integrin and couples them to the actin cytoskeleton. ILK is found at costameres and has also been localized to the Z-disc area where this protein interacts with a host of different proteins, including MLP [26] or c-Src [53]. It has also been implicated in Akt-mediated survival signalling. An ILK nonsense mutation has been identified in zebrafish which leads to a “lost contact” phenotype indicating that cells, particularly endothelial cells and cardiac myocytes, lose contact with their surrounding cells. In addition, a human ILK mutation (A262V) has been described in a DCM patient. This mutation, when injected into an ILK-deficient zebrafish, did not rescue the phenotype, while wildtype ILK does. Among other effects, ILK A262V was also associated with a decrease in capillary density in human myocardial tissue. By affecting both, cardiac myocytes and endothelial cells, ILK A262V causes cardiomyopathy and associated heart failure via a novel molecular mechanism [54].

3.5. Melusin. Melusin is a muscle-specific protein located at costameres near the Z-disc, where it binds to the cytoplasmic domain of $\beta1$ integrin [55]. Homozygous deletion of this gene is not associated with a spontaneous phenotype, but leads to a reduced left ventricular hypertrophy and a transition to DCM following transverse aortic constriction (TAC). More interestingly, deficiency of this protein is not associated with any loss of sensitivity to humoral factors such as angiotensin II or phenylephrine in terms of a myocardial hypertrophic response. Further analysis revealed that following pressure overload glycogen synthase kinase 3 β (GSK 3 β) and Akt phosphorylation were blunted in melusin deficient hearts [56]. Conversely, melusin overexpression is protective after TAC [57]. In addition, a search for melusin mutations in human heart failure patients revealed the presence of three different genetic variations, but a clear genotype-phenotype relationship could not be established [58].

Thus, melusin is an element of the integrin-dependent cardiac mechanosensor machinery, it may be indispensable

for adaptive cardiac remodelling, and melusin might serve as a therapeutic target in heart failure.

3.6. Calsarcin 1 (*FATZ2*, *Myozenin2*). The calsarcins have initially been cloned via their ability to interact with the protein phosphatase calcineurin, and they are localized to the Z-disc [59]. Further research showed that calsarcin 1 knock-out animals do not have any spontaneous phenotype, but, when subjected to biomechanical stress, for example, TAC, they respond with increased calcineurin activity, massive hypertrophy, and heart failure, which suggests that calsarcin1 inhibits calcineurin function [60]. Recently HCM-associated mutations have been identified in this gene, making it another candidate gene for cardiomyopathy [61].

3.7. Four-and-Half-Domain-LIM Proteins 1/2/3 (*FHL1/2/3*). This group of proteins contains an amino-terminal zinc finger/half LIM domain followed by four complete LIM domains. This arrangement has led to the designation of this class of proteins as four and a half LIM domain proteins (FHL). It encompasses currently five different members, of which FHL 1, 2, and 3 are expressed in striated muscle where they localize to the sarcomeric Z-disc/I-band area. But they can also sometimes be found in the nucleus [62]. FHL1 knock-out animals subjected to TAC which undergo protective remodelling—a favourable outcome. It has been suggested that this protein plays an important role in the mechanism of pathological hypertrophy by sensing biomechanical stress responses via the N2B titin stretch sensor domain. This initiates changes in the titin- and MAPK-mediated responses [63]. FHL1, 2, and 3 interact with extracellular-regulated kinases (Erk), with, particularly, FHL2 as an inhibitor of Erk-mediated transcriptional events [62].

Human mutations in *FHL1* have been identified in patients affected by X linked myopathy with postural muscle atrophy (XMPMA, probably a form of Emery Dreyfuss Muscular Dystrophy) [64] and scapuloperoneal (SP) syndrome [65] as well as in patients with reducing body myopathy (RBM). The latter is characterized by progressive muscle weakness and the presence of cytoplasmic aggregates (“aggresomes”) [66–68]. Aggresomes are inclusion bodies formed when the cellular degradation machinery, usually the ubiquitin proteasome system (UPS), is impaired or overwhelmed. This leads to an accumulation of proteins for disposal. The aggresomal response can be interpreted as protective in the presence of a high load of damaged, abnormal or misfolded protein within the cytoplasm which fails to be degraded by the UPS and before autophagy is fully engaged. A careful analysis of these aggregates in RBM show that they contain a number of different proteins, such as desmin, ubiquitin, the lysosome-associated protein LAMP1, and the endoplasmic reticulum chaperone GRP78 [68]. How mutations in *FHL1* are precisely linked to these aggresomes and may be to autophagy remains unclear, but the presence of E3 ubiquitin ligases at the sarcomeric Z-disc and the defects observed in this system in RBM link both together.

3.8. Enigma/Enigma Homologue (*ENH*)/Cypher Family and Actinin-Binding LIM Proteins (*ALP*). The enigma family of proteins consists of enigma, ENH, and cypher (mouse) (*Zasp* (human isoform), Oracle) and is defined by an amino-terminal PDZ domain as well as by one to three carboxy-terminal LIM domains [69]. All of them are expressed in striated muscle and localize to the Z-disc, including enigma [69], ENH [70], and cypher [71].

The ALP family consists of four proteins, namely, ALP (PDLIM3), CLP36 (CLIM1, Elfin, PDLIM1), RIL (PDLIM4), and Mystique (SLIM, PDLIM2), which are all expressed in the heart. Each member of this family contains an N-terminal PDZ domain and a C-terminal LIM domain, and actinin-associated LIM protein (ALP) is also present at the Z-disc [72].

ENH and enigma [70] and cypher [71] interact with protein kinase C and influences this important pathway. In contrast, ALP is important for actin filament organization [73]. Most of the genes in these two groups have been knocked out with striking different phenotypes. For example, the ALP knock-out mouse develops a pronounced right ventricular cardiomyopathy, where a developmental pathway is responsible for this phenotype [72]. In this context, ENH-deficient animals have recently been generated and develop a DCM-like phenotype [74]. Cypher is expressed in at least six different isoforms and plays an essential role in striated muscle structure and function. Mice homozygous null for cypher die during the first week because of congenital myopathy with symptoms that include decreased milk intake, limb muscle weakness, cyanosis, and cardiomyopathy [71].

Electron microscopy in these mice revealed severely disorganized skeletal and cardiac muscle with discontinuous/punctuate Z-discs. These findings are somewhat more severe but similar to defects found in MLP-deficient mice [22, 75]. The fact that homozygous deletion of this gene in animals leads to neonatal death implies that, although cypher is not necessary for myofibrillogenesis, it stabilizes Z-discs after the organism starts to sustain its own cardiovascular system. Conditional cypher knock-out animals support this conclusion, where deletion of this gene in adult animals also leads to a severe cardiomyopathy and heart failure phenotype, with Z-disc defects [76].

Knocking in two different skeletal-muscle-specific isoforms to the cypher locus produces partial cardiac rescue, with animals surviving up to one year [77]. In addition, human mutations have also been identified in the cypher (*ZASP*) gene which produces dilated and or hypertrophic cardiomyopathy, in left ventricular noncompaction [78–80]. Another set of human mutations has been found in patients affected by myofibrillar myopathy (MFM), a disorder in which disintegration of the Z-disc and then of the myofibrils is followed by abnormal accumulation of multiple proteins such as desmin, α B crystalline, and dystrophin. Clinically the disease is characterized by progressive muscle weakness, often starting or involving distal muscles, but limb girdle and scapuloperoneal distributions may also occur. Cardiomyopathy and peripheral neuropathy are frequently present. To date all MFM-causing mutations are present in Z-disc proteins:

Zasp, BAG3 (please see next chapter), desmin, α B crystalline, myotilin, and filamin C [81].

The disease causing molecular mechanism for all of the observed phenotypes, in the knock-out animals or in the patients, is not well defined. However, it is possible that the D626N ZASP mutation, which changes the affinity to PKC, might cause the phenotype via alterations in this pathway [78]. Beside skeletal muscle and cardiac phenotypes, ZASP mutations also produce neuropathy, and; hence, the spectrum of phenotypes caused by mutations in this gene has been called zaspopathies [82]. (For an excellent review on this topic, please see [83].)

3.9. Bcl2-Associated Athanogene (BAG3). Bcl2-associated athanogene (BAG) family proteins belong to an evolutionary conserved group of Hsp70/HSC70 binding cochaperones with up to six different members. They all contain a conserved carboxy-terminal Hsp70/HSC70-binding domain but differ significantly in their amino-terminal architecture, which points to different functions of different family members in cell biology. BAG3 is localized to the sarcomeric Z-disc, and BAG3-deficient animals are born in the expected Mendelian ratios, undistinguishable from wild-type littermates within the first days after birth but develop, during the first and second weeks, severe skeletal and cardiac muscle pathologies characterized by myofibrillar degeneration and apoptosis which leads to death at the age of 4 weeks [84]. In addition, human mutations in BAG3 have been found in patients affected by MFM (please see above) [85], and probably, most importantly, BAG3 recently has been identified as a novel significant candidate gene for human cardiomyopathy and associated heart failure in large genome-wide association studies (GWA) [86, 87].

3.10. Myotilin. Myotilin is a 57 kDa cytoskeletal protein, localized to the sarcomeric Z-disc and important for the stability of thin filaments during muscle contraction. It binds F-actin, crosslinks actin filaments, and prevents latrunculin A-induced filament disassembly. Mutations in this gene have been associated with limb-girdle muscular dystrophy and myofibrillar myopathies (“myotilinopathies”). Von Nandestadh and coworkers [88] analyzed the molecular mechanisms underlying myotilinopathies and found at least two different calpain cleavage sites in myotilin and that the protein is degraded by the UPS. It turned out that proteolysis inhibitor induced reduction in myotilin protein turnover, which results in formation of intracellular myotilin and actin-containing aggregates which are similar to the aggregates observed in MFM. Moreover, myotilinopathy causing mutations prevent or at least significantly slow down myotilin protein degradation.

3.11. Alpha-B Crystalline and HSPB7. Alpha crystallins are composed of two gene products: alpha-A and alpha-B (for acidic and basic). Alpha crystallins can be induced by heat shock and are members of the small heat shock protein (sHSP or HSP20) family. They act as molecular chaperones, but they do not renature proteins and release them in

the fashion of a true chaperone, instead they hold them in large soluble aggregates, and posttranslational modifications decrease their ability to chaperone. Two additional functions of alpha crystallins are an autokinase activity and participation in the intracellular architecture. Alpha-A and alpha-B gene products are differentially expressed: alpha-A is preferentially restricted to the lens, and alpha-B is expressed widely in many tissues and organs and particularly in the heart. Alpha-B crystallin interacts with desmin, vimentin, and actin and is localized to the Z-disc [89, 90]. Moreover, elevated expression of alpha-B crystallin occurs in many neurological diseases and a missense mutation cosegregated in a family with a desmin-related myopathy [91]. Particularly, the R120G alpha-B crystallin mutation has been analyzed in great detail and increases autophagy in a transgenic mouse model. Autophagy is likely to be an adaptive response to an increase in misfolded proteins, and p62 promotes aggresome formation and autophagy which protects cardiac myocytes against proteotoxic stress [92].

HSPB7 or cardiovascular heat shock protein (cvHSP) is a 170 amino acid protein with high expression in myocardium. The mRNA is induced in monocrotaline-induced right ventricular hypertrophy but downregulated in left ventricular hypertrophy following TAC. Moreover, the protein interacts with alpha filamin and with actin-binding protein 280 [93] and has been found to colocalize with alpha-B crystallin [94]. However, recently a variety of different GWAs pointed to *HSPB7* as an important novel candidate gene for DCM [87, 95–97].

3.12. Desmin. Desmin, which is muscle-specific expressed, belongs together with vimentin and lamin A/C to the intermediate filaments (IF), a group of related proteins that share common structural and sequence features, such as the central alpha helical rod and amino-terminal as well as carboxy-terminal globular domains. Desmin is a major IF and present in almost every cell type. In cardiac myocytes desmin connects desmosomes not only with the Z-disc but also with other organelles. Mutations in this gene cause a variety of cardiac diseases (beside the above-discussed MFM). These include desmin-related myopathy [98, 99], limb-girdle muscular dystrophy [100]. They also cause several cardiomyopathies such as dilated cardiomyopathy (DCM) [101], arrhythmogenic right-ventricular cardiomyopathy (ARVC) [102], cardiomyopathy with advanced AV block and arrhythmia [103], familial restrictive cardiomyopathy [104], and DCM with conduction system defects [105]. Desmin interacts with a variety of proteins, and, because it is elastic, it can sense deformation in a cellular structure. It has been linked directly to mechanosensation [106] and might well have a function via the “tensegration” of the intracellular cytoskeletal network; that is, its elasticity may cause a conformational change in response to any type of mechanical stimulation.

3.13. Nebulin/Nebulette. Nebulin is a giant 600–900 kDa filamentous protein present in skeletal muscle whereas the much shorter 100 kDa-related nebullette is present in cardiac tissue. Nebulin/nebullette run along actin filaments, and patients

with mutations in nebulin develop nemaline myopathy, which is characterized by weakness, hypotonia, and depressed or absent deep tendon reflexes. Interestingly two different nebulin knock-out mouse models recapitulate all major features of this disease and are available for further analysis [107, 108]. (For an elegant recent review on nebulin, please see [109].)

3.14. Phosphatases (Calcineurin/PPP3CA): Protein Kinases (PKC). Calcineurin is a heterodimer of a 58 to 64 kDa catalytic subunit, comprising calcineurin A and a 19 kDa regulatory subunit, calcineurin B, and is well known to be one of the major four Ser/Thr phosphatases found in eukaryotic cells implicated in the control of cardiac hypertrophy as well as associated heart failure [110]. Numerous articles have pointed to the importance of this phosphatase, which dephosphorylates nuclear factor activated T-cells (NFAT), enables nuclear translocation of this transcription factor, and initiates changes in gene expression, which in the majority of cases leads to hypertrophy and associated heart failure. Within the scope of this paper it is impossible to review completely the importance of calcineurin; however, it colocalizes with MLP at the sarcomeric Z-disc, and MLP is necessary for calcineurin activation [21].

Protein kinase C (PKC) belongs to a large family of serine/threonine kinases with at least 12 different members and plays major roles in cardiac physiology in mediating hypertrophy and remodelling. They are classically subdivided into three groups: (i) classical calcium sensitive (α , β I, β II, γ), (ii) novel isoforms which lack the calcium sensitive C2 domain (ϵ , δ , h , θ), (iii) atypical isoforms (ζ , λ murine- ι in human) which cannot be activated by calcium, diacylglycerol, or by phorbol esters (reviewed in [111]). In particular, PKC ϵ is localized to the Z-disc [112] and it translocates to the nucleus upon biomechanical stress (on TAC) [113], where this kinase most probably elicits a physiological type of hypertrophy or at least exerts protective functions [114]. This view is supported by transgenic over-expression of a constitutive active PKC ϵ in a mouse model where concentric hypertrophy but not heart failure was observed [115].

In this context, protein kinase D (PKD) translocates to the Z-disc in response to GPCR stimulation via norepinephrine, angiotensin II, and endothelin 1 and is activated via forming a complex with PKC ϵ —an effect particularly important after α adrenergic receptor triggered hypertrophy, where PKC ϵ -mediated PKD activation was essential [116]. This type of hypertrophy might be antagonized by the MuRF1, which is present at the sarcomeric Z-disc and which inhibits PKC ϵ [117].

3.15. Protein Degradation (Muscle Ring Fingers—MuRF): Calpain. Protein degradations via the UPS and via different autophagy pathways are important processes in cardiac biology. The UPS recognizes specific proteins and places polyubiquitin chains on them for subsequent destruction by the proteasome. This process is important not only for misfolded and damaged proteins, but also in regulating a variety of different cell signalling pathways involved in proliferation,

adaptation to stress, regulation of atrophy/hypertrophy-myocardial remodelling, sarcopenia, and cell survival. However, the UPS may also exert protective functions during ischemia/reperfusion or during myocardial remodelling. Some ubiquitinated proteins aggregate and cannot be degraded via the UPS, in which case cytosolic receptors such as p62, NBR, and histone deacetylase 6 recognize aggregated ubiquitinated proteins and target them for autophagy (for excellent recent reviews, please see [118–120]). Here, because of limited space, we just point out that E3 ubiquitin ligases MuRF1 and MuRF3 are localized to the sarcomeric Z-disc [121, 122] in addition to atrogin 1, which mediates calcineurin degradation and might also have major implications for cardiac function [123]. Interestingly, MuRFs interact with serum response factor and seem to play a major role in the initiation of myocardial hypertrophy [124], and particularly MuRF1 may have additional functions in muscle fatigue and twitch potentiation [125].

In addition, calpain 1, which is an important protease particularly for the selective degradation of cell cycle components and for the regulation of apoptosis (together with caspases) and for the cleavage of cell membrane-cytoskeleton components, has also been shown to colocalize with myotilin at the sarcomeric Z-disc [126].

3.16. Transcription Factors and Mitogen-Activated Protein Kinases (MAPK). The sarcomeric Z-disc harbours a number of important transcription factors, such as NFAT, which is a target of the phosphatase calcineurin and which has been implicated in the onset of maladaptive myocardial hypertrophy. Another example is clock, a helix loop helix transcription factor involved in the circadian regulation of myocardial function. The protein localizes to the Z-disc and increases its expression as well as translocating into the nucleus upon an increase in contractility. It also decreases its expression on loss of contractility. It has been suggested that this protein links glucose and fatty acid metabolism to myofilament crossbridge activity [127]. In addition, MLP, telethonin and, FHL proteins shuttle into the nucleus, where they function as cofactors of transcription [62, 128, 129] and/or affect p53 [51]. It has also become clear that a variety of MAPKs such as Erk2 and p38 converge at the sarcomeric Z-disc/I-band area and interact with FHL1 and 2 among others [62, 63, 130].

In conclusion, the sarcomeric Z-disc may well act as a central structure linking myofilament activity, mechanosensation, mechanotransduction, and transcriptional activity, an effect which may be called Z-disc mechanotranscriptional coupling.

4. Summary

The sarcomeric Z-disc, barely detectable in conventional light microscopy, is a far more complex structure than initially recognised. Novel protein/protein interaction discovery strategies have led to the identification of a variety of novel Z-disc proteins which also led to the discovery of novel functional aspects. The Z-disc is not only important for mechanical stability and force transmission but also for signalling,

mechanosensation, mechanotransduction, apoptosis, and cell survival. The sarcomeric Z-disc might also be important for protein turnover via the UPS and autophagy and has molecular links to the t-tubular system as well as to the sarcoplasmic reticulum. Links to energy turnover point to additional important but less well-studied aspects. It is important to stress that proteins localized at the sarcomeric Z-disc might also be present at other locations such as the nucleus, and, for a variety of different Z-disc proteins, nuclear shuttling has been demonstrated (for an excellent review see: [131]). Mutations in Z-disc genes give rise to Z-discopathies, a heterogeneous group of diseases encompassing various cardiomyopathies such as DCM, HCM, ARVC, titinopathies, zaspopathies, myotilinopathies, myofibrillar myopathy, and muscular dystrophies such as the LGMD and XMPMA (please see table and figure). Next generation sequencing is expected to significantly speed up the mutation discovery process, and we can expect that within the next few years a variety of novel mutations located in Z-disc genes will be discovered. This will probably lead to the identification of novel and so far unknown Z-discopathies and may also lead to a better understanding of the underlying molecular mechanism as well as to the development of novel therapeutic strategies.

Moreover, most probably because of the numerous different functions carried by various genetic Z-disc protein mutations, this could lead to perturbations in a vast array of different systems, and the sarcomeric Z-disc is becoming a “hotspot” for cardiomyopathy-causing mutations [18].

It is possible to define central or core Z-disc proteins such as α actinin which serve probably primarily a mechanical function. Another set of proteins may be called transversal or partial Z-disc proteins such as titin, nebulin, or actin which may serve a mechanical function as well but which may have additional implications, for example, in signal transduction, contractility, relaxation, and passive elasticity. In addition, peripheral Z-disc proteins such as telethonin, calsarcin, calcineurin, and MLP may be important for cell signalling, communication, and survival. These proteins can be found at various locations such as the nucleus, costameres, intercalated discs, M-lines, I-bands, and the cytoplasm.

4.1. Future Directions. Future research needs to focus on the link between the sarcomeric Z-disc (probably via MLP), acetylation/deacetylation, and calcium sensitivity. To date a clear genotype-phenotype relationship is not possible for cardiomyopathy and heart-failure-causing mutations. More effort has to be invested in analyzing the relationship between a mutation, its effects on protein function (i.e., poison peptide?), and its effects on protein metabolism in general (i.e., proteinopathy). The link between mechanosensation, mechanotransduction, and apoptosis as well as autophagy needs more investigation. In addition, telethonin might link the sarcomeric Z-disc to the t-tubular system, to the sarcoplasmic reticulum, and directly to apoptosis—these links should be exploited for development of novel therapeutic strategies to combat heart failure, an otherwise lethal condition.

The link between the sarcomeric Z-disc, gene expression, and cell survival, which can be called Z-disc transcriptional coupling, as well as the link between mechanical activity and apoptosis (mechanoptosis) can probably be exploited for novel therapeutic strategies [51].

Finally, Z-disc biology is an exciting newly emerging field and will certainly provide important stimuli for biology and physiology.

Abbreviations

ARVC:	Arrhythmogenic right ventricular cardiomyopathy
DCM:	Dilated cardiomyopathy
GPCR:	G-protein-coupled receptor
HCM:	Hypertrophic cardiomyopathy
IF:	Intermediate filament
LGMD:	Limb-girdle muscular dystrophy
LIM:	Lin11, Isl 1, and Mec 3 motive
PKC/D:	Protein kinase C/D
RBM:	Reducing body myopathy
SP:	Scapuloperoneal
TAC:	Transverse aortic constriction
UPS:	Ubiquitin proteasome system
XMPMA:	X-linked myopathy with postural muscle atrophy.

Acknowledgments

The authors are grateful to Dr. Pradeep Luther for helpful comments and in-depth discussions on the structural aspects of the sarcomeric Z-disc. R. Knöll is supported by the British Heart Foundation (PG/11/34/28793), the Deutsche Forschungsgemeinschaft (Kn 448/9-1 and Kn 448/10-1), FP7-PEOPLE-2011-IRSES Proposal No. 291834—Acronym: SarcoSi and Fritz Thyssen Foundation.

References

- [1] P. K. Luther, “Three-dimensional reconstruction of a simple Z-band in fish muscle,” *Journal of Cell Biology*, vol. 113, no. 5, pp. 1043–1055, 1991.
- [2] P. Zou, N. Pinotsis, S. Lange et al., “Palindromic assembly of the giant muscle protein titin in the sarcomeric Z-disc,” *Nature*, vol. 439, no. 7073, pp. 229–233, 2006.
- [3] P. K. Luther, J. S. Barry, and J. M. Squire, “The three-dimensional structure of a vertebrate wide (slow muscle) Z-band: lessons on Z-band assembly,” *Journal of Molecular Biology*, vol. 315, no. 1, pp. 9–20, 2002.
- [4] P. K. Luther, “The vertebrate muscle Z-disc: sarcomere anchor for structure and signalling,” *Journal of Muscle Research and Cell Motility*, vol. 30, no. 5–6, pp. 171–185, 2009.
- [5] J. M. Squire, H. A. Al-Khayat, C. Knupp, and P. K. Luther, “Molecular architecture in muscle contractile assemblies,” *Advances in Protein Chemistry*, vol. 71, pp. 17–87, 2005.
- [6] K. A. Clark, A. S. McElhinny, M. C. Beckerle, and C. C. Gregorio, “Striated muscle cytoarchitecture: an intricate web of form and function,” *Annual Review of Cell and Developmental Biology*, vol. 18, pp. 637–706, 2002.

- [7] D. Frank and N. Frey, "Cardiac Z-disc signaling network," *The Journal of Biological Chemistry*, vol. 286, pp. 9897–9904, 2011.
- [8] D. Frank, C. Kuhn, H. A. Katus, and N. Frey, "The sarcomeric Z-disc: a nodal point in signalling and disease," *Journal of Molecular Medicine*, vol. 84, no. 6, pp. 446–468, 2006.
- [9] F. Sheikh, M. L. Bang, S. Lange, and J. Chen, "'Z'eroing in on the role of Cypher in striated muscle function, signaling, and human disease," *Trends in Cardiovascular Medicine*, vol. 17, no. 8, pp. 258–262, 2007.
- [10] P. K. Luther, R. Padron, S. Ritter, R. Craig, and J. M. Squire, "Heterogeneity of Z-band structure within a single muscle sarcomere: implications for sarcomere assembly," *Journal of Molecular Biology*, vol. 332, no. 1, pp. 161–169, 2003.
- [11] R. W. Rowe, "The ultrastructure of Z disks from white, intermediate, and red fibers of mammalian striated muscles," *Journal of Cell Biology*, vol. 57, no. 2, pp. 261–277, 1973.
- [12] M. A. Goldstein, L. H. Michael, J. P. Schroeter, and R. L. Sass, "Z band dynamics as a function of sarcomere length and the contractile state of muscle," *FASEB Journal*, vol. 1, no. 2, pp. 133–142, 1987.
- [13] M. A. Goldstein, L. H. Michael, J. P. Schroeter, and R. L. Sass, "Structural states in the Z band of skeletal muscle correlate with states of active and passive tension," *Journal of General Physiology*, vol. 92, no. 1, pp. 113–119, 1988.
- [14] M. A. Goldstein, J. P. Schoeter, and R. L. Sass, "Two structural states of the vertebrate Z band," *Electron Microscopy Reviews*, vol. 3, no. 2, pp. 227–248, 1990.
- [15] M. Yamaguchi, M. Izumimoto, R. M. Robson, and M. H. Stromer, "Fine structure of wide and narrow vertebrate muscle Z-lines. A proposed model and computer simulation of Z-line architecture," *Journal of Molecular Biology*, vol. 184, no. 4, pp. 621–643, 1985.
- [16] C. M. Hampton, D. W. Taylor, and K. A. Taylor, "Novel structures for alpha-actinin:F-actin interactions and their implications for actin-membrane attachment and tension sensing in the cytoskeleton," *Journal of Molecular Biology*, vol. 368, no. 1, pp. 92–104, 2007.
- [17] B. Mohapatra, S. Jimenez, J. H. Lin et al., "Mutations in the muscle LIM protein and alpha-actinin-2 genes in dilated cardiomyopathy and endocardial fibroelastosis," *Molecular Genetics and Metabolism*, vol. 80, no. 1-2, pp. 207–215, 2003.
- [18] J. M. Bos and M. J. Ackerman, "Z-disc genes in hypertrophic cardiomyopathy: stretching the cardiomyopathies?" *Journal of the American College of Cardiology*, vol. 55, pp. 1136–1138, 2010.
- [19] C. Chiu, R. D. Bagnall, J. Ingles et al., "Mutations in alpha-actinin-2 cause hypertrophic cardiomyopathy: a genome-wide analysis," *Journal of the American College of Cardiology*, vol. 55, no. 11, pp. 1127–1135, 2010.
- [20] H. A. Louis, J. D. Pino, K. L. Schmeichel, P. Pomies, and M. C. Beckerle, "Comparison of three members of the cysteine-rich protein family reveals functional conservation and divergent patterns of gene expression," *Journal of Biological Chemistry*, vol. 272, no. 43, pp. 27484–27491, 1997.
- [21] J. Heineke, H. Ruetten, C. Willenbockel et al., "Attenuation of cardiac remodeling after myocardial infarction by muscle LIM protein-calcineurin signaling at the sarcomeric Z-disc," *Proceedings of the National Academy of Sciences of the United States of America*, vol. 102, no. 5, pp. 1655–1660, 2005.
- [22] R. Knöll, M. Hoshijima, H. M. Hoffman et al., "The cardiac mechanical stretch sensor machinery involves a Z disc complex that is defective in a subset of human dilated cardiomyopathy," *Cell*, vol. 111, no. 7, pp. 943–955, 2002.
- [23] R. Knöll, S. Kostin, S. Klede et al., "A common MLP (muscle LIM protein) variant is associated with cardiomyopathy," *Circulation Research*, vol. 106, pp. 695–704, 2010.
- [24] Y. Kong, M. J. Flick, A. J. Kudla, and S. F. Konieczny, "Muscle LIM protein promotes myogenesis by enhancing the activity of MyoD," *Molecular and Cellular Biology*, vol. 17, no. 8, pp. 4750–4760, 1997.
- [25] E. Ehler, R. Horowitz, C. Zuppinger et al., "Alterations at the intercalated disk associated with the absence of muscle LIM protein," *Journal of Cell Biology*, vol. 153, no. 4, pp. 763–772, 2001.
- [26] R. Postel, P. Vakeel, J. Topczewski, R. Knöll, and J. Bakkers, "Zebrafish integrin-linked kinase is required in skeletal muscles for strengthening the integrin-ECM adhesion complex," *Developmental Biology*, vol. 318, no. 1, pp. 92–101, 2008.
- [27] M. J. Flick and S. F. Konieczny, "The muscle regulatory and structural protein MLP is a cytoskeletal binding partner of beta1-spectrin," *Journal of Cell Science*, vol. 113, no. 9, pp. 1553–1564, 2000.
- [28] R. Knöll, G. Iaccarino, G. Tarone et al., "Towards a re-definition of 'cardiac hypertrophy' through a rational characterization of left ventricular phenotypes: a position paper of the Working Group 'Myocardial Function' of the ESC," *European Journal of Heart Failure*, vol. 13, pp. 811–819, 2011.
- [29] B. J. Maron, J. A. Towbin, G. Thiene et al., "Contemporary definitions and classification of the cardiomyopathies: an American heart association scientific statement from the council on clinical cardiology, heart failure and transplantation committee; quality of care and outcomes research and functional genomics and translational biology interdisciplinary working groups; and council on epidemiology and prevention," *Circulation*, vol. 113, no. 14, pp. 1807–1816, 2006.
- [30] V. Papalouka, D. A. Arvanitis, E. Vafiadaki et al., "Muscle Lim protein interacts with cofilin 2 and regulates F-actin dynamics in cardiac and skeletal muscle," *Molecular and Cellular Biology*, vol. 29, no. 22, pp. 6046–6058, 2009.
- [31] S. Arber and P. Caroni, "Specificity of single LIM motifs in targeting and LIM/LIM interactions in situ," *Genes and Development*, vol. 10, no. 3, pp. 289–300, 1996.
- [32] M. P. Gupta, S. A. Samant, S. H. Smith, and S. G. Shroff, "HDAC4 and PCAF bind to cardiac sarcomeres and play a role in regulating myofilament contractile activity," *Journal of Biological Chemistry*, vol. 283, no. 15, pp. 10135–10146, 2008.
- [33] B. Buyandelger, K. E. Ng, S. Miodic et al., "MLP (muscle LIM protein) as a stress sensor in the heart," *Pflügers Archiv*, vol. 462, no. 1, pp. 135–142, 2011.
- [34] M. Bertz, M. Wilmanns, and M. Rief, "The titin-telethonin complex is a directed, superstable molecular bond in the muscle Z-disc," *Proceedings of the National Academy of Sciences of the United States of America*, vol. 106, no. 32, pp. 13307–13310, 2009.
- [35] O. Mayans, P. F. M. van der Ven, M. Wilm et al., "Structural basis for activation of the titin kinase domain during myofibrillogenesis," *Nature*, vol. 395, no. 863, p. 869, 1998.
- [36] R. S. Haworth, F. Cuello, T. J. Herron et al., "Protein kinase D is a novel mediator of cardiac troponin I phosphorylation and regulates myofilament function," *Circulation Research*, vol. 95, no. 11, pp. 1091–1099, 2004.
- [37] A. Kontogianni-Konstantopoulos, E. M. Jones, D. B. Van Rossum, and R. J. Bloch, "Obscurin is a ligand for small ankyrin 1 in skeletal muscle," *Molecular Biology of the Cell*, vol. 14, no. 3, pp. 1138–1148, 2003.

- [38] T. Furukawa, Y. Ono, H. Tsuchiya et al., "Specific interaction of the potassium channel beta-subunit minK with the sarcomeric protein T-cap suggests a T-tubule-myofibril linking system," *Journal of Molecular Biology*, vol. 313, no. 4, pp. 775–784, 2001.
- [39] A. Mazzone, P. R. Strege, D. J. Tester et al., "A mutation in telethonin alters Nav1.5 function," *Journal of Biological Chemistry*, vol. 283, no. 24, pp. 16537–16544, 2008.
- [40] R. Zhang, J. Yang, J. Zhu, and X. Xu, "Depletion of zebrafish Tcap leads to muscular dystrophy via disrupting sarcomere-membrane interaction, not sarcomere assembly," *Human Molecular Genetics*, vol. 18, no. 21, pp. 4130–4140, 2009.
- [41] L. F. Tian, H. Y. Li, B. F. Jin et al., "MDM2 interacts with and downregulates a sarcomeric protein, TCAP," *Biochemical and Biophysical Research Communications*, vol. 345, no. 1, pp. 355–361, 2006.
- [42] S. H. Witt, H. Granzier, C. C. Witt, and S. Labeit, "MURF-1 and MURF-2 target a specific subset of myofibrillar proteins redundantly: towards understanding MURF-dependent muscle ubiquitination," *Journal of Molecular Biology*, vol. 350, no. 4, pp. 713–722, 2005.
- [43] N. Frey and E. N. Olson, "Calsarcin-3, a novel skeletal muscle-specific member of the calsarcin family, interacts with multiple Z-disc proteins," *Journal of Biological Chemistry*, vol. 277, no. 16, pp. 13998–14004, 2002.
- [44] G. Nicholas, M. Thomas, B. Langley et al., "Titin-cap associates with, and regulates secretion of, Myostatin," *Journal of Cellular Physiology*, vol. 193, no. 1, pp. 120–131, 2002.
- [45] N. Nakano, H. Hori, M. Abe et al., "Interaction of BMP10 with Tcap may modulate the course of hypertensive cardiac hypertrophy," *American Journal of Physiology*, vol. 293, no. 6, pp. H3396–H3403, 2007.
- [46] K. Mihatsch, M. Nestler, H. P. Saluz, A. Henke, and T. Munder, "Proapoptotic protein Siva binds to the muscle protein telethonin in cardiomyocytes during coxsackieviral infection," *Cardiovascular Research*, vol. 81, no. 1, pp. 108–115, 2009.
- [47] A. Ferreiro, M. Mezmezian, M. Olive et al., "Telethonin-deficiency initially presenting as a congenital muscular dystrophy," *Neuromuscular Disorders*, vol. 21, no. 6, pp. 433–438, 2011.
- [48] E. S. Moreira, T. J. Wiltshire, G. Faulkner et al., "Limb-girdle muscular dystrophy type 2G is caused by mutations in the gene encoding the sarcomeric protein telethonin," *Nature Genetics*, vol. 24, no. 2, pp. 163–166, 2000.
- [49] M. Olive, A. Shatunov, L. Gonzalez et al., "Transcription-terminating mutation in telethonin causing autosomal recessive muscular dystrophy type 2G in a European patient," *Neuromuscular Disorders*, vol. 18, no. 12, pp. 929–933, 2008.
- [50] T. Hayashi, T. Arimura, M. Itoh-Satoh et al., "Tcap gene mutations in hypertrophic cardiomyopathy and dilated cardiomyopathy," *Journal of the American College of Cardiology*, vol. 44, no. 11, pp. 2192–2201, 2004.
- [51] R. Knöll, W. A. Linke, P. Zou et al., "Telethonin deficiency is associated with maladaptation to biomechanical stress in the mammalian heart," *Circulation Research*, vol. 109, no. 7, pp. 758–769, 2011.
- [52] A. Lange, S. A. Wickstrom, M. Jakobson, R. Zent, K. Sainio, and R. Fassler, "Integrin-linked kinase is an adaptor with essential functions during mouse development," *Nature*, vol. 461, no. 7266, pp. 1002–1006, 2009.
- [53] Y. B. Kim, S. Choi, M. C. Choi et al., "Cell adhesion-dependent cofilin serine 3 phosphorylation by the integrin-linked kinase-c-Src complex," *Journal of Biological Chemistry*, vol. 283, no. 15, pp. 10089–10096, 2008.
- [54] R. Knöll, R. Postel, J. Wang et al., "Laminin-alpha4 and integrin-linked kinase mutations cause human cardiomyopathy via simultaneous defects in cardiomyocytes and endothelial cells," *Circulation*, vol. 116, no. 5, pp. 515–525, 2007.
- [55] M. Brancaccio, S. Guazzone, N. Menini et al., "Melusin is a new muscle-specific interactor for beta(1) integrin cytoplasmic domain," *Journal of Biological Chemistry*, vol. 274, no. 41, pp. 29282–29288, 1999.
- [56] M. Brancaccio, L. Fratta, A. Notte et al., "Melusin, a muscle-specific integrin beta(1)-interacting protein, is required to prevent cardiac failure in response to chronic pressure overload," *Nature Medicine*, vol. 9, no. 1, pp. 68–75, 2003.
- [57] M. De Acetis, A. Notte, F. Accornero et al., "Cardiac overexpression of melusin protects from dilated cardiomyopathy due to long-standing pressure overload," *Circulation Research*, vol. 96, no. 10, pp. 1087–1094, 2005.
- [58] V. Palumbo, L. Segat, L. Padovan et al., "Melusin gene (ITGB1BP2) nucleotide variations study in hypertensive and cardiopathic patients," *BMC Medical Genetics*, vol. 10, article 140, 2009.
- [59] N. Frey, J. A. Richardson, and E. N. Olson, "Calsarcins, a novel family of sarcomeric calcineurin-binding proteins," *Proceedings of the National Academy of Sciences of the United States of America*, vol. 97, no. 26, pp. 14632–14637, 2000.
- [60] N. Frey, T. Barrientos, J. M. Shelton et al., "Mice lacking calsarcin-1 are sensitized to calcineurin signaling and show accelerated cardiomyopathy in response to pathological biomechanical stress," *Nature Medicine*, vol. 10, no. 12, pp. 1336–1343, 2004.
- [61] A. Osio, L. Tan, S. N. Chen et al., "Myozenin 2 is a novel gene for human hypertrophic cardiomyopathy," *Circulation Research*, vol. 100, no. 6, pp. 766–768, 2007.
- [62] N. H. Purcell, D. Darwis, O. F. Bueno, J. M. Muller, R. Schule, and J. D. Molkentin, "Extracellular signal-regulated kinase 2 interacts with and is negatively regulated by the LIM-only protein FHL2 in cardiomyocytes," *Molecular and Cellular Biology*, vol. 24, no. 3, pp. 1081–1095, 2004.
- [63] F. Sheikh, A. Raskin, P. H. Chu et al., "An FHL1-containing complex within the cardiomyocyte sarcomere mediates hypertrophic biomechanical stress responses in mice," *Journal of Clinical Investigation*, vol. 118, no. 12, pp. 3870–3880, 2008.
- [64] C. Windpassinger, B. Schoser, V. Straub et al., "An X-linked myopathy with postural muscle atrophy and generalized hypertrophy, termed XMPMA, is caused by mutations in FHL1," *American Journal of Human Genetics*, vol. 82, no. 1, pp. 88–99, 2008.
- [65] C. M. Quinzii, T. H. Vu, K. C. Min et al., "X-linked dominant scapulo-peroneal myopathy is due to a mutation in the gene encoding four-and-a-half-LIM protein 1," *American Journal of Human Genetics*, vol. 82, no. 1, pp. 208–213, 2008.
- [66] J. Schessl, A. Columbus, Y. Hu et al., "Familial reducing body myopathy with cytoplasmic bodies and rigid spine revisited: identification of a second LIM domain mutation in FHL1," *Neuropediatrics*, vol. 41, no. 1, pp. 43–46, 2010.
- [67] J. Schessl, A. L. Taratuto, C. Sewry et al., "Clinical, histological and genetic characterization of reducing body myopathy caused by mutations in FHL1," *Brain*, vol. 132, no. 2, pp. 452–464, 2009.

- [68] J. Schessl, Y. Zou, M. J. McGrath et al., "Proteomic identification of FHL1 as the protein mutated in human reducing body myopathy," *Journal of Clinical Investigation*, vol. 118, no. 3, pp. 904–912, 2008.
- [69] P. M. Guy, D. A. Kenny, and G. N. Gill, "The PDZ domain of the LIM protein enigma binds to beta-tropomyosin," *Molecular Biology of the Cell*, vol. 10, no. 6, pp. 1973–1984, 1999.
- [70] S. Kuroda, C. Tokunaga, Y. Kiyohara et al., "Protein-protein interaction of zinc finger LIM domains with protein kinase C," *Journal of Biological Chemistry*, vol. 271, no. 49, pp. 31029–31032, 1996.
- [71] Q. Zhou, P. H. Chu, C. Huang et al., "Ablation of Cypher, a PDZ-LIM domain Z-line protein, causes a severe form of congenital myopathy," *Journal of Cell Biology*, vol. 155, no. 3, pp. 605–612, 2001.
- [72] M. Pashmforoush, P. Pomies, K. L. Peterson et al., "Adult mice deficient in actinin-associated LIM-domain protein reveal a developmental pathway for right ventricular cardiomyopathy," *Nature Medicine*, vol. 7, no. 5, pp. 591–597, 2001.
- [73] H. F. Han and M. C. Beckerle, "The ALP-enigma protein ALP-1 functions in actin filament organization to promote muscle structural integrity in *Caenorhabditis elegans*," *Molecular Biology of the Cell*, vol. 20, no. 9, pp. 2361–2370, 2009.
- [74] H. Cheng, K. Kimura, A. K. Peter et al., "Loss of enigma homolog protein results in dilated cardiomyopathy," *Circulation Research*, vol. 107, no. 3, pp. 348–356, 2010.
- [75] S. Arber, J. J. Hunter, J. Ross Jr. et al., "MLP-deficient mice exhibit a disruption of cardiac cytoarchitectural organization, dilated cardiomyopathy, and heart failure," *Cell*, vol. 88, no. 3, pp. 393–403, 1997.
- [76] M. Zheng, H. Cheng, X. Li et al., "Cardiac-specific ablation of Cypher leads to a severe form of dilated cardiomyopathy with premature death," *Human Molecular Genetics*, vol. 18, no. 4, pp. 701–713, 2009.
- [77] C. Huang, Q. Zhou, P. Liang et al., "Characterization and in vivo functional analysis of splice variants of cypher," *Journal of Biological Chemistry*, vol. 278, no. 9, pp. 7360–7365, 2003.
- [78] T. Arimura, T. Hayashi, H. Terada et al., "A Cypher/ZASP mutation associated with dilated cardiomyopathy alters the binding affinity to protein kinase C," *Journal of Biological Chemistry*, vol. 279, no. 8, pp. 6746–6752, 2004.
- [79] M. Vatta, B. Mohapatra, S. Jimenez et al., "Mutations in Cypher/ZASP in patients with dilated cardiomyopathy and left ventricular non-compaction," *Journal of the American College of Cardiology*, vol. 42, no. 11, pp. 2014–2027, 2003.
- [80] Y. Xing, F. Ichida, T. Matsuoka et al., "Genetic analysis in patients with left ventricular noncompaction and evidence for genetic heterogeneity," *Molecular Genetics and Metabolism*, vol. 88, no. 1, pp. 71–77, 2006.
- [81] D. Selcen and A. G. Engel, "Myofibrillar myopathies," *Handbook of Clinical Neurology*, vol. 101, pp. 143–154, 2011.
- [82] D. Selcen and A. G. Engel, "Mutations in ZASP define a novel form of muscular dystrophy in humans," *Annals of Neurology*, vol. 57, no. 2, pp. 269–276, 2005.
- [83] M. Zheng, H. Cheng, I. Banerjee, and J. Chen, "ALP/Enigma PDZ-LIM domain proteins in the heart," *Journal of Molecular Cell Biology*, vol. 2, no. 2, pp. 96–102, 2010.
- [84] S. Homma, M. Iwasaki, G. D. Shelton, E. Engvall, J. C. Reed, and S. Takayama, "BAG3 deficiency results in fulminant myopathy and early lethality," *American Journal of Pathology*, vol. 169, no. 3, pp. 761–773, 2006.
- [85] D. Selcen, F. Muntoni, B. K. Burton et al., "Mutation in BAG3 causes severe dominant childhood muscular dystrophy," *Annals of Neurology*, vol. 65, no. 1, pp. 83–89, 2009.
- [86] N. Norton, D. Li, M. J. Rieder et al., "Genome-wide studies of copy number variation and exome sequencing identify rare variants in BAG3 as a cause of dilated cardiomyopathy," *American Journal of Human Genetics*, vol. 88, no. 3, pp. 273–282, 2011.
- [87] E. Villard, C. Perret, F. Gary et al., "A genome-wide association study identifies two loci associated with heart failure due to dilated cardiomyopathy," *European Heart Journal*, vol. 32, pp. 1065–1076, 2011.
- [88] P. von Nandelstadh, R. Souymani, M. Baumann, and O. Carpen, "Analysis of myotilin turnover provides mechanistic insight into the role of myotilinopathy-causing mutations," *Biochemical Journal*, vol. 436, no. 1, pp. 113–121, 2011.
- [89] F. Bennardini, A. Wrzosek, and M. Chiesi, "Alpha B-Crystallin in cardiac tissue: association with actin and desmin filaments," *Circulation Research*, vol. 71, no. 2, pp. 288–294, 1992.
- [90] I. D. Nicholl and R. A. Quinlan, "Chaperone activity of alpha-crystallins modulates intermediate filament assembly," *EMBO Journal*, vol. 13, no. 4, pp. 945–953, 1994.
- [91] P. Vicart, A. Caron, P. Guicheney et al., "A missense mutation in the alphaB-crystallin chaperone gene causes a desmin-related myopathy," *Nature Genetics*, vol. 20, no. 1, pp. 92–95, 1998.
- [92] Q. Zheng, H. Su, M. J. Ranek, and X. Wang, "Autophagy and p62 in cardiac proteinopathy," *Circulation Research*, vol. 109, pp. 296–308, 2011.
- [93] S. Krief, J. F. Faivre, P. Robert et al., "Identification and characterization of cvHsp. A novel human small stress protein selectively expressed in cardiovascular and insulin-sensitive tissues," *Journal of Biological Chemistry*, vol. 274, no. 51, pp. 36592–36600, 1999.
- [94] A. Brodehl, I. Martin, T. Gawlowski, I. Stork, J. Gummert, and H. Milting, "The small heat shock proteins cvHSP and α -B-Crystallin are colocalized and interact in human myocardial tissue," *Clinical Research in Cardiology*, vol. 99, supplement 1, p. 467, 2010.
- [95] T. P. Cappola, M. Li, J. He et al., "Common variants in HSPB7 and FRMD4B associated with advanced heart failure," *Circulation*, vol. 3, no. 2, pp. 147–154, 2010.
- [96] S. J. Matkovich, D. J. Van Booven, A. Hindes et al., "Cardiac signaling genes exhibit unexpected sequence diversity in sporadic cardiomyopathy, revealing HSPB7 polymorphisms associated with disease," *Journal of Clinical Investigation*, vol. 120, no. 1, pp. 280–289, 2010.
- [97] K. Stark, U. B. Esslinger, W. Reinhard et al., "Genetic association study identifies HSPB7 as a risk gene for idiopathic dilated cardiomyopathy," *PLoS Genetics*, vol. 6, no. 10, article e1001167, 2010.
- [98] M. C. Dalakas, A. Dagvadorj, B. Goudeau et al., "Progressive skeletal myopathy, a phenotypic variant of desmin myopathy associated with desmin mutations," *Neuromuscular Disorders*, vol. 13, no. 3, pp. 252–258, 2003.
- [99] M. C. Dalakas, K. Y. Park, C. Semino-Mora, H. S. Lee, K. Sivakumar, and L. G. Goldfarb, "Desmin myopathy, a skeletal myopathy with cardiomyopathy caused by mutations in the desmin gene," *The New England Journal of Medicine*, vol. 342, no. 11, pp. 770–780, 2000.
- [100] M. C. Walter, P. Reilich, A. Huebner et al., "Scapuloperoneal syndrome type Kaeser and a wide phenotypic spectrum of adult-onset, dominant myopathies are associated with

- the desmin mutation R350P," *Brain*, vol. 130, no. 6, pp. 1485–1496, 2007.
- [101] D. Li, T. Tapscoft, O. Gonzalez et al., "Desmin mutation responsible for idiopathic dilated cardiomyopathy," *Circulation*, vol. 100, no. 5, pp. 461–464, 1999.
- [102] B. Klauke, S. Kossmann, A. Gaertner et al., "De novo desmin-mutation N116S is associated with arrhythmogenic right ventricular cardiomyopathy," *Human Molecular Genetics*, vol. 19, no. 23, pp. 4595–4607, 2010.
- [103] E. Otten, A. Asimaki, A. Maass et al., "Desmin mutations as a cause of right ventricular heart failure affect the intercalated disks," *Heart Rhythm*, vol. 7, no. 8, pp. 1058–1064, 2010.
- [104] P. Pruszczyk, A. Kostera-Pruszczyk, A. Shatunov et al., "Restrictive cardiomyopathy with atrioventricular conduction block resulting from a desmin mutation," *International Journal of Cardiology*, vol. 117, no. 2, pp. 244–253, 2007.
- [105] M. R. G. Taylor, D. Slavov, L. Ku et al., "Prevalence of desmin mutations in dilated cardiomyopathy," *Circulation*, vol. 115, no. 10, pp. 1244–1251, 2007.
- [106] H. Herrmann, H. Bar, L. Kreplak, S. V. Strelkov, and U. Aebi, "Intermediate filaments: from cell architecture to nanomechanics," *Nature Reviews Molecular Cell Biology*, vol. 8, no. 7, pp. 562–573, 2007.
- [107] M. L. Bang, X. Li, R. Littlefield et al., "Nebulin-deficient mice exhibit shorter thin filament lengths and reduced contractile function in skeletal muscle," *Journal of Cell Biology*, vol. 173, no. 6, pp. 905–916, 2006.
- [108] C. C. Witt, C. Burkart, D. Labeit et al., "Nebulin regulates thin filament length, contractility, and Z-disk structure in vivo," *EMBO Journal*, vol. 25, no. 16, pp. 3843–3855, 2006.
- [109] S. Labeit, C. A. C. Ottenheijm, and H. Granzier, "Nebulin, a major player in muscle health and disease," *FASEB Journal*, vol. 25, no. 3, pp. 822–829, 2011.
- [110] J. D. Molkentin, J. R. Lu, C. L. Antos et al., "A calcineurin-dependent transcriptional pathway for cardiac hypertrophy," *Cell*, vol. 93, no. 2, pp. 215–228, 1998.
- [111] A. C. Newton, "Protein kinase C: poised to signal," *American Journal of Physiology*, vol. 298, no. 3, pp. 395–402, 2010.
- [112] S. L. Robia, J. Ghanta, V. G. Robu, and J. W. Walker, "Localization and kinetics of protein kinase C-epsilon anchoring in cardiac myocytes," *Biophysical Journal*, vol. 80, no. 5, pp. 2140–2151, 2001.
- [113] X. Gu and S. P. Bishop, "Increased protein kinase C and isozyme redistribution in pressure-overload cardiac hypertrophy in the rat," *Circulation Research*, vol. 75, no. 5, pp. 926–931, 1994.
- [114] G. Wu, T. Toyokawa, H. Hahn, and G. W. Dorn II, "Epsilon protein kinase C in pathological myocardial hypertrophy. Analysis by combined transgenic expression of translocation modifiers and Galphaq," *The Journal of Biological Chemistry*, vol. 275, Article ID 10.1074/jbc.C000380200, pp. 29927–29930, 2000.
- [115] Y. Takeishi, P. Ping, R. Bolli, D. L. Kirkpatrick, B. D. Hoit, and R. A. Walsh, "Transgenic overexpression of constitutively active protein kinase C epsilon causes concentric cardiac hypertrophy," *Circulation Research*, vol. 86, no. 12, pp. 1218–1223, 2000.
- [116] M. Iwata, A. Maturana, M. Hoshijima et al., "PKCepsilon-PKD1 signaling complex at Z-discs plays a pivotal role in the cardiac hypertrophy induced by G-protein coupling receptor agonists," *Biochemical and Biophysical Research Communications*, vol. 327, pp. 1105–1113, 2005.
- [117] R. Arya, V. Kedar, J. R. Hwang et al., "Muscle ring finger protein-1 inhibits PKC{epsilon} activation and prevents cardiomyocyte hypertrophy," *Journal of Cell Biology*, vol. 167, no. 6, pp. 1147–1159, 2004.
- [118] V. Arndt, N. Dick, R. Tawo et al., "Chaperone-assisted selective autophagy is essential for muscle maintenance," *Current Biology*, vol. 20, no. 2, pp. 143–148, 2010.
- [119] G. Mearini, S. Schlossarek, M. S. Willis, and L. Carrier, "The ubiquitin-proteasome system in cardiac dysfunction," *Biochimica et Biophysica Acta*, vol. 1782, no. 12, pp. 749–763, 2008.
- [120] M. S. Willis, W. H. D. Townley-Tilson, E. Y. Kang, J. W. Homeister, and C. Patterson, "Sent to destroy: the ubiquitin proteasome system regulates cell signaling and protein quality control in cardiovascular development and disease," *Circulation Research*, vol. 106, no. 3, pp. 463–478, 2010.
- [121] T. Centner, J. Yano, E. Kimura et al., "Identification of muscle specific ring finger proteins as potential regulators of the titin kinase domain," *Journal of Molecular Biology*, vol. 306, no. 4, pp. 717–726, 2001.
- [122] J. A. Spencer, S. Eliazar, R. L. Ilaria Jr., J. A. Richardson, and E. N. Olson, "Regulation of microtubule dynamics and myogenic differentiation by MURF, a striated muscle RING-finger protein," *Journal of Cell Biology*, vol. 150, no. 4, pp. 771–784, 2000.
- [123] H. H. Li, V. Kedar, C. Zhang et al., "Atrogin-1/muscle atrophy F-box inhibits calcineurin-dependent cardiac hypertrophy by participating in an SCF ubiquitin ligase complex," *Journal of Clinical Investigation*, vol. 114, no. 8, pp. 1058–1071, 2004.
- [124] M. S. Willis, C. Ike, L. Li, D. Z. Wang, D. J. Glass, and C. Patterson, "Muscle ring finger 1, but not muscle ring finger 2, regulates cardiac hypertrophy in vivo," *Circulation Research*, vol. 100, no. 4, pp. 456–459, 2007.
- [125] S. Labeit, C. H. Kohl, C. C. Witt, D. Labeit, J. Jung, and H. Granzier, "Modulation of muscle atrophy, fatigue and MLC phosphorylation by MuRF1 as indicated by hindlimb suspension studies on MuRF1-KO mice," *Journal of Biomedicine and Biotechnology*, vol. 2010, Article ID 693741, 9 pages, 2010.
- [126] F. Raynaud, C. Jond-Necand, A. Marcilhac, D. Furst, and Y. Benyamin, "Calpain 1-gamma filamin interaction in muscle cells: a possible in situ regulation by PKC-alpha," *The International Journal of Biochemistry and Cell Biology*, vol. 38, no. 3, pp. 404–413, 2006.
- [127] L. Qi and S. Y. Boateng, "The circadian protein Clock localizes to the sarcomeric Z-disk and is a sensor of myofilament cross-bridge activity in cardiac myocytes," *Biochemical and Biophysical Research Communications*, vol. 351, no. 4, pp. 1054–1059, 2006.
- [128] S. Y. Boateng, R. J. Belin, D. L. Geenen et al., "Cardiac dysfunction and heart failure are associated with abnormalities in the subcellular distribution and amounts of oligomeric muscle LIM protein," *American Journal of Physiology*, vol. 292, no. 1, pp. H259–H269, 2007.
- [129] S. Y. Boateng, S. E. Senyo, L. Qi, P. H. Goldspink, and B. Russell, "Myocyte remodeling in response to hypertrophic stimuli requires nucleocytoplasmic shuttling of muscle LIM protein," *Journal of Molecular and Cellular Cardiology*, vol. 47, no. 4, pp. 426–435, 2009.
- [130] S. Vahebi, A. Ota, M. Li et al., "p38-MAPK induced dephosphorylation of alpha-tropomyosin is associated with depression of myocardial sarcomeric tension and ATPase activity," *Circulation Research*, vol. 100, no. 3, pp. 408–415, 2007.
- [131] S. Lange, E. Ehler, and M. Gautel, "From A to Z and back? Multicompartment proteins in the sarcomere," *Trends in Cell Biology*, vol. 16, no. 1, pp. 11–18, 2006.

Review Article

Tropomodulin Capping of Actin Filaments in Striated Muscle Development and Physiology

David S. Gokhin and Velia M. Fowler

Department of Cell Biology, The Scripps Research Institute, La Jolla, CA 92037, USA

Correspondence should be addressed to Velia M. Fowler, velia@scripps.edu

Received 30 June 2011; Accepted 18 August 2011

Academic Editor: Aikaterini Kontrogianni-Konstantopoulos

Copyright © 2011 D. S. Gokhin and V. M. Fowler. This is an open access article distributed under the Creative Commons Attribution License, which permits unrestricted use, distribution, and reproduction in any medium, provided the original work is properly cited.

Efficient striated muscle contraction requires precise assembly and regulation of diverse actin filament systems, most notably the sarcomeric thin filaments of the contractile apparatus. By capping the pointed ends of actin filaments, tropomodulins (Tmods) regulate actin filament assembly, lengths, and stability. Here, we explore the current understanding of the expression patterns, localizations, and functions of Tmods in both cardiac and skeletal muscle. We first describe the mechanisms by which Tmods regulate myofibril assembly and thin filament lengths, as well as the roles of closely related Tmod family variants, the leiomodins (Lmods), in these processes. We also discuss emerging functions for Tmods in the sarcoplasmic reticulum. This paper provides abundant evidence that Tmods are key structural regulators of striated muscle cytoarchitecture and physiology.

1. Introduction

Striated muscle cells are composed of densely packed myofibrils, which are, in turn, composed of large numbers of sarcomeres that repeat in series. In sarcomeres, actin (thin) filaments slide past myosin (thick) filaments to produce sarcomere shortening and, thus, contractile force. The precise temporal and spatial orchestration of actin filament assembly and architecture is critical for muscle contractile function [1–3]. Notably, precise regulation of actin filament lengths is a key feature of striated muscle sarcomeres and confers muscle-specific biomechanical and contractile properties (sarcomere length-tension relationships) [4–6]. Such finely tuned actin assembly is made possible by the regulatory actions of actin-binding proteins. While a host of proteins are known to nucleate filament assembly, cap the fast-growing (barbed) ends of actin filaments, or bind along the sides of filaments, only the tropomodulin (Tmod) family of proteins caps the slow-growing (pointed) filament ends [7–12]. Tmods (~40 kDa) are present in all metazoans, including flies and worms [13–15], with four Tmod isoforms expressed in mammalian cells; Tmod1 is predominantly expressed in terminally differentiated, postmitotic cells (such as erythrocytes, lens fiber cells, neurons, and striated muscle), Tmod2

is in neuronal tissues, Tmod3 is nearly ubiquitous, and Tmod4 is restricted to skeletal muscle fibers [16–26]. Thus, the Tmod isoforms relevant to actin filament regulation in mammalian striated muscles are Tmod1, Tmod3, and Tmod4. Tmods are dynamic caps that inhibit actin monomer association and dissociation from actin filament pointed ends [12, 27–30]; for a review, see [8]. Tmods also bind the terminal tropomyosins (TMs) of TM-coated actin filaments, and, through TM-isoform-specific binding [16–18, 31–39], they regulate the tightness of actin filament pointed-end capping and, thus, actin filament stability and lengths [12, 15, 19, 30, 36, 37, 40–42]; for reviews, see [1, 8, 43]. Aside from their pointed-end capping activities, some Tmods also possess actin monomer-binding and nucleation activities [40, 44, 45]. In addition to Tmods, striated muscles also contain leiomodulin2 (Lmod2), a larger Tmod family variant (~65 kDa) with a potent actin-nucleating activity that can be regulated by TM [21, 46]. It is also noteworthy that the closely related Lmod1, which is predominantly expressed in smooth muscles, is additionally present in a subset of extraocular striated muscle fibers [47, 48].

The amino acid sequences of Tmods share ~80% similarity, and Tmods share a common domain structure

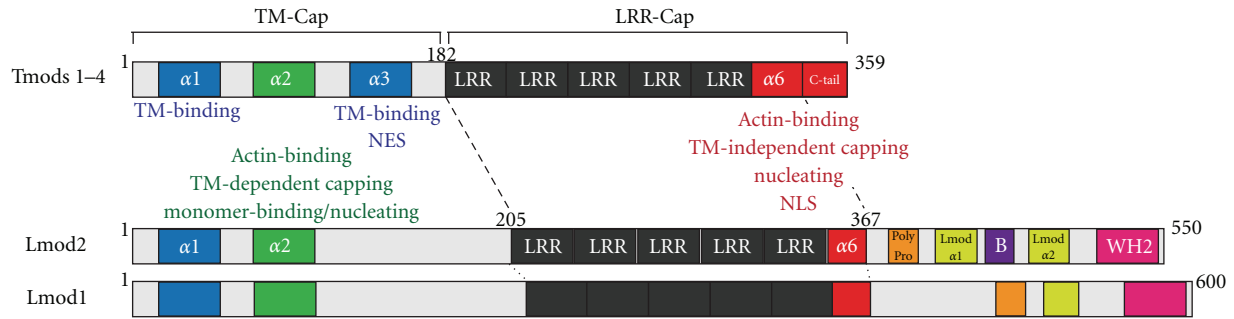


FIGURE 1: Schematic of the molecular sequence and domain organization of Tmods and Lmods found in vertebrate striated muscle. Tmods contain an N-terminal TM-Cap domain and a C-terminal LRR-Cap domain, whose α -helices possess distinct combinations of TM-binding and actin-regulatory activities, as shown. The α -helices are numbered sequentially within each domain, and the NES and NLS of Tmods are highlighted. Lmods also contain a C-terminal extension with a polyproline region, two predicted α -helices, a basic region, and a WH2 domain.

with two major domains: an unstructured and extended N-terminal half, the TM/pointed-end actin capping (TM-Cap) domain, and a compactly folded C-terminal half, the leucine-rich repeat/pointed-end actin capping (LRR-Cap) domain (Figure 1). The N-terminal TM-Cap domain is disordered in solution [32, 49–51], except for one α -helix (residues 24–35), which provides the first TM-binding site, and two downstream predicted α -helices (residues 65–75 and 126–135), which bind actin or provide the second TM-binding site, respectively [22, 34, 36–39, 42, 45, 51–53] (Figure 1). The C-terminal LRR-Cap domain of Tmods consists of a series of five leucine-rich repeats (LRRs) that are composed of tandem repeats of a parallel α -helix/ β -sheet pair, followed by a nonhomologous C-terminal α -helix ($\alpha 6$) and C-terminal tail, which, together, provide an actin pointed-end capping site [40, 54–56] (Figure 1). Tmod's TM-Cap is the unique TM-regulated actin pointed-end capping domain of the Tmod family, with TM enhancing the capping activity of the TM-Cap domain several thousand-fold [12, 30, 36–38, 40, 42]. On the other hand, Tmod's LRR-Cap domain provides a unique actin pointed-end capping domain for TM-free actin filaments [40, 54, 56]. The TM-Cap domain can also bind actin monomers, and the TM-Cap and the LRR-Cap domains are both required for actin nucleation [44, 45]. These distinct actin-regulatory activities of the TM-Cap and LRR-Cap domains and their constituent α -helices, with respect to monomer-binding, filament capping, and filament nucleation [40, 42, 44, 45] (Figure 1), impart Tmods with isoform-specific actin-regulatory functions. Lmod1 and Lmod2 contain the $\alpha 1$ - and $\alpha 2$ -helices, but not the $\alpha 3$ -helix, of the TM-Cap domain, as well as the complete LRR-Cap domain of Tmods, followed by a nonhomologous, ~150-residue-long C-terminal extension [21, 46]. This extension contains a polyproline region, two predicted α -helices, a basic region, and a WASP homology 2 (WH2) domain, which, in Lmod2, imparts strong actin-nucleating activity [46] (Figure 1).

Tmod family members play important roles in myofibril assembly and thin filament length regulation and are essential for striated muscle development and contractile function in both vertebrates and invertebrates. Tmod1 (possibly in

combination with Lmod2 [46, 57, 58]) caps the pointed ends of the sarcomeric thin filaments in cardiac muscle, whereas a combination of Tmod1 and/or Tmod4 caps thin filament pointed ends in skeletal muscle [11, 19, 31, 59–62] (Table 1, Figures 2 and 3). The relative proportions of Tmod1 and Tmod4 in skeletal muscle have not been measured directly but may depend on the muscle twitch speed, with Tmod4 predominating in fast skeletal muscle in chickens [19]. By contrast, Tmod3 is normally not associated with the sarcomeric thin filaments but, instead, appears to cap and stabilize cytoplasmic (nonmuscle) γ -actin filaments in the sarcoplasmic reticulum (SR) of skeletal muscle [63] (Table 1, Figure 3). In mice, an SR-associated (or T-tubule) compartment flanking the Z-line also contains Tmod1 and Tmod4 [63]. Tmod1 is also associated with costameric $\alpha 2$ -spectrin at the sarcolemma of fast chicken skeletal muscle fibers [19] (Table 1). Two recent reviews have discussed the roles of Tmods in regulating actin dynamics in myofibril assembly and thin filament length regulation in some detail [1, 64]. Therefore, in this paper, we will cover areas that have not been previously discussed and emphasize new and recent discoveries.

2. Tmods in Muscle Development and Myofibril Assembly

Tmod1 is one of the earliest sarcomeric proteins expressed during the development of cardiac and skeletal muscle, matching the expression patterns of the basic structural components of sarcomeres. During mouse embryonic development, *Tmod1* mRNA and protein are first detected at E8.0 in the developing heart tube as well as in the blood islands of the yolk sac [23, 59, 68], coinciding with sarcomeric α -actinin and α -myosin heavy chain (α -MHC) expression [59, 65, 73]. Tmod1 persists throughout mouse heart development, with expression especially high in the atrium and lower in the ventricle at E15.5 in mid-gestation [65], similar to α -MHC expression [73]. In chicken heart development, *Tmod1* transcripts are expressed at Hamburger-Hamilton stage 11 in the looping heart tube, earlier than those of *Lmod2* [58], and Tmod1 protein is detected coordinately with cardiac

TABLE 1: Expression and localization of Tmods and Lmods in striated muscle.

Protein	Striated muscle expression	Localization in striated muscle	References
Tmod1	Cardiac and skeletal muscle	Thin filament pointed ends	[11, 28, 31, 59, 60, 62, 65–67]
		SR- or T-tubule-associated compartment*	[63]
		Sarcolemma	[19]
Tmod3	Cardiac and skeletal muscle	SR**	[63]
Tmod4	Skeletal muscle	Thin filament pointed ends	[19, 31]
		SR- or T-tubule-associated compartment	[63]
Lmod1	Slow extraocular muscle fibers	A-band	[47]
Lmod2	Cardiac muscle	Thin filament pointed ends	[46, 57, 58]
		A-band	[57]

*To date, the putative SR-associated or T-tubule localization of Tmod1 has only been observed in skeletal muscle.

**Tmod3 is expressed ubiquitously, including in cardiac muscle [20, 21], but Tmod3 expression levels and localization in mature cardiomyocytes are uncertain, because Tmod3 is abundant in endothelial cells in all tissues [27].

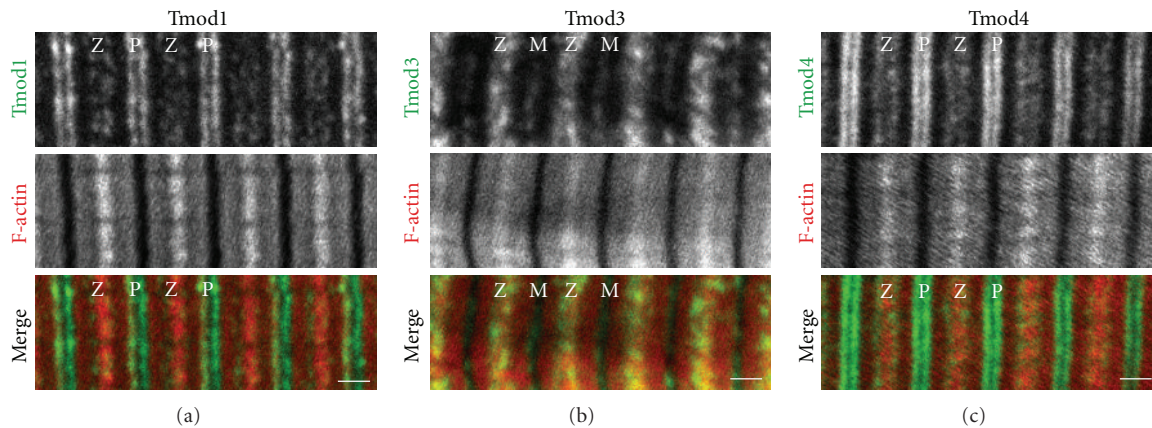


FIGURE 2: Immunofluorescence localization of Tmods in skeletal muscle. Panels depict longitudinal cryosections of mouse tibialis anterior muscle immunostained for (a) Tmod1, (b) Tmod3, or (c) Tmod4, phalloidin-stained for F-actin, and imaged by confocal microscopy, prepared as in [31, 63]. Note the predominant localization of Tmod1 and Tmod4 at the pointed ends of the phalloidin-stained thin filaments. Tmod1 and Tmod4 also exhibit Z-line-flanking localizations, corresponding to an SR- or T-tubule-associated compartment. By contrast, the M-line and Z-line-flanking localization of Tmod3 is a signature of the SR [63]. Z, Z-line; M, M-line; P, thin filament pointed ends. Bars, 1 μm .

actin and myosin in cardiomyocytes differentiating from explants of precardiac mesoderm [74]. In mouse skeletal muscle development, *Tmod1* mRNA is first detected in the developing somites at E9.5, progressing in a caudal-to-rostral fashion during embryonic development, resembling the expression patterns of α -MHC and other sarcomeric proteins [23, 59]. By E14.5–15.5, *Tmod1* mRNA and protein are abundant in the developing skeletal muscles of the trunk and limbs, as well as the diaphragm [23, 31]. In chickens, *Tmod1* mRNA and protein are expressed in embryonic skeletal muscle at 12 and 18 days of development, while *Tmod4* mRNA and protein are not expressed in skeletal muscle until after hatching [19]. The timing and patterns of *Tmod3* and *Tmod4* mRNA expression during mammalian muscle development have not been investigated although Tmod3 and Tmod4 proteins are detected at E15.5 in developing mouse hindlimb and back muscles [31]. Thus, in summary,

Tmod1 expression patterns are consistent with the notion that Tmod1 is an integral structural component of the sarcomeric contractile machinery in both cardiac and skeletal muscle.

To understand how sarcomeric actin filament (thin filament) assembly and lengths are coordinated with the precisely orchestrated spatiotemporal assembly of myofibril components during development, Tmod1 assembly into myofibrils has been studied in the developing embryonic mouse and chick heart and in cultured cardiomyocytes. In the developing mouse heart, Tmod1 associates with nascent myofibrils containing nonstriated actin (i.e., with unregulated lengths) during initial stages of myofibrillogenesis and gradually becomes striated coordinately with actin, as myofibrils mature and precise thin filament lengths are specified [59] (R. B. Nowak and V. M. Fowler, unpublished data). This mirrors the results of experiments on cultured chick

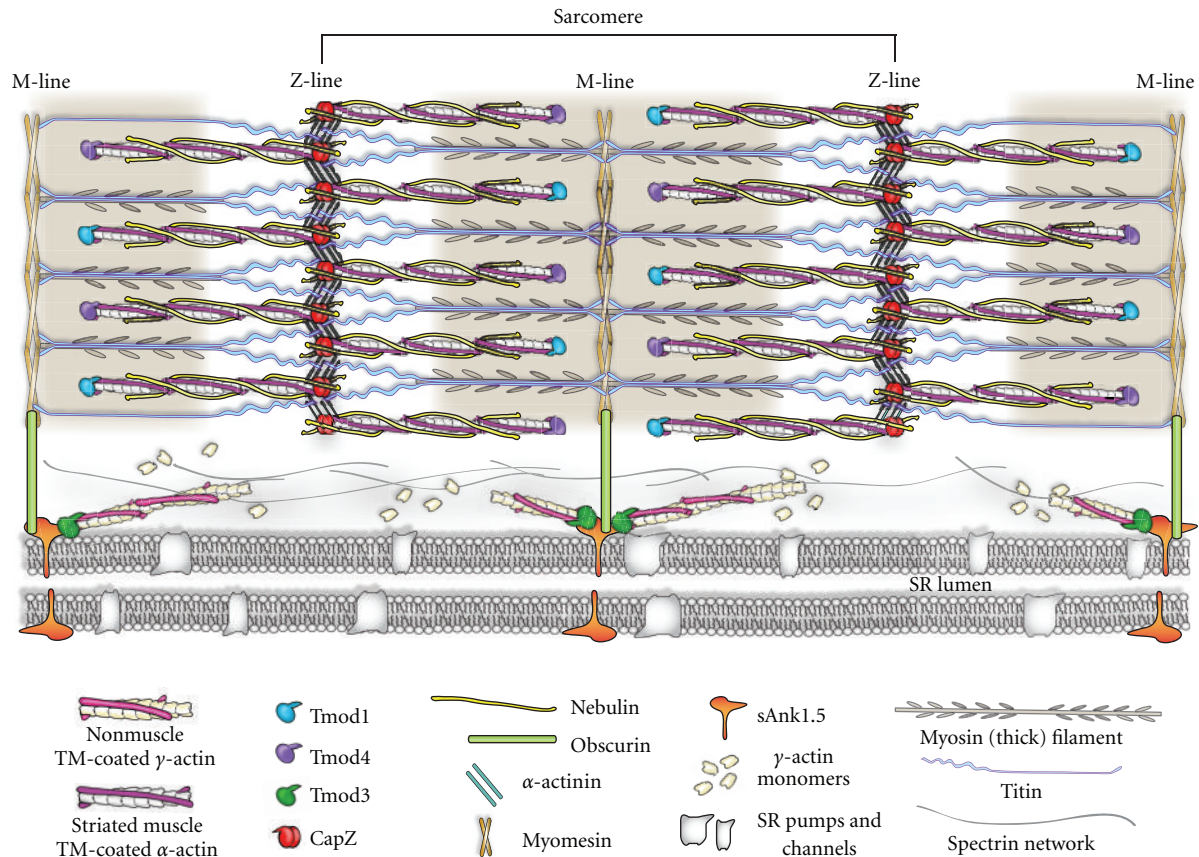


FIGURE 3: Model diagram of Tmods in the sarcomeres and SR of skeletal muscle. Thin filaments, consisting of α -actin subunits, are capped at their pointed ends by a combination of Tmod1 and Tmod4 in skeletal muscle, whereas Tmod3 is associated with cytoplasmic (nonmuscle) γ -actin filaments in the SR. The exact stoichiometries and distributions of Tmod1 versus Tmod4 on the thin filament pointed ends are unknown. Tmod-capped thin filaments extend past the distal N-terminus of nebulin into the middle of the sarcomere. By contrast, in cardiac muscle (not shown here), thin filament pointed ends are capped solely by Tmod1 and do not contain nebulin. Filaments composed of γ -actin, nonmuscle TMs, and Tmod3 are anchored to the SR membrane via sAnk1.5 and laterally connected by a spectrin network. Tmod3/nonmuscle TM/ γ -actin filaments are connected to myofibrils via Tmod3 binding to sAnk1.5, which links to obscurin, which, in turn, is linked to myomesin and titin at the M-line. To date, Tmod3's localization with respect to the cardiac SR remains undetermined. Note that for clarity, the thick filaments are not drawn to scale with respect to the thin filaments.

skeletal myotubes, in which Tmod1 assembles into puncta in nascent myofibrils in lamellipodial extensions containing nonstriated actin early in myofibrillogenesis and gradually becomes striated along with actin as myofibrils mature [61]. By contrast, in whole-mount preparations of embryonic chicken hearts, in chick cardiac mesoderm explants, and in developing axolotl hearts, Tmod1 localizes to puncta at the cell membrane, where myofibril assembly is initiated early in development, but as myofibrillogenesis nears completion later in development, thin filaments appear to become striated (i.e., length-regulated) prior to capping by Tmod1 [66, 67, 74]. Similarly, in embryonic chick cardiomyocyte cultures, Tmod1 assembles onto thin filaments after TM and all other major sarcomeric proteins have assembled, and after actin becomes striated, suggesting that Tmod1 capping is not required for thin filament length regulation during myofibril assembly [60]. These differences in the timing of Tmod1 assembly are not explained by variations in Tmod isoforms, because Tmod1 caps the thin filament pointed

ends in all of these systems [19, 59, 61, 66, 67, 74]. Instead, alterations in Tmod1 conformation and epitope accessibility at various stages of myofibril assembly may play a role, because a Tmod1 polyclonal antibody or a Tmod1 monoclonal antibody (mAb95) detects Tmod1 in nonstriated actin structures at the membrane and in mature striated myofibrils in embryonic chicken hearts, skeletal myotubes, and axolotl hearts [61, 66, 67, 74], whereas another antibody, mAb9, did not detect any Tmod1 associated with nonstriated actin structures near cell membranes in either chick or axolotl hearts [66, 67]. Since mAb9 binds to the actin-capping site in the LRR-Cap domain of Tmod1 [28, 40], Tmod1's actin-capping activity at thin filament pointed ends may vary during myofibril assembly, thus masking or revealing this epitope. Based on these studies, Tmod1 may have an early function in regulating actin pointed-end dynamics in the initial stages of myofibril assembly at the membrane and a later function in maintaining thin filament lengths in mature myofibrils [60, 65, 66].

TABLE 2: Summary of myofibril assembly and thin filament length phenotypes in Tmod1 perturbation experiments.

Perturbation	Model system	Experimental strategy	Resulting phenotype	References
Reduced Tmod1 levels	Mouse embryonic heart	Gene knockout	Myofibril disorganization, nonstriated actin	[59, 65, 68]
	Mouse embryonic stem cells	Gene knockout	Myofibril disorganization, nonstriated actin	[69]
	Mouse skeletal muscle	Gene knockout	No effect*	[31]
	Rat cardiomyocytes	Antisense cDNA expression	Thin filament elongation, nonstriated actin	[70]
	<i>Drosophila</i> primary muscle cells**	RNAi knockdown	Sarcomere length irregularity, thin filament elongation	[71]
	<i>C. elegans</i> body wall muscle***	RNAi knockdown, <i>unc94/tmd-1</i> mutant alleles	Myofibril disorganization, nonstriated actin, myofibril attachment defects	[14, 15]
Inhibition of Tmod1 function	Chick cardiomyocytes	Antibody inhibition of actin capping	Thin filament elongation, nonstriated actin	[28]
	Chick cardiomyocytes	Antibody inhibition of TM binding	Thin filament disassembly	[41]
Tmod1 overexpression	Chick cardiomyocytes	cDNA expression	Thin filament shortening	[29]
	Rat cardiomyocytes	cDNA expression	Myofibril disorganization, thin filament shortening	[70]
	Adult mouse heart	α -Myosin heavy chain promoter-driven <i>Tmod1</i> transgene	Myofibril disorganization, thin filament shortening, intercalated disc defects	[72]
	<i>Drosophila</i> indirect flight muscle**	HSP-90-driven <i>Tmod</i> transgene	Thin filament shortening	[13]
	<i>Drosophila</i> primary muscle cells**	<i>Dmef-GAL4, UAS-Tmod</i> transgene	Thin filament shortening	[71]

* No myofibril assembly or thin filament length alterations occur in Tmod1-null mouse skeletal muscle, but extrasarcomeric SR defects do occur due to Tmod3 translocation from the SR to the thin filament pointed ends.

** *Drosophila* Tmod was knocked down or overexpressed.

*** *C. elegans* UNC94/TMD-1 was knocked down or overexpressed.

An essential requirement for Tmod1 in cardiac development and myofibril assembly is demonstrated by the phenotype of Tmod1-null mice [59, 68] (Table 2). Deletion of Tmod1 is embryonic-lethal, with Tmod1-null embryos appearing morphologically normal through E7.5 but exhibiting defects in cardiac looping morphogenesis, chamber formation, and myofibrillogenesis by E8.5, which result in aborted establishment of the circulation and death by E9.5-10.5 [59, 65, 68]. The primary defect of Tmod1-null mice is in the myocardium, because cardiomyocyte-specific expression of Tmod1, via a Tmod1 transgene expressed using an α -MHC promoter, can completely reverse essentially all of the pathological phenotypes observed in the Tmod1-null mouse, including the cardiac looping defect, aberrant myofibril assembly, defects in yolk sac vasculogenesis, and embryonic lethality [65]. In the absence of Tmod1, myofibrils in the developing mouse heart are unable to mature from primitive I-Z-I bodies with nonstriated actin, resulting in incompletely assembled thin filaments and impaired contractility [59, 65, 68]. However, these results are distinct from an *in vitro* model of myofibril assembly in cardiomyocytes differentiating from mouse embryonic stem cells in Tmod1-null embryoid

bodies, where occasional thin and wispy myofibrils do assemble with regulated thin filament lengths [69]. Similar to the Tmod1-null embryonic heart, contractility is also impaired in this *in vitro* model, due to reduced numbers and defective maturation of myofibrils and cardiomyocytes [69]. The unexpected presence of some myofibrils with regulated thin filament lengths in absence of Tmod1 is unlikely to be due to compensation by Tmod4, since *Tmod4* mRNA is not expressed in the embryonic stem cells or embryoid bodies [69]. However, *Tmod3* mRNA is present, and while *Tmod3* mRNA levels are unchanged upon deletion of Tmod1 [69], Tmod3 protein may have assembled onto the thin filament pointed ends, structurally compensating for absence of Tmod1, similar to compensation by Tmod3 protein in Tmod1-null skeletal muscles [31].

In contrast to cardiac muscle, deletion of Tmod1 from mouse skeletal muscle does not appear to affect skeletal muscle development or myofibril assembly *in vivo* [31] (Table 2). This is most likely due to the additional presence of Tmod4 at the thin filament pointed ends, which may protect embryonic skeletal muscles from the myofibril assembly defects observed in Tmod1-deficient cardiac myofibrils (Figures 2

and 3). In addition, in adult Tmod1-null muscles, Tmod3 translocates from extrasarcomeric sites to cap thin filament pointed ends together with Tmod4, thus maintaining correct thin filament lengths and sarcomere structure, structurally compensating for the absence of Tmod1 as skeletal muscle matures [31, 63]. Taken together, these studies indicate that, in mice, complete removal of pointed-end capping by Tmods severely disrupts both muscle development and myofibril assembly (in cardiac muscle), but partial removal has no obvious effects (in skeletal muscle). The minimum stoichiometry of Tmods that are required to sustain the normal developmental program and myofibrillogenesis in skeletal muscle remains unclear.

An intriguing question raised by these studies is the relationship between Tmod1's role in myofibril assembly and Tmod1's role in muscle development [31, 59, 65, 68, 69]. Namely, is Tmod1's primary role to regulate myofibrillogenesis, with defects in cardiac looping and chamber formation in Tmod1-null hearts as secondary consequences of impaired contractility? Alternatively, could Tmod1 also function in an independent pathway to regulate cardiac morphogenesis and development? Interestingly, Tmod1 is trafficked through the nucleus in cultured skeletal myocytes and cardiomyocytes, as well as fibroblasts, and Tmod1, Tmod2, and Tmod3 all contain a pattern-4 nuclear localization signal (NLS; residues 340–343 of Tmod1; Figure 1), whereas Tmod4 and the *Drosophila* Tmod homologue contain arginine- and lysine-containing motifs that are similar to pattern-4 NLSs [75]. Similarly, Tmod1 contains a nuclear export signal (NES; residues 134–136; Figure 1) that, when mutated, results in Tmod1 accumulation in the nucleus [75]. Tmod1 accumulation in the nuclei of differentiating C2C12 mouse myoblasts results in depressed expression of muscle-specific genes and delayed myogenic differentiation *in vitro* [75]. Tmod1's NES is contained within the TM-binding α 3-helix (Figure 1), and mutation of these residues to eliminate TM binding leads to nuclear accumulation of Tmod1, indicating that the TM-binding and nuclear export activities of Tmod1 may function coordinately [52, 75]. Tmod1 may also influence muscle development via Tmod1 capping and stabilization of TM-actin filaments, thereby depleting the actin monomer pool and regulating muscle gene expression via the actin/myocardin-related transcription factor/serum response factor circuitry [76].

Recent studies of Tmod function in invertebrates provide clues to a network of actin regulatory proteins that orchestrate actin filament organization in myofibril assembly and control thin filament lengths in sarcomeres [64] (Table 2). In the obliquely striated body-wall muscle of *C. elegans*, mutation or RNAi depletion of the Tmod homolog UNC94/TMD-1 leads to severe actin filament disorganization of actin filament bundles with accumulation near cell-cell boundaries and impaired motility [14, 15]. In addition, defects are also observed in the organization of muscle dense bodies, the myofibril attachment sites at the membrane [14]. The actin organization and myofibril assembly defects in *unc94/tmd-1* mutants are strikingly similar to those observed in *C. elegans* mutants for actin-depolymerizing

factor (ADF)/cofilin, actin-interacting protein 1, and profilin, which also regulate sarcomeric actin filament assembly and stability [15, 77–79]. ADF/cofilin enhances dissociation of actin subunits from the pointed end [80], while TMD-1 inhibits ADF/cofilin-induced actin depolymerization by a TM-dependent pointed-end capping mechanism *in vitro* [15]. These biochemical interactions imply that TMD-1 would be antagonistic to ADF/cofilin function *in vivo*. However, unexpectedly, TMD-1 cooperates synergistically with ADF/cofilin to control sarcomeric actin organization and motility, with double mutants more severely affected than single mutants [15]. These *in vivo* genetic interactions could be explained if, in muscle cells, TMD-1 and ADF/cofilin both prevent excessive actin elongation at the thin filament pointed end by TMD-1 capping the pointed end and ADF/cofilin inducing pointed-end disassembly. The identification of *cofilin2* gene mutations in patients with nemaline myopathy, a skeletal muscle disease characterized by accumulations of aberrant actin filament bundles and muscle weakness [81], suggests conserved mechanisms to regulate sarcomeric actin assembly and organization that may also involve Tmods [15]; for reviews, see [1, 64].

3. Tmods and Thin Filament Length Regulation in Striated Muscle Sarcomeres

Once thin filaments are assembled into sarcomeres and myofibrils during muscle development, Tmods function to regulate thin filament lengths by controlling actin filament elongation and shortening at pointed ends [1] (Table 2). In cardiac myofibrils, where thin filament pointed ends are capped by Tmod1, actin dynamics and thin filament lengths are inversely proportional to Tmod1 levels [29, 70]. This was observed directly in experiments in which rhodamine-labeled skeletal muscle α -actin (ρ - α -actin) was microinjected into living chick cardiomyocytes, allowing direct visualization of actin monomer incorporation at both the barbed and pointed ends [29]. Inhibition of actin dynamics at the barbed and pointed ends has distinct effects: overexpression of GFP-Tmod1 reduces actin incorporation at pointed ends and leads to thin filament shortening, but cytochalasin D inhibition of barbed-end dynamics has no effect on lengths [29]. Furthermore, microinjection of an antibody that inhibits Tmod1's actin pointed-end capping activity by binding to the actin capping site in the C-terminal α 6-helix of the LRR-Cap [28, 40] results in elongation of thin filaments from their pointed ends and inhibition of cardiomyocyte beating [28]. Thus, while actin monomer exchange occurs at both barbed and pointed ends in striated muscle sarcomeres, only subunit exchange at pointed ends directly determines thin filament length. Moreover, both ρ - α -actin microinjection into cardiomyocytes [29] and GFP- α -actin expression in living mouse skeletal muscle [82] revealed preferential incorporation at thin filament pointed ends, indicating that the pointed ends are more dynamic than the barbed ends. The interaction between Tmod1 and cardiac TM is essential for thin filament length regulation by Tmod1; monoclonal antibody inhibition of the TM-binding

site in the TM-Cap α 1-helix causes Tmod1 dissociation and thin filament depolymerization from the pointed end [41]. Indeed, Tmod1 targeting to pointed ends in cardiomyocytes depends on prior assembly of TM [60] and on both the α 1- and α 3-helices in the TM-Cap domain [56]. Thus, actin, Tmod1, and TM synergize to maintain thin filament lengths in cardiomyocytes.

While cultured cardiomyocytes provide a useful system to study Tmod targeting to thin filament pointed ends and length regulation, they provide less insight into the physiological ramifications of altered thin filament regulation when Tmod1 levels are perturbed. α -MHC-driven transgenic overexpression of Tmod1 in the *in vivo* mouse heart leads to shorter thin filaments, consistent with increased pointed-end capping in these hearts [72] (Table 2). Mice with Tmod1-overexpressing hearts develop a dilated cardiomyopathy between P14 and P28, which occurs concomitantly with a loss of myofibrillar organization, featuring defects that reflect the *in vitro* scenario with striking similarity [70, 72]. The onset of dilation does not appear to alter the extent of Tmod1 overexpression, indicating that these processes are not directly coupled to one another, but rather, overexpression of Tmod1 appears to trigger a cascade of compensatory responses, including myocardial remodeling, changes in intercalated discs, and myocardial Ca^{2+} handling that lead to dilated cardiomyopathy [83–88].

The notion that the extent of pointed-end capping by Tmods is inversely proportional to thin filament length is not unique to cardiomyocytes and is supported by studies in *Drosophila melanogaster* indirect flight muscle (Table 2). Transient overexpression of *Drosophila* Tmod during indirect flight muscle development via the HSP-90 promoter inhibits actin elongation from thin filament pointed ends and reduces thin filament lengths [13]. Note that the *Drosophila* Tmod gene was originally misidentified as responsible for the *Sanpodo* (*spdo*) asymmetric cell division phenotype [89, 90], but *spdo* was later determined to be a tetraspanin membrane protein in the Notch signaling pathway [90–92]. Thin filament lengths in *Drosophila* are also regulated by sarcomere length short (SALS), a *Drosophila* WH2-domain-containing protein that is required for GFP-actin incorporation at pointed ends and thin filament elongation during myofibril assembly in developing larval muscles [71]. Genetic manipulation of SALS and Tmod levels in primary embryonic muscle cells revealed that SALS promotes the lengthening of thin filaments by antagonizing the pointed-end capping activity of Tmod [71], analogous to a proposed function of Lmod2 in cardiomyocytes (see Section 5) [58], which do not contain the insect-specific SALS protein [71]. However, similar to Tmod, SALS appears to cap actin filament pointed ends *in vitro*, which is puzzling based on its *in vivo* function in promoting pointed-end elongation [71]. Further biochemical studies are required to clarify cooperative and/or competitive actin regulation by SALS and Tmod. Presumably, *Drosophila* indirect flight muscle cells are programmed to maintain a balance between SALS and Tmod to optimize thin filament lengths in a manner that promotes muscle contraction and flight, as flies with excess Tmod and shortened thin filaments are unable to fly [13].

In the case of myofibrils in mammalian skeletal muscle, thin filament length regulation is further complicated by the presence of a combination of Tmod isoforms (Tmod1 and Tmod4) at the pointed ends [11, 19, 31] (Figures 2 and 3). Partially depleting the Tmod isoform inventory of skeletal muscle by deleting Tmod1 does not alter thin filament lengths *in vivo*, presumably because Tmod3 can structurally substitute for the absence of Tmod1 by leaving its SR compartment (see Section 6) to cap thin filament pointed ends in conjunction with Tmod4 [31, 63]. The switch from Tmod1/Tmod4-based capping to Tmod3/Tmod4-based capping of thin filament pointed ends produces physiological changes despite unchanged thin filament lengths; these changes include depressed isometric stress production, impaired locomotor activity, and fiber type reprogramming toward a faster phenotype [31]. Given that this Tmod1-null skeletal muscle phenotype is distinct from the more striking thin filament length misregulation phenotypes observed as a consequence of Tmod1 perturbations in cardiac muscle (Table 2), the minimum Tmod isoform types and levels that are required to maintain correct thin filament lengths in skeletal muscle sarcomeres remain unclear. Indeed, the stoichiometry of Tmods at thin filament pointed ends in rat psoas skeletal muscle, which likely contains Tmod1 and Tmod4 [11, 20, 21, 31] (V. M. Fowler, unpublished data), has been determined to be between 1.2–1.6 Tmods/pointed end, based on quantitative immunoprecipitation using Tmod1 antibodies [11], but this may have been an underestimate due to antibody cross-reactivity with Tmod4 in the absence of prior cross-adsorption [31]. To fully address this quandary *in vivo*, Tmod1 and Tmod4 isoform stoichiometries at thin filament pointed ends need to be measured for various skeletal muscles, and Tmod3-null, Tmod4-null, and Tmod1/Tmod3/Tmod4-double- and triple-null mice need to be developed for future studies.

4. Tmod/Nebulin Interactions and Thin Filament Length Regulation in Skeletal Muscle

In addition to being capped by both Tmod1 and Tmod4, skeletal muscle thin filaments are also distinct from cardiac thin filaments because they contain giant (~600–900 kDa) nebulin molecules that coextend with actin along their lengths (Figure 3). Several recent reviews have discussed the roles of nebulin in thin filament length regulation and actomyosin crossbridge activity [93–96], but, here, we will focus on aspects of nebulin relevant to Tmods. Nebulin's N-terminal domain is located near thin filament pointed ends and contains an interaction site for Tmods [97], while nebulin's C-terminal domain is located at the barbed filament end in the Z-line, containing an interaction site for CapZ [98, 99]. Tmod1, Tmod4, and the C-terminal LRR-Cap domain of Tmod1 bind to an N-terminal module (M1M2M3) of nebulin *in vitro*, based on solid-phase ELISA-binding assays with nebulin fragments and blot overlay assays with full-length nebulin [54, 97]. Binding of native nebulin and Tmods purified from mammalian skeletal muscle has also been

demonstrated in blot overlay assays, but this interaction is weak [97, 100]. Tmod4 binds to nebulin more strongly than Tmod1, and TM does not appear to affect the interaction between Tmods and nebulin [97]. However, the effect of the nebulin M1M2M3 module on Tmod's ability to cap the pointed ends of TM-coated or TM-free actin filaments has not been investigated *in vitro*.

Previous models of nebulin's layout within the thin filament have asserted that nebulin is a "molecular ruler" that orchestrates thin filament assembly and lengths. The ruler hypothesis argues that nebulin specifies the number of actin monomers that can polymerize and fill the space between its C-terminal CapZ-binding site and its N-terminal Tmod-binding M1M2M3 module, which would presumably localize to their respective thin filament ends [1, 3, 93, 101, 102]. Such an arrangement predicts that shorter or longer nebulin splice variants [103–105] produce shorter or longer thin filaments, respectively, and account for the correlation between nebulin isoform size and thin filament length [106, 107]. However, surprisingly, recent data have demonstrated instead that the nebulin M1M2M3 module is located only ~ 0.9 – $1.0 \mu\text{m}$ away from the Z-line in all mature mammalian muscles studied, whereas the thin filament pointed ends extend from $\sim 0.1 \mu\text{m}$ up to $\sim 0.4 \mu\text{m}$ further from the Z-line, well past the nebulin M2M3M3 module [1, 31, 108] (Figure 3). Moreover, despite the interactions between Tmods and the nebulin M1M2M3 module *in vitro*, Tmod1 and Tmod4 are located at the extreme pointed ends of the thin filaments and do not colocalize with the nebulin M1M2M3 module in mature mouse, rabbit, and chicken muscles [31, 108], as well as in human muscles (D. S. Gokhin and V. M. Fowler, unpublished data). Thus, Tmods likely do *not* interact with nebulin in mature mammalian muscles *in vivo* [31, 108]. Furthermore, in neonatal nebulin-null mice, Tmod1 is correctly localized to the pointed ends of the thin filaments, whose lengths are now uniformly $\sim 1.0 \mu\text{m}$, up to $\sim 30\%$ shorter than in wild-type muscles (as determined by Tmod1 localization and phalloidin staining) [109]. Thin filament lengths in the absence of nebulin are identical across all muscles and, curiously, are similar to the distance at which the nebulin M1M2M3 module normally resides with respect to the Z-line [31, 108]. In addition, thin filaments in nebulin-null mouse skeletal muscles appear to partially degenerate during muscle use as the mice develop, until lethality occurs between P7 and P21 [99, 109], explaining the broad Tmod localization observed across the I-bands at P10 [6]. Irregular thin filament disassembly during muscle development or use may also explain the broad Tmod localization pattern associated with the nonuniform and shorter filament lengths in the muscles of human nemaline myopathy patients that contain reduced nebulin levels [6]. Likewise, thin filaments in nebulin siRNA-treated chick skeletal myotubes are unusually prone to latrunculin A-induced actin depolymerization [110]. Based on these observations, nebulin appears to both mechanically and molecularly stabilize a large, ~ 1.0 - μm -long core region of the thin filament, whose length defines the minimum thin filament length that a skeletal muscle sarcomere can stably maintain. In conjunction, actin dynamics at the thin filament

pointed ends (regulated by Tmod1 and Tmod4) are proposed to specify the lengths of the nebulin-free, ~ 0.1 to ~ 0.4 - μm -long thin filament extensions beyond the M1M2M3 module of nebulin [1, 29, 31, 108, 110]. However, the actin dynamics properties and actomyosin crossbridge-regulatory characteristics of these nebulin-free extensions (compared to those of the "canonical" nebulin-coated thin filament cores) have not been studied directly.

It remains uncertain how the nebulin M1M2M3 module, or other nebulin modules, could regulate Tmod-mediated capping "at a distance" in order to specify precise muscle-specific thin filament lengths determined by the variable lengths of the nebulin-free thin filament extensions [1, 31, 108]. This conundrum is highlighted by an elegant recent experiment in chick skeletal myotubes, in which endogenous nebulin was replaced by a shorter mininebulin containing the N- and C-termini of human nebulin but lacking 18 (out of 22) central superrepeats [110]. Even in the presence of mininebulin, the thin filaments still extended well past the N-terminal end of mininebulin and were capped by Tmod1 at their normal location in the center of the sarcomere [110]. Nevertheless, the dynamics of GFP- α -actin, GFP-Tmod1, and GFP-TM were enhanced in the absence of nebulin, and dynamics were reduced (rescued) by introducing mininebulin, as measured by fluorescence recovery after photobleaching (FRAP). This suggests that nebulin may alter the long-range conformation of the TM polymer and/or actin molecules in the thin filament, thereby indirectly stabilizing Tmod capping of actin and TM at the pointed end some distance away from the nebulin molecule itself [110]. The maximum distance from which nebulin can affect Tmod dynamics remains elusive, but it is most likely on the order of ~ 0.3 – $0.4 \mu\text{m}$, which is the longest thin filament pointed-end extension measured to date [108] (D. S. Gokhin and V. M. Fowler, unpublished data). It is also possible that the nebulin M1M2M3 module may interact directly with Tmod at as-yet-unidentified developmental junctures or during the early stages of myofibril assembly when thin filaments may be shorter [61, 111, 112]. Thus, in skeletal muscle, thin filament lengths are likely regulated in a complex fashion by the dynamic properties of Tmods, nebulin, actin, and TM in combination. Heterogeneous expression of thin filament-associated protein isoforms may determine muscle-specific thin filament lengths that are essential for specifying muscle-specific sarcomere length-tension relationships for joint motion and mammalian motility [4–6].

5. Lmods in Actin Nucleation, Thin Filament Assembly, and Length Regulation

A plethora of actin nucleators have been identified in nonmuscle cells that promote assembly of actin filaments into lamellipodia, filopodia, or stress fibers via actin assembly at barbed filament ends [113]. In striated muscle, the formin-homology-domain protein FHOD3 regulates actin assembly and myofibril integrity in rat cardiomyocytes [114, 115],

while the C-terminal SH3 domain of nebulin activated by N-WASP promotes *de novo* assembly of thin filaments at Z-lines during sarcomerogenesis [116]. The larger Tmod family member, Lmod2, which is localized to stripes flanking the M-line in cultured cardiomyocytes [46, 57, 58], also exhibits a potent actin nucleating activity *in vitro*, which is enhanced by TM [46]. In rat cardiomyocytes, siRNA knockdown of Lmod2 results in defective myofibril assembly with disorganized, thin, and wispy myofibrils, implicating Lmod2 in the assembly of thin filaments and myofibrils [46]. Based on the *in vitro* properties of Lmod2, *de novo* Lmod2-nucleated filaments assembling into sarcomeres could grow from their barbed ends with Lmod2 remaining at their pointed ends [46, 57, 58]. However, this mechanism would be somewhat surprising, since previous studies have shown that thin filaments in sarcomeres elongate from their pointed ends (see Section 3) [13, 29, 71]. In agreement with the latter, overexpression of Lmod2 in embryonic chick cardiomyocytes displaced Tmod1 from pointed ends and led to thin filament lengthening [58]. By analogy to SALS function in *Drosophila* myocytes (see Section 3) [71], Lmod2 has been proposed to “fine-tune” thin filament lengths in mature cardiomyocyte sarcomeres by competing with and antagonizing the activity of Tmod1 at the thin filament pointed ends [58]. Alternatively, since the Lmod2 WH2 nucleation domain is required for thin filament elongation in this system [58], it is possible that this filament lengthening could be due to *de novo* nucleation and elongation of new filaments that are then incorporated into existing sarcomeres. Testing these models and integrating Lmod2 functions with those of the FHOD3 and nebulin-SH3 actin nucleators will require the determination of the sites of actin incorporation and filament elongation during thin filament assembly and turnover during myofibrillogenesis, as compared to myofibril maturation and maintenance during muscle contraction and adaptation *in vivo*.

Lmod2 has also been suggested to play a role in regulating actomyosin contractility in mature sarcomeres. In neonatal rat cardiomyocytes, Lmod2 colocalizes with myosin in the A-band (i.e., in broad stripes flanking Tmod1 at the pointed ends) [57]. This A-band localization of Lmod2 was only observed in mature myofibrils and depended on myosin activity as well as on the availability of free actin monomers [57]. Indeed, the myofibril disruption observed upon siRNA knockdown of Lmod2 [46] could potentially be due to effects on myosin activity, which influences myofibril assembly and organization under some conditions [57, 117–120]. The relationship of the A-band localization of Lmod2 in rat cardiomyocytes [57] to the pointed-end localization of Lmod2 in embryonic chick cardiomyocytes [58] is unclear, since full-length Lmod2 is a strong actin nucleator that produces barbed-end elongation *in vitro* and does not cap actin filament pointed ends [46, 57, 58]. However, truncated Lmod2 missing the WH2 domain caps pointed ends in a TM-dependent manner [58], suggesting that additional regulatory factors that inhibit nucleation activity may convert Lmod2 to pointed-end capping in cells. Further studies will be required to determine whether the disparate localizations reported in different studies are due to Lmod isoform or

species differences or differences in myofibril maturation in rat as opposed to chicken cardiomyocytes. Additional work will also be required to resolve the reported discrepancies in Lmod2 functions, including knockout models for Lmods to determine *in vivo* functions.

Considerably less is known about Lmod1, which is predominantly expressed in smooth muscle cells, in which thin filament lengths are not precisely regulated or aligned. In hypercontracted smooth muscle, which reveals a subdomain organization of α -actinin-containing dense bodies alternating with actin filament-rich regions, both Lmod1 and Tmod1 are concentrated in the actin filament-rich regions between the dense bodies [48]. This suggests that Lmod1 and Tmod1 may be associated with the pointed ends of variable-length smooth muscle thin filaments extending from the dense bodies. However, in extraocular striated muscle, Lmod1 colocalizes with the typical myosin-staining doublet in the A-bands of slow muscle fibers [47], similar to Lmod2 in rat cardiomyocytes [57]. This contrasts with Tmod1, which localizes to a single stripe in the middle of the sarcomere in these unstretched muscles, as expected from the close proximity of the locations of the thin filament pointed ends from each half-sarcomere [47, 48]. This suggests that, unlike Tmod1, which caps the thin filament pointed ends, Lmod1 may interact with the regions of thin filaments that interact with myosin in the A-band, or Lmod1 may possibly bind directly to myosin. Lmod1 binds striated muscle TM *in vitro* [48], but its function has otherwise not been studied. (A third Lmod gene, Lmod3, has been identified (human gene ID, 56203; mRNA, NM_198271), but its protein localization and function remain unknown).

6. Tmods and the SR

The SR is a membrane system that wraps around myofibrils and serves as the Ca^{2+} reservoir for muscle contraction. The skeletal muscle SR contains an actin filament network composed of cytoplasmic γ -actin (in contrast to myofibrils, which contain skeletal muscle α -actin) [63]. γ -Actin is thought to be involved in the compensatory remodeling response of skeletal muscle to muscular dystrophy, based on its dramatic upregulation in diverse animal models of the disease [121, 122]. While the filament-level architecture of the γ -actin network is unknown, it likely shares features with Tmod-capped actin filament architectures in nonmuscle cells, such as epithelial cells, lens fiber cells, and red blood cells [123–125]. In mouse skeletal muscle, the predominant Tmod isoform associated with γ -actin in the SR is Tmod3, which shares a localization pattern with γ -actin and nonmuscle TMs in an SR microdomain at the M-line and flanking the Z-line [63] (Figures 2 and 3). Tmod3 appears to be tethered to the SR at the M-line via an interaction with small ankyrin 1.5 (sAnk1.5) [63], a 17-kDa splice variant of ankyrin-R (ankyrin 1) with a hydrophobic transmembrane segment [126–128]. The Tmod3/sAnk1.5 complex in the SR contains γ -actin and nonmuscle TMs (TM5NM1 and TM4) and is not associated with sarco/endoplasmic reticulum Ca^{2+} -ATPase or the ryanodine receptor. Instead, Tmod3-capped γ -actin filaments may be components of an SR-to-myofibril

mechanical linking system, the best-characterized component of which is the giant (~720 kDa) protein obscurin, which links sAnk1.5 in the SR to myomesin and titin in the M-line [129, 130]. The mouse skeletal muscle SR also contains a minor Z-line-flanking microdomain containing Tmod1 and Tmod4, which, based on its localization pattern, may be associated with the SR or T-tubule system [63].

Counterintuitively, deletion of Tmod1 in mice enables the study of the functional significance of Tmod3 in the SR, because Tmod3 vacates the SR and moves to the thin filament pointed ends in adult Tmod1-null muscle [31, 63]. Thus, Tmod1 deletion appears to be a proxy for “conditional” Tmod3 deletion from the SR. In this scenario, loss of Tmod3 from the SR selectively destabilizes its associated complex with sAnk1.5 and perturbs the localizations of γ -actin, nonmuscle TMs, and sAnk1.5. This leads to aberrant SR swelling, depressed Ca^{2+} release, and myofibril misalignment [63]. Notably, previously identified SR-associated membrane skeleton proteins, β 2-spectrin and ankyrin-B, which are involved in targeting SR-associated ion channels in the heart [131–134], are not associated with the Tmod3/sAnk1.5 complex, and are not perturbed by deletion of Tmod1 and redistribution of Tmod3 from the SR to the thin filament pointed ends [63]. This suggests that Tmod3, γ -actin, and nonmuscle TMs define a novel membrane skeleton-like network associated with sAnk1.5 in the SR, which mechanically stabilizes the SR, facilitates SR Ca^{2+} release, and provides connectivity among adjacent myofibrils via linkages between sAnk1.5 and obscurin [63, 130, 135]. Certainly, creation of a Tmod3-null mouse is required to demonstrate rigorously that the SR phenotype is indeed due to the redistribution of Tmod3 from the SR to the thin filament pointed ends, rather than due to deletion of Tmod1 from a different SR compartment or from the T-tubules. In addition, by analogy to nebulin-null mice [136], it is also possible that effects of Tmod1 deletion on actin pointed-end dynamics and thin filament stability may lead to secondary effects on SR Ca^{2+} handling (see Section 7). Future work needs to focus on the molecular architecture of the SR-associated γ -actin cytoskeletal network at the Z- and M-lines and the mechanisms that drive isoform-specific sorting of actins and Tmods in striated muscle. Furthermore, whether Tmod3 plays a role in the cardiac SR analogous to its role in the skeletal muscle SR remains to be determined. It is tempting to speculate that the upregulation of γ -actin that occurs in muscular dystrophy might influence Ca^{2+} handling in the SR in addition to its better-characterized role in binding to dystrophin and mechanically fortifying the sarcolemma; such a model would be consistent with evidence implicating aberrant SR Ca^{2+} handling in the pathogenesis of muscular dystrophy [137–139].

7. Potential Relevance of Tmods to Hereditary Muscle Diseases

A persistent question is whether or not Tmods are directly involved in the pathogenesis of human nemaline myopathy, a skeletal muscle wasting disease that afflicts ~1 : 50,000 individuals, arises from mutations in thin filament-associated

proteins, and is marked by the presence of aberrant actin bundles and so-called “nemaline bodies” consisting of thin filament material [140–142]. In human skeletal muscles, a combination of Tmod1 and Tmod4 caps the pointed ends of the thin filaments (D. S. Gokhin and V. M. Fowler, unpublished data), identical to mouse muscles [31, 63], and mutations in almost all known thin filament-associated proteins, including α -actin (*ACTA1*), β - and γ -TM isoforms (*TPM2* and *TPM3*), troponin I and T isoforms (*TNNI2*, *TNNI1*, and *TNNT3*), and nebulin (*NEB*) [140–142], have been found to produce various degrees of hereditary nemaline myopathy. A nemaline myopathy-linked ADF/cofilin (*CFL2*) mutation has also been identified, implying that aberrant regulation of actin dynamics and turnover in thin filaments can lead to muscle pathologies (see Section 2) [81]. While Tmod1 deletion in mice produces mild muscle pathology with depressed isometric stress production, nemaline bodies are not observed, most likely due to structural compensation by Tmod3, which caps the thin filament pointed ends with Tmod4 in the absence of Tmod1, thus preserving thin filament stability and length regulation [31, 63]. Nevertheless, it is possible that weakened and more dynamic Tmod3/Tmod4 binding to the thin filament pointed ends may alter TM-troponin regulation of actomyosin cross-bridge activity and thereby contribute to muscle weakness [31]; similar changes in productive actomyosin crossbridge formation have been observed in nebulin-null mice as well as in human nemaline myopathy [143–147]. However, the phenotype of Tmod1-null skeletal muscle is distinct from classical nemaline myopathy, because Tmod1-null muscle is not overtly myopathic [31], and Tmod3 translocation from the SR to thin filament pointed ends is accompanied by SR defects and myofibril misalignment that can account for the muscle weakness [63]. Furthermore, no Tmod mutations have yet been identified as a basis for nemaline myopathy.

Clearly, Tmod perturbations can cause muscle pathology in mice, and mutations in the proteins that comprise the Tmod-associated thin filament structures (i.e., disease “hotspots”) in skeletal muscle cause hereditary diseases in humans. However, despite Tmods being integral structural components of thin filaments, they are, thus far, conspicuously absent from the list of thin filament proteins that cause nemaline myopathy. Indeed, Tmods appear to be the *only* thin filament proteins with no as-yet-identified mutations that cause nemaline myopathy. Why might this be the case? The most likely answer is that Tmods are essential genes in humans. Deletion of Tmod1 is embryonic lethal in mice due to defects in cardiac looping morphogenesis and myofibril assembly, resulting in aborted development early in embryogenesis [59, 68]; indeed, studies of Tmod1’s functions in noncardiac tissues *in vivo* require cardiac-specific rescue of Tmod1 to permit animal development and progression into adulthood [31, 63, 65, 124, 125]. Thus, it would be reasonable to predict that wholesale Tmod1 deletion would be lethal in humans as well. However, it is conceivable that Tmod1 mutations resulting in milder Tmod1 functional deficits or partially reduced Tmod1 levels could be associated with hereditary myopathies in humans. Tmod4 mutations are another possibility; in humans, Tmod4 is only present

in skeletal muscle [20, 21] and is a good candidate gene for skeletal muscle disease, because its perturbation would not be expected to cause cardiac defects. Nonetheless, the most probable reason that no myopathy-linked Tmod1 or Tmod4 mutations have yet been identified is compensation by other Tmod isoforms (i.e., Tmod3), as shown in mice [31, 63]. Additional studies on the individuals who are diagnosed with a nemaline myopathy of unknown genetic etiology [140] are required for the identification of putative Tmod mutations associated with nemaline myopathy or other skeletal muscle myopathies.

In addition to the potential involvement of Tmod1 and Tmod4 capping of α -actin thin filaments in nemaline myopathy, putative Tmod3 capping of γ -actin filaments in the SR [63] may play a role in muscular dystrophy. Tmod3 capping of γ -actin filaments occurs in conjunction with nonmuscle TM5NM1 and TM4 binding to the sides of γ -actin filaments, which is essential for normal excitation-contraction coupling, SR function, and maintaining a nondystrophic condition [148–150]. γ -Actin is dramatically upregulated in dystrophic muscle [121, 122], but whether this affects SR structure or function or specific SR-associated γ -actin-regulatory proteins (e.g., Tmod3 and nonmuscle TM5NM1 and TM4) remains unknown. Indeed, γ -actin upregulation without compensatory alterations in the pool of γ -actin-regulatory proteins may result in uncontrolled γ -actin polymerization, which may adversely affect the structure, stability, and function of the SR and/or sarcolemma. Another possibility is that muscular dystrophy-induced misregulation of γ -actin-regulatory proteins may alter γ -actin turnover in a manner that is toxic to the muscle cell via mechanisms involving aberrant Ca^{2+} handling [137, 138]. It is important to recognize that such proposals are speculative at this point. However, given this clinical context, they highlight the fact that the future of the “Tmods in muscle” field lies in dissecting the molecular mechanisms by which Tmods cap and stabilize actin filaments during development and disease, exploring the abilities of Tmods to regulate muscle physiology and contractility, and uncovering potential links between Tmod perturbations and muscle pathology.

Acknowledgments

This work was supported by NIH Grant no. R01-HL083464 (to V. M. Fowler) and NHLBI vascular biology training grant T32-HL007195-34 (to D. S. Gokhin). The authors gratefully acknowledge Sawako Yamashiro for assistance with preparing Figure 1 and for contributions to the initial version of this paper text. They also acknowledge Roberta B. Nowak for assistance with preparing Figure 3.

References

- [1] R. S. Littlefield and V. M. Fowler, “Thin filament length regulation in striated muscle sarcomeres: pointed-end dynamics go beyond a nebulin ruler,” *Seminars in Cell and Developmental Biology*, vol. 19, no. 6, pp. 511–519, 2008.
- [2] K. A. Clark, A. S. McElhinny, M. C. Beckerle, and C. C. Gregorio, “Striated muscle cytoarchitecture: an intricate web of form and function,” *Annual Review of Cell and Developmental Biology*, vol. 18, pp. 637–706, 2002.
- [3] R. Littlefield and V. M. Fowler, “Defining actin filament length in striated muscle: rulers and caps or dynamic stability?” *Annual Review of Cell and Developmental Biology*, vol. 14, pp. 487–525, 1998.
- [4] D. S. Gokhin, M. L. Bang, J. Zhang, J. Chen, and R. L. Lieber, “Reduced thin filament length in nebulin-knockout skeletal muscle alters isometric contractile properties,” *American Journal of Physiology—Cell Physiology*, vol. 296, no. 5, pp. C1123–C1132, 2009.
- [5] H. L. M. Granzier, H. A. Akster, and H. E. D. J. Ter Keurs, “Effect of thin filament length on the force-sarcomere length relation of skeletal muscle,” *American Journal of Physiology—Cell Physiology*, vol. 260, no. 5, pp. C1060–C1070, 1991.
- [6] C. A. C. Ottenheijm, C. C. Witt, G. J. Stienen, S. Labeit, A. H. Beggs, and H. Granzier, “Thin filament length dysregulation contributes to muscle weakness in nemaline myopathy patients with nebulin deficiency,” *Human Molecular Genetics*, vol. 18, no. 13, pp. 2359–2369, 2009.
- [7] L. M. Coluccio, “An end in sight: tropomodulin,” *Journal of Cell Biology*, vol. 127, no. 6, pp. 1497–1499, 1994.
- [8] R. S. Fischer and V. M. Fowler, “Tropomodulins: life at the slow end,” *Trends in Cell Biology*, vol. 13, no. 11, pp. 593–601, 2003.
- [9] V. M. Fowler, “Regulation of actin filament length in erythrocytes and striated muscle,” *Current Opinion in Cell Biology*, vol. 8, no. 1, pp. 86–96, 1996.
- [10] V. M. Fowler, “Capping actin filament growth: tropomodulin in muscle and nonmuscle cells,” *Society of General Physiologists Series*, vol. 52, pp. 79–89, 1997.
- [11] V. M. Fowler, M. A. Sussmann, P. G. Miller, B. E. Flucher, and M. P. Daniels, “Tropomodulin is associated with the free (pointed) ends of the thin filaments in rat skeletal muscle,” *Journal of Cell Biology*, vol. 120, no. 2, pp. 411–420, 1993.
- [12] A. Weber, C. R. Pennise, G. G. Babcock, and V. M. Fowler, “Tropomodulin caps the pointed ends of actin filaments,” *Journal of Cell Biology*, vol. 127, no. 6, pp. 1627–1635, 1994.
- [13] M. Mardahl-Dumesnil and V. M. Fowler, “Thin filaments elongate from their pointed ends during myofibril assembly in *Drosophila* indirect flight muscle,” *Journal of Cell Biology*, vol. 155, no. 6, pp. 1043–1053, 2001.
- [14] T. O. Stevenson, K. B. Mercer, E. A. Cox et al., “*unc-94* encodes a tropomodulin in *Caenorhabditis elegans*,” *Journal of Molecular Biology*, vol. 374, no. 4, pp. 936–950, 2007.
- [15] S. Yamashiro, E. A. Cox, D. L. Baillie, J. D. Hardin, and S. Ono, “Sarcomeric actin organization is synergistically promoted by tropomodulin, ADF/cofilin, AIP1 and profilin in *C. elegans*,” *Journal of Cell Science*, vol. 121, no. 23, pp. 3867–3877, 2008.
- [16] V. M. Fowler, “Identification and purification of a novel M(r) 43,000 tropomyosin-binding protein from human erythrocyte membranes,” *Journal of Biological Chemistry*, vol. 262, no. 26, pp. 12792–12800, 1987.
- [17] V. M. Fowler, “Tropomodulin: a cytoskeletal protein that binds to the end of erythrocyte tropomyosin and inhibits tropomyosin binding to actin,” *Journal of Cell Biology*, vol. 111, no. 2, pp. 471–482, 1990.
- [18] A. Watakabe, R. Kobayashi, and D. M. Helfman, “N-tropomodulin: a novel isoform of tropomodulin identified as the major binding protein to brain tropomyosin,” *Journal of Cell Science*, vol. 109, part 9, pp. 2299–2310, 1996.
- [19] A. Almenar-Queralt, A. Lee, C. A. Conley, L. R. De Pouplana, and V. M. Fowler, “Identification of a novel tropomodulin

- isoform, skeletal tropomodulin, that caps actin filament pointed ends in fast skeletal muscle," *Journal of Biological Chemistry*, vol. 274, no. 40, pp. 28466–28475, 1999.
- [20] P. R. Cox and H. Y. Zoghbi, "Sequencing, expression analysis, and mapping of three unique human tropomodulin genes and their mouse orthologs," *Genomics*, vol. 63, no. 1, pp. 97–107, 2000.
- [21] C. A. Conley, K. L. Fritz-Six, A. Almenar-Queralt, and V. M. Fowler, "Leiomodins: larger members of the tropomodulin (Tmod) gene family," *Genomics*, vol. 73, no. 2, pp. 127–139, 2001.
- [22] L. A. Sung, V. M. Fowler, K. Lambert, M. A. Sussman, D. Karr, and S. Chien, "Molecular cloning and characterization of human fetal liver tropomodulin. A tropomyosin-binding protein," *Journal of Biological Chemistry*, vol. 267, no. 4, pp. 2616–2621, 1992.
- [23] M. Ito, B. Swanson, M. A. Sussman, L. Kedes, and G. Lyons, "Cloning of tropomodulin cDNA and localization of gene transcripts during mouse embryogenesis," *Developmental Biology*, vol. 167, no. 1, pp. 317–328, 1995.
- [24] R. S. Fischer, A. Lee, and V. M. Fowler, "Tropomodulin and tropomyosin mediate lens cell actin cytoskeleton reorganization in vitro," *Investigative Ophthalmology and Visual Science*, vol. 41, no. 1, pp. 166–174, 2000.
- [25] M. A. Sussman, J. W. McAvoy, M. Rudisill et al., "Lens tropomodulin: developmental expression during differentiation," *Experimental Eye Research*, vol. 63, no. 2, pp. 223–232, 1996.
- [26] M. K. Woo and V. M. Fowler, "Identification and characterization of tropomodulin and tropomyosin in the adult rat lens," *Journal of Cell Science*, vol. 107, part 5, pp. 1359–1367, 1994.
- [27] R. S. Fischer, K. L. Fritz-Six, and V. M. Fowler, "Pointed-end capping by tropomodulin3 negatively regulates endothelial cell motility," *Journal of Cell Biology*, vol. 161, no. 2, pp. 371–380, 2003.
- [28] C. C. Gregorio, A. Weber, M. Bondad, C. R. Pennise, and V. M. Fowler, "Requirement of pointed-end capping by tropomodulin to maintain actin filament length in embryonic chick cardiac myocytes," *Nature*, vol. 377, no. 6544, pp. 83–86, 1995.
- [29] R. Littlefield, A. Almenar-Queralt, and V. M. Fowler, "Actin dynamics at pointed ends regulates thin filament length in striated muscle," *Nature Cell Biology*, vol. 3, no. 6, pp. 544–551, 2001.
- [30] A. Weber, C. R. Pennise, and V. M. Fowler, "Tropomodulin increases the critical concentration of barbed end-capped actin filaments by converting ADP.P(i)-actin to ADP-actin at all pointed filament ends," *Journal of Biological Chemistry*, vol. 274, no. 49, pp. 34637–34645, 1999.
- [31] D. S. Gokhin, R. A. Lewis, C. R. McKeown et al., "Tropomodulin isoforms regulate thin filament pointed-end capping and skeletal muscle physiology," *Journal of Cell Biology*, vol. 189, no. 1, pp. 95–109, 2010.
- [32] N. J. Greenfield and V. M. Fowler, "Tropomyosin requires an intact N-terminal coiled coil to interact with tropomodulin," *Biophysical Journal*, vol. 82, no. 5, pp. 2580–2591, 2002.
- [33] C. Vera, A. Sood, K. M. Gao, L. J. Yee, J. J. C. Lin, and L. A. Sung, "Tropomodulin-binding site mapped to residues 7-14 at the N-terminal heptad repeats of tropomyosin isoform 5," *Archives of Biochemistry and Biophysics*, vol. 378, no. 1, pp. 16–24, 2000.
- [34] G. G. Babcock and V. M. Fowler, "Isoform-specific interaction of tropomodulin with skeletal muscle and erythrocyte tropomyosins," *Journal of Biological Chemistry*, vol. 269, no. 44, pp. 27510–27518, 1994.
- [35] M. A. Sussman and V. M. Fowler, "Tropomodulin binding to tropomyosins. Isoform-specific differences in affinity and stoichiometry," *European Journal of Biochemistry*, vol. 205, no. 1, pp. 355–362, 1992.
- [36] A. S. Kostyukova, A. Choy, and B. A. Rapp, "Tropomodulin binds two tropomyosins: a novel model for actin filament capping," *Biochemistry*, vol. 45, no. 39, pp. 12068–12075, 2006.
- [37] A. S. Kostyukova and S. E. Hitchcock-DeGregori, "Effect of the structure of the N terminus of tropomyosin on tropomodulin function," *Journal of Biological Chemistry*, vol. 279, no. 7, pp. 5066–5071, 2004.
- [38] A. S. Kostyukova, S. E. Hitchcock-DeGregori, and N. J. Greenfield, "Molecular Basis of Tropomyosin Binding to Tropomodulin, an Actin-capping Protein," *Journal of Molecular Biology*, vol. 372, no. 3, pp. 608–618, 2007.
- [39] V. N. Uversky, S. P. Shah, Y. Gritsyna, S. E. Hitchcock-DeGregori, and A. S. Kostyukova, "Systematic analysis of tropomodulin/tropomyosin interactions uncovers fine-tuned binding specificity of intrinsically disordered proteins," *Journal of Molecular Recognition*, vol. 24, pp. 647–655, 2011.
- [40] V. M. Fowler, N. J. Greenfield, and J. Moyer, "Tropomodulin contains two actin filament pointed end-capping domains," *Journal of Biological Chemistry*, vol. 278, no. 41, pp. 40000–40009, 2003.
- [41] R. E. Mudry, C. N. Perry, M. Richards, V. M. Fowler, and C. C. Gregorio, "The interaction of tropomodulin with tropomyosin stabilizes thin filaments in cardiac myocytes," *Journal of Cell Biology*, vol. 162, no. 6, pp. 1057–1068, 2003.
- [42] A. S. Kostyukova, B. A. Rapp, A. Choy, N. J. Greenfield, and S. E. Hitchcock-DeGregori, "Structural requirements of tropomodulin for tropomyosin binding and actin filament capping," *Biochemistry*, vol. 44, no. 12, pp. 4905–4910, 2005.
- [43] A. S. Kostyukova, "Tropomodulin/tropomyosin interactions regulate actin pointed end dynamics," *Advances in Experimental Medicine and Biology*, vol. 644, pp. 283–292, 2008.
- [44] R. S. Fischer, E. G. Yarmola, K. L. Weber et al., "Tropomodulin 3 binds to actin monomers," *Journal of Biological Chemistry*, vol. 281, no. 47, pp. 36454–36465, 2006.
- [45] S. Yamashiro, K. D. Speicher, D. W. Speicher, and V. M. Fowler, "Mammalian tropomodulins nucleate actin polymerization via their actin monomer binding and filament pointed end-capping activities," *Journal of Biological Chemistry*, vol. 285, no. 43, pp. 33265–33280, 2010.
- [46] D. Chereau, M. Boczkowska, A. Skwarek-Maruszewska et al., "Leiomodin is an actin filament nucleator in muscle cells," *Science*, vol. 320, no. 5873, pp. 239–243, 2008.
- [47] C. A. Conley and V. M. Fowler, "Localization of the human 64 kD autoantigen D1 to myofibrils in a subset of extraocular muscle fibers," *Current Eye Research*, vol. 19, no. 4, pp. 313–322, 1999.
- [48] C. A. Conley, "Leiomodin and tropomodulin in smooth muscle," *American Journal of Physiology—Cell Physiology*, vol. 280, no. 6, pp. C1645–C1656, 2001.
- [49] A. Kostyukova, K. Maeda, E. Yamauchi, I. Krieger, and Y. Maéda, "Domain structure of tropomodulin: distinct properties of the N-terminal and C-terminal halves," *European Journal of Biochemistry*, vol. 267, no. 21, pp. 6470–6475, 2000.

- [50] A. S. Kostyukova, E. I. Tiktopulo, and Y. Maéda, "Folding properties of functional domains of tropomodulin," *Biophysical Journal*, vol. 81, no. 1, pp. 345–351, 2001.
- [51] N. J. Greenfield, A. S. Kostyukova, and S. E. Hitchcock-DeGregori, "Structure and tropomyosin binding properties of the N-terminal capping domain of tropomodulin 1," *Biophysical Journal*, vol. 88, no. 1, pp. 372–383, 2005.
- [52] K. Y. Kong and L. Kedes, "Leucine 135 of tropomodulin-1 regulates its association with tropomyosin, its cellular localization the integrity of sarcomeres," *Journal of Biological Chemistry*, vol. 281, no. 14, pp. 9589–9599, 2006.
- [53] C. Vera, J. Lao, D. Hamelberg, and L. Amy Sung, "Mapping the tropomyosin isoform 5 binding site on human erythrocyte tropomodulin: further insights into E-Tmod/TM5 interaction," *Archives of Biochemistry and Biophysics*, vol. 444, no. 2, pp. 130–138, 2005.
- [54] I. Krieger, A. Kostyukova, A. Yamashita, Y. Nitani, and Y. Maéda, "Crystal structure of the C-terminal half of tropomodulin and structural basis of actin filament pointed-end capping," *Biophysical Journal*, vol. 83, no. 5, pp. 2716–2725, 2002.
- [55] S. Lu, J. Symersky, S. Li et al., "Structural genomics of *Caenorhabditis elegans*: crystal structure of the tropomodulin C-terminal domain," *Proteins*, vol. 56, no. 2, pp. 384–386, 2004.
- [56] T. Tsukada, L. Kotlyanskaya, R. Huynh et al., "Identification of residues within tropomodulin-1 responsible for its localization at the pointed ends of the actin filaments in cardiac myocytes," *Journal of Biological Chemistry*, vol. 286, no. 3, pp. 2194–2204, 2011.
- [57] A. Skwarek-Maruszewska, M. Boczkowska, A. L. Zajac et al., "Different localizations and cellular behaviors of leiomodlin and tropomodulin in mature cardiomyocyte sarcomeres," *Molecular Biology of the Cell*, vol. 21, no. 19, pp. 3352–3361, 2010.
- [58] T. Tsukada, C. T. Pappas, N. Moroz, P. B. Antin, A. S. Kostyukova, and C. C. Gregorio, "Leiomodlin-2 is an antagonist of tropomodulin-1 at the pointed end of the thin filaments in cardiac muscle," *Journal of Cell Science*, vol. 123, no. 18, pp. 3136–3145, 2010.
- [59] K. L. Fritz-Six, P. R. Cox, R. S. Fischer et al., "Aberrant myofibril assembly in tropomodulin1 null mice leads to aborted heart development and embryonic lethality," *Journal of Cell Biology*, vol. 163, no. 5, pp. 1033–1044, 2003.
- [60] C. C. Gregorio and V. M. Fowler, "Mechanisms of thin filament assembly in embryonic chick cardiac myocytes: tropomodulin requires tropomyosin for assembly," *Journal of Cell Biology*, vol. 129, no. 3, pp. 683–695, 1995.
- [61] A. Almenar-Queralt, C. C. Gregorio, and V. M. Fowler, "Tropomodulin assembles early in myofibrillogenesis in chick skeletal muscle: evidence that thin filaments rearrange to form striated myofibrils," *Journal of Cell Science*, vol. 112, part 8, pp. 1111–1123, 1999.
- [62] M. A. Sussman, S. Sakhi, P. Barrientos, M. Ito, and L. Kedes, "Tropomodulin in rat cardiac muscle: localization of protein is independent of messenger RNA distribution during myofibrillar development," *Circulation Research*, vol. 75, no. 2, pp. 221–232, 1994.
- [63] D. S. Gokhin and V. M. Fowler, "Cytoplasmic γ -actin and tropomodulin isoforms link to the sarcoplasmic reticulum in skeletal muscle fibers," *Journal of Cell Biology*, vol. 194, no. 1, pp. 105–120, 2011.
- [64] S. Ono, "Dynamic regulation of sarcomeric actin filaments in striated muscle," *Cytoskeleton*, vol. 67, no. 11, pp. 677–692, 2010.
- [65] C. R. McKeown, R. B. Nowak, J. Moyer, M. A. Sussman, and V. M. Fowler, "Tropomodulin1 is required in the heart but not the yolk sac for mouse embryonic development," *Circulation Research*, vol. 103, no. 11, pp. 1241–1248, 2008.
- [66] E. Ehler, V. M. Fowler, and J. C. Perriard, "Myofibrillogenesis in the developing chicken heart: role of actin isoforms and of the pointed end actin capping protein tropomodulin during thin filament assembly," *Developmental Dynamics*, vol. 229, no. 4, pp. 745–755, 2004.
- [67] M. D. McLean, R. W. Zajdel, S. Dube, H. Thurston, and D. K. Dube, "Tropomodulin expression in developing hearts of normal and cardiac mutant Mexican axolotl," *Cardiovascular Toxicology*, vol. 6, no. 2, pp. 85–98, 2006.
- [68] X. Chu, J. Chen, M. C. Reedy, C. Vera, K. L. P. Sung, and L. A. Sung, "E-Tmod capping of actin filaments at the slow-growing end is required to establish mouse embryonic circulation," *American Journal of Physiology—Heart and Circulatory Physiology*, vol. 284, no. 5, pp. H1827–H1838, 2003.
- [69] Y. Ono, C. Schwach, P. B. Antin, and C. C. Gregorio, "Disruption in the tropomodulin1 (Tmod1) gene compromises cardiomyocyte development in murine embryonic stem cells by arresting myofibril maturation," *Developmental Biology*, vol. 282, no. 2, pp. 336–348, 2005.
- [70] M. A. Sussman, S. Baqué, C. S. Uhm et al., "Altered expression of tropomodulin in cardiomyocytes disrupts the sarcomeric structure of myofibrils," *Circulation Research*, vol. 82, no. 1, pp. 94–105, 1998.
- [71] J. Bai, J. H. Hartwig, and N. Perrimon, "SALS, a WH2-domain-containing protein, promotes sarcomeric actin filament elongation from pointed ends during *Drosophila* muscle growth," *Developmental Cell*, vol. 13, no. 6, pp. 828–842, 2007.
- [72] M. A. Sussman, S. Welch, N. Cambon et al., "Myofibril degeneration caused by tropomodulin overexpression leads to dilated cardiomyopathy in juvenile mice," *Journal of Clinical Investigation*, vol. 101, no. 1, pp. 51–61, 1998.
- [73] G. E. Lyons, S. Schiaffino, D. Sassoon, P. Barton, and M. Buckingham, "Developmental regulation of myosin gene expression in mouse cardiac muscle," *Journal of Cell Biology*, vol. 111, no. 6, pp. 2427–2436, 1990.
- [74] D. E. Rudy, T. A. Yatskievych, P. B. Antin, and C. C. Gregorio, "Assembly of thick, thin, and titin filaments in chick precardiac explants," *Developmental Dynamics*, vol. 221, no. 1, pp. 61–71, 2001.
- [75] K. Y. Kong and L. Kedes, "Cytoplasmic nuclear transfer of the actin-capping protein tropomodulin," *Journal of Biological Chemistry*, vol. 279, no. 29, pp. 30856–30864, 2004.
- [76] E. N. Olson and A. Nordheim, "Linking actin dynamics and gene transcription to drive cellular motile functions," *Nature Reviews Molecular Cell Biology*, vol. 11, no. 5, pp. 353–365, 2010.
- [77] S. Ono, "The *Caenorhabditis elegans* unc-78 gene encodes a homologue of actin-interacting protein 1 required for organized assembly of muscle actin filaments," *Journal of Cell Biology*, vol. 152, no. 6, pp. 1313–1319, 2001.
- [78] K. Mohri, K. Ono, R. Yu, S. Yamashiro, and S. Ono, "Enhancement of actin-depolymerizing factor/cofilin-dependent actin disassembly by actin-interacting protein 1 is required for organized actin filament assembly in the

- Caenorhabditis elegans* body wall muscle,” *Molecular Biology of the Cell*, vol. 17, no. 5, pp. 2190–2199, 2006.
- [79] S. Ono, K. Mohri, and K. Ono, “Microscopic evidence that actin-interacting protein 1 actively disassembles actin-depolymerizing factor/cofilin-bound actin filaments,” *Journal of Biological Chemistry*, vol. 279, no. 14, pp. 14207–14212, 2004.
- [80] S. Ono, “Mechanism of depolymerization and severing of actin filaments and its significance in cytoskeletal dynamics,” *International Review of Cytology*, vol. 258, pp. 1–82, 2007.
- [81] P. B. Agrawal, R. S. Greenleaf, K. K. Tomczak et al., “Nemaline myopathy with minicores caused by mutation of the CFL2 gene encoding the skeletal muscle actin-binding protein, cofilin-2,” *American Journal of Human Genetics*, vol. 80, no. 1, pp. 162–167, 2007.
- [82] H. Papponen, T. Kaisto, S. Leinonen, M. Kaakinen, and K. Metsikkö, “Evidence for γ -actin as a Z disc component in skeletal myofibers,” *Experimental Cell Research*, vol. 315, no. 2, pp. 218–225, 2009.
- [83] M. A. Sussman, S. Welch, N. Gude et al., “Pathogenesis of dilated cardiomyopathy: molecular, structural, and population analyses in tropomodulin-overexpressing transgenic mice,” *American Journal of Pathology*, vol. 155, no. 6, pp. 2101–2113, 1999.
- [84] E. Ehler, R. Horowitz, C. Zuppinger et al., “Alterations at the intercalated disk associated with the absence of muscle LIM protein,” *Journal of Cell Biology*, vol. 153, no. 4, pp. 763–772, 2001.
- [85] H. W. Lim, L. J. De Windt, J. Mante et al., “Reversal of cardiac hypertrophy in transgenic disease models by calcineurin inhibition,” *Journal of Molecular and Cellular Cardiology*, vol. 32, no. 4, pp. 697–709, 2000.
- [86] S. Welch, D. Plank, S. Witt et al., “Cardiac-specific IGF-1 expression attenuates dilated cardiomyopathy in tropomodulin-overexpressing transgenic mice,” *Circulation Research*, vol. 90, no. 6, pp. 641–648, 2002.
- [87] M. A. Sussman, S. Welch, A. Walker et al., “Hypertrophic defect unmasked by calcineurin expression in asymptomatic tropomodulin overexpressing transgenic mice,” *Cardiovascular Research*, vol. 46, no. 1, pp. 90–101, 2000.
- [88] M. A. Sussman, H. W. Lim, N. Gude et al., “Prevention of cardiac hypertrophy in mice by calcineurin inhibition,” *Science*, vol. 281, no. 5383, pp. 1690–1693, 1998.
- [89] C. A. Dye, J. K. Lee, R. C. Atkinson, R. Brewster, P. L. Han, and H. J. Bellen, “The *Drosophila* sanpodo gene controls sibling cell fate and encodes a tropomodulin homolog, an actin/tropomyosin-associated protein,” *Development*, vol. 125, no. 10, pp. 1845–1856, 1998.
- [90] J. B. Skeath and C. Q. Doe, “Sanpodo and Notch act in opposition to Numb to distinguish sibling neuron fates in the *Drosophila* CNS,” *Development*, vol. 125, no. 10, pp. 1857–1865, 1998.
- [91] A. B. Babaoglan, K. M. O’Connor-Giles, H. Mistry, A. Schickedanz, B. A. Wilson, and J. B. Skeath, “Sanpodo: a context-dependent activator and inhibitor of Notch signaling during asymmetric divisions,” *Development*, vol. 136, no. 24, pp. 4089–4098, 2009.
- [92] K. M. O’Connor-Giles and J. B. Skeath, “Numb inhibits membrane localization of sanpodo, a four-pass transmembrane protein, to promote asymmetric divisions in *Drosophila*,” *Developmental Cell*, vol. 5, no. 2, pp. 231–243, 2003.
- [93] C. T. Pappas, K. T. Bliss, A. Zieseniss, and C. C. Gregorio, “The Nebulin family: an actin support group,” *Trends in Cell Biology*, vol. 21, no. 1, pp. 29–37, 2011.
- [94] S. Labeit, C. A. C. Ottenheijm, and H. Granzier, “Nebulin, a major player in muscle health and disease,” *FASEB Journal*, vol. 25, no. 3, pp. 822–829, 2011.
- [95] C. A. C. Ottenheijm and H. Granzier, “New insights into the structural roles of nebulin in skeletal muscle,” *Journal of Biomedicine and Biotechnology*, vol. 2010, 2010.
- [96] C. A. C. Ottenheijm and H. Granzier, “Lifting the nebula: novel insights into skeletal muscle contractility,” *Physiology*, vol. 25, no. 5, pp. 304–310, 2010.
- [97] A. S. McElhinny, B. Kolmerer, V. M. Fowler, S. Labeit, and C. C. Gregorio, “The N-terminal end of nebulin interacts with tropomodulin at the pointed ends of the thin filaments,” *Journal of Biological Chemistry*, vol. 276, no. 1, pp. 583–592, 2001.
- [98] C. T. Pappas, N. Bhattacharya, J. A. Cooper, and C. C. Gregorio, “Nebulin interacts with CapZ and regulates thin filament architecture within the Z-disc,” *Molecular Biology of the Cell*, vol. 19, no. 5, pp. 1837–1847, 2008.
- [99] C. C. Witt, C. Burkart, D. Labeit et al., “Nebulin regulates thin filament length, contractility, and Z-disk structure in vivo,” *EMBO Journal*, vol. 25, no. 16, pp. 3843–3855, 2006.
- [100] R. Chitose, A. Watanabe, M. Asano et al., “Isolation of nebulin from rabbit skeletal muscle and its interaction with actin,” *Journal of Biomedicine and Biotechnology*, vol. 2010, 2010.
- [101] V. M. Fowler, C. R. McKeown, and R. S. Fischer, “Nebulin: does it measure up as a ruler?” *Current Biology*, vol. 16, no. 1, pp. R18–R20, 2006.
- [102] A. S. McElhinny, S. T. Kazmierski, S. Labeit, and C. C. Gregorio, “Nebulin: the nebulous, multifunctional giant of striated muscle,” *Trends in Cardiovascular Medicine*, vol. 13, no. 5, pp. 195–201, 2003.
- [103] S. Labeit and B. Kolmerer, “The complete primary structure of human nebulin and its correlation to muscle structure,” *Journal of Molecular Biology*, vol. 248, no. 2, pp. 308–315, 1995.
- [104] K. Donner, M. Sandbacka, V. L. Lehtokari, C. Wallgren-Pettersson, and K. Pelin, “Complete genomic structure of the human nebulin gene and identification of alternatively spliced transcripts,” *European Journal of Human Genetics*, vol. 12, no. 9, pp. 744–751, 2004.
- [105] D. Buck, B. D. Hudson, C. A. C. Ottenheijm, S. Labeit, and H. Granzier, “Differential splicing of the large sarcomeric protein nebulin during skeletal muscle development,” *Journal of Structural Biology*, vol. 170, no. 2, pp. 325–333, 2010.
- [106] M. Kruger, J. Wright, and K. Wang, “Nebulin as a length regulator of thin filaments of vertebrate skeletal muscles: correlation of thin filament length, nebulin size, and epitope profile,” *Journal of Cell Biology*, vol. 115, no. 1, pp. 97–107, 1991.
- [107] S. Labeit, T. Gibson, A. Lakey et al., “Evidence that nebulin is a protein-ruler in muscle thin filaments,” *FEBS Letters*, vol. 282, no. 2, pp. 313–316, 1991.
- [108] A. Castillo, R. Nowak, K. P. Littlefield, V. M. Fowler, and R. S. Littlefield, “A nebulin ruler does not dictate thin filament lengths,” *Biophysical Journal*, vol. 96, no. 5, pp. 1856–1865, 2009.
- [109] M. L. Bang, X. Li, R. Littlefield et al., “Nebulin-deficient mice exhibit shorter thin filament lengths and reduced contractile

- function in skeletal muscle,” *Journal of Cell Biology*, vol. 173, no. 6, pp. 905–916, 2006.
- [110] C. T. Pappas, P. A. Krieg, and C. C. Gregorio, “Nebulin regulates actin filament lengths by a stabilization mechanism,” *Journal of Cell Biology*, vol. 189, no. 5, pp. 859–870, 2010.
- [111] J. W. Sanger, P. Chowrashi, N. C. Shaner et al., “Myofibrillogenesis in skeletal muscle cells,” *Clinical Orthopaedics and Related Research*, no. 403, pp. S153–S162, 2002.
- [112] J. W. Sanger, J. Wang, B. Holloway, A. Du, and J. M. Sanger, “Myofibrillogenesis in skeletal muscle cells in zebrafish,” *Cell Motility and the Cytoskeleton*, vol. 66, no. 8, pp. 556–566, 2009.
- [113] M. D. Welch and R. D. Mullins, “Cellular control of actin nucleation,” *Annual Review of Cell and Developmental Biology*, vol. 18, pp. 247–288, 2002.
- [114] T. Iskratsch, S. Lange, J. Dwyer, A. L. Kho, C. Dos Remedios, and E. Ehler, “Formin follows function: a muscle-specific isoform of FHOD3 is regulated by CK2 phosphorylation and promotes myofibril maintenance,” *Journal of Cell Biology*, vol. 191, no. 6, pp. 1159–1172, 2010.
- [115] K. Taniguchi, R. Takeya, S. Suetsugu et al., “Mammalian formin Fhod3 regulates actin assembly and sarcomere organization in striated muscles,” *Journal of Biological Chemistry*, vol. 284, no. 43, pp. 29873–29881, 2009.
- [116] K. Takano, H. Watanabe-Takano, S. Suetsugu et al., “Nebulin and N-WASP cooperate to cause IGF-1-induced sarcomeric actin filament formation,” *Science*, vol. 330, no. 6010, pp. 1536–1540, 2010.
- [117] M. Kagawa, N. Sato, and T. Obinata, “Effects of BTS (N-benzyl-p-toluene sulphonamide), an inhibitor for myosin-actin interaction, on myofibrillogenesis in skeletal muscle cells in culture,” *Zoological Science*, vol. 23, no. 11, pp. 969–975, 2006.
- [118] Y. Soeno, Y. Shimada, and T. Obinata, “BDM (2,3-butanedione monoxime), an inhibitor of myosin actin interaction, suppresses myofibrillogenesis in skeletal muscle cells in culture,” *Cell and Tissue Research*, vol. 295, no. 2, pp. 307–316, 1999.
- [119] I. Ramachandran, M. Terry, and M. B. Ferrari, “Skeletal muscle myosin cross-bridge cycling is necessary for myofibrillogenesis,” *Cell Motility and the Cytoskeleton*, vol. 55, no. 1, pp. 61–72, 2003.
- [120] A. Skwarek-Maruszewska, P. Hotulainen, P. K. Mattila, and P. Lappalainen, “Contractility-dependent actin dynamics in cardiomyocyte sarcomeres,” *Journal of Cell Science*, vol. 122, no. 12, pp. 2119–2126, 2009.
- [121] L. M. Hanft, D. J. Bogan, U. Mayer, S. J. Kaufman, J. N. Kornegay, and J. M. Ervasti, “Cytoplasmic γ -actin expression in diverse animal models of muscular dystrophy,” *Neuromuscular Disorders*, vol. 17, no. 7, pp. 569–574, 2007.
- [122] L. M. Hanft, I. N. Rybakova, J. R. Patel, J. A. Rafael-Fortney, and J. M. Ervasti, “Cytoplasmic γ -actin contributes to a compensatory remodeling response in dystrophin-deficient muscle,” *Proceedings of the National Academy of Sciences of the United States of America*, vol. 103, no. 14, pp. 5385–5390, 2006.
- [123] K. L. Weber, R. S. Fischer, and V. M. Fowler, “Tmod3 regulates polarized epithelial cell morphology,” *Journal of Cell Science*, vol. 120, no. 20, pp. 3625–3632, 2007.
- [124] R. B. Nowak, R. S. Fischer, R. K. Zoltoski, J. R. Kuszak, and V. M. Fowler, “Tropomodulin1 is required for membrane skeleton organization and hexagonal geometry of fiber cells in the mouse lens,” *Journal of Cell Biology*, vol. 186, no. 6, pp. 915–928, 2009.
- [125] J. D. Moyer, R. B. Nowak, N. E. Kim et al., “Tropomodulin 1-null mice have a mild spherocytic elliptocytosis with appearance of tropomodulin 3 in red blood cells and disruption of the membrane skeleton,” *Blood*, vol. 116, no. 14, pp. 2590–2599, 2010.
- [126] P. G. Gallagher and B. G. Forget, “An alternate promoter directs expression of a truncated, muscle-specific isoform of the human ankyrin 1 gene,” *Journal of Biological Chemistry*, vol. 273, no. 3, pp. 1339–1348, 1998.
- [127] P. G. Gallagher, W. T. Tse, A. L. Scarpa, S. E. Lux, and B. G. Forget, “Structure and organization of the human Ankyrin-1 gene,” *Journal of Biological Chemistry*, vol. 272, no. 31, pp. 19220–19228, 1997.
- [128] N. C. Porter, W. G. Resneck, A. O’Neill, D. B. Van Rossum, M. R. Stone, and R. J. Bloch, “Association of small ankyrin 1 with the sarcoplasmic reticulum,” *Molecular Membrane Biology*, vol. 22, no. 5, pp. 421–432, 2005.
- [129] A. Fukuzawa, S. Lange, M. Holt et al., “Interactions with titin and myomesin target obscurin and obscurin-like 1 to the M-band—implications for hereditary myopathies,” *Journal of Cell Science*, vol. 121, no. 11, pp. 1841–1851, 2008.
- [130] P. Bagnato, V. Barone, E. Giacomello, D. Rossi, and V. Sorrentino, “Binding of an ankyrin-1 isoform to obscurin suggests a molecular link between the sarcoplasmic reticulum and myofibrils in striated muscles,” *Journal of Cell Biology*, vol. 160, no. 2, pp. 245–253, 2003.
- [131] P. J. Mohler, J. Q. Davis, and V. Bennett, “Ankyrin-B coordinates the Na/K ATPase, Na/Ca exchanger, and InsP3 receptor in a cardiac T-tubule/SR microdomain,” *PLoS Biology*, vol. 3, no. 12, Article ID e423, 2005.
- [132] P. J. Mohler, W. Yoon, and V. Bennett, “Ankyrin-B targets β 2-spectrin to an intracellular compartment in neonatal cardiomyocytes,” *Journal of Biological Chemistry*, vol. 279, no. 38, pp. 40185–40193, 2004.
- [133] P. J. Mohler, J. J. Schott, A. O. Gramolini et al., “Ankyrin-B mutation causes type 4 long-QT cardiac arrhythmia and sudden cardiac death,” *Nature*, vol. 421, no. 6923, pp. 634–639, 2003.
- [134] S. Tuvia, M. Buhusi, L. Davis, M. Reedy, and V. Bennett, “Ankyrin-B is required for intracellular sorting of structurally diverse Ca²⁺ homeostasis proteins,” *Journal of Cell Biology*, vol. 147, no. 5, pp. 995–1007, 1999.
- [135] A. Kontrogianni-Konstantopoulos, E. M. Jones, D. B. Van Rossum, and R. J. Bloch, “Obscurin is a ligand for small ankyrin 1 in skeletal muscle,” *Molecular Biology of the Cell*, vol. 14, no. 3, pp. 1138–1148, 2003.
- [136] C. A. C. Ottenheijm, C. Fong, P. Vangheluwe et al., “Sarcoplasmic reticulum calcium uptake and speed of relaxation are depressed in nebulin-free skeletal muscle,” *FASEB Journal*, vol. 22, no. 8, pp. 2912–2919, 2008.
- [137] J. S. H. Tay, P. S. Lai, P. S. Low, W. L. Lee, and G. C. Gan, “Pathogenesis of Duchenne muscular dystrophy: the calcium hypothesis revisited,” *Journal of Paediatrics and Child Health*, vol. 28, no. 4, pp. 291–293, 1992.
- [138] F. W. Hopf, P. R. Turner, and R. A. Steinhardt, “Calcium misregulation and the pathogenesis of muscular dystrophy,” *Sub-cellular Biochemistry*, vol. 45, pp. 429–464, 2007.
- [139] S. A. Goonasekera, C. K. Lam, D. P. Millay et al., “Mitigation of muscular dystrophy in mice by SERCA overexpression in skeletal muscle,” *Journal of Clinical Investigation*, vol. 121, no. 3, pp. 1044–1052, 2011.

- [140] D. Sanoudou and A. H. Beggs, "Clinical and genetic heterogeneity in nemaline myopathy—a disease of skeletal muscle thin filaments," *Trends in Molecular Medicine*, vol. 7, no. 8, pp. 362–368, 2001.
- [141] J. Ochala, "Thin filament proteins mutations associated with skeletal myopathies: defective regulation of muscle contraction," *Journal of Molecular Medicine*, vol. 86, no. 11, pp. 1197–1204, 2008.
- [142] N. G. Laing and C. Wallgren-Pettersson, "161st ENMC International Workshop on nemaline myopathy and related disorders, Newcastle upon Tyne, 2008," *Neuromuscular Disorders*, vol. 19, no. 4, pp. 300–305, 2009.
- [143] M. Chandra, R. Manidi, S. Ford et al., "Nebulin alters cross-bridge cycling kinetics and increases thin filament activation. A novel mechanism for increasing tension and reducing tension cost," *Journal of Biological Chemistry*, vol. 284, no. 45, pp. 30889–30896, 2009.
- [144] C. A. C. Ottenheijm, P. Hooijman, E. T. DeChene, G. J. Stienen, A. H. Beggs, and H. Granzier, "Altered myofilament function depresses force generation in patients with nebulin-based nemaline myopathy (NEM2)," *Journal of Structural Biology*, vol. 170, no. 2, pp. 334–343, 2010.
- [145] M. L. Bang, M. Caremani, E. Brunello et al., "Nebulin plays a direct role in promoting strong actin-myosin interactions," *FASEB Journal*, vol. 23, no. 12, pp. 4117–4125, 2009.
- [146] J. Ochala, V. L. Lehtokari, H. Iwamoto et al., "Disrupted myosin cross-bridge cycling kinetics triggers muscle weakness in nebulin-related myopathy," *FASEB Journal*, vol. 25, no. 6, pp. 1903–1913, 2011.
- [147] J. Ochala, H. Iwamoto, L. Larsson, and N. Yagi, "A myopathy-linked tropomyosin mutation severely alters thin filament conformational changes during activation," *Proceedings of the National Academy of Sciences of the United States of America*, vol. 107, no. 21, pp. 9807–9812, 2010.
- [148] A. J. Kee, G. Schevzov, V. Nair-Shalliker et al., "Sorting of a nonmuscle tropomyosin to a novel cytoskeletal compartment in skeletal muscle results in muscular dystrophy," *Journal of Cell Biology*, vol. 166, no. 5, pp. 685–696, 2004.
- [149] N. Vlahovich, A. J. Kee, C. D. Van der Poel et al., "Cytoskeletal tropomyosin Tm5NM1 is required for normal Excitation-contraction coupling in skeletal muscle," *Molecular Biology of the Cell*, vol. 20, no. 1, pp. 400–409, 2009.
- [150] N. Vlahovich, G. Schevzov, V. Nair-Shaliker et al., "Tropomyosin 4 defines novel filaments in skeletal muscle associated with muscle remodelling/regeneration in normal and diseased muscle," *Cell Motility and the Cytoskeleton*, vol. 65, no. 1, pp. 73–85, 2008.

Review Article

The Evolution of the Mitochondria-to-Calcium Release Units Relationship in Vertebrate Skeletal Muscles

Clara Franzini-Armstrong¹ and Simona Boncompagni²

¹ Department of Cell and Developmental Biology, School of Medicine, University of Pennsylvania, Philadelphia, PA 19104, USA

² Center for Research on Ageing and Department of Neuroscience and Imaging, Università Gabriele d'Annunzio, 66100 Chieti, Italy

Correspondence should be addressed to Clara Franzini-Armstrong, armstroc@mail.med.upenn.edu

Received 5 July 2011; Accepted 10 August 2011

Academic Editor: Aikaterini Kontrogianni-Konstantopoulos

Copyright © 2011 C. Franzini-Armstrong and S. Boncompagni. This is an open access article distributed under the Creative Commons Attribution License, which permits unrestricted use, distribution, and reproduction in any medium, provided the original work is properly cited.

The spatial relationship between mitochondria and the membrane systems, more specifically the calcium release units (CRUs) of skeletal muscle, is of profound functional significance. CRUs are the sites at which Ca^{2+} is released from the sarcoplasmic reticulum during muscle activation. Close mitochondrion-CRU proximity allows the organelles to take up Ca^{2+} and thus stimulate aerobic metabolism. Skeletal muscles of most mammals display an extensive, developmentally regulated, close mitochondrion-CRU association, fostered by tethering links between the organelles. A comparative look at the vertebrate subphylum however shows that this specific association is only present in the higher vertebrates (mammals). Muscles in all other vertebrates, even if capable of fast activity, rely on a less precise and more limited mitochondrion-CRU proximity, despite some tethering connections. This is most evident in fish muscles. Clustering of free subsarcolemmal mitochondria in proximity of capillaries is also more frequently achieved in mammalian than in other vertebrates.

1. Introduction

Mitochondria have two functional requirements: they need oxygen and also some stimulation by Ca^{2+} [1–3]. The latter event has been disputed for a while, but it is now clear that mitochondria take up some of the Ca^{2+} released from the endoplasmic reticulum (ER) under physiological conditions, a step that has important effects on a variety of their functions, including the stimulation of aerobic metabolism. The uptake has been initially difficult to pinpoint, but specifically targeted aequorin [4] gave a first clear evidence for Ca^{2+} entry into the mitochondria of living cells, and fluorometric measurements of mitochondrial dehydrogenases activity provided an early fast measurement of mitochondrial Ca^{2+} uptake *in vivo* [5]. The concept has been developed that this uptake is strictly dependent on a planned proximity between the organelles and certain components of the ER. The so-called high Ca^{2+} microdomain hypothesis proposes that the proximity is necessary because the relatively low mitochondrial affinity for Ca^{2+} [1, 6–8] means that uptake will occur

only if the mitochondrion is near the source, so that it experiences a sudden increase of the cytoplasmic Ca^{2+} level to relatively high values [9–11]. Close proximities between ER and mitochondria are indeed frequent and well documented in liver cells, where the ER, both RER and SER, is frequently tightly wrapped around the mitochondria profiles [12, 13] even in organisms as low as fish. Visible tethering connections between ER and mitochondria are sufficiently strong in liver and myocardium of mammals to maintain the association during cellular fractionation [14, 15]. More recently, an even more direct interaction between ER components and the outer mitochondrial membrane has been proposed, based on a physical link between the voltage-dependent anion channel (VDAC) of the outer mitochondrial membrane and I_p3 receptors of the ER, allowing direct coupling between Ca^{2+} release and mitochondrial uptake [16].

Cardiac and skeletal muscle cells are inherently crowded due to their content of myofibrils, and the mitochondria share the narrow intermyofibrillar spaces with the sarcoplasmic reticulum (SR); transverse (T) tubules; dyads/triads;

glycogen granules and lipid droplets as well as the basic cytoskeletal network. Among these organelles, the triads/dyads, constituted of junctional SR (jSR) and T tubules, function as calcium release units (CRUs) through which Ca^{2+} exits the SR during muscle activation. CRUs are located at specific and frequent intervals and form a discontinuous ring around the myofibrils following the path of the T tubule network. Given the narrowness of the shared spaces, it is not surprising that mitochondria and CRUs often rub elbows. In skeletal and cardiac muscles of rodents, the proximity is sufficient for mitochondria to take up Ca^{2+} even during the time course of a single twitch [17, 18]. Even though the uptake by individual organelles is small, it can affect the rate of relaxation in fibers that are rich in mitochondria [19] and in rat fibers the buffering action of mitochondria may be sufficient to reduce the frequency of detectable spontaneous releases [20].

Pertinent questions are (1) is the CRU-mitochondria relationship random, or is there a higher structural hierarchy that specifically establishes the relative positioning of the two organelles in skeletal muscle and (2) is the same structural relationship present in muscles of all vertebrates. Structural and functional evidence points to a planned 3-D relationship between the two organelles [21, 22] but not for all mitochondria and perhaps not in all muscles. Taking advantage of different kinetic properties of Ca^{2+} chelators, Shkryl and Shirokova [23] demonstrated that two functional categories of mitochondria coexist in skeletal muscle of the rat: those that take up some of the Ca^{2+} released by the SR during muscle activation even in the presence of fast Ca^{2+} chelators and those that do not. The former are, it must be presumed, closely juxtaposed to CRUs, the latter are at some distance. The structural equivalent of this functional phenomenon is the well-specified position of mitochondria relative to CRUs in the muscle fibers from the same species, as well as from other mammals. Muscles of course are of primary importance in any activity from food gathering, to eating, to defense and, indirectly, to reproduction and in some cases to heat production. Based on the fundamental tenet of evolution that features offering survival advantage are retained, it may be expected that any variation essential for the effective performance of muscles would appear as an early event in evolution. As an example, the orderly arrangement of thin and thick filaments in cross-striated sarcomeres, offering the possibility of rapid movements, is an early evolutionary event, that is found in insects, all chordates, and, even, in a slightly rudimentary form in some molluscan muscles. An early appearance of a tight mitochondrion/CRU relationship in vertebrate evolution would indicate that this particular arrangement is of overriding functional usefulness to both mitochondria and skeletal muscle; a later appearance would indicate that it is advantageous but not essential.

In order to establish the evolutionary significance of specific mitochondria/CRU relationships, we launched a widespread exploration of muscle ultrastructure within the vertebrate subphylum. To that effect, we examined muscle samples from a few organisms in each class, from fish to mammals, relying on the existing literature for further data.

2. Materials and Methods

Skeletal muscles were fixed in a variety of vertebrates. Most images came from an extensive archive present in the laboratory, other from muscles that were fixed specifically for this project. Fish: *Lampetra planeri* (larvae); *Eptatretus stouti* (Hagfish); *Lepisosteus osseus* (Gar fish); *Citharichthys sordidus* (pacific sand dab); *Danio rerio* (zebrafish); *Poecilia reticulata* (guppy); *Poecilia latipinna* var. (black molly), toadfish (*Opsanus tau*); amphibia (*Rana pipiens*, *R. temporaria*); Reptiles (*Boa constrictor*, *Nerodia sipedon*, *Anolis carolinensis*); Birds (*Meleagris gallopavo*; *fringilla* sp., *Gallus gallus*); Mammals (*Mus rattus*, *Rattus* sp., *Felis catus*).

The animals were euthanized by a variety of means (cervical dislocation and/or an overdose of anesthetic: CO_2 , ether, isoflurane, sodium pentobarbital). After euthanasia, the muscles were exposed and either fixed in situ by dripping the fixative on them, or carefully dissected tendon-to-tendon, pinned in Sylgard dish (Dow Corning) at resting length and immersed in fixative. Fixation was in 3–9% glutaraldehyde in 0.1 M cacodylate buffer (pH 7.2) at room temperature. The muscles were stored in fixative at 4°C for variable periods of time, then postfixed in 2% OsO_4 in the same buffer for 1–2 hr at 4°C, en block stained in saturated uranyl acetate, with several washes after each step, and embedded in Epon 812. Muscles for domestic chicken and kangaroo (*Macropus* sp.) were simply obtained from the supermarket, and small samples were treated as the freshly dissected muscles. Ultrathin sections (about 40 nm) were cut in an ultramicrotome Leica Ultracut R (Leica Microsystem, Austria) using a Diatome diamond knife (Diatome Ltd. Biel, Switzerland) and stained in uranyl acetate and lead citrate solutions.

3. Results and Discussion

3.1. Mammals. The following description, based on published electron micrographs of various muscles from laboratory rat and mouse [22, 24–26] and extensive unpublished observations by the two authors, offers the background for the overall distribution of mitochondria in muscles of placental mammals. Many mitochondria in these muscles lie within transverse planes that are positioned in close proximity of the triads (CRUs), between them and the nearby Z line, and thus have a preferential location opposite to the I bands of the sarcomere (Figure 1(a)). These mitochondria are very thin and elongated and closely follow the junctional SR sacs of CRUs over long distances, frequently coming to distances of ~25 nm from the SR surface (Figure 1(b); [22]. Some fibers (e.g., type IIX and IIB in mouse) have almost exclusively this type of mitochondrial disposition. A second additional set of mitochondria is present in fibers that are richer in these organelles (e.g., type I and IIA in mouse). These mitochondria are larger in diameter; they are longitudinally oriented and may span the distance of several sarcomeres, encompassing I and A bands and Z lines. Appropriate sections show that these mitochondria extend transversely oriented arm-like branches as they pass at the level of the I band and these branches are those that follow along the length of triads (Figure 1(b)). It is not clear

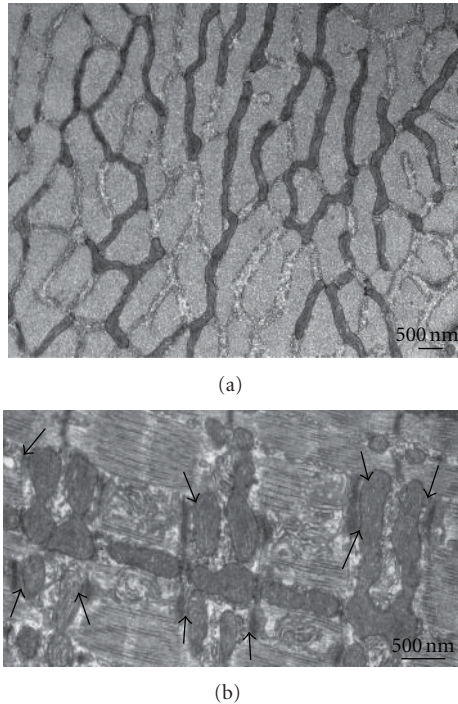


FIGURE 1: Cross (a) and longitudinal (b) sections of muscle fibers from the mouse EDL muscle. In (a), slender, elongated approximately cylindrical mitochondria profiles occupy the intermyofibrillar spaces, running transversely for long distances between the myofibrils at the I band level. In (b), the longitudinal axis of the fiber runs from left to right at a slight angle. Longitudinally arranged mitochondria send out transverse branches at the level of the I band, that correspond to those seen in (a). The transverse mitochondria branches run parallel to triads (CRUs) and are closely apposed to the junctional SR (arrows) over long distances.

whether all the longitudinally arranged mitochondria are directly connected to transverse extensions, but in general it can be assumed that these two sets of mitochondria are part of the same continuum. A different set of mitochondria (not shown) resides at peripheral sites, between the most peripheral myofibrils and the plasmalemma. These mitochondria are piled up into irregular mounds that project over the fiber surface and they are closely apposed to each other, but at some distance from the nearest myofibrils and CRUs. Capillaries are usually located in proximity of these peripheral clusters of mitochondria, so that these organelles are not near sites of Ca^{2+} release from the SR, but they are in close proximity to the capillaries. Indeed, peripheral grouping of mitochondria in mammalian fibers is mostly present in “red,” richly vascularized muscles. These peripheral mitochondria may not “sense” the SR Ca^{2+} release, but are near oxygen sources. Unfortunately, although the mitochondria content of more exotic mammal, such as the cheetah known for the fastest running speed, has been explored [27], no information of the actual positioning of mitochondria relative to CRU is available for these muscles.

Two pieces of evidence indicate that the specific targeting of mitochondria at the I band and their structural coupling to CRUs in mammalian muscles are not due to chance.

First is the fact that association of mitochondria with CRUs is acquired as a developmentally regulated event during postnatal differentiation in mouse [22] and during a recapitulation of these events in the recovery of human denervated atrophic muscle induced by electrical stimulation [28]. Secondly, strong connecting tethers link the junctional SR of CRUs to adjacent mitochondria (Figures 2(a) and 2(c), arrows) [22, 26]. The tethers link directly the SR membrane to the outer mitochondrial membrane and seem to be strong enough to hold them together if they are pulled apart (such as if the fiber is exposed to hypotonic solutions).

An extensive mitochondrion-CRU association has been detected in muscles from the domestic cat (unpublished observations): from the guinea pig [29] and from human muscles [21, 30, 31]. Taken together, these facts indicated that a major subset of mitochondria in mammalian muscle are in a specifically planned close structural and functional proximity to the SR, and more specifically with the domains (CRUs) that are responsible for Ca^{2+} release during excitation-contraction coupling. The association of the selected mitochondria with CRUs is very extensive, since approximately a quarter of the elongated mitochondrion outer surface is in very close proximity to a jSR element and is maintained by connecting tethers. This disposition seems to be common to muscles from placental mammalian that have been examined by ultrastructure.

It can also be inferred that the mitochondria that are not tethered to CRUs may be free to move and perhaps the peripartetic organelles are those aggregated in the subplasmalemmal spaces. Their presence is driven to the proximity of capillaries by the necessity of a high anaerobic profile. Indeed, the highly aerobic diaphragm of the smallest mammal, the shrew, is intensively vascularized and displays an extensive array of peripheral mitochondria [32].

One notable exception to the specific mitochondrion-CRU alignment in mammalian muscles is found in the superfast cricothyroid muscle that produces the ultrasound used by the bats for echolocation [33]. In these muscles, the mitochondria are not at the triads, but are located in long longitudinal lines between the myofibrils, a disposition that is typical of all nonmammalian vertebrates (see below).

Additionally, a muscle from a marsupial also shows no specific relationship between mitochondria positioning and CRUs (unpublished observations).

3.2. Birds. Birds, like mammals, are homoeothermic, and some of them exhibit very fast and continuously active muscles. It would be expected that if specific relationships between mitochondria and CRUs and between mitochondria and capillaries were of overriding functional importance, such relationships would be found in muscles from this group. We were surprised to find that pectoral muscles in domestic chicken and turkey (admittedly not very active muscles), and also the leg and flight muscles of finches (that are quite active) display mitochondria that are located in single longitudinal columns between the myofibrils, with no specific relationship to CRUs (Figure 3; see [34, 35]). Even in the flight muscles of hummingbirds, mitochondria are not especially associated with CRUs. It is likely however that

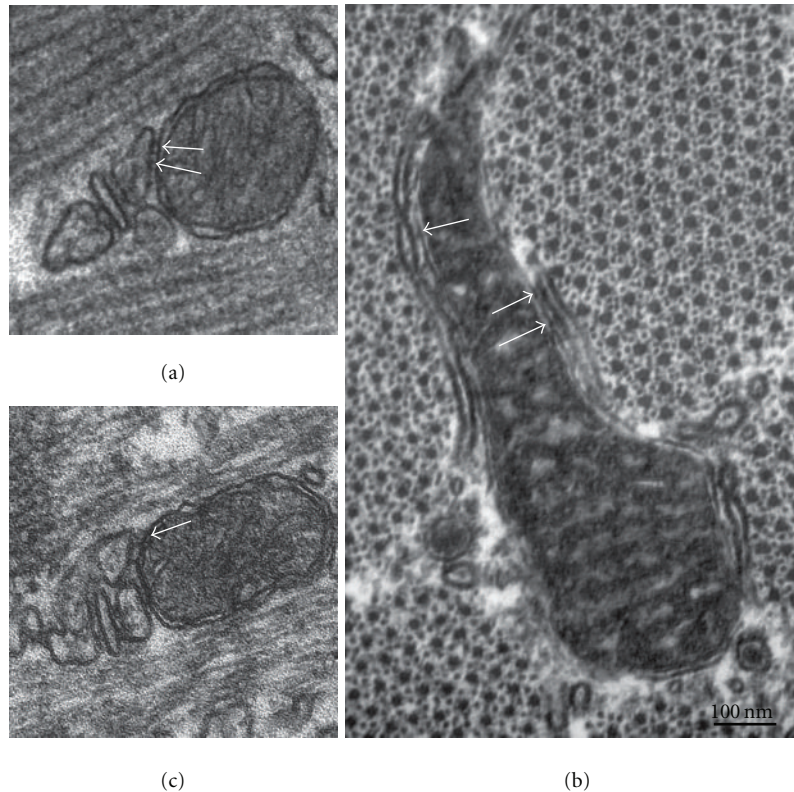


FIGURE 2: Higher magnifications highlighting association of mitochondria and SR (a)–(c). Tethering connections anchor mitochondria to the jSR of the triads (CRUs) in images of mouse EDL ((a) and (c), white arrows). Similar tethers (white arrows) anchor mitochondria to the longitudinal SR, not necessarily to CRUs, in the leg muscle from a finch (b).

the disposition of longitudinal mitochondria in the intermyofibrillar spaces is not entirely random. Each mitochondrion is in very close proximity to SR elements along its length, and it seems to be anchored to them by tethers that greatly resemble those in mammalian muscles (compare arrows in Figure 2(b) with Figures 2(a) and 2(c)). We argue that tethering to SR is responsible for holding the mitochondria within the intermyofibrillar spaces and keeping them from moving out and aggregating into subplasmalemmal clusters.

Longitudinal mitochondria have a chance of being at a short distance from one or more CRUs along their length as they run past the level of the sarcomere at which CRUs are located (Figure 3(b), arrows). The frequency of such encounters depends on the size of the mitochondrion and on the frequency of triads along the T tubule network. Note also that this configuration offers a very limited close proximity between the mitochondrion surface and the CRU.

Strikingly, the frequency of mitochondria in leg and flight muscles of the finch is actually lower than in the mouse leg muscle, despite the apparent similarity in the fast and continuously active movements in these two species.

In the species mentioned above, there also seems to be no accumulation of mitochondria in proximity of capillaries even within the more aerobic muscles. Such accumulations however are present in highly specialized muscles. The mitochondria respiration rates in the flight muscle of hummingbirds is about two times higher than that of locomotory mus-

cles in mammals running at their maximum aerobic capacities. Capillary volume density is correspondingly higher, and mitochondria are packed so highly that they almost compromise the ability to produce force by crowding out myofibrils [36]. Most relevant is the fact that mitochondria are precisely clustered at a high density right at the capillary borders [37].

3.3. Reptiles. We examined the body muscles of two snakes (*Boa constrictor* and *Nerodia sipedon*) and the leg muscles of a lizard (*Anolis carolinensis*) as examples of reptile muscles that are used for a variety of slow to fast movements. The slower tortoise muscles have also been described [38]. Three different types of muscle fibres in *Boa c.* showed the distinctive characteristics of tonic (large myofibrils, limited membrane systems, and few mitochondria) probably used when the snake crushes its prey, phasic “red” (smaller myofibrils, slightly higher mitochondria content) probably used when the snake moves around for longer periods of time, and phasic “white” (smaller myofibrils, low mitochondria content) probably used when the snake strikes a prey. The lizard leg muscles had small myofibrils and frequent triads as to be expected from the very fast movements of these graceful animals when in search of prey.

A noticeable feature of these reptilian muscles is a scarcity of mitochondria in keeping with the general motile pattern of prolonged immobility alternated with brief periods of fast activity. The overall distribution pattern is the same as

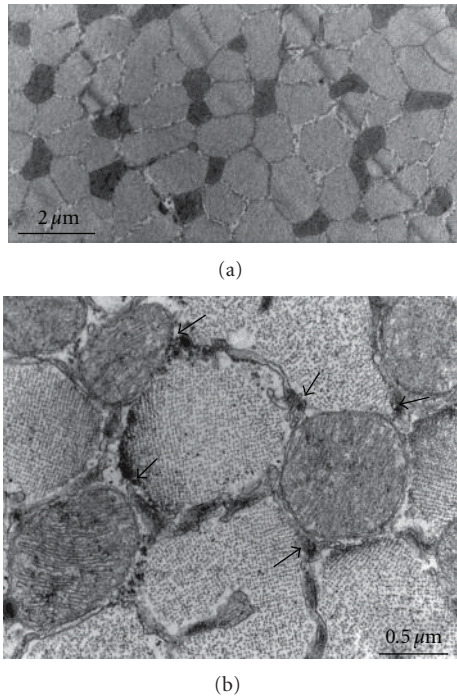


FIGURE 3: Breast muscle from the finch shown in cross-sections (a) and (b). In the finch, as in other birds, mitochondria are located in single longitudinally oriented rows between the myofibrils. A limited proximity between mitochondria and CRUs (arrows in (b)) occurs where the mitochondria cross the level at which T tubules are located. Accumulations of mitochondria at the fiber edges are not present in the flight muscles of many birds, indicating that the mitochondria are not free to escape from the myofibrillar domains of the fibers, probably due to tethering; see Figure 2.

in birds: and the same comments apply: mitochondria are located in single columns occupying the intermyofibrillar spaces, with no special relationship to CRUs and no accumulation at capillaries (Figure 4, from the lizard).

As in the case of birds, a fast, continuously active muscle provides an ultimate example of functionally designed organization. “Sound production is one of the most energetically costly activities in animals” [39]. Despite extremely reduced tension production that minimizes contractile use of ATP [39] and some other mechanical tradeoffs strategies [40], the rattlesnakes tail shaker muscle is a fascinating example of the adaptations necessary to produce and maintain extremely fast contraction-relaxation rates [41]. Mitochondria are indeed at high density in these muscles and large clusters are for the most part fairly close to capillaries, but they do not bear a specific spatial relationship to CRUs [42].

3.4. Amphibia. In muscles of amphibia, as exemplified by various species of *Rana* (*R. pipiens*, *R. temporaria* [43, 44]; see also [45] for *Rana japonica* and [46] for *Rana nigromaculata*), the large majority of the mitochondria tend to be located between the myofibrils [46]. Frog mitochondria are fairly large; they are positioned in single file between the myofibrils and an individual organelle may run for the length of one-

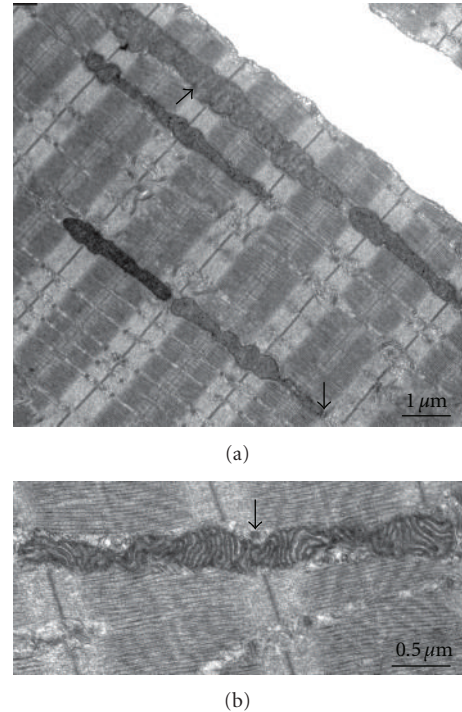


FIGURE 4: Longitudinal sections of leg muscles from a small lizard, as an example from reptiles. The myofibrils are small, and the CRUs (triads) are frequent, as expected from a rapid muscle. Mitochondria are not frequent, and they are located in single longitudinal rows between the myofibrils. An occasional proximity to CRU occurs when the mitochondria cross the T tubule network (arrows, see also Figures 3 and 5 for birds and amphibia).

two sarcomeres (Figure 5). There is no peripheral clustering at the fiber edge. The disposition is the same in sartorius and gastrocnemius where mitochondria are unusually scarce (Figure 5) and in the iliofibularis where they are more frequent.

In general, none of the *Rana* muscles have a content of mitochondria comparable to that of rat or mouse, indicating a limited reliance on oxidative phosphorylation and there are no descriptions of muscle with an extensive mitochondria accumulation. Tonic fibers that sustain prolonged periods of activity (e.g., those used in the mating amplexus) have an even lower density of mitochondria, in keeping with the fact that although the contractions are prolonged, they involve very slow cycling cross-bridges and thus require a limited amount of ATP.

3.5. Fish. At the lower end of the vertebrate subphylum, we collected images from tail musculature of a variety of fish, from primitive to more advanced. For example, see [47–50]. All muscles fibers, including the “red” ones used for powering swimming motion [51], contain elongated mitochondria that are either located in longitudinal slits between myofibrils (Figure 6(a)) or, more frequently, at the fibers’ edges, under the plasmalemma (Figure 6(b)). An interesting variation relative to birds, reptiles, and amphibia is the fact that intermyofibrillar mitochondria are most

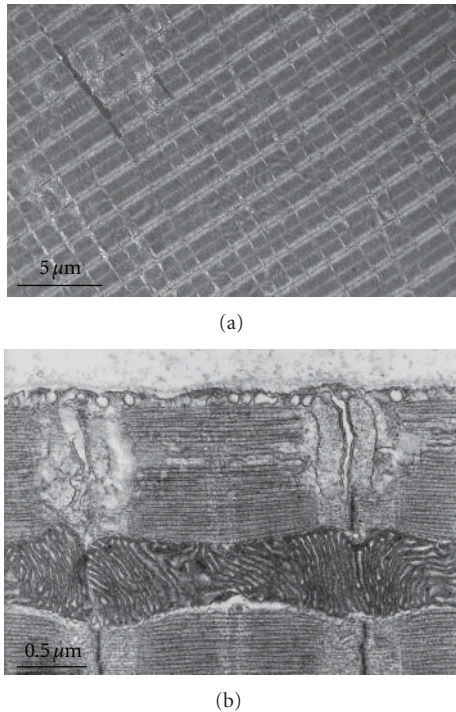


FIGURE 5: Images from the frog gastrocnemius (a) and sartorius (b) in longitudinal sections. The predominant location of mitochondria is similar to that of birds and reptiles, again providing limited contacts with CRUs. Note overall scarcity of mitochondria in these muscles gastrocnemius. Others have more frequent mitochondria but still no large clusters at the periphery.

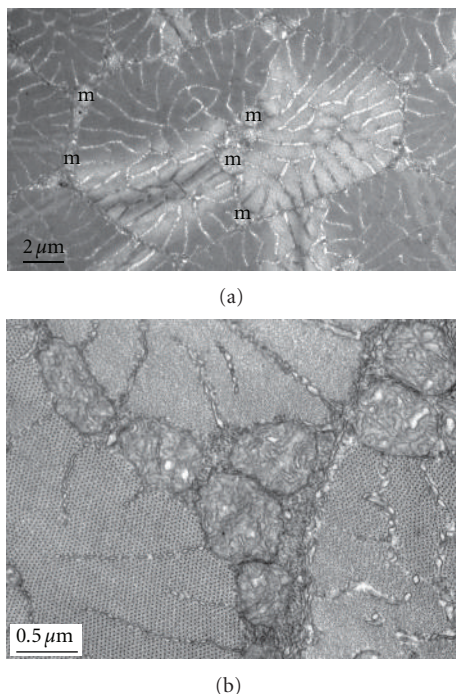


FIGURE 6: Cross-sections of small fibers in zebrafish. These images illustrate two characteristics of mitochondria (m) disposition in fish muscles. There is a tendency for clustering of the organelles in small groups that are mostly segregated to the fibers' edges. In this manner, proximity of the mitochondrion' surface to CRUs is quite limited.

often, particularly if more numerous, collected into small, longitudinally aligned clusters. This tendency is strongly emphasized in the case of cold adaptation in fish such as the striped bass, that results in an increase of mitochondrial volume density by as much as 230% [52]. While in the fish exposed to warmer water the mitochondria are positioned in single longitudinal rows between the myofibrils, in the cold-adapted fish the mitochondria are accumulated in large clusters both between the myofibrils and at the fiber periphery. The direct effect of clustering is that of decreasing the probability that an individual mitochondrion comes to close proximity to a CRU. Higher oxidative capacity relates to higher mitochondrial content, but not to a better contact with CRUs [53, 54].

Interestingly, in superfast sound-producing swimbladder musculature of *Opsanus tau* (toadfish), where the mitochondria are not frequent [55, 56] and of *Porichthys notatus* (midshipman) where they are quite abundant [57], mitochondria are almost completely excluded from the regions of the fiber containing myofibrils and placed instead in the central core and outer subplasmalemmal ring. The physiology of these fast-acting muscle fibers, like those of the rattlesnake, has been modified for superfast repetitive contractions with little force production [58], thus reducing their ATP requirements.

4. Conclusions

This brief comparative look at skeletal muscles shows that a well-regulated, close, extensive association between mitochondria and CRUs is present only in mammalian skeletal muscles. In other vertebrate muscles, the mitochondria-CRU proximity is far less extensive and less well regulated. Since the presumably privileged mitochondrial disposition of mammalian muscles is a relatively late event in evolutionary times, it must confer some advantage, but it may not be essential to muscle function. Apparently, coupling of muscle activation to stimulation of mitochondrial aerobic ATP production must occur even in the absence of the mammalian-type associations.

It is hard to actually pinpoint the precise advantage that extensive mitochondria-CRU association confers. Even assuming that some Ca^{2+} uptake by mitochondria is absolutely essential, it must be remembered that this uptake must be limited in order to avoid the total collapse of the mitochondrion's inner membrane potential. So, it is not entirely clear that the extensive ER/SR-mitochondria contacts that are present in liver and in mammalian skeletal muscle are necessary and/or advantageous relative to the more fleeting contacts between CRU and mitochondria of muscles in lower vertebrates.

Perhaps the answer, in the case of mammalian skeletal muscle, lies in the fact that mitochondria-CRU contacts foster the differentiation of complex mitochondrial shapes. Increases in cytosolic calcium levels above resting seem to reduce mitochondrial motility [59], so an initial association of large mitochondria with CRUs may have a positive feedback effect, enhancing and stabilizing further associations. Mitochondria that are not tethered to SR and thus end up in peripheral clusters are smaller and not as extensive as the

CRU-associated ones. During postnatal muscle fiber maturation in mouse, extension of mitochondria into branched pattern and their association with CRUs occur in parallel [22]. A direct effect of this unique mitochondria tendency towards extension for long distances both longitudinally and transversely is the effective spread of information over relatively large regions of the fiber, and this may have some specific advantages. For example, mitochondria-based superoxide flashes (mSOF) in resting and activated mouse FDB fibers occur simultaneously over extended regions reflecting the complex mitochondrial network [60]. Considering that a moderate level of superoxide production has physiological effects (discussed in [60]), coordination of its production is certainly of advantage.

It is, however, also noteworthy that extensive CRU-mitochondria contacts are avoided in a mammalian fast-acting muscle capable of prolonged activity: the bat cricothyroid, used for echolocation [33]. Additionally, mitochondria tethering is “loosened” in a mouse muscle with a leaky mutation of the RyR [61] emphasizing the inherent risks of a close proximity of mitochondria to Ca^{2+} sources. Perhaps fish muscles have the best solution. Mitochondria clustering in those muscles has the effect of reducing the portion of each organelle’s outline that faces directly towards a CRU, thus reducing the influence of CRU’s Ca^{2+} release on mitochondria and allowing the development of some of the fastest known muscle fibers, where mitochondria interfere very little with Ca^{2+} cycling.

Abbreviations

CRU:	Ca^{2+} release unit
EDL:	Extensor digitorum longus
FDB:	Flexor digitorum brevis muscle
EM:	Electron microscopy
SR:	Sarcoplasmic reticulum
jSR:	Junctional SR
T tubule:	Transverse tubule.

Acknowledgments

The authors thank Dr. Angela Dulhunty from the Australian National University for kindly providing a sample of Kangaroo muscle, Mr. Mathew Close for lizard and snake muscles, and Mrs. Inna Martinyuk for electron microscopy support. This work was supported by NIH Grant RO1 H 48093 to C. Franzini Armstrong.

References

- [1] C. S. Rossi and A. L. Lehninger, “Stoichiometry of respiratory stimulation, accumulation of Ca^{++} and phosphate, and oxidative phosphorylation in rat liver mitochondria,” *The Journal of Biological Chemistry*, vol. 239, pp. 3971–3980, 1964.
- [2] R. S. Balaban, “Cardiac energy metabolism homeostasis: role of cytosolic calcium,” *Journal of Molecular and Cellular Cardiology*, vol. 34, no. 10, pp. 1259–1271, 2002.
- [3] P. S. Brookes, Y. Yoon, J. L. Robotham, M. W. Anders, and S. S. Sheu, “Calcium, ATP, and ROS: a mitochondrial love-hate triangle,” *American Journal of Physiology—Cell Physiology*, vol. 287, no. 4, pp. C817–C833, 2004.
- [4] R. Rizzuto, A. W. M. Simpson, M. Brini, and T. Pozzan, “Rapid changes of mitochondrial Ca^{2+} revealed by specifically targeted recombinant aequorin,” *Nature*, vol. 358, no. 6384, pp. 325–327, 1992.
- [5] G. Hajnoczky, L. D. Robb-Gaspers, M. B. Seitz, and A. P. Thomas, “Decoding of cytosolic calcium oscillations in the mitochondria,” *Cell*, vol. 82, no. 3, pp. 415–424, 1995.
- [6] B. Chance, G. R. Williams, W. F. Holmes, and J. Higgins, “Respiratory enzymes in oxidative phosphorylation. V. A mechanism for oxidative phosphorylation,” *The Journal of Biological Chemistry*, vol. 217, no. 1, pp. 439–451, 1955.
- [7] E. Carafoli, C. S. Rossi, and A. L. Lehninger, “Uptake of Adenine Nucleotides by Respiring Mitochondria During Active Accumulation of Ca^{++} and Phosphate,” *The Journal of Biological Chemistry*, vol. 240, pp. 2254–2261, 1965.
- [8] A. Scarpa and P. Graziotti, “Mechanisms for intracellular calcium regulation in heart. I. Stopped flow measurements of Ca^{++} uptake by cardiac mitochondria,” *Journal of General Physiology*, vol. 62, no. 6, pp. 756–772, 1973.
- [9] R. Rizzuto, M. Brini, M. Murgia, and T. Pozzan, “Microdomains with high Ca^{2+} close to IP_3 -sensitive channels that are sensed by neighboring mitochondria,” *Science*, vol. 262, no. 5134, pp. 744–747, 1993.
- [10] R. Rizzuto, P. Pinton, W. Carrington et al., “Close contacts with the endoplasmic reticulum as determinants of mitochondrial Ca^{2+} responses,” *Science*, vol. 280, no. 5370, pp. 1763–1766, 1998.
- [11] R. Rizzuto and T. Pozzan, “Microdomains of intracellular Ca^{2+} : molecular determinants and functional consequences,” *Physiological Reviews*, vol. 86, no. 1, pp. 369–408, 2006.
- [12] G. Csordás, P. Várnai, T. Golenár et al., “Imaging interorganelle contacts and local calcium dynamics at the ER-mitochondrial interface,” *Molecular Cell*, vol. 39, no. 1, pp. 121–132, 2010.
- [13] C. A. Mannella, K. Buttle, B. K. Rath, and M. Marko, “Electron microscopic tomography of rat-liver mitochondria and their interactions with the endoplasmic reticulum,” *BioFactors*, vol. 8, no. 3-4, pp. 225–228, 1998.
- [14] G. C. Shore and J. R. Tata, “Two fractions of rough endoplasmic reticulum from rat liver. I. Recovery of rapidly sedimenting endoplasmic reticulum in association with mitochondria,” *Journal of Cell Biology*, vol. 72, no. 3, pp. 714–725, 1977.
- [15] C. García-Pérez, G. Hajnoczky, and G. Csordás, “Physical coupling supports the local Ca^{2+} transfer between sarcoplasmic reticulum subdomains and the mitochondria in heart muscle,” *Journal of Biological Chemistry*, vol. 283, no. 47, pp. 32771–32780, 2008.
- [16] G. Szabadkai, K. Bianchi, P. Várnai et al., “Chaperone-mediated coupling of endoplasmic reticulum and mitochondrial Ca^{2+} channels,” *Journal of Cell Biology*, vol. 175, no. 6, pp. 901–911, 2006.
- [17] R. Rudolf, M. Mongillo, P. J. Magalhães, and T. Pozzan, “In vivo monitoring of Ca^{2+} uptake into mitochondria of mouse skeletal muscle during contraction,” *Journal of Cell Biology*, vol. 166, no. 4, pp. 527–536, 2004.
- [18] V. K. Sharma, V. Ramesh, C. Franzini-Armstrong, and S. S. Sheu, “Transport of Ca^{2+} from sarcoplasmic reticulum to mitochondria in rat ventricular myocytes,” *Journal of Bioenergetics and Biomembranes*, vol. 32, no. 1, pp. 97–104, 2000.
- [19] J. M. Gillis, “Inhibition of mitochondrial calcium uptake slows down relaxation in mitochondria-rich skeletal muscles,”

- Journal of Muscle Research and Cell Motility*, vol. 18, no. 4, pp. 473–483, 1997.
- [20] E. V. Isaeva and N. Shirokova, “Metabolic regulation of Ca^{2+} release in permeabilized mammalian skeletal muscle fibres,” *Journal of Physiology*, vol. 547, part 2, pp. 453–462, 2003.
 - [21] T. Ogata and Y. Yamasaki, “Ultra-high-resolution scanning electron microscopy of mitochondria and sarcoplasmic reticulum arrangement in human red, white, and intermediate muscle fibers,” *Anatomical Record*, vol. 248, no. 2, pp. 214–223, 1997.
 - [22] S. Boncompagni, A. E. Rossi, M. Micaroni et al., “Mitochondria are linked to calcium stores in striated muscle by developmentally regulated tethering structures,” *Molecular Biology of the Cell*, vol. 20, no. 3, pp. 1058–1067, 2009.
 - [23] V. M. Shkryl and N. Shirokova, “Transfer and tunneling of Ca^{2+} from sarcoplasmic reticulum to mitochondria in skeletal muscle,” *Journal of Biological Chemistry*, vol. 281, no. 3, pp. 1547–1554, 2006.
 - [24] A. Rambourg and D. Segretain, “Three-dimensional electron microscopy of mitochondria and endoplasmic reticulum in the red muscle fiber of the rat diaphragm,” *Anatomical Record*, vol. 197, no. 1, pp. 33–48, 1980.
 - [25] T. Ogata and Y. Yamasaki, “Scanning electron-microscopic studies on the three-dimensional structure of mitochondria in the mammalian red, white and intermediate muscle fibers,” *Cell and Tissue Research*, vol. 241, no. 2, pp. 251–256, 1985.
 - [26] A. E. Rossi, S. Boncompagni, and R. T. Dirksen, “Sarcoplasmic reticulum-mitochondrial symbiosis: bidirectional signaling in skeletal muscle,” *Exercise and Sport Sciences Reviews*, vol. 37, no. 1, pp. 29–35, 2009.
 - [27] T. M. Williams, G. P. Dobson, O. Mathieu-Costello, D. Morsbach, M. B. Worley, and J. A. Phillips, “Skeletal muscle histology and biochemistry of an elite sprinter, the African cheetah,” *Journal of Comparative Physiology, B*, vol. 167, no. 8, pp. 527–535, 1997.
 - [28] S. Boncompagni, H. Kern, K. Rossini et al., “Structural differentiation of skeletal muscle fibers in the absence of innervation in humans,” *Proceedings of the National Academy of Sciences of the United States of America*, vol. 104, no. 49, pp. 19339–19344, 2007.
 - [29] B. R. Eisenberg, A. M. Kuda, and J. B. Peter, “Stereological analysis of mammalian skeletal muscle. I. Soleus muscle of the adult guinea pig,” *Journal of Cell Biology*, vol. 60, no. 3, pp. 732–754, 1974.
 - [30] A. G. Engel and B. Q. Banker, “Ultrastructural changes in diseased muscle,” in *Myology*, A. G. Engel and C. Franzini-Armstrong, Eds., vol. 1, chapter 31, pp. 749–888, McGraw-Hill, 3rd edition, 2004.
 - [31] S. Boncompagni, L. d’Amelio, S. Fulle, G. Fanò, and F. Protasi, “Progressive disorganization of the excitation-contraction coupling apparatus in aging human skeletal muscle as revealed by electron microscopy: a possible role in the decline of muscle performance,” *Journals of Gerontology, Series A*, vol. 61, no. 10, pp. 995–1008, 2006.
 - [32] O. Mathieu-Costello, S. Morales, J. Savolainen, and M. Vornanen, “Fiber capillarization relative to mitochondrial volume in diaphragm of shrew,” *Journal of Applied Physiology*, vol. 93, no. 1, pp. 346–353, 2002.
 - [33] J. P. Revel, “The sarcoplasmic reticulum of the bat cricothroid muscle,” *The Journal of cell biology*, vol. 12, pp. 571–588, 1962.
 - [34] A. F. Howatson, “The structure of pigeon breast muscle mitochondria,” *The Journal of Biophysical and Biochemical Cytology*, vol. 2, supplement 4, pp. 363–368, 1956.
 - [35] S. G. Page, “Structure and some contractile properties of fast and slow muscles of the chicken,” *Journal of Physiology*, vol. 205, no. 1, pp. 131–145, 1969.
 - [36] I. Grinyer and J. C. George, “Some observations on the ultra-structure of the hummingbird pectoral muscles,” *Canadian Journal of Zoology*, vol. 47, no. 5, pp. 771–773, 1969.
 - [37] R. K. Suarez, J. R. B. Lighton, G. S. Brown, and O. Mathieu-Costello, “Mitochondrial respiration in hummingbird flight muscles,” *Proceedings of the National Academy of Sciences of the United States of America*, vol. 88, no. 11, pp. 4870–4873, 1991.
 - [38] S. G. Page, “Fine structure of tortoise skeletal muscle,” *Journal of Physiology*, vol. 197, no. 3, pp. 709–715, 1968.
 - [39] K. E. Conley and S. L. Lindstedt, “Minimal cost per twitch in rattlesnake tail muscle,” *Nature*, vol. 383, no. 6595, pp. 71–72, 1996.
 - [40] B. R. Moon, J. J. Hopp, and K. E. Conley, “Mechanical trade-offs explain how performance increases without increasing cost in rattlesnake tailshaker muscle,” *Journal of Experimental Biology*, vol. 205, part 5, pp. 667–675, 2002.
 - [41] L. C. Rome, D. A. Syme, S. Hollingworth, S. L. Lindstedt, and S. M. Baylor, “The whistle and the rattle: the design of sound producing muscles,” *Proceedings of the National Academy of Sciences of the United States of America*, vol. 93, no. 15, pp. 8095–8100, 1996.
 - [42] P. J. Schaeffer, K. E. Conley, and S. L. Lindstedt, “Structural correlates of speed and endurance in skeletal muscle: the rattlesnake tailshaker muscle,” *Journal of Experimental Biology*, vol. 199, part 2, pp. 351–358, 1996.
 - [43] C. Franzini-Armstrong, “Studies of the triad. 3. Structure of the junction in fast twitch fibers,” *Tissue and Cell*, vol. 47, no. 2, pp. 488–499, 1970.
 - [44] C. Franzini-Armstrong, “Studies of the triad. IV. Structure of the junction in frog slow fibers,” *Journal of Cell Biology*, vol. 56, no. 1, pp. 120–128, 1973.
 - [45] I. Sato, K. Konishi, M. Sunohara, and A. Mikami, “Enzyme activities and morphology of Japanese brown frog (*Rana japonica*) mitochondria in the tibialis anterior muscle during hibernation and active life,” *Canadian Journal of Zoology*, vol. 79, no. 7, pp. 1316–1321, 2001.
 - [46] T. Ogata and Y. Yamasaki, “High-resolution scanning electron-microscopic studies on the three-dimensional structure of mitochondria and sarcoplasmic reticulum in the different twitch muscle fibers of the frog,” *Cell and Tissue Research*, vol. 250, no. 3, pp. 489–497, 1987.
 - [47] C. Franzini-Armstrong and K. R. Porter, “Sarcolemmal invaginations constituting the T system in fish muscle fibers,” *Journal of Cell Biology*, vol. 22, pp. 675–696, 1964.
 - [48] C. Franzini-Armstrong, W. F. Gilly, E. Aladjem, and D. Appelt, “Golgi stain identifies three types of fibres in fish muscle,” *Journal of Muscle Research and Cell Motility*, vol. 8, no. 5, pp. 418–427, 1987.
 - [49] V. Di Biase and C. Franzini-Armstrong, “Evolution of skeletal type e-c coupling: a novel means of controlling calcium delivery,” *Journal of Cell Biology*, vol. 171, no. 4, pp. 695–704, 2005.
 - [50] J. Schredelseker, V. Di Biase, G. J. Obermair et al., “The $\beta 1a$ subunit is essential for the assembly of dihydropyridine-receptor arrays in skeletal muscle,” *Proceedings of the National Academy of Sciences of the United States of America*, vol. 102, no. 47, pp. 17219–17224, 2005.
 - [51] M. A. Freadman, “Role partitioning of swimming musculature of striped Bass *Morone saxatilis* Walbaum and Bluefish, *Pomatomus saltatrix* L.,” *Journal of Fish Biology*, vol. 15, no. 4, pp. 417–423, 1979.

- [52] S. Egginton and B. D. Sidell, "Thermal acclimation induces adaptive changes in subcellular structure of fish skeletal muscle," *American Journal of Physiology*, vol. 256, no. 1, part 2, pp. R1–R9, 1989.
- [53] K. M. O'Brien, C. Skilbeck, B. D. Sidell, and S. Egginton, "Muscle fine structure may maintain the function of oxidative fibres in haemoglobinless Antarctic fishes," *Journal of Experimental Biology*, vol. 206, part 2, pp. 411–421, 2003.
- [54] I. A. Johnston, J. Calvo, H. Guderley, D. Fernandez, and L. Palmer, "Latitudinal variation in the abundance and oxidative capacities of muscle mitochondria in perciform fishes," *Journal of Experimental Biology*, vol. 201, part 1, pp. 1–12, 1998.
- [55] K. E. Loesser, J. Rafi, and M. L. Fine, "Embryonic, juvenile, and adult development of the toadfish sonic muscle," *Anatomical Record*, vol. 249, no. 4, pp. 469–477, 1997.
- [56] D. Appelt, V. Shen, and C. Franzini-Armstrong, "Quantitation of Ca ATPase, feet and mitochondria in superfast muscle fibres from the toadfish, *Opsanus tau*," *Journal of Muscle Research and Cell Motility*, vol. 12, no. 6, pp. 543–552, 1991.
- [57] M. K. Lewis, P. C. Nahirney, V. Chen et al., "Concentric intermediate filament lattice links to specialized Z-band junctional complexes in sonic muscle fibers of the type I male midshipman fish," *Journal of Structural Biology*, vol. 143, no. 1, pp. 56–71, 2003.
- [58] L. C. Rome and S. L. Lindstedt, "The quest for speed: muscles built for high-frequency contractions," *News in Physiological Sciences*, vol. 13, no. 6, pp. 261–268, 1998.
- [59] M. Yi, D. Weaver, and G. Hajnóczky, "Control of mitochondrial motility and distribution by the calcium signal: a homeostatic circuit," *Journal of Cell Biology*, vol. 167, no. 4, pp. 661–672, 2004.
- [60] L. Wei, G. Salahura, S. Boncompagni et al., "Mitochondrial superoxide flashes: metabolic biomarkers of skeletal muscle activity and disease," *FASEB Journal*, vol. 25, pp. 3068–3078, 2011.
- [61] S. Boncompagni, A. E. Rossi, M. Micaroni et al., "Characterization and temporal development of cores in a mouse model of malignant hyperthermia," *Proceedings of the National Academy of Sciences of the United States of America*, vol. 106, no. 51, pp. 21996–22001, 2009.

Research Article

Both Basic and Acidic Amino Acid Residues of IpTx_a Are Involved in Triggering Substate of RyR1

In Ra Seo,^{1,2} Dae Eun Kang,^{1,2} Dong Woo Song,^{1,2} and Do Han Kim^{1,2}

¹ Systems Biology Research Center, Gwangju Institute of Science and Technology (GIST), Gwangju 500-712, Republic of Korea

² School of Life Sciences, Gwangju Institute of Science and Technology (GIST), 1 Oryong-dong, Buk-gu, Gwangju 500-712, Republic of Korea

Correspondence should be addressed to Do Han Kim, dhkim@gist.ac.kr

Received 1 June 2011; Revised 5 August 2011; Accepted 10 August 2011

Academic Editor: Aikaterini Kontrogianni-Konstantopoulos

Copyright © 2011 In Ra Seo et al. This is an open access article distributed under the Creative Commons Attribution License, which permits unrestricted use, distribution, and reproduction in any medium, provided the original work is properly cited.

Imperatoxin A (IpTx_a) is known to modify the gating of skeletal ryanodine receptor (RyR1). In this paper, the ability of charged aa residues of IpTx_a to induce substate of native RyR1 in HSR was examined. Our results show that the basic residues (e.g., Lys¹⁹, Lys²⁰, Lys²², Arg²³, and Arg²⁴) are important for producing substate of RyR1. In addition, other basic residues (e.g., Lys³⁰, Arg³¹, and Arg³³) near the C-terminus and some acidic residues (e.g., Glu²⁹, Asp¹³, and Asp²) are also involved in the generation of substate. Residues such as Lys⁸ and Thr²⁶ may be involved in the self-regulation of substate of RyR1, since alanine substitution of the aa residues led to a drastic conversion to the substate. The modifications of the channel gating by the wild-type and mutant toxins were similar in purified RyR1. Taken together, the specific charge distributions on the surface of IpTx_a are essential for regulation of the channel gating of RyR1.

1. Introduction

In striated muscles, depolarization of the cell surface membranes leads to activation of ryanodine receptors (RyRs) in the junctional sarcoplasmic reticulum (SR) [1–5]. A number of endogenous RyR modulators such as calmodulin, FK506-binding proteins, calsequestrin, triadin, and HRC have been identified [6–8]. Exogenous modulators of RyRs such as toxins and peptides have also been reported [9, 10].

Imperatoxin A (IpTx_a) from the African scorpion *Pandinus imperator* is a high-affinity modulator of skeletal RyR (RyR1). It greatly increases open probability (P_o) and [³H]ryanodine binding to RyR1 at nanomolar concentration [11, 12]. Moreover, binding of IpTx_a to RyRs reconstituted in planar lipid bilayers generates marked occurrence of long-lasting openings in subconductance state (substate) [13]. Confocal imaging of skeletal muscle fibers to monitor IpTx_a-induced Ca²⁺ sparks demonstrate that the toxin induces long-duration and low-amplitude local Ca²⁺ release consistent with the observation of the prolonged substate in the presence of IpTx_a [14]. Another structurally related scorpion toxin, maurocalcine (MCA), and one specific small

fragment of II-III loop region of skeletal DHPR (Peptide A) also bind to RyR1 and modify channel activity [15–18]. MCA also strongly enhances [³H]ryanodine binding to RyR1 and induces long-lasting substate with the current amplitude of 48% of the full conductance [16, 18]. Peptide A could bind to RyR1 and could either activate or inhibit the activity of RyR1. It could also induce the long-lasting substate [15, 17, 19].

A comparison of the amino acid (aa) sequences of these RyR1-modifying probes shows a common basic aa domain and the C-terminal hydroxyl-containing side chain. The aa sequences may also contribute to the essential structure for activating RyR1 [15, 16]. Especially, a cluster of positively charged aa residues on the surface of the peptide A is critical for activation of RyR1 [19, 20]. The mutations of the specific basic residues of MCA and IpTx_a have failed to induce long-lasting substate and to potentiate [³H]ryanodine binding [20, 21]. To date, the ability of a single aa residue of IpTx_a to control the substate of RyR1 is not fully understood. Recently we have found that several basic aa residues of IpTx_a (e.g., Lys¹⁹, Arg²³, and Arg³³) are necessary for increasing open probability and inducing substate in rabbit skeletal RyR1 [22].

In the present study, to evaluate the roles of the charged aa residues of IpTx_a in modifying the RyR1 gating, synthetic wild-type and alanine-scanning mutants of IpTx_a were tested on planar lipid bilayer-incorporated RyR1. The basic aa mutants (e.g., K19A, K20A, K22A, R23A, and R24A) resulted in a significant loss of production of substate in RyR1, consistent with the previous suggestion that the critical basic domain of toxin determines its binding to the channel [15, 16, 22]. The effective domain encompassing these basic residues involved in producing substate is structurally conserved with both MCa and Peptide A [19, 23]. This suggests a common role of the highly clustered positive charges for their action on RyR1 channel gating. The mutations of some acidic residues (e.g., Asp², Asp¹³, and Glu²⁹) and basic residues within C-terminal region of IpTx_a (e.g., Lys³⁰, Arg³¹, and Arg³³) also led to a significant inhibition on the gating. When Lys⁸ and Thr²⁶ were replaced by alanine, the substate was predominant indicating that these two residues are essential for the functions of the toxin. In addition, the effects of the wild-type and mutant toxins on the gating behavior of RyR1 are strikingly similar when the native RyR1 in SR and the purified RyR1 are used for the incorporation into bilayers, suggesting that generation of the substate is due to a direct binding of the toxin to RyR1.

2. Materials and Methods

2.1. Materials. Porcine brain phosphatidylethanolamine and phosphatidylserine were purchased from Avanti Polar Lipids, Inc. All other reagents were from Sigma.

2.2. Chemical Synthesis of Wild-Type and Mutant IpTx_a Peptides. The peptide synthesis was conducted by a peptide synthesizer (Applied Biosystems model 433A). The linear precursors of wild-type and mutant IpTx_a were synthesized by solid-phase Fmoc chemistry starting from Fmoc-Arg (2,2,5,7,8-pentamethylchroman-6-sulphonyl)-Alko or Fmoc-Ala-Alko resin using a variety of blocking groups for amino acid protection. After cleavage by trifluoroacetic acid, crude linear peptides were extracted with 2 M ethanoic acid, diluted to final peptide concentration of 25 μM in a solution of 1 M ammonium acetate and 2.5 mM reduced/0.25 mM oxidized glutathione adjusted to pH 7.8 with aqueous NH₄OH, and stirred slowly at 4°C for 2-3 days. In the redox buffer system, oxidized glutathione acts as oxidase and assists in the formation of disulfide bonds whereas reduced glutathione functions as disulfide isomerase and facilitates formation of correct disulfide bonds by promoting rapid reshuffling of incorrect disulfide pairings. A 10:1 mixture of reduced and oxidized glutathione was suggested to be an efficient redox buffer system for producing disulfide bonds in IpTx_a [21]. The folding reactions were monitored by HPLC. The crude oxidized products were purified by successive chromatography with CM-cellulose CM-52 and preparative HPLC with C18 silica columns. The purity of all analogues were in the range of 60 to 95% as measured by analytical HPLC and MALDI-TOF-MS (matrix-assisted laser desorption ionization-time-of-flight MS) measurements (see

Supplementary Figure 1 (in Supplementary material available online at doi: 10.1155/2011/386384)).

2.3. Preparation of Junctional SR Vesicles from Rabbit Skeletal Muscle. A heavy fraction of fragmented SR vesicles (HSR) containing junctional SR was prepared from rabbit fast-twitch back and leg muscles as described previously [24].

2.4. Planar Lipid Bilayers. Single-channel recordings of rabbit skeletal RyR1 incorporated into planar lipid bilayers were carried out as described previously [25–27]. Lipid bilayers, consisting of brain tissue phosphatidylethanolamine and phosphatidylserine (1:1) in decane (20 mg/mL) were formed across a hole of approximately 200 μm diameter. Thinning of the bilayer was monitored by bilayer capacitance. The basic composition of the *cis/trans* solution consisted of 300 mM cesium methanesulfonate, 10 mM Tris/Hepes (pH 7.2), 2 mM EGTA, and 1.998 mM CaCl₂ ([Ca²⁺]_{free} = 10 μM) [27]. [Ca²⁺]_{free} was calculated using the “Chelator” program (Theo Schoenmaker). Cs⁺ was selected as the charge carrier to ensure precise control of free [Ca²⁺], to increase the channel conductance, and to avoid any contribution from potassium channels present in the SR membrane [12]. Chloride channels were inhibited by using the impermeant anion methanesulfonate [12]. Incorporation of ion channels was carried out as described by Miller and Racker [25] and confirmed by recording the characteristically high single-channel conductance of RyRs [27, 28]. The *trans* side was maintained at ground and the *cis* side was clamped at –30 mV relative to the ground. After addition of the IpTx_a to the *cis* chamber, the single channel data were collected at –30 mV for 2–5 min. The channel activity was recorded on a DTR-1204 Digital Recorder (Biologic Science Instrument) and displayed on a Tektronix TDS 340A oscilloscope. Recordings were filtered with an 8-pole low-pass Bessel filter at 1 kHz and digitalized through a Digidata 1200 series interface (Axon Instruments). Data acquisition and analysis were done with the Axon Instruments software, pClamp v7.0.

Data were analyzed using the Hill equation described previously [12, 13, 15]:

$$P_{\text{substate}} = \frac{(P_{\text{substate, max}})}{[1 + (EC_{50}/[IpTx_a])^{nH}]} \text{ or} \quad (1)$$

$$P_o = \frac{(P_o, \text{max})}{[1 + (EC_{50}/[IpTx_a])^{nH}]},$$

where (P_o, max) is the P_o observed at saturating concentrations of IpTx_a, EC_{50} is the IpTx_a concentration for which 50% of P_o, max is obtained and nH is the Hill coefficient. Also, $P_{\text{substate, max}}$ is the P_{substate} observed at saturating concentrations of IpTx_a, EC_{50} is the IpTx_a concentration for which 50% of $P_{\text{substate, max}}$ is obtained, and nH is the Hill coefficient. The probability of full open state of the channel (P_o) was defined as the ratio of the time spent in the open state to the total time exclusive of time spent in the substate. The probability to obtain substate (P_{substate}) was calculated

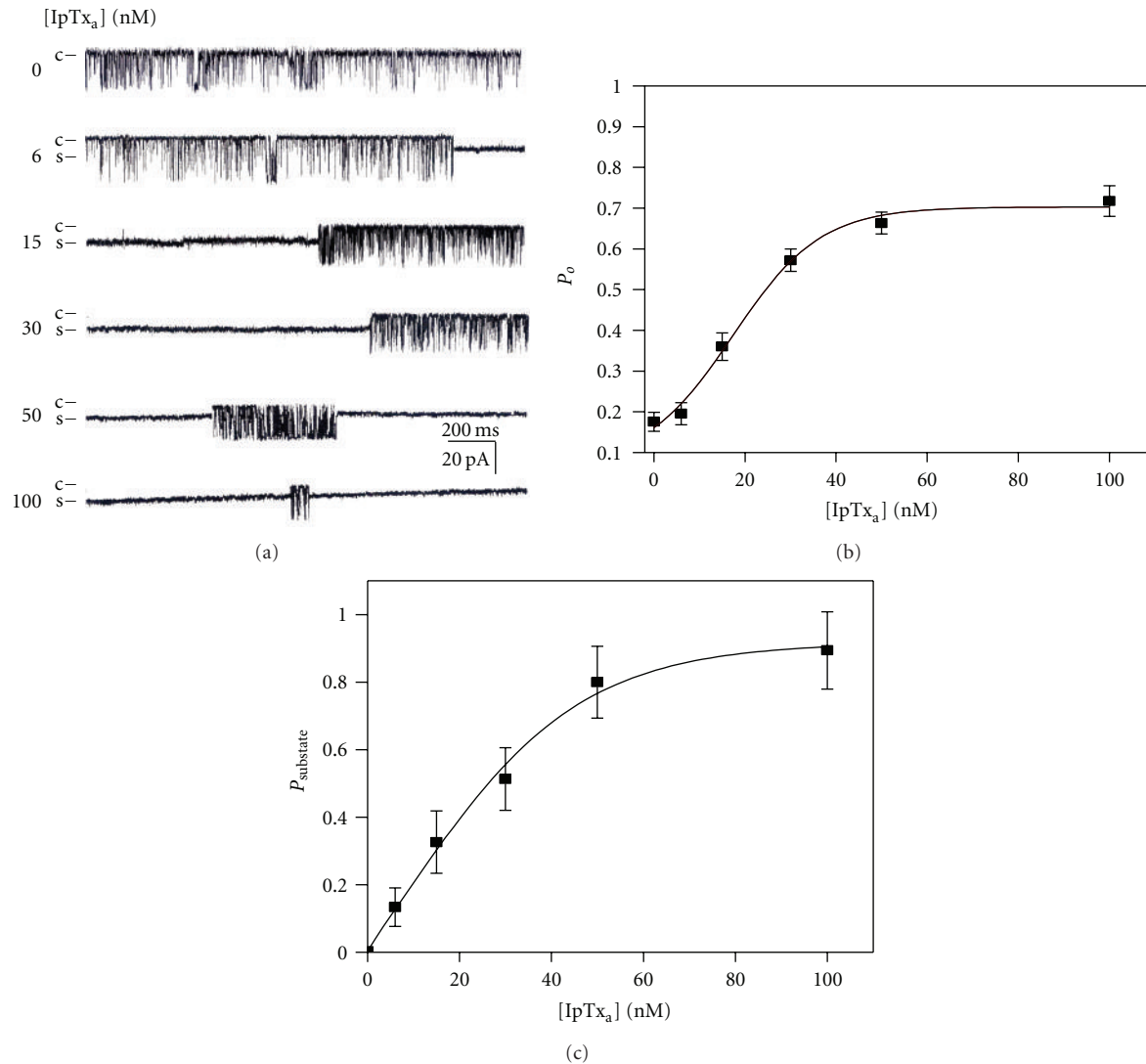


FIGURE 1: Properties of single channel gating in IpTx_a-modified native RyR1. (a) Channel current traces of a single skeletal RyR1 in planar lipid bilayers activated by various concentrations of IpTx_a. IpTx_a at 6–100 nM (final) was added to the *cis* solution to activate the channel. Channel openings are shown as downward deflections. Channel activities were recorded at a holding potential of -30 mV. (b) A plot of P_o versus concentration of IpTx_a to activate rabbit skeletal RyR1. Data points are means \pm SE of ten experiments. (c) A plot of P_{substate} versus IpTx_a concentration for rabbit skeletal RyR1. Data points are means \pm SE of 9 experiments.

as the time spent in the substate divided by a given total recording time. The durations of the substate were obtained by manual positioning of the cursors and constructing all point histograms. Mean duration of substate was measured by total substate time divided by total substate frequencies.

2.5. Statistical Analysis. Results are given as means \pm SE. Significant differences were analyzed using Student's *t*-test. Differences were considered to be significant when $P < 0.05$. The fitting of the data to the graphs were carried out using the software, Origin v7.

3. Results

3.1. Effects of IpTx_a on Single-Channel Gating Properties of RyR1. To examine how IpTx_a modifies RyR1 activity, RyR1

in HSR incorporated in planar lipid bilayers was tested in the presence or absence of synthetic wild-type IpTx_a. The chamber solutions for both *cis* (cytosolic) and *trans* (luminal) sides included 300 mM cesium methanesulfonate and 10 mM Tris-Hepes (pH 7.2). $10 \mu\text{M}$ free Ca^{2+} was added to the *cis* side to activate the incorporated RyR1. After an addition of IpTx_a to the *cis* chamber, the single channel gating properties were recorded at a holding potential of -30 mV for over 2 min at each toxin concentration. Figure 1(a) shows traces from continuous recordings in the absence and in the presence of 6, 15, 30, 50, and 100 nM IpTx_a. When the toxin concentration increased, the occurrence of substate of RyR1 was remarkably increased. To examine the effects of IpTx_a on full open state, we calculated the probability to obtain the full open state (P_o) as the time spent in the open state divided by the total time exclusive

of the time spent in the substate. The time for recorded P_o was in the range of 30 s–2 min. Figure 1(b) shows a plot of P_o versus IpTx_a concentration at 10 μ M Ca²⁺. The steady-state P_o was 0.18 ± 0.02 at 10 μ M Ca²⁺. When the concentration of IpTx_a was increased in *cis* chamber, P_o increased markedly to 0.7, suggesting that the cytosolic IpTx_a enhanced the channel activity by increasing open probability in a dose-dependent manner. Using the Hill equation (1) the parameters such as $P_{o,max}$, EC₅₀, and Hill coefficient (nH) were calculated. The calculated $P_{o,max}$ and EC₅₀ for P_o were 0.72 ± 0.02 and 17.35 ± 4.67 nM, respectively. The Hill coefficient (nH) for P_o was 1.14. Application of IpTx_a to the *trans* (SR lumen) side of chamber did not show any effect (data not shown), suggesting that increase of the full opening events of the RyR1 channel is due to interaction between the toxin and the cytosolic region of the channel.

In light of the evidence that IpTx_a could induce substate both in cardiac and skeletal RyRs [13], the effects of synthetic IpTx_a on the occurrence of substate were tested using native RyR1 in rabbit skeletal HSR. Figure 1(a) shows that an addition of IpTx_a to the *cis* side of RyR1 channel could induce the substate. The probability to obtain substate ($P_{substate}$) increased, when the concentration of IpTx_a increased from 6 to 100 nM in the *cis* chamber (Figure 1(c)). The calculated $P_{substate,max}$ and EC₅₀ for $P_{substate}$ were 0.92 ± 0.06 and 23.27 ± 2.37 nM, respectively. The Hill coefficient (nH) for $P_{substate}$ was 1.24, suggesting that IpTx_a and RyR1 do not have the cooperative bindings in the concentration range.

3.2. Effects of Alanine Scanning Mutants of IpTx_a on RyR1. In the previous studies [21, 22], it was proposed that specific basic amino acid residues on the surface of IpTx_a are required for the electrostatic interaction of the toxin with RyR1. Particularly, Gurrola et al. [15] suggested the structural domain composed of Lys¹⁹-Arg²⁴ followed by Thr²⁶ is responsible for the IpTx_a-RyR1 binding. A possible molecular interaction between IpTx_a and RyR1 was further investigated in the present study by producing various alanine scanning mutants at charged aa. We first tested the effects of IpTx_a mutants on substate of RyR1 at a holding potential of -30 mV.

The single channel traces of RyR1 activated at 30 nM wild type or mutant IpTx_a are shown in Figure 2(a). Ability of the different mutant toxins to induce substate of RyR1 was further tested using different toxin concentrations. Interestingly, both K8A and T26A mutants displayed a significantly increased substate lifetime, indicating a negative role of these residues in modifying RyR1 gating. $P_{substate,max}$ of K8A or T26A reached almost to 1, and EC₅₀ (nM) values were shifted from 23.27 ± 0.37 (wild type) to 5.70 ± 2.86 (K8A) or to 9.98 ± 1.92 (T26A; Figure 2(b) and Table 1). The mutations of the basic aa (Lys¹⁹, Lys²⁰, Lys²², Arg²³, Arg²⁴, Lys³⁰, Arg³¹, and Arg³³) significantly reduced the probability to obtain substate ($P_{substate}$), compared with the wild-type toxin (Figure 2(b) and Table 1). The effect of D15A mutant was similar to that of wild-type toxin, suggesting no major involvement of Asp¹⁵ in the binding between the toxin and RyR1. On the other hand, the substitutions of some acidic aa

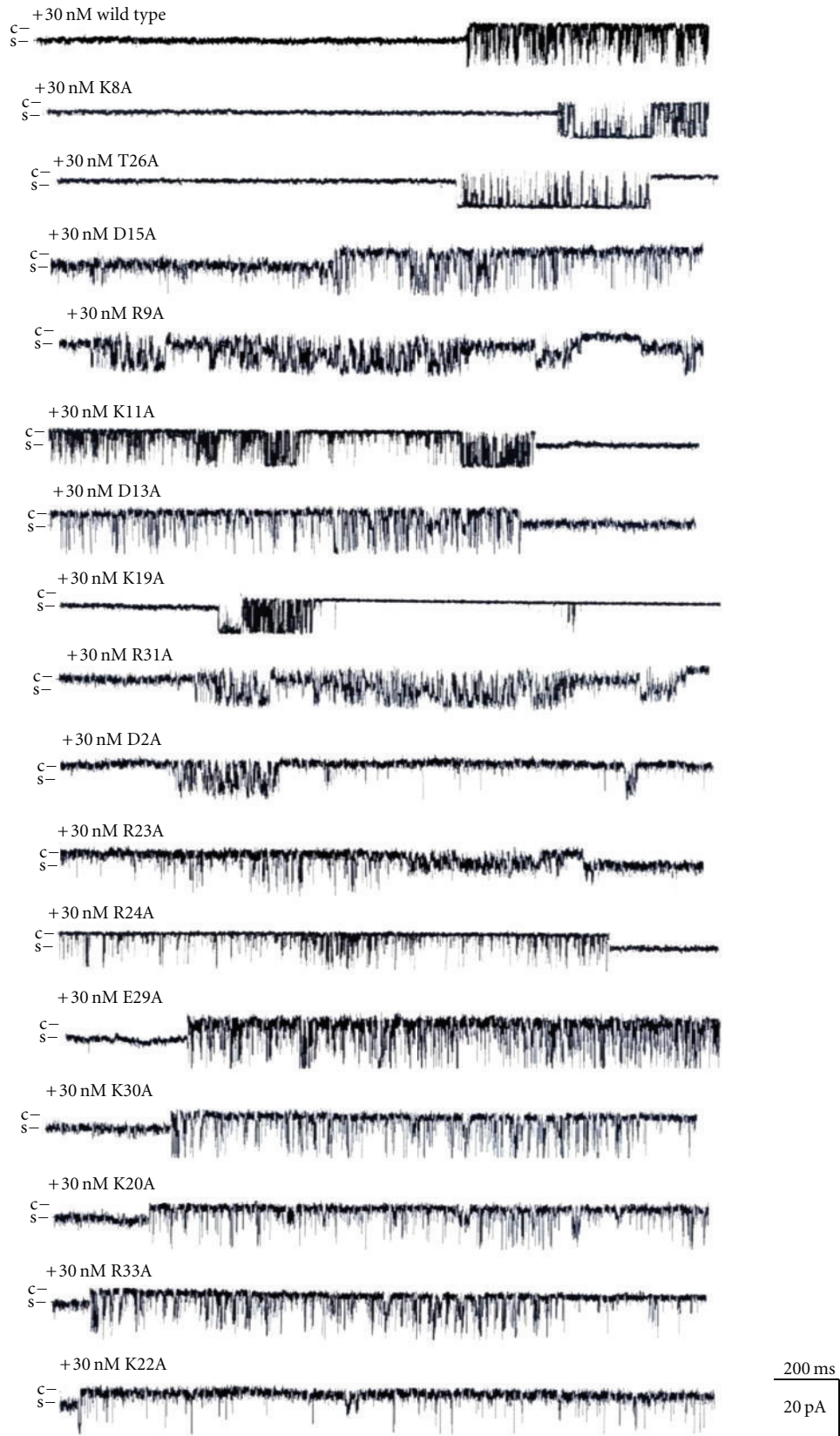
TABLE 1: Effects of the mutant IpTx_a on $P_{substate}$ of native RyR1 in SR. $P_{substate,max}$ and EC₅₀ for $P_{substate,max}$ were calculated using (1) as described in "Section 2." Values are means \pm SE of 3–9 experiments. The average lengths of the substate events were determined at 30 nM concentration. Asterisks indicate significant differences from the wild-type toxin for each parameter (Student *t*-test, $P < 0.05$). ND: not determined.

	$P_{substate}$		Mean duration of substate (s)
	$P_{substate,max}$	EC ₅₀ (nM)	
Wild type	0.92 ± 0.06	23.27 ± 2.37	4.56 ± 0.42
K8A	0.97 ± 0.01	$5.70 \pm 2.86^*$	ND
T26A	0.98 ± 0.05	$9.98 \pm 1.92^*$	$3.66 \pm 0.40^*$
D15A	0.91 ± 0.05	21.47 ± 1.92	4.50 ± 0.51
R9A	$0.75 \pm 0.05^*$	19.91 ± 3.16	$5.86 \pm 0.52^*$
K11A	$0.70 \pm 0.07^*$	21.76 ± 3.49	4.35 ± 1.07
D13A	$0.62 \pm 0.07^*$	21.72 ± 7.92	$2.76 \pm 0.25^*$
K19A	$0.43 \pm 0.07^*$	21.84 ± 6.47	$1.94 \pm 0.43^*$
R31A	$0.40 \pm 0.03^*$	19.24 ± 4.65	$3.42 \pm 0.27^*$
D2A	$0.38 \pm 0.08^*$	28.63 ± 14.02	$2.96 \pm 0.60^*$
R23A	$0.32 \pm 0.09^*$	19.54 ± 9.36	$2.50 \pm 0.26^*$
R24A	$0.26 \pm 0.08^*$	26.03 ± 7.01	$1.55 \pm 0.94^*$
E29A	$0.19 \pm 0.03^*$	$6.07 \pm 4.28^*$	$1.75 \pm 0.29^*$
K30A	$0.19 \pm 0.02^*$	$16.66 \pm 2.86^*$	$1.72 \pm 0.39^*$
K20A	$0.18 \pm 0.05^*$	18.53 ± 8.17	$3.64 \pm 0.78^*$
R33A	$0.14 \pm 0.03^*$	$16.03 \pm 5.65^*$	$1.97 \pm 0.19^*$
K22A	$0.12 \pm 0.02^*$	18.49 ± 2.88	$3.31 \pm 0.15^*$

such as Asp², Asp¹³, and Glu²⁹ by alanine alter the probability to obtain substate significantly (Figure 2 and Table 1). These results suggest that the charged aa distributed on the surface of IpTx_a contribute to the stimulatory action of the toxin and to the interaction between IpTx_a and RyR1.

3.3. Mean Duration of IpTx_a-Induced Substate. To investigate the causes for the decreased $P_{substate}$ by the mutant toxins, the average length of substate at 30 nM wild type or mutant of IpTx_a was calculated as total substate time divided by the total frequencies of substate. The recording time in each concentration was 2 min. Despite the marked increase in $P_{substate}$ as IpTx_a was increased from 6 nM to 100 nM, the mean duration of the IpTx_a induced-substate of RyR1 appeared to be similar at different [IpTx_a] (Figure 4). The average mean duration of substate of the mutants (D2A, D13A, K19A, K22A, R23A, R24A, E29A, K30A, and R33A) was significantly less than that of wild-type IpTx_a (Table 1). Some mutants (K19A, R24A, E29A, and K30A) showed more marked reduction in mean duration of substate (<2 s). The decreased mean duration of substate in the mutant toxins is due probably to the loss of their ability to induce long-lasting substate.

3.4. Effects of IpTx_a on Purified RyR1. To determine whether the activation of native RyR1 in SR by IpTx_a was due to a direct activation of RyR1 or due to an indirect activation through other proteins associated to RyR1, we added IpTx_a



(a)

FIGURE 2: Continued.

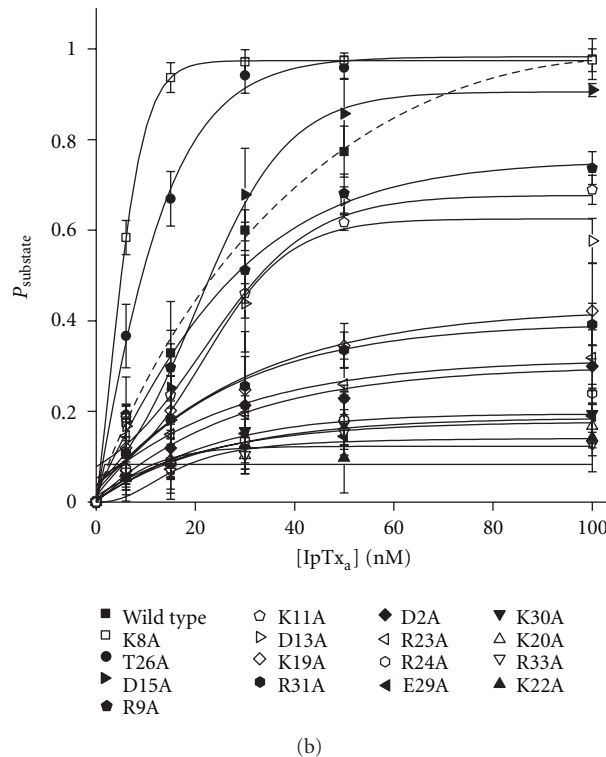


FIGURE 2: Single channel current traces of RyR1 modified by various alanine scanning IpTx_a mutants. (a) Single channel current traces of skeletal RyR1 activated in the presence of 30 nM wild-type or various mutant IpTx_a (*cis* side) at -30 mV holding potential. Single channel opening is shown as a downward deflection. (b) The plots of P_{substate} of RyR1 versus concentration of IpTx_a are shown. The data points are means \pm SE from 3–5 independent experiments.

to purified RyR1 incorporated into planar lipid bilayers (Figure 3(a)). 30 nM IpTx_a increased P_{substate} both in native and purified RyR1 in a similar extent (Figures 1 and 3). Figure 4 shows that the mean durations of substate of purified RyR1 are similar to native RyR1 at the tested concentration range, suggesting that the response of RyR1 to IpTx_a was not mediated by other RyR1-associated proteins. Purity of RyR1 at the final purification step was verified by Coomassie blue staining (Supplementary Figure 2).

3.5. Effects of IpTx_a Mutants on Purified RyR1. We further tested the effects of mutant IpTx_a (K8A, K30A, R31A, or R33A) on P_{substate} of purified RyR1. Channel activity was monitored for 2 min in the presence of 6 to 100 nM mutant toxins (Figure 5(a)). The plots of P_{substate} versus [IpTx_a] showed that the mutant toxins (K30A, R31A, and R33A) led to much smaller P_{substate} (0.16 ± 0.05 , 0.15 ± 0.02 , and 0.18 ± 0.06 , resp.) than that of wild-type IpTx_a (0.86 ± 0.05) without a significant change of EC_{50} (Figure 5(b) and Table 2). K8A led to similar $P_{\text{substate, max}}$ (0.85 ± 0.02) to wild-type toxin (Figure 5(b)). K30A and R33A produced less than 2 s of mean duration of substate (Table 2).

4. Discussion

4.1. Effects of IpTx_a Mutants on Substate of RyR1. The highly positive charges of the basic residues of IpTx_a could

contribute to the formation of its functional surface area having uniquely oriented charge distribution [15, 19, 21–23]. In the present study we tested the hypothesis that electrostatic force mediates the IpTx_a-RyR1 interaction by studying the effects of alanine scanning mutations of charged aa residues in IpTx_a on RyR1 functions.

Single point mutations of charged residues in IpTx_a generally affected the probability of occurring substate (P_{substate}) in RyR1 (Figure 2 and Table 1). Previously, it was shown that mutations in a cluster of basic residues (Lys¹⁹-Arg²⁴) decreased the ability of the toxin to activate [³H]ryanodine binding to RyR1 [15, 21]. The recombinant mutant toxins (e.g., K19A, R23A, and R24A) were less effective to increase open probability (P_o) and to induce substate of the channel [22]. Our present results demonstrate that a cluster of the basic residues 19–24 is necessary for inducing substate of RyR1, confirming the functional importance of the clustered basic residues. In addition, replacing other basic residues located in C-terminal region of IpTx_a with alanine (e.g., K30A, R31A, and R33A) also reduced the effects of the toxin on channel modification (Figure 2(b)). As described previously, the C-terminal basic residues (Lys²², Arg²³, and Arg²⁴) are aligned in the central domain of IpTx_a and possibly are responsible for activating RyR1 [21]. Our present findings agree with the previous suggestion that the positively charged region within the C-terminus is involved in the interaction with RyR1.

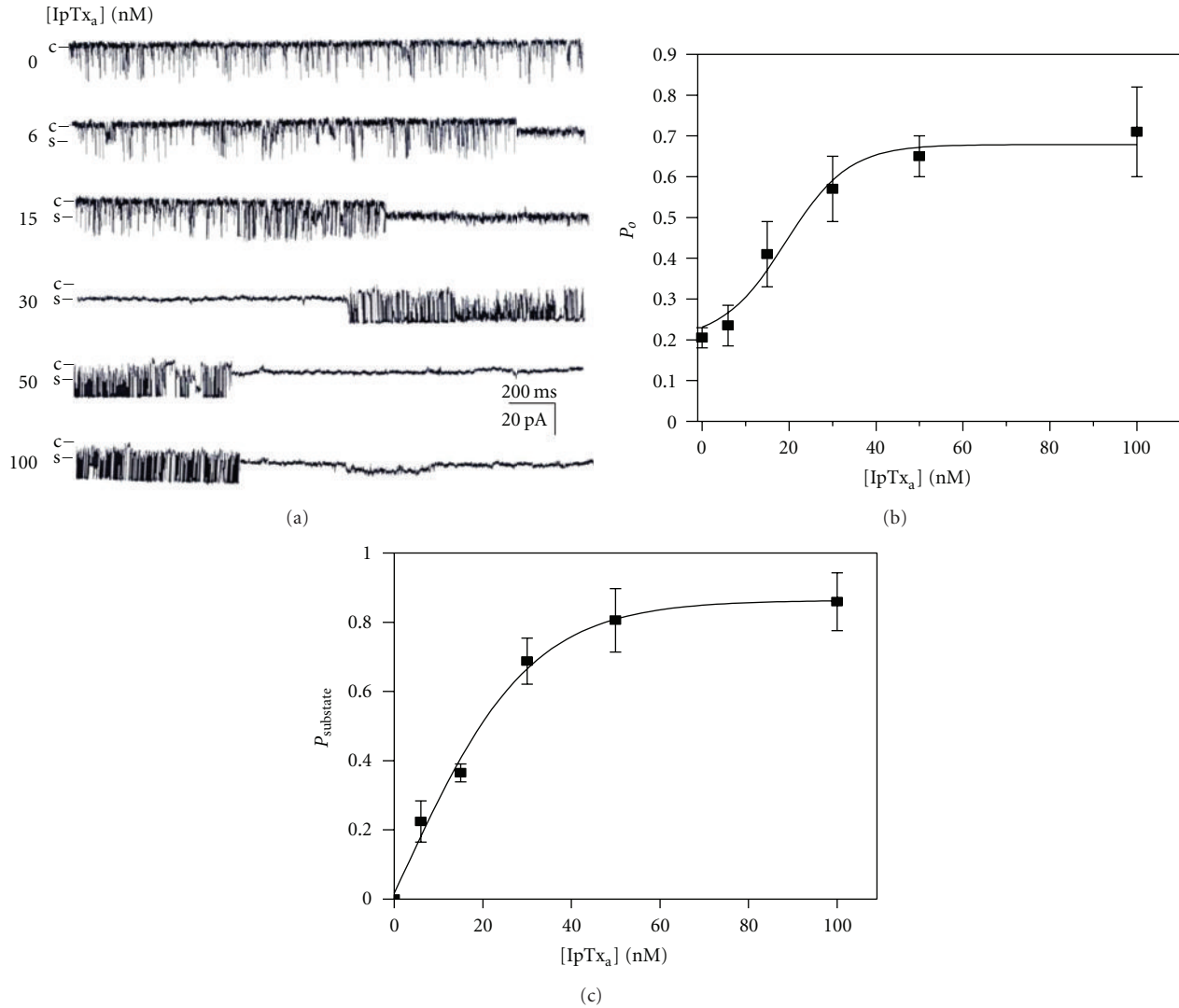


FIGURE 3: Effects of IpTx_a on purified rabbit RyR1 incorporated in planar lipid bilayers. (a) Single channel activity of purified RyR1 incorporated in planar lipid bilayers at 10 μ M Ca²⁺ with or without IpTx_a (6–100 nM) was recorded. Single channel currents are shown as downward deflections from the closed level (indicated by c). The holding potential was –30 mV. (b) The plot of P_o of purified RyR1 versus various concentrations of IpTx_a is shown. (c) The plot of P_{substate} of purified RyR1 versus various concentrations of IpTx_a is shown. The results are shown as the means \pm SE for 7 experiments.

K8A and T26A, the two mutated analogs of IpTx_a, showed dramatically decreased EC_{50} of P_{substate} compared to that of wild-type toxin, indicating higher binding affinity to RyR1 (Figures 2(b) and 5(b)). Although the ability of K8A to increase the substate lifetime of RyR1 was previously studied using recombinant IpTx_a mutant [22], the effect of K8A on [³H]ryanodine binding to RyR1 is controversial [15, 21]. T26A mutant was reported to reduce toxin-activated ryanodine binding to RyR1 [15]. The inconsistency between occurrence of substate and ryanodine binding to RyR1 affected by K8A or T26A suggests multiple independent actions of IpTx_a on different modes of channel gating. In fact, Dulhunty et al. [17] proposed an existence of multiple toxin binding sites within RyR1 including the transient activation site and substate site [17].

4.2. The Effects of IpTx_a and Peptide A on RyR1 Gating. Marked functional similarity of the three peptides, IpTx_a, MCA, and Peptide A has been proposed on the basis of their primary structural homology of a specific domain consisting of basic amino acids (Lys¹⁹-Arg²³ of IpTx_a or MCA, and Arg⁶⁸¹-Lys⁶⁸⁵ of Peptide A) [15, 17, 18, 23, 29]. Stretches of these positively charged residues tend to adopt different secondary structures such as α -helical structure for Peptide A and β -sheet structure for IpTx_a and MCA. However, their orientation on the surface of the peptides could be similar [19, 21]. Peptide A was shown to share the common binding site on RyR1 with IpTx_a and MCA and mimicked the toxin effects on RyR1 gating [15, 23, 29]. However, evidence for noncompetitive binding of MCA and peptide

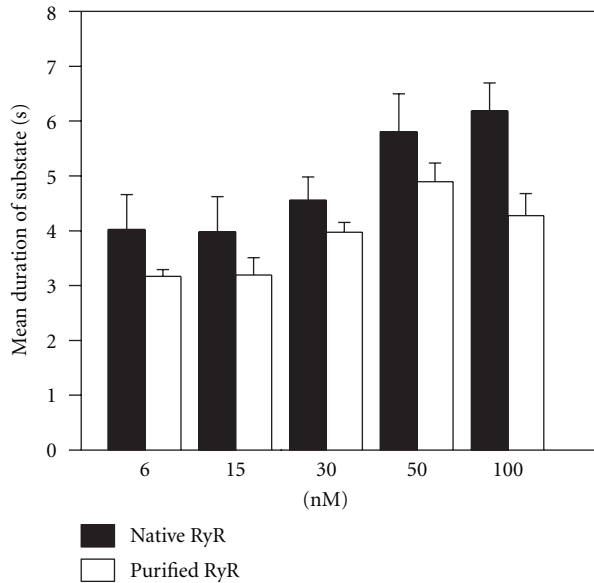
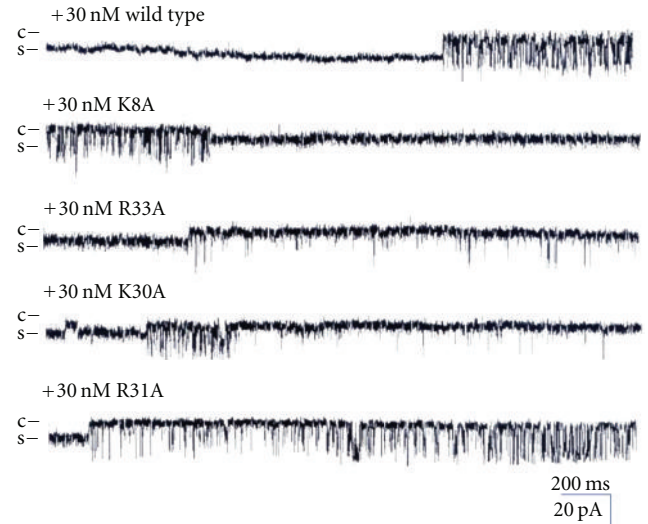


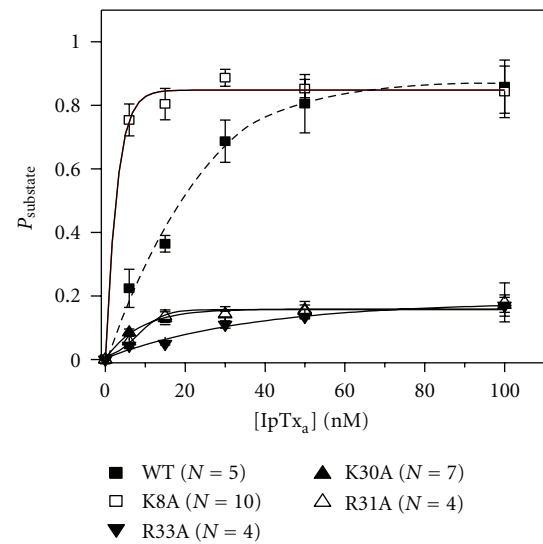
FIGURE 4: Effects of IpTx_a on the mean durations of substate of native and purified RyR1. Mean durations of the substate events in native RyR1 versus purified RyR1 were determined in the presence of 6–100 nM IpTx_a. Data points are means \pm SE for 10 experiments.

A to RyR1 was shown by [³H]ryanodine binding and real-time Surface Plasmon resonance (SPR) studies. MCA and peptide A induced distinct modification of channel gating in an additive, but not competitive, manner. This indicates the possibility of an existence of independent binding sites for the two peptides on RyR [16]. These different results have been further understood by the hypothesis that the toxins and peptide A binding sites within RyR have both common activation site and independent substate sites [17]. Although the present results show that the mutations within the structural motif shared by Peptide A inhibited substate induction (Figure 2), it is hard to find direct evidence of competitive function in the common region of RyR1. Even though our investigations were undertaken without Peptide A, it could be suggested that the prolonged substate opening triggered by IpTx_a is independent of the action of Peptide A [17]. Further study will be necessary to clarify whether the structurally conserved domains of IpTx_a and Peptide A compete for the induction of substate in RyR1.

4.3. Comparison of the Active Sites with MCA. IpTx_a and MCA share 82% aa identity in their primary structures. In addition to the similar β -sheet structure of the common stretch of the basic residues (Lys¹⁹-Arg²⁴), the solution structures of IpTx_a and MCA exhibit similar overall molecular folding [21, 30]. Because of this structural homology, these two toxins share functional similarities. Both IpTx_a and MCA strongly induce SR Ca²⁺ release and activate ryanodine binding to skeletal RyR. In addition, both peptides have the ability to induce reversible transition of RyR1 gating mode between substate and fast full open gating [12, 13, 15–17]. Previously, it was demonstrated that mutations of each basic residue within Lys¹⁹-Thr²⁶ and mutation of Lys⁸ of MCA



(a)



(b)

FIGURE 5: Properties of single channel gating in wild-type and mutant IpTx_a-modified purified RyR1. (a) Single channel currents of purified RyR1 activated in the presence of wild-type or mutant IpTx_a were measured at -30 mV holding potential. The single channel opening is shown as a downward deflection. The recordings of single channel currents were measured at 30 nM wild-type or mutant IpTx_a in the *cis* solution. (b) The plots of P_{substate} of purified RyR1 versus wild-type or mutant IpTx_a at various concentrations.

decreased the ability of the toxin to induce Ca²⁺ release and potentiate [³H]ryanodine binding in the SR [29]. Moreover, the occurrence of long-lasting substate was markedly prevented by mutations of the basic residues within Lys²⁰-Arg²⁴ of MCA [29]. This inhibitory effect was reduced, if the mutation was farther from Lys²⁴ while alanine replacement completely inhibited the substate event of skeletal RyR [17, 29]. Therefore, the previous results showing the effects of MCA mutants are partially coherent with our observations of the effects of IpTx_a mutants on RyR1 substate. In the

TABLE 2: Effects of the mutant IpTx_a on P_{substate} of purified RyR1. $P_{\text{substate, max}}$ and EC_{50} for P_{substate} of purified RyR1 were calculated as described in the legend to Table 1. Values are means \pm SE of 4–10 experiments. The average lengths of the substate events were determined at 30 nM concentration. Asterisks indicate significant differences from the wild type for each parameter (Student t -test, $P < 0.05$). ND: not determined.

	P_{substate}		Mean duration of substate (s)
	$P_{\text{substate, max}}$	EC_{50} (nM)	
Wild type	0.86 \pm 0.05	17.08 \pm 2.31	3.97 \pm 0.18
K8A	0.85 \pm 0.02	5.29 \pm 4.84*	ND
R33A	0.18 \pm 0.06*	19.25 \pm 1.05	1.43 \pm 0.09*
K30A	0.16 \pm 0.05*	15.66 \pm 5.99	1.88 \pm 0.22*
R31A	0.15 \pm 0.02*	18.23 \pm 1.65	3.15 \pm 0.10*

present study, IpTx_a mutant, R24A, was the most effective in decreasing mean duration of substate of RyR1 (Figure 3 and Table 1). R24A mutant showed comparable B_{max} value of P_{substate} with those of other mutants, R23A, K22A, and K20A, although the values were significantly less than that of wild-type IpTx_a (Figure 3 and Table 1). This suggests that the common domain clustered by positively charged residues (Lys²⁰-Arg²⁴) are responsible for the actions of two scorpion toxins to induce long-lasting substate opening of skeletal RyR1.

In spite of the high sequence identity, a significant functional difference between IpTx_a and MCa has been observed. Two toxins induced different degree of substate of RyR1 at +40 mV holding potential (28% and 48% of full conductance state for IpTx_a and MCa, resp.) [10, 13]. In addition, comparison of 3D structures of two peptides showed significantly different structural motifs near the N-terminal regions, where MCa but not IpTx_a has a β -strand and makes the hydrophobic core by connecting to the side chains of four cysteine residues, Cys¹⁰, Cys¹⁶, Cys²¹, and Cys³² [21]. Thus, the difference in the functional effect between IpTx_a and MCa on RyR1 gating appears to be due to the subtle change in the local charge distribution or a structural dissimilarity. Here we further suggest and it appears that both acidic (e.g., Asp², Asp¹³, and Glu²⁹) and basic residues of C-terminal region of IpTx_a (e.g., Lys³⁰, Arg³¹, and Arg³³) are involved in functional interaction with RyR1 in the case of IpTx_a (Figure 2(b)). To our knowledge, to date there is no report regarding to the involvement of the acidic aa residues of IpTx_a are related to the occurrence of P_{substate} of RyR1.

5. Conclusions

In this study, the ability of charged aa residues of IpTx_a to induce substate of RyR1 was examined in detail. Both basic and acidic aa residues are involved in producing substate of RyR1 supporting the hypothesis that the structural domain constituting a local cluster of charged aa is important for modifying the mode of channel gating [15, 16, 21]. Residues such as Lys⁸ and Thr²⁶ of IpTx_a are important in terms

of their inhibitory role in producing substate of RyR1. The modified channel gating properties induced by wild-type and mutant toxins were found both in native and purified RyR1. Taken together, the specific charge distributions on the surface of IpTx_a may directly regulate the gating behavior of RyR1.

Acknowledgments

The authors thank Dr. M. Samso at Virginia Commonwealth University for providing the purified rabbit RyR1. This paper was supported by the Korea MEST NRF Grant (20110002144), the 2011 GIST Systems Biology Infrastructure Establishment Grant and KISTI-KREONET. I. R. Seo, D. E. Kang, and D. W. Song equally contributed to this paper.

References

- [1] A. Tsugorka, E. Rios, and L. A. Blatter, "Imaging elementary events of calcium release in skeletal muscle cells," *Science*, vol. 269, no. 5231, pp. 1723–1726, 1995.
- [2] E. Rios, J. Ma, and A. Gonzalez, "The mechanical hypothesis of excitation-contraction (EC) coupling in skeletal muscle," *Journal of Muscle Research and Cell Motility*, vol. 12, no. 2, pp. 127–135, 1991.
- [3] W. Cheng, X. Altafaj, M. Ronjat, and R. Coronado, "Interaction between the dihydropyridine receptor Ca²⁺ channel β -subunit and ryanodine receptor type 1 strengthens excitation-contraction coupling," *Proceedings of the National Academy of Sciences of the United States of America*, vol. 102, no. 52, pp. 19225–19230, 2005.
- [4] M. D. Stern and E. G. Lakatta, "Excitation-contraction coupling in the heart: the state of the question," *FASEB Journal*, vol. 6, no. 12, pp. 3092–3100, 1992.
- [5] W. G. Wier, T. M. Egan, J. R. López-López, and C. W. Balke, "Local control of excitation-contraction coupling in rat heart cells," *Journal of Physiology*, vol. 474, no. 3, pp. 463–471, 1994.
- [6] D. M. Bers, "Macromolecular complexes regulating cardiac ryanodine receptor function," *Journal of Molecular and Cellular Cardiology*, vol. 37, no. 2, pp. 417–429, 2004.
- [7] J. J. Mackrill, "Ryanodine receptor calcium channels and their partners as drug targets," *Biochemical Pharmacology*, vol. 79, no. 11, pp. 1535–1543, 2010.
- [8] D. W. Song, J. G. Lee, H. S. Youn, S. H. Eom, and D. H. Kim, "Ryanodine receptor assembly: a novel systems biology approach to 3D mapping," *Progress in Biophysics and Molecular Biology*, vol. 105, no. 3, pp. 145–161, 2011.
- [9] R. El-Hayek, B. Antoniu, J. Wang, S. L. Hamilton, and N. Ikegami, "Identification of calcium release-triggering and blocking regions of the II-III loop of the skeletal muscle dihydropyridine receptor," *The Journal of Biological Chemistry*, vol. 270, no. 38, pp. 22116–22118, 1995.
- [10] Z. Fajloun, R. Kharrat, L. Chen et al., "Chemical synthesis and characterization of maurocalcine, a scorpion toxin that activates Ca²⁺ release channel/ryanodine receptors," *FEBS Letters*, vol. 469, no. 2-3, pp. 179–185, 2000.
- [11] H. H. Valdivia, M. S. Kirby, W. J. Lederer, and R. Coronado, "Scorpion toxins targeted against the sarcoplasmic reticulum Ca²⁺ release channel of skeletal and cardiac muscle," *Proceedings of the National Academy of Sciences of the United States of America*, vol. 89, no. 24, pp. 12185–12189, 1992.

- [12] R. El-Hayek, A. J. Lokuta, C. Arevalo, and H. H. Valdivia, "Peptide probe of ryanodine receptor function: imperatoxin A, a peptide from the venom of the scorpion *Pandinus imperator*, selectively activates skeletal-type ryanodine receptor isoforms," *The Journal of Biological Chemistry*, vol. 270, no. 48, pp. 28696–28704, 1995.
- [13] A. Tripathy, W. Resch, L. E. Xu, H. H. Valdivia, and G. Meissner, "Imperatoxin A induces subconductance states in Ca^{2+} release channels (ryanodine receptors) of cardiac and skeletal muscle," *Journal of General Physiology*, vol. 111, no. 5, pp. 679–690, 1998.
- [14] A. Shtifman, C. W. Ward, J. Wang, H. H. Valdivia, and M. F. Schneider, "Effects of imperatoxin A on local sarcoplasmic reticulum Ca^{2+} release in frog skeletal muscle," *Biophysical Journal*, vol. 79, no. 2, pp. 814–827, 2000.
- [15] G. B. Gurrola, C. Arévalo, R. Sreekumar, A. J. Lokuta, J. W. Walker, and H. H. Valdivia, "Activation of ryanodine receptors by imperatoxin A and a peptide segment of the II-III loop of the dihydropyridine receptor," *The Journal of Biological Chemistry*, vol. 274, no. 12, pp. 7879–7886, 1999.
- [16] L. Chen, E. Estève, J. M. Sabatier et al., "Maurocalcine and peptide A stabilize distinct subconductance states of ryanodine receptor type 1, revealing a proportional gating mechanism," *The Journal of Biological Chemistry*, vol. 278, no. 18, pp. 16095–16106, 2003.
- [17] A. F. Dulhunty, S. M. Curtis, S. Watson, L. Cengia, and M. G. Casarotto, "Multiple actions of imperatoxin A on ryanodine receptors: interactions with the II-III loop "A" fragment," *The Journal of Biological Chemistry*, vol. 279, no. 12, pp. 11853–11862, 2004.
- [18] B. Lukacs, M. Sztretye, J. Almassy et al., "Charged surface area of maurocalcine determines its interaction with the skeletal ryanodine receptor," *Biophysical Journal*, vol. 95, no. 7, pp. 3497–3509, 2008.
- [19] M. G. Casarotto, D. Green, S. M. Pace, S. M. Curtis, and A. F. Dulhunty, "Structural determinants for activation or inhibition of ryanodine receptors by basic residues in the dihydropyridine receptor II-III loop," *Biophysical Journal*, vol. 80, no. 6, pp. 2715–2726, 2001.
- [20] R. El-Hayek and N. Ikemoto, "Identification of the minimum essential region in the II-III loop of the dihydropyridine receptor $\alpha 1$ subunit required for activation of skeletal muscle-type excitation-contraction coupling," *Biochemistry*, vol. 37, no. 19, pp. 7015–7020, 1998.
- [21] C. W. Lee, E. H. Lee, K. Takeuchi et al., "Molecular basis of the high-affinity activation of type 1 ryanodine receptors by imperatoxin A," *Biochemical Journal*, vol. 377, no. 2, pp. 385–394, 2004.
- [22] I. R. Seo, M. R. Choi, C. S. Park, and D. H. Kim, "Effects of recombinant imperatoxin A (IpTx_3) mutants on the rabbit ryanodine receptor," *Molecules and Cells*, vol. 22, no. 3, pp. 328–335, 2006.
- [23] D. Green, S. Pace, S. M. Curtis et al., "The three-dimensional structural surface of two β -sheet scorpion toxins mimics that of an α -helical dihydropyridine receptor segment," *Biochemical Journal*, vol. 370, no. 2, pp. 517–527, 2003.
- [24] D. H. Kim, S. T. Ohnishi, and N. Ikemoto, "Kinetic studies of calcium release from sarcoplasmic reticulum in vitro," *The Journal of Biological Chemistry*, vol. 258, no. 16, pp. 9662–9668, 1983.
- [25] C. Miller and E. Racker, " Ca^{2+} induced fusion of fragmented sarcoplasmic reticulum with artificial planar bilayers," *Journal of Membrane Biology*, vol. 30, no. 1, pp. 283–300, 1976.
- [26] J. S. Smith, R. Coronado, and G. Meissner, "Single channel measurements of the calcium release channel from skeletal muscle sarcoplasmic reticulum: activation by Ca^{2+} and ATP and modulation by Mg^{2+} ," *Journal of General Physiology*, vol. 88, no. 5, pp. 573–588, 1986.
- [27] E. H. Lee, G. Meissner, and D. H. Kim, "Effects of quercetin on single Ca^{2+} release channel behavior of skeletal muscle," *Biophysical Journal*, vol. 82, no. 3, pp. 1266–1277, 2002.
- [28] F. A. Lai, H. P. Erickson, E. Rousseau, Q. Y. Liu, and G. Meissner, "Purification and reconstitution of the calcium release channel from skeletal muscle," *Nature*, vol. 331, no. 6154, pp. 315–319, 1988.
- [29] E. Estève, S. Smida-Rezgui, S. Sarkozi et al., "Critical amino acid residues determine the binding affinity and the Ca^{2+} release efficacy of maurocalcine in skeletal muscle cells," *The Journal of Biological Chemistry*, vol. 278, no. 39, pp. 37822–37831, 2003.
- [30] A. Mosbah, R. Kharrat, Z. Fajloun et al., "A new fold in the scorpion toxin family, associated with an activity on a ryanodine-sensitive calcium channel," *Proteins*, vol. 40, no. 3, pp. 436–442, 2000.

Review Article

The Recent Understanding of the Neurotrophin's Role in Skeletal Muscle Adaptation

Kunihiro Sakuma¹ and Akihiko Yamaguchi²

¹ *Research Center for Physical Fitness, Sports and Health, Toyohashi University of Technology, 1-1 Hibarigaoka, Tenpaku-cho, Toyohashi 441-8580, Japan*

² *School of Dentistry, Health Sciences University of Hokkaido, Kanazawa, Ishikari-Tobetsu, Hokkaido 061-0293, Japan*

Correspondence should be addressed to Kunihiro Sakuma, ksakuma@las.tut.ac.jp

Received 27 May 2011; Accepted 24 July 2011

Academic Editor: Aikaterini Kontrogianni-Konstantopoulos

Copyright © 2011 K. Sakuma and A. Yamaguchi. This is an open access article distributed under the Creative Commons Attribution License, which permits unrestricted use, distribution, and reproduction in any medium, provided the original work is properly cited.

This paper summarizes the various effects of neurotrophins in skeletal muscle and how these proteins act as potential regulators of the maintenance, function, and regeneration of skeletal muscle fibers. Increasing evidence suggests that this family of neurotrophic factors influence not only the survival and function of innervating motoneurons but also the development and differentiation of myoblasts and muscle fibers. Muscle contractions (e.g., exercise) produce BDNF mRNA and protein in skeletal muscle, and the BDNF seems to play a role in enhancing glucose metabolism and may act for myokine to improve various brain disorders (e.g., Alzheimer's disease and major depression). In adults with neuromuscular disorders, variations in neurotrophin expression are found, and the role of neurotrophins under such conditions is beginning to be elucidated. This paper provides a basis for a better understanding of the role of these factors under such pathological conditions and for treatment of human neuromuscular disease.

1. Introduction

Neurotrophins are best known for their roles in regulating neuronal survival, plasticity, growth, and death [1, 2]. As such, they have been studied predominantly in the context of nervous system development and function. However, accumulating evidence suggests that neurotrophins play a more widespread role than originally thought. Accordingly, they are now the focus of study in numerous cell populations across multiple tissue systems. Of these populations, skeletal muscle is of particular interest, because it acts as an abundant source of neurotrophic support throughout development [3, 4]. In addition, skeletal muscle expresses several neurotrophin receptors, providing the basis for neurotrophin signaling within the muscle compartment [5]. Indeed, neurotrophin knockout mice often exhibit distinct defects in muscle development and function, and to date neurotrophin- (NT-) 4/5 has been implicated in muscle fiber transformation, NT-3 in muscle spindle formation, and nerve growth factor (NGF) in dystrophic muscle pathology [6–8]. Expression profiling has shown that brain-derived

neurotrophic factor (BDNF) is differentially expressed in skeletal muscle under various physiological and pathological conditions [4]. Several studies have demonstrated that physical exercise can increase circulating BDNF levels in both healthy humans [9, 10] and patients with multiple sclerosis [11]. More recently, Matthews et al. [12] clearly showed the production of BDNF mRNA and protein by human skeletal muscle after 2 hours of ergometer bicycle exercise. In addition, denervation causes alterations of muscle neurotrophin levels [3, 13, 14], and, in several animal studies, reduced NGF and NT-3 mRNA as well as NGF protein levels have been observed in diabetic muscle [15–18], whereas an increase in BDNF mRNA levels has been reported [15, 19].

Glial-cell-line-derived neurotrophic factor (GDNF) was first discovered in glial cells and supports dopaminergic neurons of the central nervous system [20]. GDNF induces sprouting and muscle fiber reinnervation [21] and may be involved in the maintenance of cell body size and the cholinergic phenotype of motoneurons [22]. Earlier studies showed the marked expression of GDNF at neuromuscular junction (NMJ) during early myogenesis and then negligible

levels. However, several researchers observed clear expression in normal muscles of mice, after denervation, and merosin-deficient muscular dystrophy in adult animals.

This paper focuses on the effects of neurotrophins (NGF, BDNF, NT-4/5, and GDNF) on skeletal muscle and how they act as potential regulators of the development, maintenance, function, and regeneration of skeletal muscle fibers. In mice carrying null mutations in the NT-3 or tropomyosin-related kinase (Trk)C gene, numbers of proprioceptive neurons and muscle spindles are dramatically decreased [8, 23]. Conversely, the embryonic overexpression of NT-3 in developing limb or muscle increases the number of proprioceptive neurons [24, 25]. However, the muscle morphology in these models is poorly described. In this paper, we did not describe a possible role of NT-3 and the receptor (TrkC) in muscle fiber; only a few studies found some role of NT-3 to muscle morphology [26, 27].

2. Normal Distribution of Neurotrophins and Their Receptors in Adult Skeletal Muscle

2.1. Neurotrophins. The level of BDNF expression in animals fuels debate as well. Low levels were reported in developing and postnatal avian and rodent skeletal muscle [3, 28–32]. However, other studies including our own could not detect any BDNF expression in developing muscle of mice and rats [14, 33]. Indeed, neither Western blotting nor immunohistochemistry revealed immunoreactivity in the soleus and several fast-type muscles in Wistar rats at 2–12 weeks of age. To investigate this issue in more detail, recent studies have applied intensified *in situ* hybridization (ISH) techniques for electron microscopy to detect BDNF mRNA in muscle and, in particular, to determine the cell types (muscle fibers, satellite cells, Schwann cells, fibroblasts, and endothelial cells) that synthesize BDNF. These studies suggest the expression of BDNF to be confined to myofibers in adult rat muscle [34] and that other cells in normal muscle do not contribute to BDNF expression. However, Mousavi and Jasmin [35] demonstrated more recently the expression of BDNF in normal satellite cells of several muscles in adult mice. Using three different methods (reverse transcription-PCR, *in situ* hybridization, and immunofluorescence), they found the clear colocalization of both BDNF and the receptor p75^{NTR} with Pax3, a marker of satellite cells, in the diaphragm, soleus, and EDL muscle of mature mice. Furthermore, they showed that BDNF was not expressed at significant levels within mature myofibers and did not accumulate within subsynaptic regions of neuromuscular junctions. Consistent with these observations, Liem et al. [34] reported that subsynaptic regions of NMJs in soleus muscle were devoid of BDNF transcripts. The expression of BDNF in NMJs has been controversial. It has been hypothesized that skeletal-muscle-derived BDNF enhances the survival of innervating motor neurons throughout their lifespan and potentiates neuromuscular transmission [36, 37]. This hypothesis is supported by several lines of evidence including, for example, the expression of BDNF in skeletal muscle and retrograde transport of exogenously applied BDNF to distinct motor neuron cell bodies [3, 38,

39]. As postulated by Mousavi and Jasmin [35], mature NMJs unlike the central nervous system (CNS) may be stable arrangements that do not require BDNF signaling for remodeling and modulation of neuromuscular transmission.

NT-4/5 expression is dependent on the activity of neuromuscular synapses. Electrical stimulation of motor nerves enhanced NT-4/5 expression in skeletal muscle, and a blockade of neuromuscular endplates with bungarotoxin led to reduced NT-4/5 expression [39]. Although NT-4/5 expression appears relatively strong in skeletal muscle of adult rats, several studies including our own suggest the expression of NT-4/5 to be dependent on fiber type [14, 40]. One study found NT-4/5 to be equally distributed in both muscle types in humans [40], while another, using *in situ* hybridization and immunohistochemistry, found NT-4/5 to be selectively expressed in the slow-twitch fibers of mice. In contrast, our Western blot analysis [14] demonstrated that NT-4/5 expression is higher in fast-type (extensor digitorum longus, tibialis anterior, and gastrocnemius) than slow-type (soleus) muscles. Immunohistochemical analysis revealed NT-4/5 protein within vesicle-like structures that are diffusely distributed in the cytosol of muscle fibers in the tibialis anterior muscle. Low levels of NT-4/5 immunoreactivity were also observed around the edge of soleus muscle fibers. Furthermore, Carrasco and English [7] found, using Fisher 344 rats, that intramuscular injections of recombinant NT-4/5 (1.5 μ g) into the soleus muscle of neonates significantly accelerated the normal fast-to-slow myosin heavy chain (MHC) isoform transformation. The sequestration of endogenous NT-4/5 with TrkB-IgG prevented this transformation from occurring. Intriguingly, administration of another TrkB ligand did not affect the normal course of the transformation in this muscle. In their study, the developmental upregulation of NT-4/5 mRNA expression in rat soleus muscle fibers occurred earlier than the upregulation of MHCI mRNA expression associated with muscle fiber transformation. This finding would indicate that the NT-4/5 protein is expressed more abundantly in the soleus muscle because of the slow-type characteristics. Although the expression pattern of NT-4/5 appears to differ depending on the species of animal and with postnatal growth, NT-4/5 is important for maintaining various functions (fiber-type conversion, survival of motoneuron, the formation of NMJ, etc.) in skeletal muscle.

The expression of GDNF has been found in a variety of tissues and cells outside of the CNS, including skeletal muscle and Schwann cells [21, 41, 42]. Earlier studies indicated that GDNF is important to the survival of motoneurons during myogenesis and regulates the postnatal change from multi-innervation to single innervation. In general, GDNF expression seems to peak during early myogenesis and to be negligible in mature skeletal muscle. A more recent study clearly demonstrated the existence of GDNF mRNA and protein in both slow-type soleus and fast-type EDL muscles, especially the former [43].

2.2. Neurotrophin Receptors. Figure 1 indicates possible interactions between several neurotrophins and these receptors in mammalian muscle. The low-affinity NT receptor

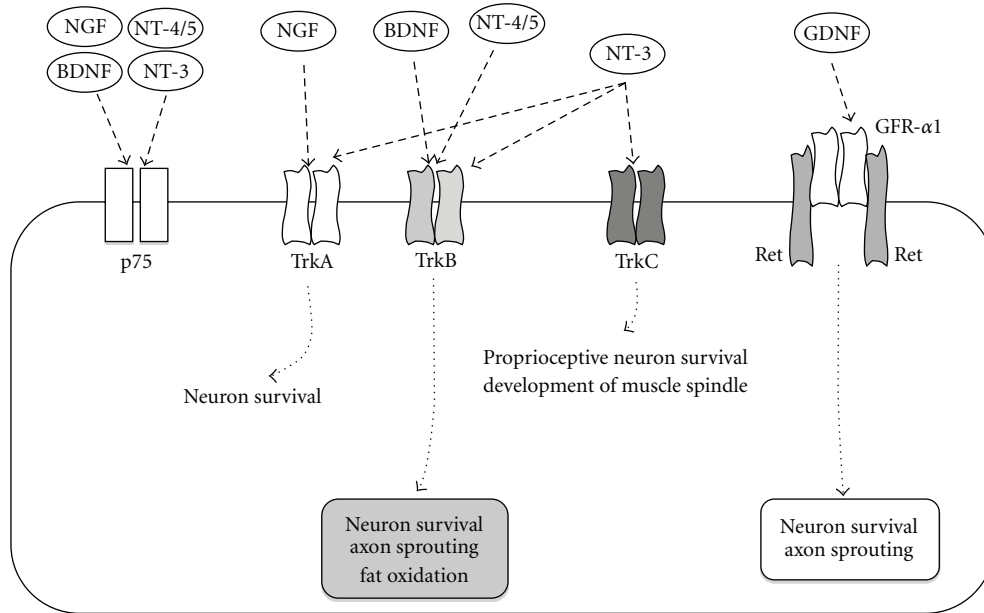


FIGURE 1: The interaction (preference of binding) between neurotrophins and these receptors. The low-affinity receptor $p75^{NTR}$ binds all neurotrophins with similar affinity but not different kinetics. Trk receptors are a family of transmembrane glycoprotein, which includes three members, TrkA, TrkB, and TrkC. The full-length TrkA, TrkB, and TrkC have estimated molecular weights of 140, 145, and 145 kDa, respectively. Each Trk preferentially binds a single neurotrophin. TrkA is the receptor for NGF, both BDNF and NT-4/5 bind to TrkB, and NT-3 is the ligand for TrkC. GDNF dimer forms a complex with GFR- α 1, and this complex induces dimerization of Ret. BDNF: brain-derived neurotrophic factor, GDNF: glial cell-line derived neurotrophic factor, and NT-4/5: neurotrophin-4/5.

($p75^{NTR}$) binds both neurotrophin precursor proteins and all mature neurotrophins. It is expressed in developing rat myoblasts and in adult rat and chicken muscle [44–46]. In chicks, all somitic cells strongly express $p75^{NTR}$ mRNA during early development [47]. Subsequently, as the somite becomes subdivided into the dermatome, myotome, and sclerotome, $p75^{NTR}$ mRNA expression becomes high in dermatome and sclerotome and decreases to low levels in the myotome [45].

In the adult rat, both the long form of TrkA mRNA and a short isoform that lacks 18 base pairs coding for an insert in the extracellular region are expressed in skeletal muscle [45]. TrkB is also found in the muscle of adult mice [48]. Our group found that the truncated TrkB was highly expressed in muscle, but the full-length TrkB was also detectable, at least at low levels [14, 45]. TrkB expression varies depending on the type of skeletal muscle [14, 45]. TrkB is more abundant around the edge of myofibers of the soleus muscle than gastrocnemius muscle. Full-length TrkB and TrkB-T1 appear in close proximity to motor endplates in skeletal muscle. In contrast, a more recent study [49] using real-time PCR detected both the truncated and full-length TrkB mRNA in the predominantly fast-twitch medial gastrocnemius muscles. It is possible that the equivocal results regarding the expression of TrkB in skeletal muscle are due to methodological differences, because there are discrepant sensitivities between the sensitivity of techniques utilized to establish protein versus mRNA expression changes. Other studies have found the colocalization of TrkB with mitochondrial membrane [50] and endothelial cells

[51] in skeletal muscle, although the role of TrkB at these locations is not entirely understood.

Both GDNF receptor (GFR) α 1 and GFR α 2 are expressed abundantly in the developing and adult central and peripheral nervous systems [52, 53]. GFR α 3 mRNA was detected in spleen, lung, liver, heart, and kidney, but not in brain, skeletal muscle, or testis [54].

2.3. Neurotrophins at NMJs. Whether and if so how neurotrophins modulate the development and function of motor endplates in skeletal muscle has still not been fully elucidated. Neurotrophins have been shown to potentiate the spontaneous activity of developing neuromuscular synapses in culture [55, 56]. The situation *in vivo*, however, is less clear. Overexpression of NT-4/5 in myoblasts in developing *Xenopus laevis* embryos leads to the enhanced release of acetylcholine in innervating motor terminals, and additional postsynaptic effects were observed with increased mean burst duration of low-conductance acetylcholine (ACh) receptor (AChR) channels [57]. NT-4/5 overexpression in myocytes leads to the enhanced spontaneous activation of skeletal muscle [57]. This suggests that NT-4/5 modulates neuromuscular transmission and that this involves effects via pre- and postsynaptic TrkB receptors. Indeed, a more recent study [58] using confocal microscopy clearly demonstrated immunoreactivity to BDNF, NT-4/5, p75, and TrkB at NMJs in the mouse levator auris longus muscle.

Both BDNF and NT-4/5 acted on TrkB receptors in the pre- and postsynaptic part of the NMJ [59, 60]. BDNF and NT-4/5 inhibited agrin-induced AChR clustering in cultured

chicken myotubes, whereas NGF and NT-3 had no effect [60].

It was demonstrated that GDNF enhanced spontaneous neurotransmitter release in amphibian neuron-myocyte cocultures and isolated neuromuscular preparations from mice [61]. Treating frog neuron-muscle co-cultures with GDNF increased the frequency as well as amplitude of spontaneous synaptic currents [62]. In addition, using quantitative data from double-labeled imaging, Yang and Nelson [63] found that GDNF induced a quick and substantial increase in AChR insertion as well as lateral movement into AChR aggregates in the surface membrane of mouse primary cultured muscle cells. Furthermore, transgenic mice with muscle-specific overexpression of GDNF exhibit hyperinnervation of the muscle at birth and delayed synapse elimination [21]. Although all of the findings made *in vitro* and with transgenic mice show that GDNF plays an important role in the formation and maturation of NMJs, there is no direct evidence (e.g., immunofluorescence) that the GDNF protein exists at NMJs in normal mammalian skeletal muscle *in vivo*.

3. Effect of Exercise on Neurotrophin and Neurotrophin Receptor Expression

Increased physical activity has been shown to alter the structure and function of the NMJ. Exercise increases the size and degree of branching of motor nerve terminals at the NMJ [64], the total area of both pre- and postsynaptic elements [65], and the amount of ACh released [66]. Endurance exercise in young animals results in the hypertrophy of nerve terminals and an increase in neurotransmitter release [67]. Increased exercise training has also been shown to have effects on neurotrophic factor expression in mammalian skeletal muscle. BDNF mRNA expression has consistently been shown to increase in the CNS and peripheral nervous system (PNS) in a dose-dependent manner following exercise [68, 69]. Recently, brief treadmill training bouts over 5 days were found to produce large increases in BDNF mRNA in soleus muscle [70, 71] that do not follow the positive dose-response relationship originally demonstrated in the nervous system with voluntary wheel running [68, 69, 72, 73]. As BDNF and NT-4/5 can initiate intracellular signaling through the same cell surface receptor, TrkB [74, 75], it is of interest that NT-4/5 has not been evaluated following similar exercise. To date, only one study has addressed the issue of exercise-induced NT-4/5 expression, finding no significant elevation of NT-4/5 protein levels in the vastus lateralis of two aerobically trained individuals.

In Sprague-Dawley rats exercised on a treadmill at speeds of up to 20 m/min with a 5% incline, BDNF mRNA expression was enhanced in soleus muscle following 5 days (184%) but not 10 days of exercise. NT-4/5 and TrkB mRNA levels were not affected at either time point. The exercise-elicited increase in BDNF expression in muscle seems to influence neurotrophin levels in motoneurons. Gómez-Pinilla et al. [69] indicated a marked increase in BDNF mRNA but not protein in soleus muscle after 5 consecutive days of treadmill training. In contrast, ELISA and immunohistochemistry

showed an increase in the protein but not mRNA in lumbar motoneurons after this training. It is known that motoneurons can retrogradely transport BDNF that has been injected into skeletal muscle [76] or the sciatic nerve [77, 78] and that the administration of BDNF can prevent the degeneration of motoneurons [76, 78]. These findings raise the question of whether these neurotrophic factors play a role in the routine maintenance and plasticity of the neuromuscular system.

Wehrwein et al. [43] showed that GDNF protein content increased with involuntary exercise in skeletal muscle but decreased with hindlimb suspension. This adaptation of GDNF protein content elicited by exercise seems to be dependent on muscle fiber type. More recently, McCullough et al. [79] found that low-intensity exercise (10 m/min, 45 min/day, 2 weeks) increased and decreased the amount of GDNF in the soleus and EDL muscles, respectively, corresponding with the change in the average endplate area. Such a change in GDNF content was observed after both 4 hours of electrical stimulation and mechanical stretching in both muscles. Interestingly, pretreatment with α -bungarotoxin blocked the stretch-induced decrease in GDNF protein in EDL muscle and uncovered a stretch-induced increase in the protein in soleus muscle. Therefore, ACh may act on nAChRs to regulate GDNF protein content. The application of GDNF increased spontaneous transmitter release from motor nerve terminals in skeletal muscles of both neonatal mice [61] and from nerve muscle co-cultures [62]. Treatment with exogenous GDNF caused continuous synaptic remodeling and axonal branching at the NMJ [80]. Figure 2 provides an overview of molecular pathway of neurotrophic factors to regulate to neurotransmission, hypertrophy, or fat oxidation in skeletal muscle.

4. Possible Role of Neurotrophins during Muscle Regeneration

Experimental results indicate neurotrophins (particularly NGF) to be involved in muscle regeneration. NGF improved the muscle-regenerating capacity of muscle stem cells in dystrophic muscle [81]. In addition, phenotypic knockout of NGF resulted in skeletal muscle atrophy and dystrophy in adult mice [6, 82]. In humans, regenerating muscle fibers from patients affected by Duchenne and Becker muscular dystrophies consistently express NGF, as do myofibroblasts and mast cells. Interestingly rest fibers from healthy subjects did not show NGF immunoreactivity or NGF protein [6]. Moreover, regenerating myofibers expressed NGF receptors, TrkA-receptor [83] as well as p75^{NTR} [84]. Taken together, these results indicate that, in dystrophic muscles, NGF expression might be able to trigger and favor the regeneration process. In fact, Deponti et al. [85] provided the direct evidence that NGF-p75^{NTR} signaling regulates the differentiation of satellite cells *in vivo*. They utilized a tissue-permeable form of a NGF-competing peptide (P75^{NTR}TAT4) or the control peptide TAT4 starting 48 h after damage (cardiotoxin injection). Six days after the cardiotoxin injection, regenerating centro-nucleated fibers

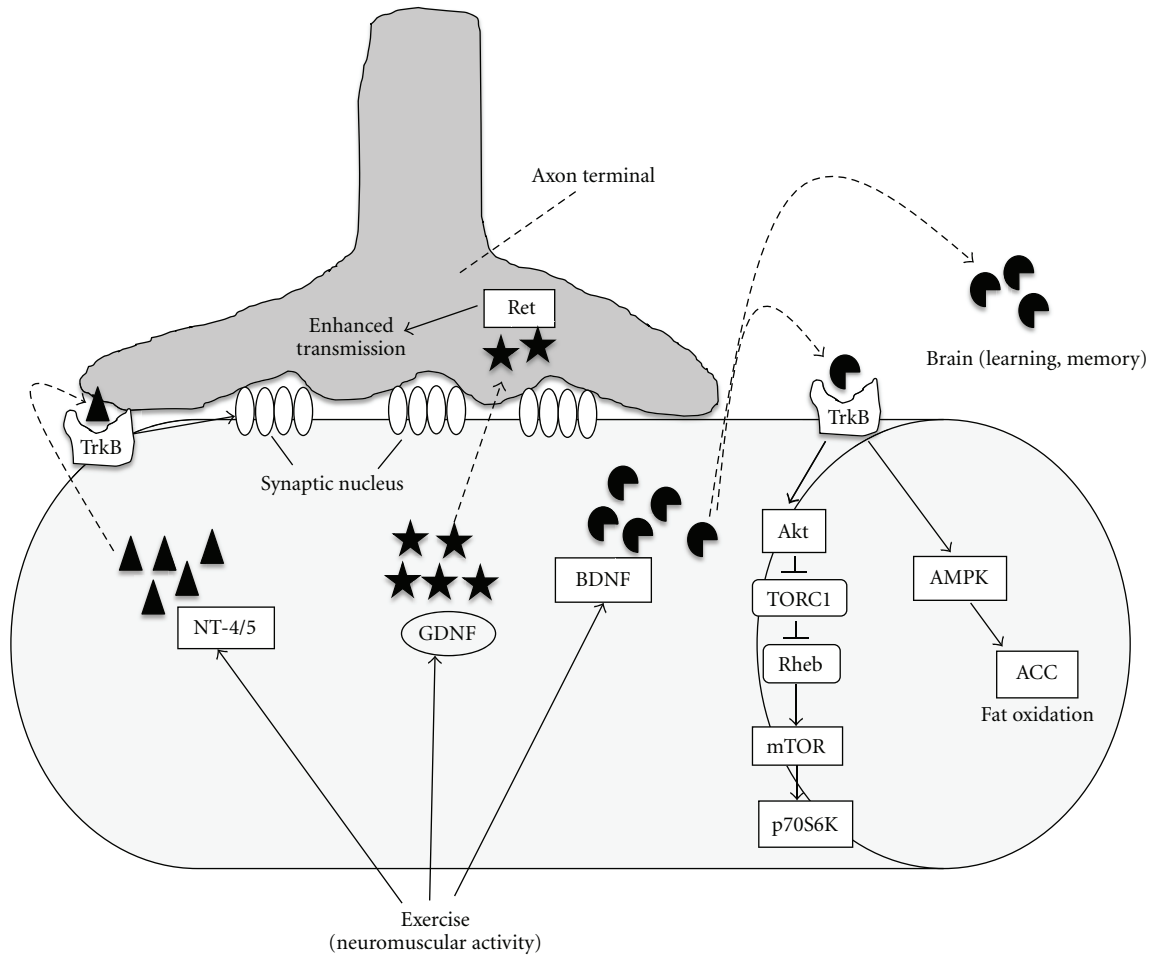


FIGURE 2: Schematic diagram of the functional role of skeletal muscle-derived neurotrophic factors after exercise. Exercise (neuromuscular activity) increases BDNF expression in skeletal muscle. In the patients with spinal cord injury, BDNF stimulates protein synthesis by activating Akt/mTOR/p70S6K pathway through TrkB receptor on muscle membrane. BDNF also promotes the fat oxidation through AMPK-ACC signaling. BDNF produced by skeletal muscle after exercise may circulate into brain to improve the impaired learning and/or depression. Increased GDNF protein after exercise promotes the amount of neurotransmitter (e.g., ACh) at NMJ by conjugating with Ret in presynaptic region (axon terminal). NT-4/5 may possess similar role of GDNF. BDNF: brain-derived neurotrophic factor, GDNF: glial cell-line derived neurotrophic factor, NT-4/5: neurotrophin-4/5, NMJ: neuromuscular junction, TORC1: a component of TOR signaling complex 1, Rheb: Ras homolog enriched in brain, mTOR: mammalian target of rapamycin, AMPK: AMP-activated protein kinase, and ACC: acetyl CoA carboxylase.

were present in the control, whereas no regeneration was apparent in the muscles treated with P75^{NTR}TAT4. At 10 days, regeneration occurred also in the P75^{NTR}TAT4-treated animals, however, it was significantly less extensive than in controls with a persistence of embryonic MHC. At this time, they observed the marked upregulation in RhoA-GTP expression in regenerating muscle treated with P75^{NTR}TAT4 compared to control muscle. During muscle regeneration *in vivo*, NGF-p75^{NTR} signaling seems to promote myogenic differentiation by inhibiting RhoA-GTP as demonstrated *in vitro* using pull-down assays [85].

The role of BDNF in skeletal muscle development and function has been difficult to determine due in part to the early postnatal death of the BDNF knockout mouse (BDNF^{-/-}) [86]. More recently, Clow and Jasmin [87] generated a mouse in which BDNF is specifically depleted

from skeletal muscle cells to examine the functional role of muscle-derived BDNF *in vivo*. Mice carrying the LoxP-targeted BDNF allele (BDNF^{f/f}) were crossed with Myf5-Cre mice to generate BDNF^{f/wt};Myf5-Cre progeny, and then backcrossed with BDNF^{f/f} homozygotes to produce BDNF^{f/f};Myf5-Cre mice (BDNF^{MKO}). At P7, BDNF transcript levels were decreased by ~50% in BDNF^{MKO} muscles compared with controls. Although overall muscle histology is not affected in the absence of muscle-BDNF, they observed the decreased expression (by 30%) of a satellite cell marker, Pax7. After the injection with cardiotoxin, BDNF-depleted muscle showed lower levels of differentiation-promoting factors such as myogenin, MyoD, and embryonic MHC as well as the delayed appearance of newly centrally nucleated fibers in the regenerating muscle during 1–5 days [87]. Furthermore, treatment with exogenous BDNF protein was

sufficient to rescue normal gene expression and myotube size in BDNF^{MKO} mice probably due to the upregulation of Pax7 expression.

In contrast, a previous study by this same group showed that siRNA-mediated depletion of BDNF resulted in the precocious differentiation of rat L6 myoblasts [35]. There are many possible causes for the disparity observed between these studies. First, there are intrinsic differences in the properties of immortalized cell lines and primary cultures. Second, the developmental timing of BDNF depletion differed between these studies. These differences, in conjunction with the different mechanisms used to deplete BDNF expression (siRNA transfection versus transgenic knock-out) could result in altered responses of satellite cells to signals that promote growth, differentiation, or both. Finally, it becomes important to consider that many features of embryonic muscle development are recapitulated during muscle regeneration, with similar changes in muscle gene expression, physiological properties, and functional characteristics. In BDNF^{MKO} muscle, Pax7 expression is decreased, satellite cell differentiation is defective, and regeneration is delayed.

GDNF signaling seems to have an important role during muscle regeneration. Using *in situ* hybridization histochemistry, Kami et al. [88] investigated whether the expression of GDNF-linked molecules significantly changes in regenerating muscle. They utilized muscle contusion to elicit extensive damage, because this approach directly damages muscle cells, blood vessels, intramuscular nerves, and extracellular matrix components. They found that muscle contusion induced increases in GDNF and GFR α 1 mRNAs in Schwann cell-like cells in the intramuscular nerves. GFR α 1 and RET mRNA expression in motoneurons was upregulated. We have also observed such motoneuronal activation after muscle damage with bupivacaine [14]. Our immunoprecipitation analysis clearly showed the phosphorylation of TrkB in the spinal cord at 1 day after pharmacological muscle damage (bupivacaine). These findings suggest that a rapid and prominent increase in the receptor components for GDNF or TrkB in motoneurons is important for the regeneration of intramuscular motor nerves damaged by muscle contusion and bupivacaine injections.

5. Neurotrophin and Neuromuscular Disorders

5.1. Sarcopenia. Aging is associated with a progressive decline of muscle mass, quality, and strength, a condition known as sarcopenia [89]. Age-related muscle loss is a result of reductions in the size and number of muscle fibers possibly due to a multifactorial process that involves physical activity, nutritional intake, oxidative stress, and hormonal changes [90, 91]. The specific contribution of each of these factors is unknown but there is emerging evidence that the disruption of several positive regulators (Akt and SRF (serum response factor)) of muscle hypertrophy with age is an important feature in the progression of sarcopenia [92–94]. In addition, marked motoneuron loss and aberrant neuromuscular sprouting have been observed in aged mammals. Neurotrophic factors expressed in skeletal muscle

are essential to motoneuron survival and muscle fiber innervation during development. Spinal motoneurons express cognate receptors for these neurotrophic factors, and during aging, major changes take place in their expression pattern. Whereas the expression of TrkB and Trk C is downregulated, that of the components of the GDNF receptor (GFR α 1 and Ret) is upregulated [95]. This pattern of regulation mirrors the altered expression of the corresponding neurotrophic factors in target muscles [22]. GDNF, one of the most potent neurotrophic factors for motoneurons, is markedly up-regulated in human as well as rat muscle tissue during aging [22]. In addition, muscle-derived CNTF receptor- α is considered to play an important role in muscle fiber innervation/reinnervation [96]. Edström et al. [97] showed increased levels of CNTF receptor- α in sarcopenic muscle compared with normal adult muscle. The increase in GDNF and CNTF receptor- α in sarcopenic muscles probably reflects signaling from regenerating/denervated muscle fibers to attract motor axons. Although this is evidence for increased GDNF signaling from muscle to motoneurons during aging, it is not sufficient to restore appropriate innervation of the muscle fibers.

5.2. Myopathies. As in animal models, pathological situations can modify neurotrophin expression. NGF concentrations were measured by enzyme immunoassay in muscle biopsies from subjects with amyotrophic lateral sclerosis (ALS) or inflammatory myopathies [13]. NGF levels were significantly (140%) higher in patients with ALS than in the control subjects. In inflammatory myopathies, the increase was not significant. Age and gender had no influence on NGF concentrations in muscle. However, both mRNA and protein levels of NGF, BDNF, and NT-4/5 were increased in postmortem biopsies tissue of 15 ALS patients in comparison to controls, suggesting that some of the earlier data have to be reinvestigated and only biopsies from individuals with a postmortem period of less than 3 h should be tested [98]. During the course of the disease, upregulation of BDNF expression is observed in the early phase and the increase of NGF and NT-4/5, in later stages. In the spinal cord of ALS patients, a reduction in BDNF and no significant change in the amount of NT-4/5 were observed in spite of the elevated NGF expression. A decreased level of phosphorylated TrkB protein was also detected, suggesting impaired TrkB signaling [99]. Importantly, p75^{NTR} expression was induced in spinal cord motoneurons and denervated Schwann cells in ALS [100, 101]. Collectively, these results suggest that motor neurons switch from BDNF to NGF responsiveness in human ALS. Systemic administration of a modified cyclic decapeptide p75^{NTR} antagonist conjugated to the TAT4 cell permeabilization sequence to presymptomatic transgenic SOD1^{G93A} mice affected neither disease onset nor disease progression, as determined by hindlimb locomotion, grip strength, and survival [102].

In muscle from patients with DMD, NGF was expressed in regenerating fibers and connective tissue myofibroblast [103]. Rest fibers from dystrophic patients, as well as muscle fibers from healthy subjects and regenerative muscle fibers in patients with polymyositis (PM), did not show NGF

immunoreactivity. In another study, NT-4/5 protein and mRNA were found in both type I and type II fibers of healthy aerobically trained athletes and patients with mitochondrial encephalomyopathies [40]. However, in ragged-red fibers, which are present more frequently in highly oxidative type I fibers than in glycolytic type II fibers of patients with mitochondrial encephalomyopathies, NT-4/5 expression is upregulated in contrast to muscle fibers from healthy subjects.

P75^{NTR} expression has also been found in normal and pathological human muscle [84, 104]. Normal muscle cells from 12- to 22-week-old fetuses stained strongly for P75^{NTR} [84]. In adult muscle, only intramuscular nerve endings showed immunoreactivity with no staining detected in muscle fibers [84]. The outer surface of some regenerating muscle fibers, in muscle biopsy specimens from patients with muscular dystrophies, was positively stained for P75^{NTR} [84, 104]. P75^{NTR} mRNA expression was also detected using *in situ* hybridization in such cells.

Some muscular dystrophies would affect the amount of neurotrophin in the CNS as well as skeletal muscle. Our previous study [105] indicated the upregulation of GDNF protein and reciprocal downregulation of NT-4/5 protein in cerebellum and spinal cord motoneurons of merosin-deficient *dy* mice. In particular, our immunohistochemical analysis using *dy* mice clearly showed the marked enhancement of GDNF protein in the Purkinje and granule cells of the cerebellum and in many lumbar motoneurons. At this time, the microtubule-associated protein-2 (MAP-2) protein level was markedly decreased in these regions. Therefore, GDNF expression in the cerebellum and spinal cord appears to play a role in the fundamental disorders caused by a lack of merosin. Nico et al. [106] found marked immunoreactivity of NGF in neurons, astrocytes, and ependymal cells in the *mdx* brain different to the faint NGF expression only in neurons and astrocytes. In addition, they demonstrated that *mdx* brain possessed NGFRs on both glial and endothelial cells different to the absence of NGFR protein expression in endothelial cells in controls. Since some muscular dystrophies include a disorder of the CNS, elevated and/or decreased neurotrophin levels may further degrade the pathological symptoms.

5.3. Spinal Cord Injury. Spinal cord injury is a devastating neurological condition that produces muscular paresis/paralysis caudal to the lesion level, leading to a pronounced loss of muscle mass and severe muscle atrophy [107]. This paraplegia-induced muscle atrophy increases the risk of developing secondary health problems such as cardiovascular disease and diabetes in paraplegic patients [108]. Muscular disuse severely reduces the expression of BDNF protein and mRNA in both lumbar spinal cord and soleus muscle in acute and chronic stages after spinal cord injury. This trophic factor can activate rapamycin (mTOR), a protein that participates in mammalian cell size control and plays an important role in muscular tropism [109]. Furthermore, paraplegia-induced muscle atrophy in rats has been associated with a downregulation of the mTOR signaling pathway [110].

Studies have shown that repetitive motor activity, such as cycling exercise training, accelerates muscle size restoration after complete spinal cord injury in rats [111, 112]. In addition, treadmill training has been shown to diminish the extent of muscle atrophy [107] and restores BDNF levels in both the lumbar spinal cord and soleus muscle [113] in moderate spinal cord injury models. Furthermore, more recently, Ilha et al. [114] conducted a 9-week step-program for rats with complete spinal cord transection (SCT) at T8-T9. Step training, initiated immediately after SCT in rats, partially reverted muscular atrophy in chronic paralyzed soleus muscle possibly due to BDNF upregulation. Therefore, BDNF produced in response to treadmill training appears to ameliorate the symptoms of spinal cord injuries.

5.4. Diabetes. BDNF has been identified as a key component of the hypothalamic pathway that controls body weight and energy homeostasis [115]. Most recently, Pederson et al. have shown that BDNF appears to be a major player not only in central metabolic pathways but also as a regulator of metabolism in skeletal muscle [13]. Interestingly, individuals with both obesity and type 2 diabetes possess low levels of circulating BDNF [116] similar to patients with Alzheimer's disease [117], major depression [118], or acute coronary syndrome [119]. In a human *in vivo* model, Pedersen et al. [120] demonstrated that the cerebral output of BDNF was inhibited under hyperglycemic clamp conditions. The latter finding may explain the concomitant finding of low circulating levels of BDNF in individuals with type 2 diabetes and the association between low plasma BDNF levels and the severity of insulin resistance [116]. The human data are in accordance with reports from animal models suggesting that BDNF also plays a role in insulin resistance and in energy balance. BDNF administration has beneficial effects on glucose homeostasis and improves insulin resistance in obese diabetic animal models, such as C57BL/KsJ-db/db mice, even when food intake is controlled [121, 122]. It was found that BDNF mRNA and protein expression were increased in human skeletal muscle after exercise; however, muscle-derived BDNF appeared not to be released into the circulation. Since BDNF increased the phosphorylation of AMP-activated protein kinase (AMPK) and acetyl CoA carboxylase and enhanced fat oxidation both *in vitro* and *ex vivo*, contraction-induced muscle-derived BDNF may increase fat oxidation in an AMPK-dependent fashion.

6. Conclusions

This paper summarized and highlighted the current understanding of the normal distribution and functional role of neurotrophin in skeletal muscle during exercise, regeneration, and disorders. In particular, many researchers are interested in the important role of BDNF in learning and memory [123] or glucose metabolism as well as adaptations in skeletal muscle. A strategy for controlling the amount of BDNF may be also effective in the future treatment of various muscular disorders.

Acknowledgment

This work was supported by a research Grant-in-Aid for Scientific Research C (no. 23500778) from the Ministry of Education, Science, Culture, Sports, Science and Technology of Japan.

References

- [1] R. W. Oppenheim, "Cell death during development of the nervous system," *Annual Review of Neuroscience*, vol. 14, pp. 453–501, 1991.
- [2] L. F. Reichardt, "Neurotrophin-regulated signalling pathways," *Philosophical Transactions of the Royal Society B*, vol. 361, no. 1473, pp. 1545–1564, 2006.
- [3] O. Griesbeck, A. S. Parsadanian, M. Sendtner, and H. Thoenen, "Expression of neurotrophins in skeletal muscle: quantitative comparison and significance for motoneuron survival and maintenance of function," *Journal of Neuroscience Research*, vol. 42, no. 1, pp. 21–33, 1995.
- [4] G. Chevrel, R. Hohlfeld, and M. Sendtner, "The role of neurotrophins in muscle under physiological and pathological conditions," *Muscle and Nerve*, vol. 33, no. 4, pp. 462–476, 2006.
- [5] E. V. Pitts, S. Potluri, D. M. Hess, and R. J. Balice-Gordon, "Neurotrophin and Trk-mediated signaling in the neuromuscular system," *International Anesthesiology Clinics*, vol. 44, no. 2, pp. 21–76, 2006.
- [6] S. Capsoni, F. Ruberti, E. Di Daniel, and A. Cattaneo, "Muscular dystrophy in adult and aged anti-NGF transgenic mice resembles an inclusion body myopathy," *Journal of Neuroscience Research*, vol. 59, no. 4, pp. 553–560, 2000.
- [7] D. I. Carrasco and A. W. English, "Neurotrophin 4/5 is required for the normal development of the slow muscle fiber phenotype in the rat soleus," *Journal of Experimental Biology*, vol. 206, no. 13, pp. 2191–2200, 2003.
- [8] P. Ernfors, K. F. Lee, J. Kucera, and R. Jaenisch, "Lack of neurotrophin-3 leads to deficiencies in the peripheral nervous system and loss of limb proprioceptive afferents," *Cell*, vol. 77, no. 4, pp. 503–512, 1994.
- [9] L. T. Ferris, J. S. Williams, and C. L. Shen, "The effect of acute exercise on serum brain-derived neurotrophic factor levels and cognitive function," *Medicine and Science in Sports and Exercise*, vol. 39, no. 4, pp. 728–734, 2007.
- [10] S. Rojas Vega, H. K. Strüder, B. Vera Wahrmann, A. Schmidt, W. Bloch, and W. Hollmann, "Acute BDNF and cortisol response to low intensity exercise and following ramp incremental exercise to exhaustion in humans," *Brain Research*, vol. 1121, no. 1, pp. 59–65, 2006.
- [11] S. M. Gold, K. H. Schulz, S. Hartmann et al., "Basal serum levels and reactivity of nerve growth factor and brain-derived neurotrophic factor to standardized acute exercise in multiple sclerosis and controls," *Journal of Neuroimmunology*, vol. 138, no. 1-2, pp. 99–105, 2003.
- [12] V. B. Matthews, M. B. Åström, M. H. S. Chan et al., "Brain-derived neurotrophic factor is produced by skeletal muscle cells in response to contraction and enhances fat oxidation via activation of AMP-activated protein kinase," *Diabetologia*, vol. 52, no. 7, pp. 1409–1418, 2009.
- [13] H. J. Sturenburg and K. Kunze, "Tissue nerve growth factor concentrations in neuromuscular diseases," *European Journal of Neurology*, vol. 5, no. 5, pp. 487–490, 1998.
- [14] K. Sakuma, K. Watanabe, M. Sano et al., "A possible role for BDNF, NT-4 and TrkB in the spinal cord and muscle of rat subjected to mechanical overload, bupivacaine injection and axotomy," *Brain Research*, vol. 907, no. 1-2, pp. 1–19, 2001.
- [15] P. Fernyhough, L. T. Diemel, W. J. Brewster, and D. R. Tomlinson, "Altered neurotrophin mRNA levels in peripheral nerve and skeletal muscle of experimentally diabetic rats," *Journal of Neurochemistry*, vol. 64, no. 3, pp. 1231–1237, 1995.
- [16] P. Fernyhough, L. T. Diemel, J. Hardy, W. J. Brewster, L. Mohiuddin, and D. R. Tomlinson, "Human recombinant nerve growth factor replaces deficient neurotrophic support in the diabetic rat," *European Journal of Neuroscience*, vol. 7, no. 5, pp. 1107–1110, 1995.
- [17] C. Ihara, A. Shimatsu, H. Mizuta, H. Murabe, Y. Nakamura, and K. Nakao, "Decreased neurotrophin-3 expression in skeletal muscles of streptozotocin-induced diabetic rats," *Neuropeptides*, vol. 30, no. 4, pp. 309–312, 1996.
- [18] P. Fernyhough, L. T. Diemel, and D. R. Tomlinson, "Target tissue production and axonal transport of neurotrophin-3 are reduced in streptozocin-diabetic rats," *Diabetologia*, vol. 41, no. 3, pp. 300–306, 1998.
- [19] P. Fernyhough, K. Maeda, and D. R. Tomlinson, "Brain-derived neurotrophic factor mRNA levels are up-regulated in hindlimb skeletal muscle of diabetic rats: effects of denervation," *Experimental Neurology*, vol. 141, no. 2, pp. 297–303, 1996.
- [20] L. F. H. Lin, D. H. Doherty, J. D. Lile, S. Bektesh, and F. Collins, "GDNF: a glial cell line-derived neurotrophic factor for midbrain dopaminergic neurons," *Science*, vol. 260, no. 5111, pp. 1130–1132, 1993.
- [21] Q. T. Nguyen, A. S. Parsadanian, W. D. Snider, and J. W. Lichtman, "Hyperinnervation of neuromuscular junctions caused by GDNF overexpression in muscle," *Science*, vol. 279, no. 5357, pp. 1725–1729, 1998.
- [22] B. Ulfhake, E. Bergman, E. Edström et al., "Regulation of neurotrophin signaling in aging sensory and motoneurons: dissipation of target support?" *Molecular Neurobiology*, vol. 21, no. 3, pp. 109–135, 2000.
- [23] R. Klein, I. Silos-Santiago, R. J. Smeyne et al., "Disruption of the neurotrophin-3 receptor gene *trkC* eliminates Ia muscle afferents and results in abnormal movements," *Nature*, vol. 368, no. 6468, pp. 249–251, 1994.
- [24] R. A. Oakley, F. B. Lefcort, D. O. Clary et al., "Neurotrophin-3 promotes the differentiation of muscle spindle afferents in the absence of peripheral targets," *Journal of Neuroscience*, vol. 17, no. 11, pp. 4262–4274, 1997.
- [25] D. E. Wright, L. Zhou, J. Kucera, and W. D. Snider, "Introduction of a neurotrophin-3 transgene into muscle selectively rescues proprioceptive neurons in mice lacking endogenous neurotrophin-3," *Neuron*, vol. 19, no. 3, pp. 503–517, 1997.
- [26] M. Simon, G. Terenghi, C. J. Green, and G. R. Coulton, "Differential effects of NT-3 on reinnervation of the fast extensor digitorum longus (EDL) and the slow soleus muscle of rat," *European Journal of Neuroscience*, vol. 12, no. 3, pp. 863–871, 2000.
- [27] G. D. Sterne, G. R. Coulton, R. A. Brown, C. J. Green, and G. Terenghi, "Neurotrophin-3-enhanced nerve regeneration selectively improves recovery of muscle fibers expressing myosin heavy chains 2b," *Journal of Cell Biology*, vol. 139, no. 3, pp. 709–715, 1997.

- [28] F. C. F. Ip, J. Cheung, and N. Y. Ip, "The expression profiles of neurotrophins and their receptors in rat and chicken tissues during development," *Neuroscience Letters*, vol. 301, no. 2, pp. 107–110, 2001.
- [29] V. E. Koliatsos, M. H. Cayouette, L. R. Berkemeier, R. E. Clatterbuck, D. L. Price, and A. Rosenthal, "Neurotrophin 4/5 is a trophic factor for mammalian facial motor neurons," *Proceedings of the National Academy of Sciences of the United States of America*, vol. 91, no. 8, pp. 3304–3308, 1994.
- [30] V. E. Koliatsos, R. E. Clatterbuck, J. W. Winslow, M. H. Cayouette, and D. L. Price, "Evidence that brain-derived neurotrophic factor is a trophic factor for motor neurons in vivo," *Neuron*, vol. 10, no. 3, pp. 359–367, 1993.
- [31] P. C. Maisonpierre, L. Belluscio, B. Friedman et al., "NT-3, BDNF, and NGF in the developing rat nervous system: parallel as well as reciprocal patterns of expression," *Neuron*, vol. 5, no. 4, pp. 501–509, 1990.
- [32] T. Timmusk, N. Belluardo, M. Metsis, and H. Persson, "Widespread and developmentally regulated expression of neurotrophin-4 mRNA in rat brain and peripheral tissues," *European Journal of Neuroscience*, vol. 5, no. 6, pp. 605–613, 1993.
- [33] L. C. Schecterson and M. Bothwell, "Novel roles for neurotrophins are suggested by BDNF and NT-3 mRNA expression in developing neurons," *Neuron*, vol. 9, no. 3, pp. 449–463, 1992.
- [34] S. Liem, N. Brouwer, and J. C. Copray, "Ultrastructural localization of intramuscular expression of BDNF mRNA by silver-gold intensified non-radioactive in situ hybridization," *Histochemistry and Cell Biology*, vol. 116, pp. 545–551, 2001.
- [35] K. Mousavi and B. J. Jasmin, "BDNF is expressed in skeletal muscle satellite cells and inhibits myogenic differentiation," *Journal of Neuroscience*, vol. 26, no. 21, pp. 5739–5749, 2006.
- [36] R. W. Oppenheim, Y. Qin-Wei, D. Prevette, and Q. Yan, "Brain-derived neurotrophic factor rescues developing avian motoneurons from cell death," *Nature*, vol. 360, no. 6406, pp. 755–757, 1992.
- [37] X. H. Zhang and M. M. Poo, "Localized synaptic potentiation by BDNF requires local protein synthesis in the developing axon," *Neuron*, vol. 36, no. 4, pp. 675–688, 2002.
- [38] K. Mousavi, D. J. Parry, and B. J. Jasmin, "BDNF rescues myosin heavy chain IIB muscle fibers after neonatal nerve injury," *American Journal of Physiology*, vol. 287, no. 1, pp. C22–C29, 2004.
- [39] H. Funakoshi, N. Belluardo, E. Arenas et al., "Muscle-derived neurotrophin-4 as an activity-dependent trophic signal for adult motor neurons," *Science*, vol. 268, no. 5216, pp. 1495–1499, 1995.
- [40] U. A. Walker and E. A. Schon, "Neurotrophin-4 is up-regulated in ragged-red fibers associated with pathogenic mitochondrial DNA mutations," *Annals of Neurology*, vol. 43, no. 4, pp. 536–540, 1998.
- [41] C. E. Henderson, H. S. Phillips, R. A. Pollock et al., "GDNF: a potent survival factor for motoneurons present in peripheral nerve and muscle," *Science*, vol. 266, no. 5187, pp. 1062–1064, 1994.
- [42] H. Suzuki, A. Hase, Y. Miyata, K. Arahata, and C. Akazawa, "Prominent expression of glial cell line-derived neurotrophic factor in human skeletal muscle," *Journal of Comparative Neurology*, vol. 402, no. 3, pp. 303–312, 1998.
- [43] E. A. Wehrwein, E. M. Roskelley, and J. M. Spitsbergen, "GDNF is regulated in an activity-dependent manner in rat skeletal muscle," *Muscle and Nerve*, vol. 26, no. 2, pp. 206–211, 2002.
- [44] P. Ernfors, F. Hallbook, T. Ebendal et al., "Developmental and regional expression of β -nerve growth factor receptor mRNA in the chick and rat," *Neuron*, vol. 1, no. 10, pp. 983–996, 1988.
- [45] C. Lomen-Hoerth and E. M. Shooter, "Widespread neurotrophin receptor expression in the immune system and other nonneuronal rat tissues," *Journal of Neurochemistry*, vol. 64, no. 4, pp. 1780–1789, 1995.
- [46] M. Yamamoto, G. Sobue, K. Yamamoto, S. Terao, and T. Mitsuma, "Expression of mRNAs for neurotrophic factors (NGF, BDNF, NT-3, and GDNF) and their receptors (p75NGFR, TrkA, TrkB, and TrkC) in the adult human peripheral nervous system and nonneural tissues," *Neurochemical Research*, vol. 21, no. 8, pp. 929–938, 1996.
- [47] J. G. Heuer, C. S. von Bartheld, Y. Kinoshita, P. C. Evers, and M. Bothwell, "Alternating phases of FGF receptor and NGF receptor expression in the developing chicken nervous system," *Neuron*, vol. 5, no. 3, pp. 283–296, 1990.
- [48] R. Klein, "Role of neurotrophins in mouse neuronal development," *The FASEB Journal*, vol. 8, no. 10, pp. 738–744, 1994.
- [49] D. I. Ogborn and P. F. Gardiner, "Effects of exercise and muscle type on BDNF, NT-4/5, and TrkB expression in skeletal muscle," *Muscle and Nerve*, vol. 41, no. 3, pp. 385–391, 2010.
- [50] F. R. Wiedemann, D. Siemen, C. Mawrin, T. F. Horn, and K. Dietzmann, "The neurotrophin receptor TrkB is colocalized to mitochondrial membranes," *International Journal of Biochemistry and Cell Biology*, vol. 38, no. 4, pp. 610–620, 2006.
- [51] P. Kermani, D. Rafii, D. K. Jin et al., "Neurotrophins promote revascularization by local recruitment of TrkB + endothelial cells and systemic mobilization of hematopoietic progenitors," *The Journal of Clinical Investigation*, vol. 115, no. 3, pp. 653–663, 2005.
- [52] J. Widenfalk, C. Nosrat, A. Tomac, H. Westphal, B. Hoffer, and L. Olson, "Neurturin and glial cell line-derived neurotrophic factor receptor- β (GDNFR- β), novel proteins related to GDNF and GDNFR- α with specific cellular patterns of expression suggesting roles in the developing and adult nervous system and in peripheral organs," *Journal of Neuroscience*, vol. 17, no. 21, pp. 8506–8519, 1997.
- [53] P. Naveilhan, C. Baudet, A. Mikaelis, L. Shen, H. Westphal, and P. Ernfors, "Expression and regulation of GFR α 3, a glial cell line-derived neurotrophic factor family receptor," *Proceedings of the National Academy of Sciences of the United States of America*, vol. 95, no. 3, pp. 1295–1300, 1998.
- [54] S. Jing, Y. Yu, M. Fang et al., "GFR α -2 and GFR α -3 are two new receptors for ligands of the GDNF family," *The Journal of Biological Chemistry*, vol. 272, no. 52, pp. 33111–33117, 1997.
- [55] R. J. Kleiman, N. Tian, D. Krizaj, T. N. Hwang, D. R. Copenhagen, and L. F. Reichardt, "BDNF-induced potentiation of spontaneous twitching in innervated myocytes requires calcium release from intracellular stores," *Journal of Neurophysiology*, vol. 84, no. 1, pp. 472–483, 2000.
- [56] R. Stoop and M. M. Poo, "Synaptic modulation by neurotrophic factors: differential and synergistic effects of brain-derived neurotrophic factor and ciliary neurotrophic factor," *Journal of Neuroscience*, vol. 16, no. 10, pp. 3256–3264, 1996.
- [57] X. H. Wang and M. M. Poo, "Potentiation of developing synapses by postsynaptic release of neurotrophin-4," *Neuron*, vol. 19, no. 4, pp. 825–835, 1997.
- [58] N. Garcia, M. Tomàs, M. M. Santafe, M. A. Lanuza, N. Besalduch, and J. Tomàs, "Localization of brain-derived neurotrophic factor, neurotrophin-4, tropomyosin-related kinase b receptor, and p75NTR receptor by high-resolution

- immunohistochemistry on the adult mouse neuromuscular junction," *Journal of the Peripheral Nervous System*, vol. 15, no. 1, pp. 40–49, 2010.
- [59] A. K. Y. Fu, F. C. F. Ip, K. O. Lai, K. W. K. Tsim, and N. Y. Ip, "Muscle-derived neurotrophin-3 increases the aggregation of acetylcholine receptors in neuron-muscle co-cultures," *NeuroReport*, vol. 8, no. 18, pp. 3895–3900, 1997.
- [60] D. G. Wells, B. A. Mckechnie, S. Kelkar, and J. R. Fallon, "Neurotrophins regulate agrin-induced postsynaptic differentiation," *Proceedings of the National Academy of Sciences of the United States of America*, vol. 96, no. 3, pp. 1112–1117, 1999.
- [61] R. R. Ribchester, D. Thomson, L. J. Haddow, and Y. A. Ushkaryov, "Enhancement of spontaneous transmitter release at neonatal mouse neuromuscular junctions by the glial cell line-derived neurotrophic factor (GDNF)," *Journal of Physiology*, vol. 512, no. 3, pp. 635–641, 1998.
- [62] C. Y. Wang, F. Yang, X. P. He et al., "Regulation of neuromuscular synapse development by glial cell line-derived neurotrophic factor and neurturin," *The Journal of Biological Chemistry*, vol. 277, no. 12, pp. 10614–10625, 2002.
- [63] L. X. Yang and P. G. Nelson, "Glial cell line-derived neurotrophic factors regulates the distribution of acetylcholine receptors in mouse primary skeletal muscle cells," *Neuroscience*, vol. 128, no. 3, pp. 497–509, 2004.
- [64] M. H. Andonian and M. A. Fahim, "Effects of endurance exercise on the morphology of mouse neuromuscular junction during ageing," *Journal of Neurocytology*, vol. 16, no. 5, pp. 589–599, 1987.
- [65] M. R. Deschenes, C. M. Maresh, J. F. Crivello, L. E. Armstrong, W. J. Kraemer, and J. Covault, "The effects of exercise training of different intensities on neuromuscular junction morphology," *Journal of Neurocytology*, vol. 22, no. 8, pp. 603–615, 1993.
- [66] M. Dorlochter, A. Irintchev, M. Brinkers, and A. Wernig, "Effects of enhanced activity on synaptic transmission in mouse extensor digitorum longus muscle," *Journal of Physiology*, vol. 436, pp. 283–292, 1991.
- [67] M. A. Fahim, "Endurance exercise modulates neuromuscular junction of C57BL/6NNia aging mice," *Journal of Applied Physiology*, vol. 83, no. 1, pp. 59–66, 1997.
- [68] P. A. Adlard, V. M. Perreau, C. Engesser-Cesar, and C. W. Cotman, "The timecourse of induction of brain-derived neurotrophic factor mRNA and protein in the rat hippocampus following voluntary exercise," *Neuroscience Letters*, vol. 363, no. 1, pp. 43–48, 2004.
- [69] F. Gómez-Pinilla, Z. Ying, R. R. Roy, R. Molteni, and V. R. Edgerton, "Voluntary exercise induces a BDNF-mediated mechanism that promotes neuroplasticity," *Journal of Neurophysiology*, vol. 88, no. 5, pp. 2187–2195, 2002.
- [70] R. Cuppinf, S. Sartini, D. Agostini et al., "BDNF expression in rat skeletal muscle after acute or repeated exercise," *Archives Italiennes de Biologie*, vol. 145, no. 2, pp. 99–110, 2007.
- [71] F. Gómez-Pinilla, Z. Ying, P. Opazo, R. R. Roy, and V. R. Edgerton, "Differential regulation by exercise of BDNF and NT-3 in rat spinal cord and skeletal muscle," *European Journal of Neuroscience*, vol. 13, no. 6, pp. 1078–1084, 2001.
- [72] S. A. Neeper, F. Gómez-Pinilla, J. Choi, and C. Cotman, "Exercise and brain neurotrophins," *Nature*, vol. 373, no. 6510, article 109, 1995.
- [73] H. S. Oliff, N. C. Berchtold, P. Isackson, and C. W. Cotman, "Exercise-induced regulation of brain-derived neurotrophic factor (BDNF) transcripts in the rat hippocampus," *Molecular Brain Research*, vol. 61, no. 1-2, pp. 147–153, 1998.
- [74] R. Klein, F. Lamballe, S. Bryant, and M. Barbacid, "The trkB tyrosine protein kinase is a receptor for neurotrophin-4," *Neuron*, vol. 8, no. 5, pp. 947–956, 1992.
- [75] R. Klein, V. Nanduri, S. Jing et al., "The trkB tyrosine protein kinase is a receptor for brain-derived neurotrophic factor and neurotrophin-3," *Cell*, vol. 66, no. 2, pp. 395–403, 1991.
- [76] Y. Sagot, T. Rossé, R. Vejsada, D. Perrelet, and A. C. Kato, "Differential effects of neurotrophic factors on motoneuron retrograde labeling in a murine model of motoneuron disease," *Journal of Neuroscience*, vol. 18, no. 3, pp. 1132–1141, 1998.
- [77] R. Curtis, J. R. Tonra, J. L. Stark et al., "Neuronal injury increases retrograde axonal transport of the neurotrophins to spinal sensory neurons and motor neurons via multiple receptor mechanisms," *Molecular and Cellular Neurosciences*, vol. 12, no. 3, pp. 105–118, 1998.
- [78] Q. Yan, J. Elliott, and W. D. Snider, "Brain-derived neurotrophic factor rescues spinal motor neurons from axotomy-induced cell death," *Nature*, vol. 360, no. 6406, pp. 753–755, 1992.
- [79] M. J. McCullough, N. G. Peplinski, K. R. Kinnell, and J. M. Spitsbergen, "Glial cell line-derived neurotrophic factor protein content in rat skeletal muscle is altered by increased physical activity in vivo and in vitro," *Neuroscience*, vol. 174, pp. 234–244, 2011.
- [80] C. R. Keller-Peck, G. Feng, J. R. Sanes, Q. Yan, J. W. Lichtman, and W. D. Snider, "Glial cell line-derived neurotrophic factor administration in postnatal life results in motor unit enlargement and continuous synaptic remodeling at the neuromuscular junction," *Journal of Neuroscience*, vol. 21, no. 16, pp. 6136–6146, 2001.
- [81] M. Lavasani, A. Lu, H. Peng, J. Cummins, and J. Huard, "Nerve growth factor improves the muscle regeneration capacity of muscle stem cells in dystrophic muscle," *Human Gene Therapy*, vol. 17, no. 2, pp. 180–192, 2006.
- [82] F. Ruberti, S. Capsoni, A. Comparini et al., "Phenotypic knockout of nerve growth factor in adult transgenic mice reveals severe deficits in basal forebrain cholinergic neurons, cell death in the spleen, and skeletal muscle dystrophy," *Journal of Neuroscience*, vol. 20, no. 7, pp. 2589–2601, 2000.
- [83] M. Rende, E. Brizi, J. Conner et al., "Nerve growth factor (NGF) influences differentiation and proliferation of myogenic cells in vitro via TrKA," *International Journal of Developmental Neuroscience*, vol. 18, no. 8, pp. 869–885, 2000.
- [84] P. Baron, E. Scarpini, G. Meola et al., "Expression of the low-affinity NGF receptor during human muscle development, regeneration, and in tissue culture," *Muscle and Nerve*, vol. 17, no. 3, pp. 276–284, 1994.
- [85] D. Deponti, R. Buono, G. Catanzaro et al., "The low-affinity receptor for neurotrophins p75NTR plays a key role for satellite cell function in muscle repair acting via RhoA," *Molecular Biology of the Cell*, vol. 20, no. 16, pp. 3620–3627, 2009.
- [86] P. Ernfors, K. F. Lee, and R. Jaenisch, "Mice lacking brain-derived neurotrophic factor develop with sensory deficits," *Nature*, vol. 368, no. 6467, pp. 147–150, 1994.
- [87] C. Clow and B. J. Jasmin, "Brain-derived neurotrophic factor regulates satellite cell differentiation and skeletal muscle regeneration," *Molecular Biology of the Cell*, vol. 21, no. 13, pp. 2182–2190, 2010.
- [88] K. Kami, Y. Morikawa, Y. Kawai, and E. Senba, "Leukemia inhibitory factor, glial cell line-derived neurotrophic factor, and their receptor expressions following muscle crush

- injury," *Muscle and Nerve*, vol. 22, no. 11, pp. 1576–1586, 1999.
- [89] D. G. Candow and P. D. Chilibeck, "Differences in size, strength, and power of upper and lower body muscle groups in young and older men," *Journals of Gerontology—Series A Biological Sciences and Medical Sciences*, vol. 60, no. 2, pp. 148–156, 2005.
- [90] R. N. Baumgartner, D. L. Waters, D. Gallagher, J. E. Morley, and P. J. Garry, "Predictors of skeletal muscle mass in elderly men and women," *Mechanisms of Ageing and Development*, vol. 107, no. 2, pp. 123–136, 1999.
- [91] R. Roubenoff and V. A. Hughes, "Sarcopenia: current concepts," *Journals of Gerontology—Series A Biological Sciences and Medical Sciences*, vol. 55, no. 12, pp. M716–M724, 2000.
- [92] K. Sakuma, M. Akiho, H. Nakashima, H. Akima, and M. Yasuhara, "Age-related reductions in expression of serum response factor and myocardin-related transcription factor A in mouse skeletal muscles," *Biochimica et Biophysica Acta*, vol. 1782, no. 7–8, pp. 453–461, 2008.
- [93] K. Sakuma and A. Yamaguchi, "Molecular mechanisms in aging and current strategies to counteract sarcopenia," *Current Aging Science*, vol. 3, no. 2, pp. 90–101, 2010.
- [94] K. Sakuma and A. Yamaguchi, "Sarcopenia: molecular mechanisms and current therapeutic strategy," in *Cell Aging*, J. W. Perloft and A. H. Wong, Eds., Nova Science, Huntington, NY, USA, 2011.
- [95] H. Johnson, K. Mossberg, U. Arvidsson, F. Piehl, T. Hökfelt, and B. Ulfhake, "Increase in α -CGRP and GAP-43 in aged motoneurons: a study of peptides, growth factors, and ChAT mRNA in the lumbar spinal cord of senescent rats with symptoms of hindlimb incapacities," *Journal of Comparative Neurology*, vol. 359, no. 1, pp. 69–89, 1995.
- [96] T. M. DeChiara, R. Vejsada, W. T. Poueymirou et al., "Mice lacking the CNTF receptor, unlike mice lacking CNTF, exhibit profound motor neuron deficits at birth," *Cell*, vol. 83, no. 2, pp. 313–322, 1995.
- [97] E. Edström, M. Altun, E. Bergman et al., "Factors contributing to neuromuscular impairment and sarcopenia during aging," *Physiology and Behavior*, vol. 92, no. 1–2, pp. 129–135, 2007.
- [98] B. M. Küst, J. C. V. M. Copray, N. Brouwer, D. Troost, and H. W. G. M. Boddeke, "Elevated levels of neurotrophins in human biceps brachii tissue of amyotrophic lateral sclerosis," *Experimental Neurology*, vol. 177, no. 2, pp. 419–427, 2002.
- [99] T. Mutoh, G. Sobue, T. Hamano et al., "Decreased phosphorylation levels of TrkB neurotrophin receptor in the spinal cords from patients with amyotrophic lateral sclerosis," *Neurochemical Research*, vol. 25, no. 2, pp. 239–245, 2000.
- [100] H. Kerkhoff, F. G. I. Jennekens, D. Troost, and H. Veldman, "Nerve growth factor receptor immunostaining in the spinal cord and peripheral nerves in amyotrophic lateral sclerosis," *Acta Neuropathologica*, vol. 81, no. 6, pp. 649–656, 1991.
- [101] J. L. Seeburger, S. Tarras, H. Natter, and J. E. Springer, "Spinal cord motoneurons express p75(NGFR) and p145(trkB) mRNA in amyotrophic lateral sclerosis," *Brain Research*, vol. 621, no. 1, pp. 111–115, 1993.
- [102] B. J. Turner, S. S. Murray, L. G. Piccenna, E. C. Lopes, T. J. Kilpatrick, and S. S. Cheema, "Effect of p75 neurotrophin receptor antagonist on disease progression in transgenic amyotrophic lateral sclerosis mice," *Journal of Neuroscience Research*, vol. 78, no. 2, pp. 193–199, 2004.
- [103] P. Toti, M. Villanova, R. Vatti et al., "Nerve growth factor expression in human dystrophic muscles," *Muscle and Nerve*, vol. 27, no. 3, pp. 370–373, 2003.
- [104] J. Zhao, K. Yoshioka, T. Miike, T. Kageshita, and T. Arao, "Nerve growth factor receptor immunoreactivity on the tunica adventitia of intramuscular blood vessels in childhood muscular dystrophies," *Neuromuscular Disorders*, vol. 1, no. 2, pp. 135–141, 1991.
- [105] K. Sakuma, K. Watanabe, T. Totsuka et al., "The reciprocal change of neurotrophin-4 and glial cell line-derived neurotrophic factor protein in the muscles, spinal cord and cerebellum of the dy mouse," *Acta Neuropathologica*, vol. 104, no. 5, pp. 482–492, 2002.
- [106] B. Nico, D. Mangieri, A. De Luca et al., "Nerve growth factor and its receptors TrkA and p75 are upregulated in the brain of mdx dystrophic mouse," *Neuroscience*, vol. 161, no. 4, pp. 1057–1066, 2009.
- [107] J. E. Stevens, M. Liu, P. Bose et al., "Changes in soleus muscle function and fiber morphology with one week of locomotor training in spinal cord contusion injured rats," *Journal of Neurotrauma*, vol. 23, no. 11, pp. 1671–1681, 2006.
- [108] A. P. Buunk, R. Zurriaga, P. Gonzalez, C. Terol, and S. L. Roig, "Targets and dimensions of social comparison among people with spinal cord injury and other health problems," *British Journal of Health Psychology*, vol. 11, no. 4, pp. 677–693, 2006.
- [109] S. C. Bodine, T. N. Stitt, M. Gonzalez et al., "Akt/mTOR pathway is a crucial regulator of skeletal muscle hypertrophy and can prevent muscle atrophy in vivo," *Nature Cell Biology*, vol. 3, no. 11, pp. 1014–1019, 2001.
- [110] H. C. Dreyer, E. L. Glynn, H. L. Lujan, C. S. Fry, S. E. DiCarlo, and B. B. Rasmussen, "Chronic paraplegia-induced muscle atrophy downregulates the mTOR/S6K1 signaling pathway," *Journal of Applied Physiology*, vol. 104, no. 1, pp. 27–33, 2008.
- [111] E. E. Dupont-Versteegden, R. J. L. Murphy, J. D. Houlié, C. M. Gurley, and C. A. Peterson, "Mechanisms leading to restoration of muscle size with exercise and transplantation after spinal cord injury," *American Journal of Physiology*, vol. 279, no. 6, pp. C1677–C1684, 2000.
- [112] J. M. Nothias, T. Mitsui, J. S. Shumsky, I. Fischer, M. D. Antonacci, and M. Murray, "Combined effects of neurotrophin secreting transplants, exercise, and serotonergic drug challenge improve function in spinal rats," *Neurorehabilitation and Neural Repair*, vol. 19, no. 4, pp. 296–312, 2005.
- [113] K. J. Hutchinson, F. Gómez-Pinilla, M. J. Crowe, Z. Ying, and D. M. Basso, "Three exercise paradigms differentially improve sensory recovery after spinal cord contusion in rats," *Brain*, vol. 127, no. 6, pp. 1403–1414, 2004.
- [114] J. Ilha, N. B. da Cunha, M. Jaeger et al., "Treadmill step training-induced adaptive muscular plasticity in a chronic paraplegia model," *Neuroscience Letters*, vol. 492, no. 3, pp. 170–174, 2011.
- [115] B. E. Wisse and M. W. Schwartz, "The skinny on neurotrophins," *Nature Neuroscience*, vol. 6, no. 7, pp. 655–656, 2003.
- [116] K. S. Krabbe, A. R. Nielsen, R. Krogh-Madsen et al., "Brain-derived neurotrophic factor (BDNF) and type 2 diabetes," *Diabetologia*, vol. 50, no. 2, pp. 431–438, 2007.
- [117] C. Laske, E. Stransky, T. Leyhe et al., "Stage-dependent BDNF serum concentrations in Alzheimer's disease," *Journal of Neural Transmission*, vol. 113, no. 9, pp. 1217–1224, 2006.
- [118] F. Karege, G. Perret, G. Bondolfi, M. Schwald, G. Bertschy, and J. M. Aubry, "Decreased serum brain-derived neurotrophic factor levels in major depressed patients," *Psychiatry Research*, vol. 109, no. 2, pp. 143–148, 2002.
- [119] L. Manni, V. Nikolova, D. Vyagova, G. N. Chaldakov, and L. Aloe, "Reduced plasma levels of NGF and BDNF in patients

- with acute coronary syndromes,” *International Journal of Cardiology*, vol. 102, no. 1, pp. 169–171, 2005.
- [120] B. K. Pedersen, M. Pedersen, K. S. Krabbe, H. Bruunsgaard, V. B. Matthews, and M. A. Febbraio, “Role of exercise-induced brain-derived neurotrophic factor production in the regulation of energy homeostasis in mammals: experimental Physiology-Hot Topic Review,” *Experimental Physiology*, vol. 94, no. 12, pp. 1153–1160, 2009.
- [121] T. Nakagawa, A. Tsuchida, Y. Itakura et al., “Brain-derived neurotrophic factor regulates glucose metabolism by modulating energy balance in diabetic mice,” *Diabetes*, vol. 49, no. 3, pp. 436–444, 2000.
- [122] J. R. Tonra, M. Ono, X. Liu et al., “Brain-derived neurotrophic factor improves blood glucose control and alleviates fasting hyperglycemia in C57BLKS-Lepr(db)/lepr(db) mice,” *Diabetes*, vol. 48, no. 3, pp. 588–594, 1999.
- [123] Y. F. Liu, H. I. Chen, C. L. Wu et al., “Differential effects of treadmill running and wheel running on spatial or aversive learning and memory: roles of amygdalar brain-derived neurotrophic factor and synaptotagmin I,” *Journal of Physiology*, vol. 587, no. 13, pp. 3221–3231, 2009.